

General Disclaimer

One or more of the Following Statements may affect this Document

- This document has been reproduced from the best copy furnished by the organizational source. It is being released in the interest of making available as much information as possible.
- This document may contain data, which exceeds the sheet parameters. It was furnished in this condition by the organizational source and is the best copy available.
- This document may contain tone-on-tone or color graphs, charts and/or pictures, which have been reproduced in black and white.
- This document is paginated as submitted by the original source.
- Portions of this document are not fully legible due to the historical nature of some of the material. However, it is the best reproduction available from the original submission.

Quantitative Determination of Stratospheric Aerosol Characteristics

Skylab Investigation EREP 587

"Made available under NASA sponsorship
in the interest of early and wide dis-
semination of Earth Resources Survey
Program information and without liability
for any use made thereof."

Principal Investigator

David L. Tingey
Research and Engineering Division
Boeing Aerospace Company
Seattle, Washington

Co-Investigator

John Potter
Lockheed Electronics Company
Houston, Texas

Contract Number NAS9-13303

Boeing Document Number D180-19209-1

FINAL REPORT

for period

July 1973 through December 1975

(E76-10203) QUANTITATIVE DETERMINATION OF
STRATOSPHERIC AEROSOL CHARACTERISTICS Final
Report, Jul. 1973 - Dec. 1975 (Boeing
Aerospace Co., Seattle, Wash.) 246 p HC
\$8.00

N76-19511

Unclass
00203

CSCL 04A G3/43

prepared for

National Aeronautics and Space Administration
Lyndon B. Johnson Space Center
Houston, Texas 77058

"Made available under NASA sponsorship
in the interest of early and wide dis-
semination of Earth Resources Survey
Program information and without liability
for any use made thereof."



Research & Engineering Division
Boeing Aerospace Company



QUANTITATIVE DETERMINATION OF STRATOSPHERIC AEROSOL CHARACTERISTICS

SKYLAB INVESTIGATION EREP 587

Principal Investigator

David L. Tingey *eng*
Research and Engineering Division
Boeing Aerospace Company
Seattle, Washington

Co-Investigator

John Potter
Lockheed Electronics Company
Houston, Texas

Contract Number NAS9-13303

Boeing Document Number D180-19209-1

FINAL REPORT

for period

July 1973 through December 1975

prepared for

National Aeronautics and Space Administration
Lyndon B. Johnson Space Center
Houston, Texas 77058



PREFACE

This investigation uses the sensors of the Skylab Earth Resources Experiment Package to measure stratospheric aerosols. The data was acquired when the Skylab vehicle was in the Solar Inertial mode and the sensors were viewing the limb of the earth with the sun behind the sensors.

The investigation was designed to produce altitude profiles of aerosol attenuation coefficients for several wavelengths. The analysis techniques were also developed to invert the data for particle size distributions and number densities; however, the actual data analysis did not reach that level due to unexpected complications discovered in the data which had to be treated.

There were several contributors to this investigation beyond the Principal Investigator and the Co-Investigator. We acknowledge and appreciate the efforts of Nancy Polky who performed much of the actual implementation of the analysis techniques. We also appreciate the assistance of Dr. Bob Curran of NASA Goddard Space Flight Center who shared his software to read and calibrate the S191 data, and Dr. David E. Pitts who shared his software to calculate the effects of refraction. Ken Wahlin also assisted during the last few months of the investigation. We extend special appreciation to Bill Johnson of Lockheed Electronics Company who on several occasions provided us with information not contained in the supplied documentation.



TABLE OF CONTENTS

	<u>Page</u>
1.0 INTRODUCTION	1
2.0 APPROACH	2
2.1 ANALYSIS TECHNIQUES	2
2.1.1 Simulated Limb Brightness Curves	2
2.1.2 Inversion of Limb Brightness Curves	6
2.1.3 Inversion of Intensities for Number Density and Partizle Size Distributions	7
2.1.4 Location of Field of View	11
2.1.4.1 S192 Field of View	12
2.1.4.2 S191 Field of View	17
2.1.4.3 S190A Field of View	20
2.1.5 Noise Reduction	20
2.1.6 Refraction	23
2.2 DATA ACQUISITION	30
2.2.1 The S190A Data	30
2.2.2 The S191 Data	30
2.2.3 The S192 Data	31
2.3 DESCRIPTION OF ACQUIRED DATA	32
3.0 DATA ANALYSIS	34
3.1 THE S192 DATA	34
3.1.1 Position in Scan of Maximum Altitude Known	34
3.1.2 Position in Scan of Maximum Altitude Not Known	35
3.2 THE S191 DATA	36
3.3 THE S190A DATA	37
4.0 RESULTS	41
5.0 SUMMARY AND RECOMMENDATIONS	238
REFERENCES	240
DISTRIBUTION LIST	241



LIST OF TABLES

<u>Table</u>		<u>Page</u>
1	190 Spectral Bands	30
2	S192 Spectral Bands	32
3	S190A--Pass 47, Frame 175, Description of Acquired Data	33
4	S192--Description of Acquired Data	33
5	S191 Spectral Bands	36
6	S191 Summary Results	45
7	Multiplicative and Additive ($\times 10^{-4}$) Scale Factors for S192 Data, Passes 61 and 47	47
8	Multiplicative Scale Factors for S191 Data, Pass 47	48

LIST OF FIGURES

<u>Figure</u>		<u>Page</u>
1	Geometry of Slant Path for Simulated Limb Brightness Curves	3
2	Location of Field of View from SKYBET Ephemeris Data	11
3	S192--Exact Location of Field of View, A	13
4	S192--Exact Location of Field of View, B	14
5	S192--Altitude Increment from Geometry of Conical Scan	15
6	S192--Intersection of Conical Scan with the Earth's Surface	16
7	S191--Location of Field of View	18
8	S191--Change of Field of View	19
9	S192--Pass 47, Tape 934527, Scans 350-374, Band 3. Deviations from Polynomial Fit After Fourier Filtering	22
10	S192--Pass 61, Tape 932867, Band 1. Low Frequency Scan to Scan Noise for Four Points on the Limb	24



LIST OF FIGURES (continued)

<u>Figure</u>		<u>Page</u>
11	S192--Pass 61, Tape 932867, Band 1. Low Frequency Scan to Scan Noise for Four Points on the Limb	24
12	S192--Pass 61, Tape 932857, Band 3. Low Frequency Scan to Scan Noise for One Point on the Limb	25
13	S192--Pass 61, Tape 932857, Band 3. Low Frequency Scan to Scan Noise for the Average of Deep Space	25
14	Observation Angle at the Sensor for a Straight Line Path	26
15	Refraction Through the Layers of the Atmosphere	27
16	Observation Angle at the Sensor for a Refracted Path	28
17	Comparison of Two Refraction Models	29
18	S190A--Pass 47, D-log E Curves for Original and Duplicate Film. Roll 43-24.	39
19	S190A--Pass 47, D-log E Curves for Original and Duplicate Film. Roll 44-22	39
20	S190A--Pass 47, D-log E Curves for Original and Duplicate Film. Roll 47-32.	40
21	S190A--Pass 47, D-log E Curves for Original and Duplicate Film. Roll 48-32.	40



1.0 INTRODUCTION

The aerosol content of the atmosphere is related to the volcanic eruptions, industrial pollution, aircraft pollution, explosions on the surface of the earth, and perhaps other sources. Atmospheric scientists have long been interested in the distribution of aerosols in the atmosphere. This is reflected in the vast literature that has grown up on the subject and in the considerable efforts that have been made to determine aerosol distribution including hundreds of aircraft, rocket, and balloon flights and many ground-based studies using searchlights and lasers. Some of this was motivated by the purely scientific objective of understanding our atmosphere. However, much of it was also motivated by a desire to make practical applications of this knowledge in astronomy, meteorology, and other fields. One of the more recent areas of interest is in remote sensing. Models based on the rather sparse data available give an aerosol optical depth of about 0.05 above 20 km. An aerosol level four times this has been shown to cause error of several percent in the classification of ERTS data. It is quite likely that aerosol levels could vary by factors much larger than four. Thus there is considerable interest, both from a purely scientific standpoint and from a practical applications standpoint in aerosol distributions in the atmosphere.

The main objective of this experiment was to obtain quantitative measurements of the brightness of the earth's limb and to use these to study the distribution of aerosols in the atmosphere.

Techniques were developed to use limb measurements (by S190, S191, and S192) to obtain aerosol attenuation coefficients, number densities and particle size distributions as a function of altitude. They are described in Section 2.0. These methods were applied to S190, S191, and S192 data. Because of time and data quality limitations, it was decided to concentrate on obtaining aerosol attenuation coefficients rather than attempt the more complicated analysis required to obtain number densities and particle size distributions. The results are described in Section 4.0.



2.0 APPROACH

2.1 ANALYSIS TECHNIQUES

In analyzing the data the first task was to remove the noise insofar as possible. The techniques used to do this are described in Section 2.1.5.

After this was done the data was analyzed using two general techniques:

(1) comparing the measured limb brightness curves with simulated limb brightness curves calculated for various atmospheric models, and (2) inverting the data to obtain a vertical profile of the attenuation coefficients. The techniques for doing this are developed in this section. We also include in this section a description of a technique for inverting the data to obtain particle number densities and size distributions (Section 2.1.3). However, this technique was not used in the data analysis for the reasons given above.

2.1.1 Simulated Limb Brightness Curves

In this paragraph we derive a mathematical expression for the limb brightness curve that will allow us to simulate the brightness that would be observed by the Skylab sensors. This curve will, of course, depend on the aerosol distribution assumed for the atmosphere. All required data had a scattering angle of near 180° . The error caused by assuming the measurements to be 180° were expected to be small, and the task of modeling the slant path for non- 180° scattering was complex by comparison. All models were therefore computed for 180° backscatter. We carry out calculations for a pure Rayleigh scattering atmosphere and for two aerosol distributions found by Elterman.^{1,2} Each point on a limb brightness curve corresponds to a line of sight through the atmosphere (or sensor pointing vector) which traverses various levels in the atmosphere down to some minimum altitude x . Such a line of sight is the line $O'C$ shown in Figure 1, where O' is the position of the sensor. Here we assume $O'C$ is a straight line. In fact it is slightly curved due to refraction in the atmosphere. This effect is considered in Section 2.1.6. In Figure 1, the point A is the point of closest approach to the earth's surface and point B is some other point on the line of sight, a distance $+l$ from A. Distances on the other side of A are negative. The altitude at point B is $x + z$. The radius of the earth is R_E . This is the mean radius of the earth as defined in NASA documentation.

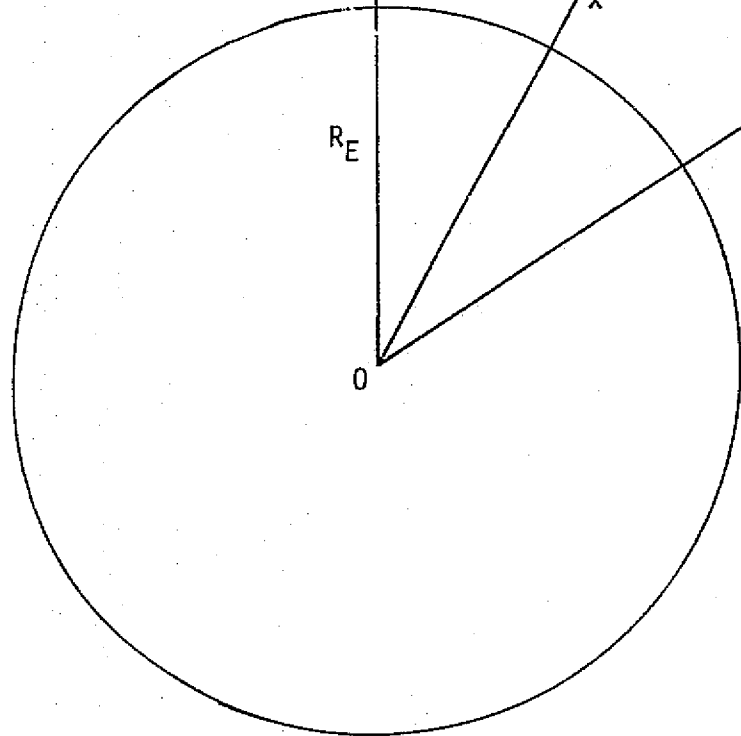


Figure 1. Geometry of Slant Path for Simulated Limb Brightness Curves



In order to compute the radiance at O' measured by a sensor pointed in the direction $O'A$ we calculate the contribution of each point B along the line of sight and add all these contributions. Only first order scattering will be included and it is assumed that the incident solar radiation is parallel to $O'C$, i.e., we consider the case of pure backscattering. Point B is illuminated by an incident solar irradiance of

$$I_0 e^{-\int_l^\infty \beta(u) du}$$

where I_0 is the solar irradiance at the top of the atmosphere and $\beta(u)$ is the atmospheric volume extinction coefficient (units km^{-1}). The integral is along the path $B O'$ and the upper limit is actually the distance $A O'$. However, since $\beta(u)$ is completely negligible (i.e., equal to zero in our models) for attitudes corresponding to the point O' and above, we have replaced the upper limit by ∞ . We shall assume that absorption is zero so β is equal to the scattering coefficient.

The proportion of this incident irradiance that is scattered back towards the point O' is given by the value of the scattering diagram or phase function $P(\theta)$ for $\theta = 180^\circ$. For a more complete discussion of extinction coefficients and phase functions, see Chandrasekhar.³ We shall write P or $P(l, 180^\circ)$ to show it is a function of l as well. The radiance $I_0 P(l, \theta=180^\circ) e^{-\int_l^\infty \beta(u) du}$ scattered towards O' from the point B is attenuated on the path $B O'$ by factor $e^{-\int_l^\infty \beta(u) du}$. Integrating over all points B along the path we obtain the following expression for the radiance along this path

$$B(X) = I_0 \int_{-\infty}^{\infty} P(l, 180^\circ) \beta(l) \exp(-2 \int_l^\infty \beta(u) du) dl \quad (1)$$

Equation 1 can be simplified if it is assumed that $P(l, 180)$ is independent of position in the atmosphere (i.e., independent of l and x). In that case one can easily show that

$$B(x) = \frac{I_0 P}{2} \left[1 - \exp\left(-2 \int_{-\infty}^{\infty} \beta(l) dl\right) \right] \quad (2)$$



In what follows we shall assume that $\beta(l)$ depends only on altitude in the atmosphere. In that case $\beta(-l) = \beta(l)$ so that

$$\int_{-\infty}^{\infty} \beta(l) dl = 2 \int_0^{\infty} \beta(l) dl. \quad (3)$$

From Figure 1

$$l^2 = (R_E + x + z)^2 - (R_E + x)^2 = z^2 + 2(R_E + x)z. \quad (4)$$

$$dl = \frac{(z + R_E + x)}{\sqrt{z^2 + 2(R_E + x)z}} dz \quad (5)$$

Now $\beta(l)$ is zero for all values of l except those corresponding to small values of $x + z$, i.e., values for which

$$z \ll R_E$$

$$x \ll R_E$$

Therefore we can replace dl in Equation (3) by

$$dl \approx \sqrt{\frac{R}{2}} \frac{dz}{\sqrt{z}} \quad (6)$$

The integral of Equation (3) can then be written

$$\int_0^{\infty} \beta(l) dl \approx \sqrt{\frac{R}{2}} \int_0^{\infty} \beta(z + x) \frac{dz}{\sqrt{z}} = \sqrt{\frac{R}{2}} \int_x^{\infty} \beta(z) \frac{dz}{\sqrt{z-x}} \quad (7)$$

Thus we finally obtain the following expression for limb brightness:

$$B(x) = \frac{I_0 P}{2} \left[1 - \exp\left(-4\sqrt{\frac{R}{2}} \int_x^{\infty} \beta(z) \frac{dz}{\sqrt{z-x}}\right) \right] \quad (8)$$

This is the expression that was used to calculate most of our simulated limb brightness curves.



2.1.2 Inversion of Limb Brightness Curves

The Weyl fractional integral⁴ of order ϕ of Φ is defined by

$$h(\Phi(\xi), x, \phi) = \frac{1}{\Gamma(\phi)} \int_x^\infty \Phi(\xi) (\xi-x)^{\phi-1} d\xi$$

It can be shown that the Weyl fractional integral and the Fourier transform are related by the expression

$$Fe^{-1} \{\Phi(x); t\} = t^\phi (\operatorname{sgn} t) \exp(\pi i \phi/2) Fe^{-1} \{h(\Phi(\xi), x, \phi); t\}$$

where the inverse Fourier transform of $f(x)$ is

$$Fe^{-1} \{f(x); t\} = \int_{-\infty}^{\infty} f(x) e^{2\pi i x t} dx = F(t)$$

Then

$$\Phi(x) = Fe \left[t^\phi (\operatorname{sgn} t) \exp(\pi i \phi/2) Fe^{-1} \{h(\Phi(\xi), x, \phi); t\} \right]$$

From Equation (8)

$$\ln \left[\frac{I_0 P(x)}{I_0 P(x) - 2B(x)} \right] = 2\sqrt{2R} \int_x^\infty \frac{\beta(q)}{\sqrt{q-x}} dq$$

Let

$$F(x) = \frac{1}{\Gamma(\frac{1}{2})} \int_x^\infty \frac{\beta(q)}{\sqrt{q-x}} dq$$

which is the Weyl fractional integral of order $1/2$ of β . Combining these last two expression yields

$$F(x) = \frac{1}{\Gamma(\frac{1}{2})} \frac{1}{2\sqrt{2R}} \ln \left[\frac{I_0 P(x)}{I_0 P(x) - 2B(x)} \right]$$

and

$$\beta(x) = Fe \{ t^{1/2} (\operatorname{sgn} t) \exp(\pi i/4) Fe^{-1} [F(x); t]; x \}$$



This expression serves to invert the limb brightness profile, B , which is contained in $F(x)$ to find the altitude profile of attenuation coefficients. Note that the wavelength dependence of the coefficients is contained only in the brightness signature, therefore the resulting profile is for a single wavelength, and must be repeated to determine wavelength dependence.

The function $P(x)$ was found by evaluating Equation (3) with and without $P(x)$ using values of β from a model of the stratosphere. A ratio of these results was then used to determine the function $P(x)$ as it is removed from the integral (mean value theorem). It was found that the $P(x)$ did not significantly vary with changes in the model. The error caused by the use of the function derived from the model on the measured data we therefore accepted as inconsequential.

2.1.3 Inversion of Intensities for Number Density and Particle Size Distributions

Scattering of radiation by aerosols which have a distribution of sizes can be represented by a Fredholm integral equation of the first kind assuming all of the particles have the same index of refraction. Using the Phillips-Twoomey inversion method^{5,6} the following development allows scattering by particles differing in index of refraction. Inverting the measured radiation from such a set of scatterers requires simultaneous integral equations for unknown size distributions with an independent measurement for each equation. Each size distribution then describes all of the particles having a common index of refraction.

Let the single integral equation be represented by

$$g(x) = \int_a^b K(x,y) f(y) dy \quad (9)$$

where $g(x)$ is the measured radiation, $f(y)$ is the aerosol size distribution, and the kernel is the scattering function. Constraints are then imposed on the error, ϵ , inherent in the measurement of $g(x)$, and the unknown function $f(y)$, such as

$$\sum_i \epsilon_i^2 \leq e, \text{ some chosen constant} \quad (10)$$



$$\int_a^b (F'(y))^2 dy = \min \quad (11)$$

where $F'(y)$ is the second or third derivative of $F(y)$.

A trial solution, $P(y)$, may also be used,

$$\int_a^b (f(y) - P(y))^2 dy = \min \quad (12)$$

Through some suitable quadrature the integrals become matrices, and an expression is obtained which incorporates the constraints through Lagrangian multipliers. The problem then is to minimize the expression

$$(G - AF)^T (G - AF) + \gamma_1 (BF)^T (BF) + \gamma_2 (F-P)^T (F-P)$$

where $A = wK$, w being the quadrature weights and A^T is the transpose of A . The matrix B is determined by the numerical approximation to Equation (11). Matrix differentiation with respect to F yields

$$A^T (AF - G) + \gamma_1 HF + \gamma_2 (F-P) = 0$$

where $B^T B = H$, and solving for F yields the solution

$$F = (A^T A + \gamma_1 H + \gamma_2)^{-1} (A^T G + \gamma_2 P) \quad (13)$$

When two sets of particles which differ by index of refraction, each having an independent size distribution, are interspersed in a volume, the measured intensities scattered from the volume are due to the combined scattering of each set. If the intensities add linearly, which is the case for the scattering of light from an incoherent source, the problem of finding the unknown size distributions can be expressed in two simultaneous integral equations.

$$I_g(x) = \int_a^b {}^1K(x,y) {}^1f(y) dy + \int_a^b {}^2K(x,y) {}^2f(y) dy \quad (14)$$



$$^2g(x) = \int_a^b {}^{21}K(x,y) {}^1f(y) dy + \int_a^b {}^{22}K(x,y) {}^2f(y) dy$$

In these equations superscripts are used to represent different functions. Again the $g(x)$ functions are the measured radiation, the kernels are the scattering functions and the f functions are the unknown particle size distributions differing in index of refraction. As before, the equations will be constrained through imposed limits on the inherent errors in the measured values and on the behavior of the unknowns in direct analogy to the solution of the single integral equation. A matrix expression is obtained,

$$\begin{aligned} & ({}^1G - {}^{11}A {}^1F - {}^{12}A {}^2F)^T ({}^1G - {}^{11}A {}^1F - {}^{12}A {}^2F) + \\ & ({}^2G - {}^{21}A {}^1F - {}^{22}A {}^2F)^T ({}^2G - {}^{21}A {}^1F - {}^{22}A {}^2F) + \\ & \gamma_1 ({}^1B {}^1F)^T ({}^1B {}^1F) + \gamma_2 ({}^2B {}^2F)^T ({}^2B {}^2F) + \gamma_3 ({}^1F - {}^1P)^T ({}^1F - {}^1P) + \gamma_4 ({}^2F - {}^2P)^T ({}^2F - {}^2P) \end{aligned}$$

which is minimized with respect to the unknowns 1F and 2F yielding two simultaneous equations.

$${}^{11}A^T ({}^{11}A {}^1F + {}^{12}A {}^2F - {}^1G) + {}^{21}A^T ({}^{21}A {}^1F + {}^{22}A {}^2F - {}^2G) + \gamma_1 {}^1B^T {}^1B {}^1F + \gamma_3 ({}^1F - {}^1P) = 0$$

$${}^{12}A^T ({}^{11}A {}^1F + {}^{12}A {}^2F - {}^1G) + {}^{22}A^T ({}^{21}A {}^1F + {}^{22}A {}^2F - {}^2G) + \gamma_2 {}^2B^T {}^2B {}^2F + \gamma_4 ({}^2F - {}^2P) = 0$$

These are then solved (${}^iH = {}^iB^T {}^iB$) yielding

$$\begin{pmatrix} F_1 \\ F_2 \end{pmatrix} = \begin{pmatrix} {}^{11}A^T {}^{11}A + {}^{21}A^T {}^{21}A + \gamma_1 {}^1H + \gamma_3 I & {}^{11}A^T {}^{12}A + {}^{21}A^T {}^{22}A \\ {}^{12}A^T {}^{11}A + {}^{22}A^T {}^{21}A & {}^{12}A^T {}^{12}A + {}^{22}A^T {}^{22}A + \gamma_2 {}^2H + \gamma_4 I \end{pmatrix}^{-1} \begin{pmatrix} {}^{11}A^T {}^1G + {}^{21}A^T {}^2G + \gamma_3 I \\ {}^{12}A^T {}^1G + {}^{22}A^T {}^2G + \gamma_4 I \end{pmatrix} \quad (15)$$



The method is quickly generalized to n equations with n unknowns. The limitations are the same as those for solving the single equation with the additional requirement that measurements and hence the kernels be independent functions. The general expression to be minimized is

$$\sum_{j=1}^N \left[(i_G - \sum_{i=1}^N j i_A i_F)^T (j_G - \sum_{i=1}^N j i_A i_F) \right] + \sum_{i=1}^N \left[\gamma_i (i_B i_F)^T (i_B i_F) + \mu_i (i_F - i_P)^T (i_F - i_P) \right]$$

Differentiation with respect to each of the unknowns yields

$$\sum_j j K_A^T \left(\sum_{i=1}^N j i_A i_F \right) + \gamma_K K_B^T K_B K_F + \mu_K (K_F - K_P) - j K_A^T j_G = 0; K=1, 2, \dots, N$$

or

$$\sum_i \left[\sum_j j K_A^T j i_A + (\gamma_K K_H + \mu_K I) \delta_{Ki} \right] i_F = \sum_j j K_A^T i_G + \mu_K K_P; K=1, 2, \dots, N \quad (16)$$

where $K_H = K_B^T K_B$.

Comparison with Equation (13), the solution for the inversion of the single integral equation, shows that a similarity in the form of the solutions is maintained. Equation (15) becomes an example of the expansion of Equations (16) necessary to obtain the solutions, in this case two solutions from two simultaneous equations.

Respective number density is obtained from the solutions for size distributions by integrating over all sizes,

$$N = \int P(a) da$$

Solutions can also be verified by calculating attenuation coefficients with the expression

$$B(\lambda) = \int C_{sca}(\lambda, a) f(a) da \text{ where}$$

C_{sca} is the scattering cross section for a spherical particle of radius a . Again $f(a)$ is the particle size distribution. This expression can also



serve to invert the attenuation coefficients to obtain the size distribution.

2.1.4 Location of the Field of View

Locating the sensor field of view was a major task. The Skylab ephemeris and ancillary data did not give an accurate enough determination for our purposes. From NASA Document PHO-TR524 Rev. A, page B-1, location of the intersection point of the sensor pointing vector and the earth ellipsoid was accurate to within 5.5 Km. tolerance when the sensor was pointing vertically downward. Extending the tolerance from a distance of 435 Km (orbital altitude) to 2400 Km (distance to the limb) gives a possible error of about 30 Km. Attempts were made to simply translate the field of view determined by Skybet, but all were unsatisfactory. Not only was the field of view unknown, but also the change in field of view between data points was unknown, as the following demonstrates:

Let \vec{SPV}' be the sensor pointing vector in ECT' , a coordinate system very close to ECT , the Earth Centered True coordinate system, and let \vec{SPV} be the sensor pointing vector in ECT . \vec{SC} is the spacecraft vector in ECT . If A is a 3×3 matrix which accounts for the error in \vec{SPV} , then

$$A \cdot \vec{SPV}' = \vec{SPV}$$

If θ is the angle between the spacecraft vector and the sensor pointing vector emanating from the spacecraft

$$\cos \theta = \frac{\vec{SPV} \cdot -\vec{SC}}{|\vec{SPV}| \cdot |\vec{SC}|} = \frac{(\vec{A} \cdot \vec{SPV}') \cdot -\vec{SC}}{|\vec{A} \cdot \vec{SPV}'| \cdot |\vec{SC}|}$$

defining h = spacecraft altitude

R = radius of the earth

x = altitude, or closest approach of the pointing vector.

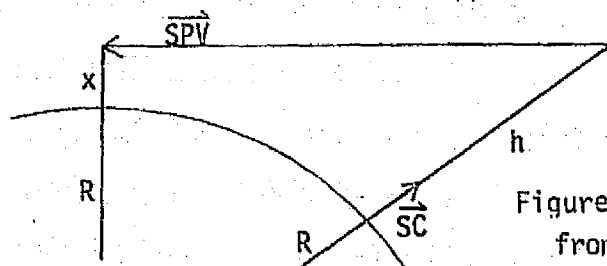


Figure 2. Location of Field of View
from SKYBET Ephemeris Data



$$\begin{aligned}
 X &= (R+h) \sin \theta - R \\
 &= (R+h) \sin \left\{ \cos^{-1} \frac{(\vec{A} \cdot \vec{SPV}_1) \cdot - \vec{SC}}{|\vec{A} \cdot \vec{SPV}_1| |\vec{SC}|} \right\} - R \\
 X_2 - X_1 &= (R+h) \left(\sin \left\{ \cos^{-1} \frac{(\vec{A} \cdot \vec{SPV}_1) \cdot - \vec{SC}}{|\vec{A} \cdot \vec{SPV}_1| |\vec{SC}|} \right\} \right. \\
 &\quad \left. - \sin \left\{ \cos^{-1} \frac{(\vec{A} \cdot \vec{SPV}_2) \cdot - \vec{SC}}{|\vec{A} \cdot \vec{SPV}_2| |\vec{SC}|} \right\} \right)
 \end{aligned}$$

which shows that the difference in altitude is not a linear relationship with the difference in sensor pointing vectors. Even if \vec{SPV}_1 and \vec{SPV}_2 are close the unknown transformation matrix \vec{A} which contains the pointing errors cannot be removed. It is simple to show with the above relationship that a 1% deviation from unity on the diagonal of A with very small (< 1%) off-diagonal contributions will produce the expected 30 Km error tolerance. It was for this reason that Skybet data was not suitable to use for field-of-view location.

2.1.4.1 S192 Field of View

We now derive an expression for the altitude of the sensor pointing vector for S192. (This expression was derived by Dr. F. E. Alzofon of Lockheed Electronics Co.) Each point on a S192 scan of the limb corresponds to a line of sight through the atmosphere (or sensor pointing vector) which traverses various levels in the atmosphere down to a minimum altitude x . The situation is shown in Figure 3. Here O is the center of the earth and Skylab is located at O' . The axis of S192 is pointed in a direction x' and the instrument is scanning in a cone as shown. The angular change from one data point to the next is $\Delta\phi \approx 0.094$ degree. $O'P$ is a specific sensor pointing vector corresponding to a specific data point on a scan. In order to interpret the data we need to know the minimum altitude r measured from the center of the earth for this (and every other) sensor pointing vector. For the purpose of this discussion we will ignore the effects of refraction. They will be discussed in Section 2.1.6.

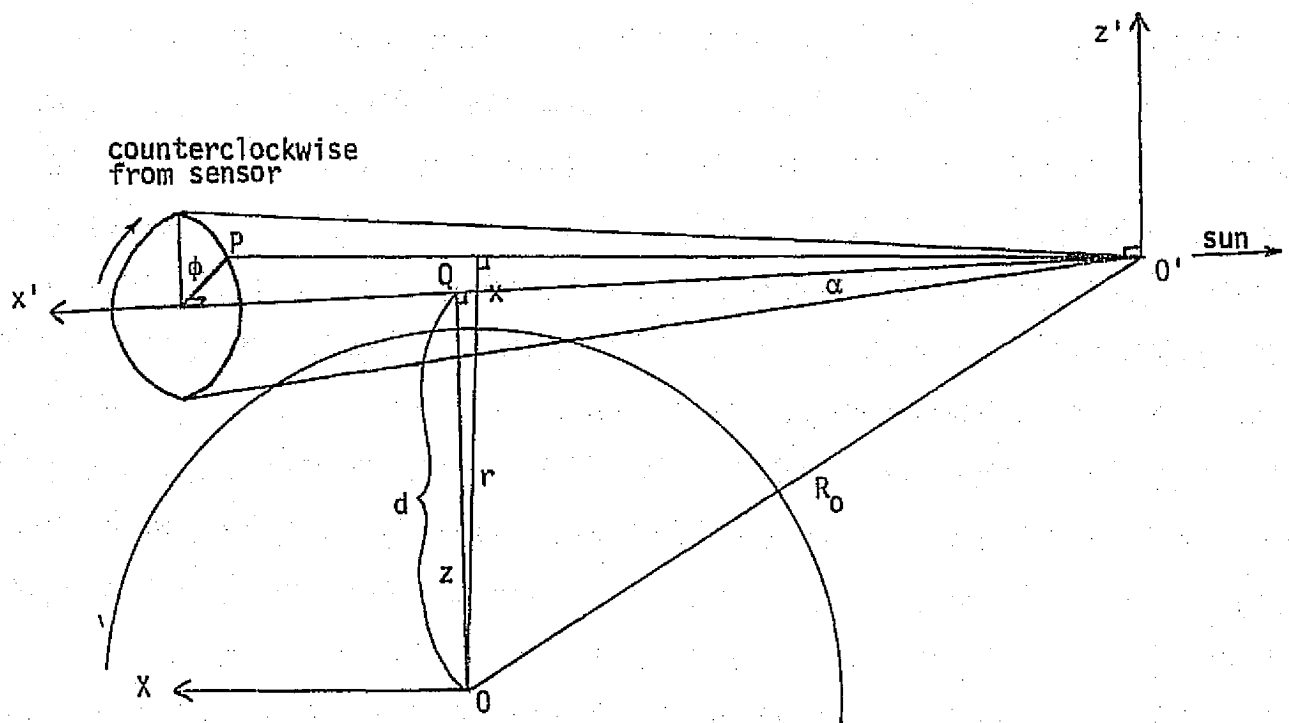


Figure 3. S192--Exact Location of Field of View, A

In order to calculate r we first define two coordinate systems centered at points O and O' with axes as shown. The axes in the two coordinate systems are parallel to each other. In the coordinate system centered at O , the equation of the line $O'P$ is given by

$$\frac{x - x_1}{l} = \frac{y - y_1}{m} = \frac{z - z_1}{n} \quad (17)$$

where x_1 , y_1 , and z_1 are the coordinates of the point O' and are given by

$$\begin{aligned} x_1 &= -\sqrt{R_0^2 - d^2} \\ y_1 &= 0 \\ z_1 &= d \end{aligned} \quad (18)$$

and l , m and n are the direction cosines of the line $O'P$. To determine l , m and n , we consider Figure 4. Clearly

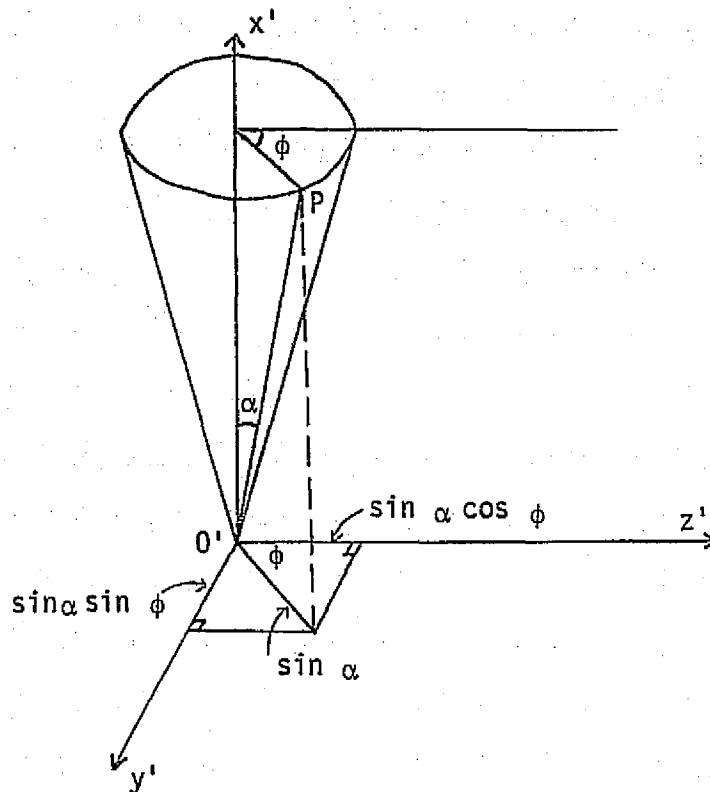


Figure 4. S192--Exact Location of Field of View, B

$$l = \cos \alpha$$

$$m = \sin \alpha \sin \phi \quad (19)$$

$$n = \sin \alpha \cos \phi$$

The equation of the sphere of radius r is

$$r^2 = x^2 + y^2 + z^2 \quad (20)$$

Solving Equations (17) and (20) together we obtain

$$A y^2 + B y + C = 0 \quad (21)$$



$$\begin{aligned} \text{where } A &= 1 + a^2 + b^2 \\ B &= 2x_1 a + 2db \\ C &= x_1^2 + d^2 - r^2 \\ a &= 1 / \tan \alpha \sin \phi \\ b &= 1 / \tan \phi \end{aligned} \quad (22)$$

Now Equation (21) has two solutions corresponding to the two points in which a line intersects a sphere. However, we are concerned with the case where these two points are the same point, i.e., where the line is tangent to the sphere. In this case

$$B^2 - 4AC = 0 \quad (23)$$

Substituting Equations (22) in (23) we obtain

$$r = \sqrt{R_0^2 - (x_1 \cos \alpha + d \sin \alpha \cos \phi)^2}$$

$$\text{where } x_1 = -\sqrt{R_0^2 - d^2}$$

The altitude of the sensor pointing vector is given by $r - R_E$.

A slightly different (and simpler) approximation to the above exact expression which does not depend on d (see Figure 3) can be obtained in the following manner.

For S192 the altitude increment is dependent on the position of the scan

relative to the earth. This can be represented as the angle of intersection, η_1 , between the scan arc and the earth's surface. All altitude increments Δx_1 can be determined from the η_1 and known characteristics of the scan arc. The arc between two adjacent points subtends an angle of $\alpha = 116.25^\circ / 1239$ pts. The arc between the first point and any

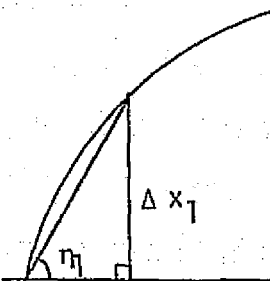


Figure 5. S192--Altitude Increment from Geometry of Conical Scan

$$\theta_i = (i-1) (116.25^\circ) / 1239$$

To express n_i in terms of n_1 and β_i it is seen in Figure 6 that $n_i = n_1 - \beta_i$, or

$$n_i = n_1 - \frac{(i-1)}{1239} (116.25^0)$$

Therefore the change in increment is

$$\Delta X_i = S \sin \eta_i$$

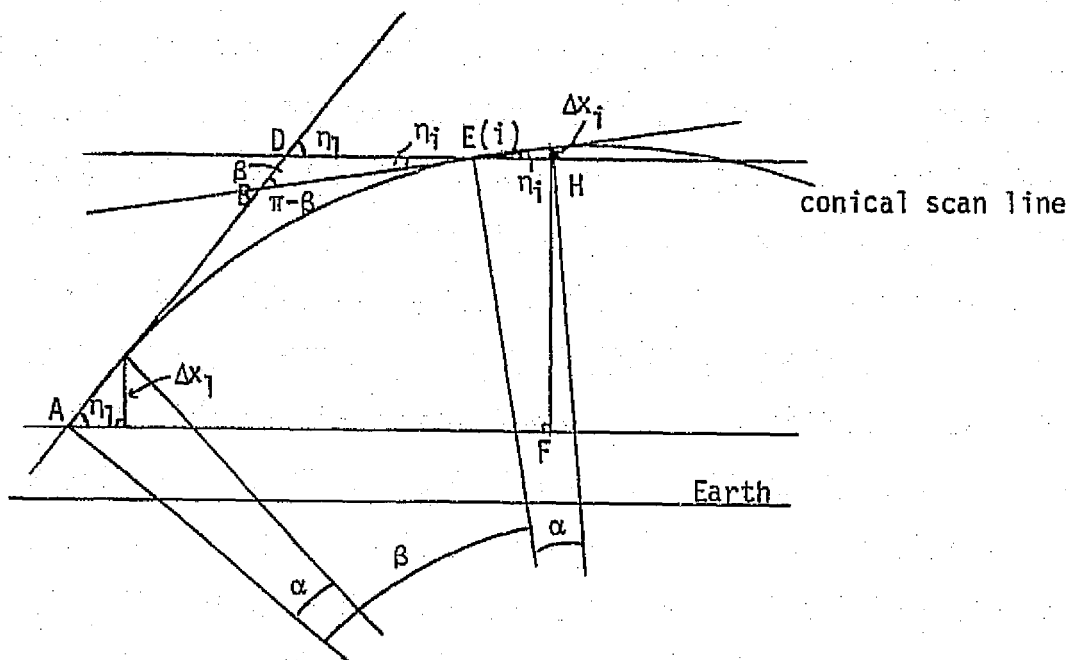


Figure 6. S192--Intersection of Conical Scan with the Earth's Surface

where S is the center-to-center spacing between points i and i + 1. S is the product of the angle subtended by the arc between two adjacent points and the distance from the sensor. The angle (.157894 milliradians) is a sensor characteristic; the distance from the sensor is a function of the altitude but almost a constant; a distance of 2400 Km was used. S then equals .378 kilometers. For the cases where the arc reaches a maximum altitude and begins



decreasing in altitude, that is, at the maximum, the tangent of the arc is parallel to the tangent to the earth; η_1 can be determined since the orientation of the scan is known. For the cases where such a maximum cannot be identified in the data, η_1 must be allowed to vary as the data is compared to the model thereby determining the unknown constants through a least-squares fit of the two curves.

2.1.4.2 S191 Field of View

The observation angle and the observation altitude for S191 was derived to be

$$\theta = \cos^{-1} (\sin \gamma \cos \beta)$$

$$X = R_0 \sin \theta - R_e$$

as follows:

The angle β is defined as the angle between the sun vector and its projection into the orbital plane. The angle γ is defined as the sun elevation angle at the spacecraft subsatellite point. The angle γ is also the angle between the sun vector and its projection into the orbit's tangent plane at the spacecraft.

Some assumptions were necessary. The sun vector was not parallel to the EREP axis vector by a small angle less than four degrees. For this derivation the two vectors were assumed parallel. Also the S191 vector is treated as equal to the EREP vector for this derivation of increment change between observation angles; the actual location was not the issue. Location was included in the derivation of scattering angle.

Where θ is the observation angle relative to the radius of orbit, from Figure 7,

$$|DB| = R_0 \cos (90 - \gamma)$$

$$= R_0 \sin \gamma$$

$$|AB| = |DB| / \cos \beta.$$

REPRODUCIBILITY OF THE
ORIGINAL PAGE IS POOR



Therefore,

$$|AB| = R_0 \sin \gamma / \cos \beta$$

$$|AD| = |AB| \sin \beta.$$

Therefore, $|AD| = R_0 \sin \gamma \sin \beta / \cos \beta.$

$$|DC| = R_0 \sin (90 - \gamma)$$

$$= R_0 \cos \gamma$$

and $|AC|^2 = |AD|^2 + |DC|^2$

then $|AC|^2 = R_0^2 \frac{\sin^2 \gamma \sin^2 \beta}{\cos^2 \beta} + R_0^2 \cos^2 \gamma.$

Also $|AC|^2 = |BA|^2 + |BC|^2 - 2|AB||BC| \cos \theta$

where $|BC| = R_0.$

Solving for $\cos \theta$ and substituting the above relationships will yield

$$\cos \theta = \sin \gamma \cos \beta.$$

In this relationship β is nearly a constant and γ is a function of time due to spacecraft orbital motion. Let L and M be the positions of the spacecraft at times T_1 and T_2 representing the acquisition times of two adjacent data points. The times are clearly related to the sensor scan rate by

$$T_2 = T_1 + \left(\frac{1}{\text{scan rate}} \right)$$

$$= T_1 + .925 \text{ sec}$$

The angle, α , defined by the extended earth radii passing through L and M respectively, is determined by the product of the orbital rate and the inverse of the scan rate.

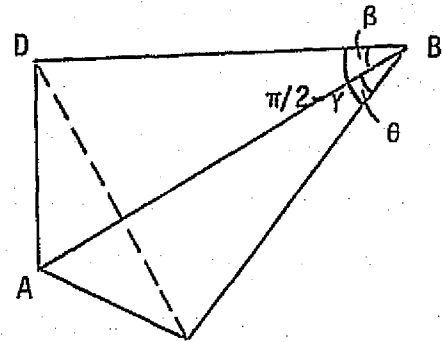


Figure 7 C

S191--Location of Field of View

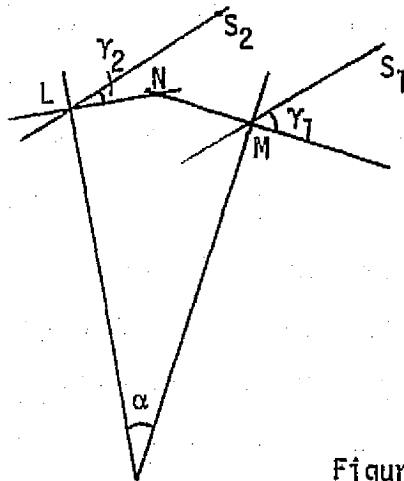


Figure 8 S191--Change of Field of View

If point N is defined by the intersection of their respective orbit tangent planes with the orbital plane and $\vec{S_1}M$ and $\vec{S_2}L$ are parallel projections of sun vectors into the orbital plane, then

$$\gamma_2 = \gamma_1 - \alpha$$

The initial observation angle θ_1 , is related to the initial estimate of lowest observed altitude, R_{min} , by

$$\theta_1 = \sin^{-1} \left[(R_e + R_{min}) / R_o \right]$$

As previously shown θ and γ are related by

$$\sin \gamma \cos \beta = \cos \theta$$

then
$$\gamma_1 = \sin^{-1} (\cos \theta_1 / \cos \beta)$$

and
$$\gamma_{i+1} = \gamma_i - \alpha$$

and
$$\theta_i = \cos^{-1} (\sin \gamma_i \cos \beta)$$

and
$$x_i = R_o \sin \theta_i - R_e$$

where x_i is the altitude of point i.



2.1.4.3 S190A Field of View

The field of view of S190A as described in NASA PHO-TR524 is $21.24^{\circ} \times 21.24^{\circ}$ which is about 900 Km at the earth's limb 2400 Km distant $(2 \left[2400 \right] \tan \frac{21.24^{\circ}}{2})$. The data frame is 57 x 57 mm. Using a micro-densitometer with a sensing aperture of 20 μ , each data point records .316 Km $(= \frac{20\mu \times 900 \text{ Km}}{57 \times 10^3 \mu})$ at the earth's limb. If data points are recorded every 20 μ , center to center spacing is also .316 Km.

The S190A densitometer scans were aligned to be approximately normal to the earth. If the alignment were in error up to 20° , the altitude increment would be between .30 Km and .32 Km.

2.1.5 Noise Reduction

Noise elements identified and treated consisted of a Gaussian or random noise, a high frequency noise, a low frequency noise, and a coherent noise generally known as "herringbone" noise.

The random noise was to be expected. Nevertheless the random nature of the noise was verified by constructing noise histograms and verifying their characteristic Gaussian shapes. The histograms were not exactly Gaussian due to the contributions of coherent noise and aerosol layer effects, however, the curves approximated the Gaussian shape well.

The random noise was obtained for histogramming by fitting the measurements on the limb with a sixth order polynomial and finding the deviations from the polynomial. This removed the effects of amplitude. Using a polynomial approximation, however, does not account for the "bumps" caused by aerosol layers, therefore the Gaussian shape of the histograms should have a small distortion as they did.

The random noise was reduced by averaging twenty-five adjacent scans. The number of scans to average was arrived at by considering the advantage of using more scans (the standard deviation decreases as the inverse of the square root of the number of scans) versus the rate of field of view shift across pixels. The shift rate was found by determining the average apparent point of earth-atmosphere interface. Two such points were found 2692 scans apart. With a change in the pixel number of 300, the rate becomes about .11 pixels per scan, or 2.8 pixels per 25 scans.



A low pass Fourier filter was applied to the result of averaging. The filter was designed to suppress high frequency noise equivalent to a period on the limb of less than about 2 Km. The filter was applied to deviations of the data (average curve) from a sixth order polynomial least squares approximation to the data. Figure 9 shows the typical result; the "herringbone" noise reported by NASA becomes obvious. The frequency measured in this data appears to be about 10 KHz. The Fourier filter was therefore modified to suppress this noise, which reduces the effective resolution to about 2.2 Km on the limb.

After the data had been Fourier filtered it was apparent that we were not successful in removing all coherent noise. A twenty-five point convolution filter was therefore applied to the data in the time domain rather than Fourier transform the data again to be filtered in the frequency domain. This filter removed much of the noise; however, some lower frequency noise remained. For this reason the sixth order polynomial fit of the data was analyzed in addition to the filtered data; this gives a general level of aerosol content.

The low frequency noise was suspected when it was noted that the least squares sixth order polynomial approximation to the data showed a shift in amplitude between several adjacent scans. A 17 cycles/sec noise was reported by NASA personnel. With a scan rate of 94.8 scans/sec we searched for a noise with a period of approximately 5.5 scans/cycle.

The frequency and amplitude were determined by plotting a selected point on a scan as a function of scan. A twenty point curve was thus derived, for example the value of data point 500 could be plotted for scans 200 through 220. Several such curves were obtained by repeating the procedure for different points on the scan. To emphasize differences and to minimize effects of amplitude, the lowest value on each twenty point curve was subtracted from the respective curves. The plots for each set of scans were then averaged to obtain a representative curve for that set. Plots were obtained both from the portion of the scan covering the limb and from the portion of the scan recording dark space. The limb plots are important simply because that is the data being analyzed for aerosol effects; it is preferable not to extrapolate results from other data into this data. The dark space plots are valuable since ideally they record no external energy; any

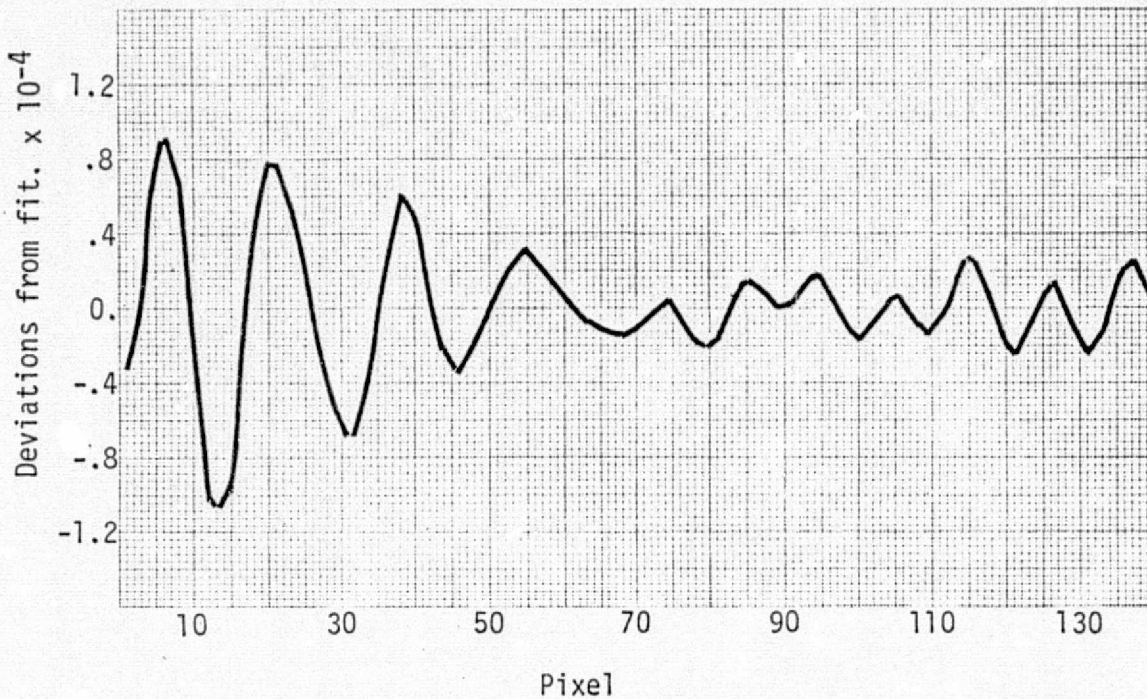


Figure 9. S192--Pass 47, Tape 934527, Scans 350-374, Band 3.
Deviations from Polynomial Fit After Fourier Filtering

REPRODUCIBILITY OF THE
ORIGINAL PAGE IS POOR



fluctuation from scan to scan should be due to the sensor alone thereby making the variations more apparent. For the limb plots the value plotted was obtained from the polynomial approximation of the data; for the dark space plots the value plotted was obtained from a straight line approximation of the data. This was necessary since the Gaussian noise would camouflage the periodic noise being sought.

Figures 10 through 12 are representative of the low frequency plots for the limb. Figure 13 is representative of the plots derived from dark space. A comparison shows that they are consistent both in amplitude and in frequency. Both sets reveal a frequency of about 5.8 scans/cycle or 16.3 cycles/sec.

The low frequency noise was therefore determined. The result on each scan is an additive constant which is unknown, but related scan to scan. However, the above procedure to suppress random noise averages twenty-five adjacent scans which covers about four cycles. Therefore, only an unknown, additive constant remains. This constant is determined by a solution of an overdetermined set of equations during the scaling process. A more complete description of the scaling process is found in Section 3.1.2.

2.1.6 Refraction

Refraction was included in the scaling of the data by assigning the appropriate observation altitude to each measured point. The model remained that which would be observed without refraction; the location of data points were distributed to remove the effects of refraction.

To develop the proper relationships the increment change in observation angle on the vertical was first determined; this increment is not that increment inherent in the design of the instrument as described in Section 2.1.4. Since we are seeking to describe an equivalent sensor which observes a path normal to the earth one need not consider what is observed but simply the observation characteristics. The geometric relationship of Figure 14 yields

$$\theta_i = \sin^{-1} \left[(R_e + X_i) / R_c \right]$$

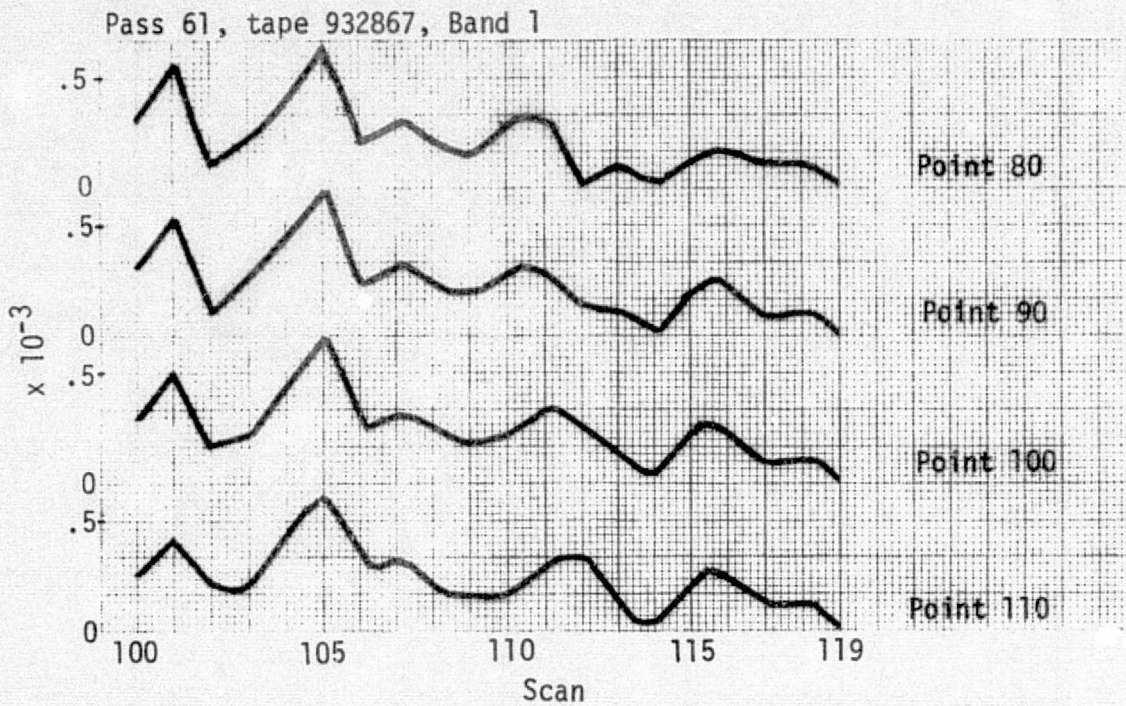


Figure 10. S192--Pass 61, Tape 932867, Band 1. Low Frequency Scan to Scan Noise for Four Points on the Limb

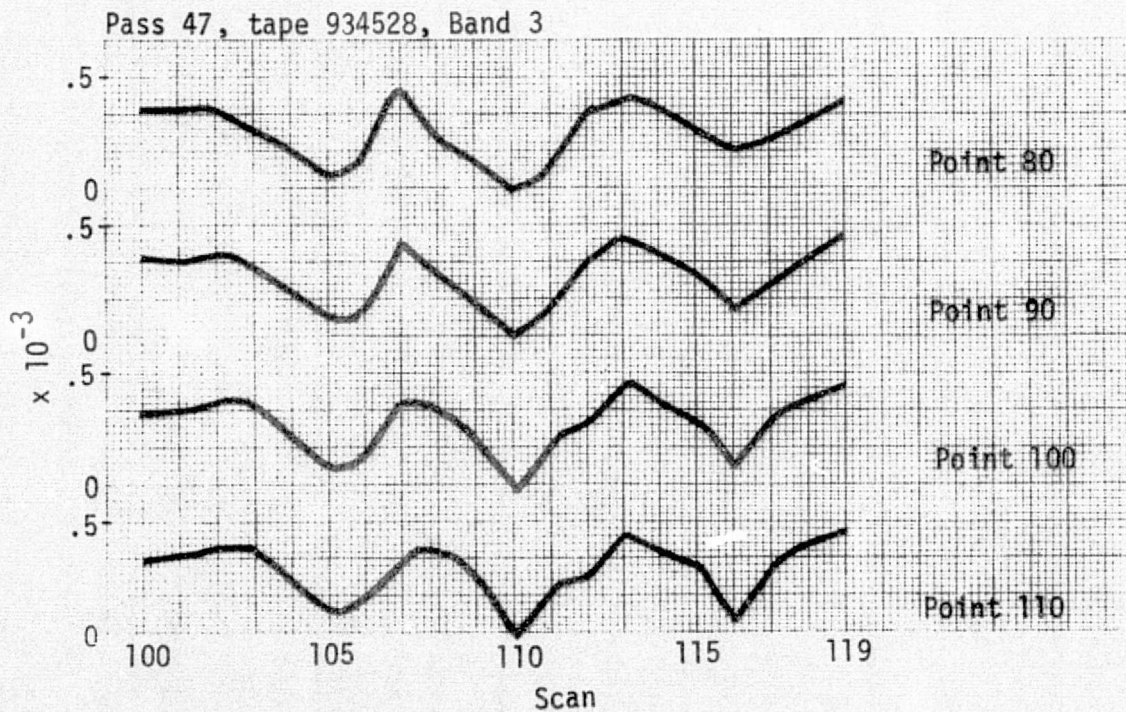


Figure 11. S192--Pass 61, Tape 932867, Band 1. Low Frequency Scan to Scan Noise for Four Points on the Limb

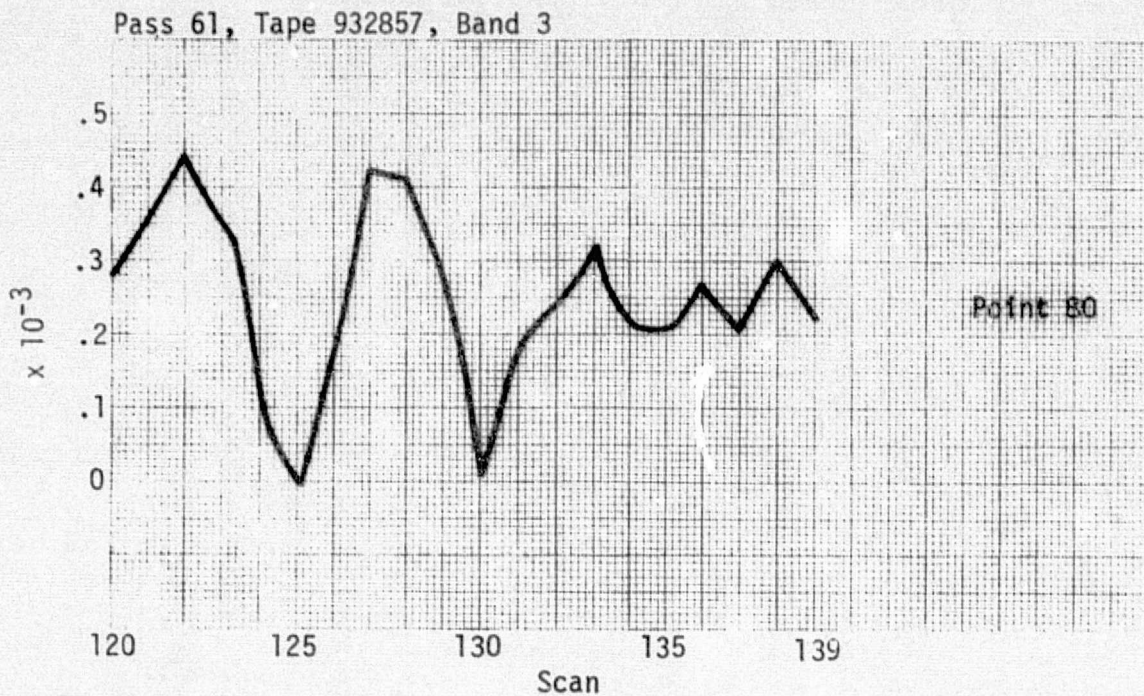


Figure 12. S192--Pass 61, Tape 932857, Band 3. Low Frequency Scan to Scan Noise for the Point on the Limb

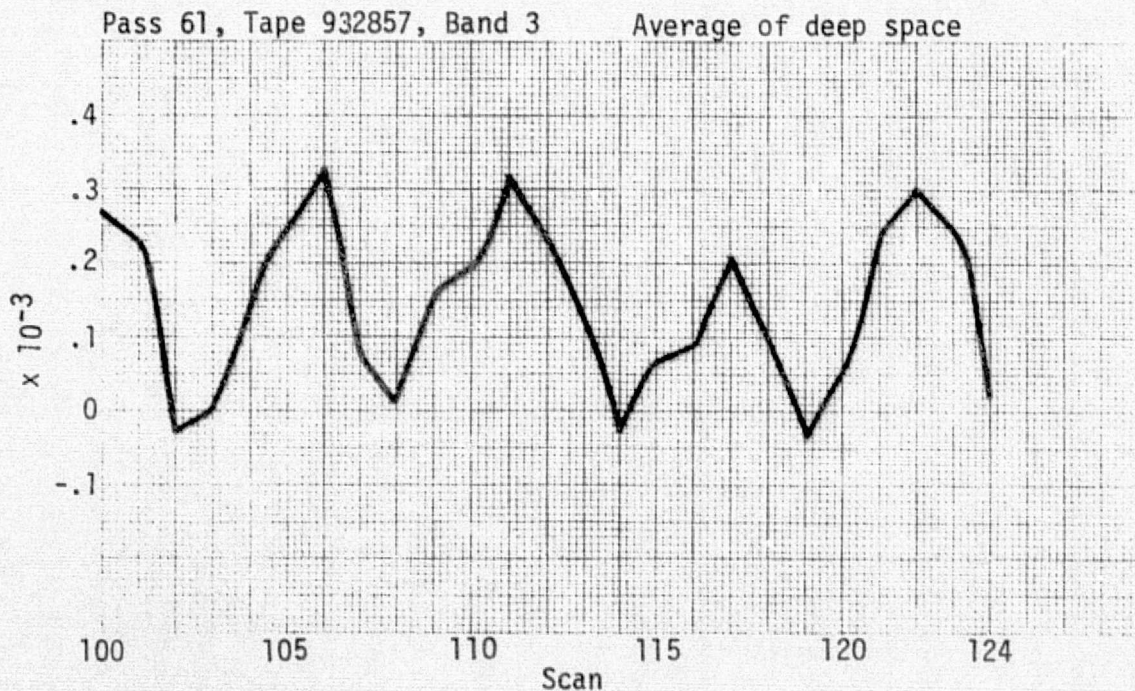


Figure 13. S192--Pass 61, Tape 932857, Band 3. Low Frequency Scan to Scan Noise for the Average of Deep Space

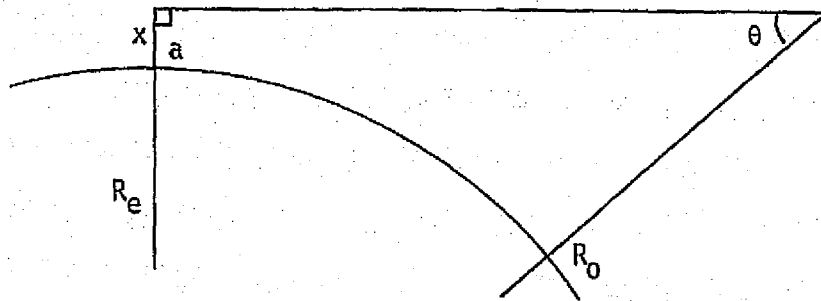


Figure 14. Observation Angle at the Sensor for a Straight Line Path

Thus for S192, an altitude provided by the derivation of Section 2.1.4.S192 can be converted to an equivalent observation angle θ . For S191 Section 2.1.4.S191 derives the observation angle directly. Knowing the observation angle, one can obtain the altitude viewed by tracing the refracted light path through the atmosphere. The data point acquired at the given observation angle is then assigned the obtained altitude, the complete set of which defines the limb brightness profile with the effects of refraction removed. This profile is then compared to the model for scaling and calibration of the data as defined in Section 3.1.2.

To trace the refracted light path the atmospheric refraction model as implemented by Dr. David E. Pitts of NASA and documented in NASA TMX-58033, "A Model Atmosphere for Earth Resources Applications"⁷ was used. For a path leaving altitude X at an angle γ from the earth's normal, this program uses the "law of sines" to find ϕ' , the angle between the path and the earth's normal at an altitude Z above X . The program considers the atmosphere as a number of layers and iterates through them until the light path emerges from the final layer. The geometry is illustrated in Figure 15, the relationship for refraction is

$$\phi' = \sin^{-1} \left(\frac{n''r'' \sin \phi''}{n'r'} \right)$$

The indices of refraction, n' and n'' , of the respective layers were computed within the same program. Because refraction was only a small effect, any inaccuracies caused by approximated input parameters would be insignificant. Therefore, one set of temperature and pressure as a function of altitude were used throughout, being provided by the U.S. Standard Atmosphere, 1962.⁸

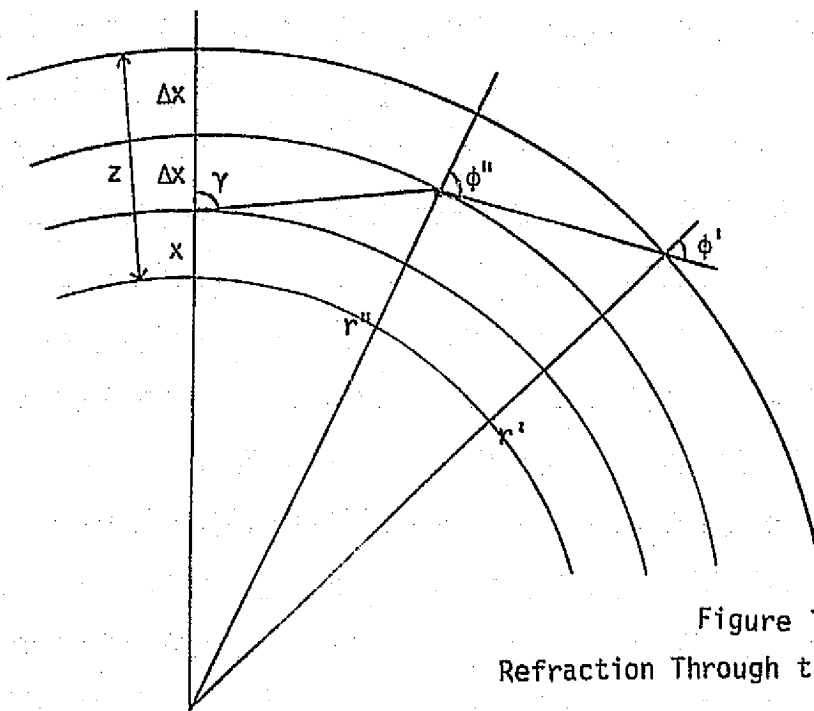


Figure 15.
Refraction Through the Layers of the Atmosphere

Because this investigation observes the lowest altitude at a tangent ($\gamma = \pi/2$) a table of altitude versus emerging angle was derived by assigning an altitude and initiating γ to be $\pi/2$ and iterating through the atmosphere to obtain the emerging angle. Because essentially no refraction occurs above 20 km iteration was terminated there. The emerging angle, ϕ' , was related to the observation angle, θ , at the spacecraft by the expression

$$\theta = \sin^{-1} \left[(R_e + 20) \sin \phi' / R_o \right]$$

as can be seen by Figure 16 is the "law of sines".

The program was verified by using another expression derived by Baum and Code⁹ which derives the amount of refraction occurring as light passes through a planetary atmosphere having exponentially decreasing density as altitude increases:

$$\phi_I = \left(\frac{2\pi R'}{H} \right)^{1/2} (n' - 1) \exp \left[(R' - R_i)/H \right]$$



where n' is the refractive index at X' , a reference altitude for which n' is known ($R' = R_e + X'$). $X_i = R' - R_e$ is the altitude of closest approach to the planet; R_e is again the radius of the earth. A scale height, H , of 8 Km was used.

The Pitts program calculates ϕ' and α' , the Baum and Code expression calculates ψ , shown in Figure 17. It can be seen that

$$\phi' = \pi/2 + \phi/2 - \alpha.$$

Comparison of the results of the two agree to better than 1% which is as accurate as the value used for the scale height parameter.

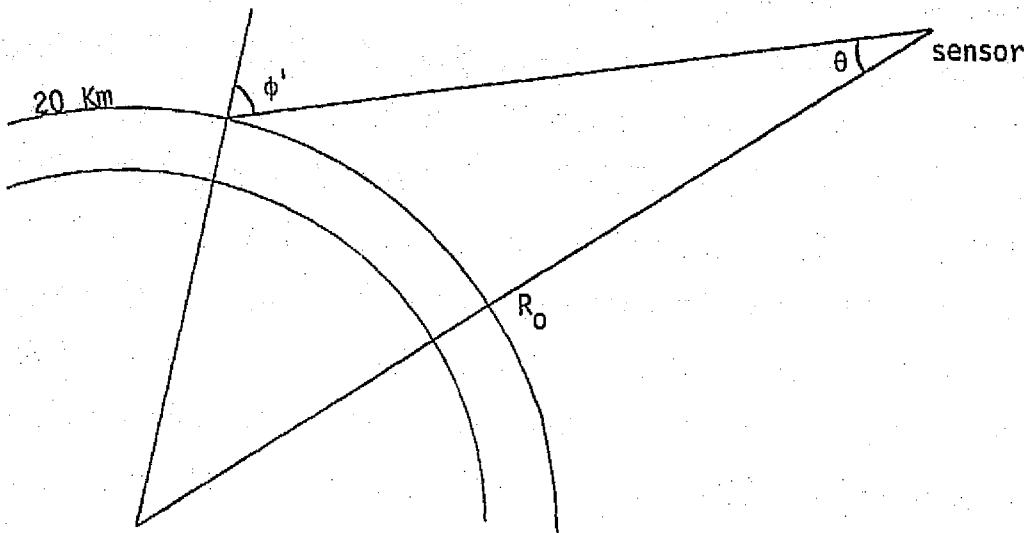


Figure 16

Observation Angle at the Sensor for a Refracted Path

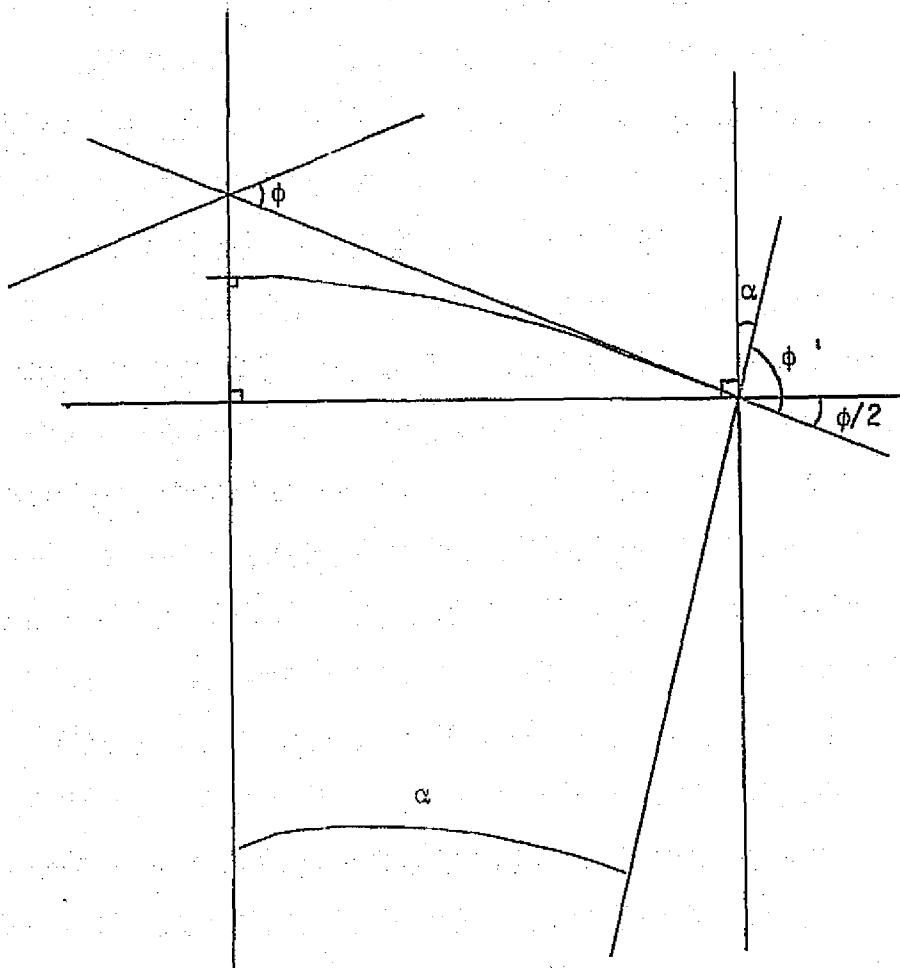


Figure 17
Comparison of Two Refraction Models



2.2 DATA ACQUISITION

This investigation used data from S190A, S191, and S192. All data was acquired with the Skylab vehicle in the solar inertial mode as opposed to the Z-Local-Vertical mode. This positions the spacecraft such that the sensors' pointing vector views the earth's limb twice per orbit. Each of these two limb passes provides a complete limb data set.

2.2.1 The S190A Data

The S190A sensor consists of six 70 mm lenses mounted in a single camera body. It produces film imagery of a scene in six spectral regions. The regions and film types are listed in Table 1.

Table 1. 190A Spectral Bands

<u>Spectral Region</u>	<u>Film Type</u>
.5 - .6 μm	B/W S0-022
.6 - .7	B/W S0-022
.7 - .8	IR B/W EK2424
.8 - .9	IR B/W EK2424
.5 - .88	IR Color EK2443
.4 - .7	High Resolution Color S0-356

The S190A camera bank was used because it provided maximum spatial resolution and minimum geometric distortion of the image.

2.2.2 The S191 Data

The S191 spectrometer was used to acquire high spectral resolution data within its field of view of one milliradian (about 2.4 Km in altitude at the earth's limb). Radiance data from the first filter wheel was used. This data includes wavelengths from 0.38 μm to 2.5 μm and has a wavelength-dependent spectral resolution of approximately 0.08 λ . We did not use the S191 data in the infrared bands and the first, or lowest, wavelength bands since it was reported that this data had errors due to off-axis rejection problem. An algorithm was developed to correct for this effect but we were



unable to acquire data corrected by this algorithm.

Approximately one spectral scan was acquired per second. In solar inertial mode the orbital motion of the satellite caused the line of sight of S191 to traverse the altitude at the earth's limb. The data was therefore acquired by fixing the sensor pointing angle relative to the spacecraft and allowing the spacecraft motion to produce the altitude scan. At one spectral scan per second the line of sight traversed about 2.4 Km in altitude when the motion of the sensor line of sight was normal to the earth and in the orbital plane. For a line of sight off of the orbital plane at an angle of about 44° , it traversed about 1.7 Km per spectral scan.

The S191 spectrometer recorded three complete scans through the limb for each complete limb data set. This was to obtain data in the same approximate region of the earth for three angles of limb observation relative to the direction of the incident solar radiation, all near 180° backscatter. The sensor was pointed just below the horizon of the spacecraft to cause the field of view to scan upward through the atmosphere. At intervals of $(35/\cos \beta)$ seconds the VTS* was manually reset to below the horizon and the process was repeated. The angle, β , is that angle defined by the intersection of the sun to earth center line and the projection of this line on the orbital plane. The first scan was initiated when the spacecraft was about 33° from the terminator on the daylight side and repeated until the vehicle was about 13° from the terminator. These guidelines were derived from the fact that near 33° from the terminator the limb becomes visible with the VTS about 10° forward; at 13° from the terminator the limb is seen behind the spacecraft at angles greater than 10° . It is during this period, at a time where the spacecraft position in orbit is 3.25° before the terminator, that the S192 scanner initiated its data acquisition for approximately five seconds. At least three frames of S190A were exposed during this period also.

2.2.3 The S192 Data

The third sensor of EREP used in this investigation was the multi-spectral conical scanner S192. Data was recorded simultaneously in thirteen spectral bands with wavelength between $.41 \mu$ and 12.5μ as shown in Table 2. The conical scan has an angle of revolution, α , of $5^{\circ}32'$. Experiment data is acquired in the front $116^{\circ}15'$, the remaining portion of the scan

*Viewfinder Tracking System



Table 2. S192 Spectral Bands

<u>Band</u>	<u>Spectral Range (μm)</u>
1	.41 - .46
2	.46 - .51
3	.52 - .56
4	.56 - .61
5	.62 - .67
6	.68 - .76
7	.78 - .88
8	.98 - 1.08
9	1.09 - 1.19
10	1.2 - 1.3
11	1.55 - 1.75
12	2.1 - 2.35
13	10.2 - 12.5

being assigned to housekeeping data. One conical scan was recorded approximately every .01 second, therefore the effect produced by motion of the spacecraft during one scan was negligible. The scanner was allowed to record several thousand limb scans as it passed through the limb. This data provided a horizontal distribution of stratospheric characteristics as well as sufficient data to reduce system noise effects.

2.3 DESCRIPTION OF ACQUIRED DATA

Analysis of the S190A data was done for Frame 175 of Pass 47 taken on September 18, 1973 at 44 minutes 8 seconds after midnight, GMT. Three microdensitometer scans were taken from the frame. The first was taken one-half inch from the left edge of the frame, the second was taken in the middle of the frame, and the third was measured one-half inch from the right edge of the frame. Table 3 lists the variable information for these three scans.

Only one S191 scan was analyzed. This was the first data take of Pass 47 taken on September 18, 1973. The scan covered from 44 minutes 19 seconds through 44 minutes 52 seconds after midnight, GMT. The sun elevation



angle at subsatellite point on earth was 2.63° and the data was acquired at 43°N , 104°W .

Eight sets of scans were analyzed from the S192 data. Table 4 summarizes the variable information of these scans. The five sets of scans from Pass 47 were taken on September 18, 1973, 44 minutes after midnight, GMT.

The three sets of scans from Pass 61 were taken on December 5, 1973, 16 hours and 45 minutes after midnight.

Table 3. S190A - Pass 47, Frame 175

	Latitude	Longitude	Sun-angle
Left	47°N	103°W	2.31°
Middle	45°N	103°W	2.21°
Right	42°N	103°W	2.16°

Table 4. S192

Pass	Tape No.	Scans	Time (sec)*	Lat-Long**	Sun-angle
47	934527	350-374	10.80	$43^{\circ}\text{N}-104^{\circ}\text{W}$	2.58°
47	934527	600-624	13.44	$43^{\circ}\text{N}-104^{\circ}\text{W}$	2.49°
47	934528	100-124	15.67	$43^{\circ}\text{N}-104^{\circ}\text{W}$	2.21°
47	934528	300-324	17.78	$43^{\circ}\text{N}-104^{\circ}\text{W}$	2.09°
47	934528	614-638	21.10	$42^{\circ}\text{N}-103^{\circ}\text{W}$	2.00°
61	932867	100-124	41.12	$45^{\circ}\text{S}-33^{\circ}\text{E}$	4.49°
61	932867	600-624	46.44	$45^{\circ}\text{S}-34^{\circ}\text{E}$	4.23°
61	932857	120-144	69.54	$45^{\circ}\text{S}-36^{\circ}\text{E}$	3.08°

*number of seconds after stated times the scans took place

**position on the earth where the earth's tangent is parallel to the sensor line of sight at its closest approach (point a of figure 14)



3.0 DATA ANALYSIS

3.1 THE S192 DATA

The first step in analyzing the S192 data was to remove the noise insofar as possible using the techniques described in Section 2.1.5. This involved the following steps:

- (1) Put data in engineering units using the calibration constants supplied on the data tape header record.
- (2) Average 25 adjacent scans.
- (3) Fit the exponential of a 6th order polynomial to the result of step (2).
- (4) Find the difference between the results of (2) and (3).
- (5) Apply a Fourier filter to the results of (4).
- (6) Apply a convolution filter to the results of (5).
- (7) Add the results of (6) to the fit found in (3) for a smoothed data scan.

In some of the S192 scans the maximum altitude was low enough that one could determine at what point in the scan it occurred. In other cases the scan extended so far into deep space that this could not be done. These two cases are treated somewhat differently.

3.1.1 Position in Scan of Maximum Altitude Known

In this case a relative altitude scale can be obtained using the methods of Section 2.1.4. However, an absolute scale cannot be directly determined because the absolute value for the maximum altitude is not known.

We attempted to determine the absolute scale by comparing the measured curve with a simulated curve calculated from Equation (8) of Section 2.1.1. By varying the altitude of the first point a least squares fit between the measured curve and the model curve was found as a function of starting altitude. The fit was found only in the last half of the curves, i.e., the higher altitudes, where the aerosol contribution is minimal and the measured data should be very close to the simulated data.



In such a comparison of curves, one expects to require some adjustment of the brightness as well as the altitude because there are uncertainties in both the measured data and the model. We assumed variations of the form $S_i = a T_i + b$ where the S_i are the model values and the T_i are the measured data values. For each choice of starting altitude, a and b are obtained through a least squares solution of an overdetermined set of equations. Scan points used for S_i and T_i were chosen to weight the second half of the curves. Only every tenth point was included from the first half of the curves. Every point was included from the second half. It was hoped that a would be very close to one, and b close to zero. In that case, one would have some confidence in the absolute altitudes obtained.

The inversion of the data was carried out in two ways. The first was to simply invert the measured data using the information of Section 2.1.2. Only the relative altitudes, which were known, are required for this. This leads to an altitude profile for β whose relative scale is known but whose absolute position in space is not known. This can be determined approximately by relating it to the absolute altitude scale determined by the procedure described above or by comparing this profile to the one in the Elterman model.

The second data inversion technique involved inverting the data after it had been transformed using the coefficients a and b determined above. The process was the same except that the data had been scaled with a and b .

3.1.2 Position in Scan of Maximum Altitude Not Known

In the case where no peak is present, the analysis is complicated by the fact that there is no direct method for determining even the relative altitudes.

In this case the data curve was also fit to the model by finding the least squares solution to the overdetermined set of linear equations, $a t_i + b = S_i$, where t_i is the measured brightness and S_i is the model brightness at the same altitude.

The altitudes were assigned using an iterative process which varies both with the assignment of an altitude to the first data point and with the assignment of the increment between the first two altitudes. As shown



earlier the first increment determines all subsequent intervals. An initial estimate of altitude was made based on the point of maximum slope of the curve. The point of maximum slope of the data is assumed to be at the same altitude as the model. This assumption could be in error by 3 Km but it serves well as a first estimate. By allowing the data to converge on a best fit the unknown constants are determined. An obvious shortcoming of this technique is the severe dependency on the model. In an attempt to bracket the results the two Elterman^{1,2} models of 1964 and 1968 were used as, respectively, a low and a high aerosol content stratosphere.

3.2 THE S191 DATA

The first step in analyzing the S191 data was to average several adjacent intensity values within a spectral scan. Although this decreases spectral resolution it was necessary in order to reduce the random noise within each data value caused by low irradiance. Table 5 gives the spectral bands created in this way

Relative altitude increments were determined as described in Section 2.1.4; the absolute altitudes were not known. In the same manner as was described in Section 3.1.1 for S192, the data was compared to a simulated curve calculated from Equation (8) of Section 2.1.1 in order to determine absolute altitudes. Again it was hoped that the scaling constants determined by the least squares solution of the comparison would only slightly modify the calibration provided with the data by NASA.

Table 5. S191 Spectral Bands

Band	Spectral Range (μm)	Average Wavelength (μm)
1	.46 - .50	.48
2	.51 - .55	.53
3	.56 - .60	.58
4	.61 - .65	.63
5	.66 - .70	.68
6	.71 - .75	.73
7	.76 - .80	.78
8	.81 - .85	.83
9	.86 - .90	.88
10	.915 - .945	.93
11	.96 - .99	.975



3.3 THE S190A DATA

Calibration of film densities is done by constructing a density vs. log exposure curve from a calibration step wedge. These curves are given for each roll of original film. We have duplicate film, so certain steps must be taken to construct this curve.

Machine calibration step wedges and the density measured at each step by PTD* are supplied. There is a separate step wedge for each of the three duplicate film types. Using the densities that we measured on these step wedges, and those supplied, a machine cross-calibration curve was constructed for each duplicate film type. With these curves, densities measured by PTD can be converted to equivalent densities which we would have measured with our densitometer.

We were supplied with the densities measured by PTD on the step wedge for each duplicate roll of film. Using the machine cross-calibration curve, these densities were converted to the densities which we would have measured. Because each step on a duplicate step wedge corresponds to the same log exposure increment as the same step on the original step wedge, log exposure values for the densities we measure can be found by a user duplicate density vs. original log exposure curve.

The original log exposure at each step is found from the log exposure at the first step of the wedge plus the log exposure increment for each step. The log exposure at the first step is supplied in the Sensitometric Data Package. These values must be adjusted for conversion from the Wratten filter, used in the construction of the step wedges to the flight type filter. These adjustment factors are also supplied in the Sensitometric Data Package. The log exposure increments were supplied by Harold Lockwood of Technicolor Graphic Services, Inc.

Log exposure is first converted to exposure, then exposure is converted to radiance values by the following equation

$$R = \frac{E \cdot 4 F^2 \cdot 10^{-7}}{\pi T t}$$

where

R = radiance incident at the lens in Watt/cm²

E = exposure in ergs/cm²

*Photographic Technology Division - NASA JSC



F = f-stop number

T = optical system transmission

t = duration of exposure in seconds

Sensitivity is lost in the film duplication process. Figures 18 through 21 show the original and duplicate characteristic curves for Rolls 43, 44, 47 and 48 (Stations 1, 2, 5 and 6) of Pass 47. The loss of sensitivity is readily observable from these curves. As many as 10 density levels (steps of the step wedge) with a change in density of 1 on the original film produce constant density on the duplicate film. Only 7 steps of the step wedge or 0.1.05 log exposure units lie within the linear portion of the curve.

The S190A data was measured as duplicate film density with a 400 x 20 μm aperture densitometer oriented with length tangent to the earth.

In addition to the convolution filter inherent in using a 400 x 20 μm aperture, the values were further filtered with a fourteen point convolution filter. This was necessary because the film grain noise still dominated the density fluctuations.

As with the other sensors, the absolute altitudes and altitude increment were unknown. In the manner described in Section 3.1.1, the data was best fit to a model brightness curve by iterating on starting altitude and increment, to determine altitudes, scaled brightness values and attenuation coefficient profiles.

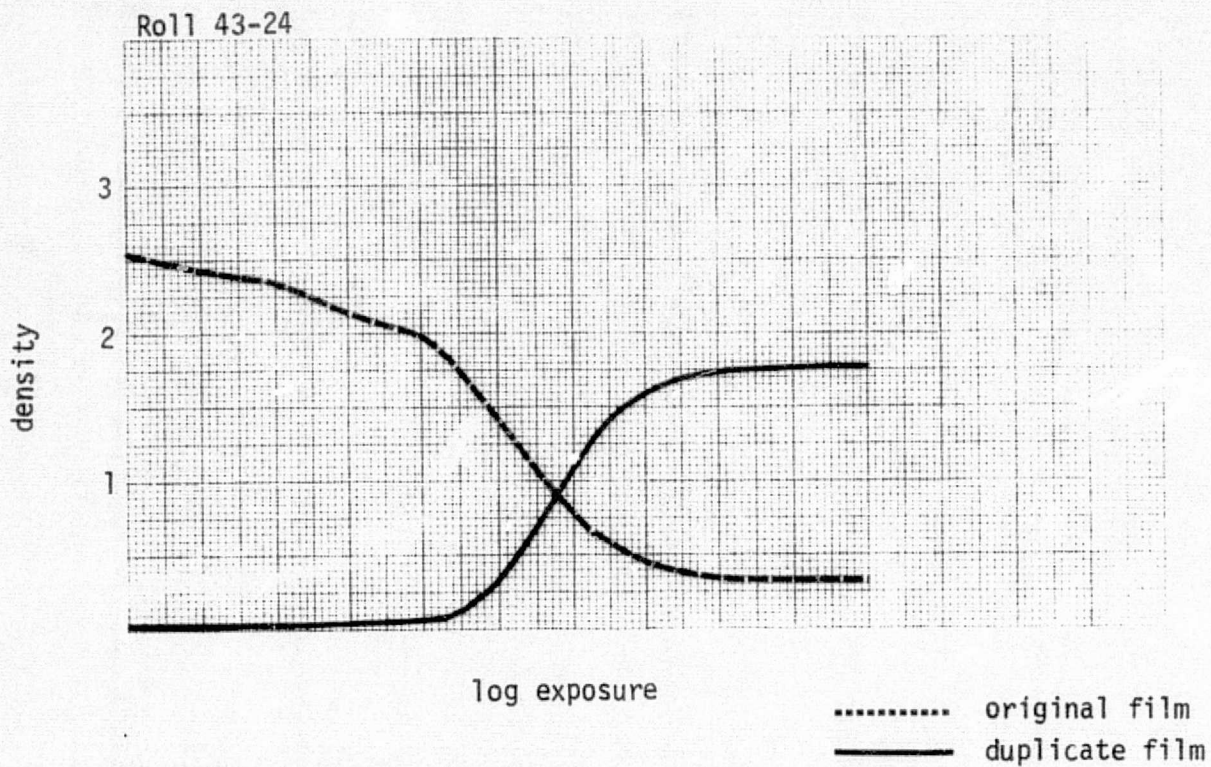


Figure 18 S190A--Pass 47, D-log E Curves for Original and Duplicate Film. Roll 43-24.

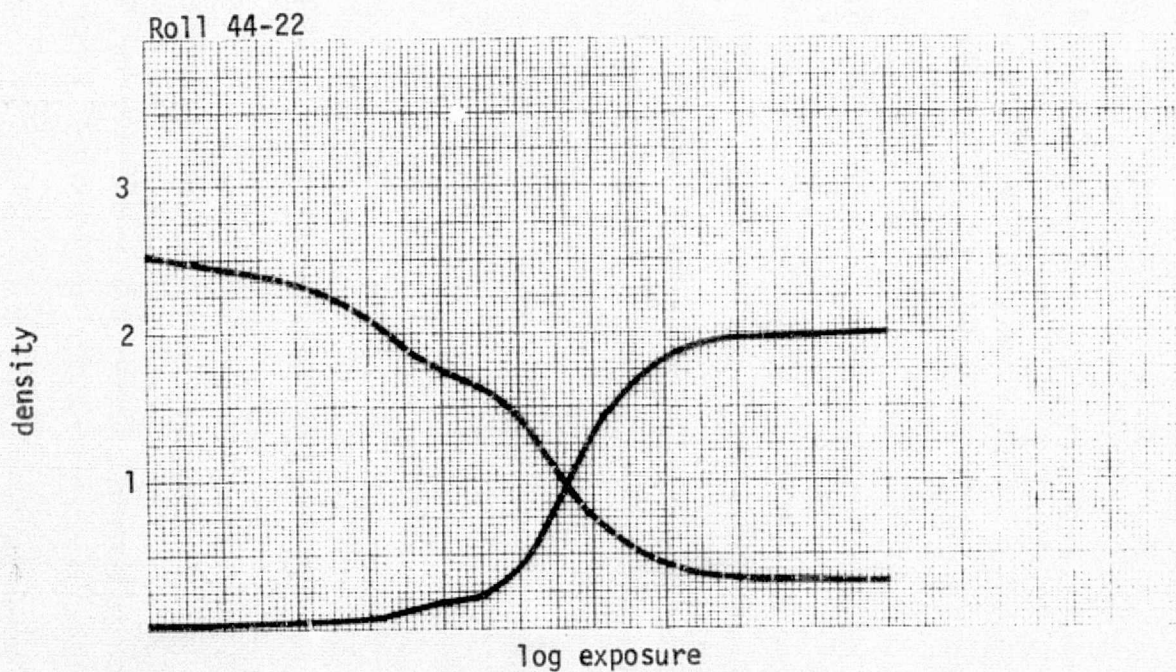


Figure 19 S190A--Pass 47, D-log E Curves for Original and Duplicate Film. Roll 44-22

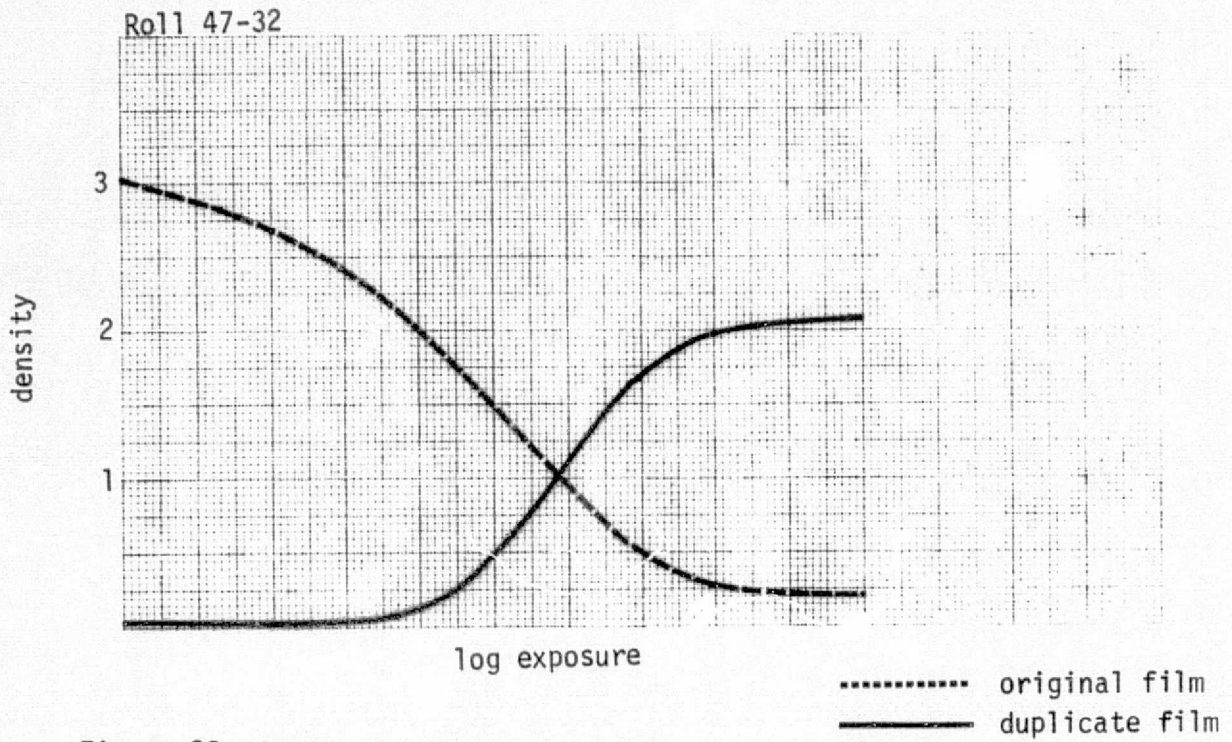


Figure 20 S190A--Pass 47, D-log Curves for Original and Duplicate Film. Roll 47-32.

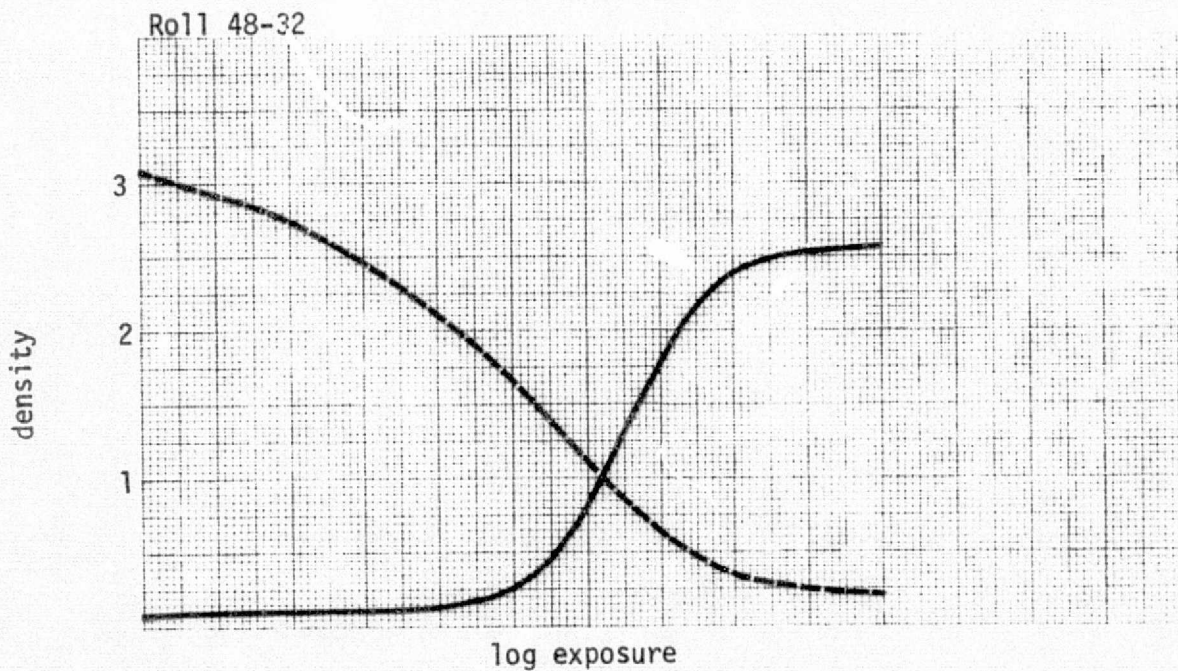


Figure 21. S190A--Pass 47, D-log E Curves for Original and Duplicate Film. Roll 48-32.



4.0 RESULTS

S192 Results

One of the more interesting results was observed in the S192 data (pages 49 through 82). A peak was apparent in the lower altitudes that was not present in the shorter wavelengths and grew with increasing wavelength beginning with band 7 (.825 μm). Figures on pages 49 through 72 are the radiance values in milliwatts/cm²- μm -str from pass 61. Each has been averaged over twenty-five scans to remove most of the random noise. However, it is apparent that some random noise still remains. The first twelve charts are from scans 100-124; the second twelve charts are from scans 600-624 showing the continuance for several kilometers. Pages 73 through 82 show a similar peak from pass 47. These ten charts were scaled to an inaccurate model which therefore nullifies the radiance and altitude values shown. However, the charts serve to illustrate the similar wavelength dependent peak. Judging from the altitude values obtained from the scaling process previously described (and illustrated below) one can estimate the altitude of the peaks to be around 11 Km. There were cirrus clouds present in the S190A imagery. We therefore suggest that the peak could be a cirrus cloud at about 36,000 ft. The wavelength dependence is due to the limb view. The blue portions of the incident light are scattered out of the incident path. The cloud scatters red light which is further reddened through its path out of the atmosphere. Hence the sensor detects only the longer wavelength radiation. The shorter wavelength radiation effectively does not reach the lower level at which the cloud is seen.

The charts of pages 83 through 87 are the attenuation coefficients for ten S192 wavelengths obtained by inverting data from pass 61. The relative altitude increment was determined by knowledge of the relative position of the highest point in the scan arc as was described earlier. The data was not scaled in intensity or altitude. The results are therefore valuable to identify relative values and fluctuations in the attenuation coefficients. Comparison with various models or previous results would be necessary to assign altitudes, however assignment can be done by comparison with the following charts. To scale them accurately in this way would require an additional least squares curve matching which was not performed. A general interpretation is also possible simply by noting the attenuation



coefficient values and the relative variations. These variations may be due to sensor noise or to aerosol variations. We were unable to complete a study of these possibilities due to other complications.

The charts of pages 88 through 159 contain the results of scaling and inverting the SI92 data for passes 47 and 61 using the variable altitude and increment scheme as previously discussed. The data is presented by pass, for the two models. Each result is represented as three charts: (1) the limb brightness measurement as scaled with the model used to scale, (2) the attenuation coefficients obtained by inverting the brightness with the model for a Rayleigh atmosphere (no aerosols) and with the model attenuation coefficients (the first and last 5 points should be disregarded due to deviations inherent in the Fourier inversion process), and (3) a ratio of the aerosol and Rayleigh coefficients to accentuate layers.

Table 7 shows the additive and multiplicative scale factors applied to the data. Since one would expect the multiplicative factor, a , to be near unity if the NASA provided calibration were close, only those results which used factors close to unity are presented here. One would also expect that the additive bias, b , would be small compared to the data. The actual criteria used to select the best results were as follows:

- 1) $.95 \leq a \leq 1.1$
- 2) $b < 0$ and $.5 \leq \frac{|b|}{\text{deep space value}} \leq 1.5$
- 3) a good agreement in brightness values between the model and the measurements for the upper half of the curve.

Among things apparent in the data is a layer centered at 40 Km about 10 Km deep, a layer at 35 Km of approximately the same depth and one at from 20 to 25 Km from 5 to 10 Km deep.

The 40 Km layer is apparent in the plots on pages 90, 99, 102, 111, 120, 135 and 156. Of these scans, all but those on pages 102 and 120 meet the criteria established above. The plot on 120 meets the criteria except that $|b|/\text{deep space value} = .35$, slightly smaller than allowed. All of these plots are for bands 1 or 2.

Pages on which the 35 Km layer can be seen are 93, 105, 108, 114, 117, 126, 132, 141, 144, 150, 153 and 159. Only the scans on pages 153 and 159 meet the criteria, and the fit for the data on page 159 (seen on page 157)



is suspicious because of the large deviation in the first half of the curve from the model and previous results.

It seems that the apparent layers seen at 35 Km and 40 Km represent a single layer which is located in the inversion process at different altitudes due to inaccurate scaling. Because five of seven scans that placed the layer at 40 Km meet the above criteria and a sixth (No. 120) almost does but only two of twelve that placed it at 35 Km meet the criteria, we conclude that 40 Km is most likely the correct altitude of the layer.

We acquire more confidence in the 40 Km results when we note that in pairs the charts represent the same data scaled to the two models; that is, Charts 90 and 111, Charts 99 and 120, and Charts 135 and 156 are the results of scaling and inverting three data sets to the 1964 and 1968 models respectively. The first two sets are band 1 from pass 47 at two different locations (different scan numbers). The third dataset is band 2 from pass 61 which, of course, is a third location. The numerical results between models remain significantly different. Within each model the results for the 40 Km layer are consistent: the 1964 model places the attenuation coefficient ratio of aerosol to Rayleigh at .1; the 1968 places the value at .23.

In reviewing the 20 Km layer one must account for the inherent error in the first few points caused by the inversion process. With this in mind, almost all of the S192 charts indicate a large 20 Km layer exists. Again, where we restrict our attention to those which satisfy the above criteria for a successful scale, charts 90, 99, 111, 135, and 156 emerge. And again we will include chart 120 which almost satisfies it. As before, Charts 90 and 111 represent the results using models 1964 and 1968 respectively, as do Charts 97 and 120 and Charts 135 and 156, for the same measured data. Each of the pair of charts represent a different location (scan number or pass). The numerical results are model dependent but consistent within each model: the 1964 model finds the attenuation coefficient ratio (aerosol:Rayleigh) to be about .1; the 1968 model finds it to be between .75 and 1.0.

S191 Results

The S191 was a much more sensitive instrument than the S192 but apparently its absolute radiometric calibration was less accurate. Hence, the criteria for selecting the best S191 scaling and inversion results were changed from the S192 criteria as follows:



- 1) $.75 < a < 1.25$
- 2) a good agreement in brightness values between the model and the measurements for the upper two thirds of the curve
- 3) No defined restriction on the bias value, b , because a deep space value was not obtained.

Where the S192 instrument was sensitive in the lower wavelengths to about 45 Km, the S191 instrument was sensitive to about 70 Km. Hence, we could require that a larger portion of the brightness curve match the model since the model is less influenced by aerosol changes in these regions. Also, the restrictions on the multiplicative scale factor, a , was relaxed as a result of the documentation stating that S191 radiometric values could be in error by 15%. The only restriction on the bias value, b , was that it be small in comparison to the data values.

Aerosol layers are apparent in many bands at about 20, 40, 50, 60, and 67 Km. Those at 20 and 40 Km are consistent with the S192 results. Charts 160-201 contain S191 charts of the results. All show several layers consistent among themselves. Charts 162, 165, 174, and 183 are those which satisfy the above criteria. Table 6 summarizes the information on these charts showing for each chart the location of an aerosol layer and the value of the attenuation coefficient ratio (aerosol:Rayleigh) at that location.

Within the 1964 model (No. 162, 165, and 174) is an indication of the wavelength dependence of the layer, and hence its aerosol size. However, one must be careful not to conclude too much from such few data points. It would be valuable to extract more points from the S191 data in the future to better derive conclusions. From the information in table 6 we note that layers at 40, 50, and 55 Km are more responsive to the longer wavelengths shown while layers at 59 and 66 Km are most responsive around $.53 \mu$ falling off at higher and lower wavelengths.

Charts 162 and 183 are the results of scaling and inverting the same data to the 1964 model and the 1968 model, respectively. Note that the same layers are evident but the derived attenuation coefficient values, and hence the ratios (aerosol:Rayleigh) are different. For example, respectively for the 1964 model and the 1968 model ratio values obtained are .07 and .24 at 23 Km, .04 and .22 at 39 Km, .09 and .26 at 48 Km, and .7 and .86 at 59 Km.



		Approximate Altitude									Wavelength	Model
Chart No. (Page No.)		15	20	30	40	50	55	60		65		
162	a)		23	29	39	48	55	59		66	.48	64
	b)		.07	.05	.04	.09	.16	.7		.04		
165	a)		19		38	49		59		67	.53	64
	b)		-.2		.2	.4		1.		.7		
174	a)	14	19	29	41	47	52	59	63	68	.71	64
	b)	.1	.08	.04	.24	.58	.43	.43	.2	.04		
183	a)		23	30	39	48	55	59		67	.48	68
	b)		.24	.2	.22	.26	.37	.86		.3		

Table 6. S191 Summary Results
(a) Aerosol Layer Altitude
(b) Aerosol:Rayleigh attenuation coefficient ratio

S190A Results

The results from the S190 sensor must be presented as only qualitative since the attempts to scale and calibrate the data were unsatisfactory. This is undoubtedly because of the limited sensitivity of the duplicate film. The film was sensitive to light intensities below 30 Km where the scaling was severely model dependent. We therefore report the findings as relative and qualitative. The altitude and coefficient numbers are only for comparison between charts with no real world meaning. The data was scaled against two models which are labeled 1964 and 1968 models. These are not the same models used for the S191 and S192 data analysis, however, because of a programming error. It was felt that there was little advantage in redoing the work since the results were not quantitative anyway and the models served well enough to assign an approximate altitude sufficient for inversion.

For station 6, $\lambda = .55 \mu$, pages 204, 207, and 210 show the results from the 1964 model. Layers are apparent at 16, 22, and 26 Km. On pages 219, 222, and 225 the same data scaled to the 1968 model shows layers at 22, 26, and 32 Km.

For station 5, $\lambda = .68 \mu$, pages 213 and 216 show the results from the



1964 model. Layers are apparent at 15, 20, and 22 Km. The 1968 model results are shown on pages 228, 231, and 234. Page 237 contains results from station 2, $\lambda = .85 \mu\text{m}$ scaled to the 1968 model.



Table 7. Multiplicative and Additive ($\times 10^{-4}$) Scale Factors
for S192 Data, Passes 61 and 47

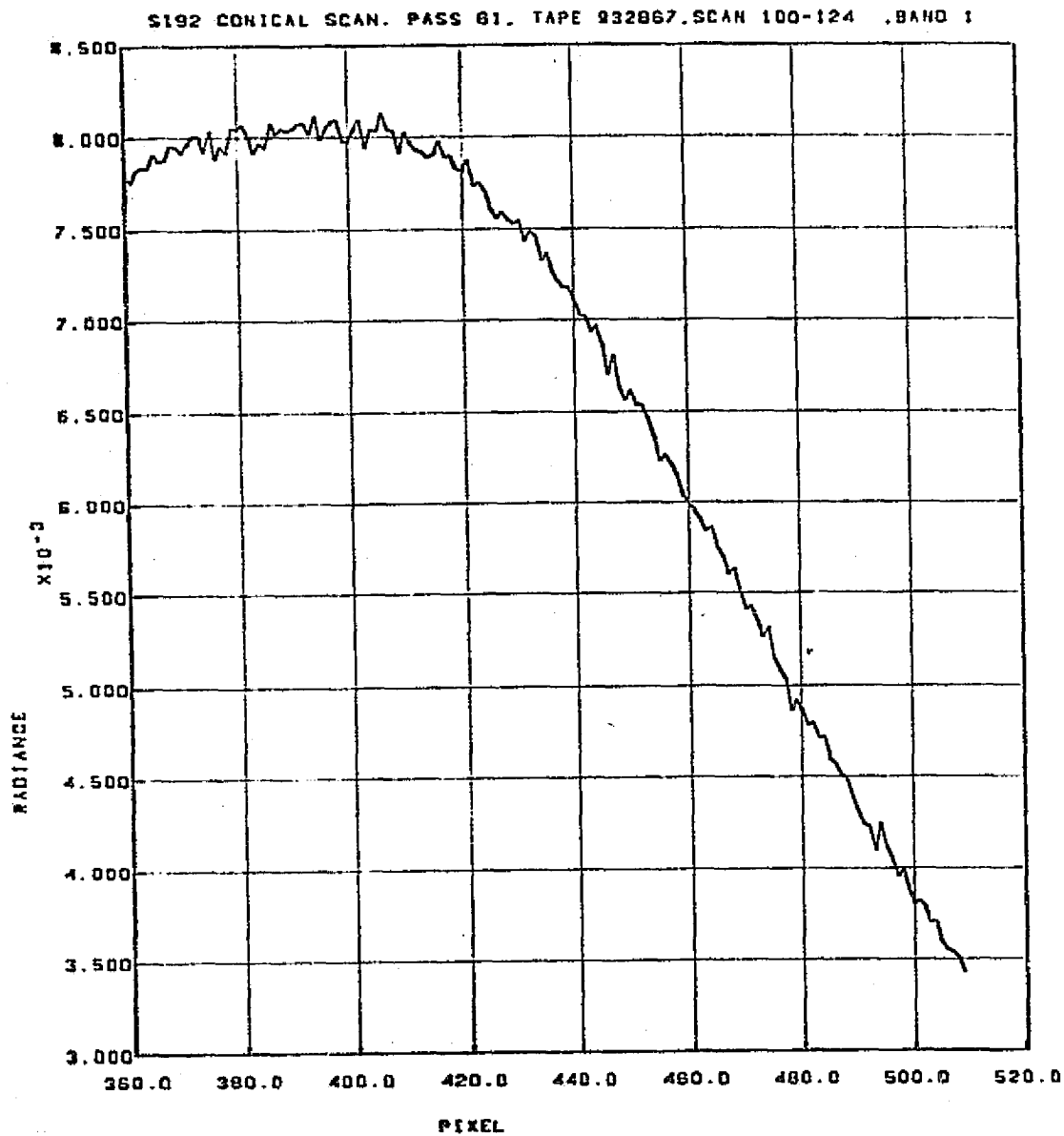
PASS 61								Dark Space
1964 Model					1968 Model			Bias Value
Scans	(100-124)	(600-624)	(120-144)	(100-124)	(600-624)	(120-144)	(x 10 ⁻⁴)	
Band								
1	a	-	.9576	-	1.0573	.9202	.9507	
	b	-	1.267	-	9.174	.6333	-1.242	
2	a	.9802	-	1.0726	-	1.105	1.0294	
	b	-1.200	-	-2.377	-	7.214	-1.716	
4	a	-	-	-	1.0621	1.1227	1.1087	
	b	-	-	-	4.049	-.9139	-1.690	

		PASS 47				Dark Space Bias Value ($\times 10^{-4}$)
		(100-124)	(350-374)	(100-124)	(350-374)	
1	a	.9990	.9956	.9545	.9522	
	b	-.8209	-.5310	-.520	-.3153	.899
2	a	-	1.1011	-	1.0608	
	b	-	-3.284	-	-2.636	1.583
3	a	.9955	1.0700	.9909	-	
	b	-3.475	-3.104	2.793	-	1.414
4	a	-	-	1.0255	-	
	b	-	-	-4.967	-	1.836
6	a	.9992	-	-	-	
	b	-2.874	-	-	-	.959
7	a	-	1.0245	-	1.0782	
	b	-	-3.333	-	-3.177	1.406



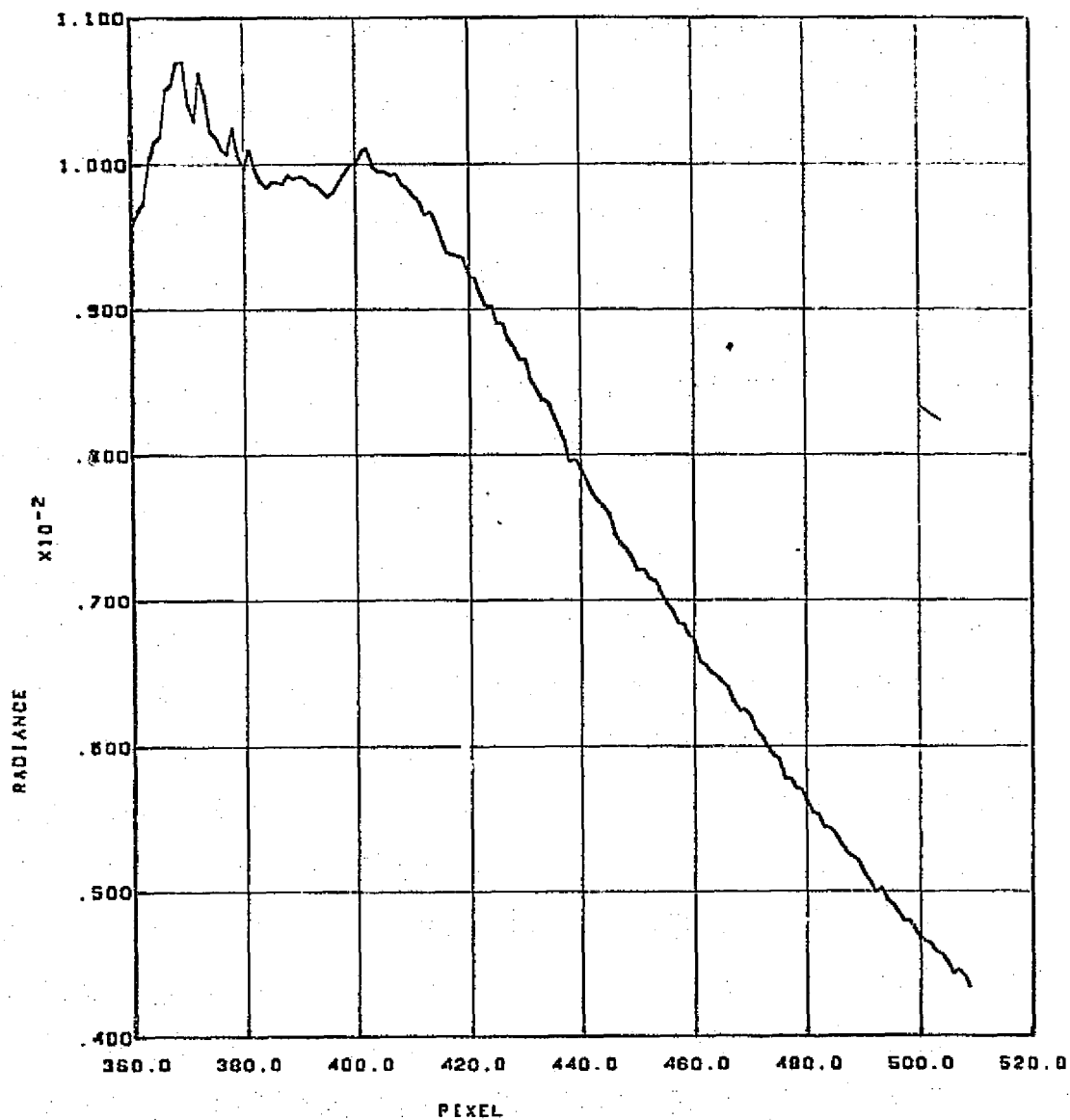
Table 8. Multiplicative Scale Factors for S191 Data, Pass 47

λ (μm)	1968 Model	1964 Model
.48	1.17	1.249
.53	.9283	.9904
.63	.5006 (x)	.5636 (x)
.68	.7477	.8978
.73	.8281	1.228
.78	.8607	1.611 (x)
.83	.8264	2.84 (x)

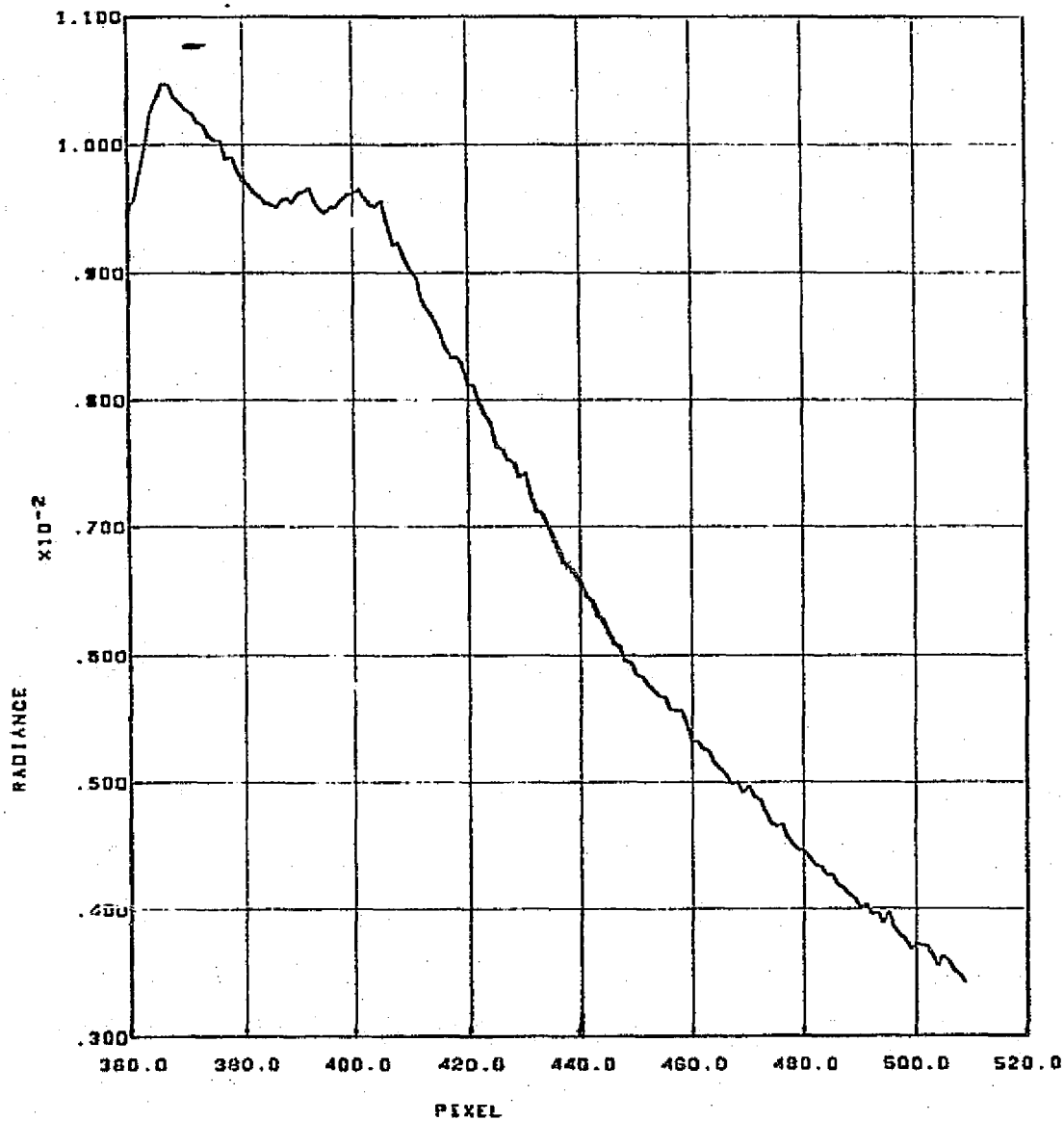


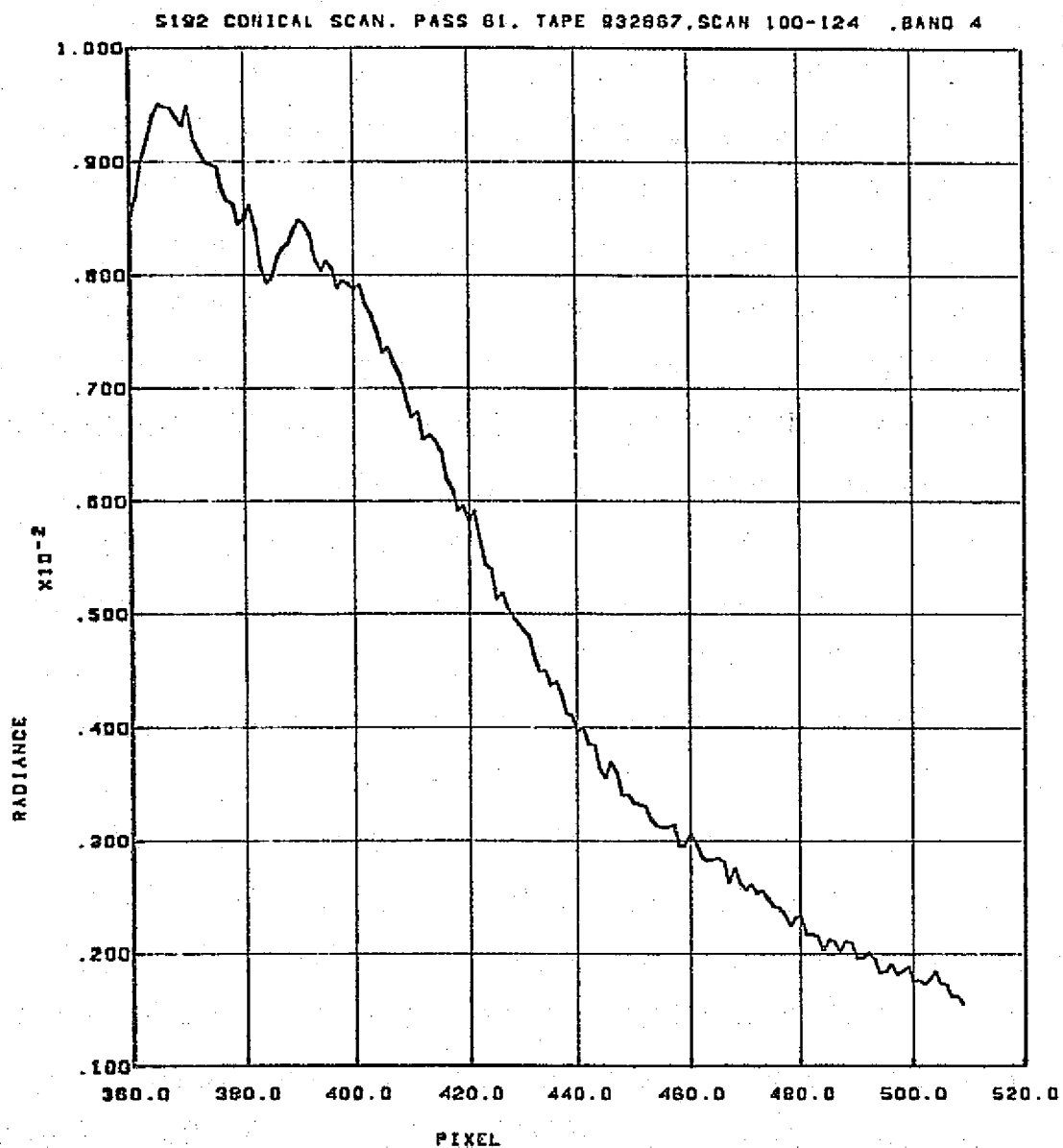
REPRODUCIBILITY OF THE
ORIGINAL PAGE IS POOR

S192 CONICAL SCAN, PASS 61, TAPE 932867, SCAN 100-124, BAND 2



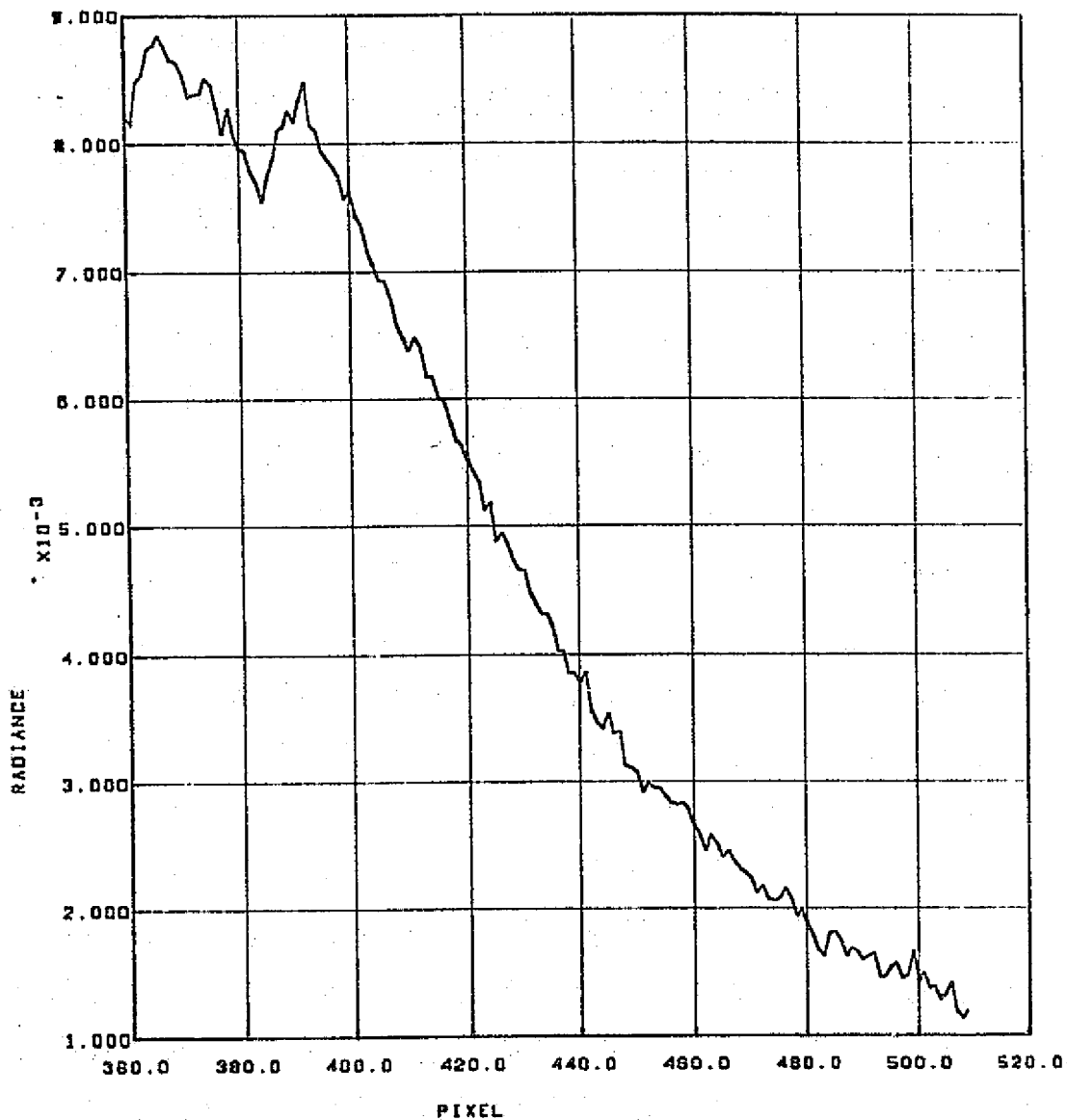
S192 CONICAL SCAN. PASS 61. TAPE 932867. SCAN 100-124 .BAND 3



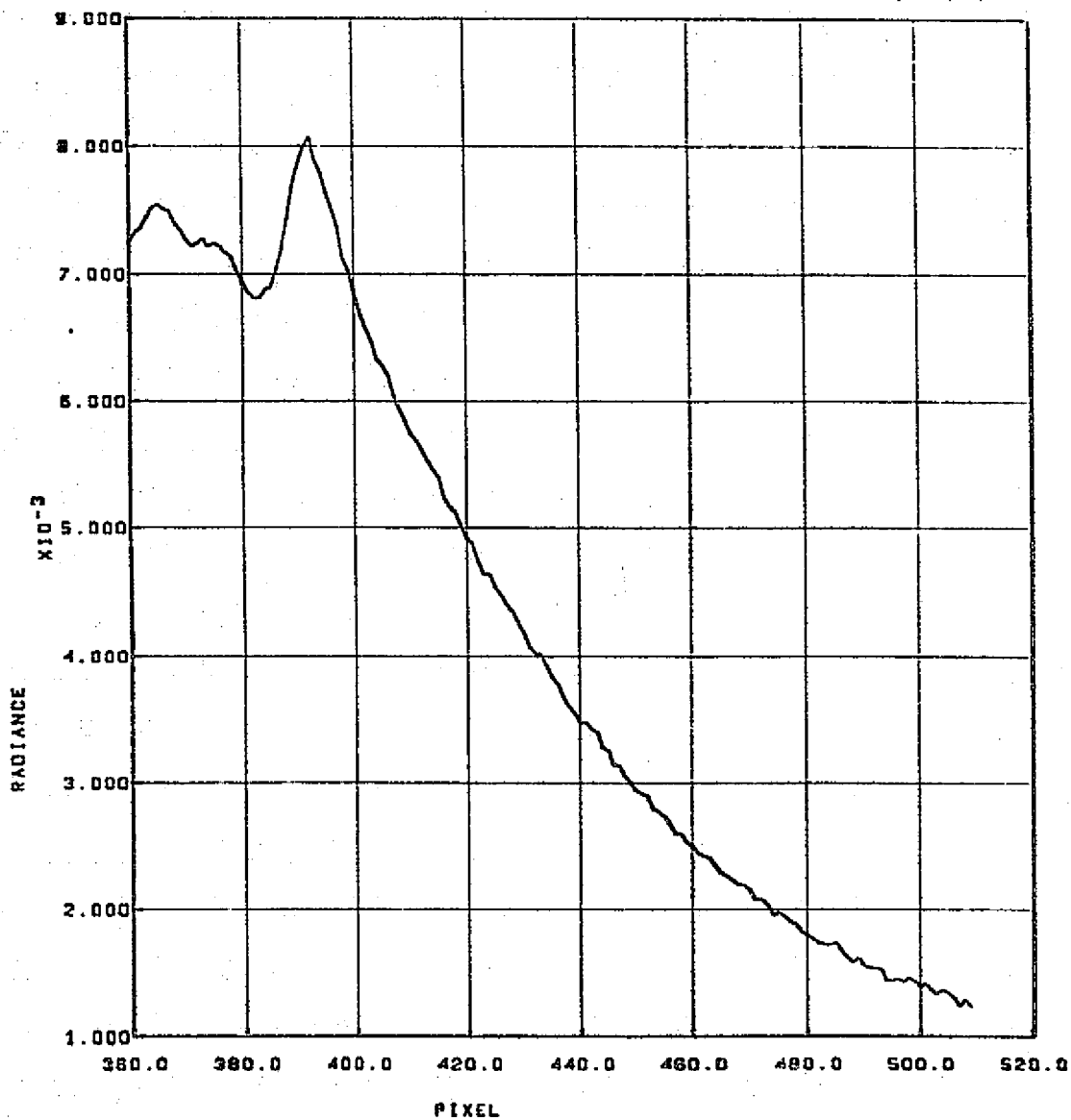


REPRODUCIBILITY OF THE
ORIGINAL PAGE IS POOR

S192 CONICAL SCAN. PASS 61. TAPE 932867. SCAN 100-124 .BAND 5

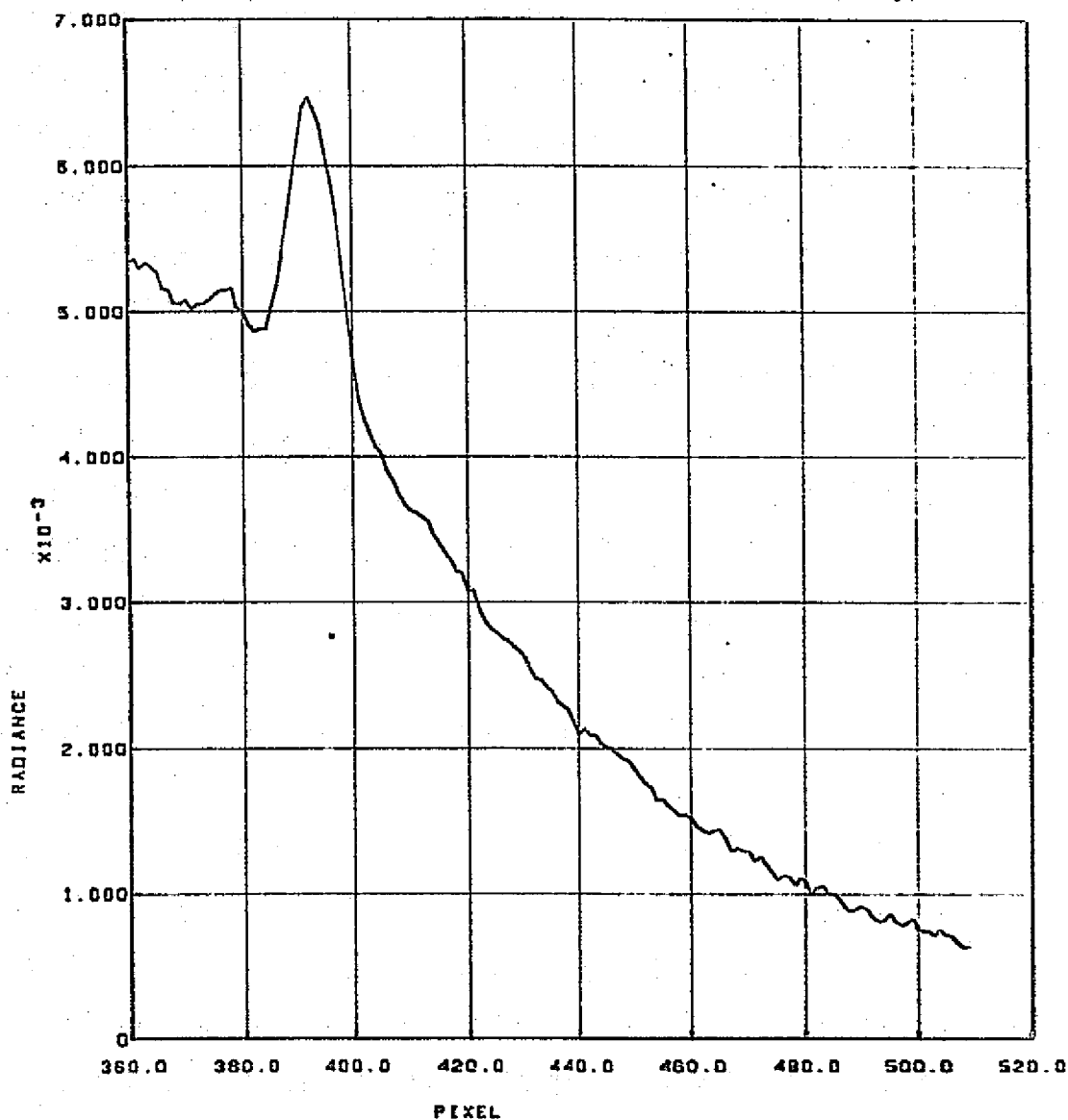


5122 CONICAL SCAN. PASS 61. TAPE 932867. SCAN 100-124 .BAND 6



811

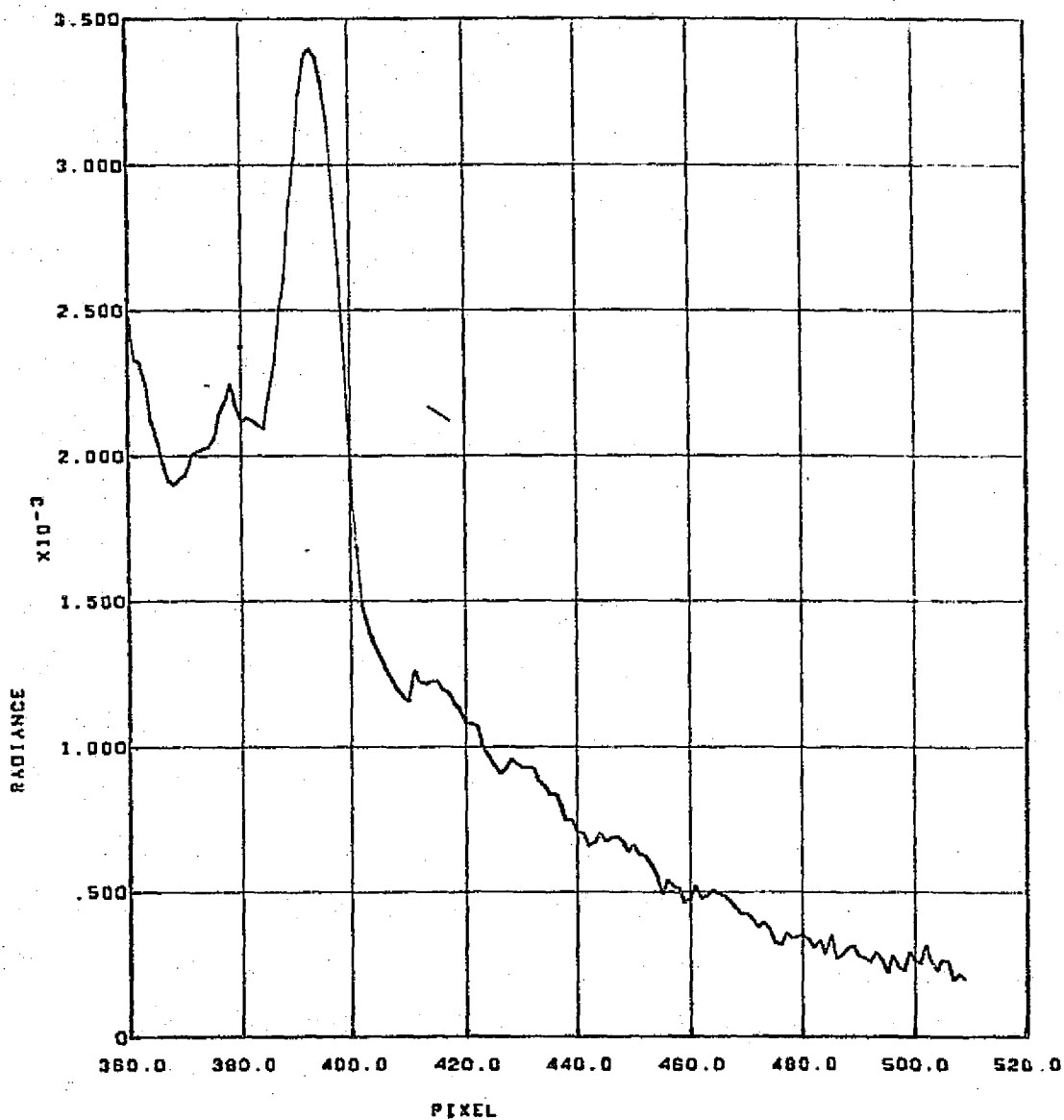
S192 CONICAL SCAN. PASS 61. TAPE 932067. SCAN 100-124 .BAND 7

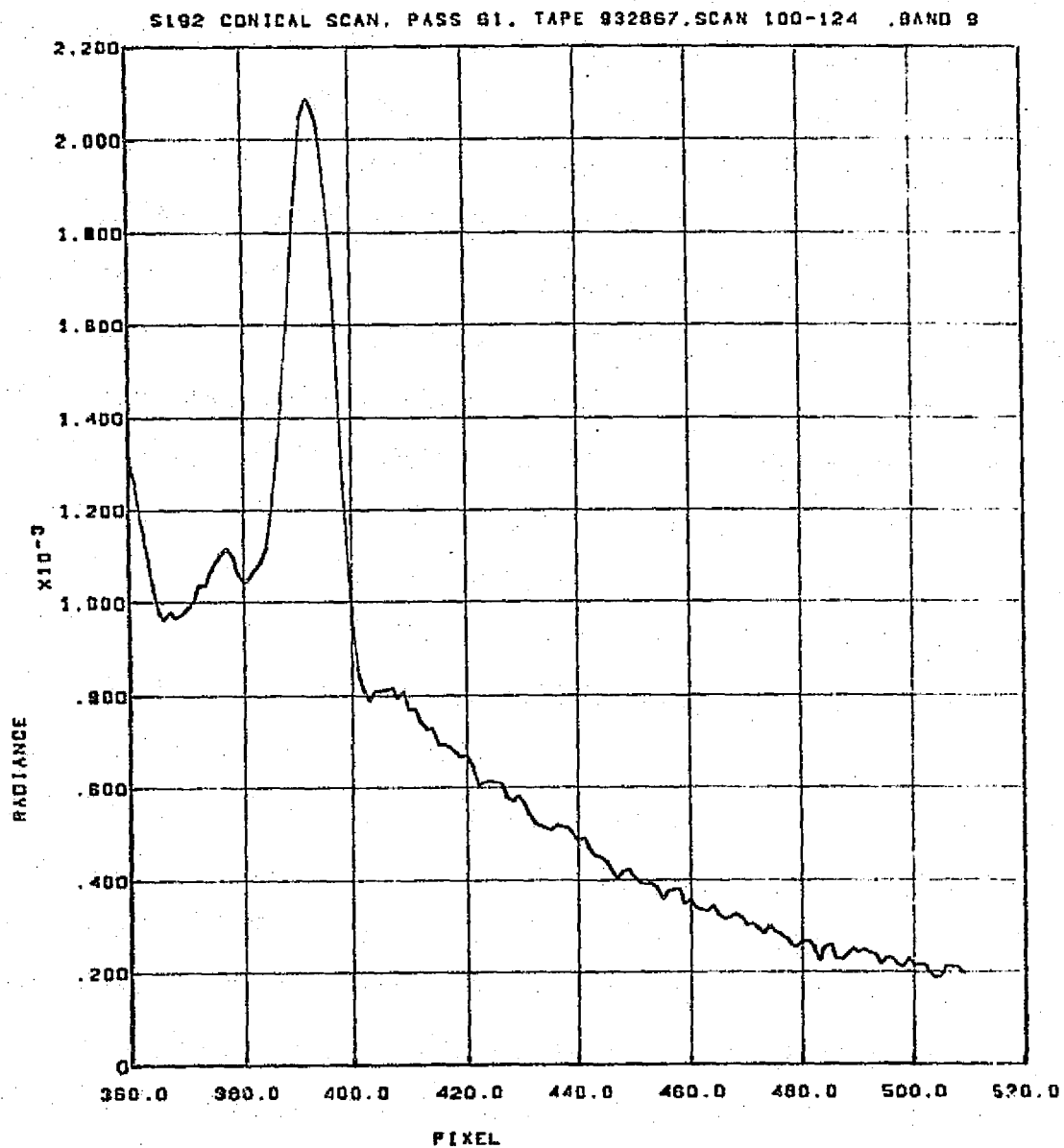


REPRODUCIBILITY OF THE
ORIGINAL PAGE IS POOR

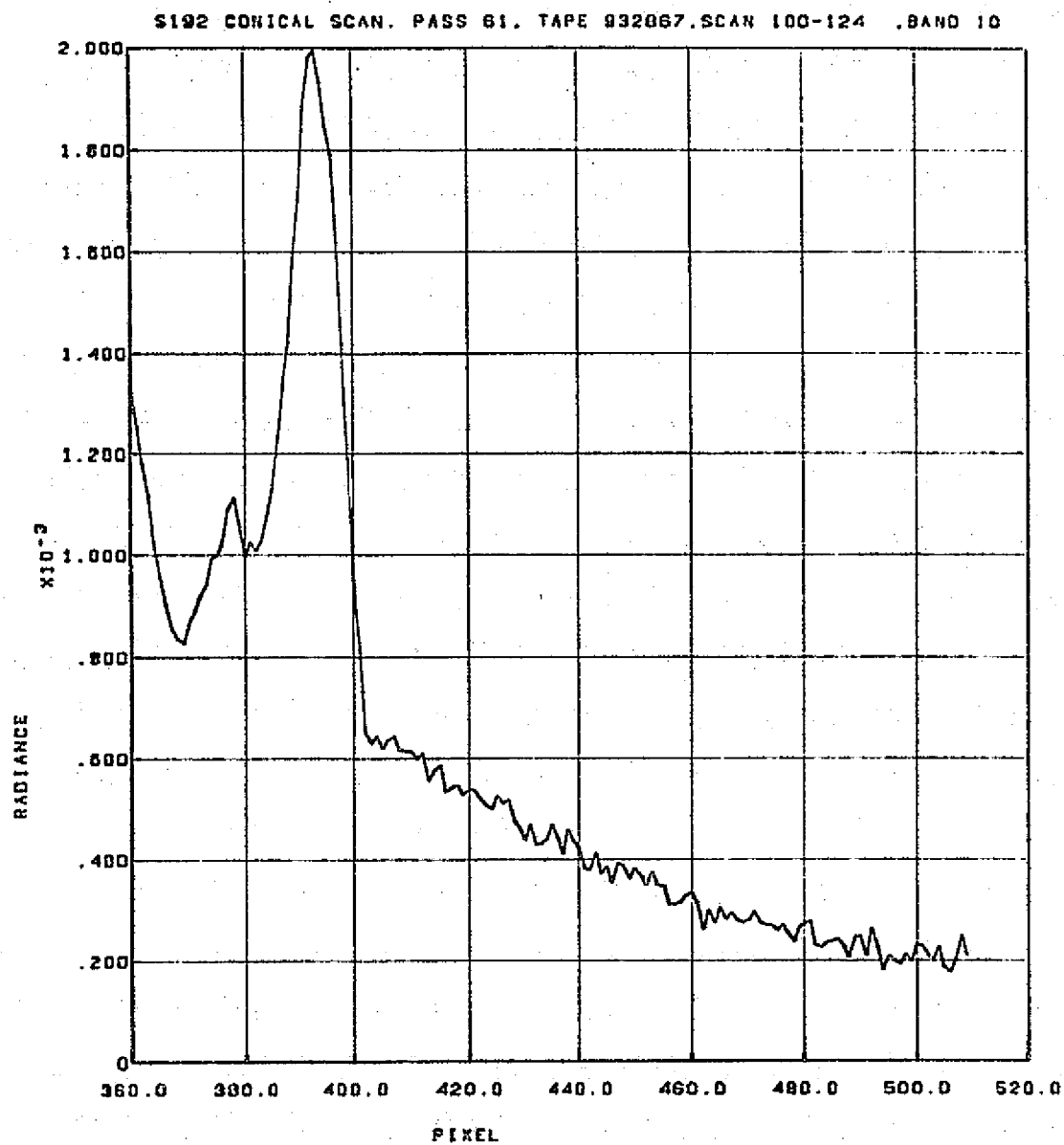
011

S192 CONICAL SCAN. PASS 61. TAPE 932867. SCAN 100-124 .BAND 8

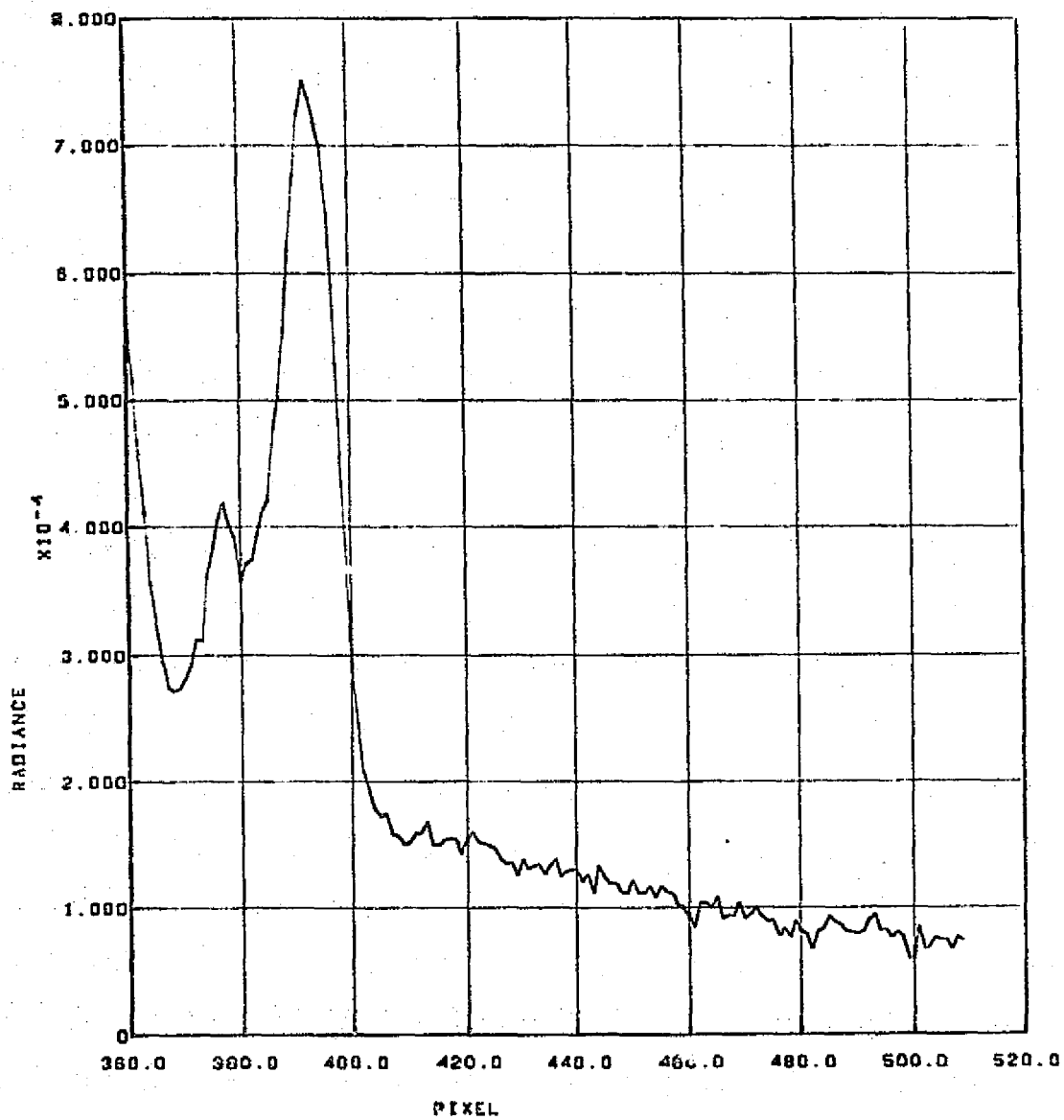


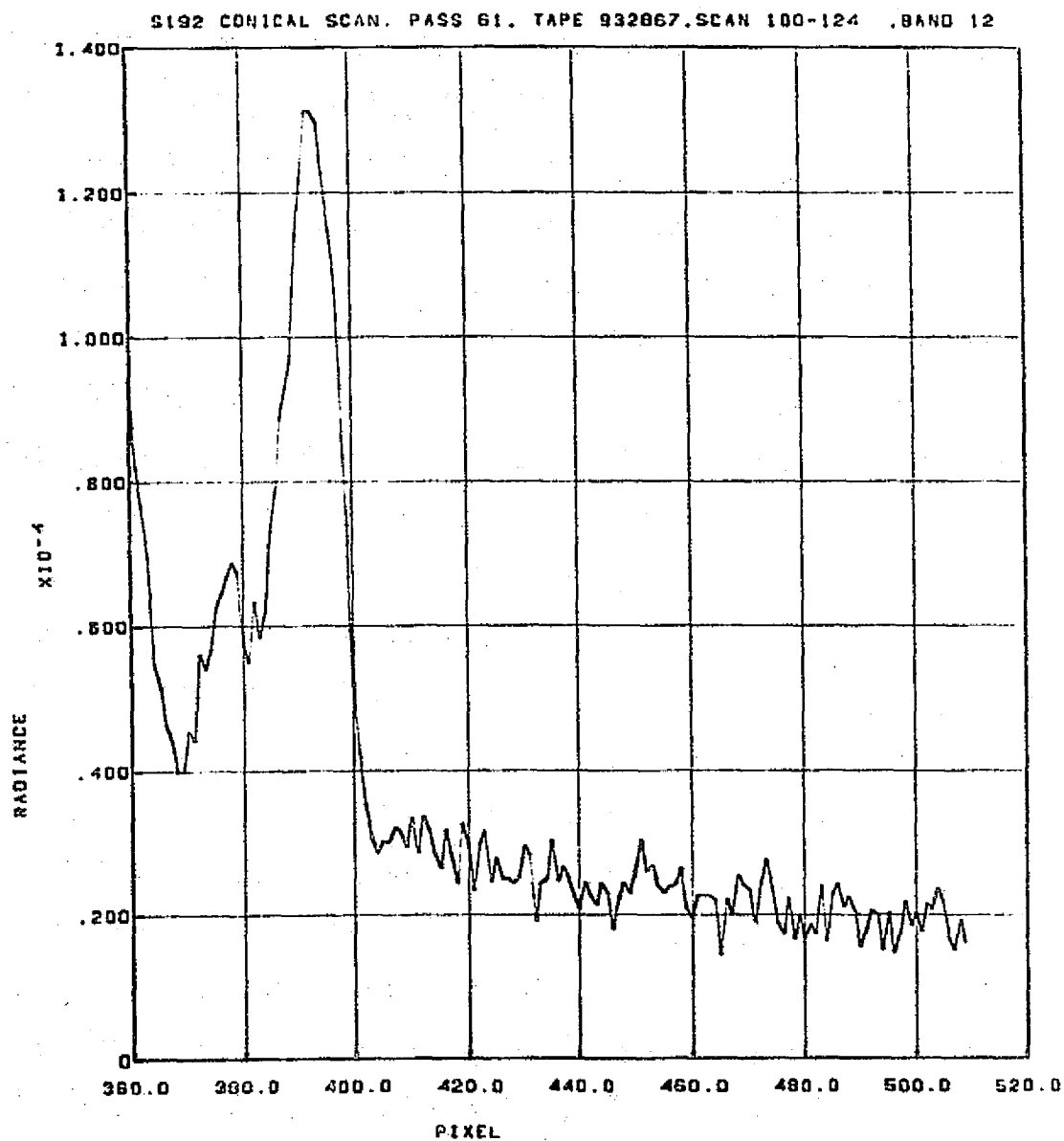


REPRODUCIBILITY OF THE
ORIGINAL PAGE IS POOR



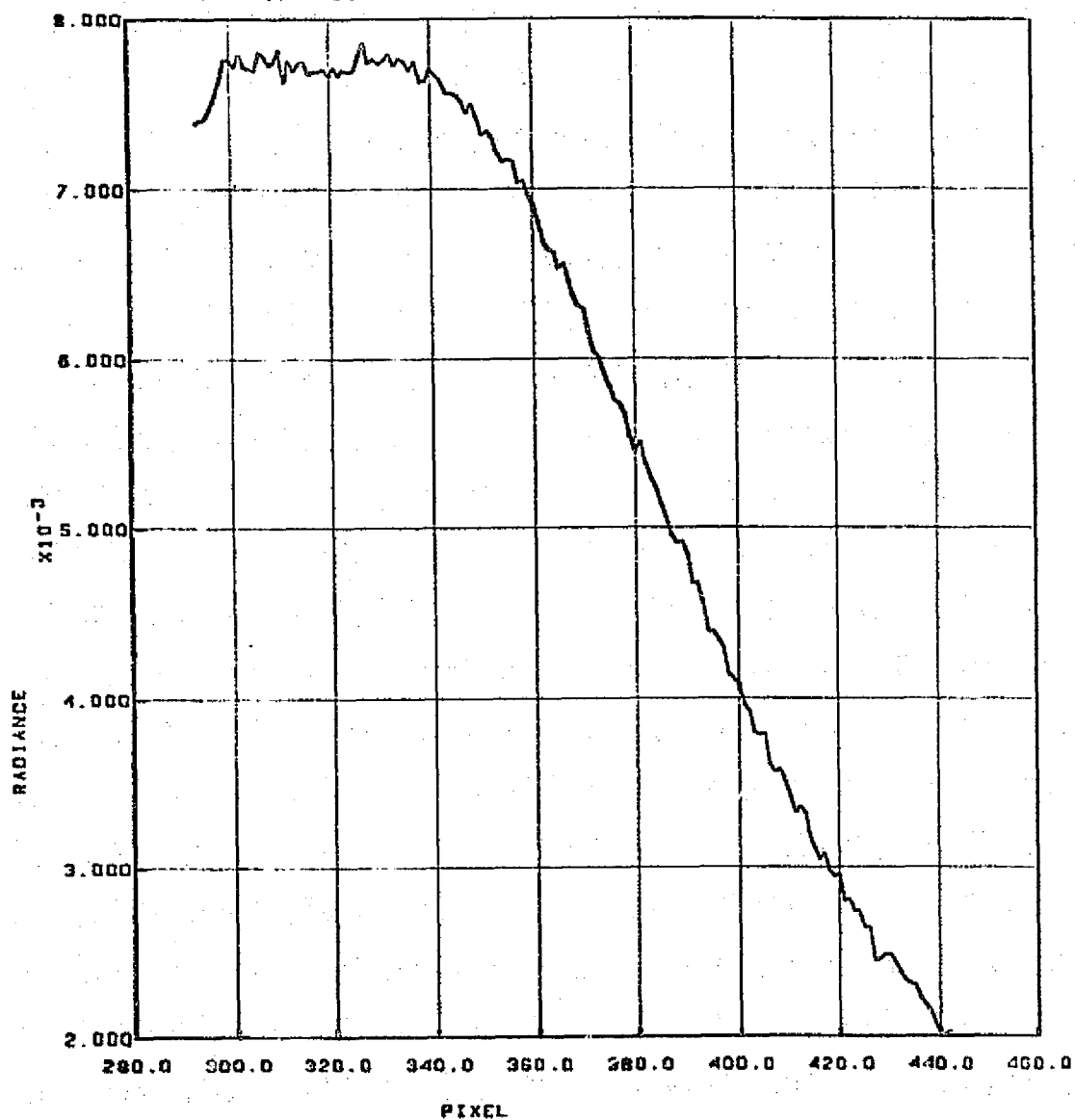
S192 CONICAL SCAN, PASS 81, TAPE 932867, SCAN 100-124, BAND 11



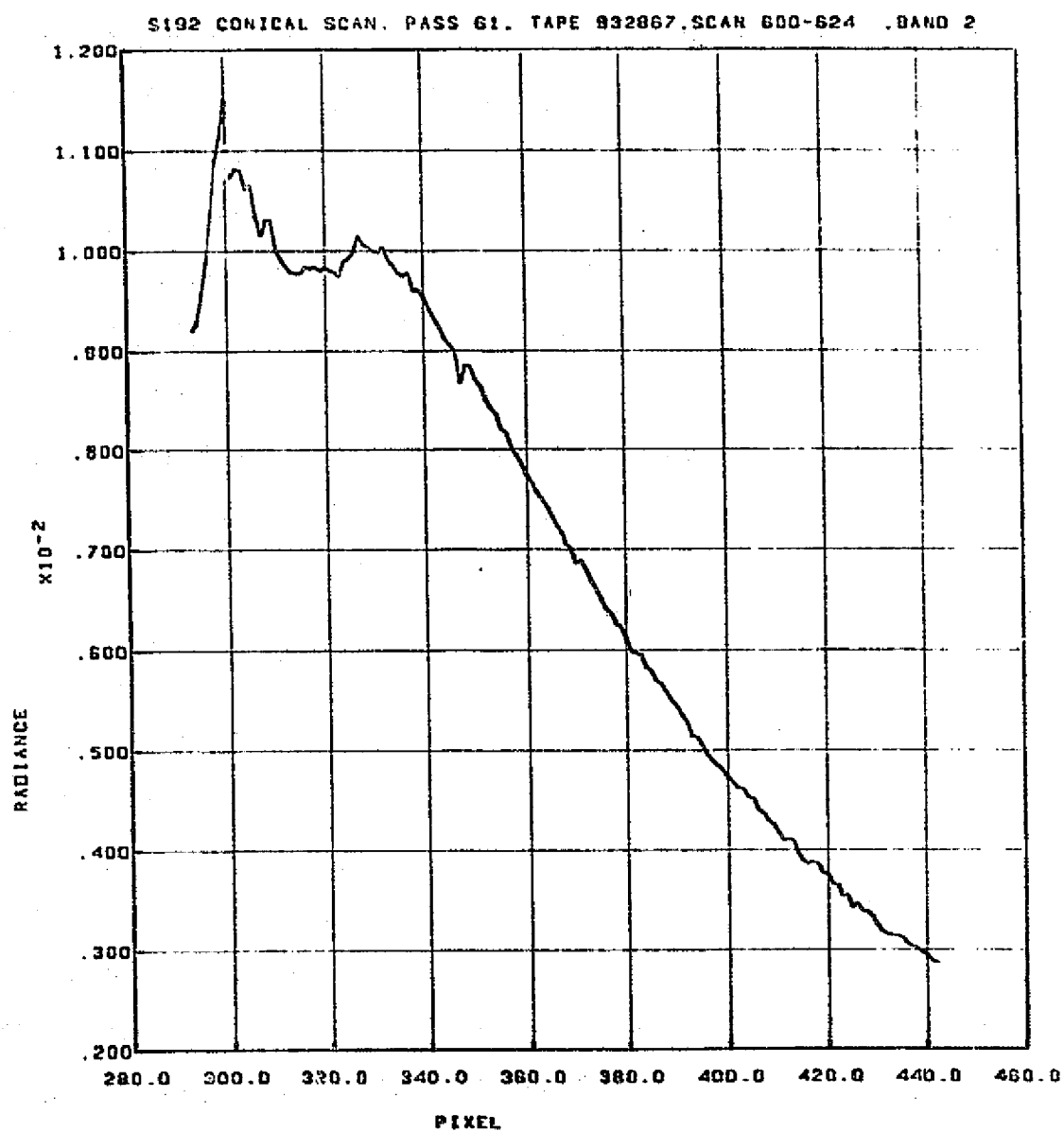


REPRODUCIBILITY OF THE
ORIGINAL PAGE IS POOR

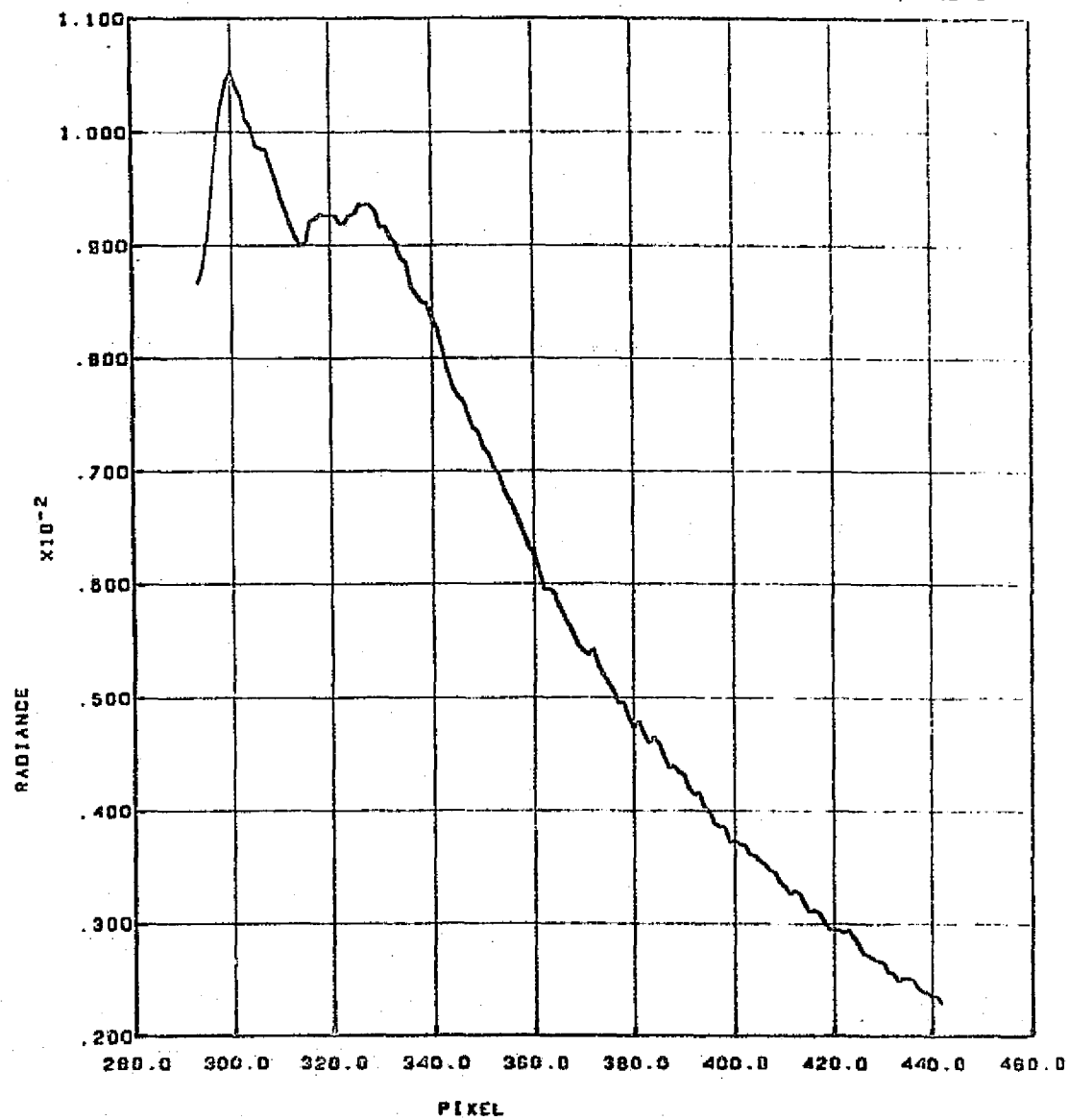
SI92 CONICAL SCAN. PASS 61. TAPE 932067. SCAN 600-624 .BAND 1



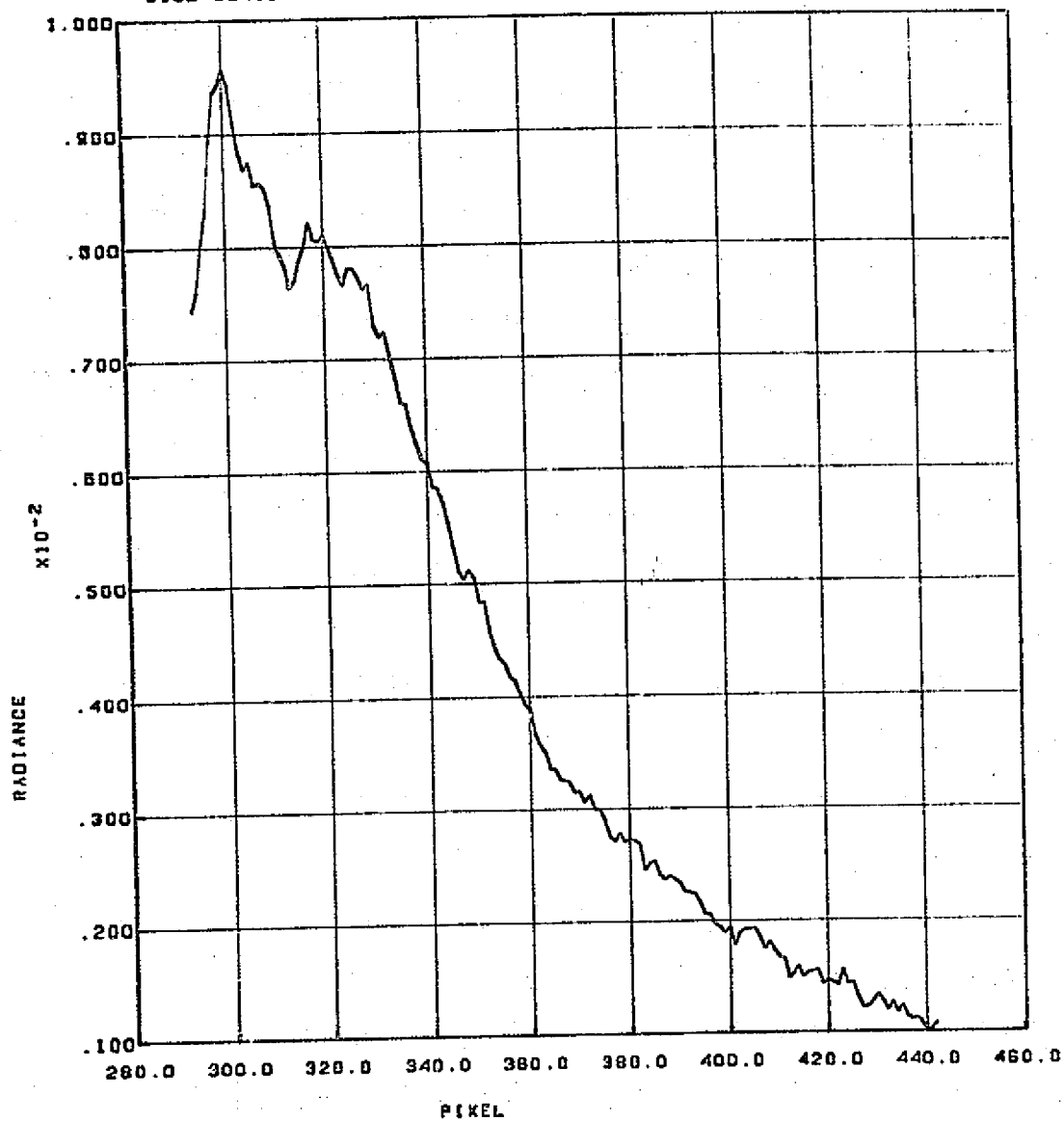
014.



S102 CONICAL SCAN. PASS 01. TAPE 932867, SCAN 600-624, BAND 3

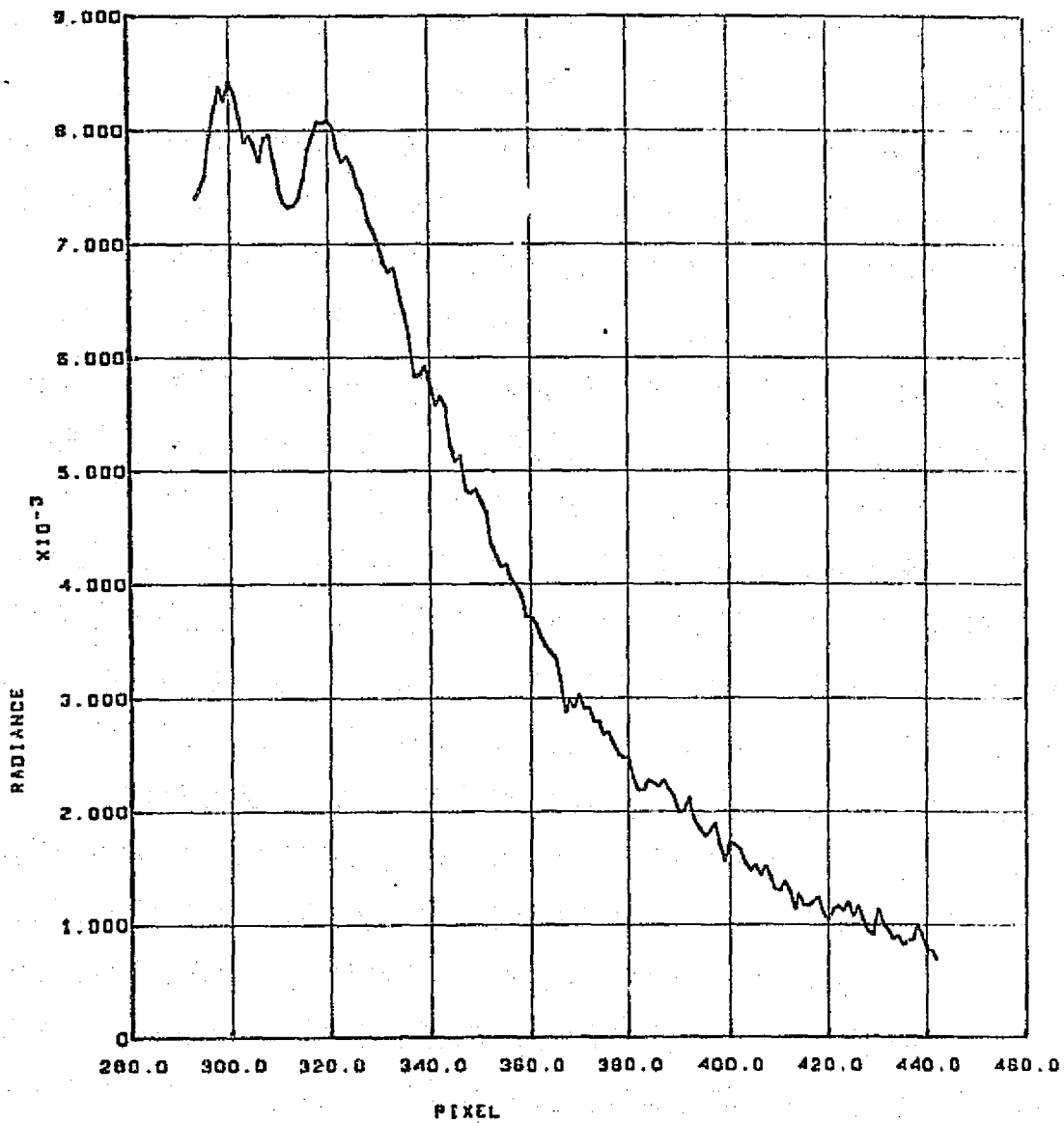


SI92 CONICAL SCAN. PASS 81. TAPE 932867. SCAN 600-624 .BAND 4

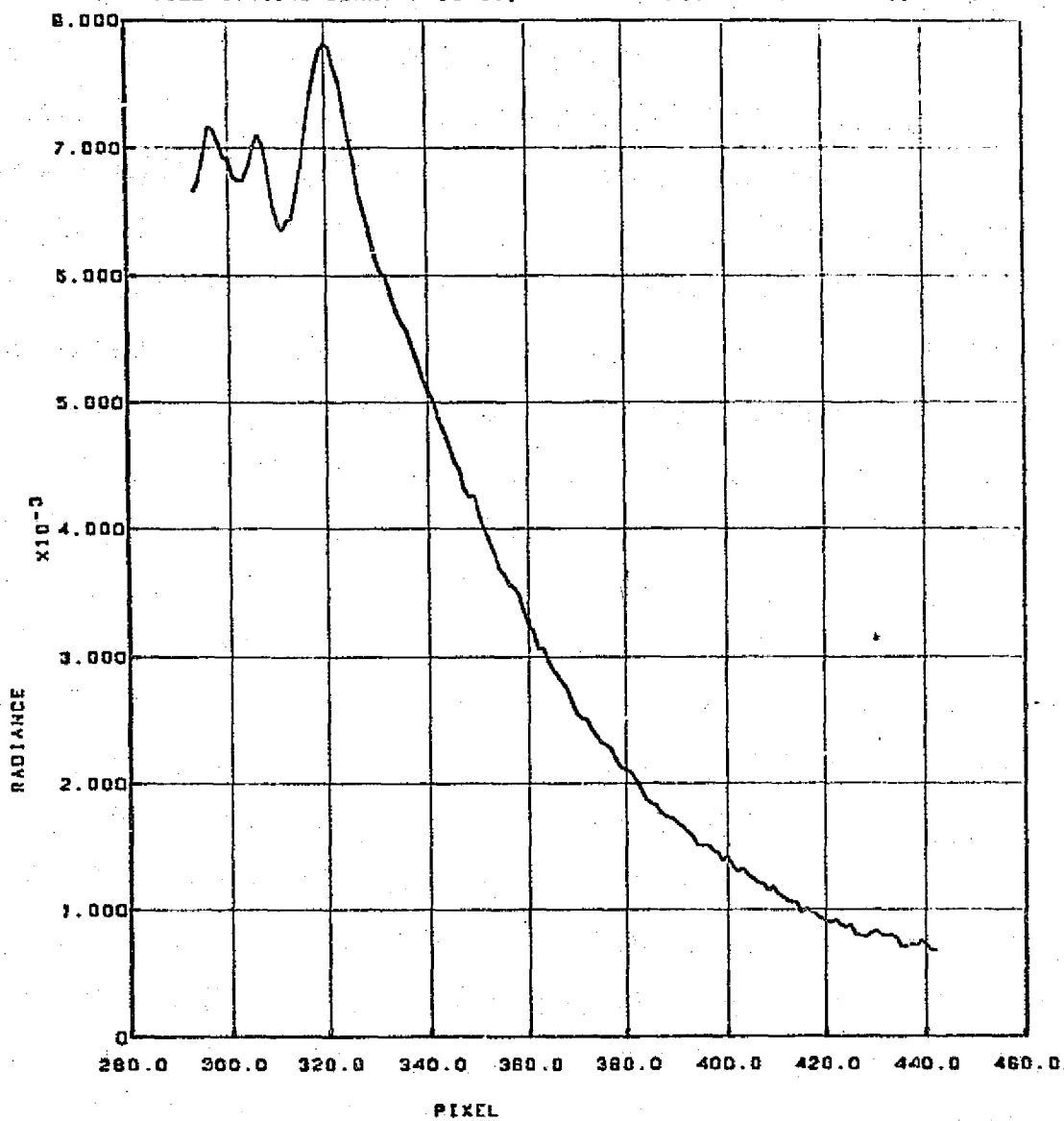


REPRODUCIBILITY OF THE
ORIGINAL PAGE IS POOR

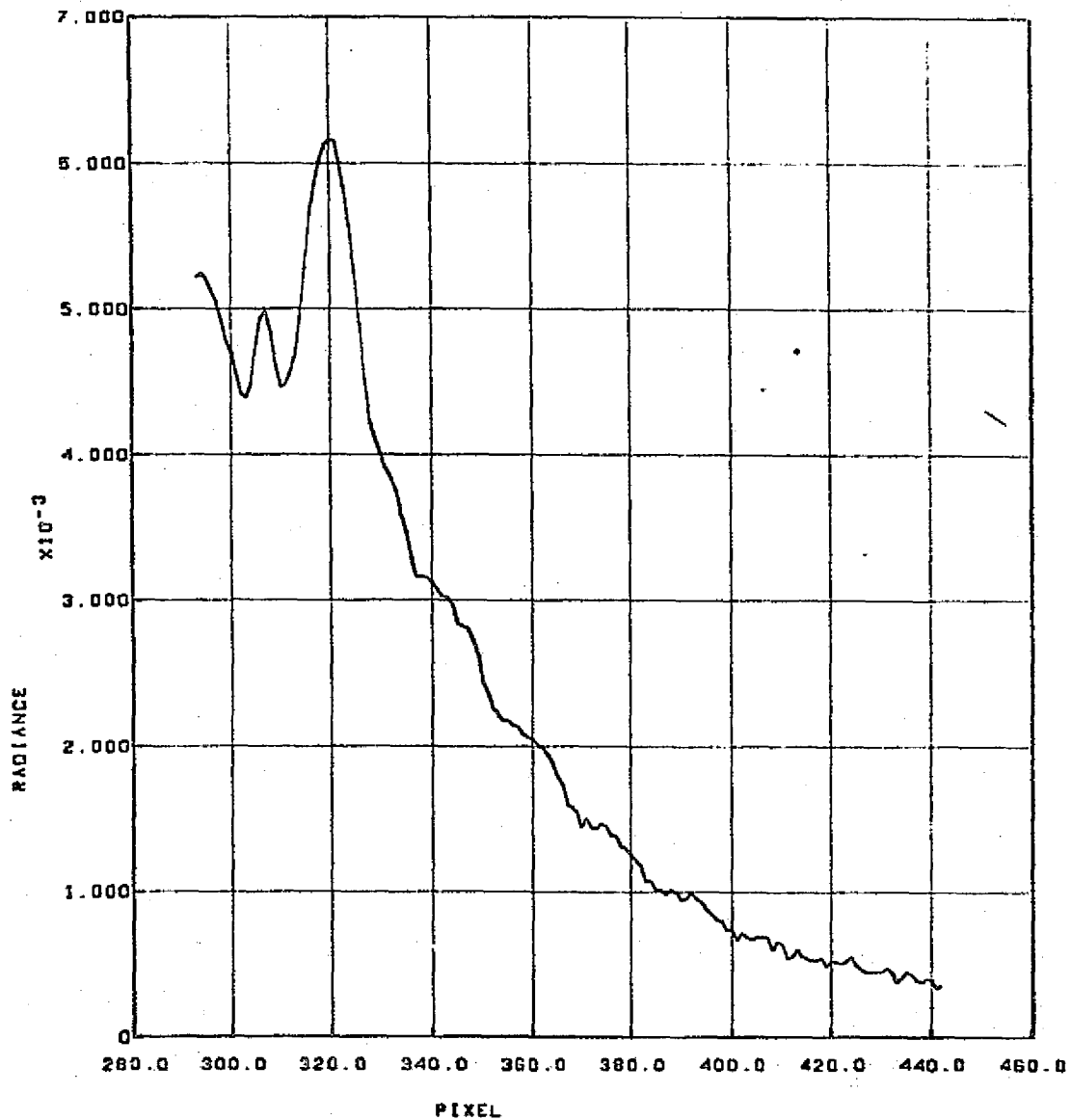
S192 CONICAL SCAN. PASS 61. TAPE 932867. SCAN 600-624 .BAND 5



S192 CONICAL SCAN. PASS 61. TAPE 932867. SCAN 600-624 .BAND 6

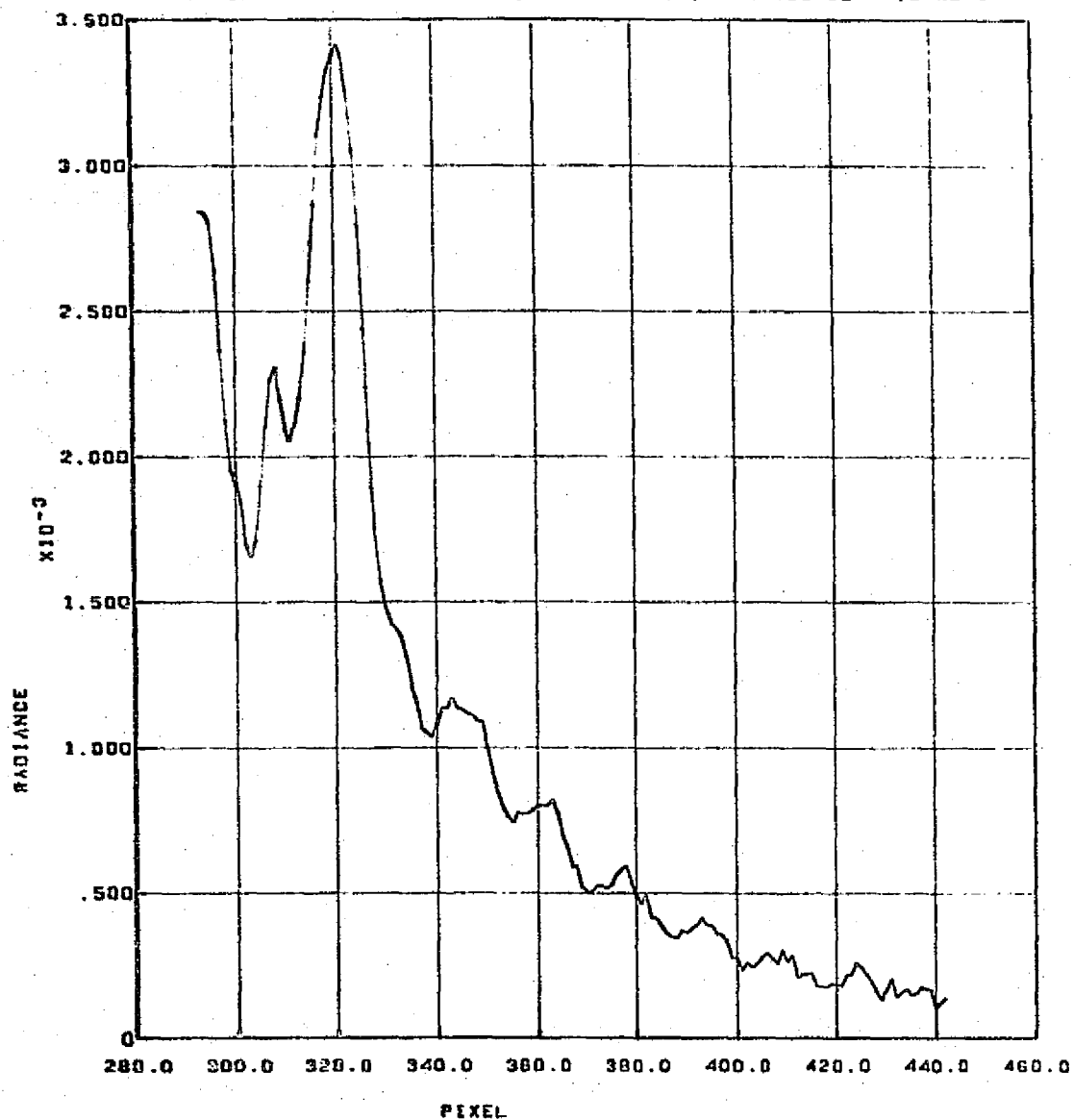


3192 CONICAL SCAN. PASS 61. TAPE 932867. SCAN 800-824 .BAND 7

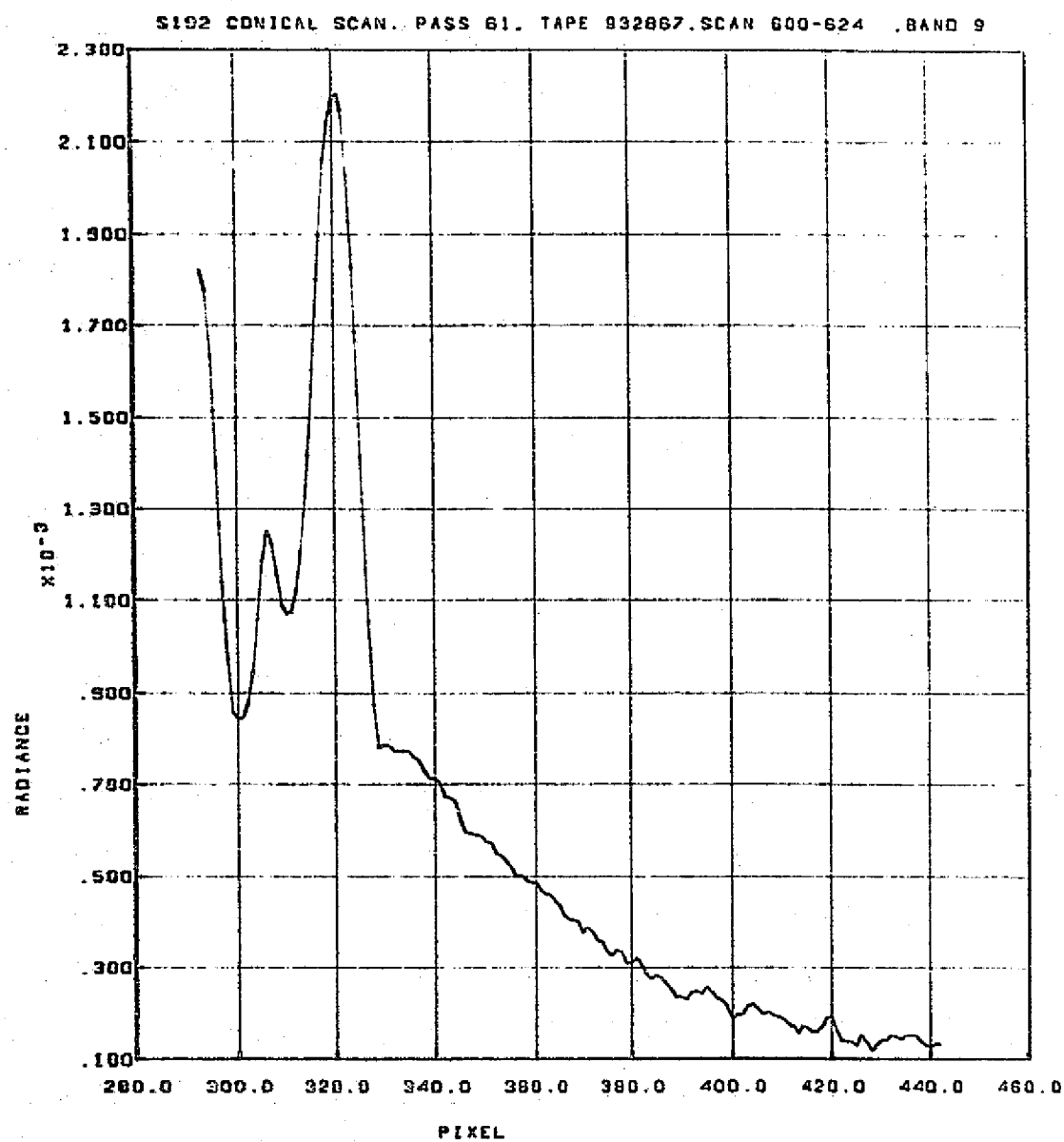


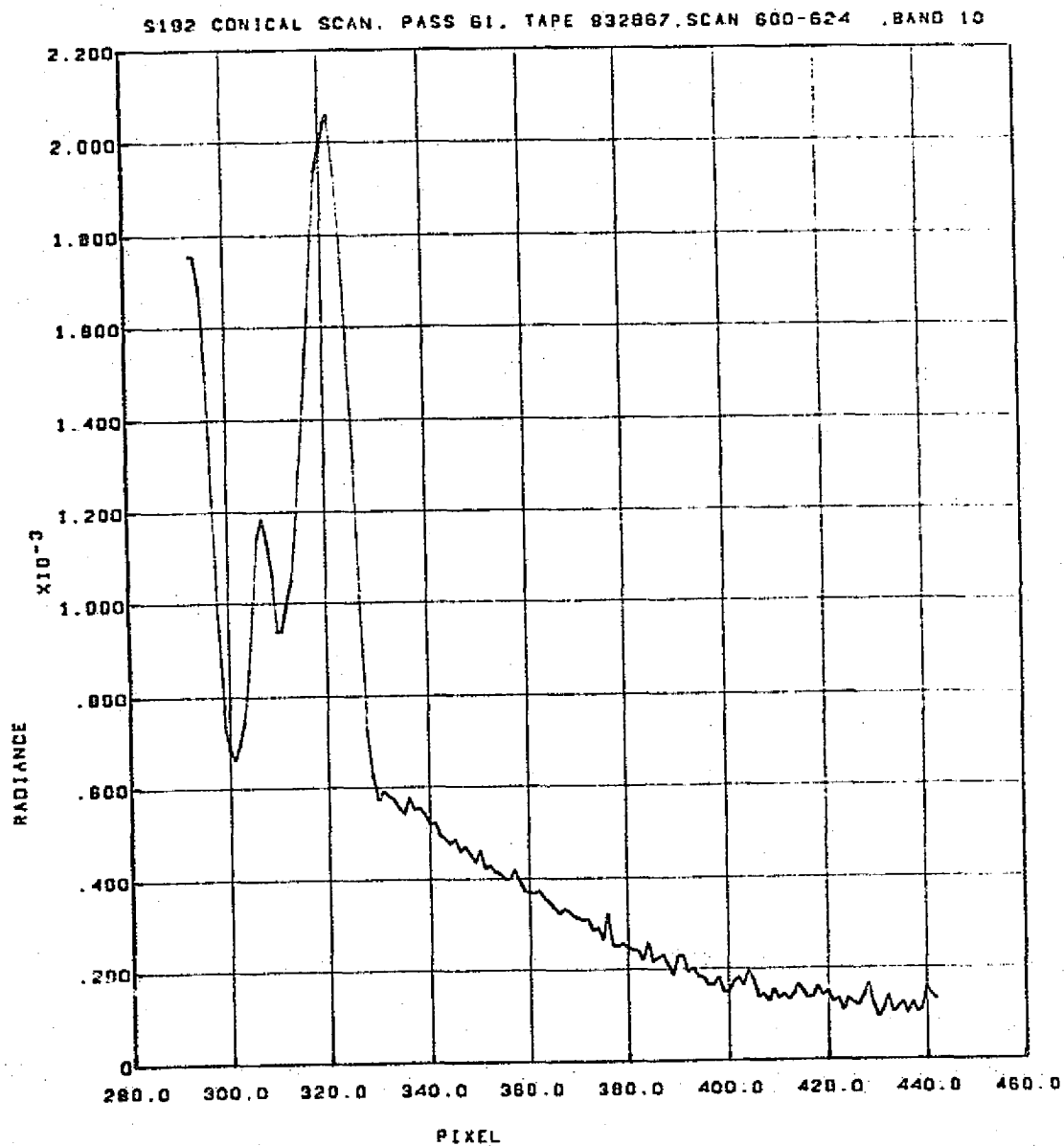
REPRODUCIBILITY OF THE
ORIGINAL PAGE IS POOR

S192 CONICAL SCAN. PASS 61. TAPE 932867, SCAN 600-624 .BAND 8



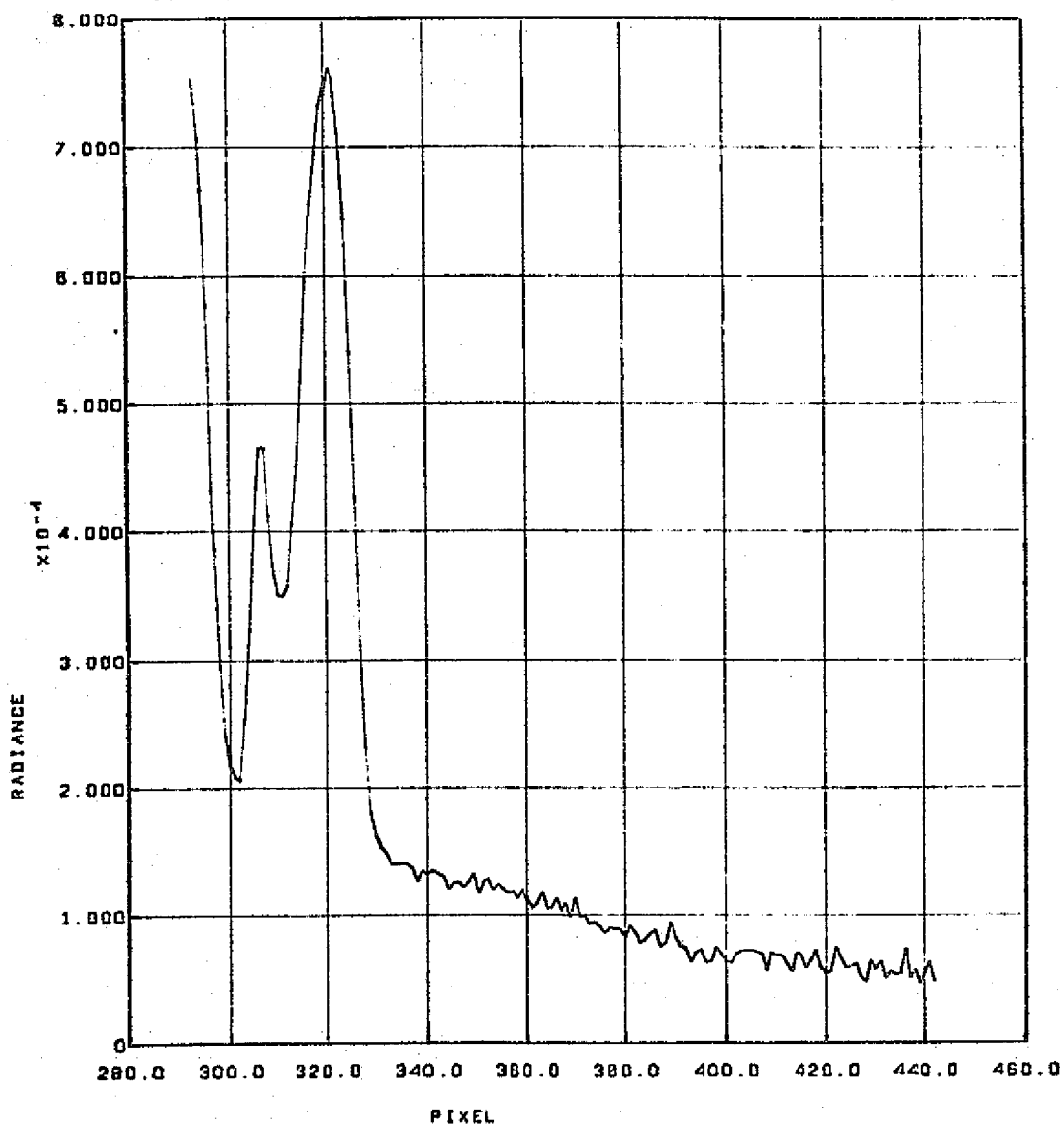
811



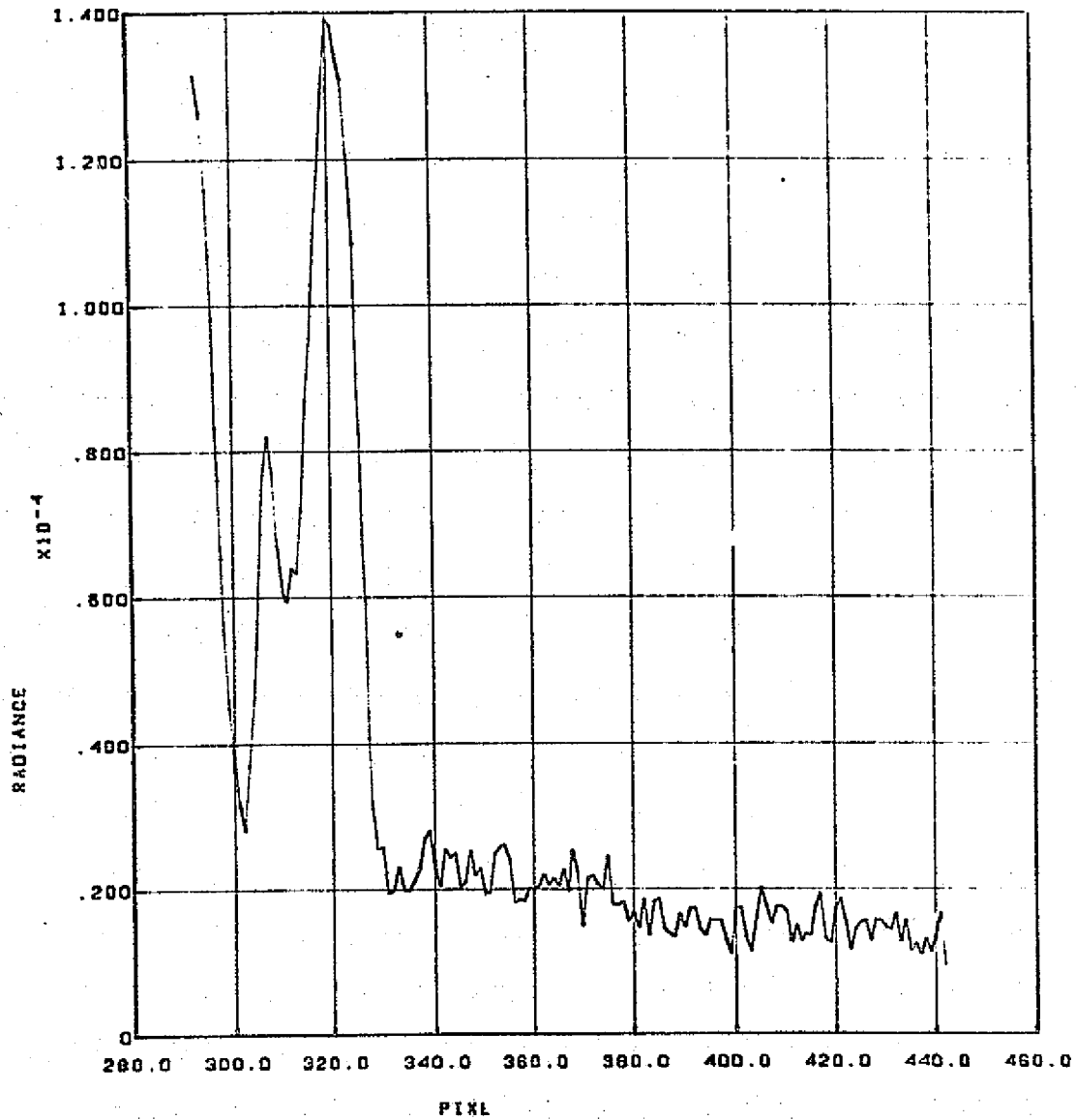


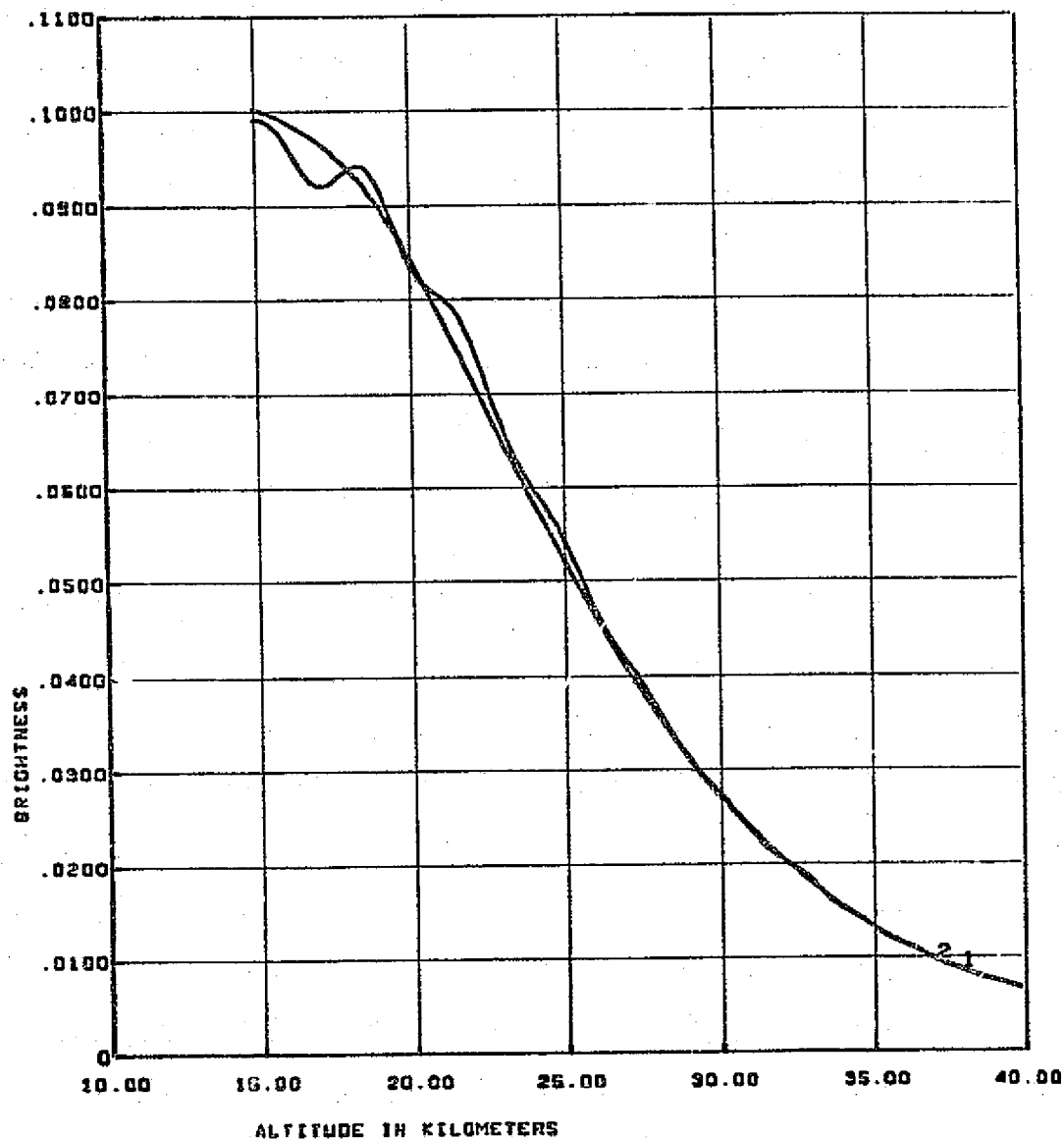
REPRODUCIBILITY OF THE
ORIGINAL PAGE IS POOR

5192 CONICAL SCAN. PASS 61. TAPE 932867. SCAN 600-624 .BAND 11



S192 CONICAL SCAN. PASS 61. TAPE 932867. SCAN 600-624 .BAND 12



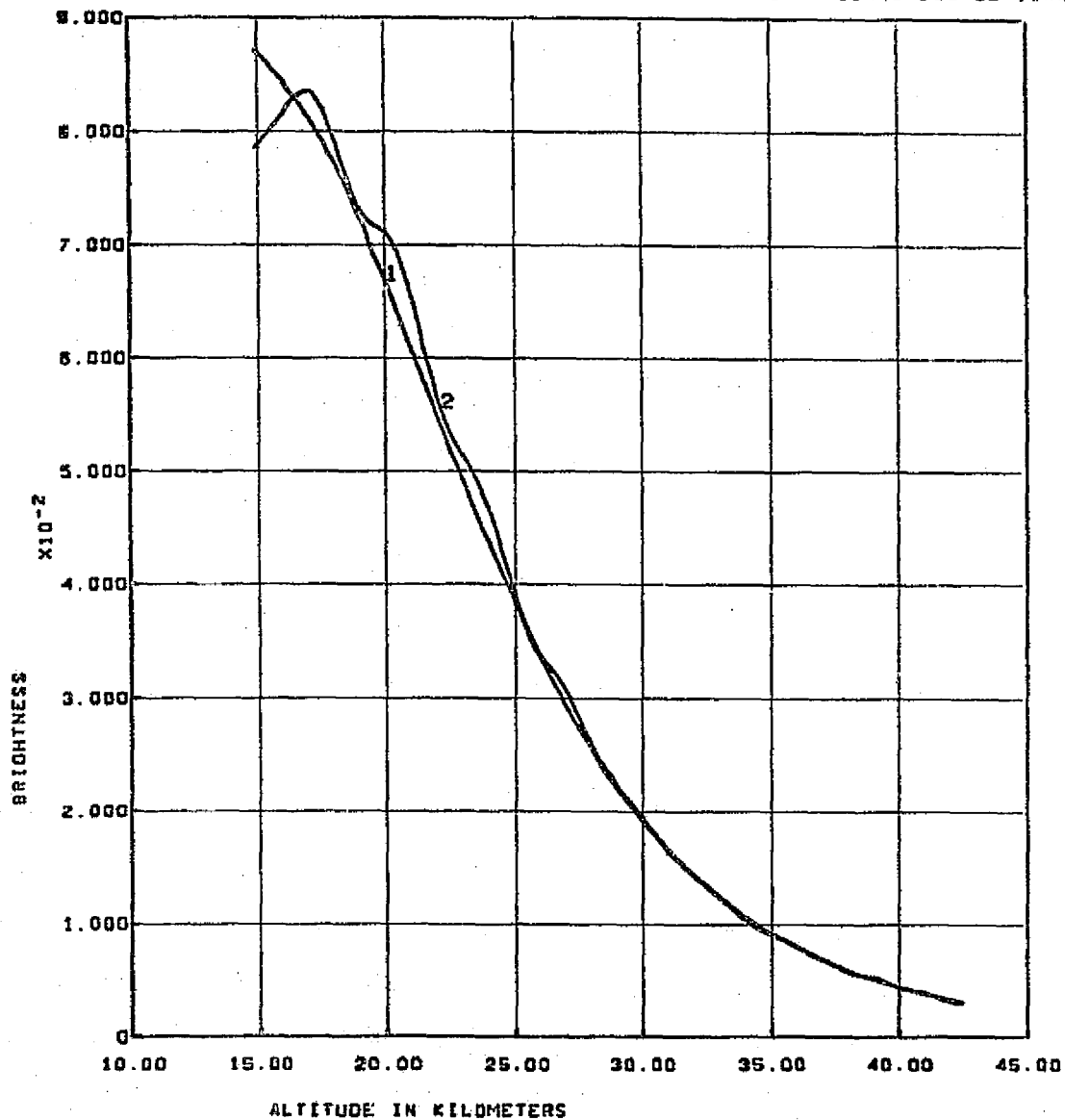


CURVE 1 - BRIGHTNESS MODEL GENERATED FROM RAYLEIGH + 1969 AEROSOL BETAS.
 CURVE 2 - MEASURED BRIGHTNESS SCALED BY 1969 MODEL.

REPRODUCIBILITY OF THE
 ORIGINAL PAGE IS POOR

5192 CONICAL SCAN. PASS 47. TAPE NUMBER 934528

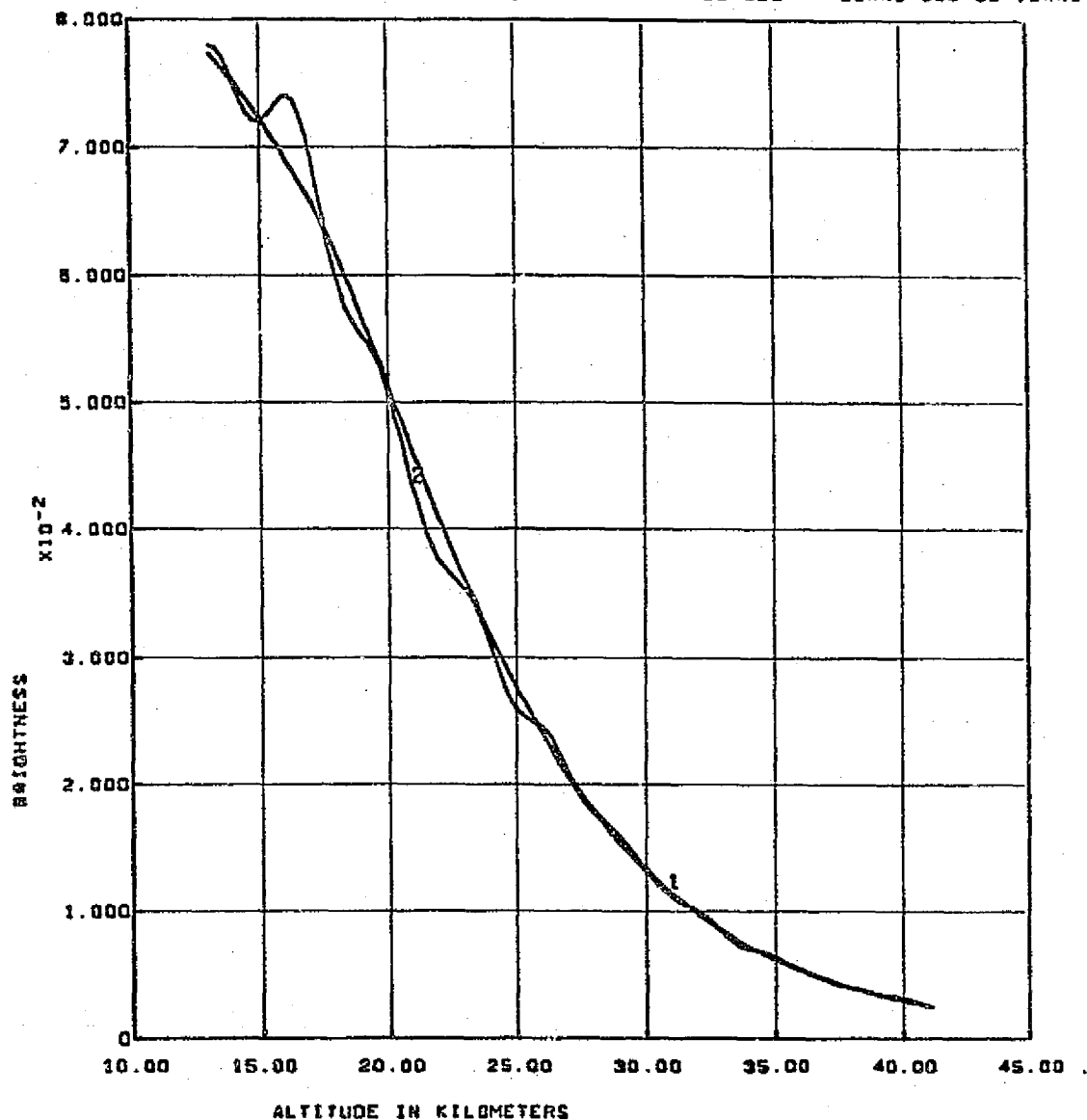
SCANS 300-324. BAND 2



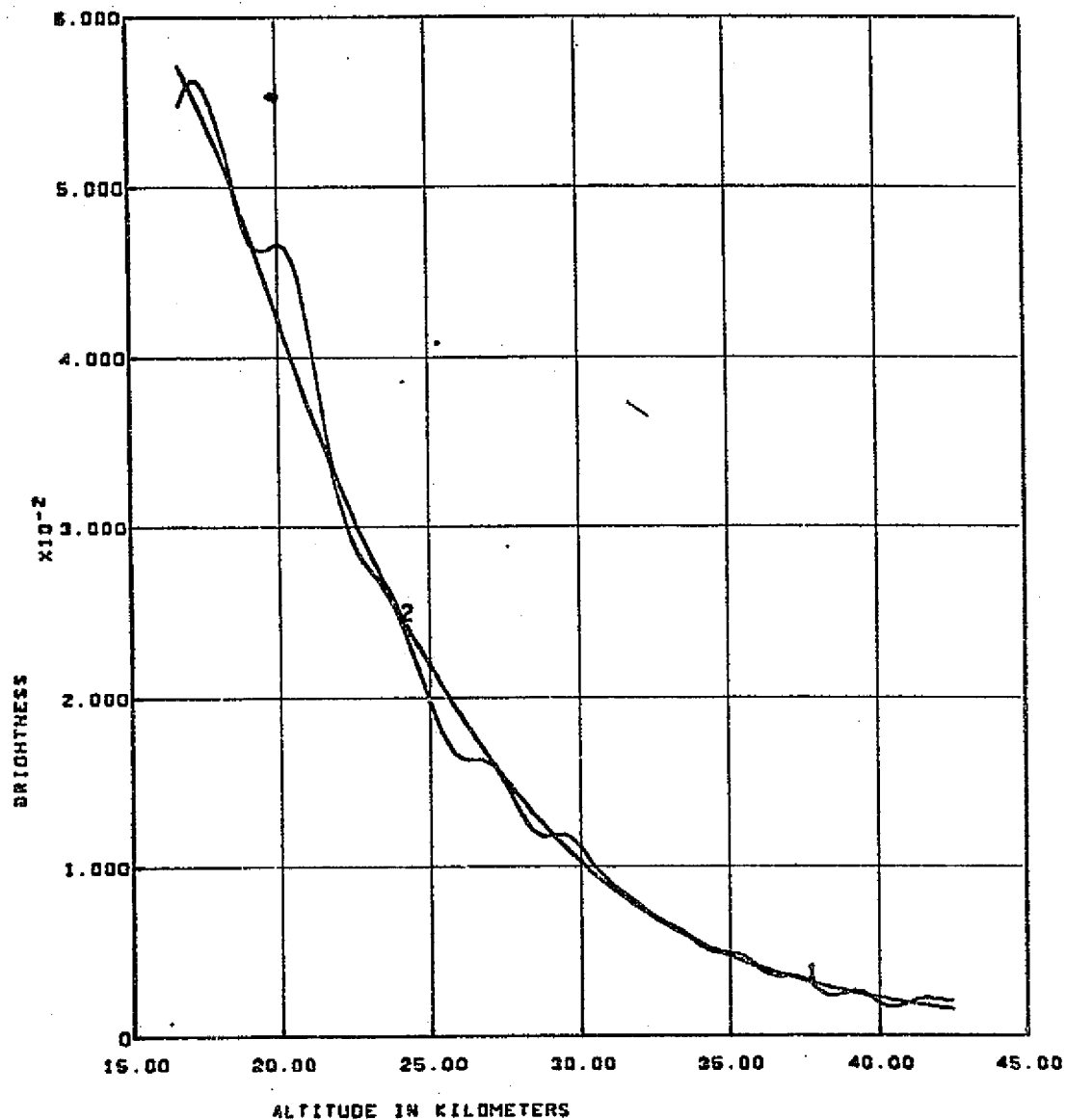
CURVE 1 - BRIGHTNESS MODEL GENERATED FROM RAYLEIGH + 1968 AEROSOL BETAS.
CURVE 2 - MEASURED BRIGHTNESS SCALED BY 1968 MODEL.

S192 CONICAL SCAN, PASS 47, TAPE NUMBER 934528

SCANS 300-324, BAND 3



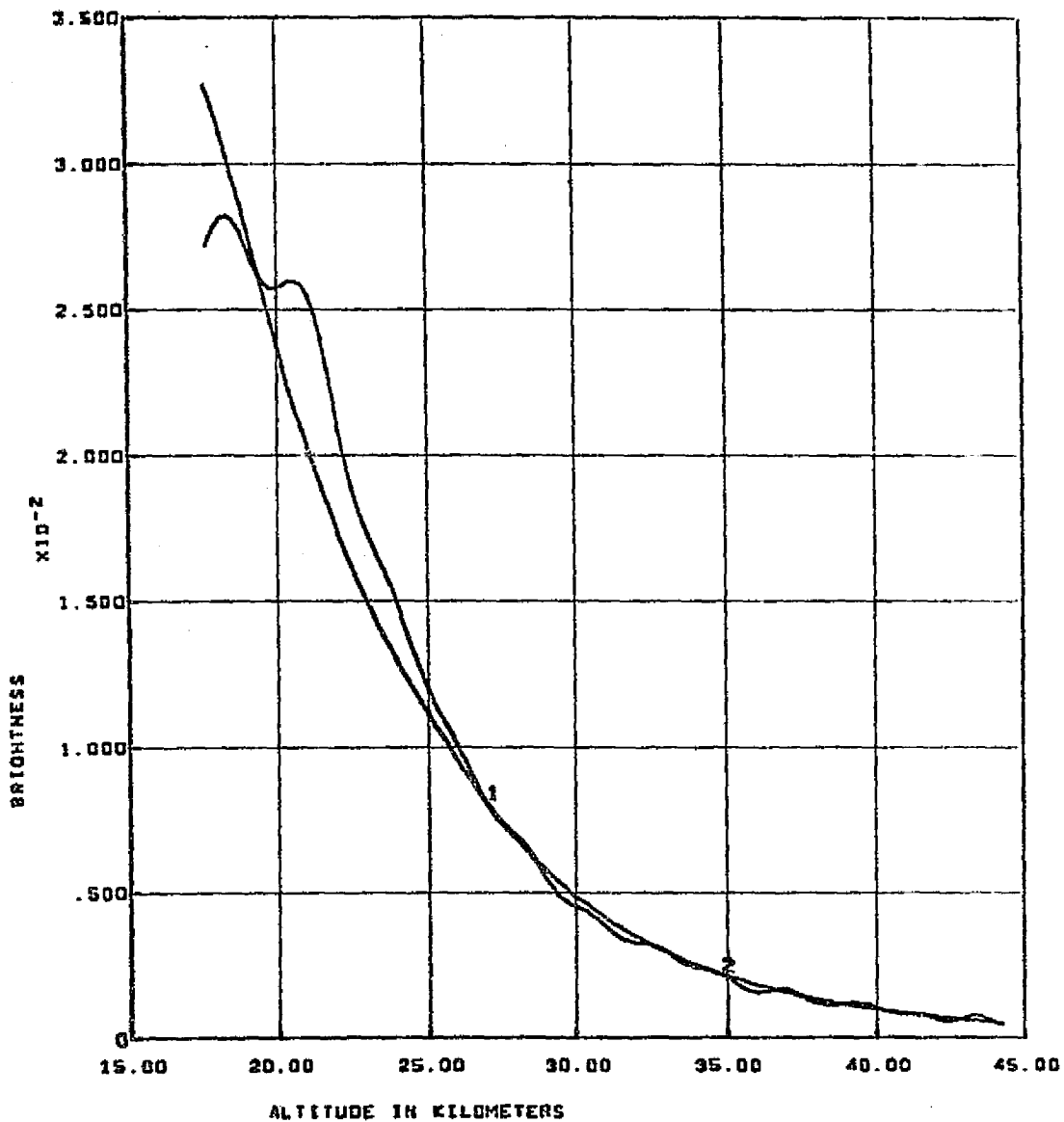
CURVE 1- BRIGHTNESS MODEL GENERATED FROM RAYLEIGH + 1960 AEROSOL BETAS.
 CURVE 2 - MEASURED BRIGHTNESS SCALED BY 1960 MODEL.



CURVE 1 - BRIGHTNESS MODEL GENERATED FROM RAYLEIGH + 1988 AEROSOL BETAS.
CURVE 2 - MEASURED BRIGHTNESS SCALED BY 1988 MODEL.

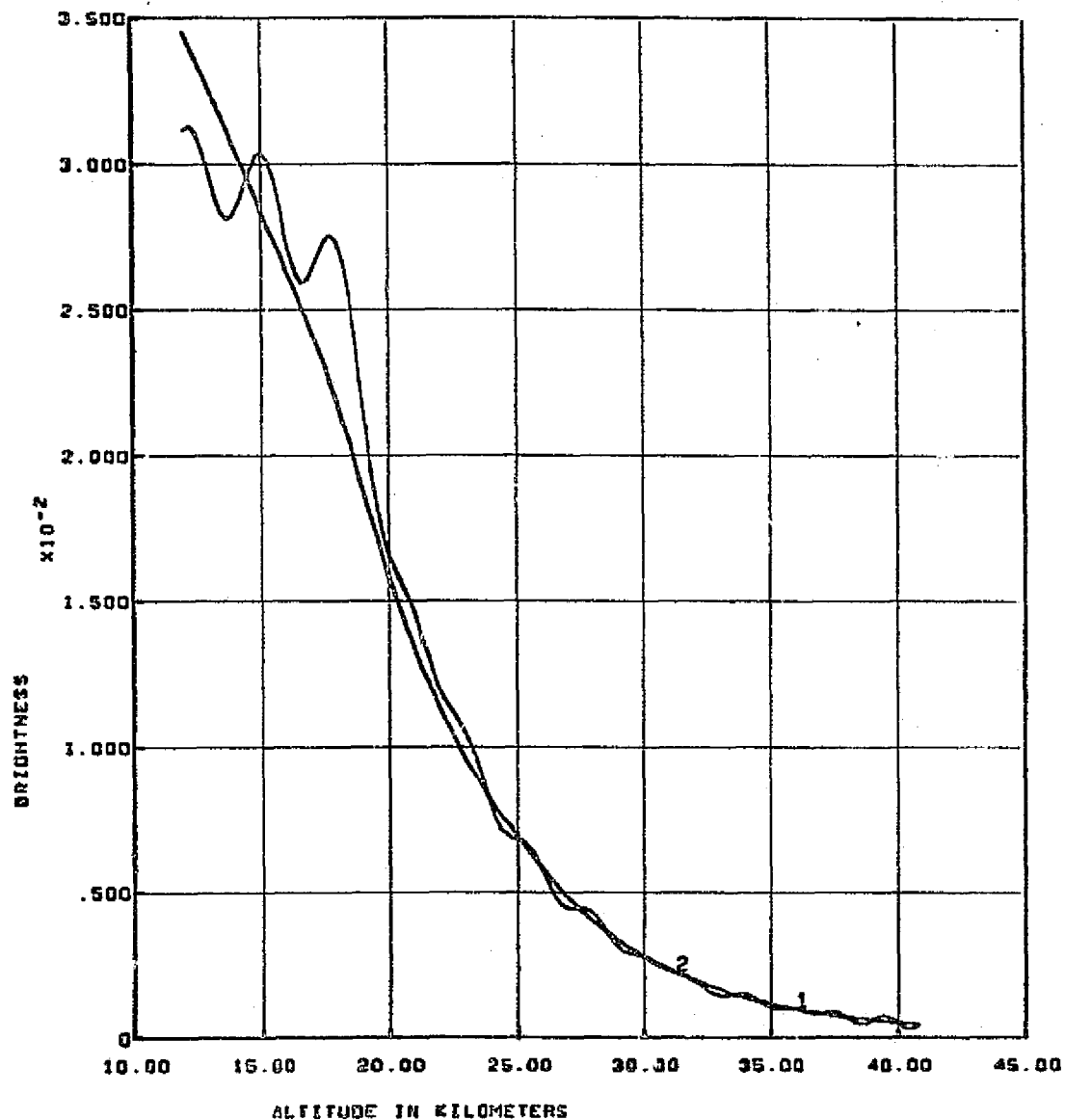
9192 CONICAL SCAN, PASS 47, TAPE NUMBER 934528

SCANS 300-324, BAND 0



CURVE 1- BRIGHTNESS MODEL GENERATED FROM RAYLEIGH + 1966 AEROSOL DATA.
CURVE 2 - MEASURED BRIGHTNESS SCALED BY 1966 MODEL.

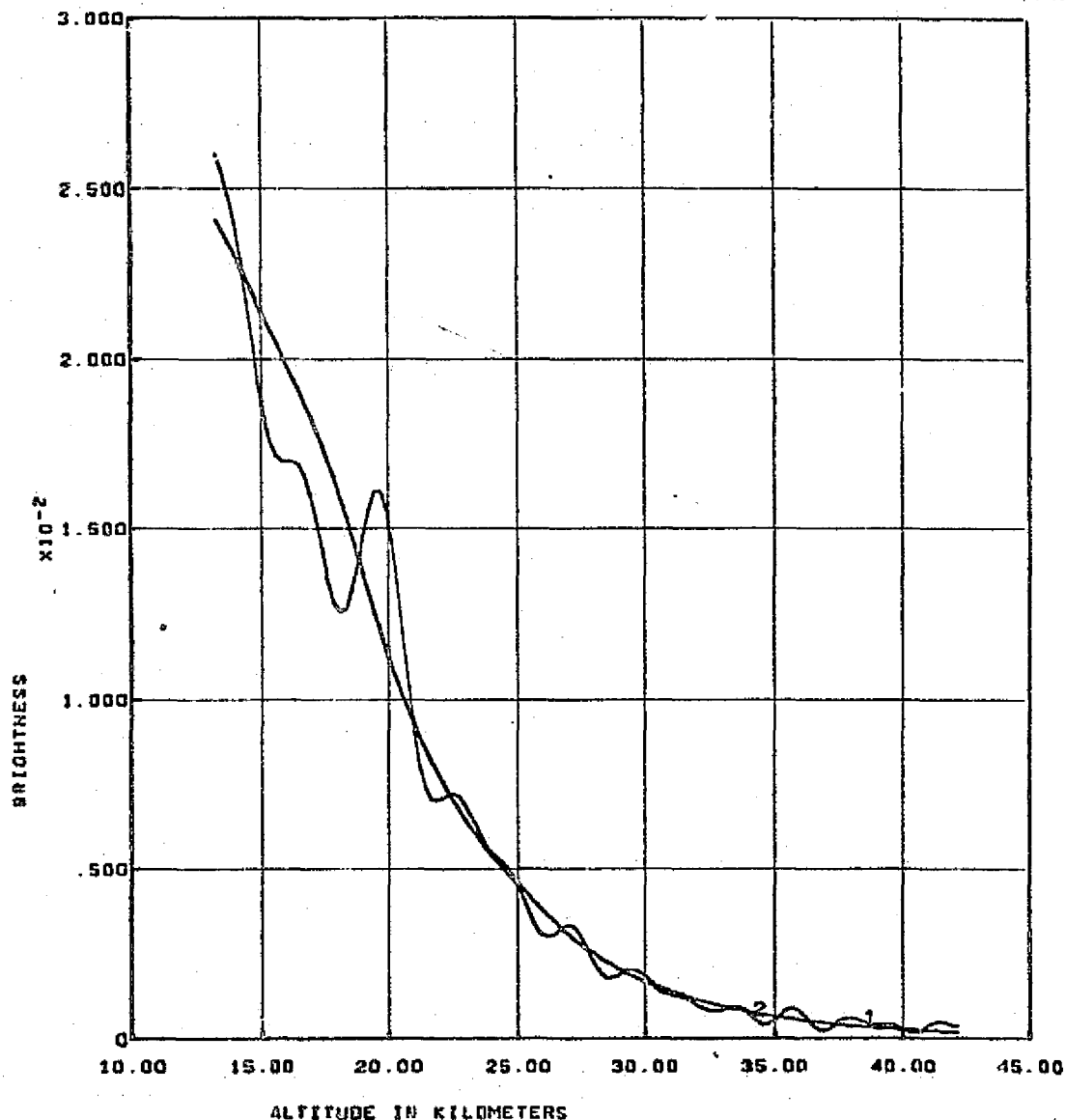
REPRODUCIBILITY OF THE
ORIGINAL PAGE IS POOR



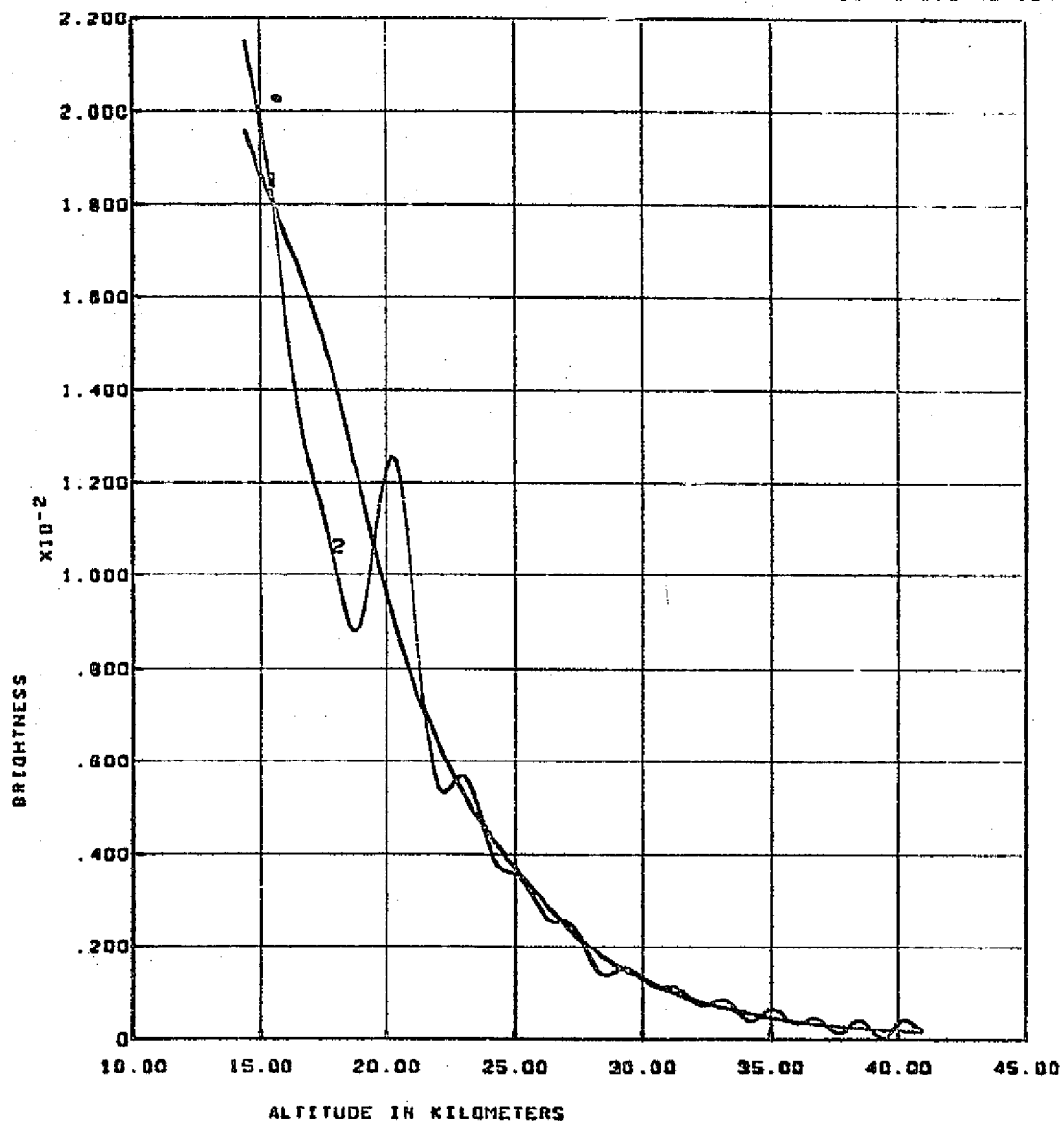
CURVE 1 - BRIGHTNESS MODEL GENERATED FROM RAYLEIGH + 1988 AEROSOL DATAS.
CURVE 2 - MEASURED BRIGHTNESS SCALED BY 1988 MODEL.

S192 CONICAL SCAN. PASS 47. TAPE NUMBER 934528

SCANS 300-324. BAND 8



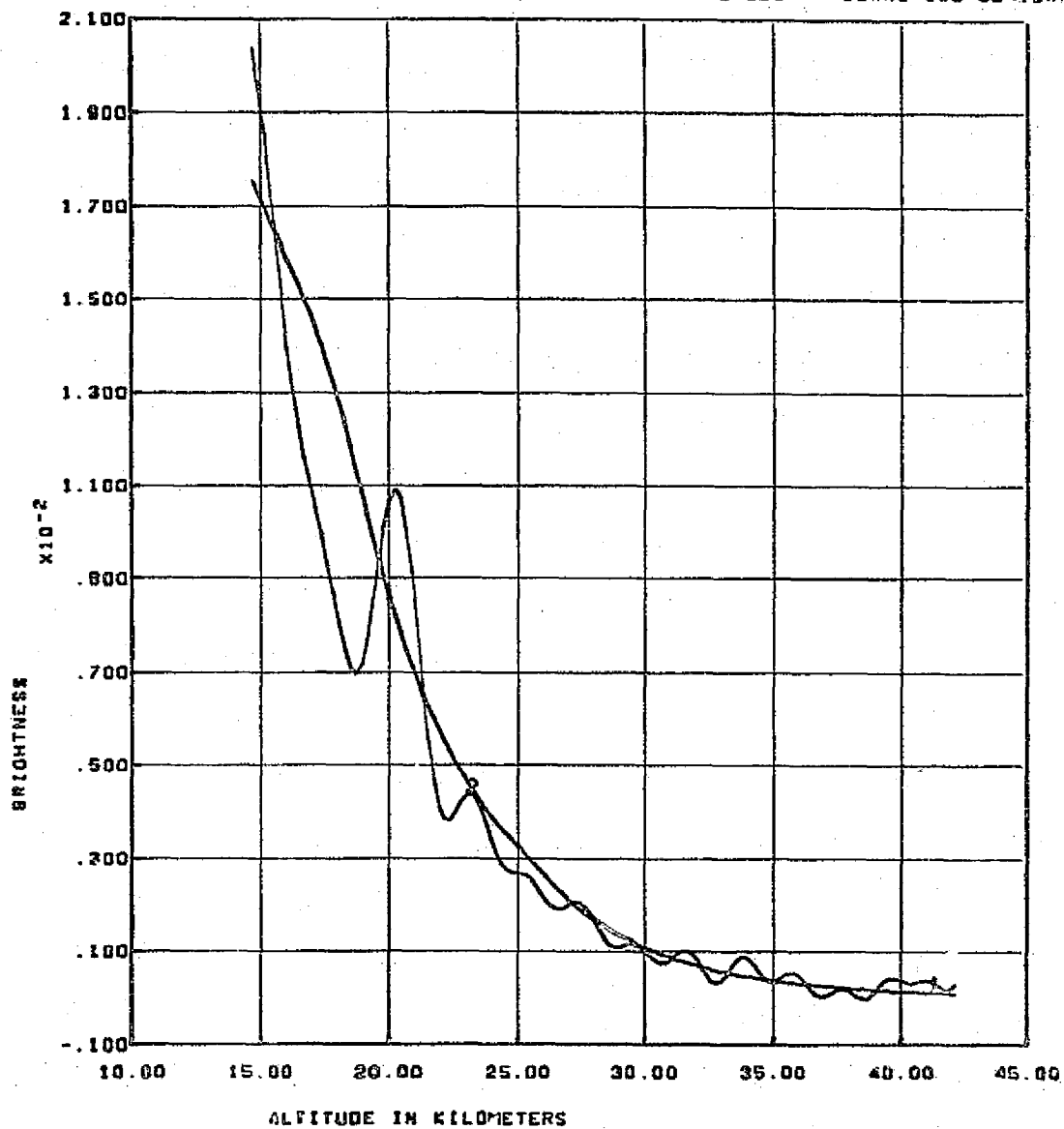
CURVE 1 - BRIGHTNESS MODEL GENERATED FROM RAYLEIGH + 1968 AEROSOL BETAS.
 CURVE 2 - MEASURED BRIGHTNESS SCALED BY 1968 MODEL.



CURVE 1 - BRIGHTNESS MODEL GENERATED FROM RAYLEIGH + 1968 AEROSOL BETAS.
CURVE 2 - MEASURED BRIGHTNESS SCALED BY 1968 MODEL.

9102 CONICAL SCAN. PASS 47. TAPE NUMBER 934528

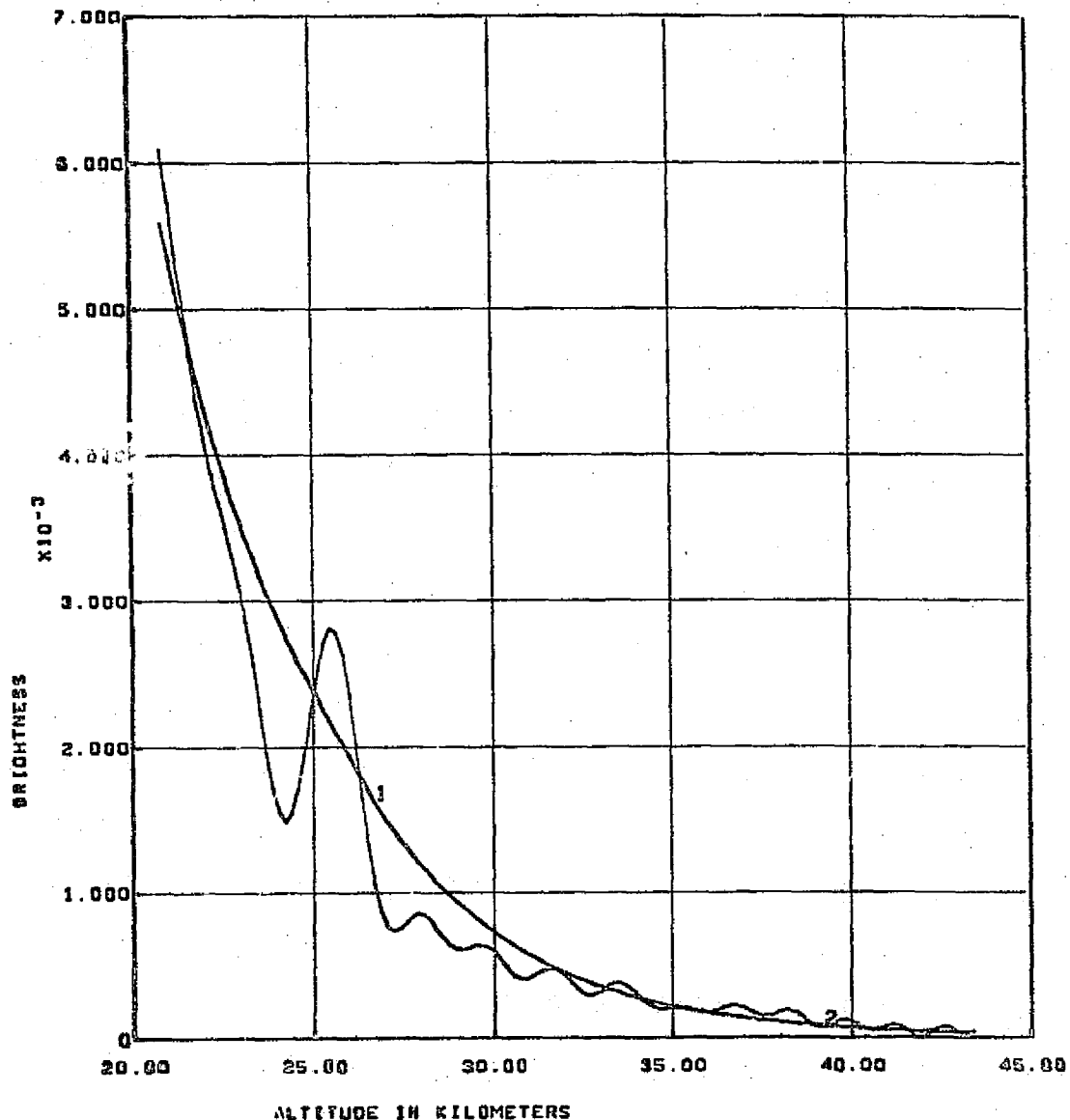
SCANS 300-324.DAND 10



CURVE 1 - BRIGHTNESS MODEL GENERATED FROM RAYLEIGH + 1988 AEROSOL DATAS.
 CURVE 2 - MEASURED BRIGHTNESS SCALED BY 1988 MODEL.

S192 CONICAL SCAN. PASS 47. TAPE NUMBER 034578

SCANS 300-324, BAND 11

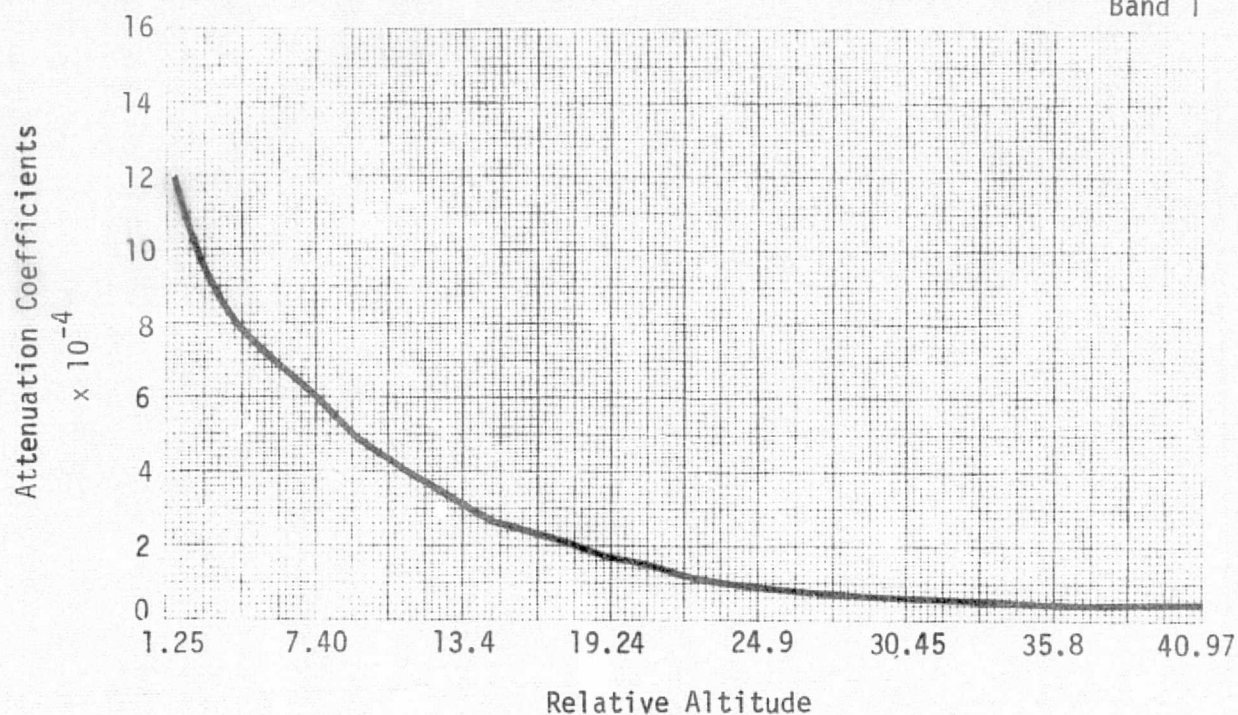


CURVE 1- BRIGHTNESS MODEL GENERATED FROM RAYLEIGH + 1989 AEROSOL BETAS.
CURVE 2 - MEASURED BRIGHTNESS SCALED BY 1989 MODEL.

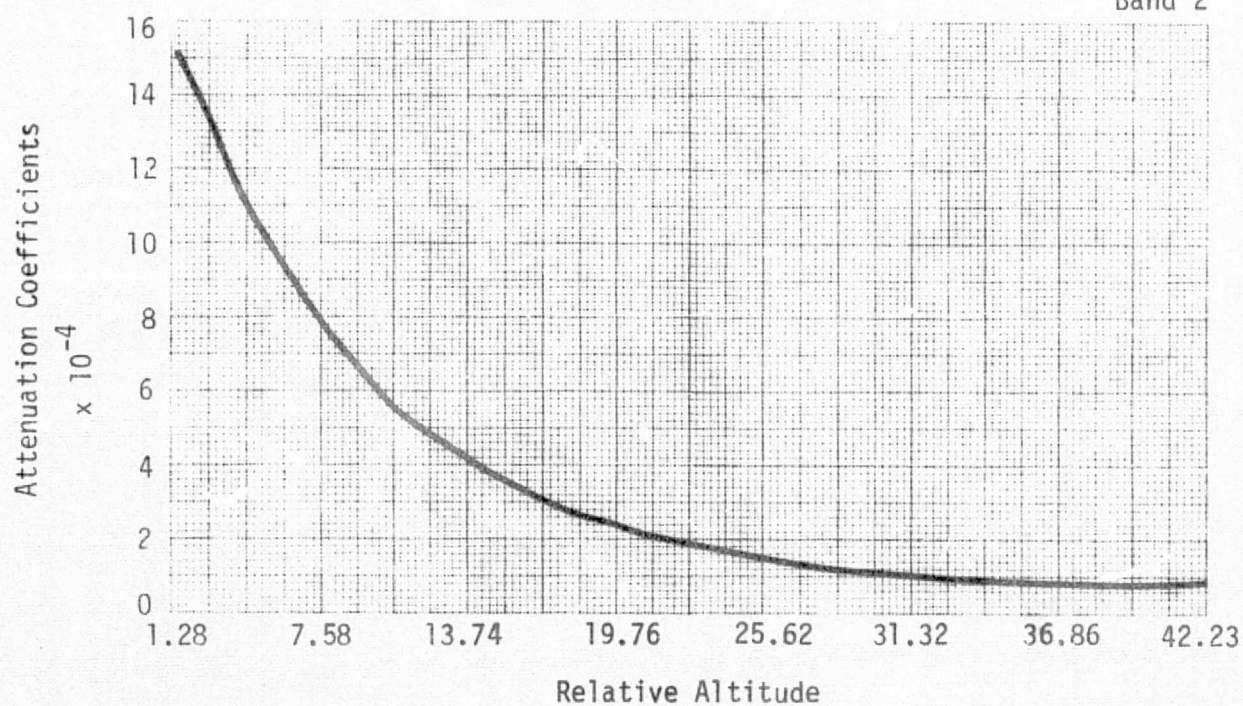
REPRODUCIBILITY OF THE
ORIGINAL PAGE IS POOR

S192 Conical Scan. Pass 61. Tape 932857. Scans 120-144

Band 1

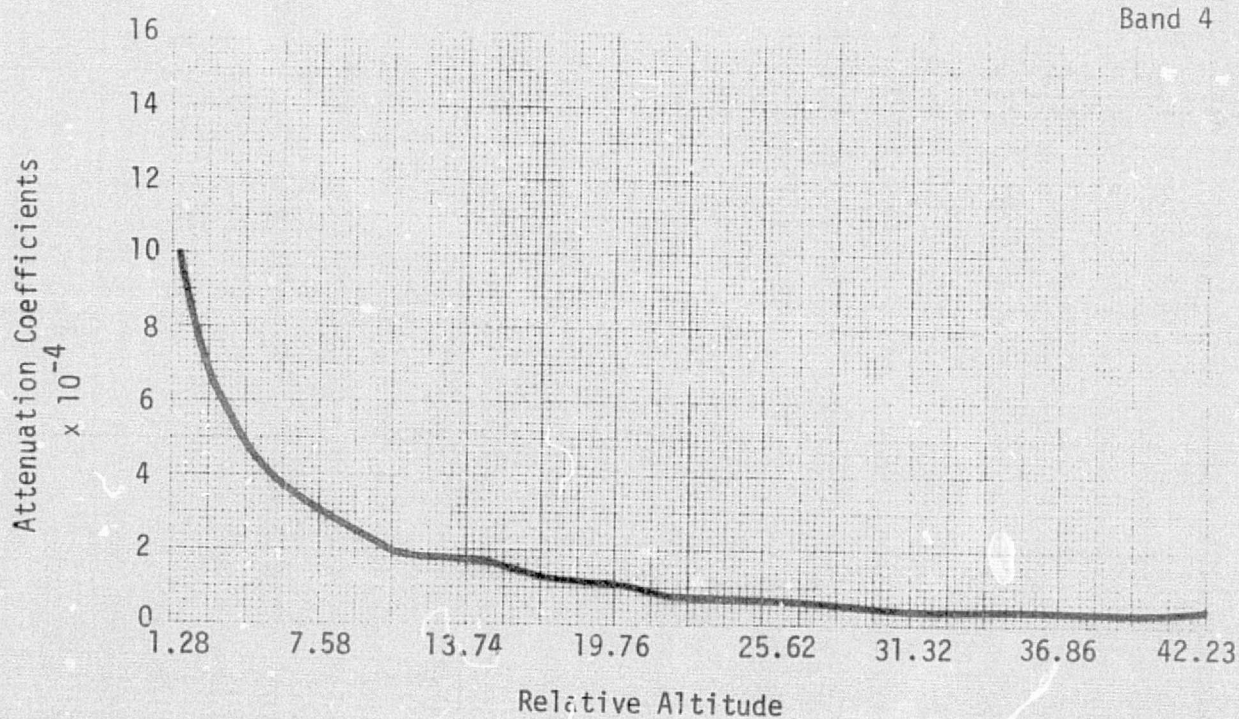
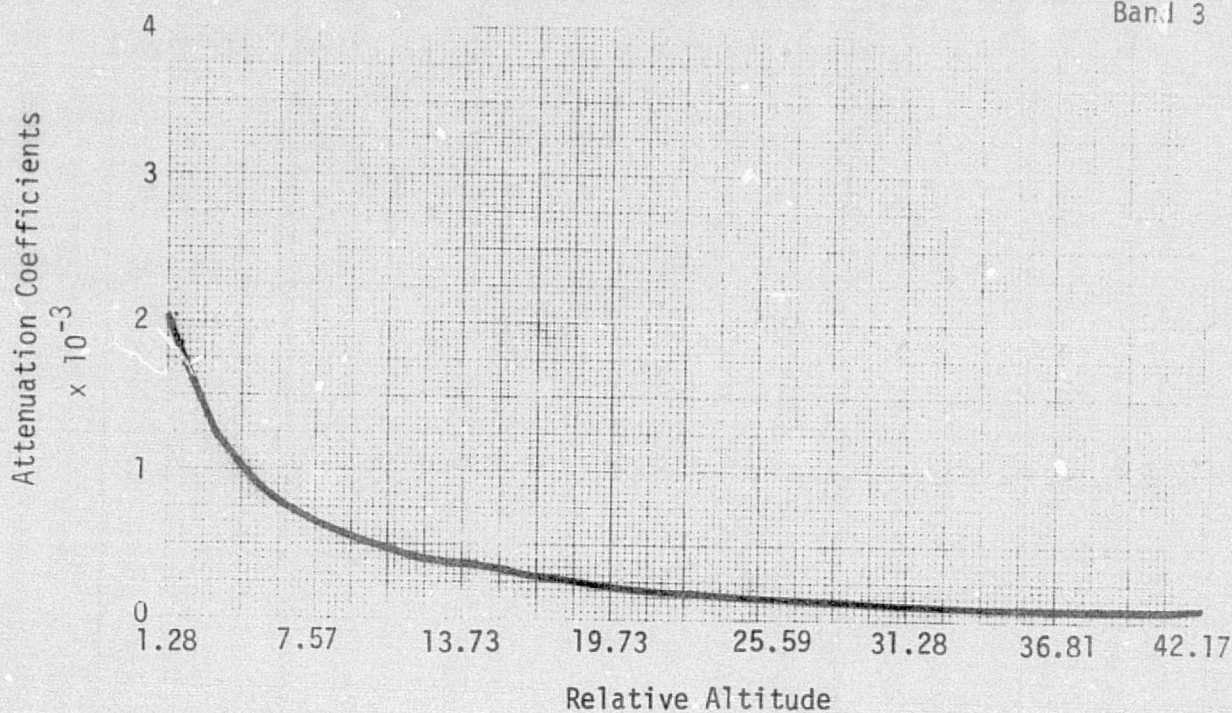


Band 2



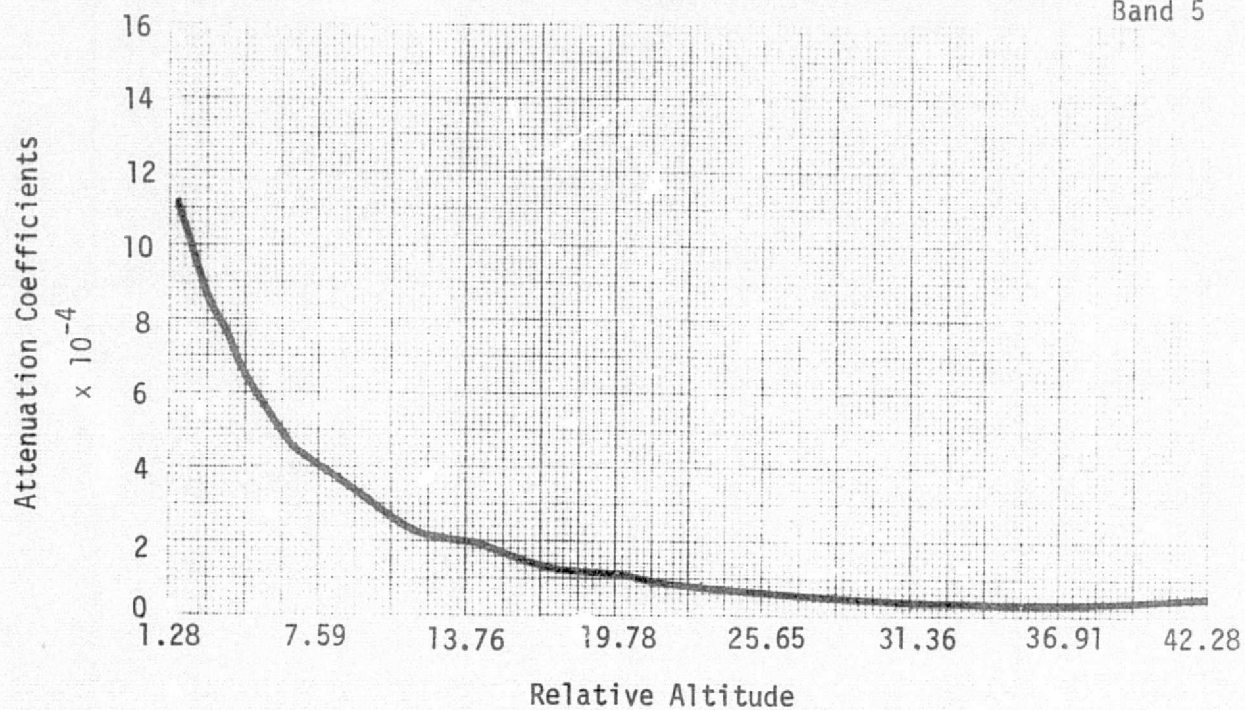
S192 Conical Scan. Pass 61. Tape 932857. Scans 120-144

Band 3

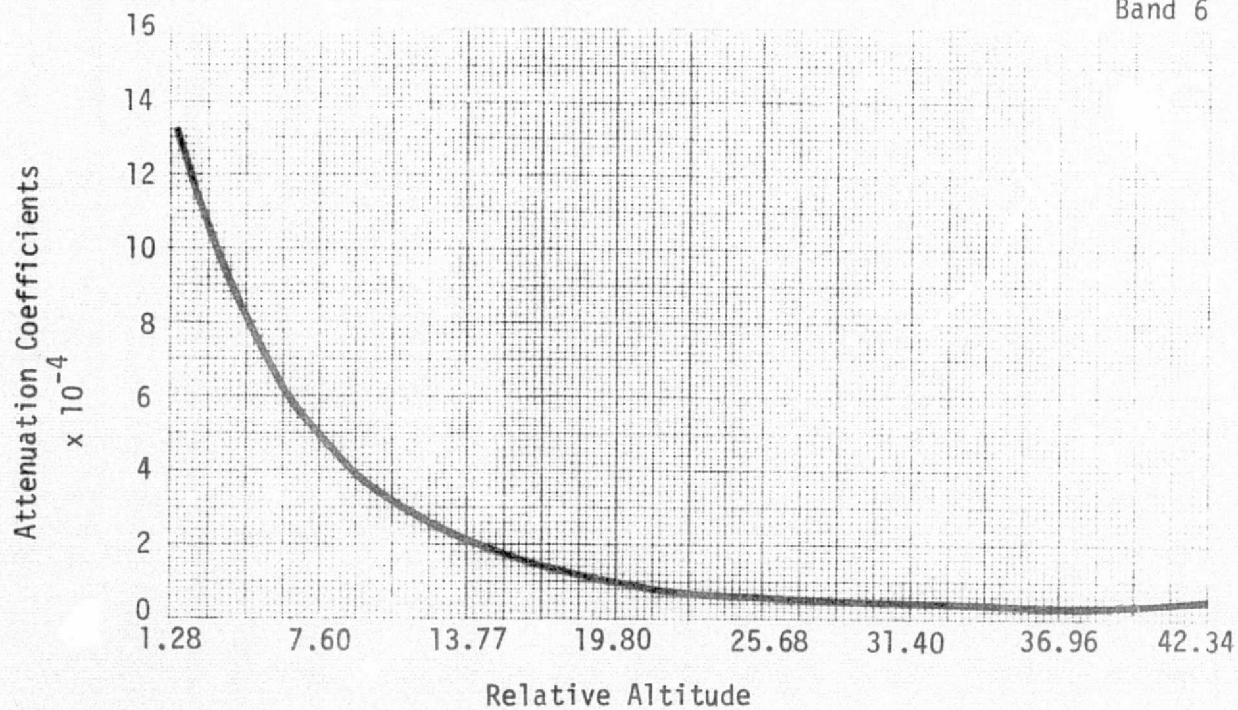


S192 Conical Scan, Pass 61. Tape 932857. Scans 120-144

Band 5

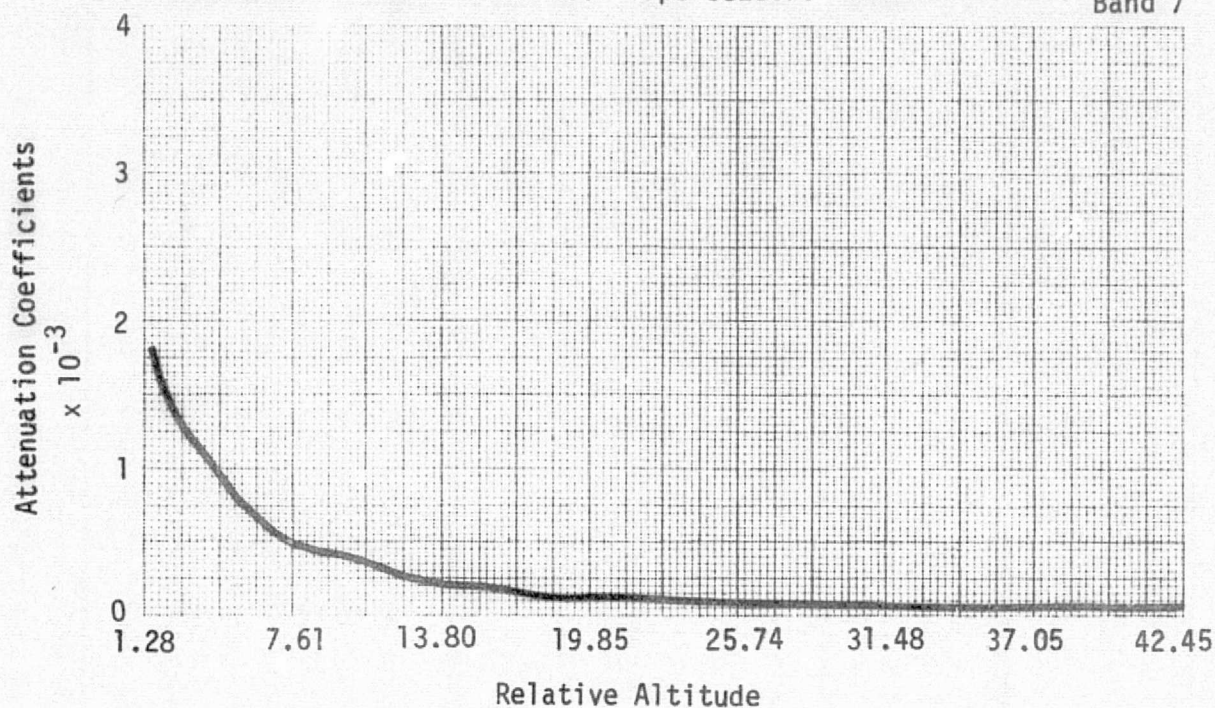


Band 6

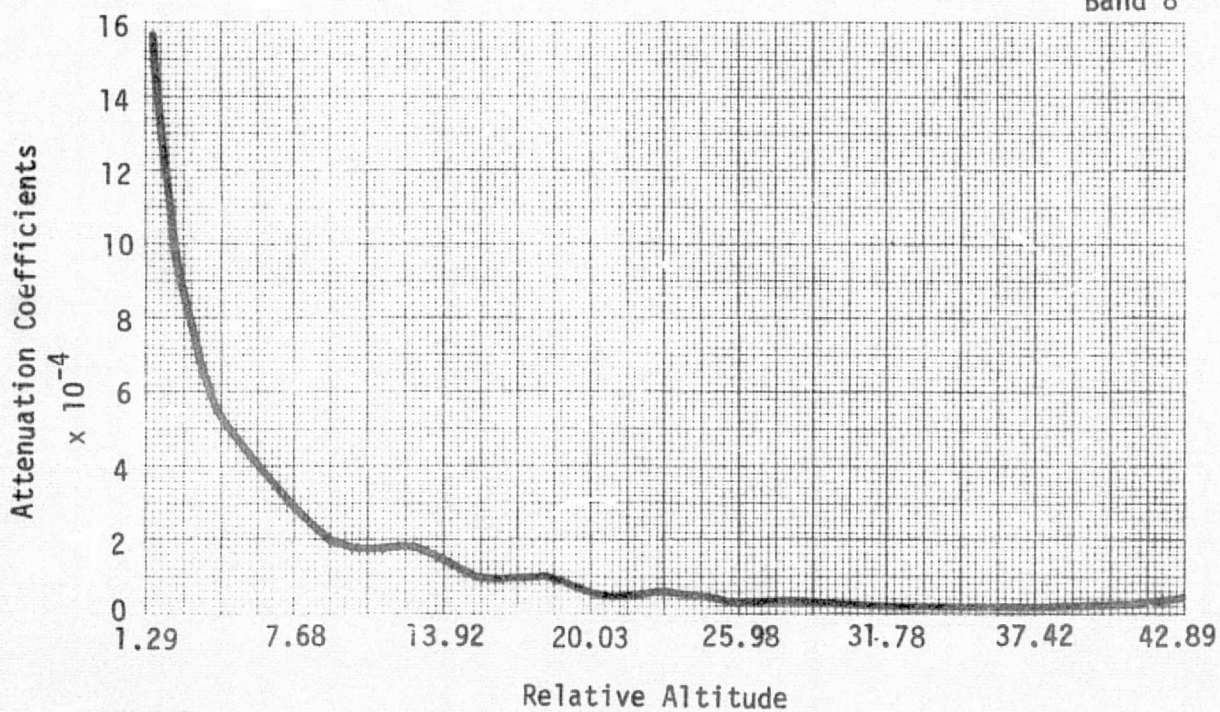


S192 Conical Scan. Pass 61. Tape 932857. Scans 120-144

Band 7

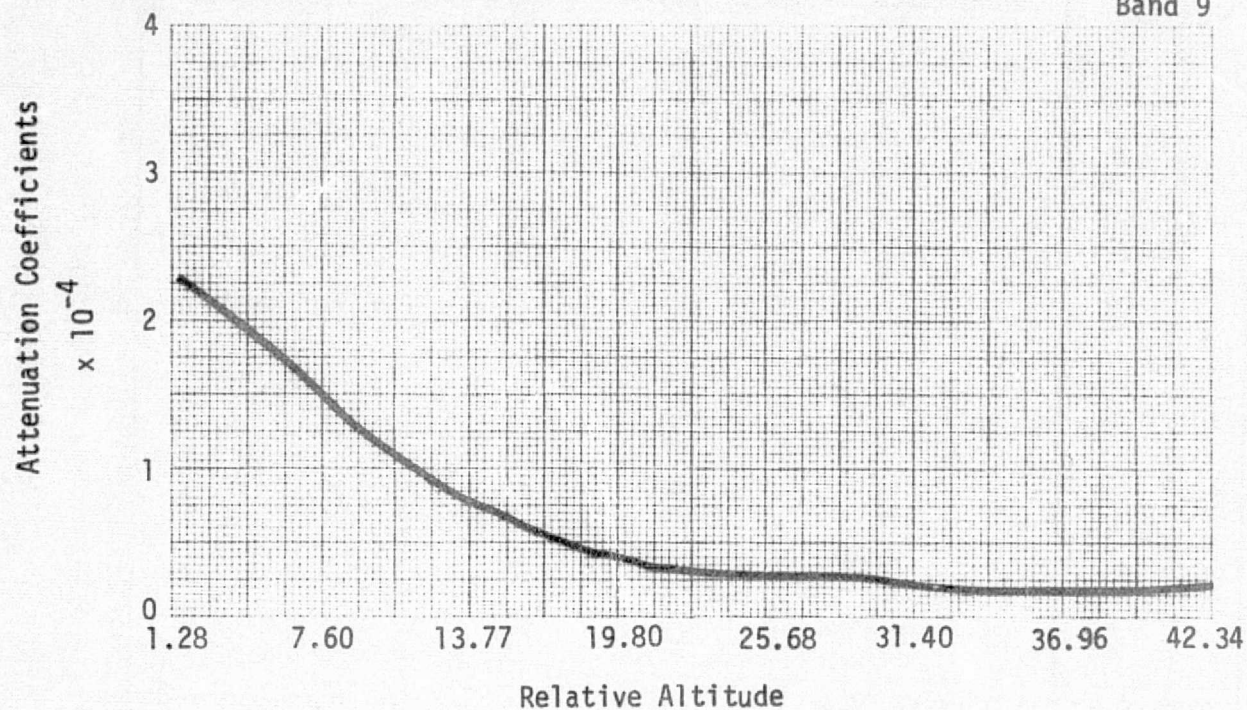


Band 8

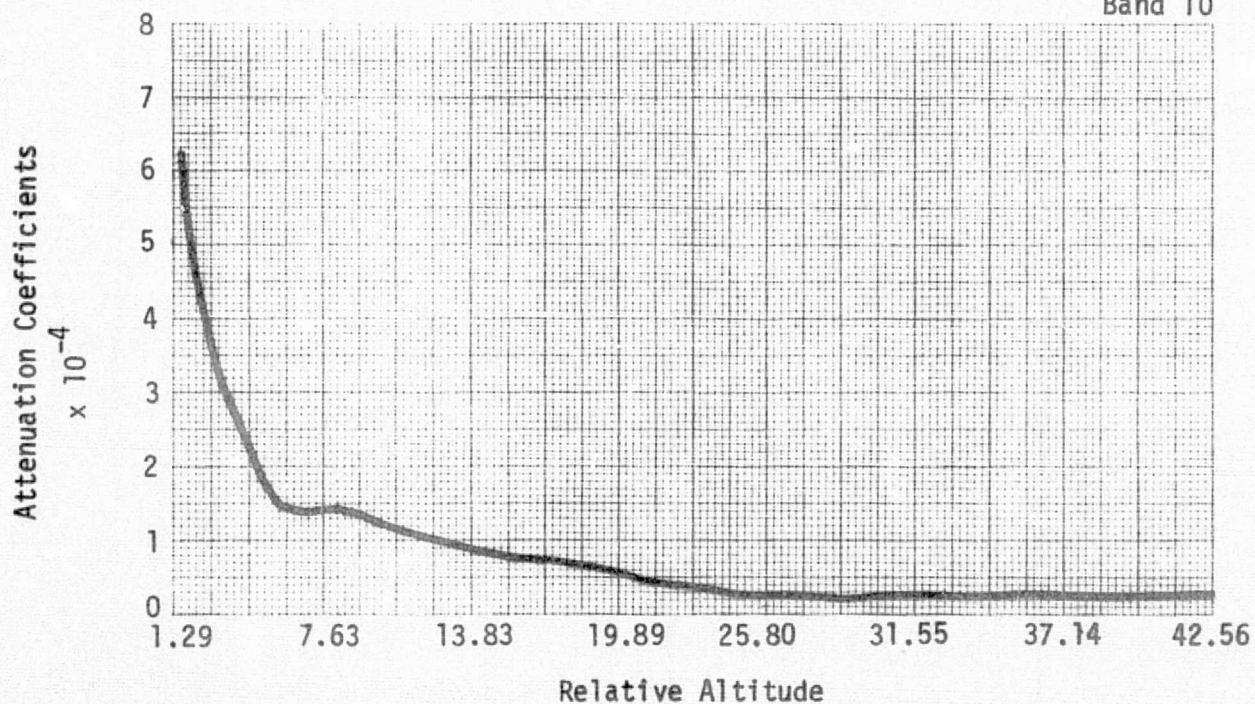


S192 Conical Scan. Pass 61. Tape 932857. Scans 120-144

Band 9



Band 10

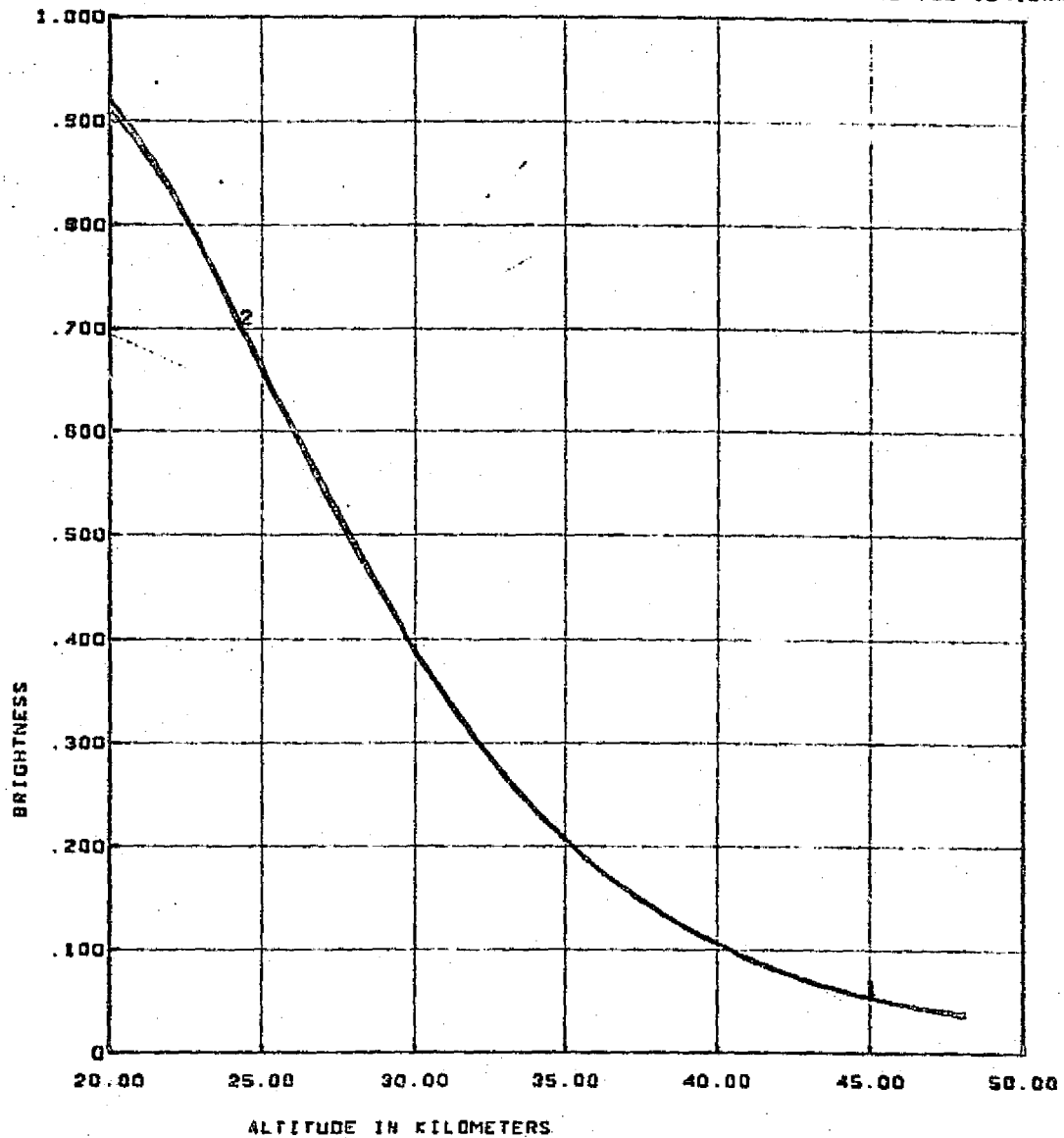


REPRODUCIBILITY OF THE
ORIGINAL PAGE IS POOR

S192 CONICAL SCAN, PASS 47, TAPE NUMBER 934528

SCANS 100-124.DAND

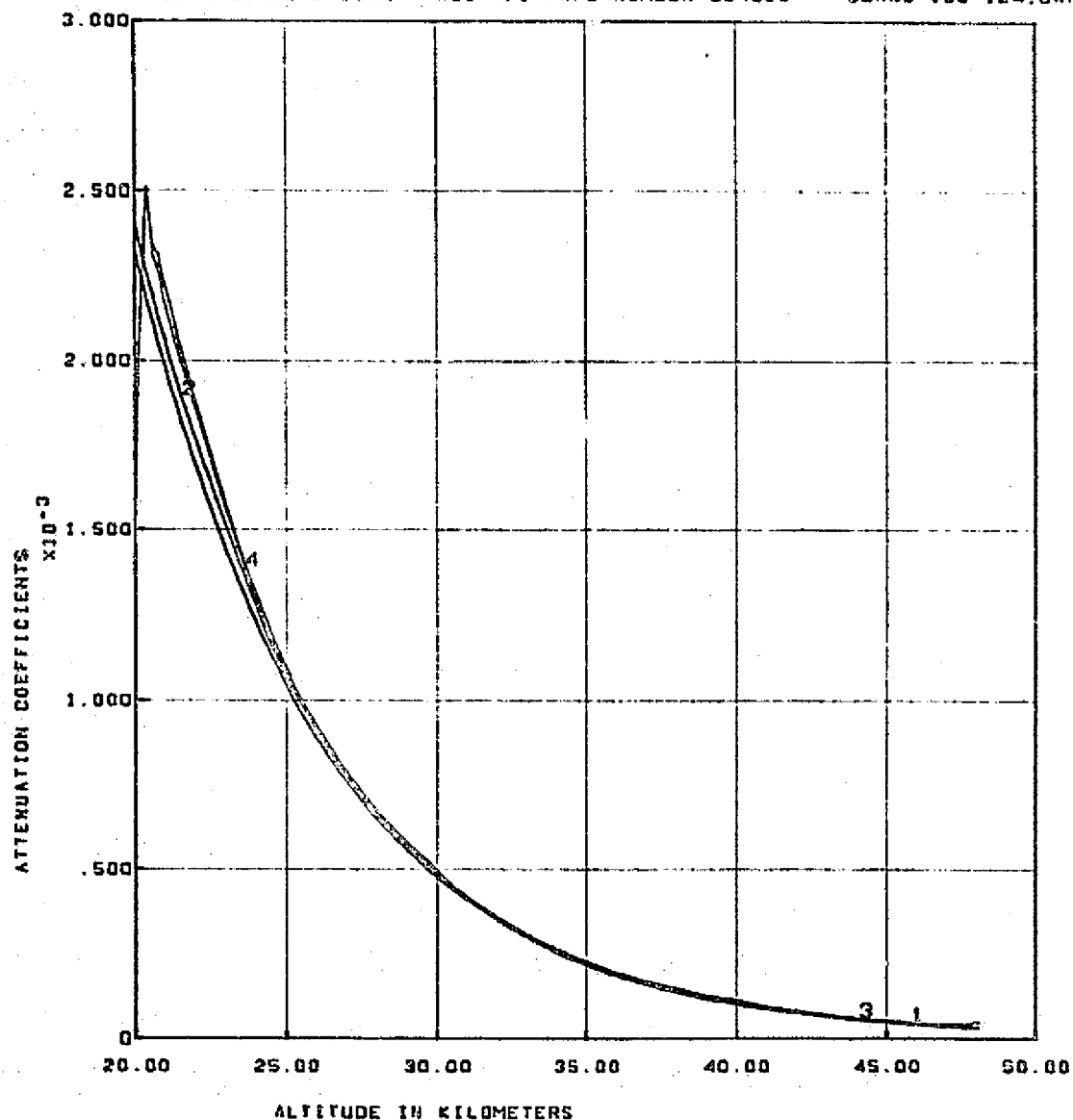
1



CURVE 1 - BRIGHTNESS MODEL GENERATED FROM RAYLEIGH + 1984 AEROSOL BETAS.
 CURVE 2 - MEASURED BRIGHTNESS SCALED BY 1984 MODEL.

S192 CONICAL SCAN. PASS 47. TAPE NUMBER 934520

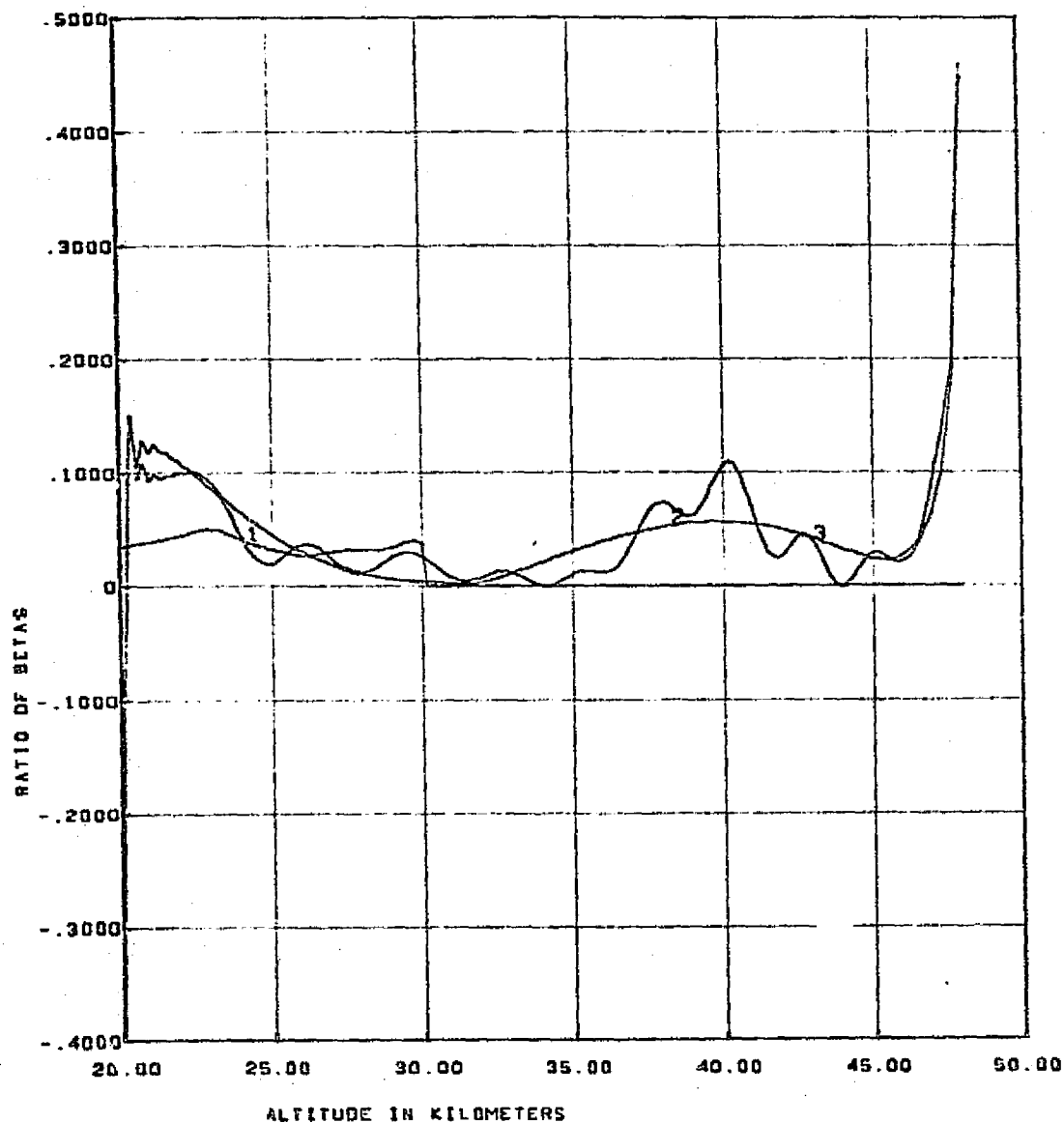
SCANS 100-124. BAND 1



ATTENUATION COEFFICIENTS - 1-RAYLEIGH, 2-RAYLEIGH + 1964 AEROSOL, 3-RESULTS FROM INVERSION OF EXPONENTIAL FIT, 4-RESULTS FROM INVERSION OF SMOOTHED BRIGHTNESS

S192 CONICAL SCAN. PASS 47. TAPE NUMBER 934528

SCANS 100-124. CAND 1

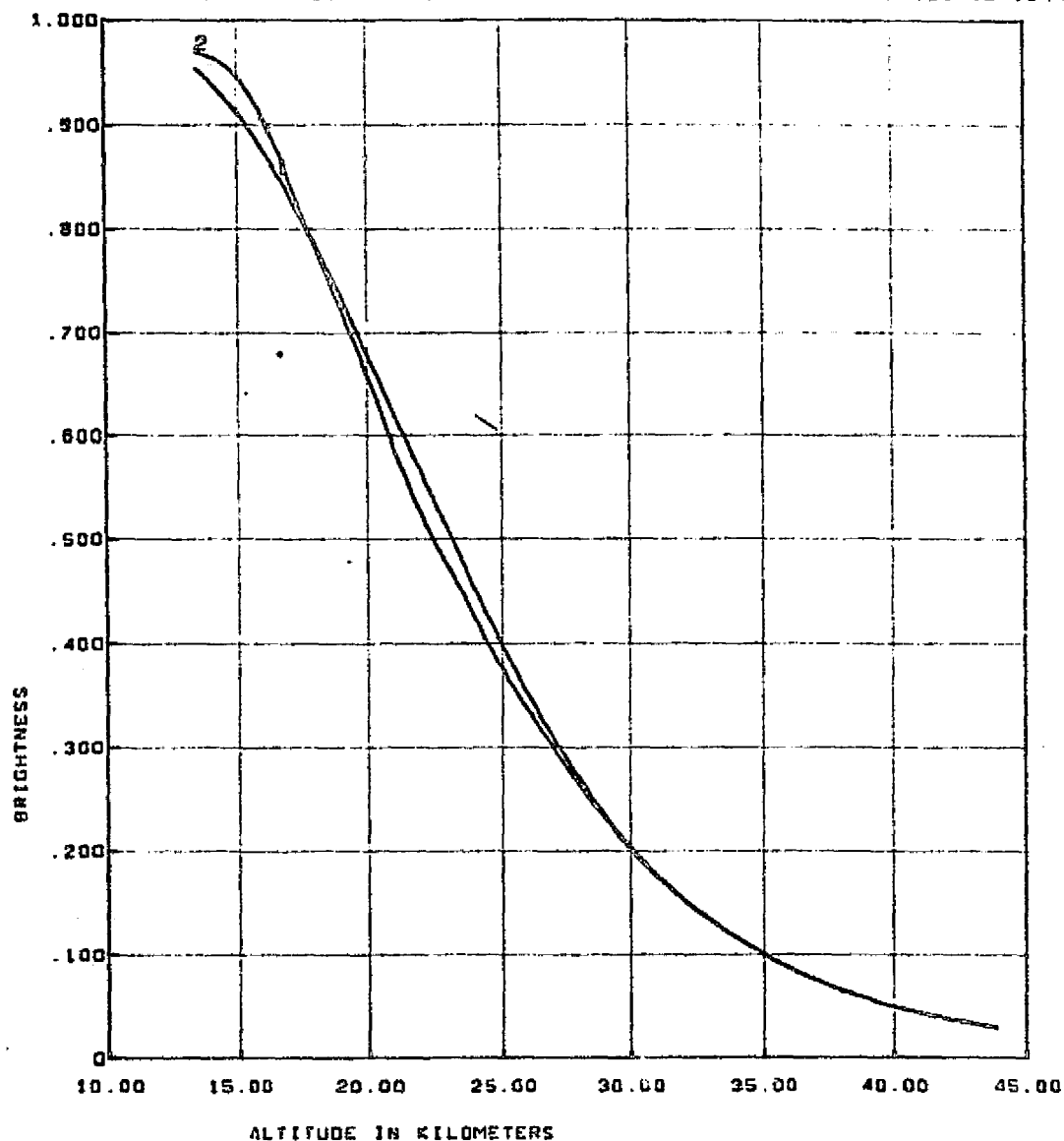


RATIO OF BETAS, AEROSOL OVER RAYLEIGH. 1-1984 MODEL AEROSOL. 2-RESULTS FROM INVERSION OF EXPONENTIAL FIT. 3-RESULTS FROM INVERSION OF SMOOTHED BRIGHTNESS

REPRODUCIBILITY OF THE
ORIGINAL PAGE IS POOR

S192 CONICAL SCAN, PASS 47, TAPE NUMBER 934528

SCANS 100-124, BAND 2

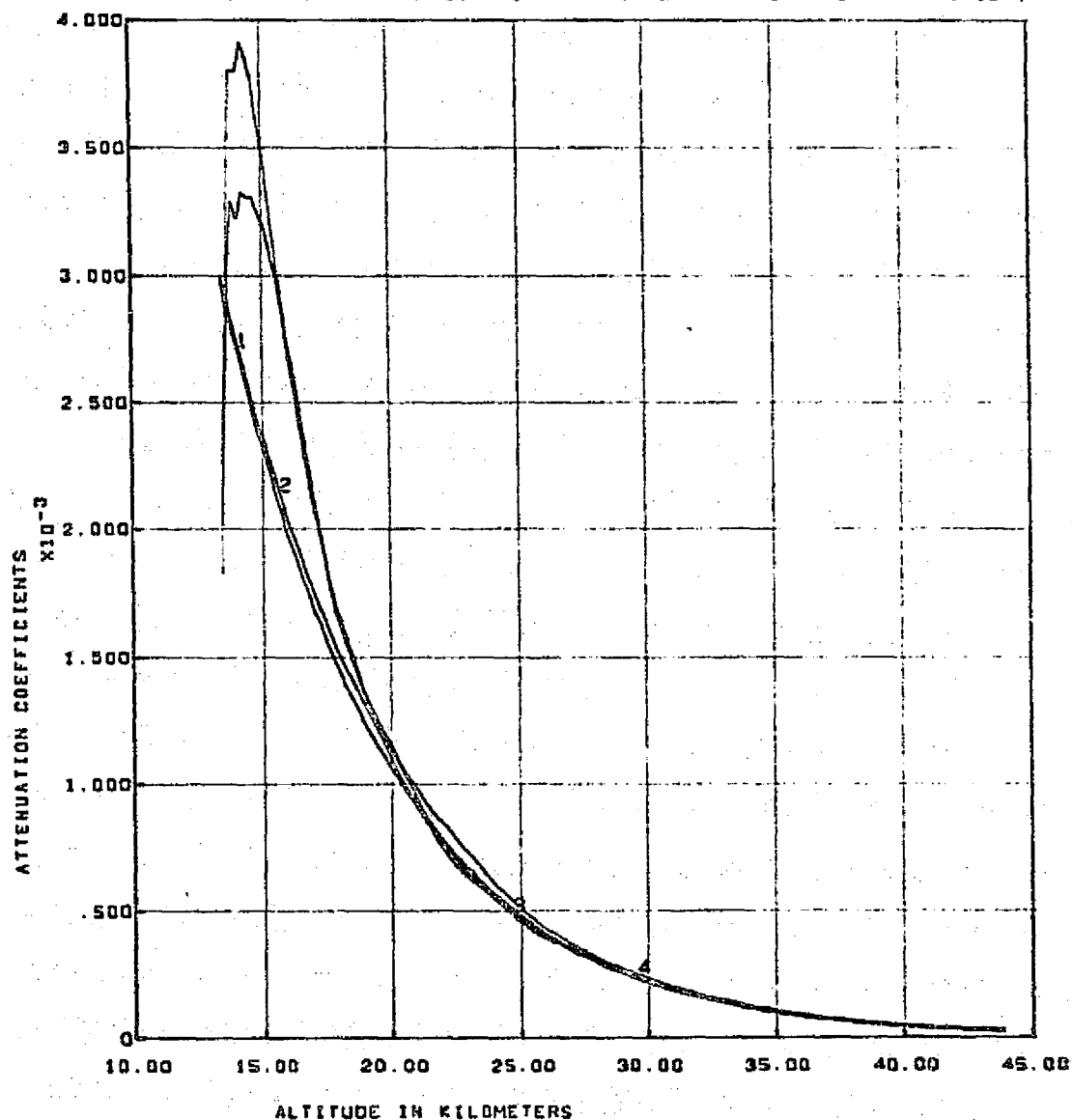


CURVE 1 - BRIGHTNESS MODEL GENERATED FROM RAYLEIGH + 1964 AEROSOL DATA.
CURVE 2 - MEASURED BRIGHTNESS SCALED BY 1964 MODEL.

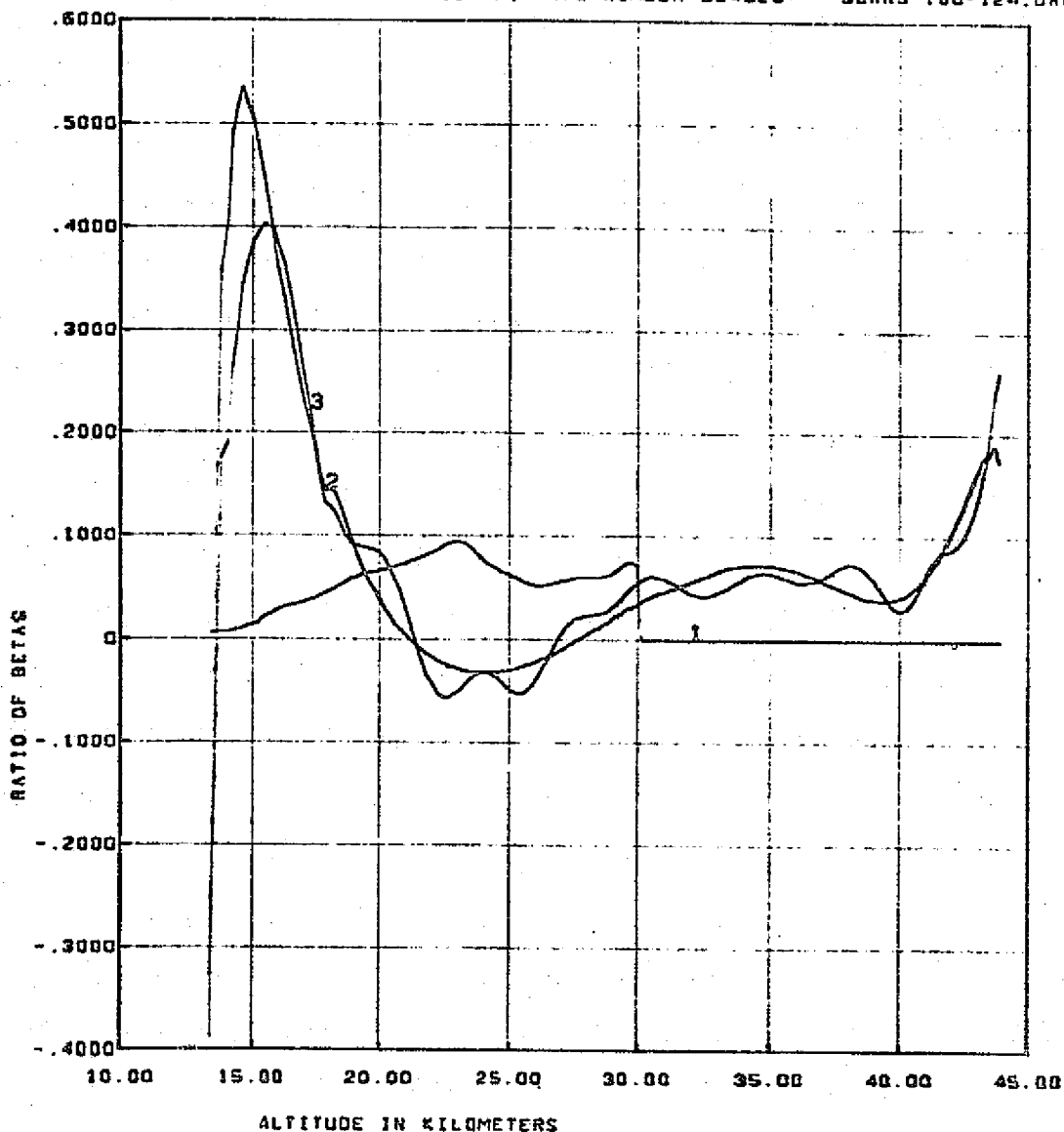
C-2

S192 CONICAL SCAN. PASS 47. TAPE NUMBER 934520

SCANS 100-124. BAND 3



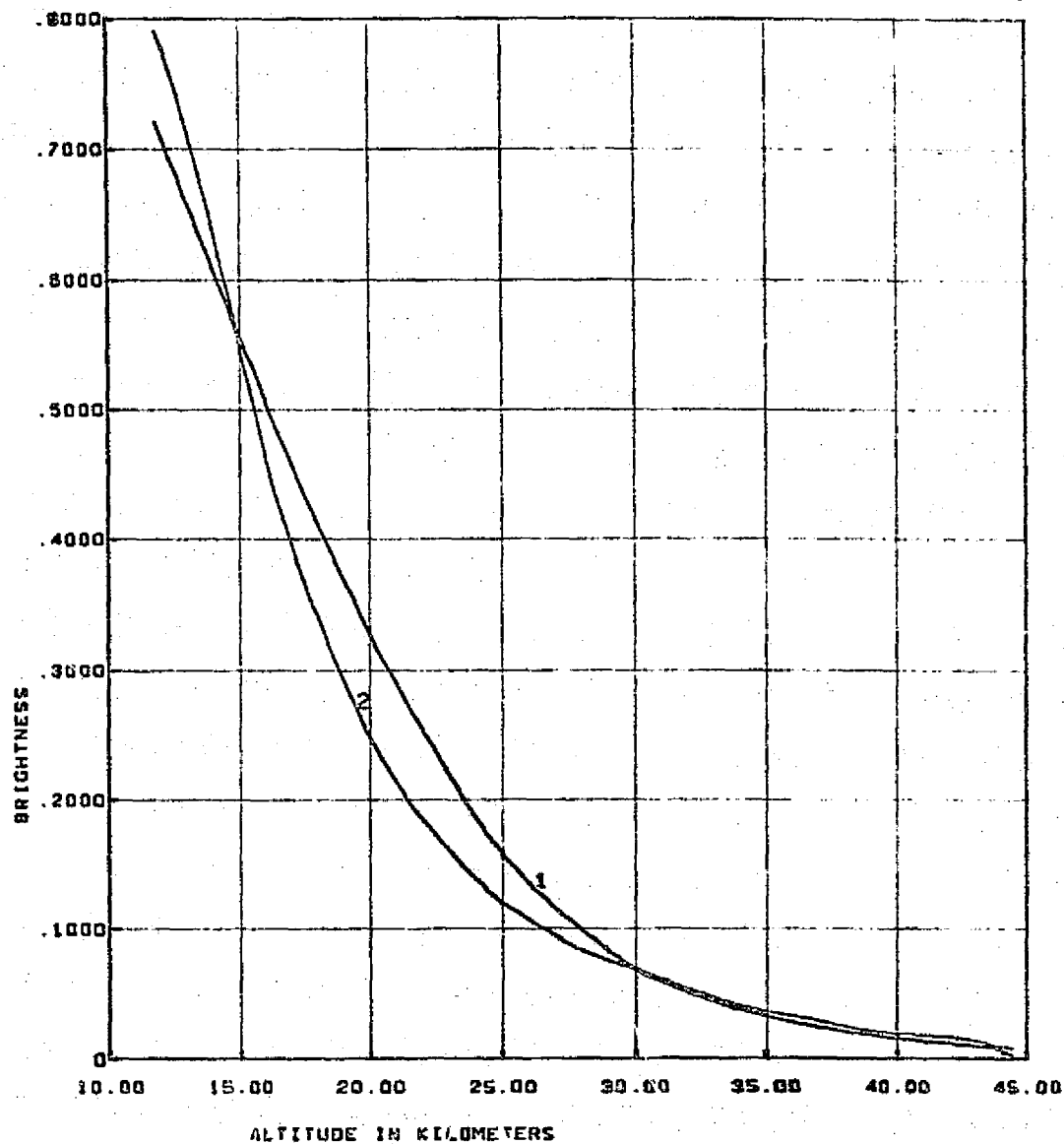
ATTENUATION COEFFICIENTS - 1-RAYLEIGH, 2-RAYLEIGH + 1984 AEROSOL, 3-RESULTS FROM INVERSION OF EXPONENTIAL FIT, 4-RESULTS FROM INVERSION OF SMOOTHED BRIGHTNESS



RATIO OF BETAS, AEROSOL OVER RAYLEIGH. 1-1984 MODEL AEROSOL. 2-RESULTS FROM INVERSION OF EXPONENTIAL FIT. 3-RESULTS FROM INVERSION OF SMOOTHED BRIGHTNESS

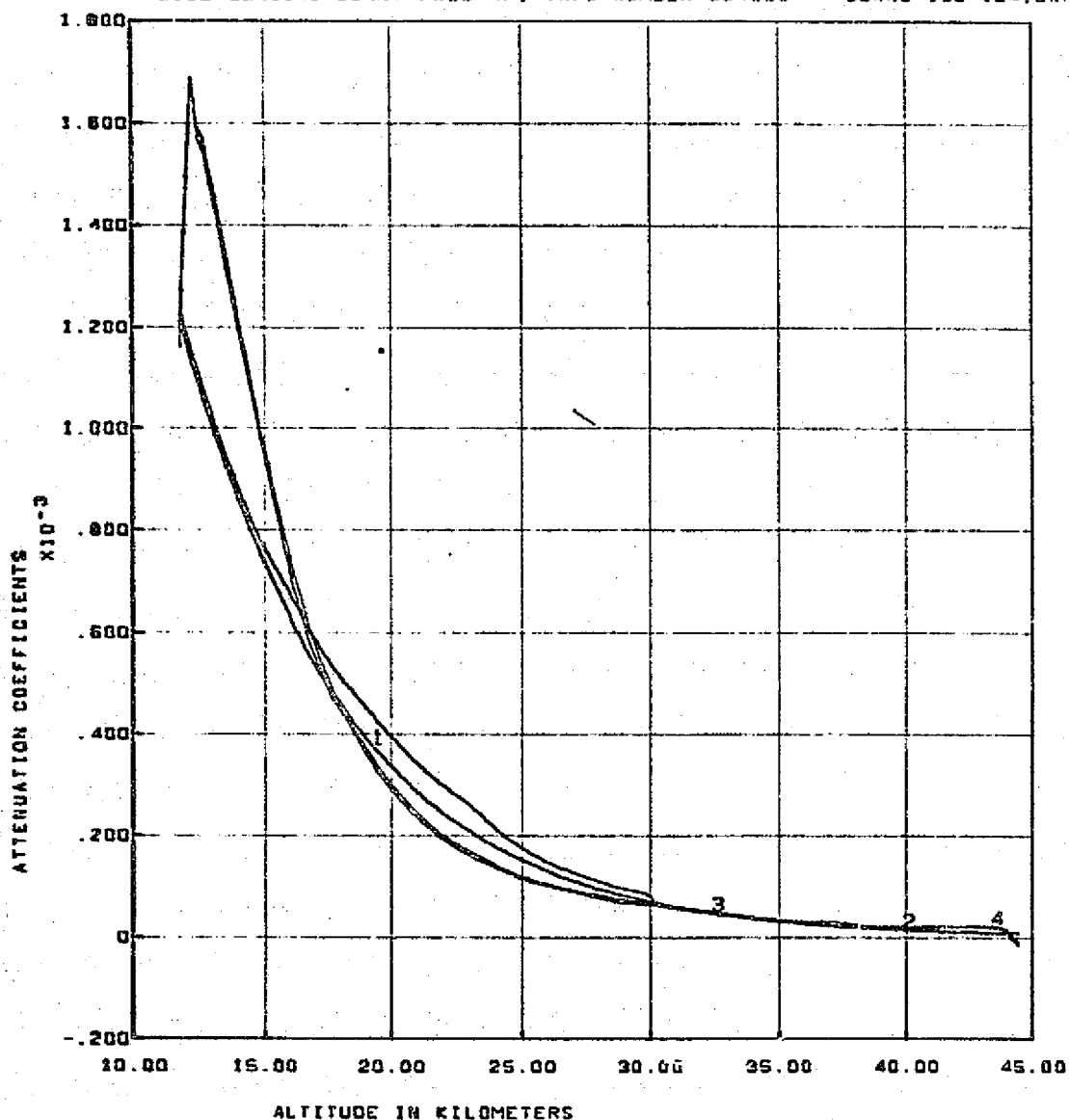
2102 CONICAL SCAN. PASS 47. TAPE NUMBER 934528

SCANS 100-124. BAND 0



CURVE 1- BRIGHTNESS MODEL GENERATED FROM RAYLEIGH + 1934 AEROSOL DATA.
CURVE 2 - MEASURED BRIGHTNESS SCALED BY 1964 MODEL.

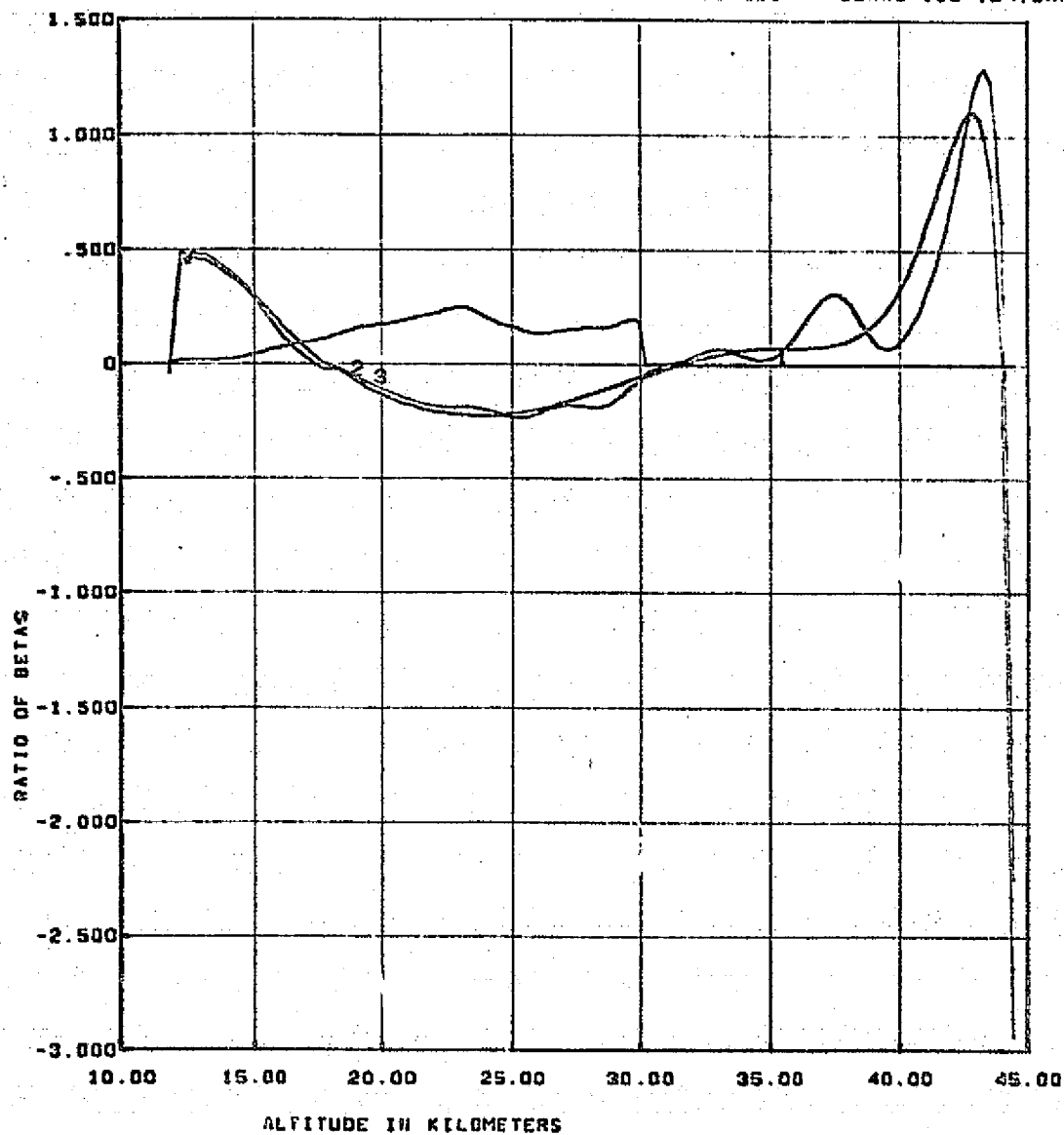
111



ATTENUATION COEFFICIENTS - 1-RAYLEIGH, 2-RAYLEIGH + 1964 AEROSOL, 3-RESULTS FROM INVERSION OF EXPONENTIAL FIT, 4-RESULTS FROM INVERSION OF SMOOTHED BRIGHTNESS

S192 CONICAL SCAN, PASS 47, TAPE NUMBER 934528

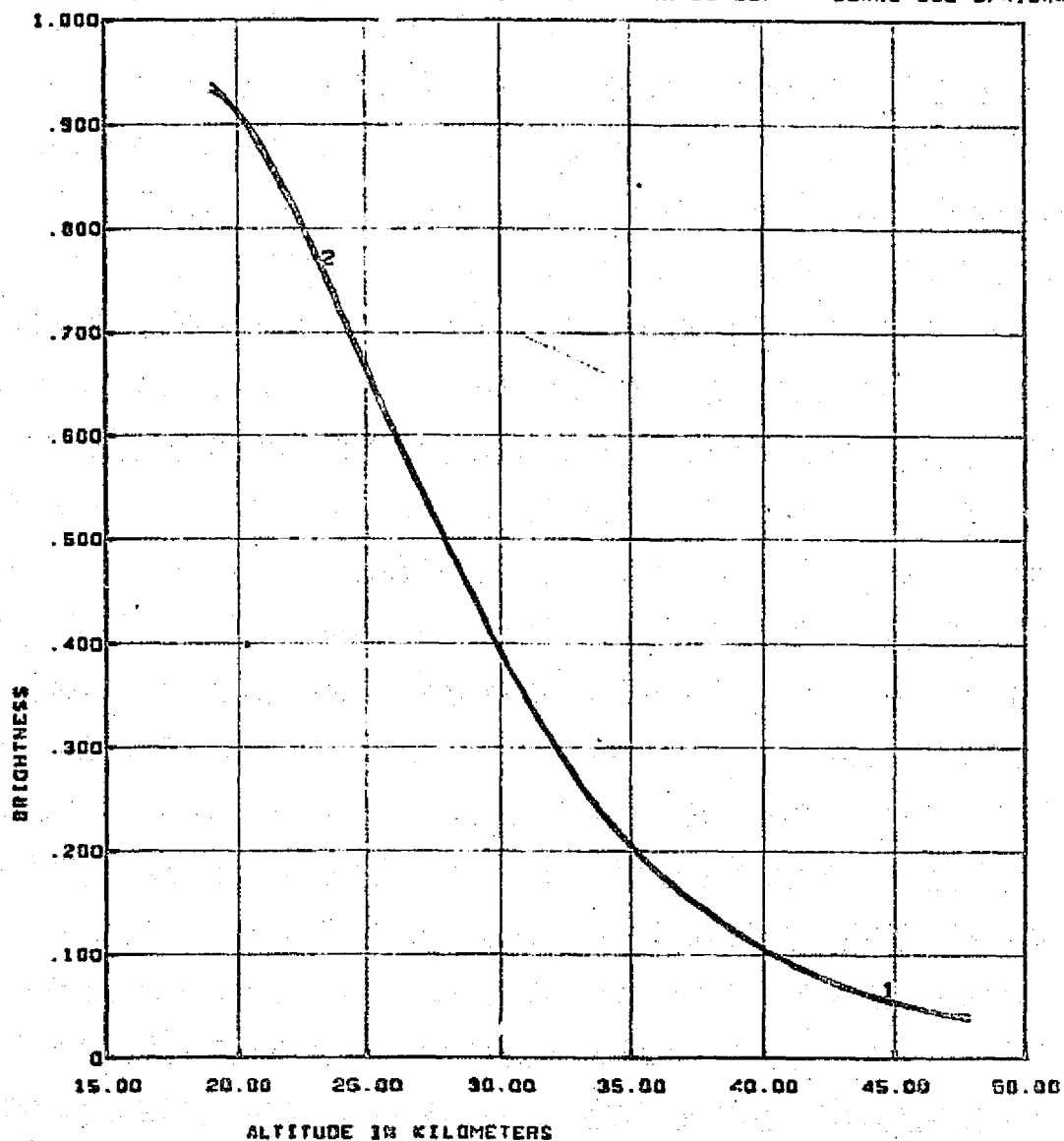
SCANS 100-124, BAND 8



RATIO OF BETAS, AEROSOL OVER RAYLEIGH. 1-1984 MODEL AEROSOL, 2-RESULTS FROM INVERSION OF EXPONENTIAL FIT, 3-RESULTS FROM INVERSION OF SMOOTHED BRIGHTNESS

S192 CONICAL SCAN. PASS 47. TAPE NUMBER 934527

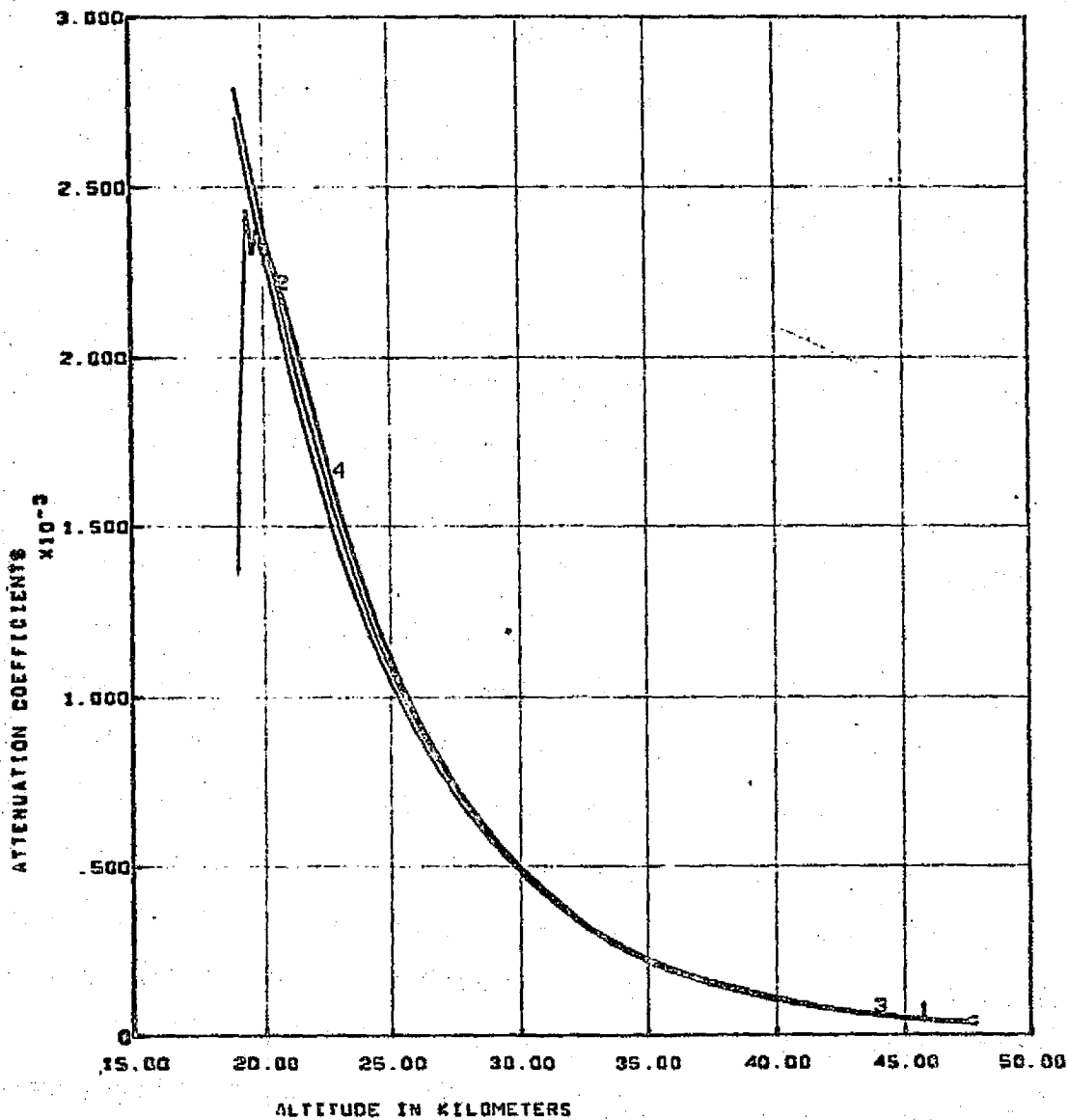
SCANS 350-374. BAND 1



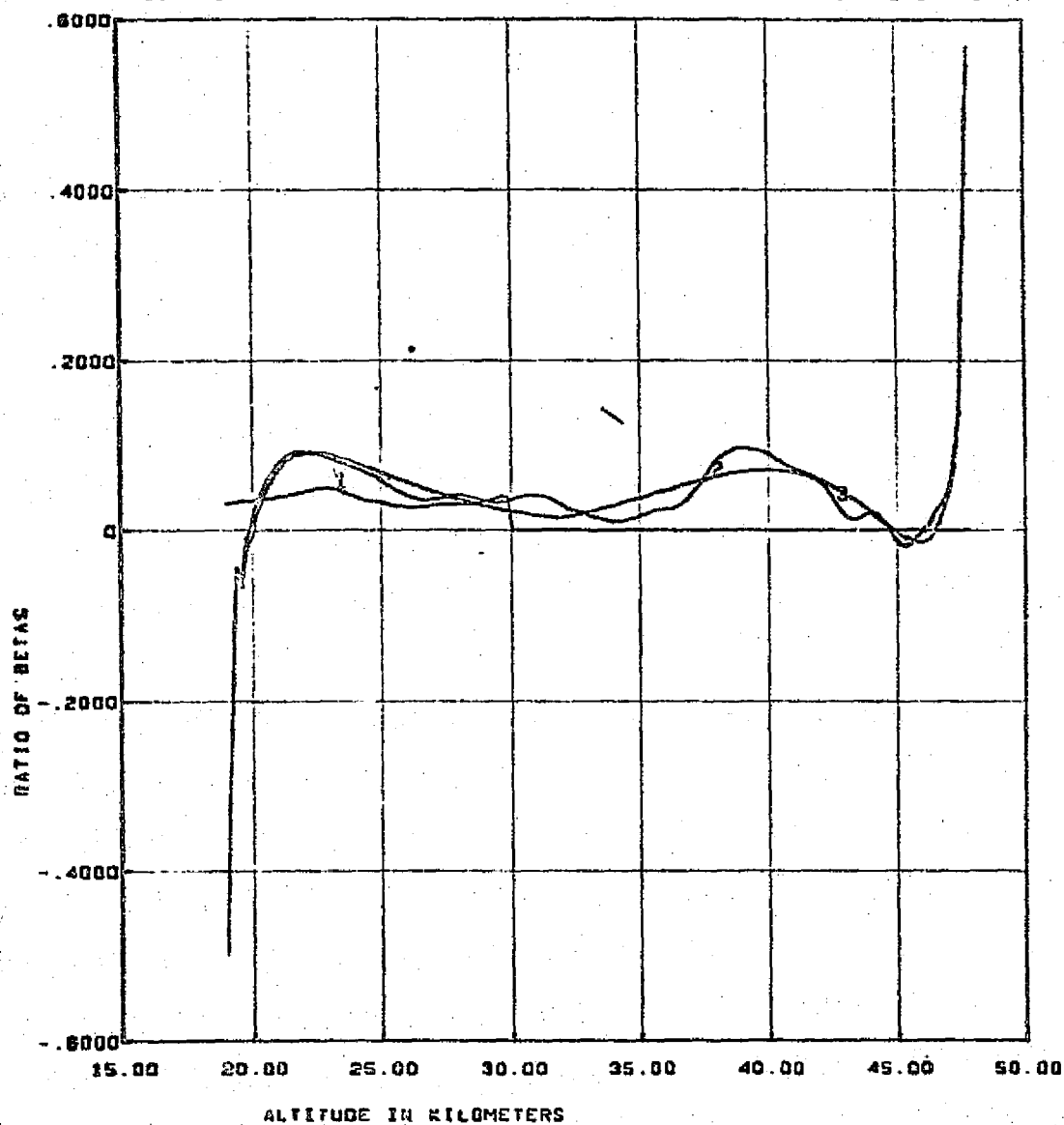
CURVE 1 - BRIGHTNESS MODEL GENERATED FROM RAYLEIGH + 1964 AEROSOL DEFFAS.
CURVE 2 - MEASURED BRIGHTNESS SCALED BY 1964 MODEL.

S192 CONICAL SCAN. PASS 47. TAPE NUMBER 934527

SCANS 350-374. DAND 1



ATTENUATION COEFFICIENTS - 1-RAYLEIGH. 2-RAYLEIGH + 1964 AEROSOL. 3-RESULTS FROM INVERSION OF EXPONENTIAL FIT. 4-RESULTS FROM INVERSION OF SMOOTHED BRIGHTNESS

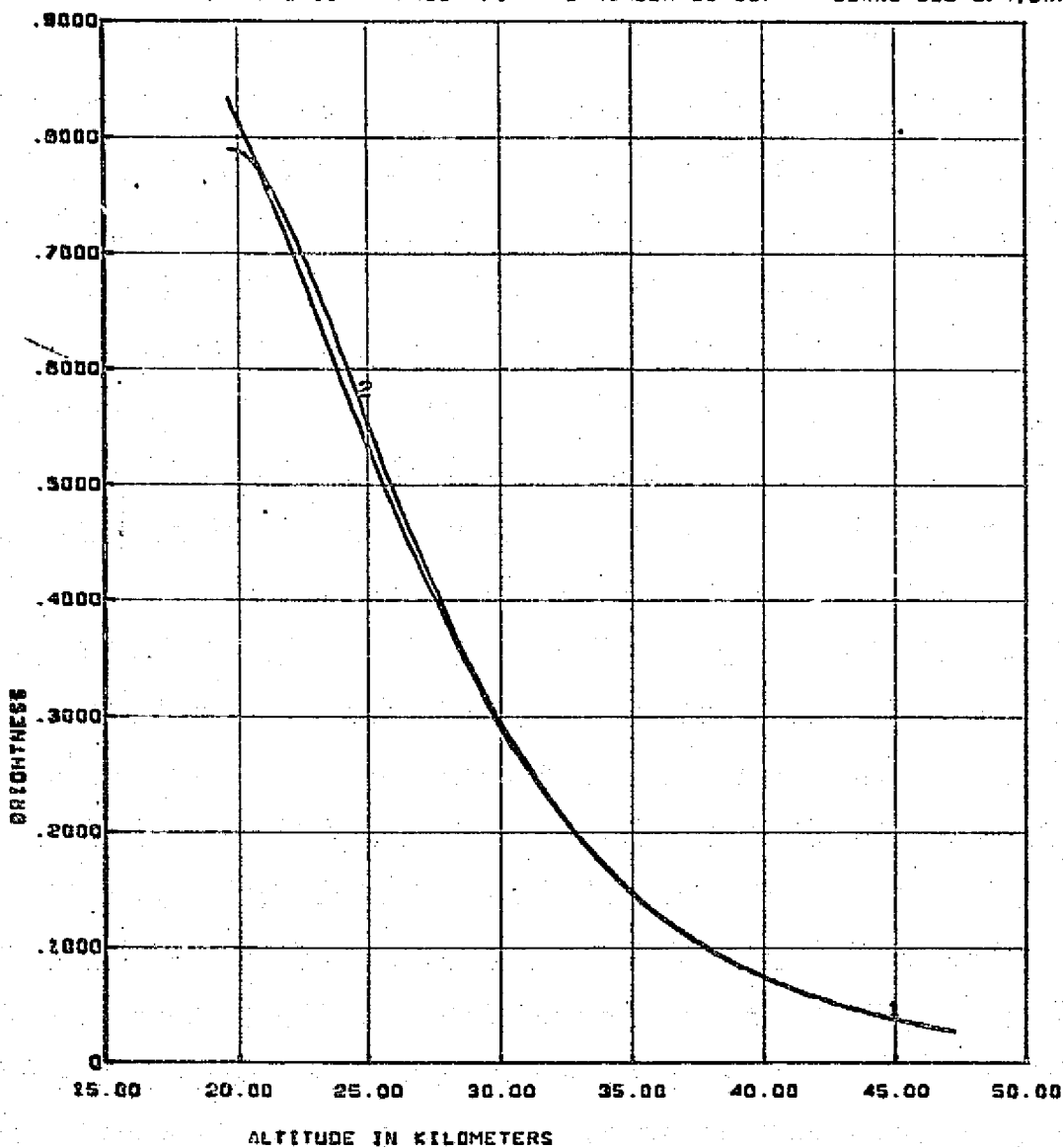


RATIO OF BETAS. AEROSOL OVER RAYLEIGH. 1-1984 MODEL AEROSOL. 2-RESULTS FROM
INVERSION OF EXPONENTIAL FIT. 3-RESULTS FROM INVERSION OF SMOOTHED BRIGHTNESS

REPRODUCIBILITY OF THE
ORIGINAL PAGE IS POOR

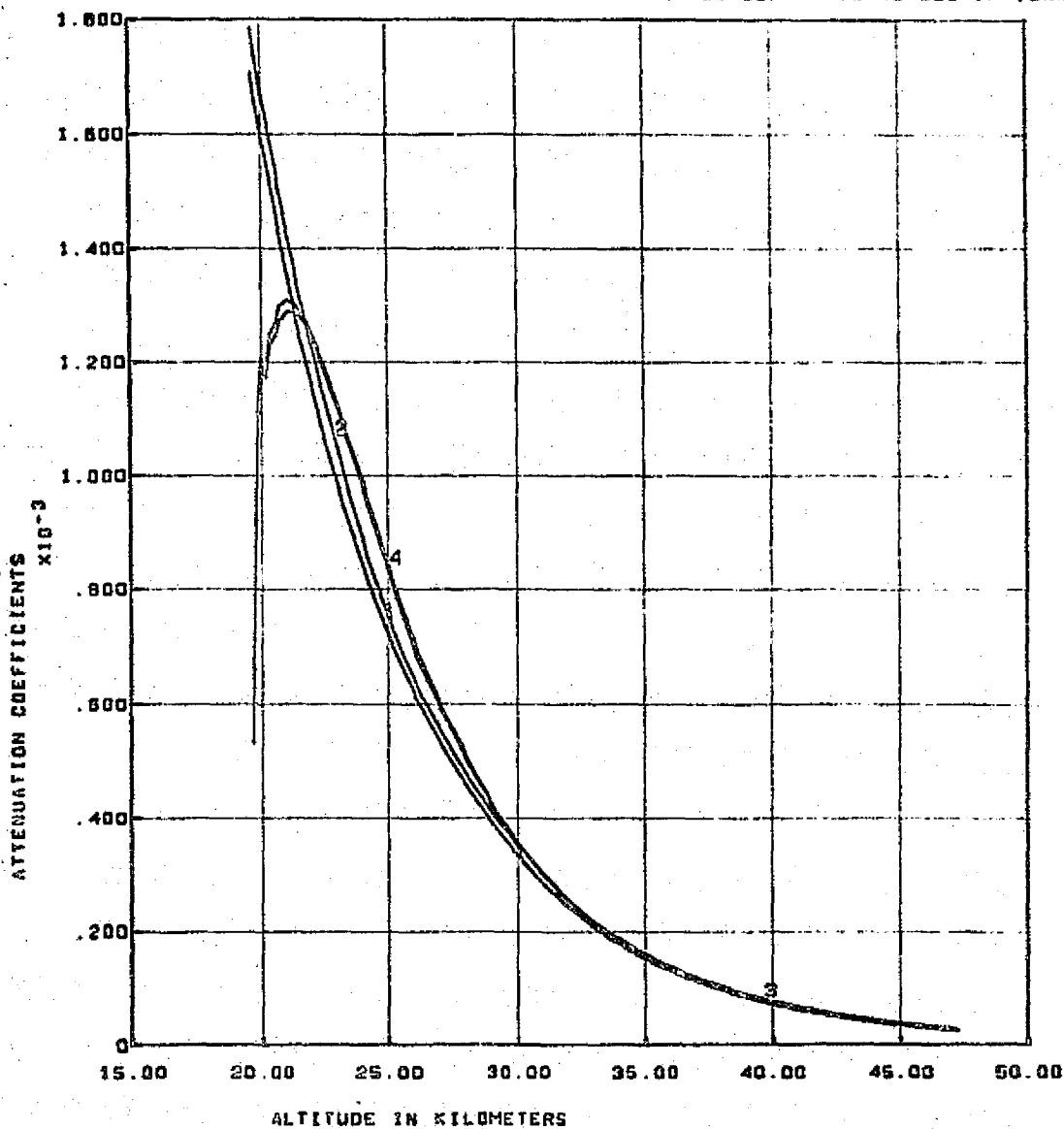
S192 CONICAL SCAN. PASS 47. TAPE NUMBER 934527

SCANS 350-374.0AND 2



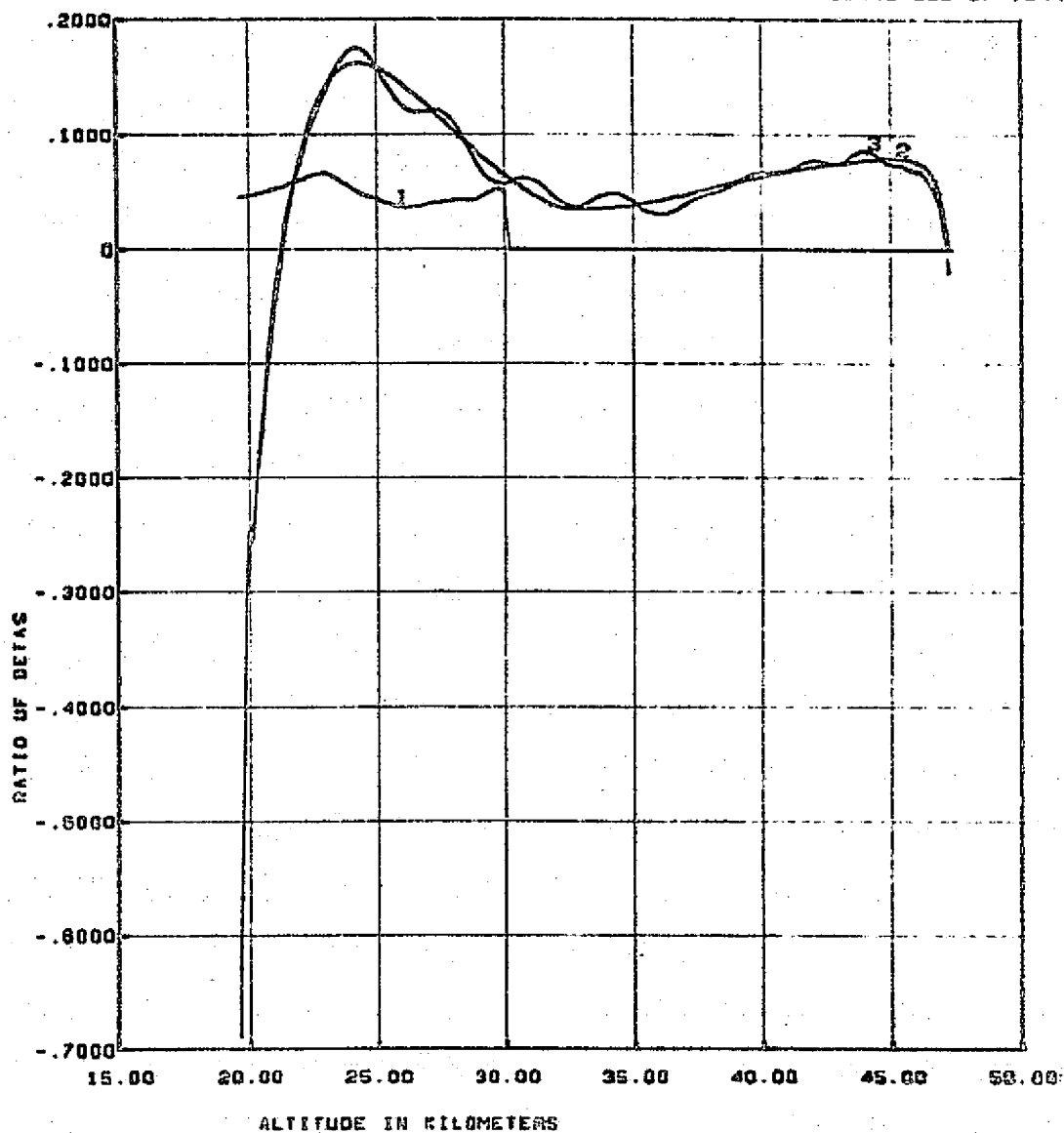
CURVE 1- BRIGHTNESS MODEL GENERATED FROM RAYLEIGH + 1964 AEROSOL DATA.
 CURVE 2 - MEASURED BRIGHTNESS SCALED BY 1964 MODEL.

S192 CONICAL SCAN. PASS 47. TAPE NUMBER 934527 SCANS 350-374.0AND 2



ATTENUATION COEFFICIENTS - 1-RAYLEIGH, 2-RAYLEIGH + 1984 AEROSOL, 3-RESULTS FROM INVERSION OF EXPONENTIAL FIT, 4-RESULTS FROM INVERSION OF SMOOTHED BRIGHTNESS

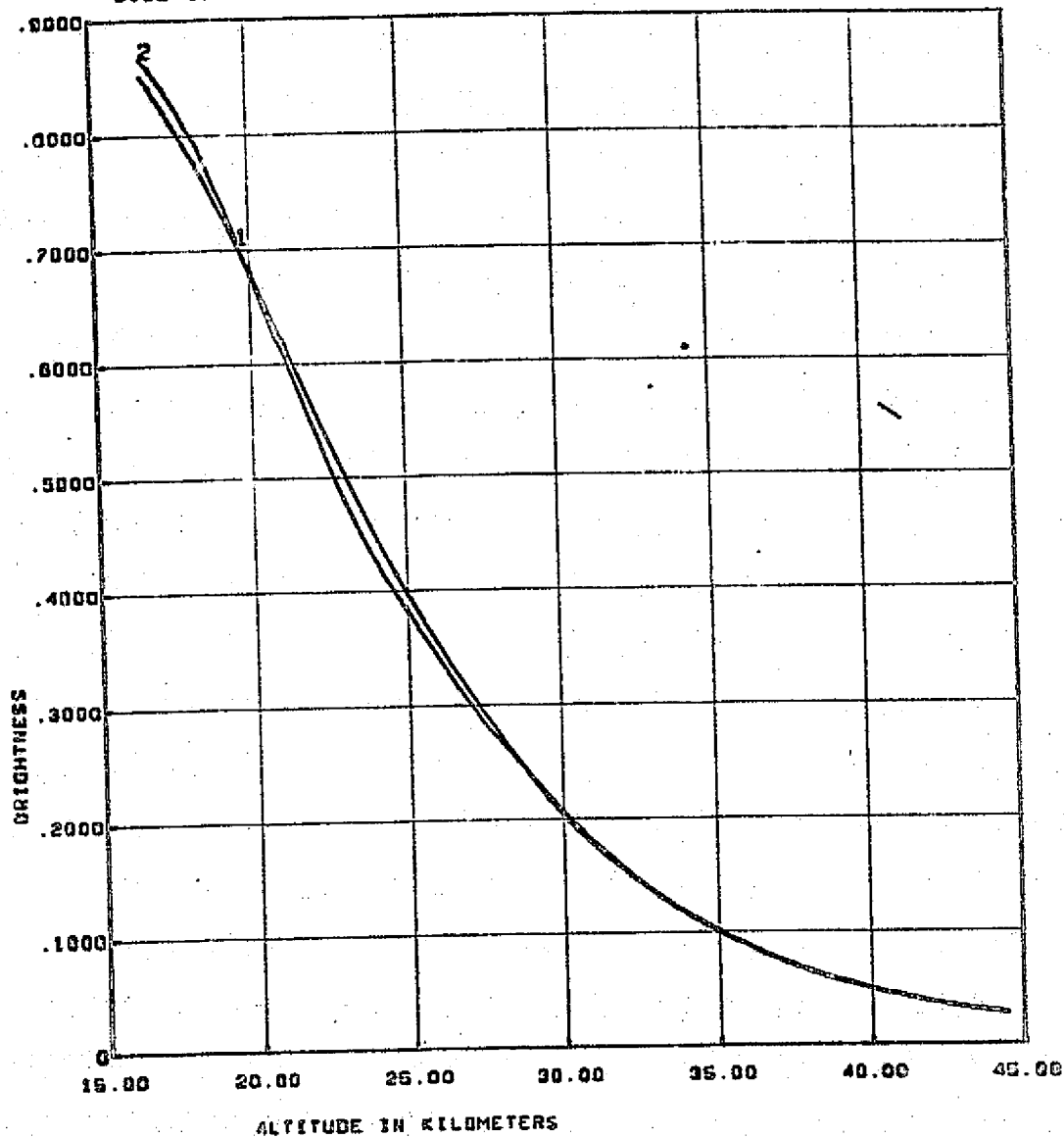
S102 CONICAL SCAN, PASS 42, TAPE NUMBER 034527 SCANS 350-374, BAND 2



RATIO OF BETAS, AEROSOL OVER RAYLEIGH. 1-1954 MODEL AEROSOL. 2-RESULTS FROM INVERSION OF EXPONENTIAL FIT. 3-RESULTS FROM INVERSION OF SMOOTHED BRIGHTNESS

S192 CONICAL SCAN. PASS 47. TAPE NUMBER 934527

SCANS 350-374. BAND 3



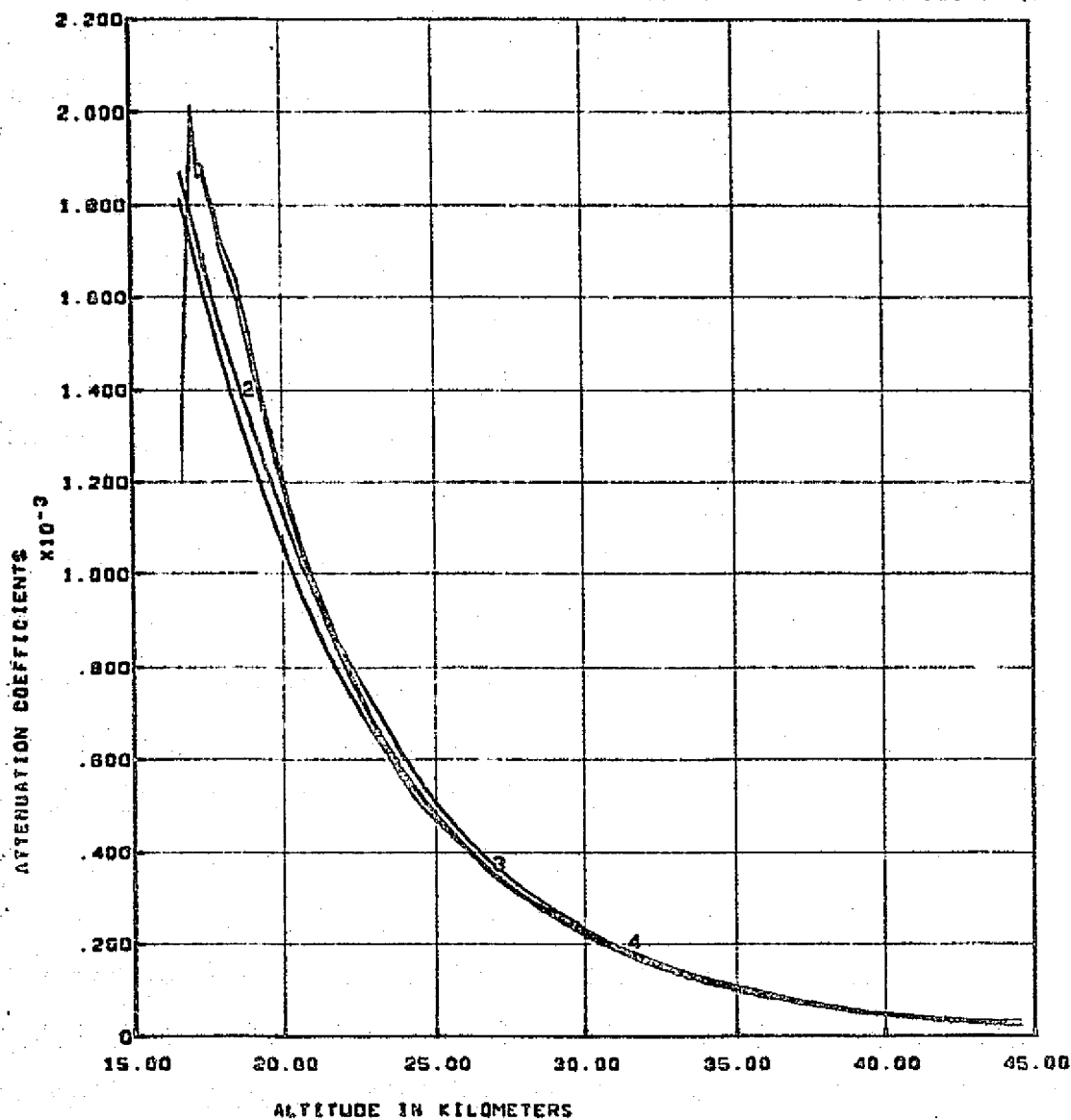
CURVE 1 - BRIGHTNESS MODEL GENERATED FROM RAYLEIGH + 1984 AEROSOL DATAS.
CURVE 2 - MEASURED BRIGHTNESS SCALED BY 1984 MODEL.

REPRODUCIBILITY OF THE
ORIGINAL PAGE IS POOR

S192 CONICAL SCAN. PASS 47. TAPE NUMBER 934527

SCANS 350-374.DAND

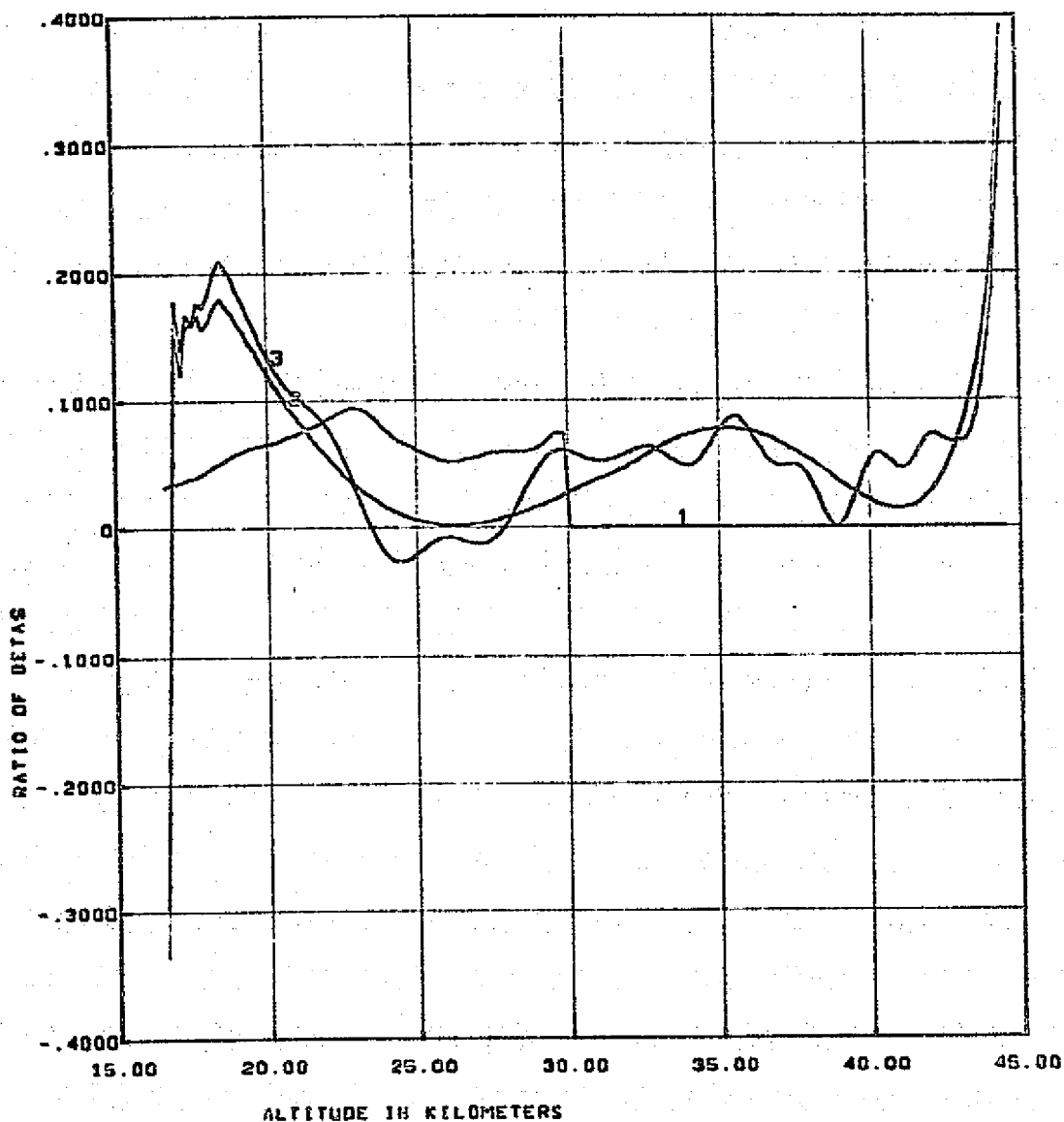
3



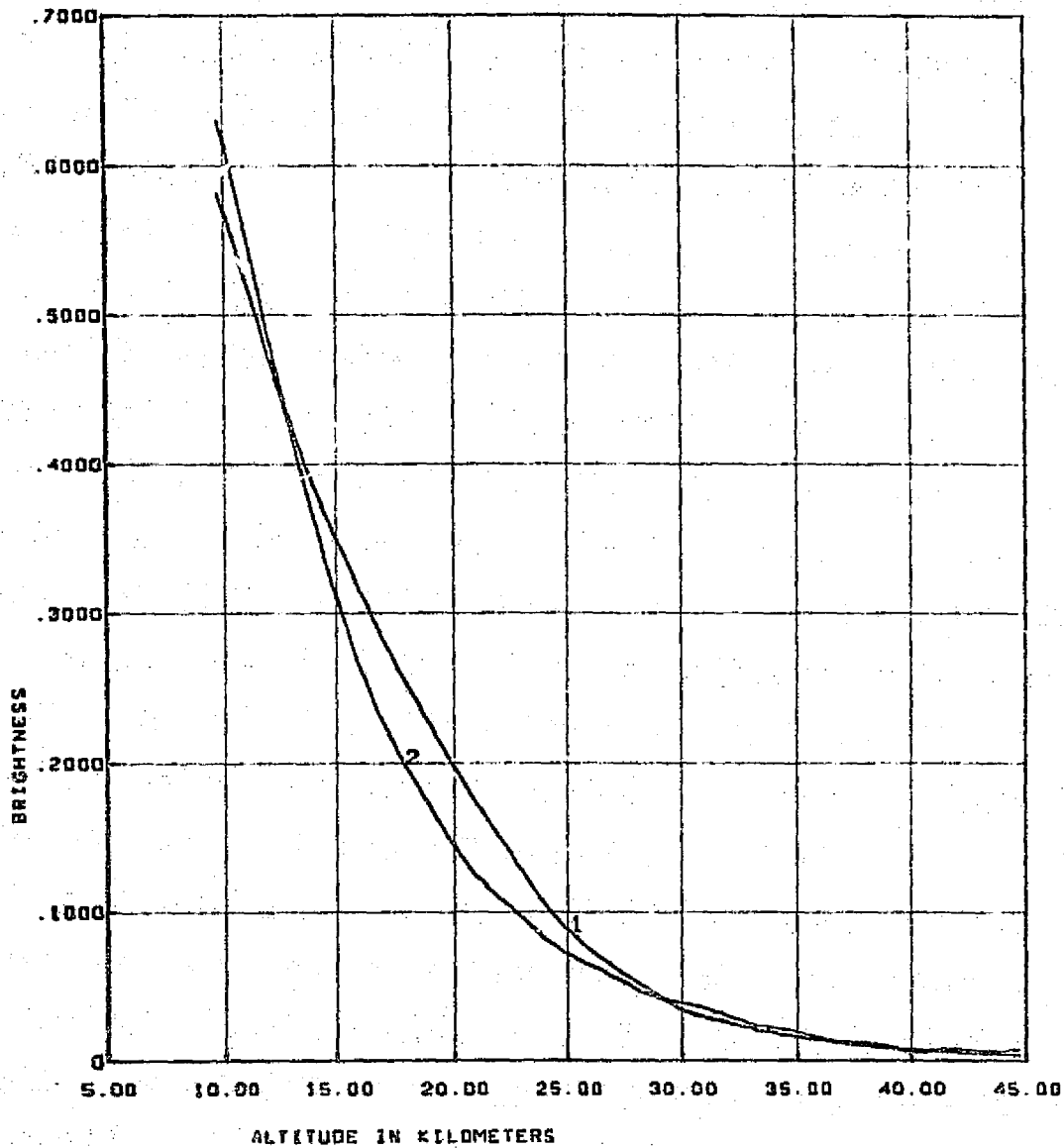
ATTENUATION COEFFICIENTS - 1-RAYLEIGH, 2-RAYLEIGH + 1984 AEROSOL, 3-RESULTS FROM INVERSION OF EXPONENTIAL FIT, 4-RESULTS FROM INVERSION OF SMOOTHED BRIGHTNESS

S192 CONICAL SCAN. PASS 47. TAPE NUMBER 934527

SCANS 350-374. BAND 3



RATIO OF BETAS. AEROSOL OVER RAYLEIGH. 1-1964 MODEL AEROSOL. 2-RESULTS FROM INVERSION OF EXPONENTIAL FIT. 3-RESULTS FROM INVERSION OF SMOOTHED BRIGHTNESS

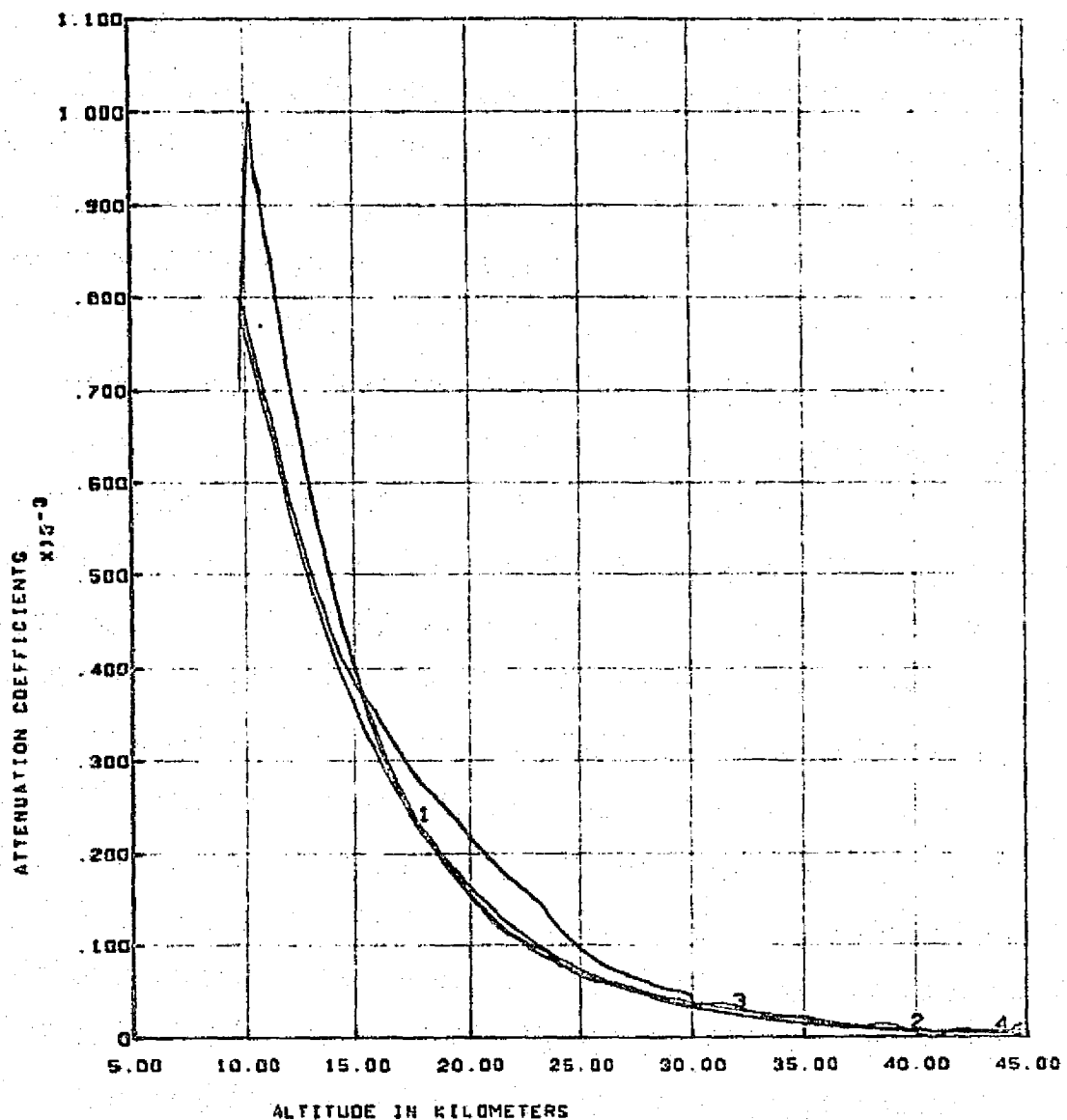


CURVE 1 - BRIGHTNESS MODEL GENERATED FROM RAYLEIGH + 1964 AEROSOL BETAS.
CURVE 2 - MEASURED BRIGHTNESS SCALED BY 1964 MODEL.

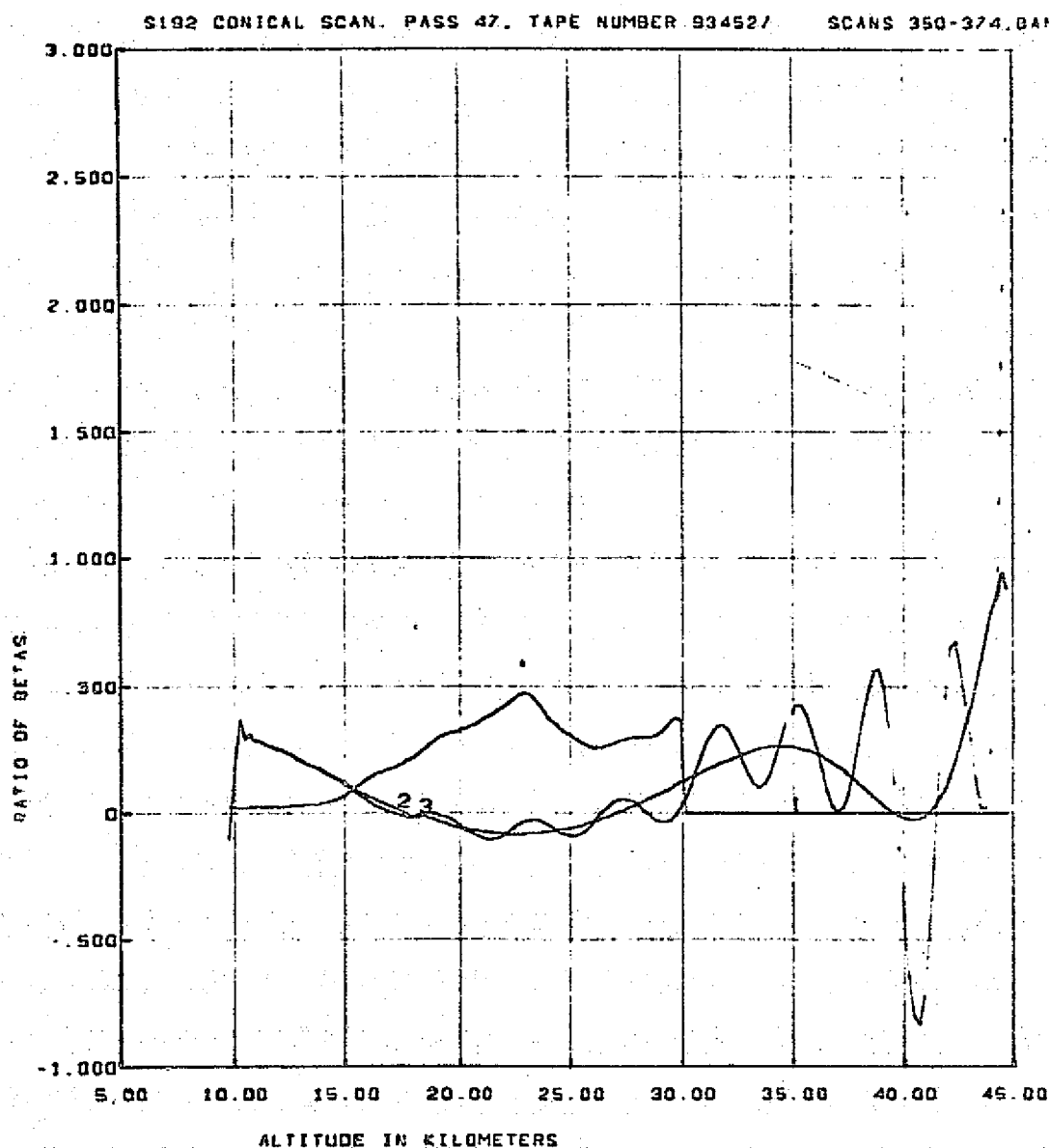
S192 CONICAL SCAN. PASS 47. TAPE NUMBER 934527

SCANS 350-374, BAND 7

011

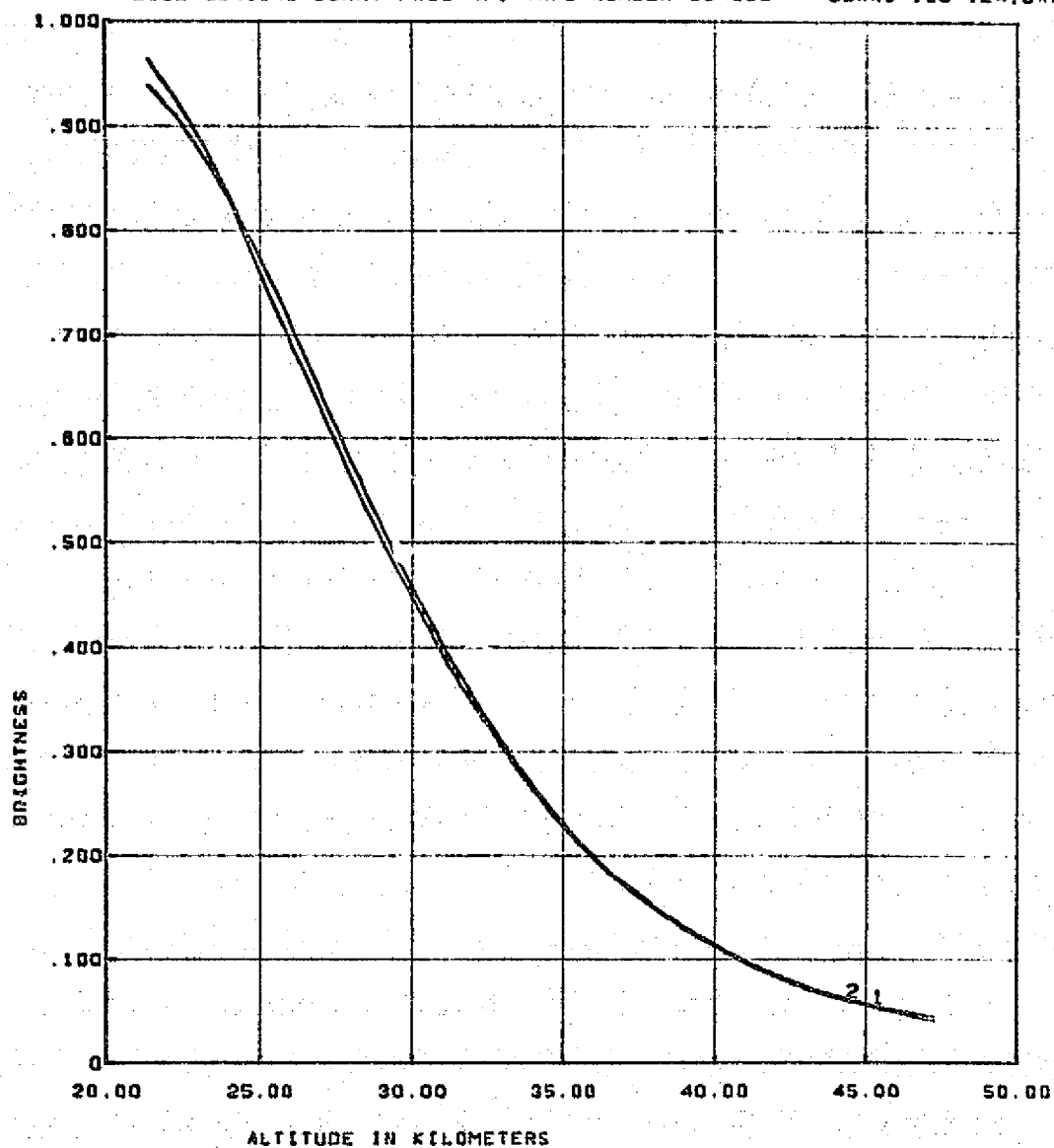


ATTENUATION COEFFICIENTS - 1-RAYLEIGH, 2-RAYLEIGH + 1984 AEROSOL, 3-RESULTS FROM INVERSION OF EXPONENTIAL FIT, 4-RESULTS FROM INVERSION OF SMOOTHED BRIGHTNESS



RATIO OF BETAS AEROSOL OVER RAYLEIGH. 1-1964 MODEL AEROSOLS 2-RESULTS FROM INVERSION OF EXPONENTIAL FIT. 3-RESULTS FROM INVERSION OF SMOOTHED BRIGHTNESS

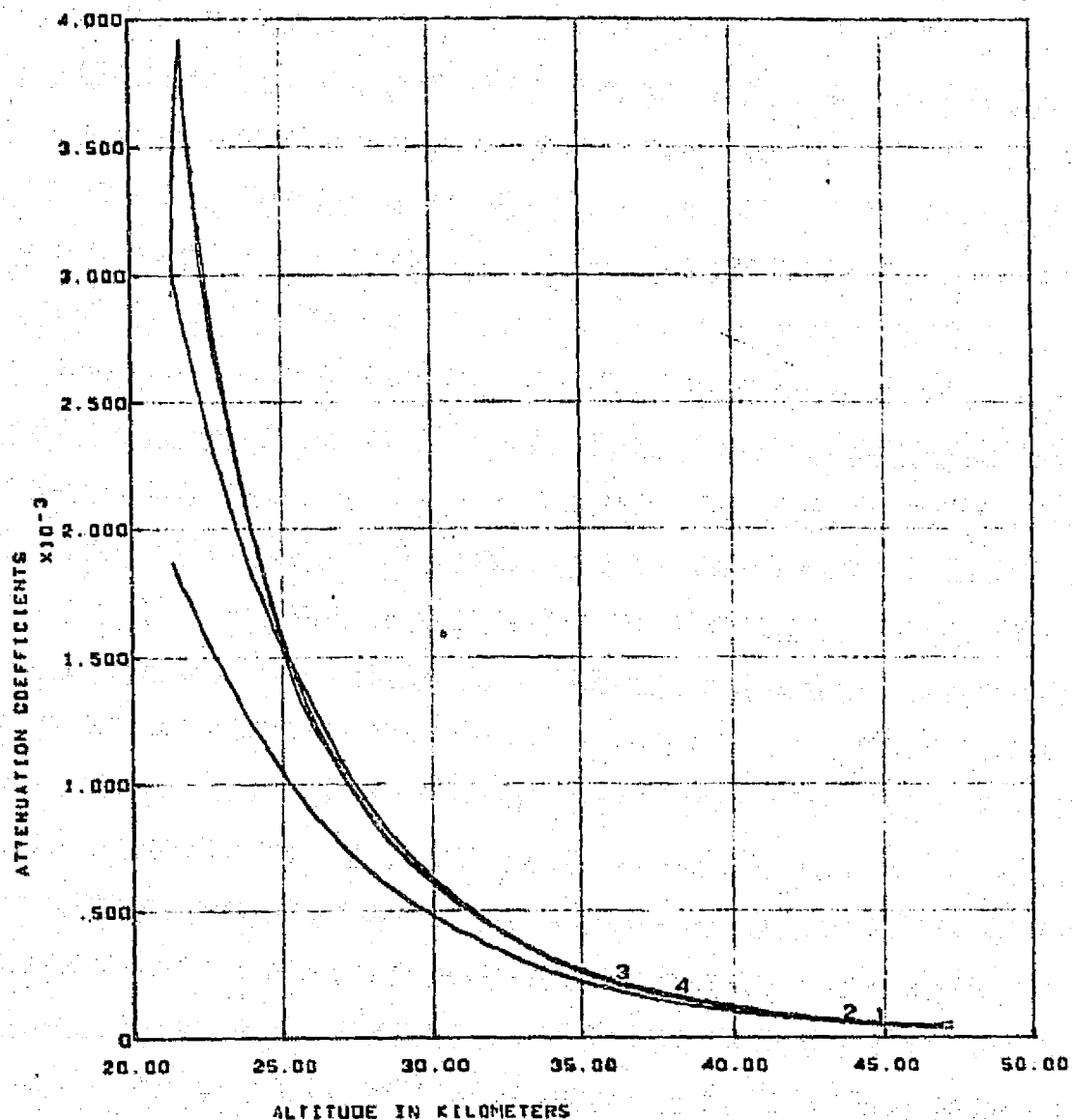
REPRODUCIBILITY OF THE ORIGINAL PAGE IS POOR



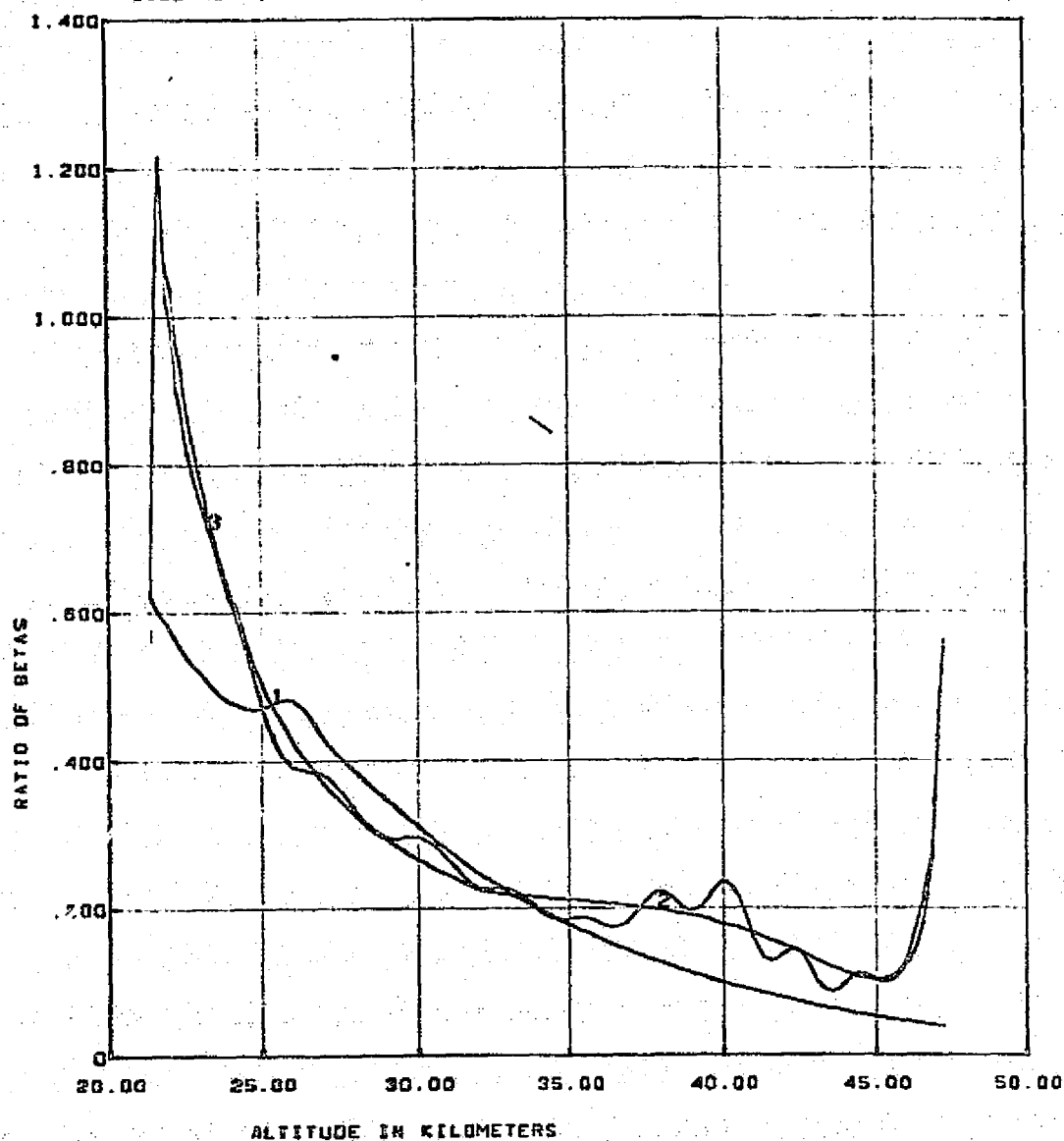
CURVE 1 - BRIGHTNESS MODEL GENERATED FROM RAYLEIGH + 1968 AEROSOL BETAS.
CURVE 2 - MEASURED BRIGHTNESS SCALED BY 1968 MODEL.

S192 CONICAL SCAN PASS 47. TAPE NUMBER 934528

SCANS 100-124, BAND 1



ATTENUATION COEFFICIENTS - 1-RAYLEIGH. 2-RAYLEIGH + 1000 AEROSOL. 3-RESULTS FROM INVERSION OF EXPONENTIAL FIT. 4-RESULTS FROM INVERSION OF SMOOTHED BRIGHTNESS

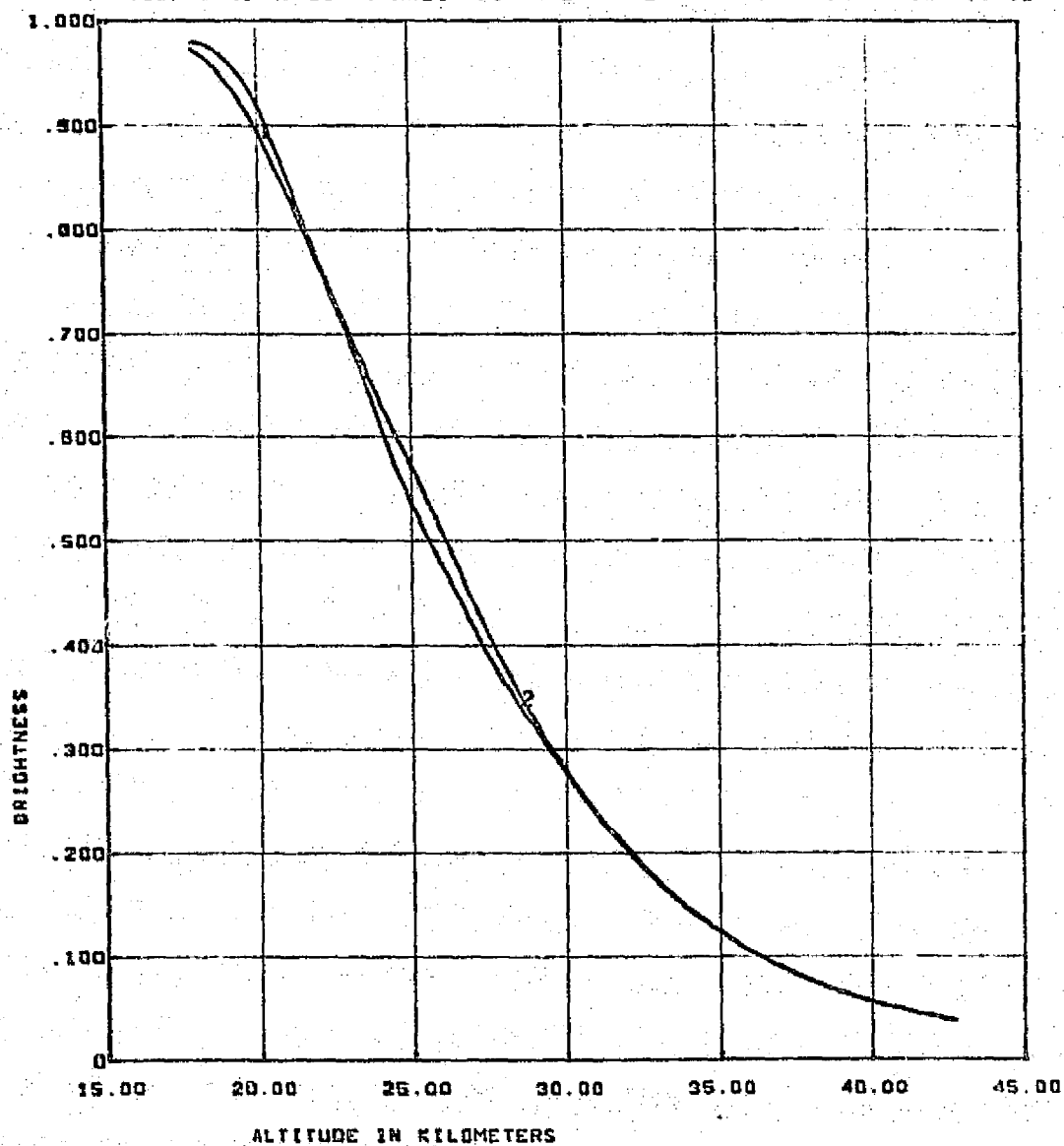


RATIO OF BETAS, AEROSOL OVER RAYLEIGH. 1-1988 MODEL AEROSOL. 2-RESULTS FROM INVERSION OF EXPONENTIAL FIT. 3-RESULTS FROM INVERSION OF SMOOTHED BRIGHTNESS

REPRODUCIBILITY OF THE
ORIGINAL PAGE IS POOR

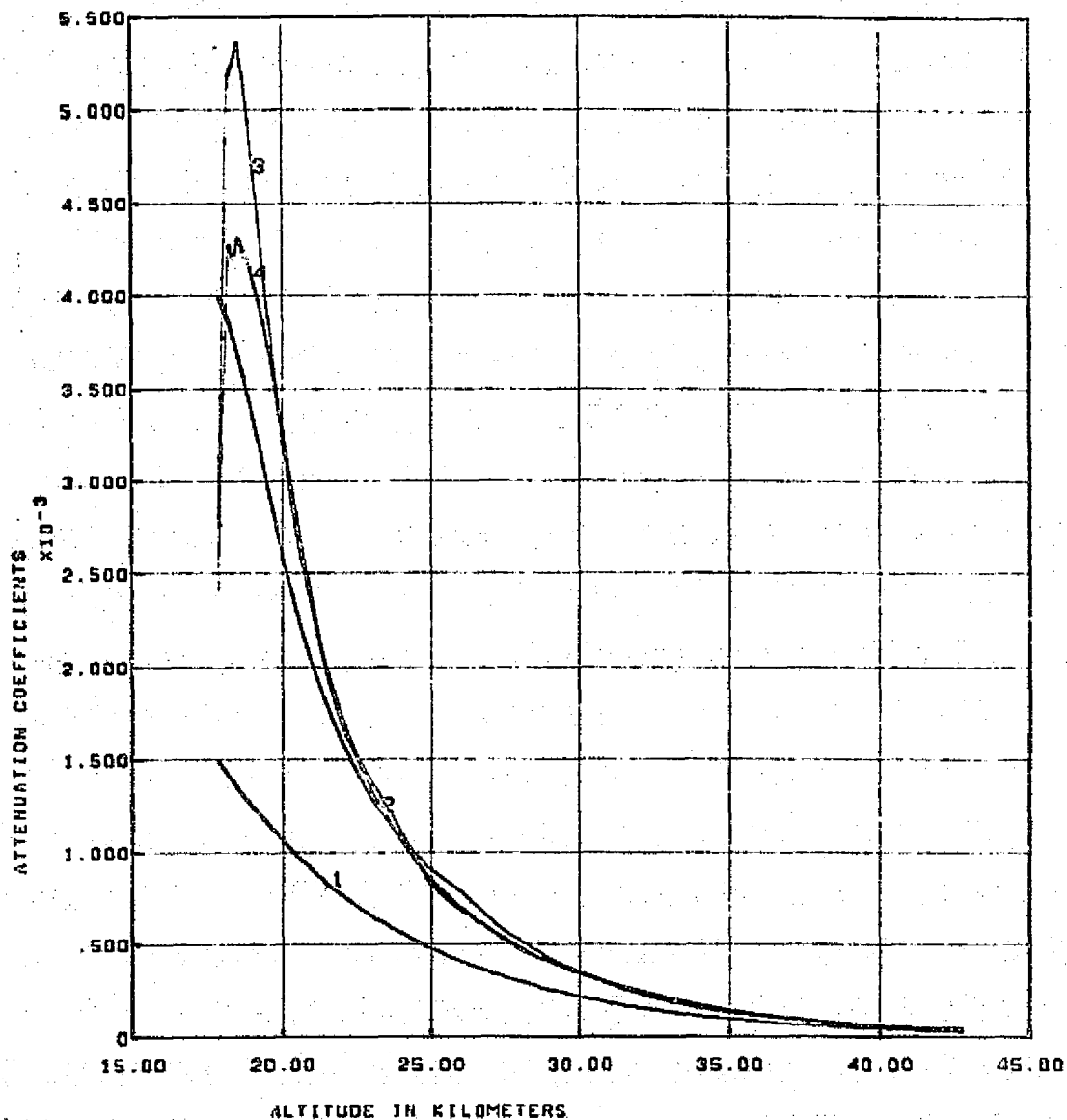
S192 CONICAL SCAN. PASS 47. TAPE NUMBER 934528

SCANS 100-124. DAND 3

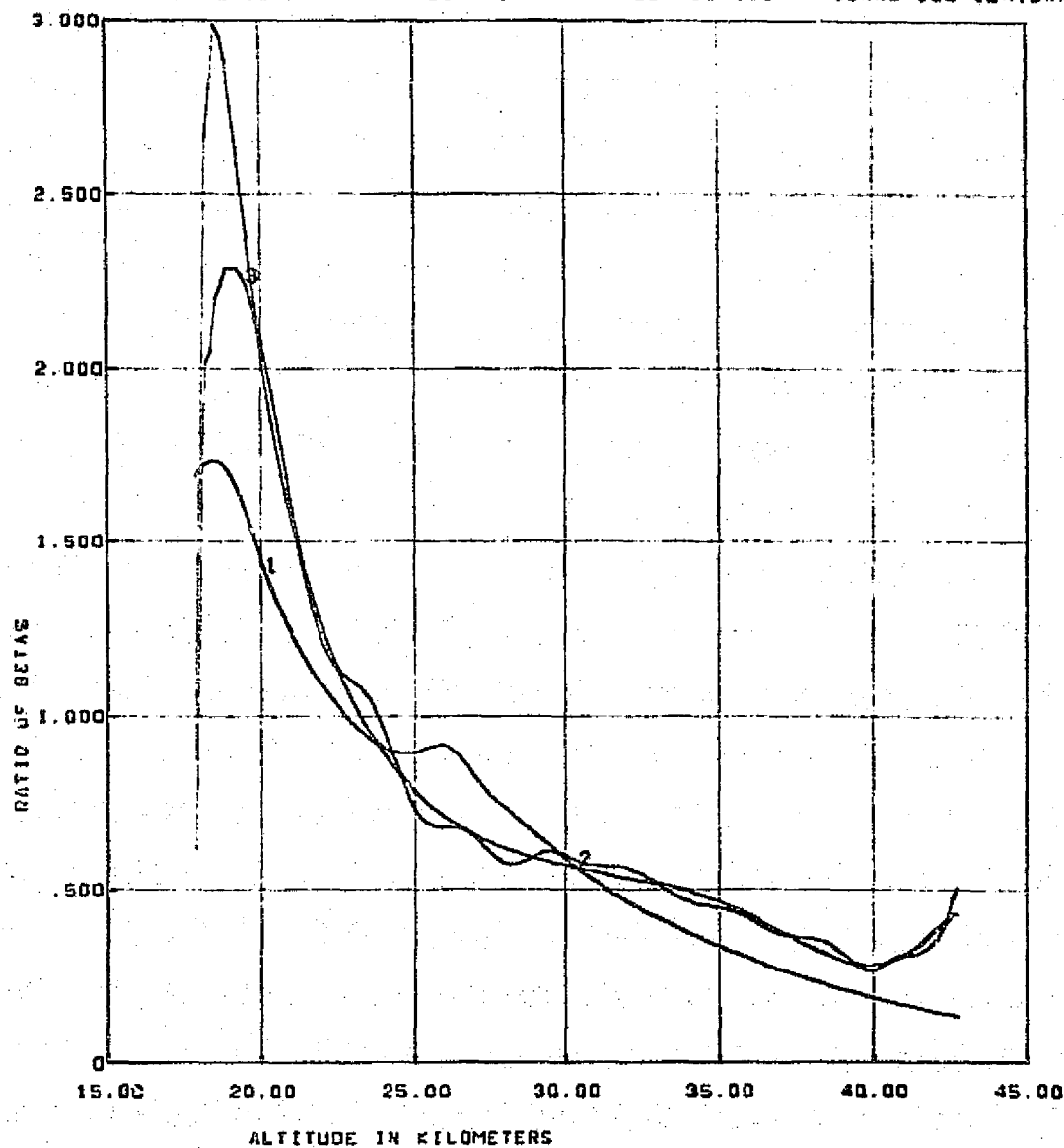


CURVE 1 - BRIGHTNESS MODEL GENERATED FROM RAYLEIGH + 1968 AEROSOL DETAS
CURVE 2 - MEASURED BRIGHTNESS SCALED BY 1968 MODEL.

S192 CONICAL SCAN. PASS 47. TAPE NUMBER 934528 SCANS 100-124. BAND 3



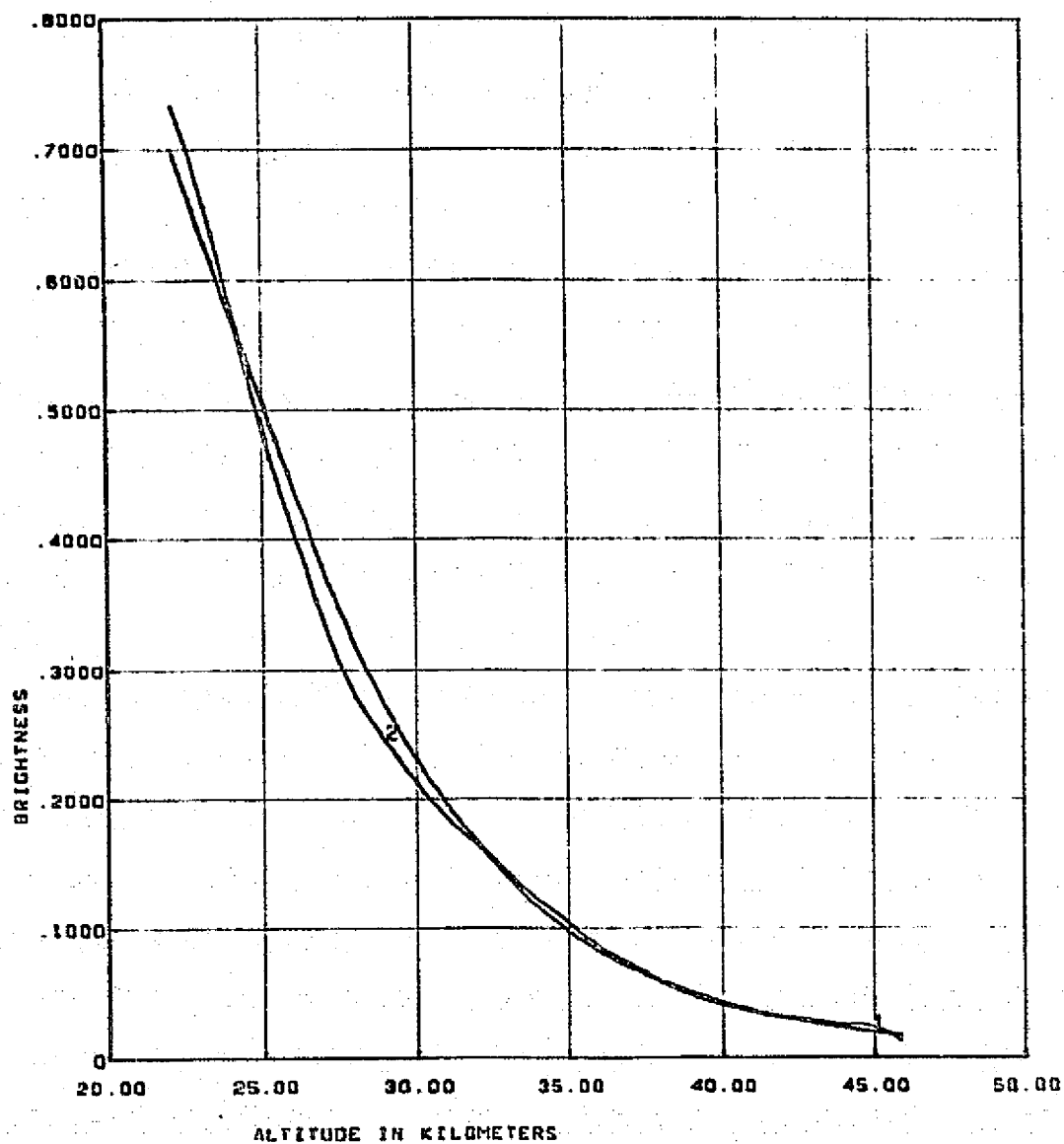
ATTENUATION COEFFICIENTS - 1-RAYLEIGH. 2-RAYLEIGH + 1960 AEROSOL. 3-RESULTS FROM INVERSION OF EXPONENTIAL FIT. 4-RESULTS FROM INVERSION OF SMOOTHED BRIGHTNESS



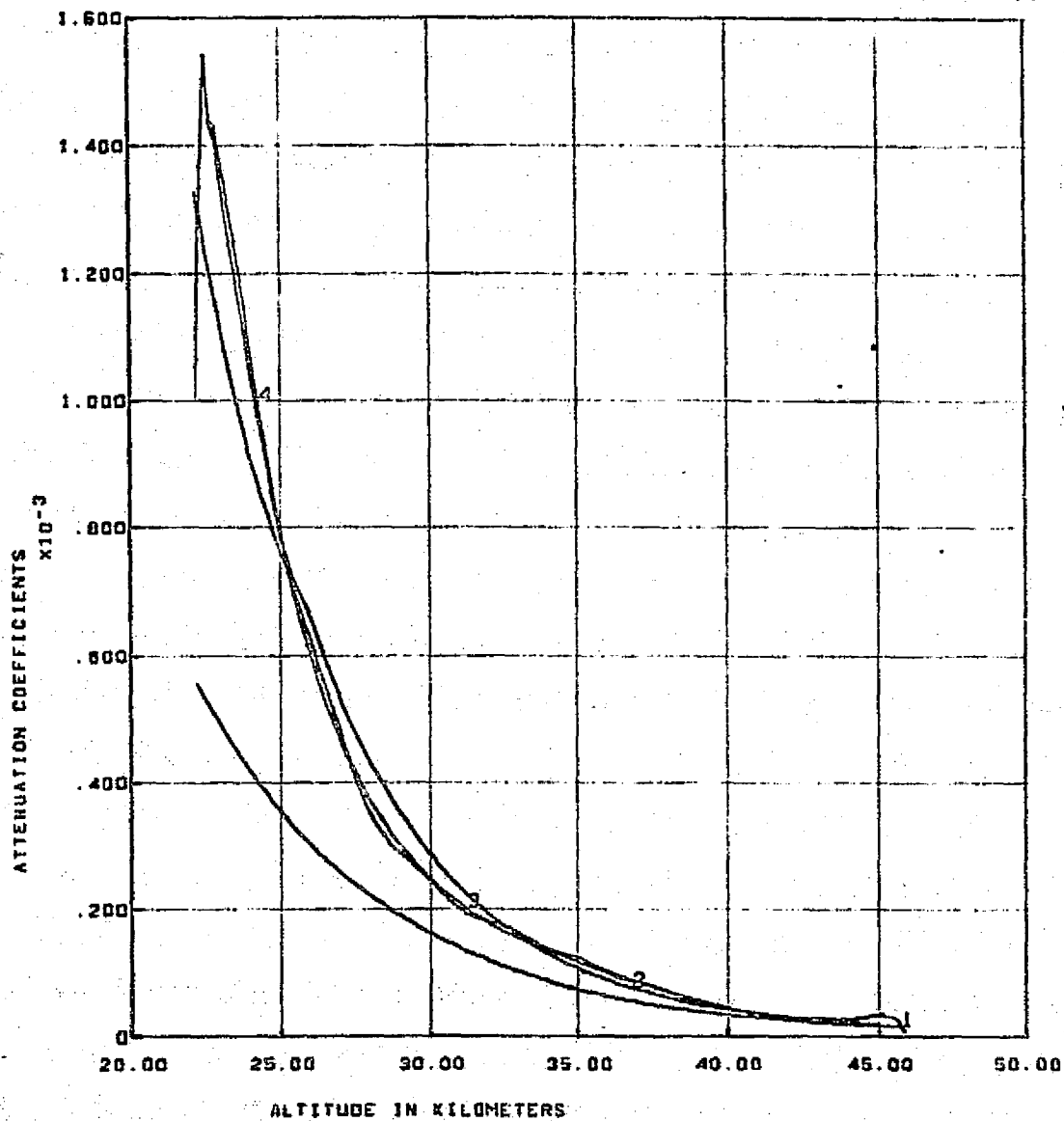
RATIO OF BETAS, AEROSOL OVER RAYLEIGH. 1-1968 MODEL AEROSOL. 2-RESULTS FROM INVERSION OF EXPONENTIAL FIT. 3-RESULTS FROM INVERSION OF SMOOTHED BRIGHTNESS

81A

S192 CONICAL SCAN. PASS 47. TAPE NUMBER 934520 SCANS 100-124.DAND 4



CURVE 1 - BRIGHTNESS MODEL GENERATED FROM RAYLEIGH + 1968 AEROSOL BETAS.
 CURVE 2 - MEASURED BRIGHTNESS SCALED BY 1968 MODEL.



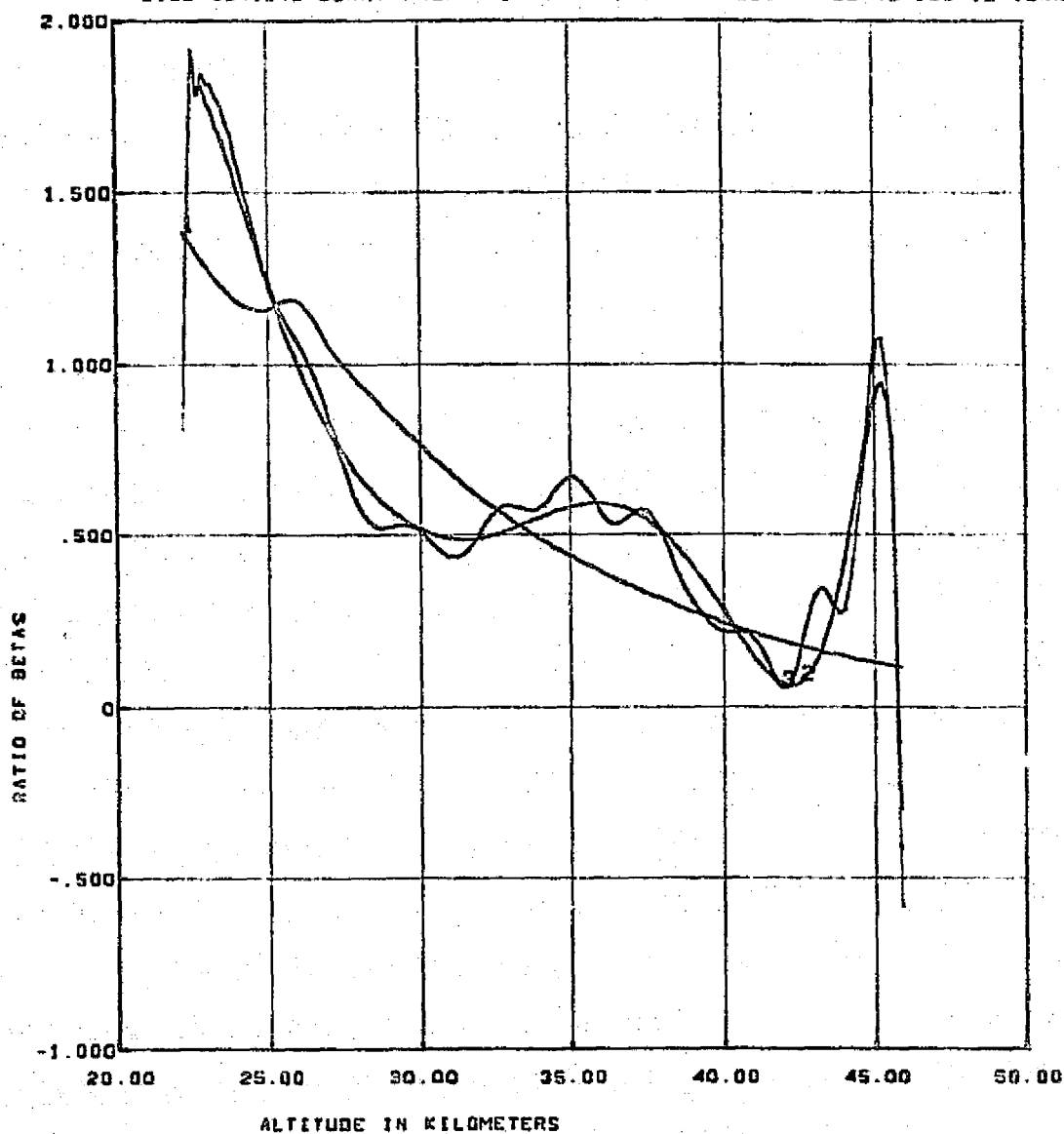
ATTENUATION COEFFICIENTS - 1-RAYLEIGH. 2-RAYLEIGH + 1966 AEROSOL. 3-RESULTS FROM INVERSION OF EXPONENTIAL FIT. 4-RESULTS FROM INVERSION OF SMOOTHED BRIGHTNESS

81A

S192 CONICAL SCAN. PASS 47. TAPE NUMBER 934528

SCANS 100-124.DAND

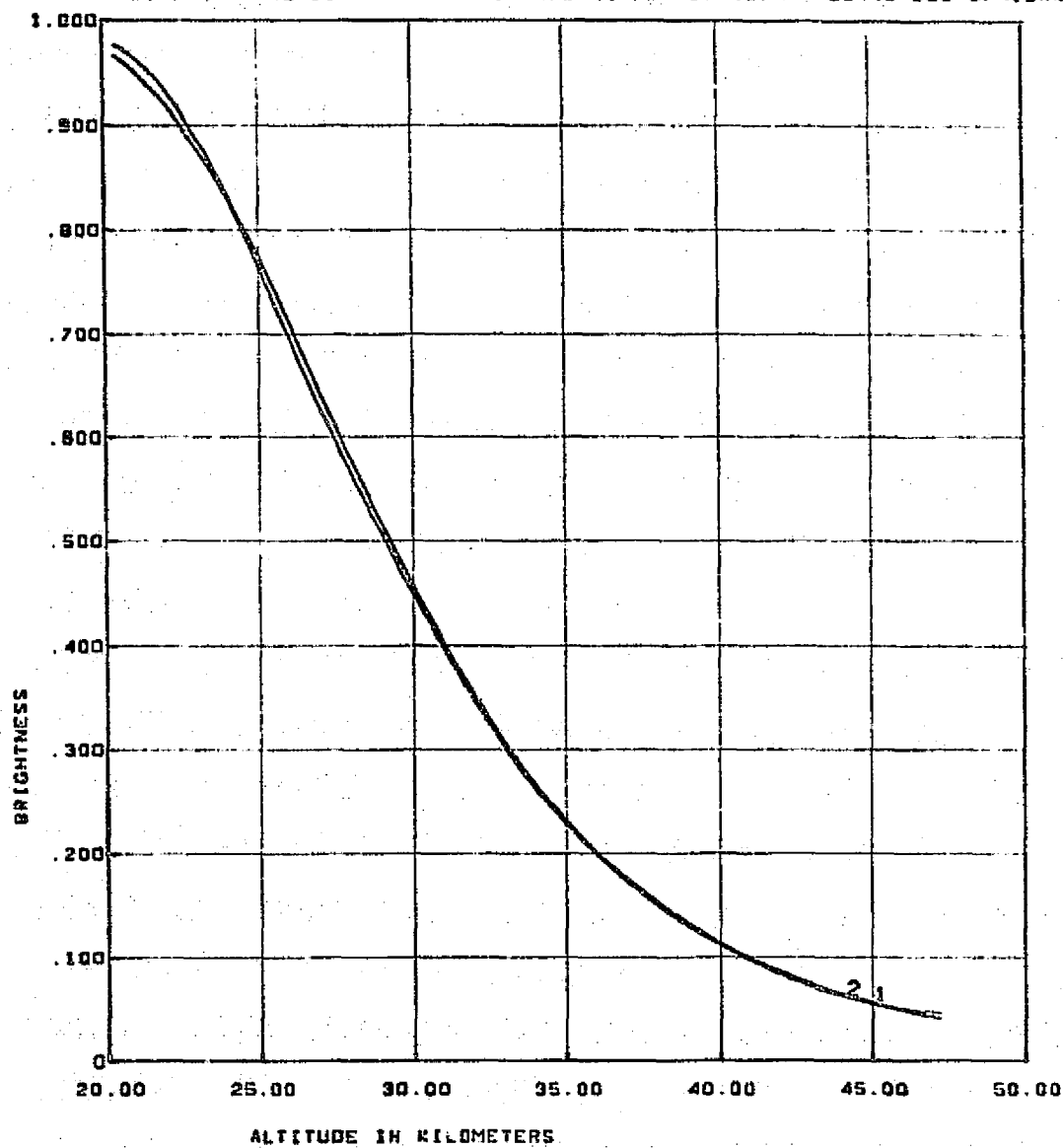
4



RATIO OF BETAS. AEROSOL OVER RAYLEIGH. 1-1000 MODEL AEROSOL. 2-RESULTS FROM INVERSION OF EXPONENTIAL FIT. 3-RESULTS FROM INVERSION OF SMOOTHED BRIGHTNESS

818.

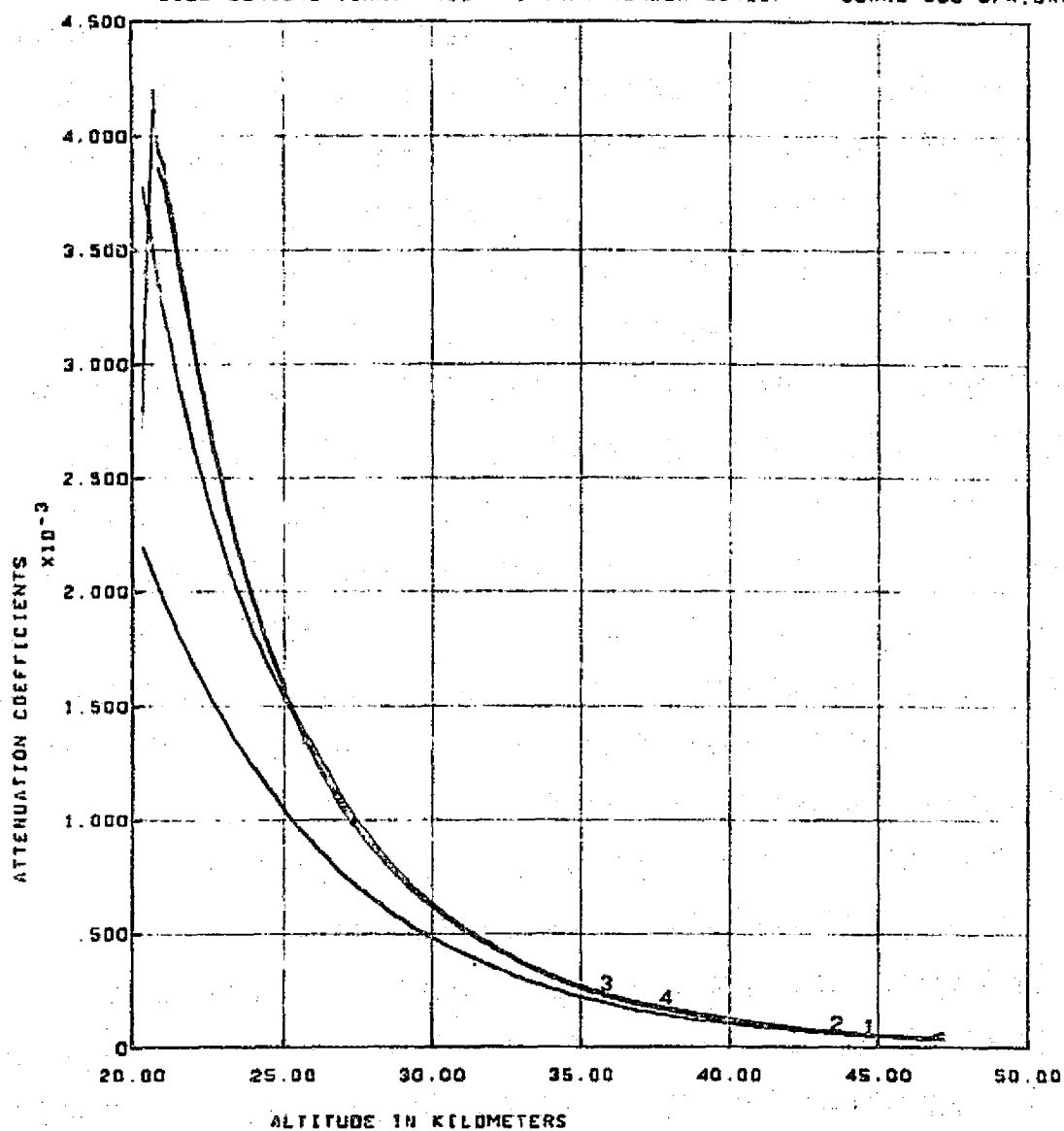
S102 CONICAL SCAN. PASS 47. TAPE NUMBER 934527 SCANS 350-374.DAND 1



CURVE 1 - BRIGHTNESS MODEL GENERATED FROM RAYLEIGH + 1880 AEROSOL BETAS.
CURVE 2 - MEASURED BRIGHTNESS SCALED BY 1880 MODEL.

S182 CONICAL SCAN. PASS 47. TAPE NUMBER 934527

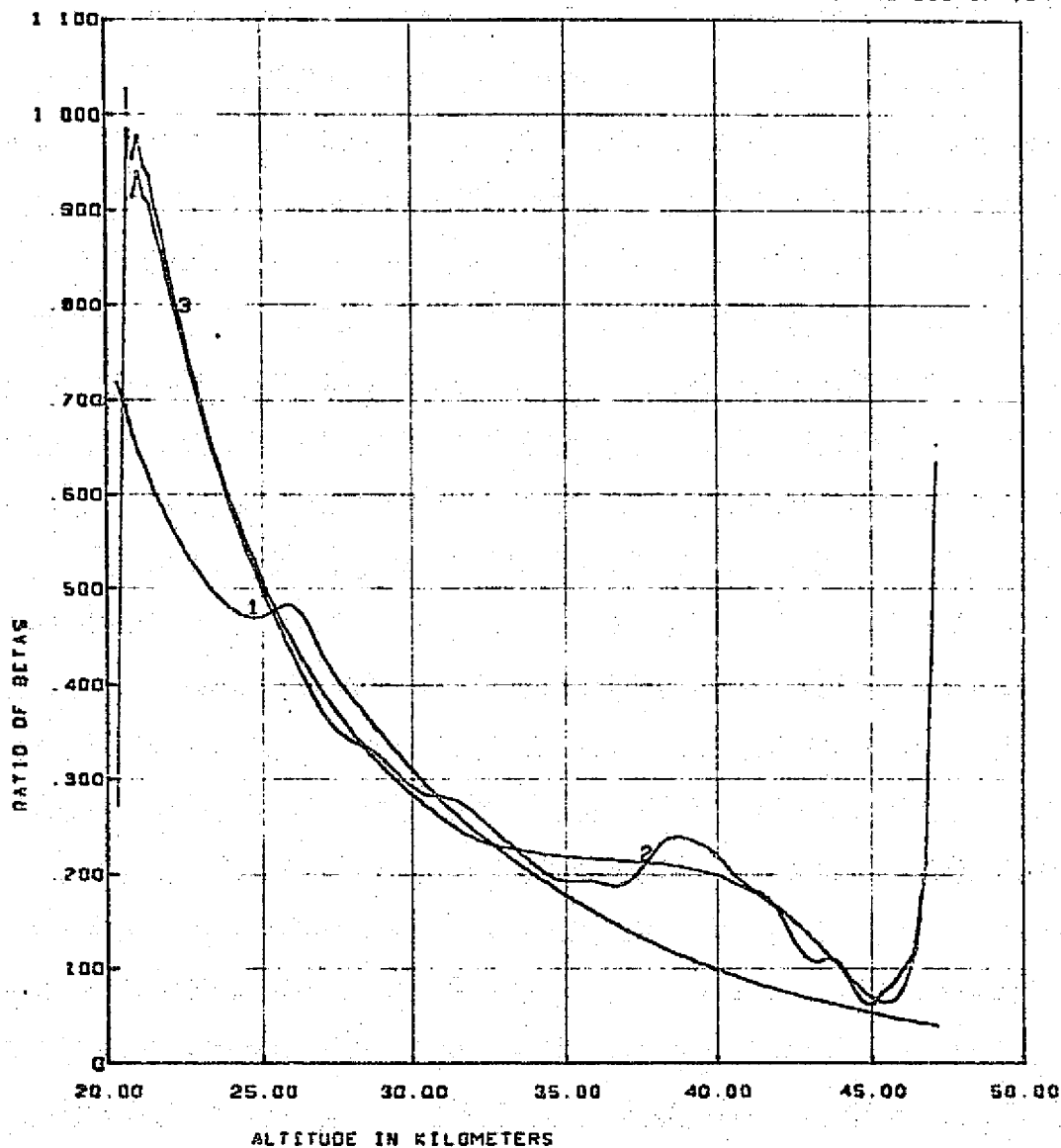
SCANS 350-374. BAND 1



ATTENUATION COEFFICIENTS - 1-RAYLEIGH, 2-RAYLEIGH + 1960 AEROSOL, 3-RESULTS FROM INVERSION OF EXPONENTIAL FIT, 4-RESULTS FROM INVERSION OF SMOOTHED BRIGHTNESS

REPRODUCIBILITY OF THE
ORIGINAL PAGE IS POOR

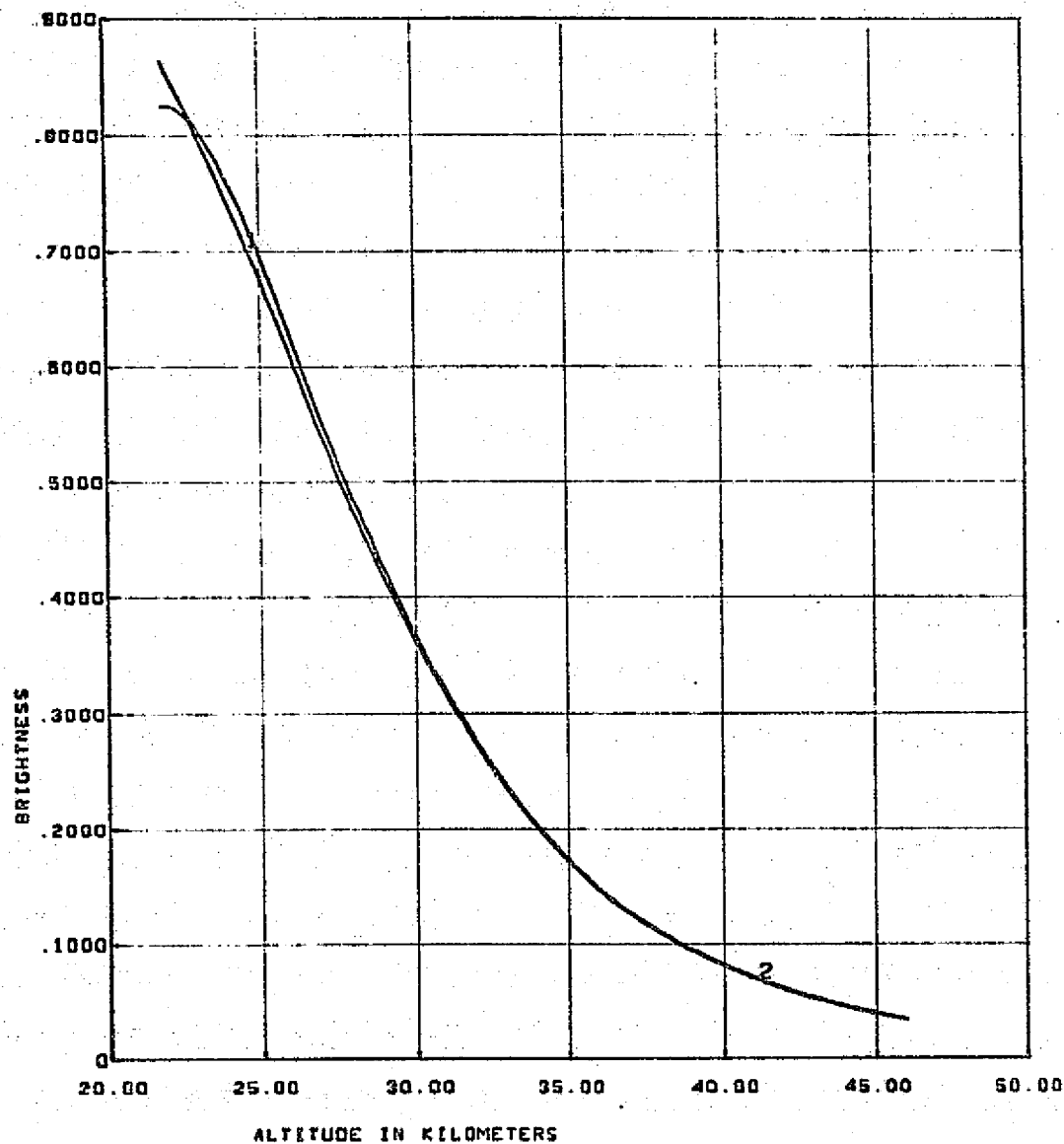
S192 CONICAL SCAN. PASS 47. TAPE NUMBER 934527 SCANS 350-374, BAND 1



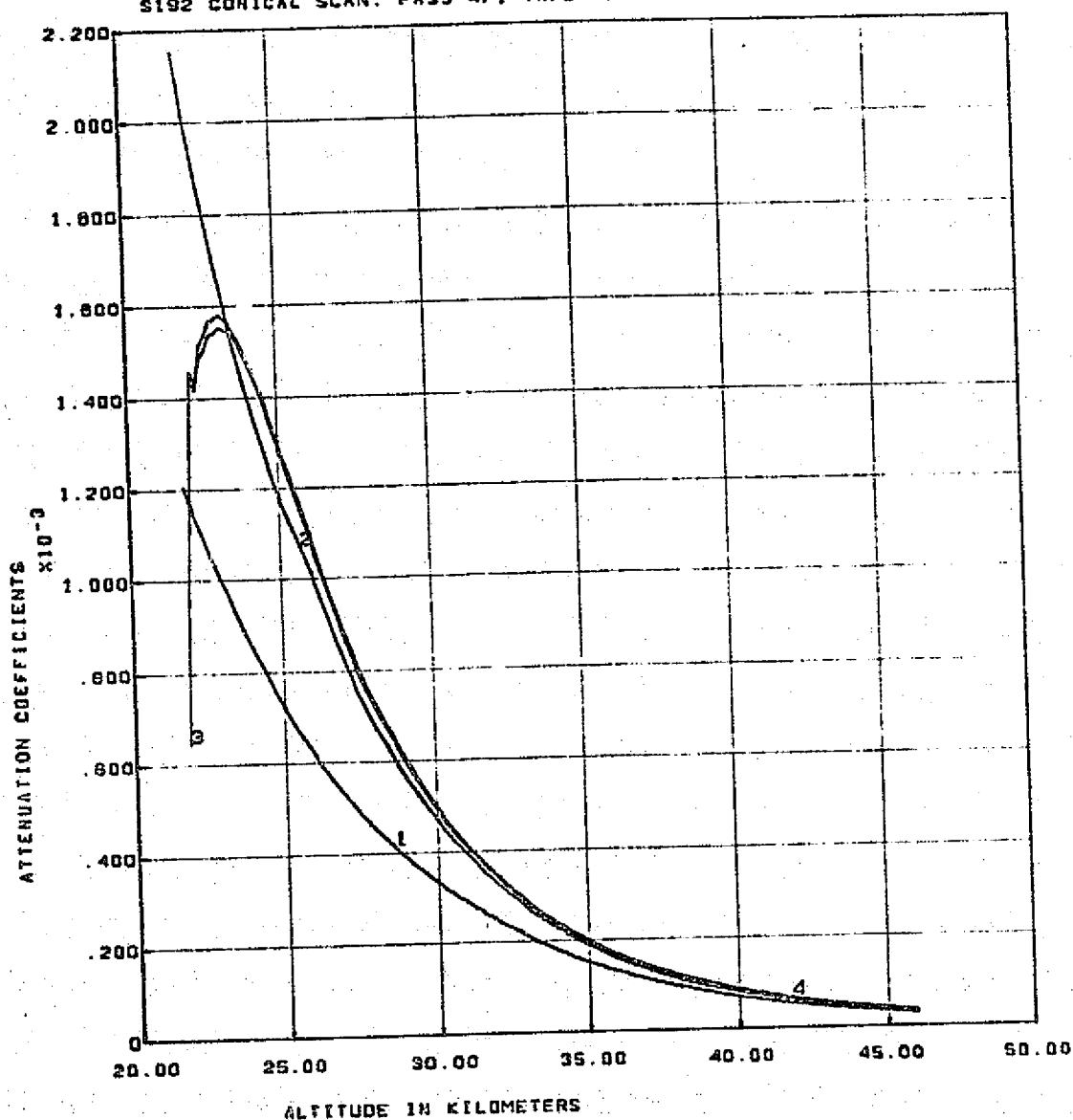
RATIO OF BETAS, AEROSOL OVER RAYLEIGH. 1-1988 MODEL AEROSOL. 2-RESULTS FROM INVERSION OF EXPONENTIAL FIT. 3-RESULTS FROM INVERSION OF SMOOTHED BRIGHTNESS

S192 CONICAL SCAN, PASS 47, TAPE NUMBER 934527

SCANS 350-374, BAND 2

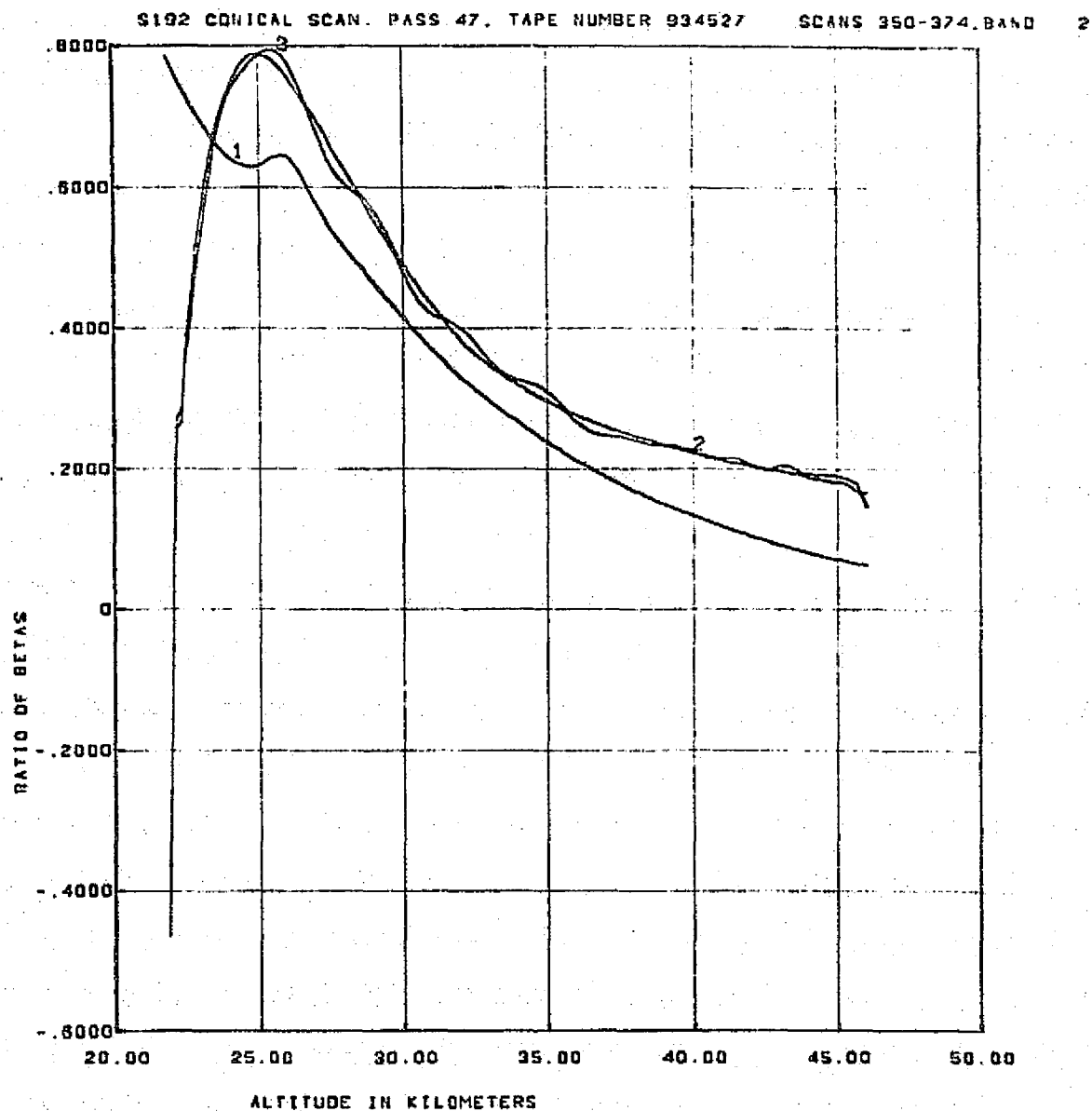


CURVE 1 - BRIGHTNESS MODEL GENERATED FROM RAYLEIGH + 1968 AEROSOL DETAS.
CURVE 2 - MEASURED BRIGHTNESS SCALED BY 1968 MODEL.



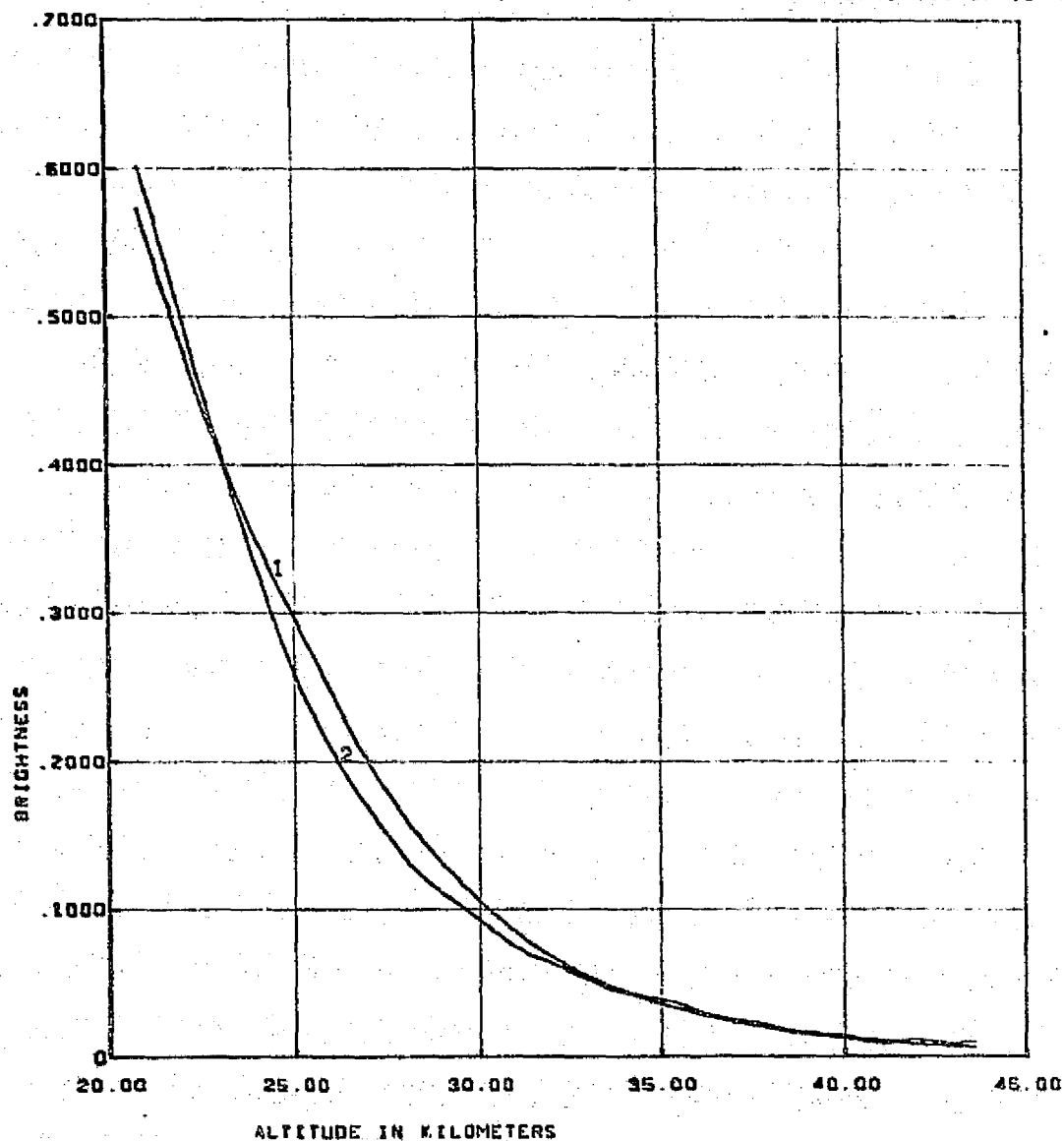
ATTENUATION COEFFICIENTS - 1-RAYLEIGH, 2-RAYLEIGH + 1968 AEROSOL, 3-RESULTS FROM INVERSION OF EXPONENTIAL FIT, 4-RESULTS FROM INVERSION OF SMOOTHED BRIGHTNESS

REPRODUCIBILITY OF THE
ORIGINAL PAGE IS POOR

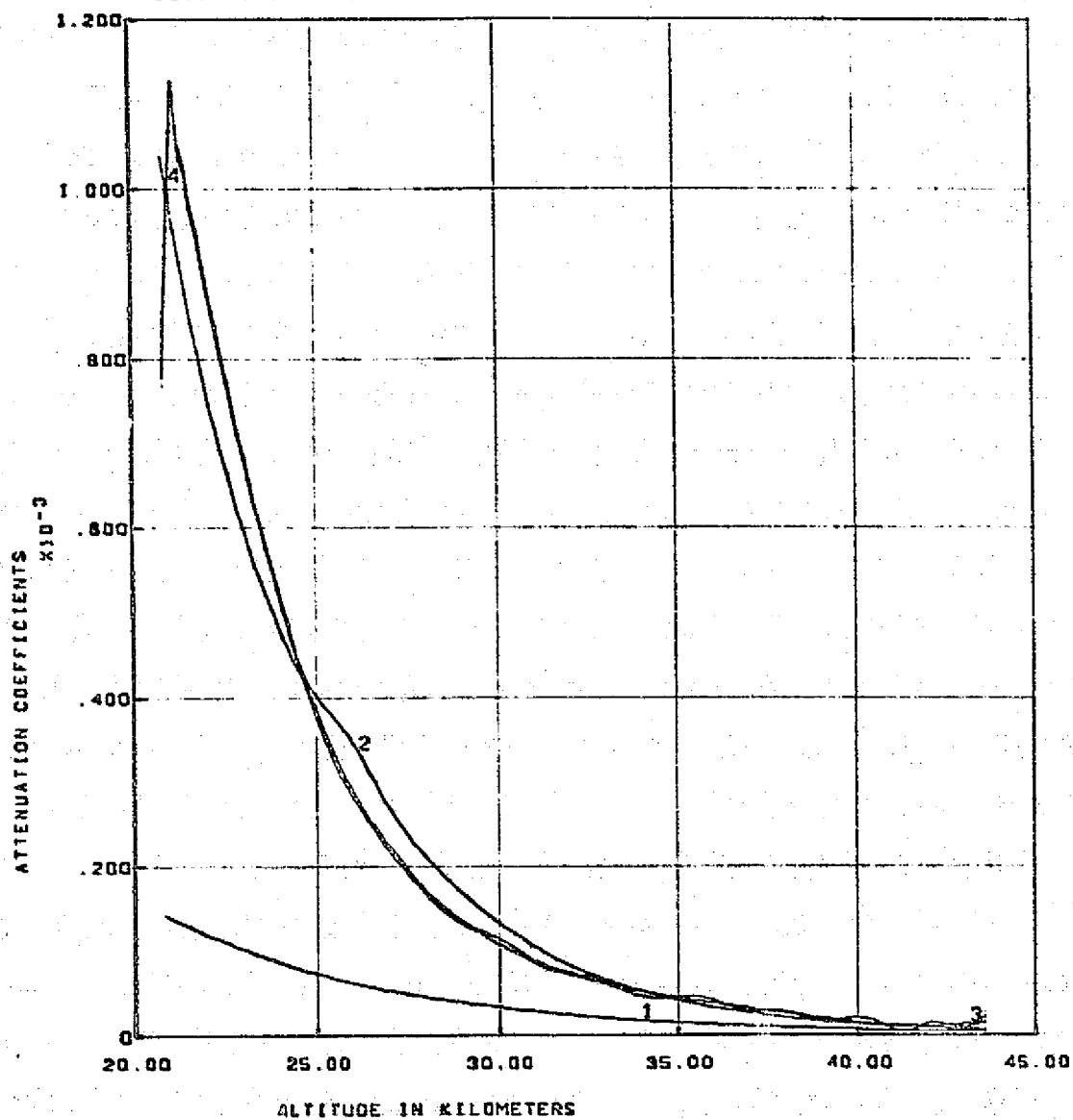


RATIO OF BETAS, AEROSOL OVER RAYLEIGH. 1-1988 MODEL AEROSOL. 2-RESULTS FROM INVERSION OF EXPONENTIAL FIT. 3-RESULTS FROM INVERSION OF SMOOTHED BRIGHTNESS

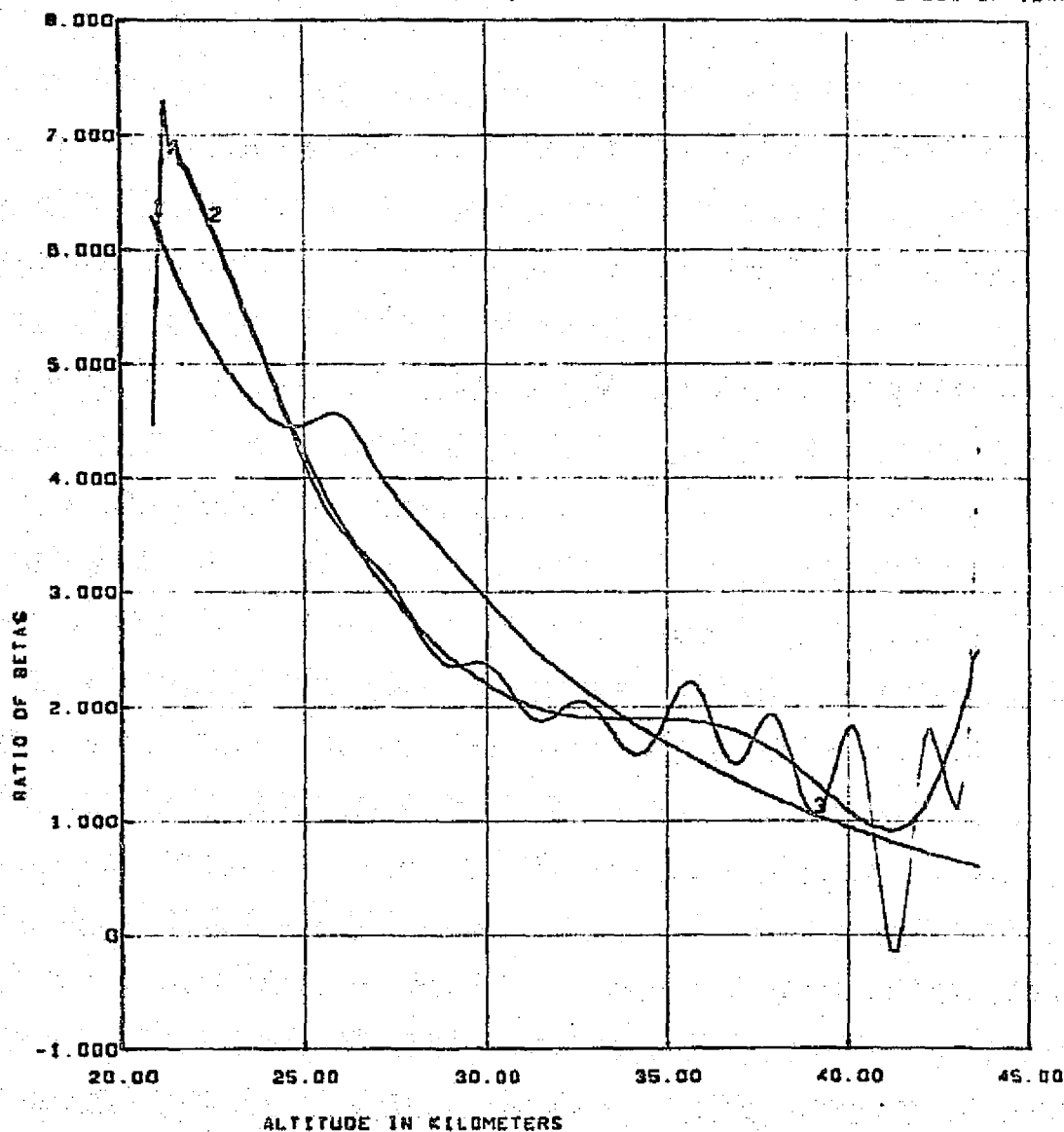
SI92 CONICAL SCAN. PASS 47. TAPE NUMBER 934527 SCANS 350-374. BAND 7



CURVE 1 - BRIGHTNESS MODEL GENERATED FROM RAYLEIGH + 1966 AEROSOL BETAS.
CURVE 2 - MEASURED BRIGHTNESS SCALED BY 1966 MODEL.



ATTENUATION COEFFICIENTS - 1-RAYLEIGH. 2-RAYLEIGH + 1968 AEROSOL. 3-RESULTS FROM INVERSION OF EXPONENTIAL FIT. 4-RESULTS FROM INVERSION OF SMOOTHED BRIGHTNESS

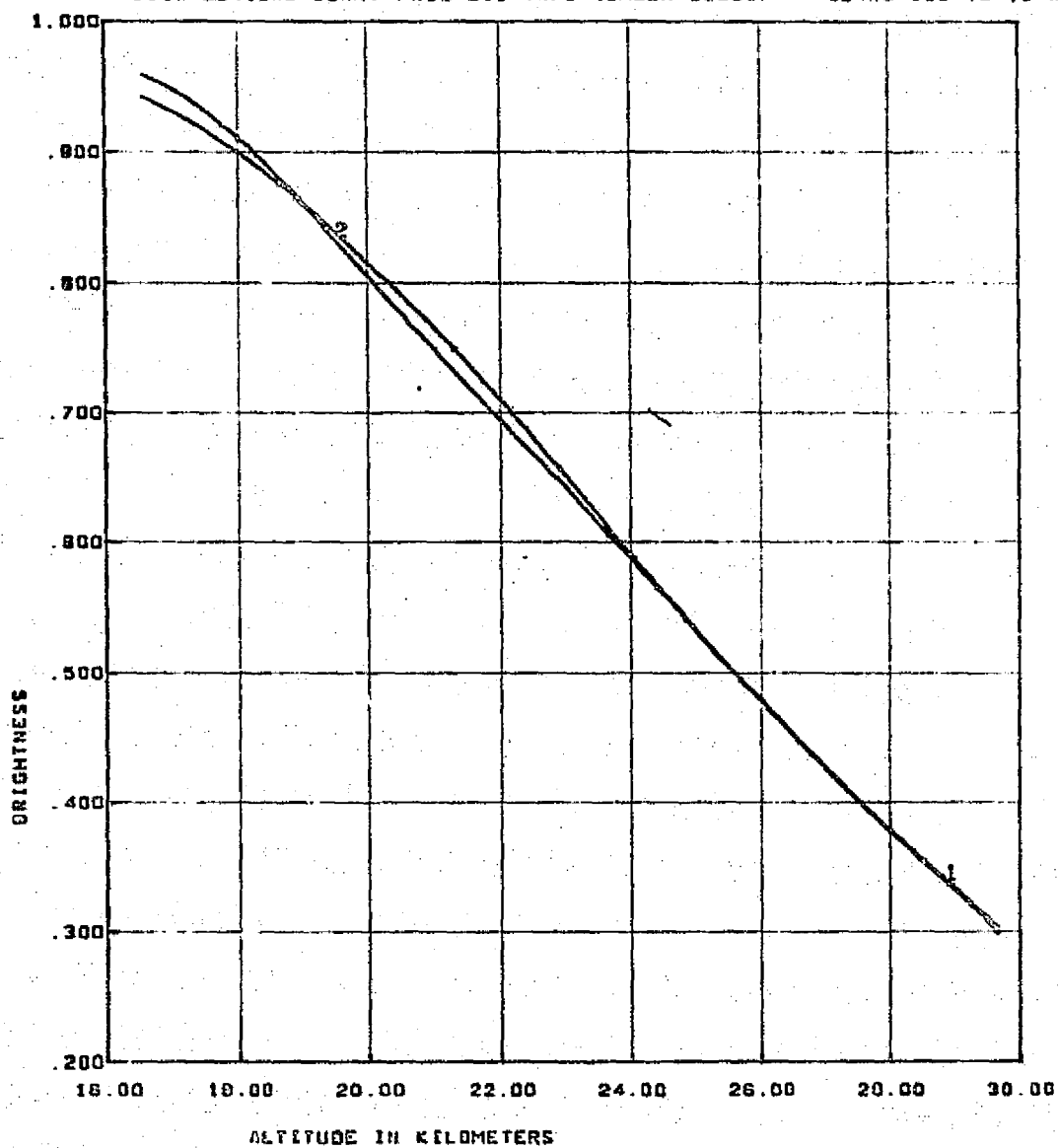


RATIO OF BETAS, AEROSOL OVER RAYLEIGH. 1-1988 MODEL AEROSOL. 2-RESULTS FROM INVERSION OF EXPONENTIAL FIT. 3-RESULTS FROM INVERSION OF SMOOTHED BRIGHTNESS

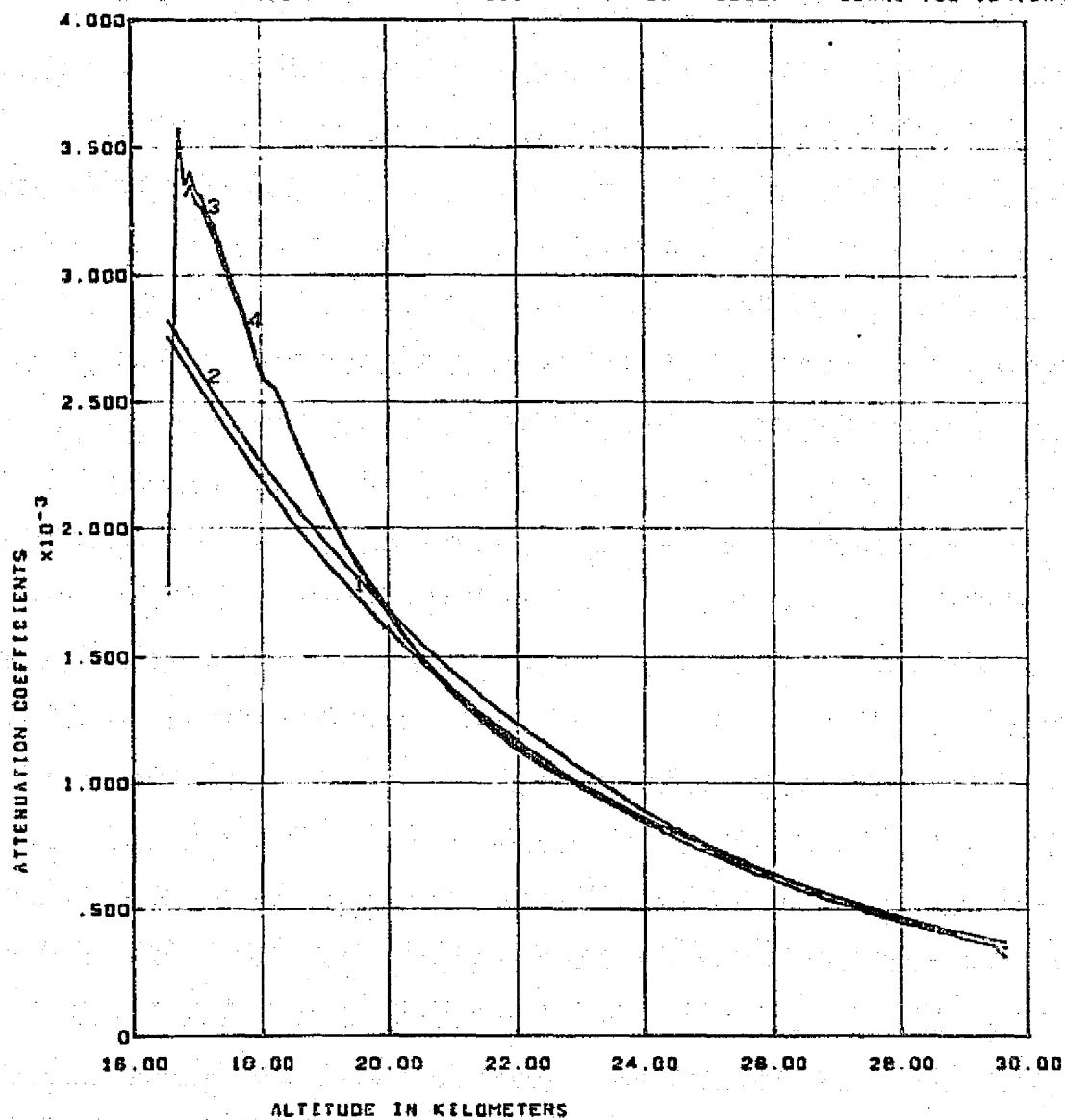
REPRODUCIBILITY OF THE
ORIGINAL PAGE IS POOR

S192 CONICAL SCAN. PASS B1. TAPE NUMBER 932887

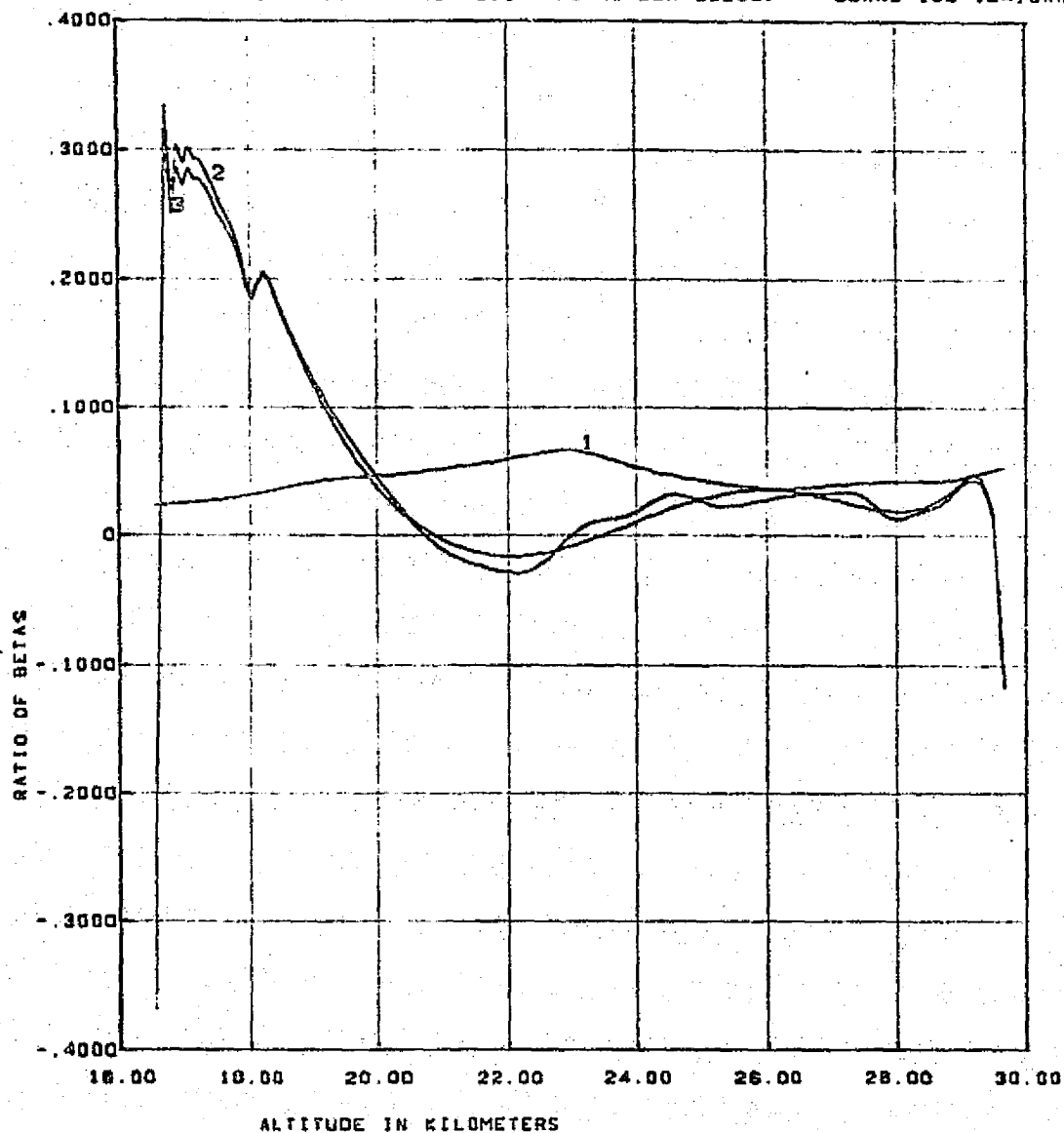
SCANS 100-124, BAND 2



CURVE 1- BRIGHTNESS MODEL GENERATED FROM RAYLEIGH + 1984 AEROSOL BETAS.
CURVE 2 - MEASURED BRIGHTNESS SCALED BY 1984 MODEL.



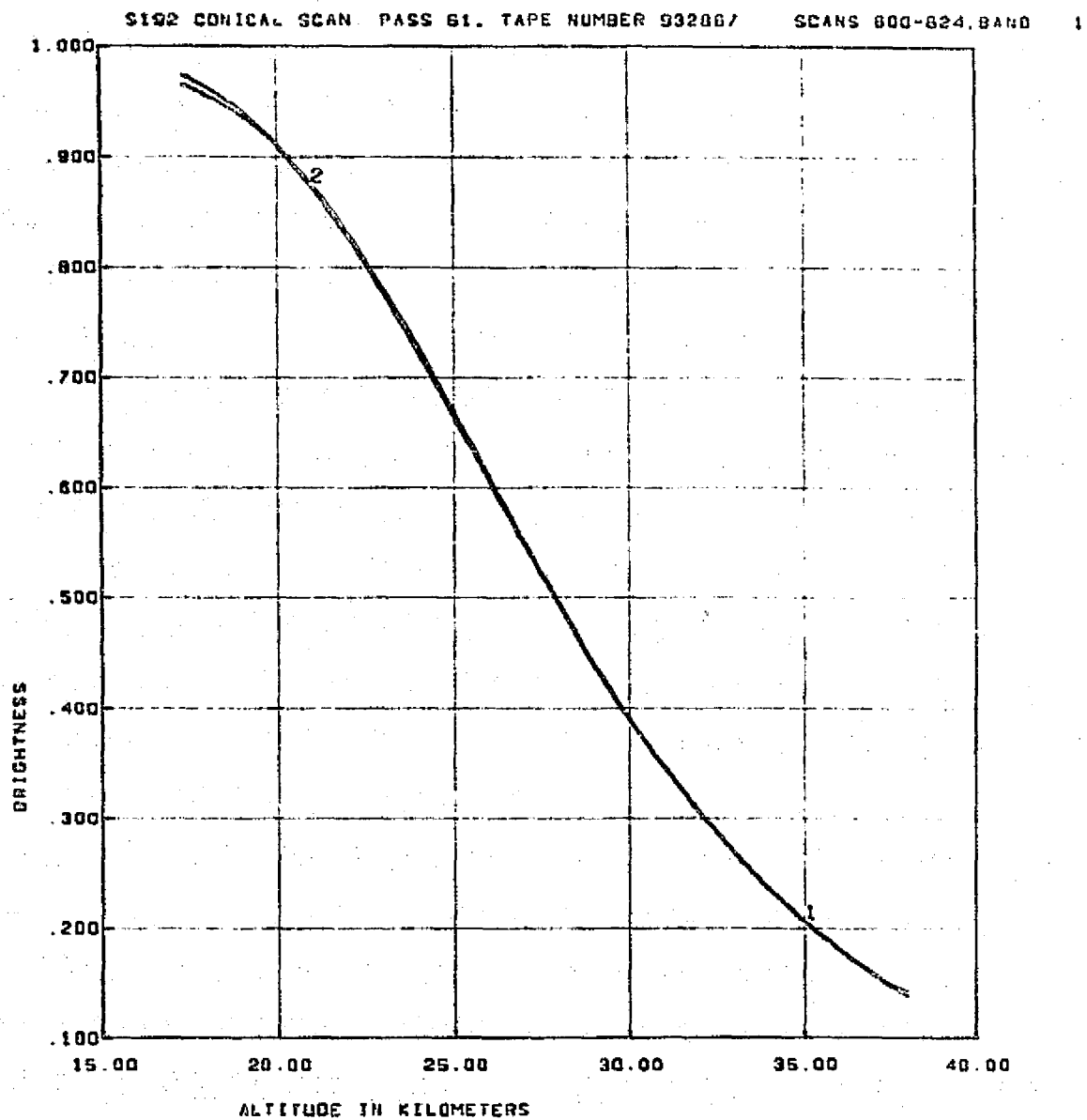
ATTENUATION COEFFICIENTS - 1-RAYLEIGH, 2-RAYLEIGH + 1984 AEROSOL, 3-RESULTS FROM INVERSION OF EXPONENTIAL FIT, 4-RESULTS FROM INVERSION OF SMOOTHED BRIGHTNESS



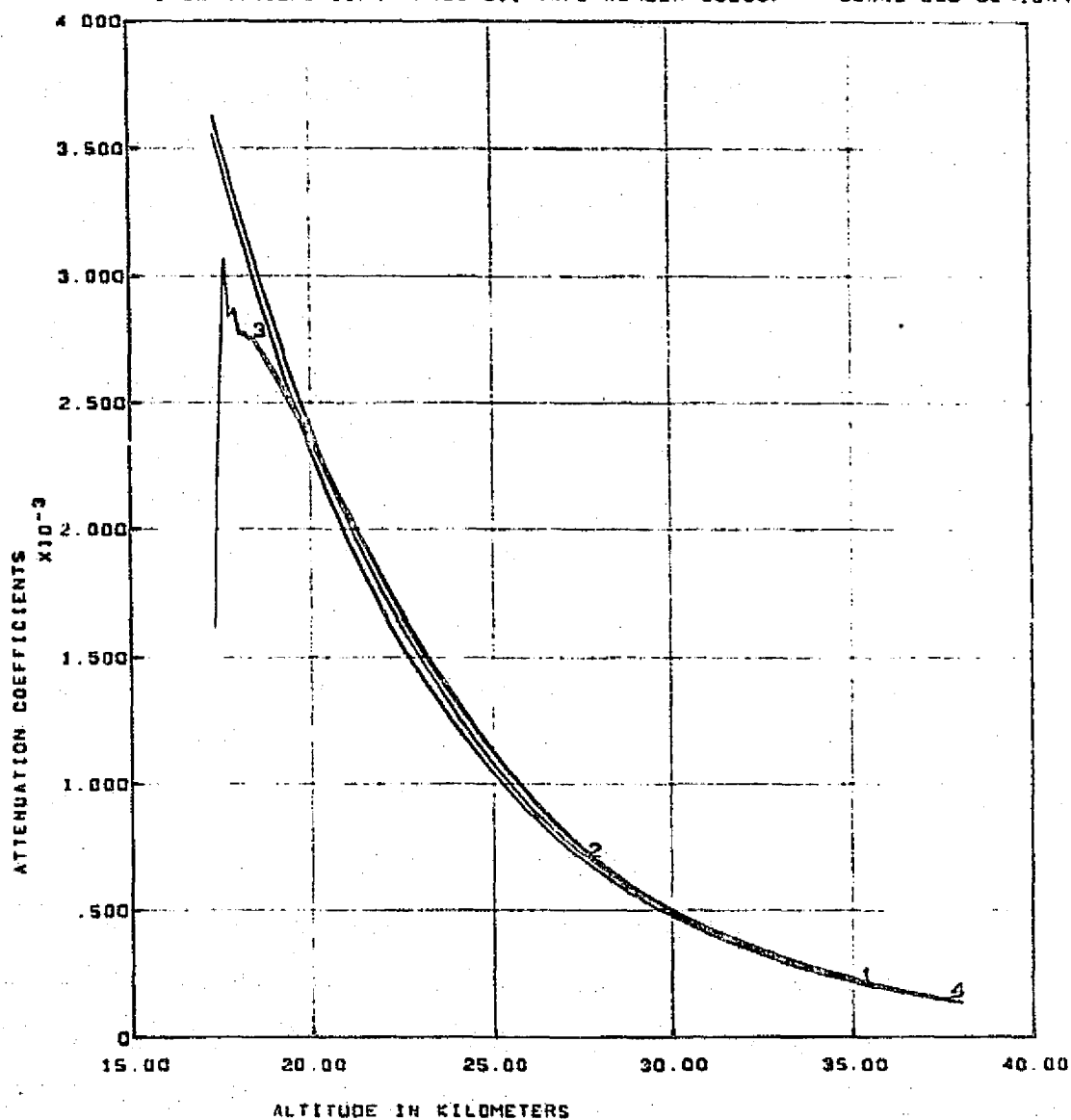
RATIO OF BETAS. AEROSOL OVER RAYLEIGH. 1-1904 MODEL AEROSOL. 2-RESULTS FROM INVERSION OF EXPONENTIAL FIT. 3-RESULTS FROM INVERSION OF SMOOTHED BRIGHTNESS

REPRODUCIBILITY OF THE
ORIGINAL PAGE IS POOR

818.



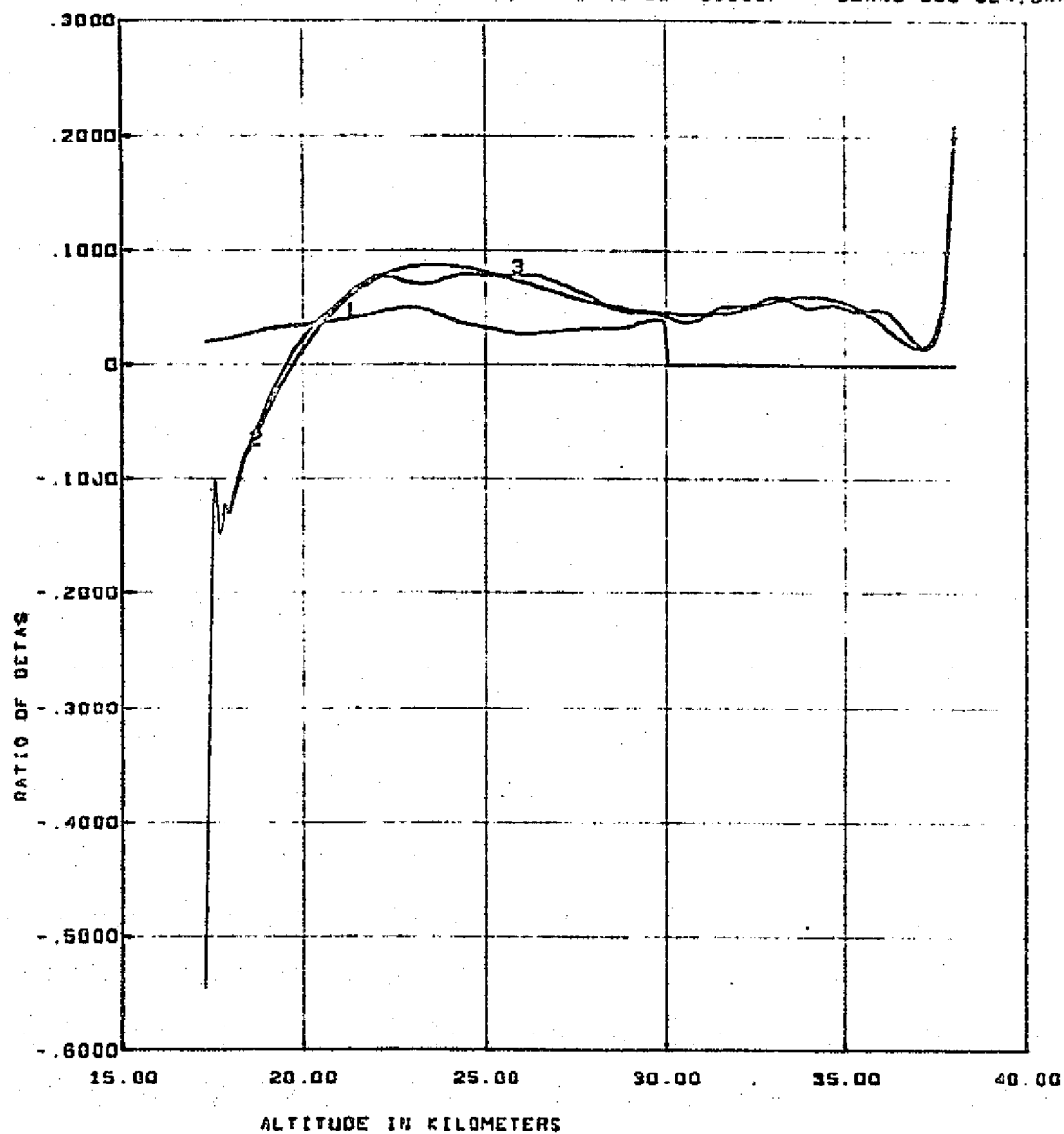
CURVE 1- BRIGHTNESS MODEL GENERATED FROM RAYLEIGH + 1964 AEROSOL BETAS
CURVE 2 - MEASURED BRIGHTNESS SCALED BY 1964 MODEL.



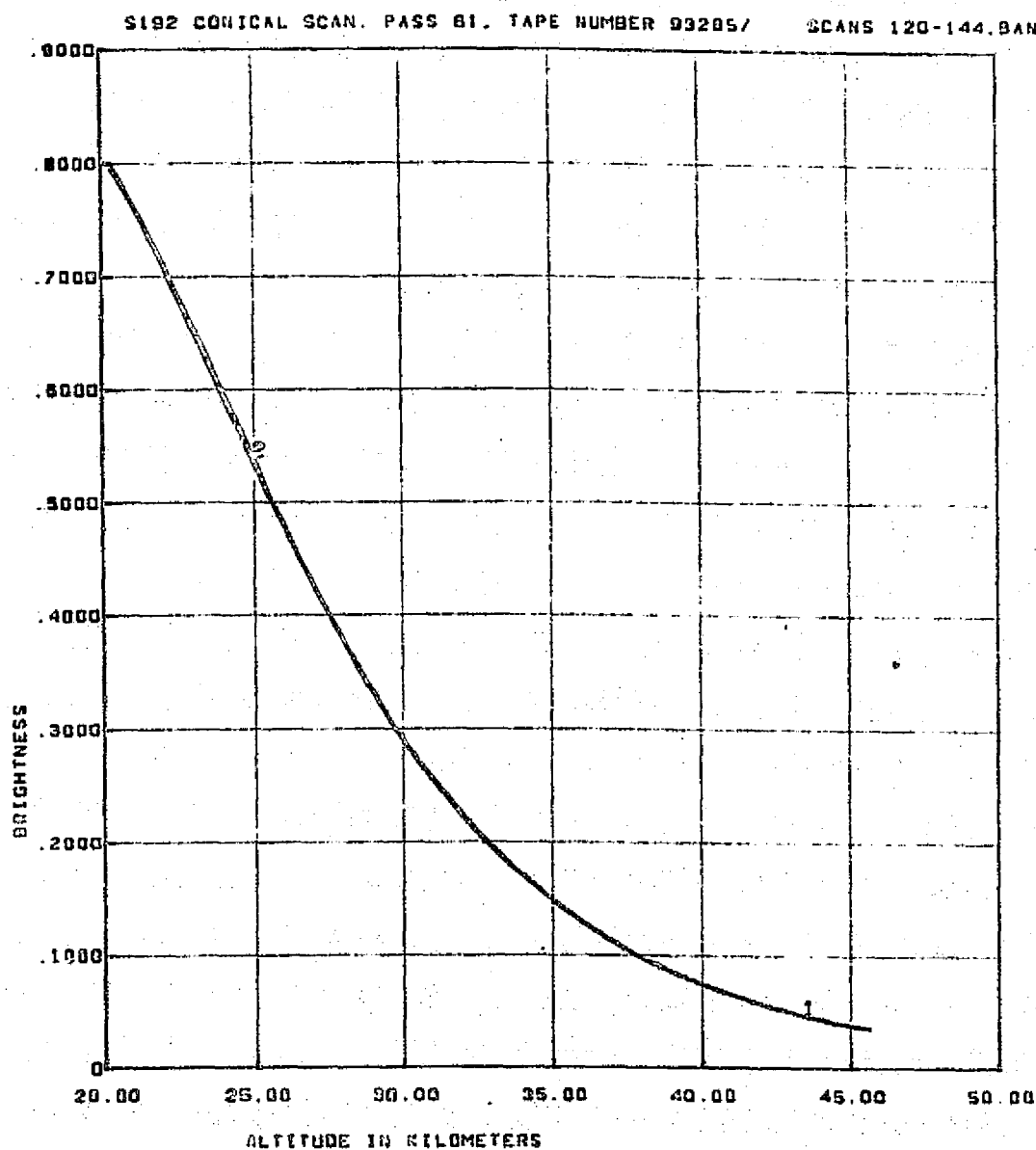
ATTENUATION COEFFICIENTS - 1-RAYLEIGH. 2-RAYLEIGH + 1964 AEROSOL. 3-RESULTS FROM INVERSION OF EXPONENTIAL FIT. 4-RESULTS FROM INVERSION OF SMOOTHED BRIGHTNESS

S192 CONICAL SCAN. PASS 61. TAPE NUMBER 932067

SCANS 600-624. BAND 1



RATIO OF BETAS. AEROSOL OVER RAYLEIGH. 1-1984 MODEL AEROSOL. 2-RESULTS FROM INVERSION OF EXPONENTIAL FIT. 3-RESULTS FROM INVERSION OF SMOOTHED BRIGHTNESS

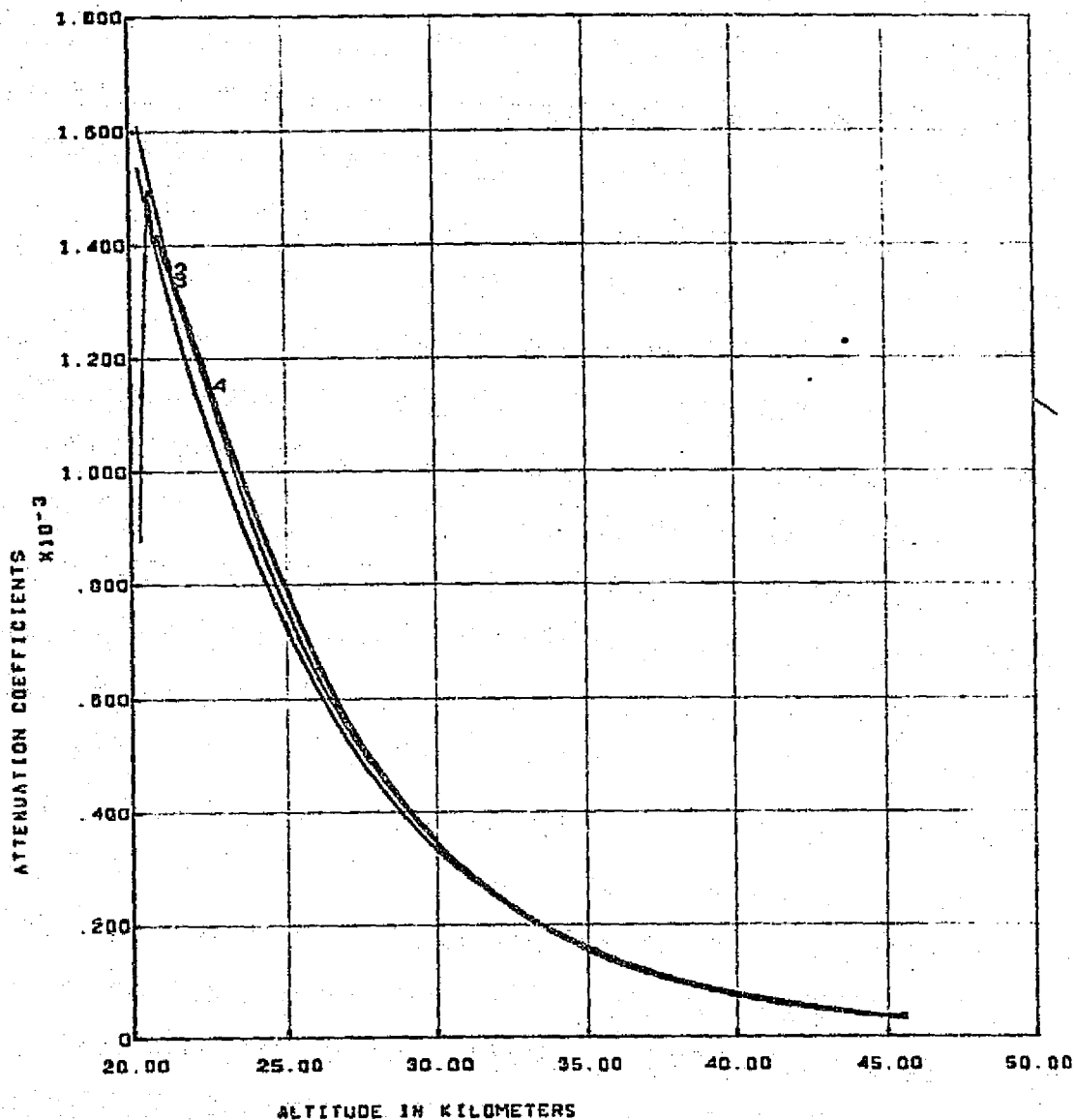


CURVE 1 - BRIGHTNESS MODEL GENERATED FROM RAYLEIGH + 1984 AEROSOL BETAS.
 CURVE 2 - MEASURED BRIGHTNESS SCALED BY 1984 MODEL.

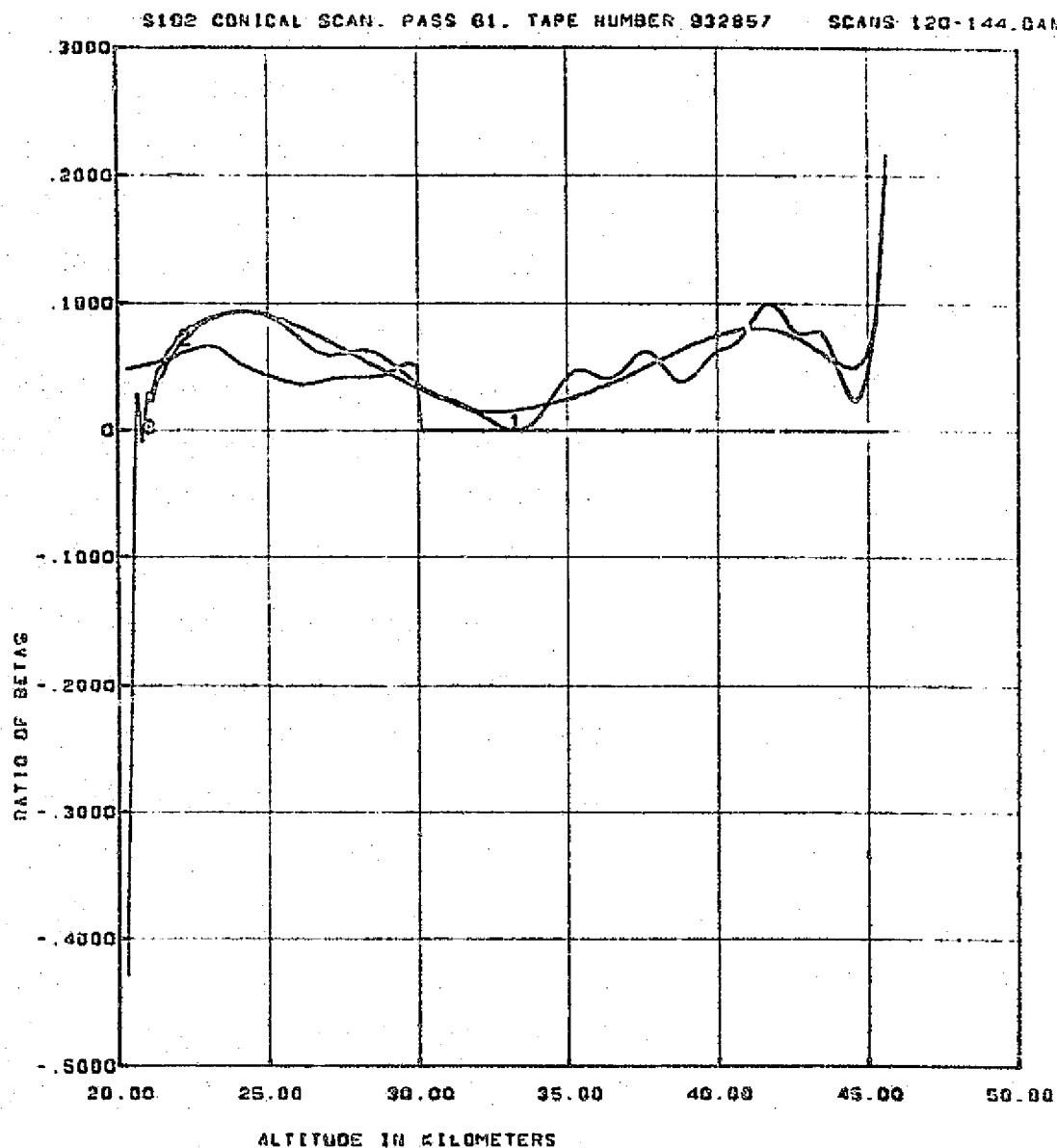
REPRODUCIBILITY OF THE
 ORIGINAL PAGE IS POOR

S192 CONICAL SCAN. PASS B1. TAPE NUMBER 932857

SCANS 120-144. BAND 2



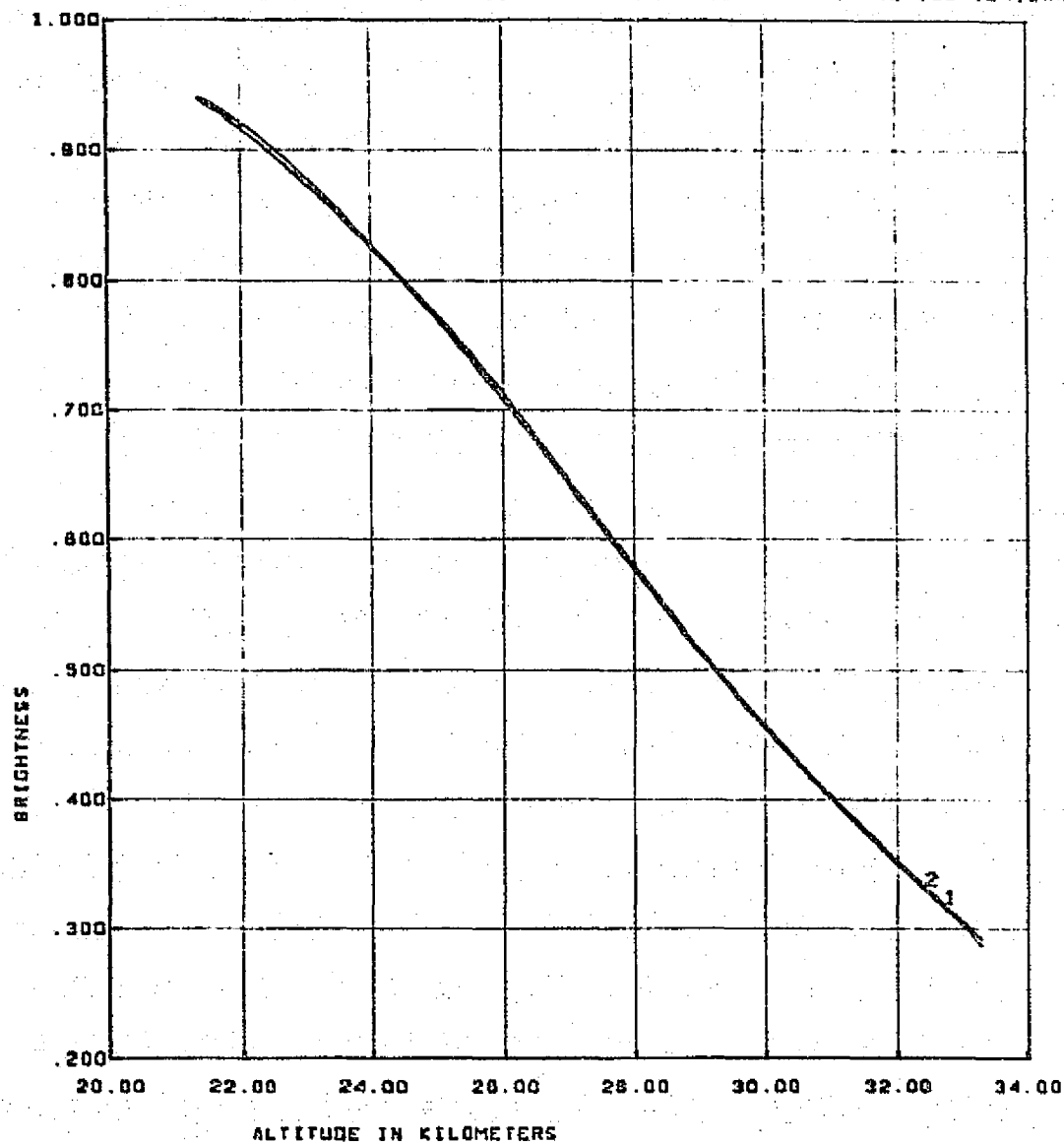
ATTENUATION COEFFICIENTS - 1-RAYLEIGH, 2-RAYLEIGH + 1954 AEROSOL, 3-RESULTS FROM INVERSION OF EXPONENTIAL FIT, 4-RESULTS FROM INVERSION OF SMOOTHED BRIGHTNESS



RATIO OF BETAS, AEROSOL OVER RAYLEIGH. 1-1964 MODEL AEROSOL. 2-RESULTS FROM INVERSION OF EXPONENTIAL FIT. 3-RESULTS FROM INVERSION OF SMOOTHED BRIGHTNESS

S192 CONICAL SCAN. PASS 81. TAPE NUMBER 932067

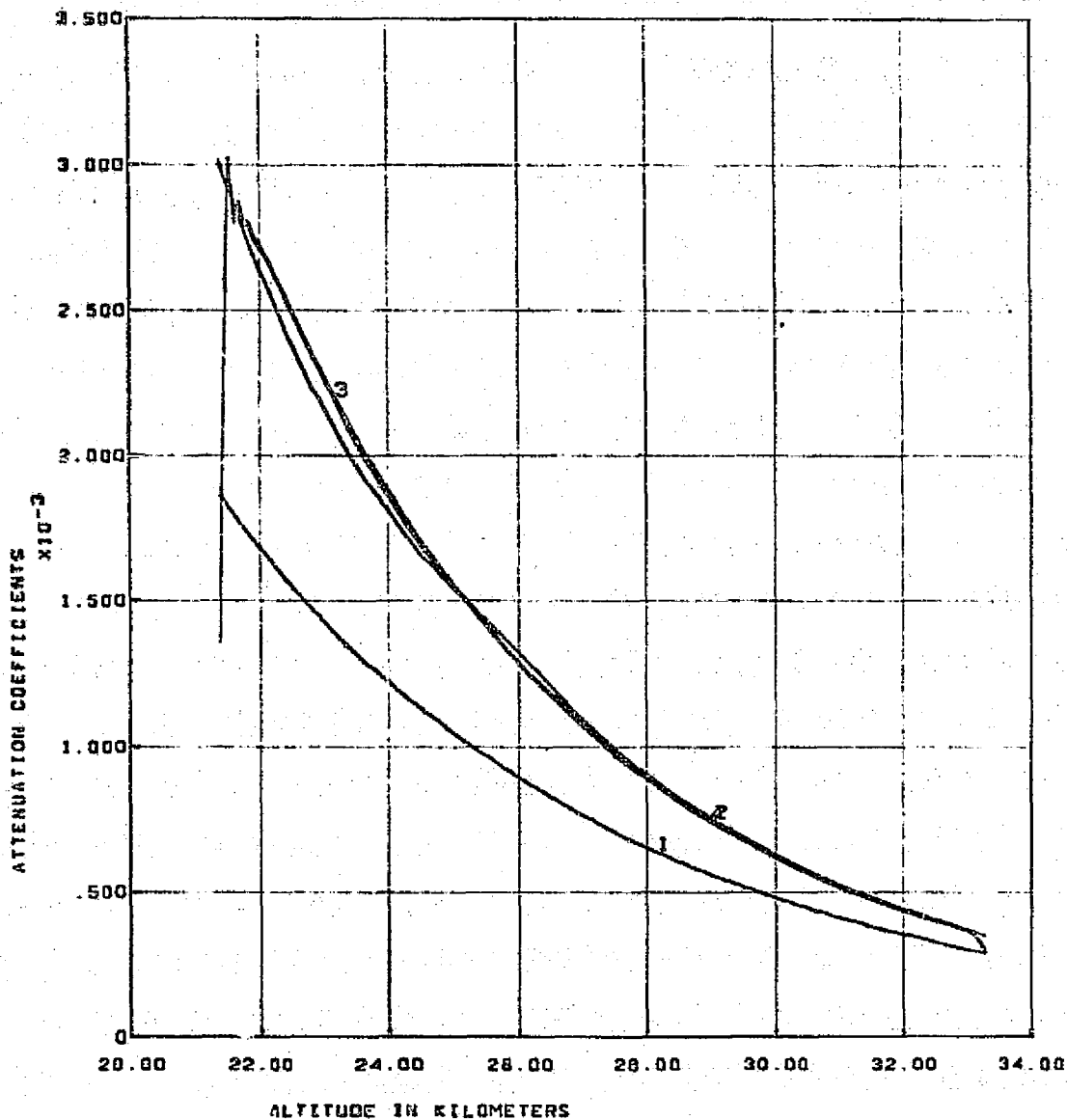
SCANS 100-124. BAND 1



CURVE 1 - BRIGHTNESS MODEL GENERATED FROM RAYLEIGH + 1968 AEROSOL BETAS.
CURVE 2 - MEASURED BRIGHTNESS SCALED BY 1968 MODEL.

S192 CONICAL SCAN. PASS 61. TAPE NUMBER 932887

SCANS 100-124. BAND 1

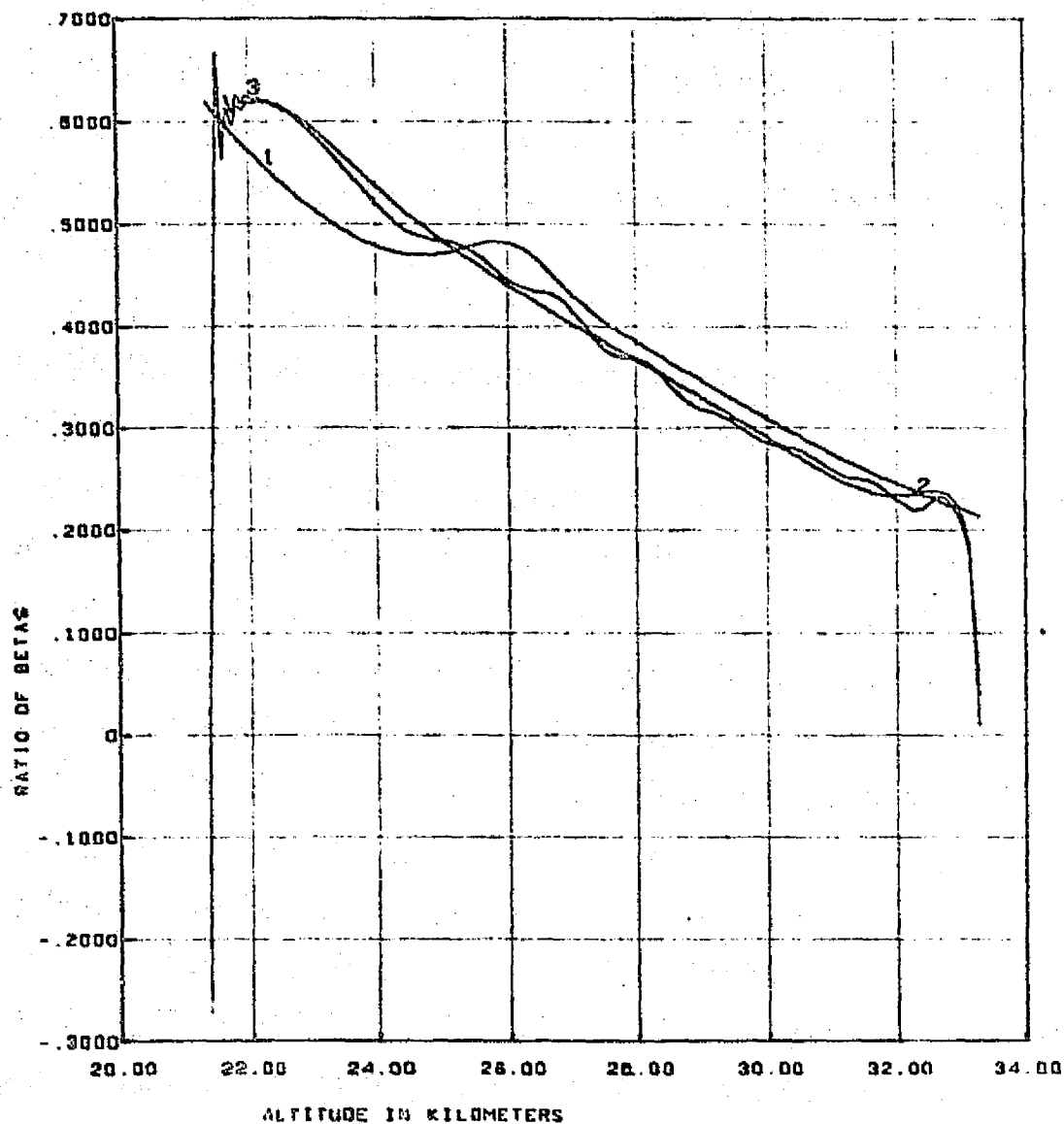


ATTENUATION COEFFICIENTS - 1-RAYLEIGH, 2-RAYLEIGH + 1988 AEROSOL, 3-RESULTS FROM INVERSION OF EXPONENTIAL FIT, 4-RESULTS FROM INVERSION OF SMOOTHED BRIGHTNESS

REPRODUCIBILITY OF THE
ORIGINAL PAGE IS POOR

5192 CONICAL SCAN, PASS G1, TAPE NUMBER 932867

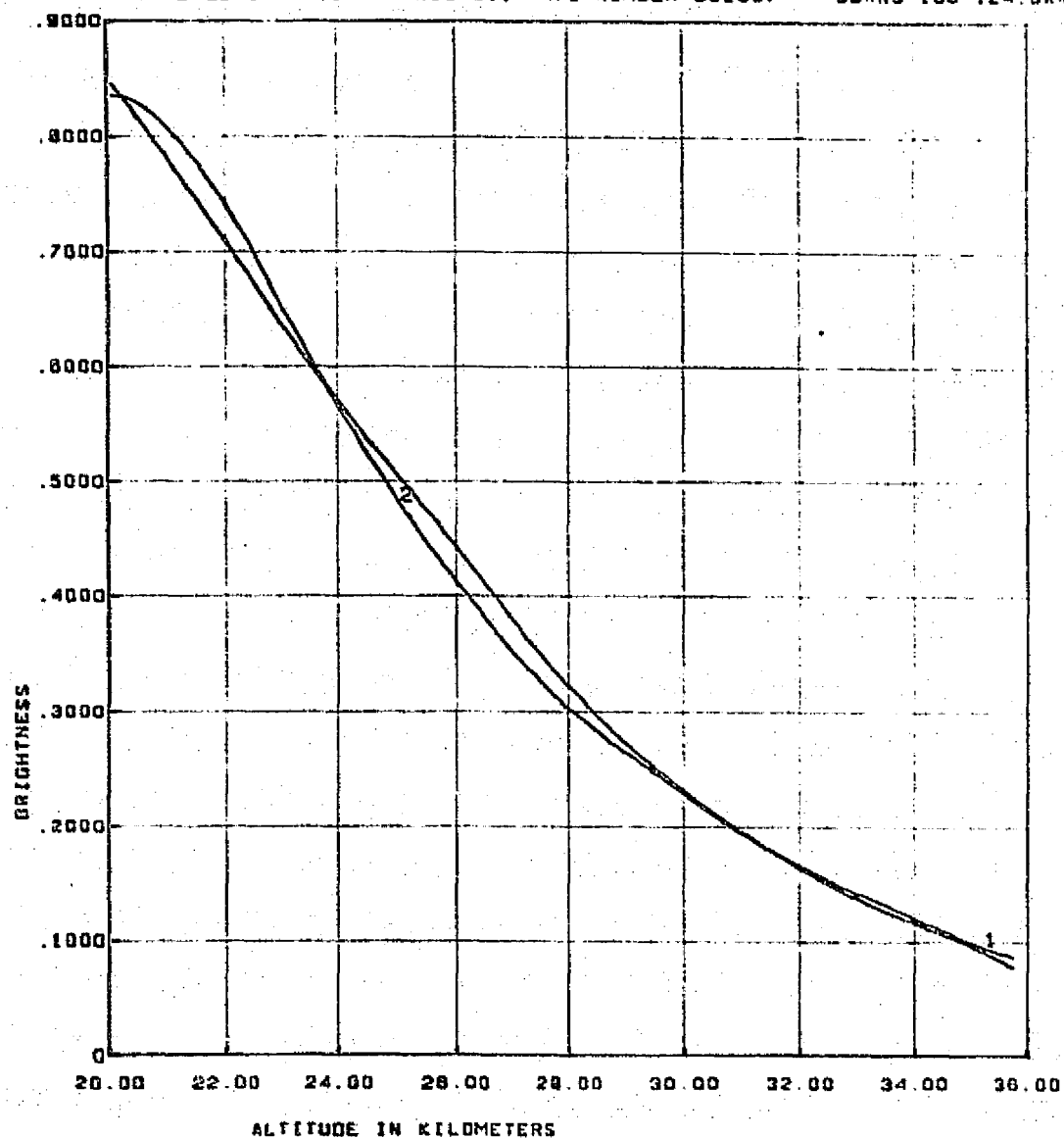
SCANS 100-124, BAND 1



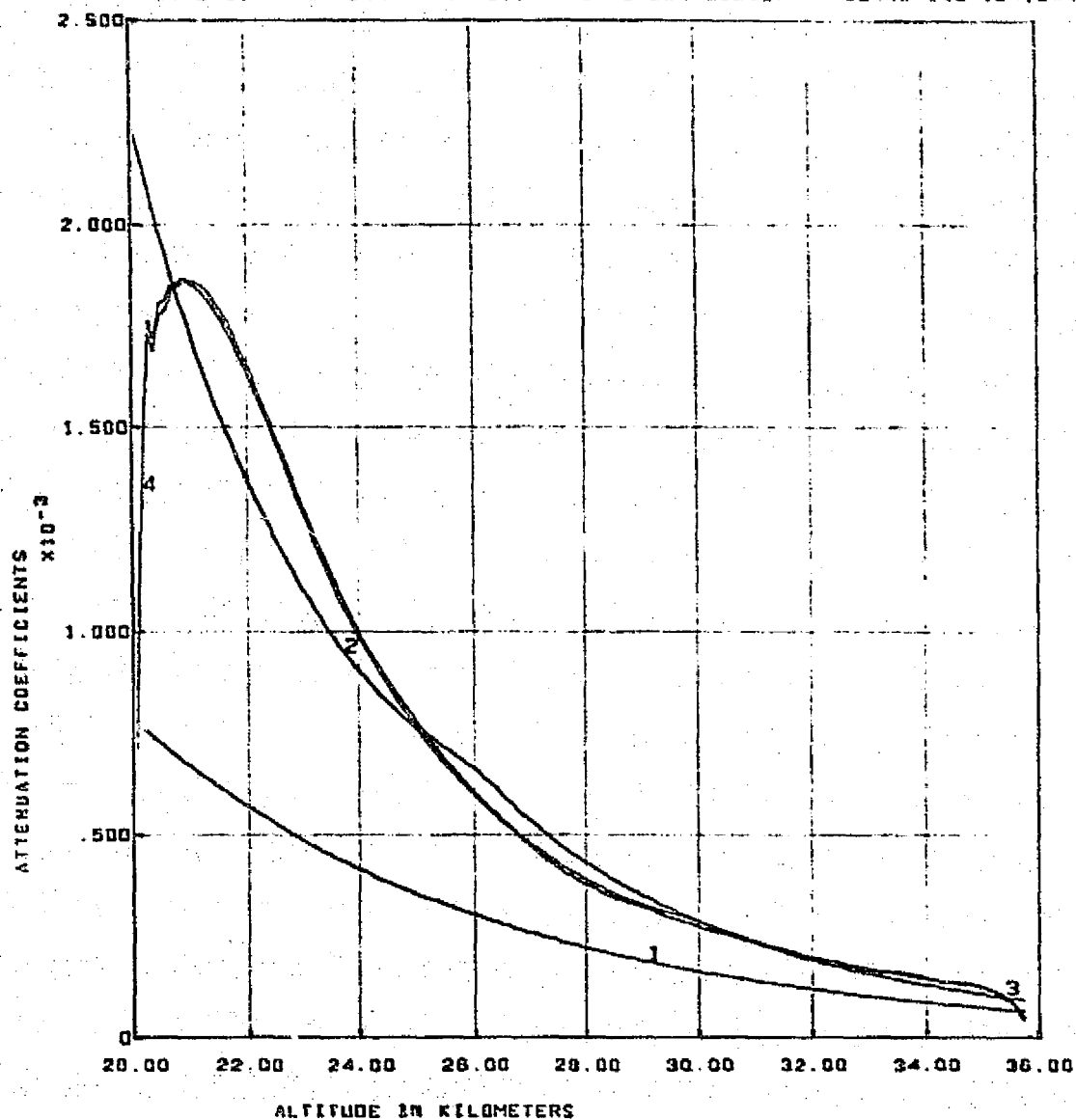
RATIO OF BETAS, AEROSOL OVER RAYLEIGH. 1-1960 MODEL AEROSOL, 2-RESULTS FROM INVERSION OF EXPONENTIAL FIT, 3-RESULTS FROM INVERSION OF SMOOTHED BRIGHTNESS

SI92 CONICAL SCAN PASS G1. TAPE NUMBER 932867

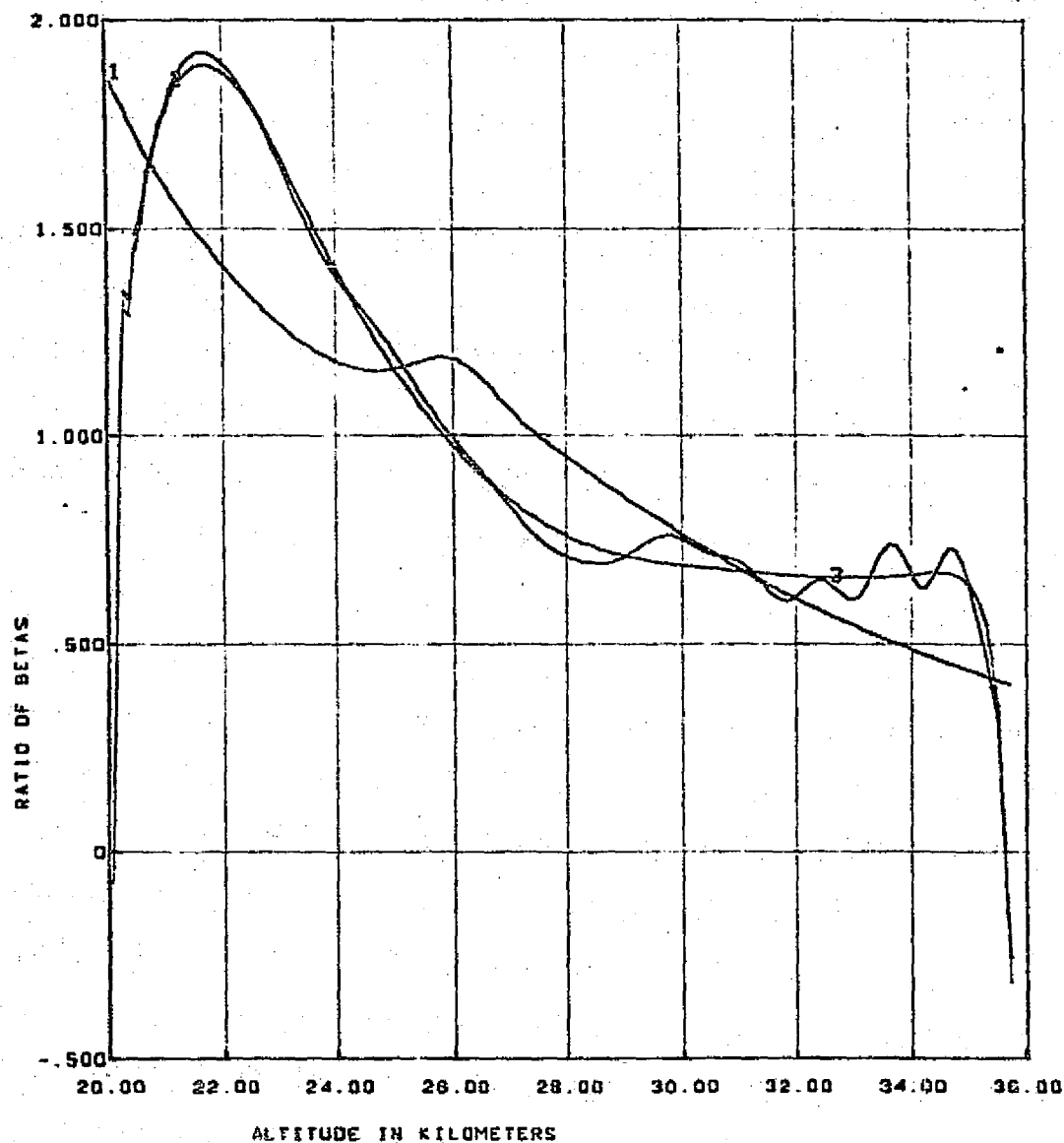
SCANS 100-124. BAND 4



CURVE 1 - BRIGHTNESS MODEL GENERATED FROM RAYLEIGH + 1960 AEROSOL BETAS
 CURVE 2 - MEASURED BRIGHTNESS SCALED BY 1960 MODEL.



ATTENUATION COEFFICIENTS - 1-RAYLEIGH. 2-RAYLEIGH + 1963 AEROSOL. 3-RESULTS FROM INVERSION OF EXPONENTIAL FIT. 4-RESULTS FROM INVERSION OF SMOOTHED BRIGHTNESS

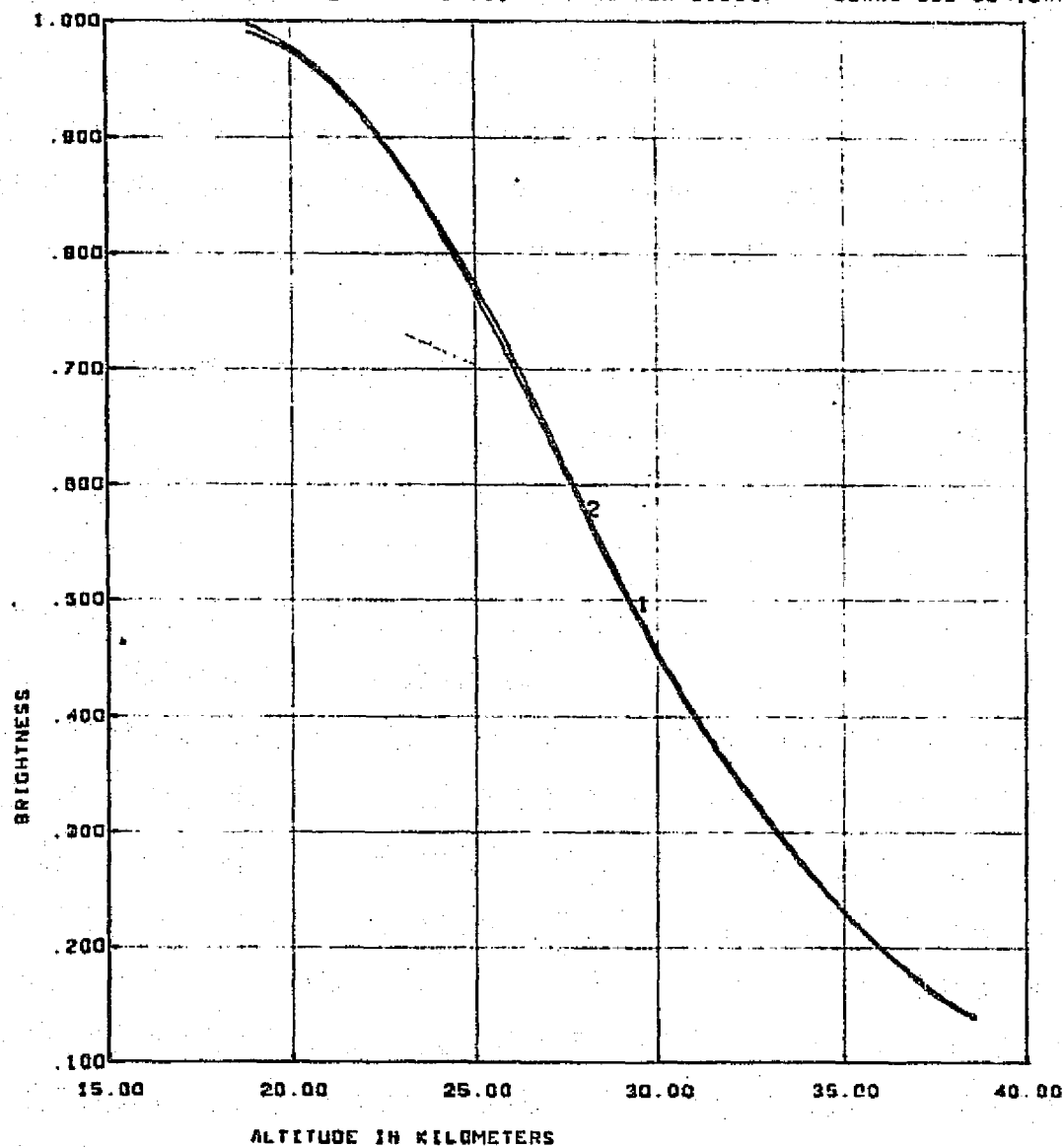


RATIO OF BETAS, AEROSOL OVER RAYLEIGH. 1-1988 MODEL AEROSOL, 2-RESULTS FROM
INVERSION OF EXPONENTIAL FIT, 3-RESULTS FROM INVERSION OF SMOOTHED BRIGHTNESS

REPRODUCIBILITY OF THE
ORIGINAL PAGE IS POOR

5192 CONICAL SCAN. PASS 81. TAPE NUMBER 932887

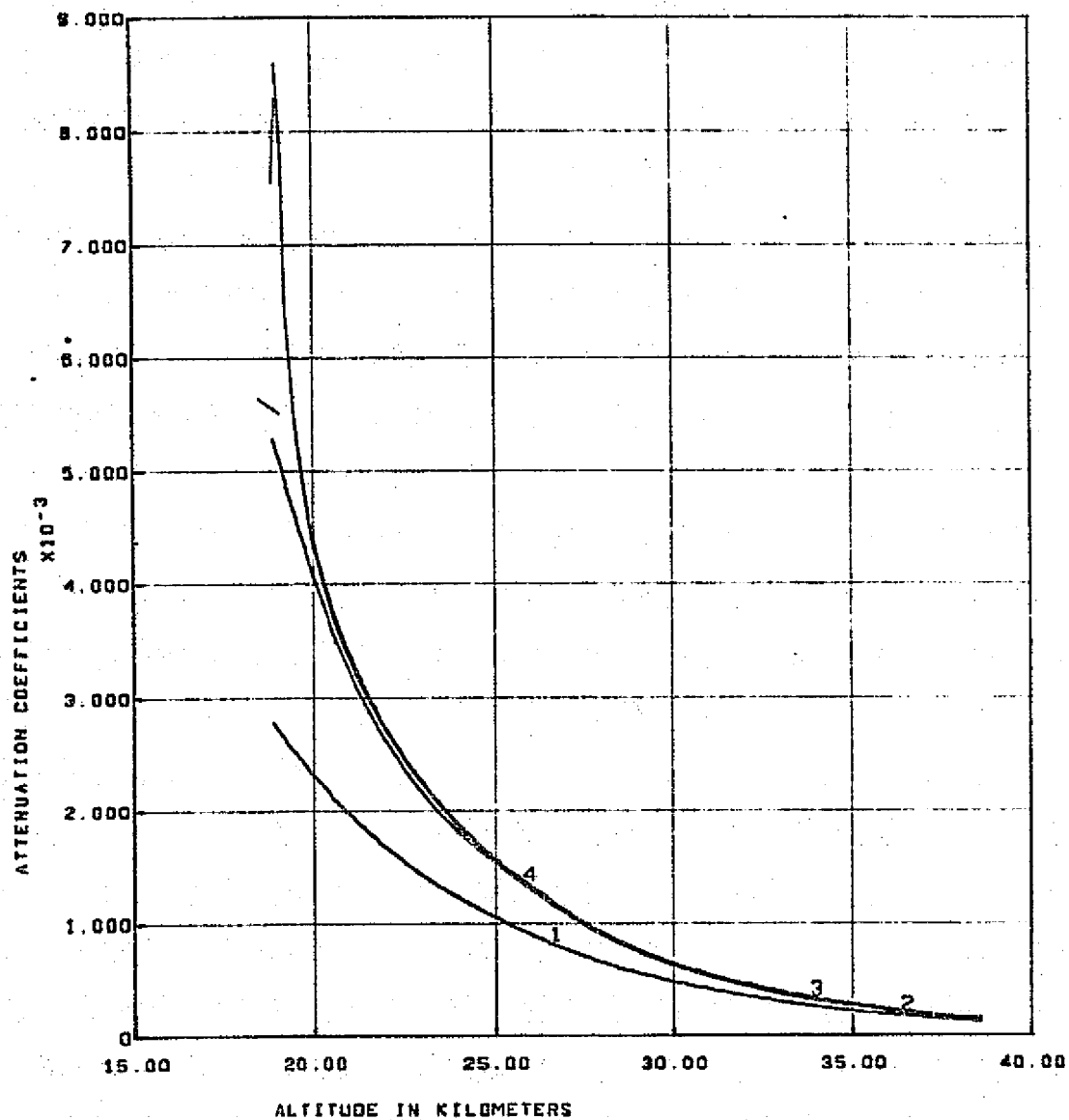
SCANS 600-624. BAND 1



CURVE 1 - BRIGHTNESS MODEL GENERATED FROM RAYLEIGH + 1968 AEROSOL BETAS.
CURVE 2 - MEASURED BRIGHTNESS SCALED BY 1968 MODEL.

S192 CONICAL SCAN. PASS G1. TAPE NUMBER 932887

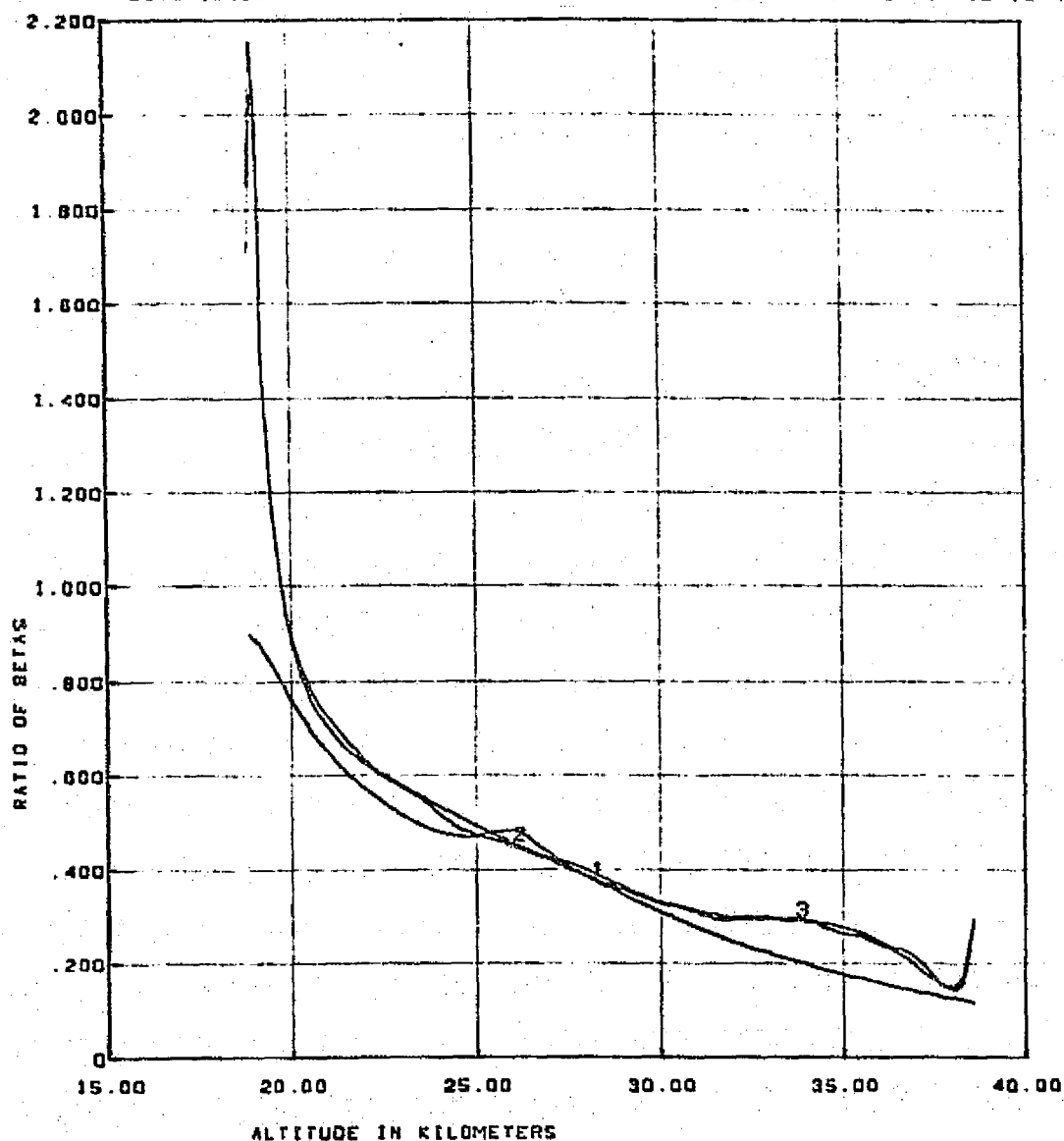
SCANS 600-824. BAND 1



ATTENUATION COEFFICIENTS - 1-RAYLEIGH. 2-RAYLEIGH + 1988 AEROSOL. 3-RESULTS FROM INVERSION OF EXPONENTIAL FIT. 4-RESULTS FROM INVERSION OF SMOOTHED BRIGHTNESS

S192 CONICAL SCAN. PASS 01. TAPE NUMBER 932067

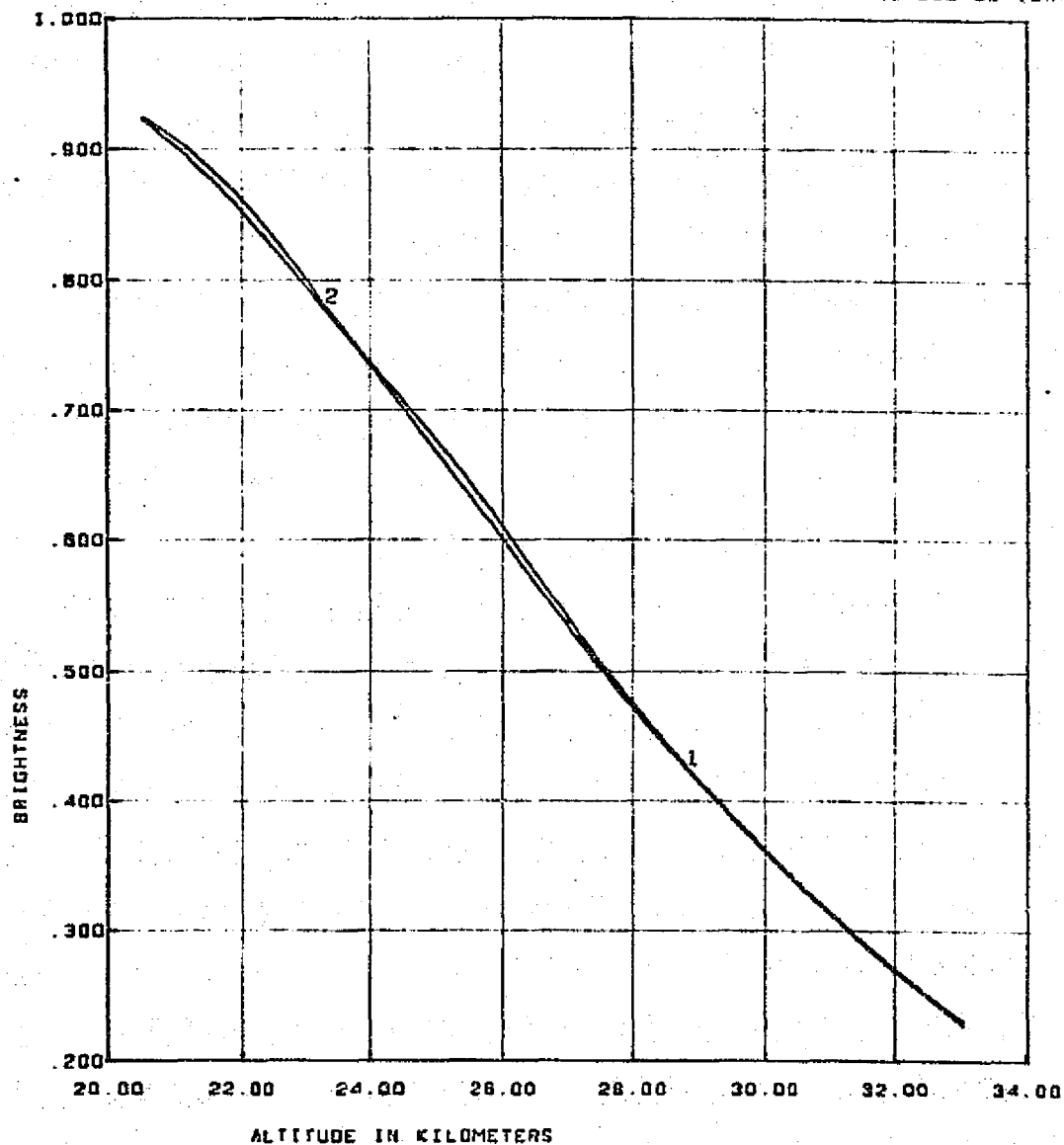
SCANS 600-624. BAND 1



RATIO OF BETAS, AEROSOL OVER RAYLEIGH, 1-1968 MODEL AEROSOL, 2-RESULTS FROM INVERSION OF EXPONENTIAL FIT, 3-RESULTS FROM INVERSION OF SMOOTHED BRIGHTNESS

\$192 CONICAL SCAN. PASS 81. TAPE NUMBER 932867

SCANS 800-824. BAND 2

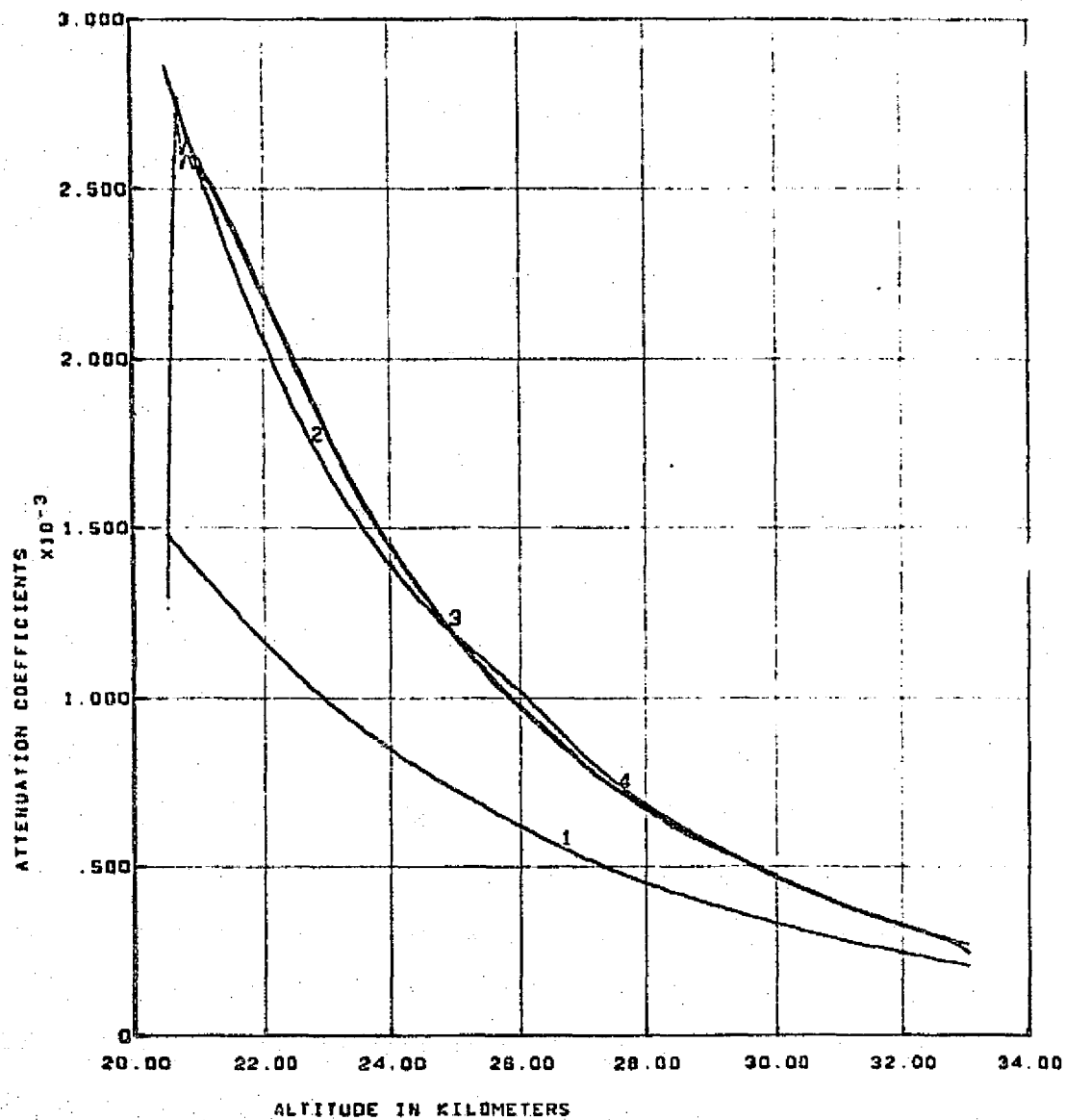


CURVE 1 - BRIGHTNESS MODEL GENERATED FROM RAYLEIGH + 1988 AEROSOL BETAS.
CURVE 2 - MEASURED BRIGHTNESS SCALED BY 1988 MODEL.

REPRODUCIBILITY OF THE
ORIGINAL PAGE IS POOR

S192 CONICAL SCAN. PASS 81. TAPE NUMBER 932867

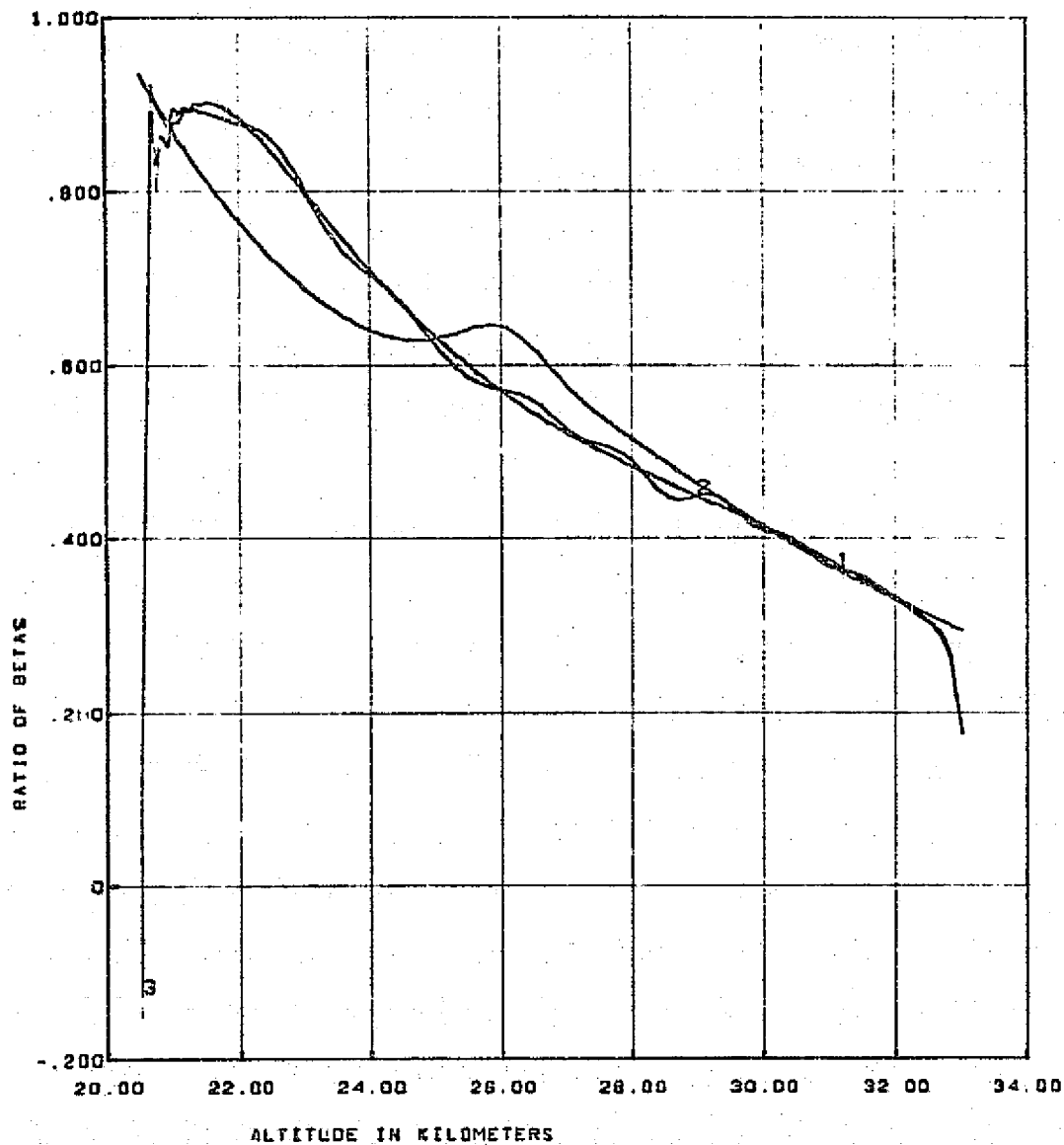
SCANS 600-624. BAND 2



ATTENUATION COEFFICIENTS - 1-RAYLEIGH. 2-RAYLEIGH + 1968 AEROSOL. 3-RESULTS FROM INVERSION OF EXPONENTIAL FIT. 4-RESULTS FROM INVERSION OF SMOOTHED BRIGHTNESS

S192 CONICAL SCAN, PASS 61, TAPE NUMBER 932867

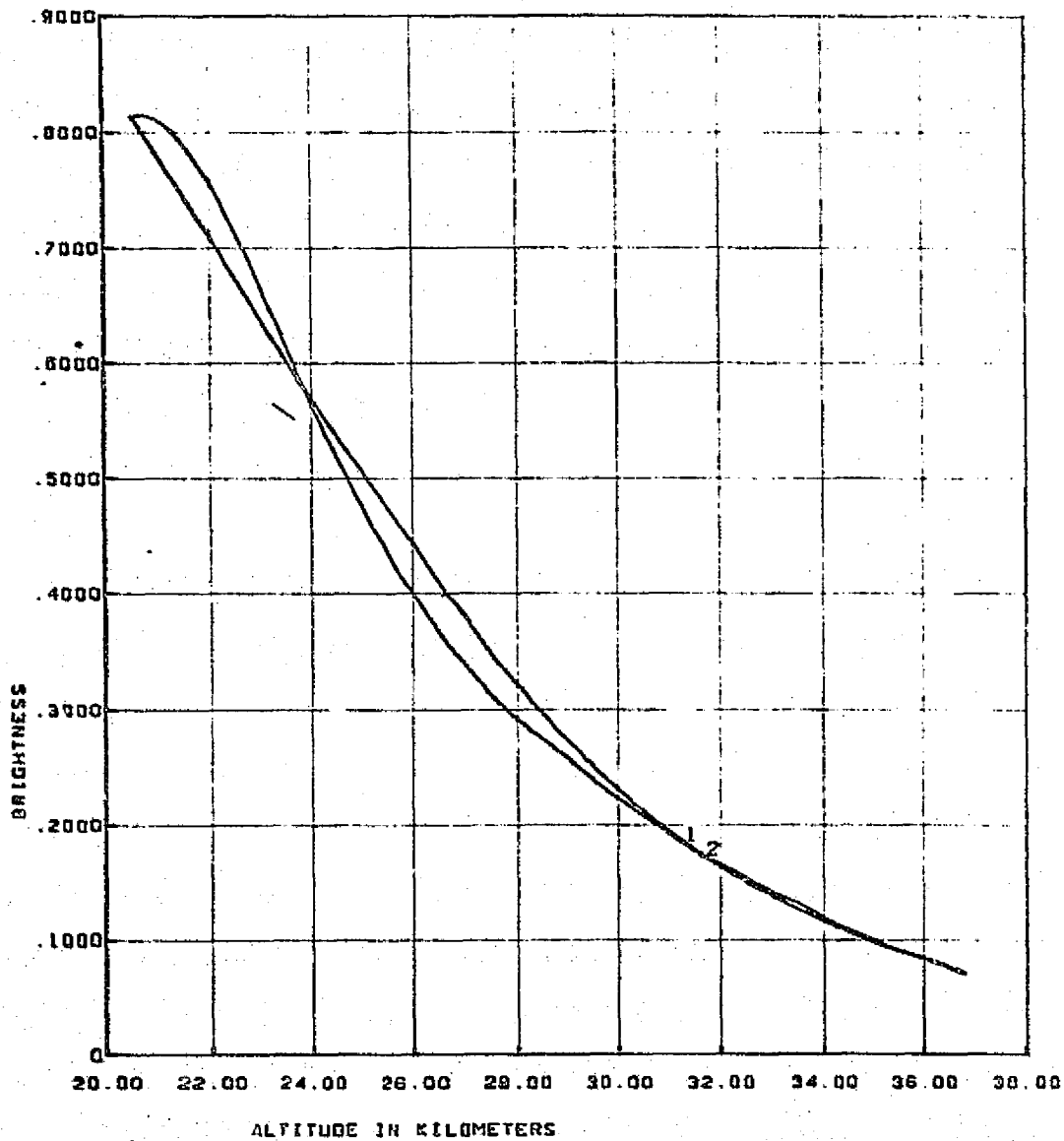
SCANS 600-624, BAND 2



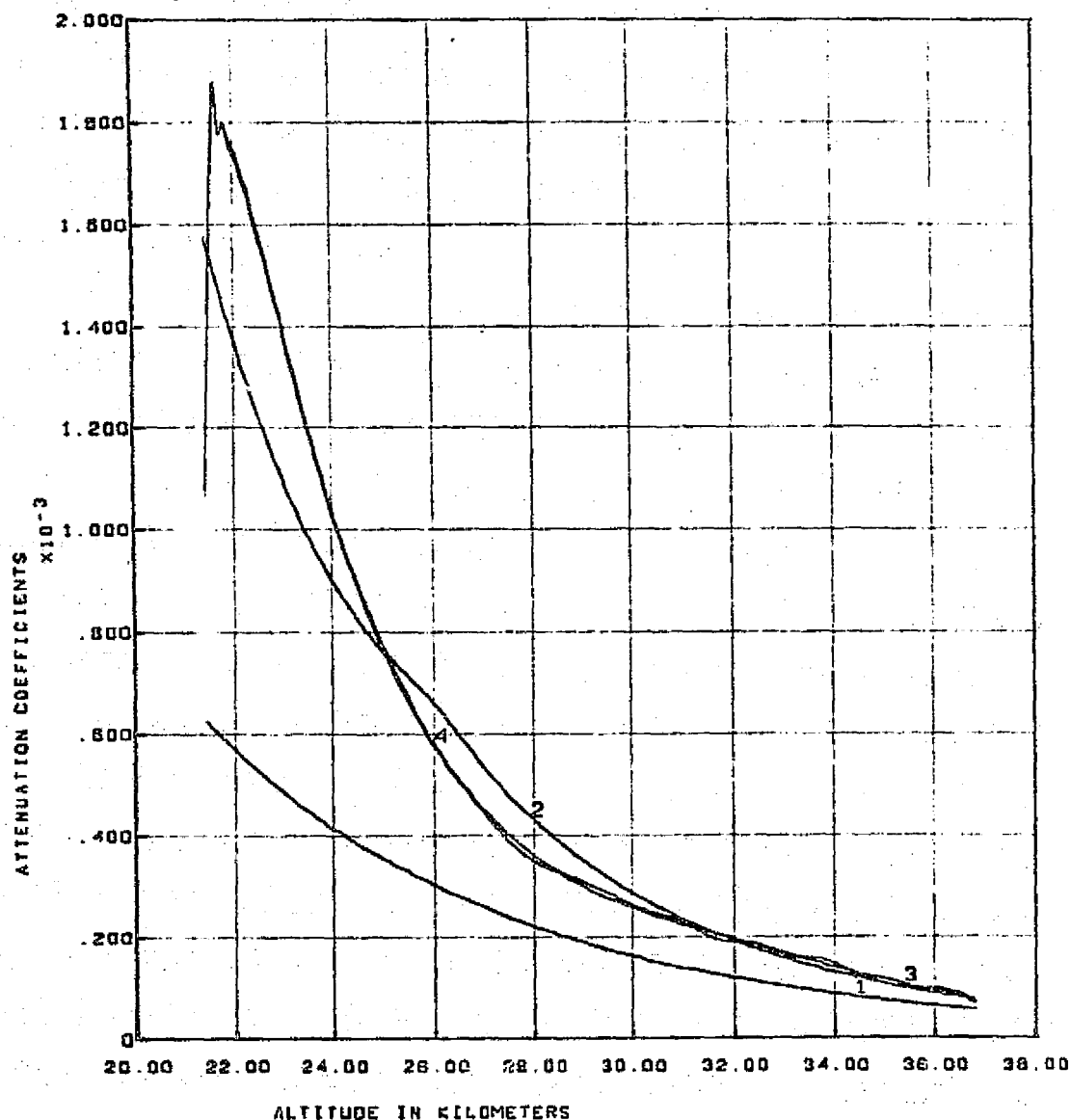
RATIO OF BETAS, AEROSOL OVER RAYLEIGH. 1-1968 MODEL AEROSOL, 2-RESULTS FROM INVERSION OF EXPONENTIAL FIT, 3-RESULTS FROM INVERSION OF SMOOTHED BRIGHTNESS

S192 CONICAL SCAN. PASS 61. TAPE NUMBER 932067

SCANS 600-624, BAND 4



CURVE 1- BRIGHTNESS MODEL GENERATED FROM RAYLEIGH + 1968 AEROSOL DETAS.
 CURVE 2 - MEASURED BRIGHTNESS SCALED BY 1968 MODEL.

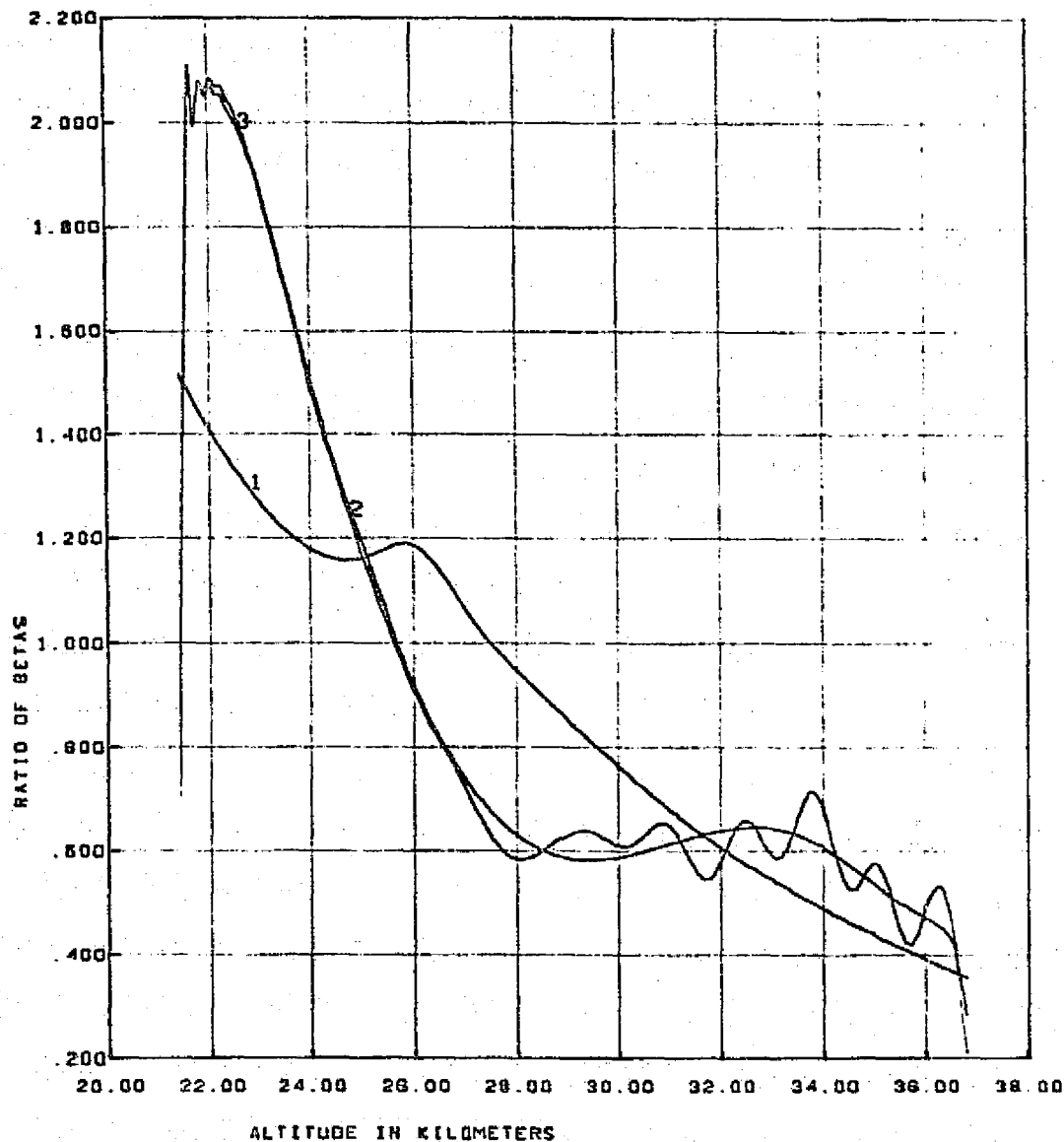


ATTENUATION COEFFICIENTS - 1-RAYLEIGH, 2-RAYLEIGH + 1968 AEROSOL, 3-RESULTS FROM INVERSION OF EXPONENTIAL FIT, 4-RESULTS FROM INVERSION OF SMOOTHED BRIGHTNESS

REPRODUCIBILITY OF THE
ORIGINAL PAGE IS POOR

S192 CONICAL SCAN, PASS 01, TAPE NUMBER 932887

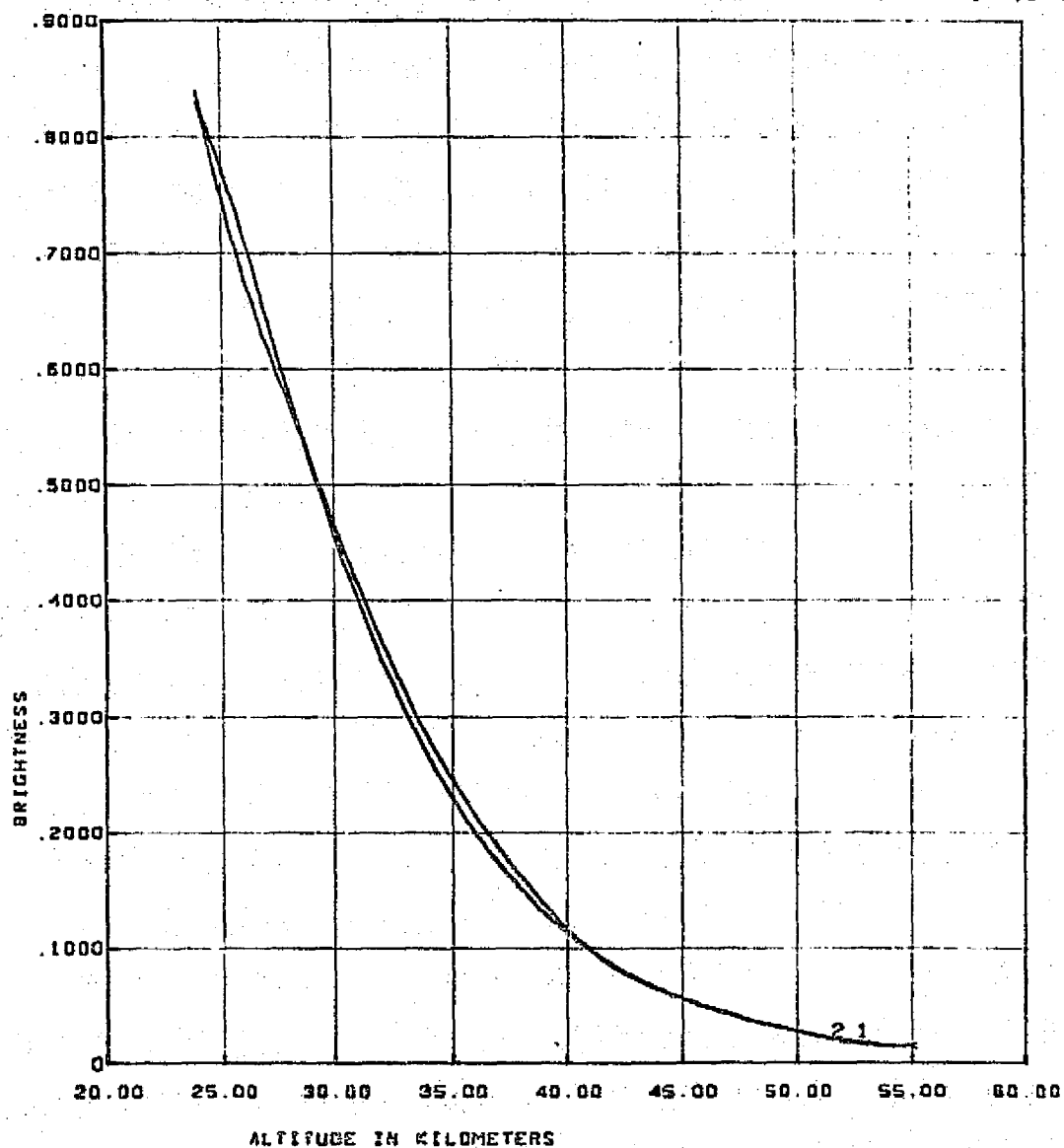
SCANS 600-624, BAND 4



RATIO OF BETAS, AEROSOL OVER RAYLEIGH. 1-1968 MODEL AEROSOL. 2-RESULTS FROM INVERSION OF EXPONENTIAL FIT. 3-RESULTS FROM INVERSION OF SMOOTHED BRIGHTNESS

S192 CONICAL SCAN, PASS 81, TAPE NUMBER 932957

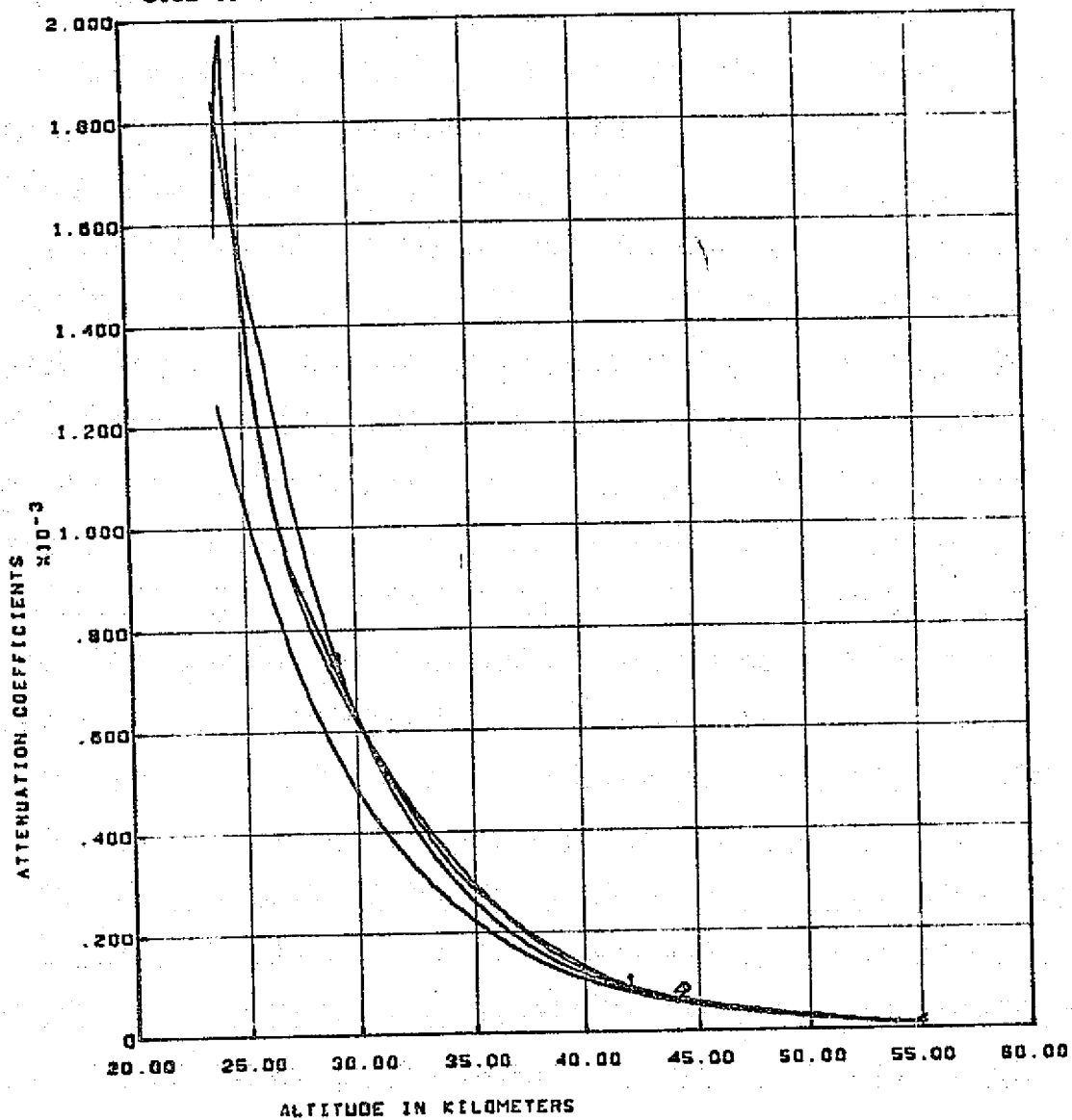
SCANS 120-144, BAND 1



CURVE 1- BRIGHTNESS MODEL GENERATED FROM RAYLEIGH + 1988 AEROSOL BETAS.
CURVE 2 - MEASURED BRIGHTNESS SCALED BY 1988 MODEL.

S192 CONICAL SCAN. PASS 61. TAPE NUMBER 932857

SCANS 120-144, BAND 1

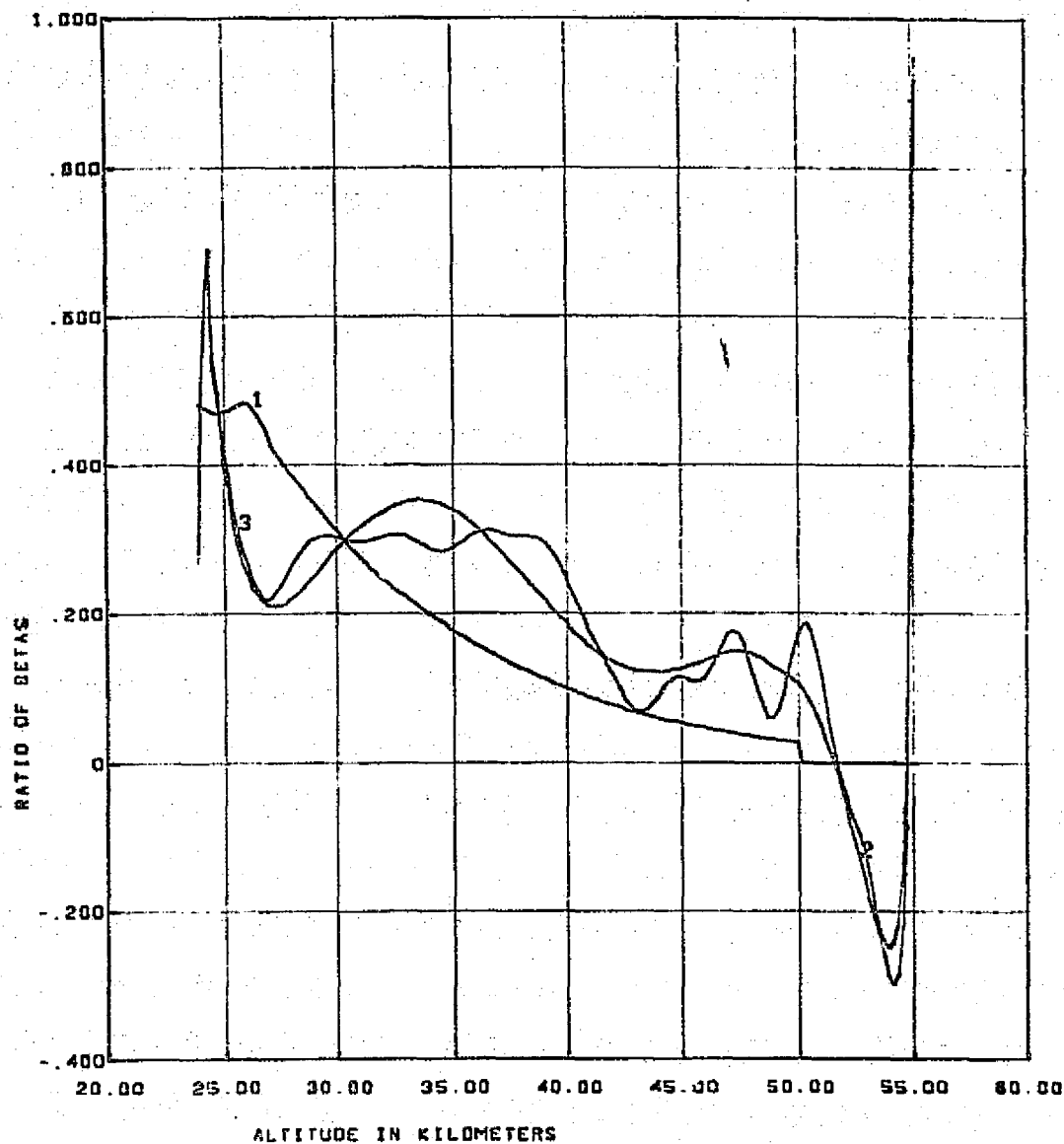


ATTENUATION COEFFICIENTS - 1-RAYLEIGH, 2-RAYLEIGH + 1988 AEROSOL, 3-RESULTS FROM INVERSION OF EXPONENTIAL FIT, 4-RESULTS FROM INVERSION OF SMOOTHED BRIGHTNESS

REPRODUCIBILITY OF THE ORIGINAL PAGE IS POOR

5192 CONICAL SCAN. PASS 81. TAPE NUMBER 932857

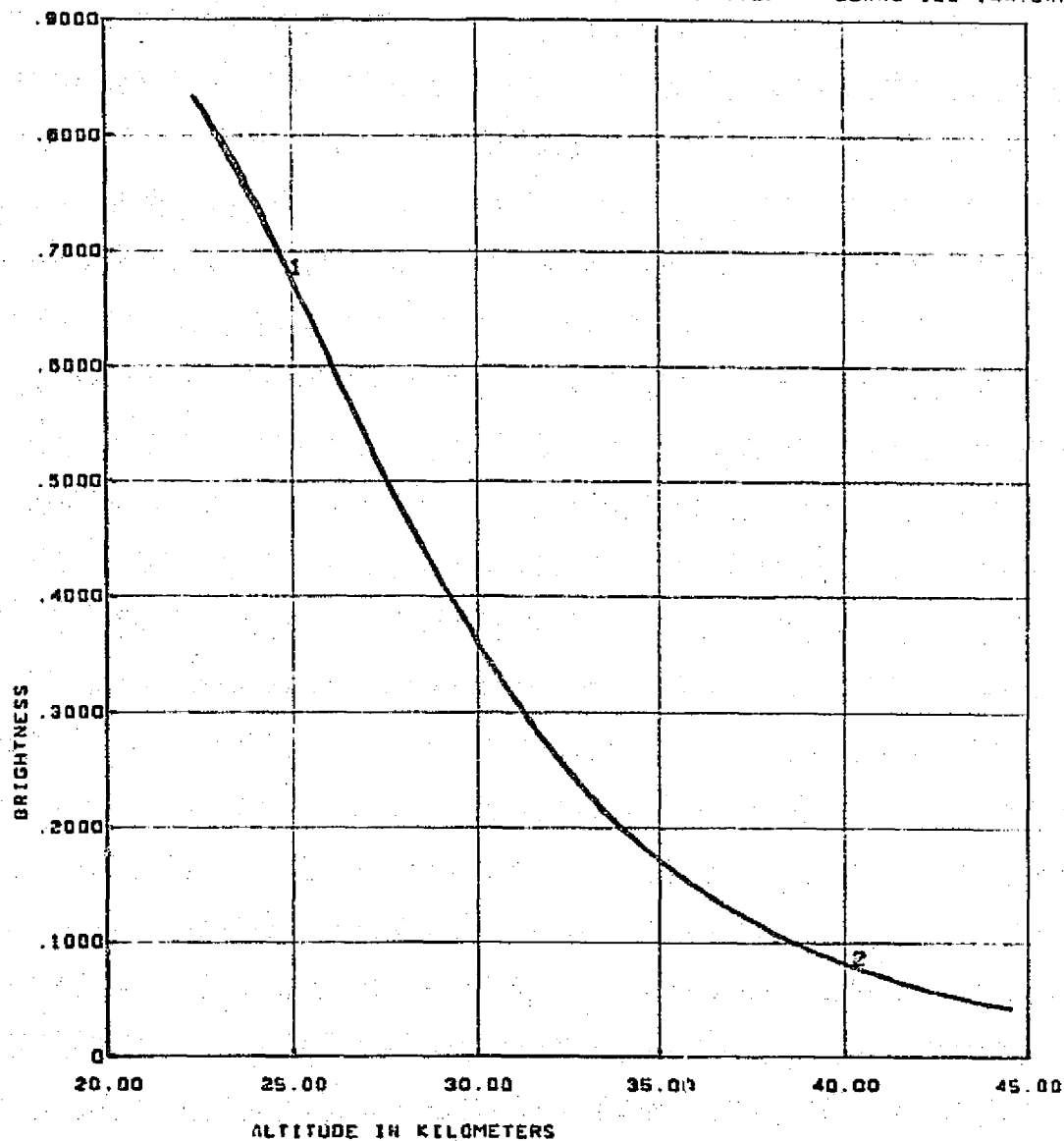
SCANS 120-144. BAND 1



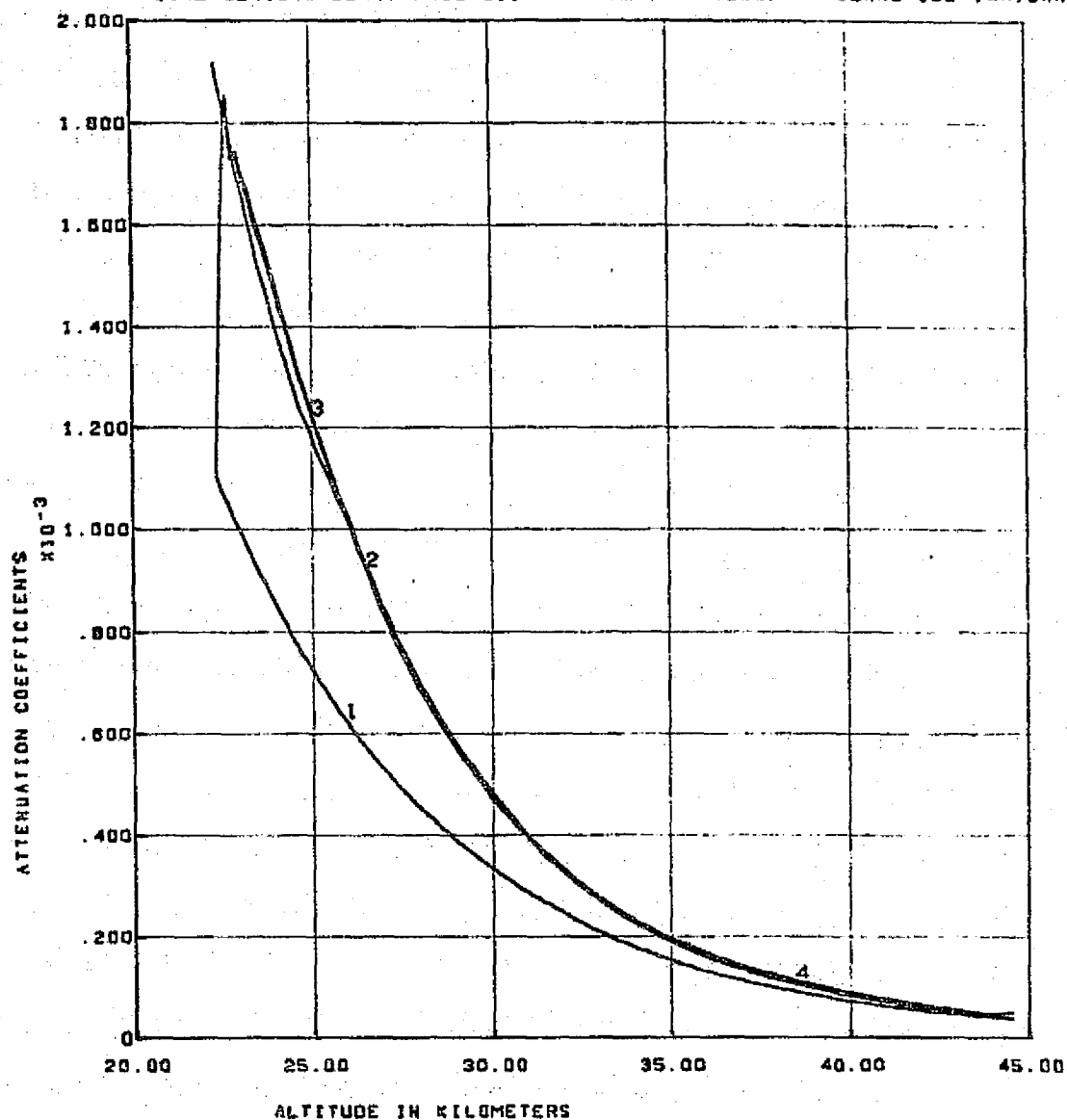
RATIO OF BETAS, AEROSOL OVER RAYLEIGH. 1-1988 MODEL AEROSOL. 2-RESULTS FROM INVERSION OF EXPONENTIAL FIT. 3-RESULTS FROM INVERSION OF SMOOTHED BRIGHTNESS

S192 CONICAL SCAN, PASS 61, TAPE NUMBER 932857

SCANS 120-144, BAND 2



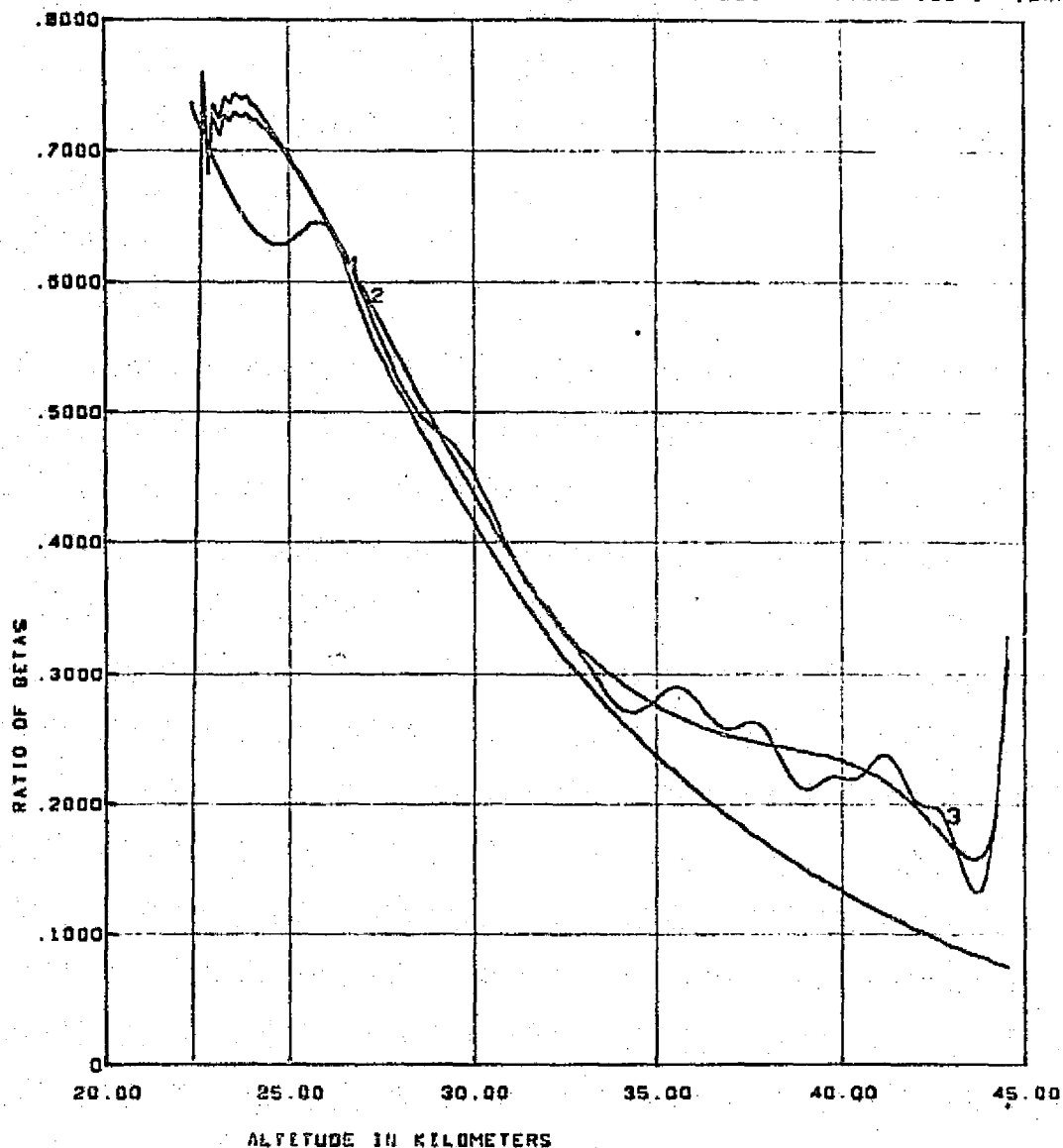
CURVE 1 - BRIGHTNESS MODEL GENERATED FROM RAYLEIGH + 1968 AEROSOL BETAS.
CURVE 2 - MEASURED BRIGHTNESS SCALED BY 1968 MODEL.



ATTENUATION COEFFICIENTS - 1-RAYLEIGH, 2-RAYLEIGH + 1968 AEROSOL, 3-RESULTS FROM INVERSION OF EXPONENTIAL FIT, 4-RESULTS FROM INVERSION OF SMOOTHED BRIGHTNESS

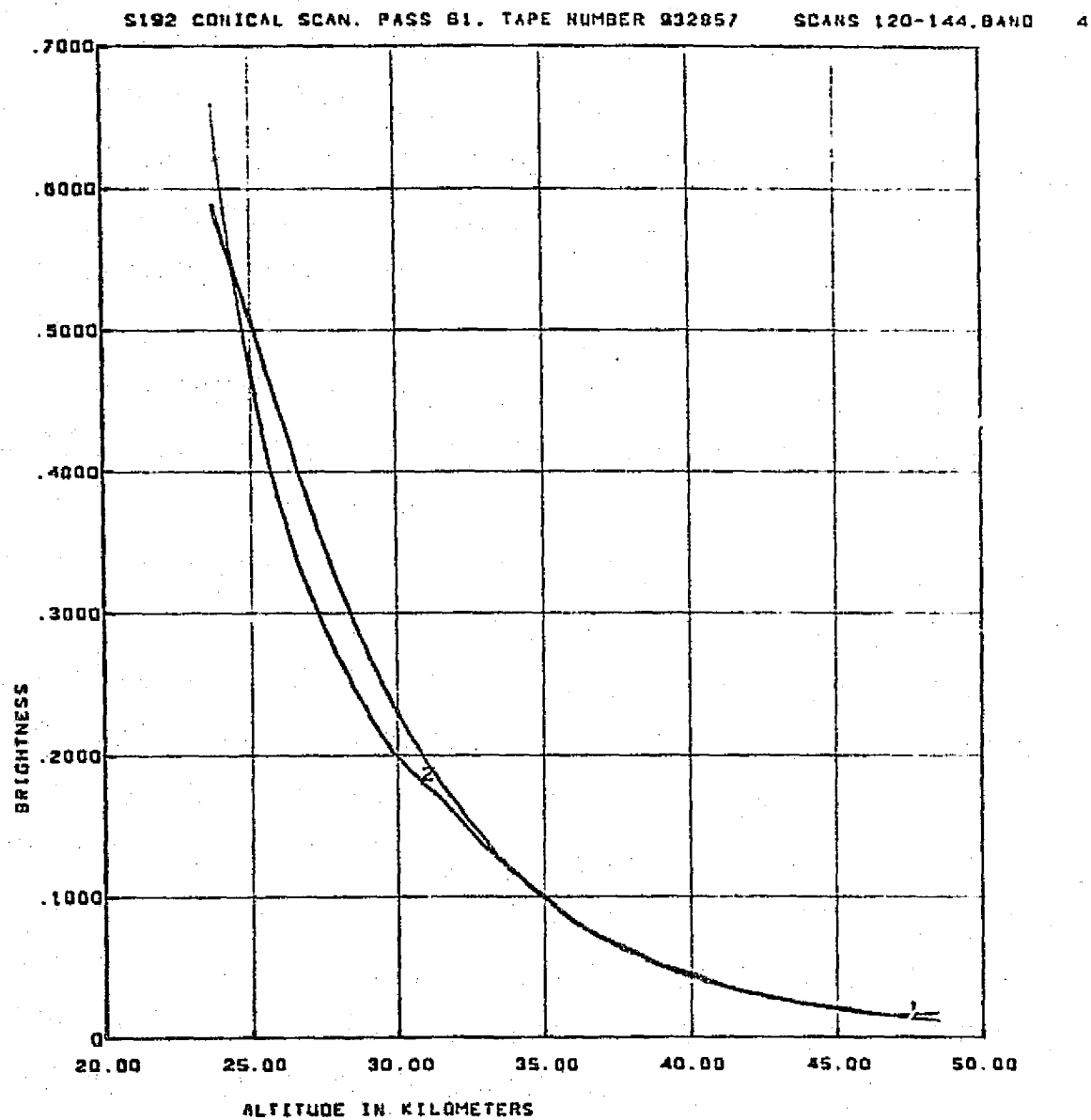
S192 CONICAL SCAN. PASS 61. TAPE NUMBER 932857

SCANS 120-144. BAND 2



RATIO OF BETAS, AEROSOL OVER RAYLEIGH. 1-1988 MODEL AEROSOL. 2-RESULTS FROM INVERSION OF EXPONENTIAL FIT. 3-RESULTS FROM INVERSION OF SMOOTHED BRIGHTNESS

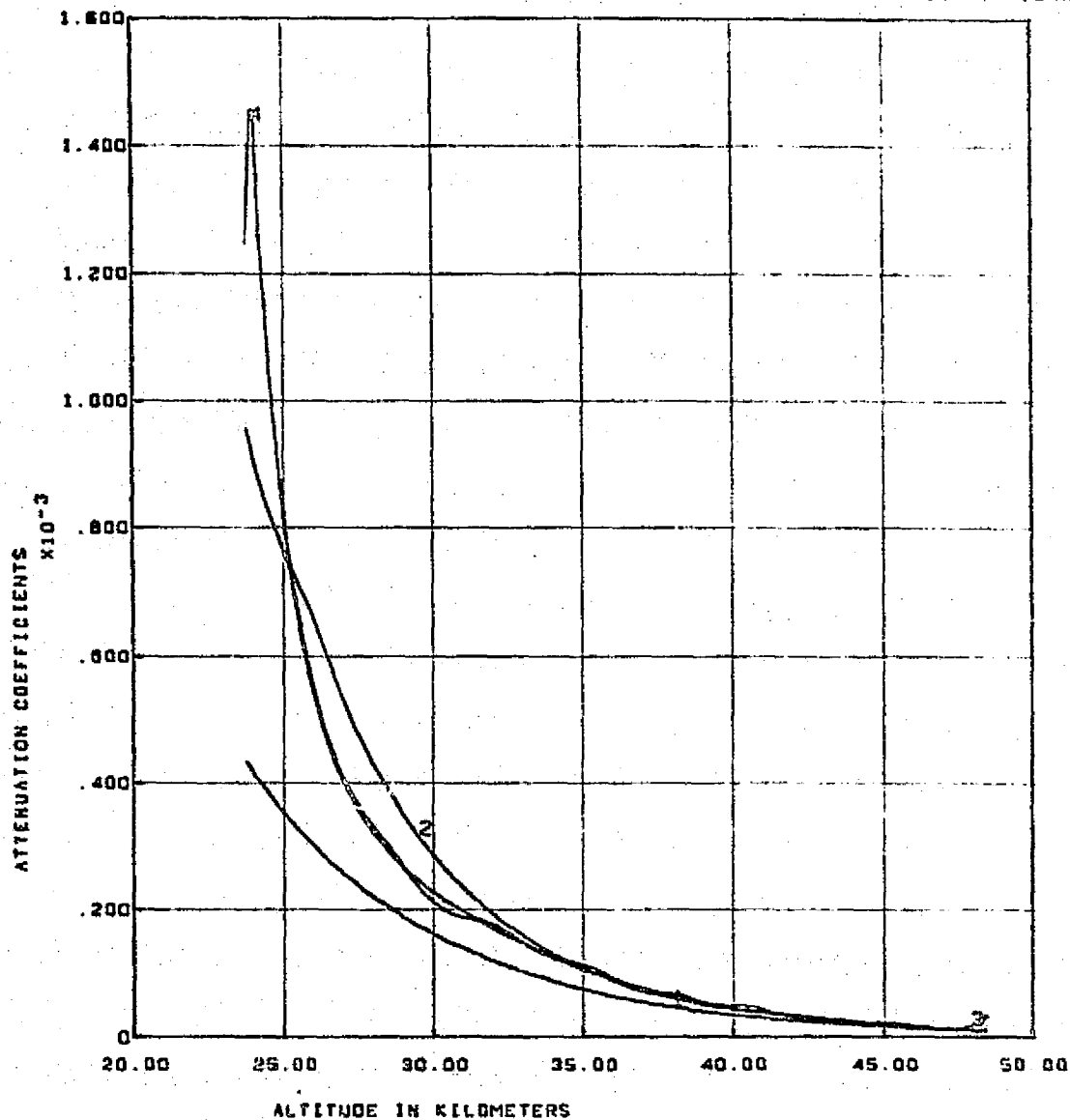
REPRODUCIBILITY OF THE ORIGINAL PAGE IS POOR



CURVE 1 - BRIGHTNESS MODEL GENERATED FROM RAYLEIGH + 1968 AEROSOL BETAS.
CURVE 2 - MEASURED BRIGHTNESS SCALED BY 1968 MODEL.

SL92 CONICAL SCAN. PASS 81. TAPE NUMBER 932857

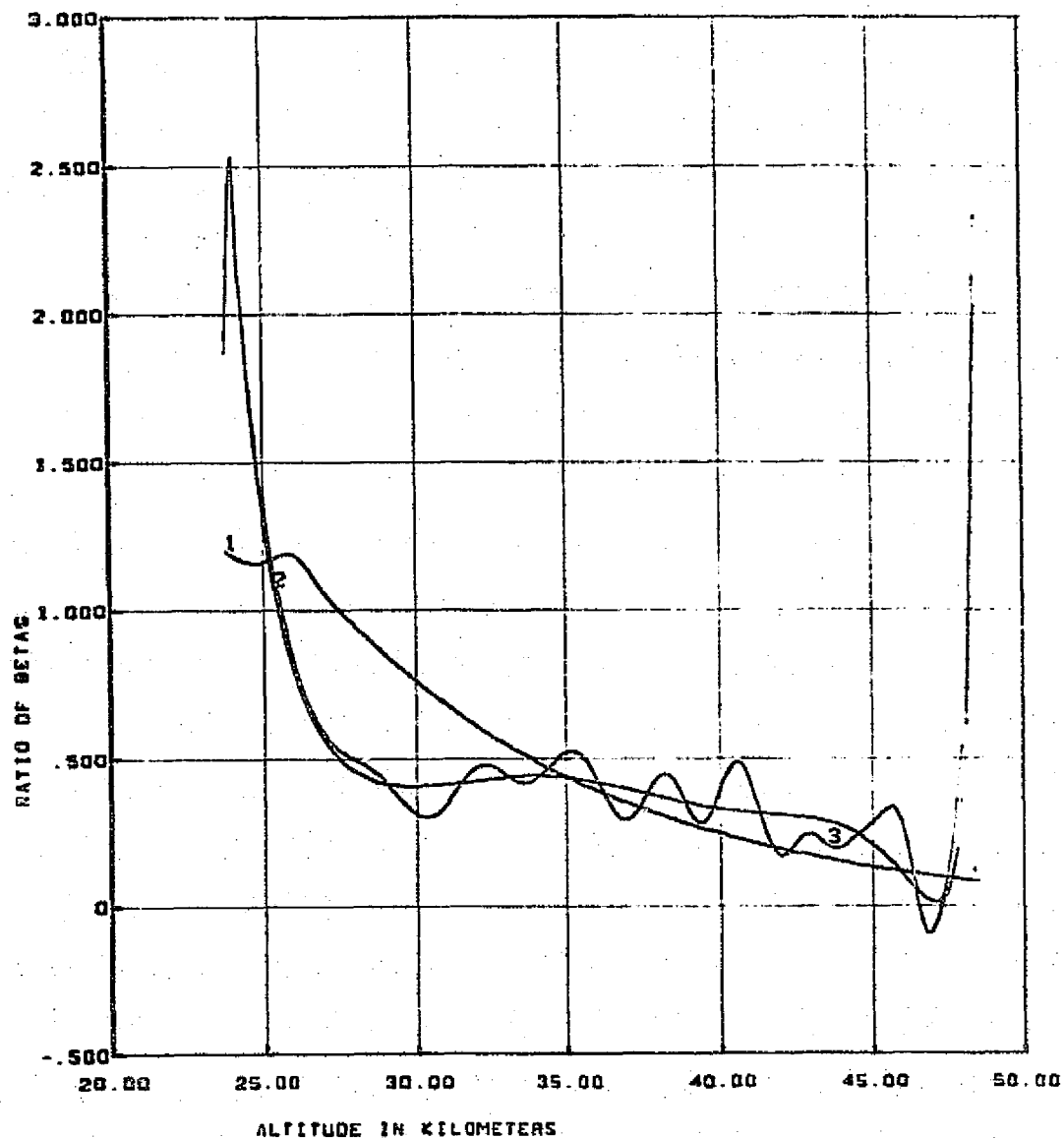
SCANS 120-144. BAND 4



ATTENUATION COEFFICIENTS - 1-RAYLEIGH, 2-RAYLEIGH + 1980 AEROSOL, 3-RESULTS FROM INVERSION OF EXPONENTIAL FIT, 4-RESULTS FROM INVERSION OF SMOOTHED BRIGHTNESS

S192 CONICAL SCAN. PASS 81. TAPE NUMBER 932857

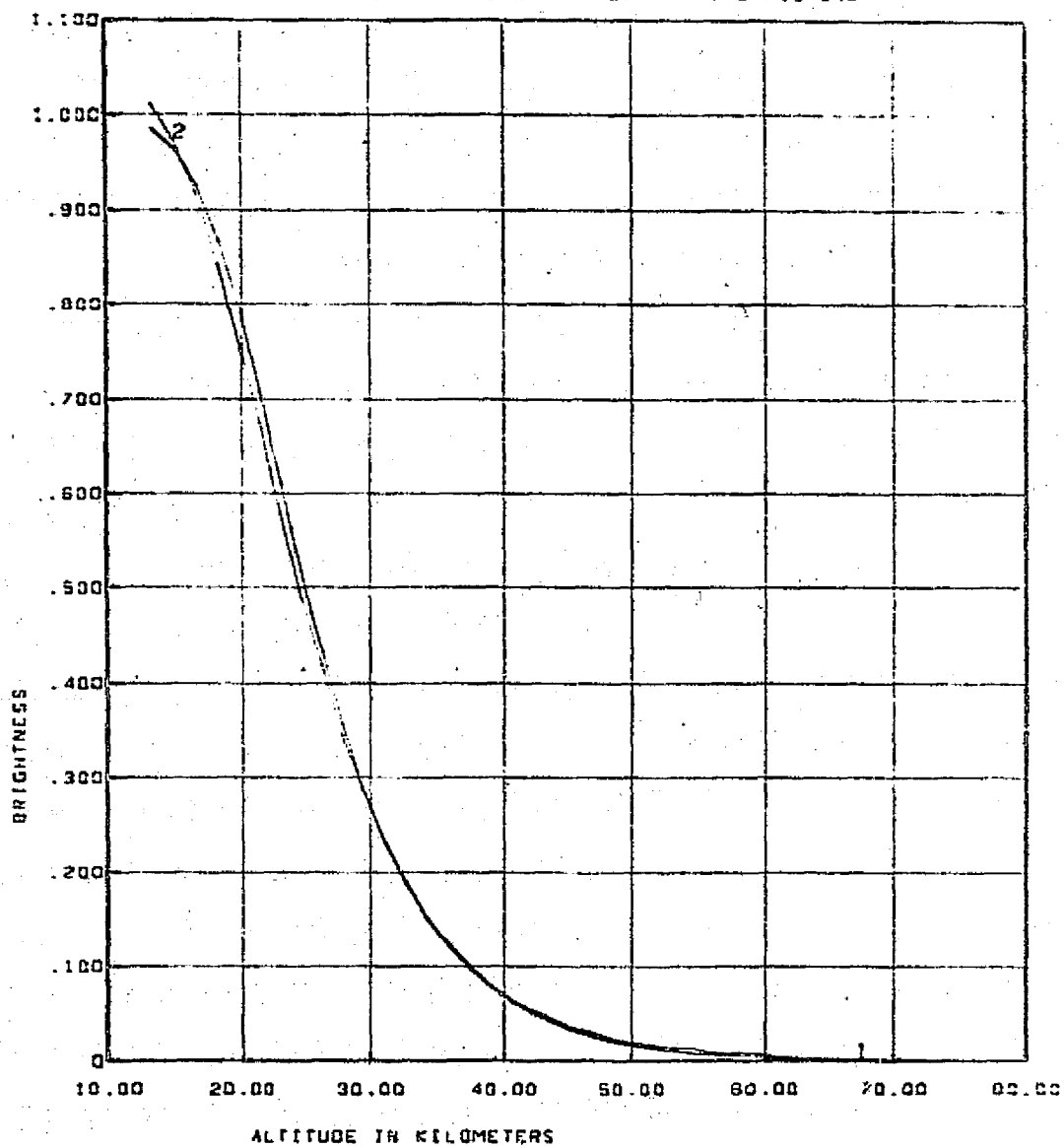
SCANS 120-144. BAND 4



RATIO OF BETAS. AEROSOL OVER RAYLEIGH. 1-1968 MODEL AEROSOL. 2-RESULTS FROM INVERSION OF EXPONENTIAL FIT. 3-RESULTS FROM INVERSION OF SMOOTHED BRIGHTNESS

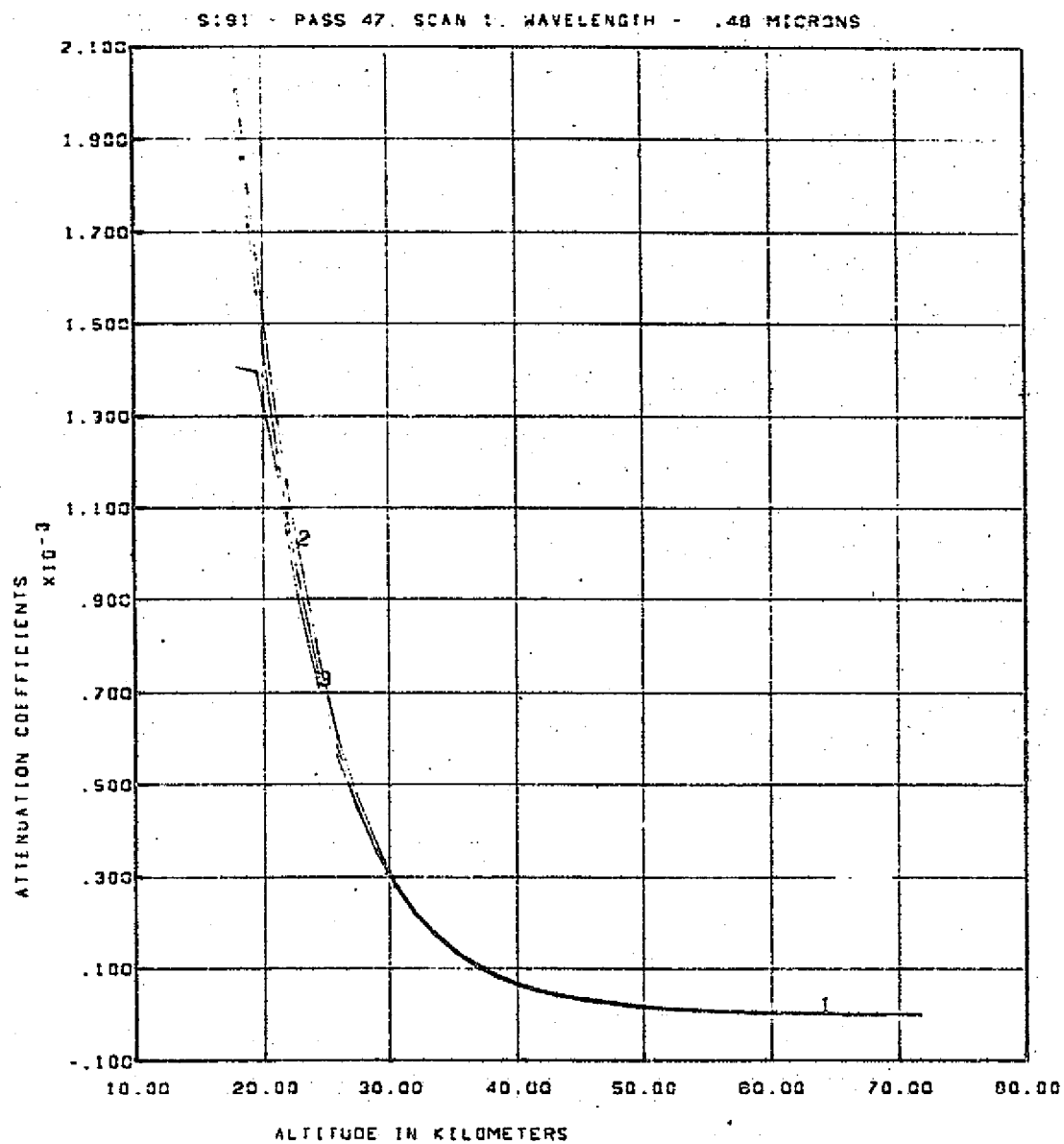
REPRODUCIBILITY OF THE ORIGINAL PAGE IS POOR

S191 - PASS 47, SCAN 1', WAVELENGTH - .48 MICRONS



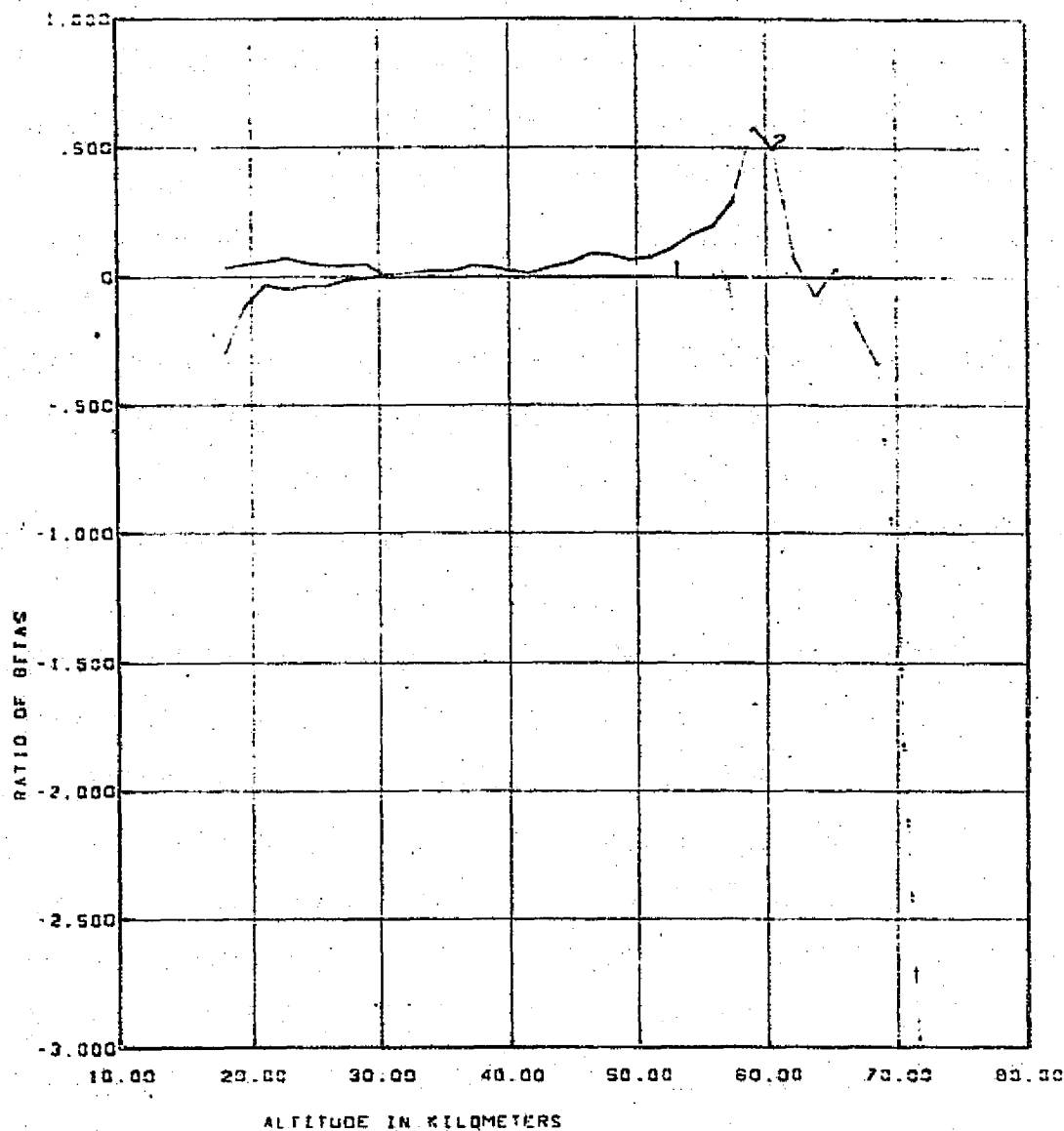
CURVE 1 - BRIGHTNESS MODEL GENERATED FROM RAYLEIGH + 1964 AEROSOL BETAS.
 CURVE 2 - MEASURED BRIGHTNESS SCALED BY 1964 MODEL.

11

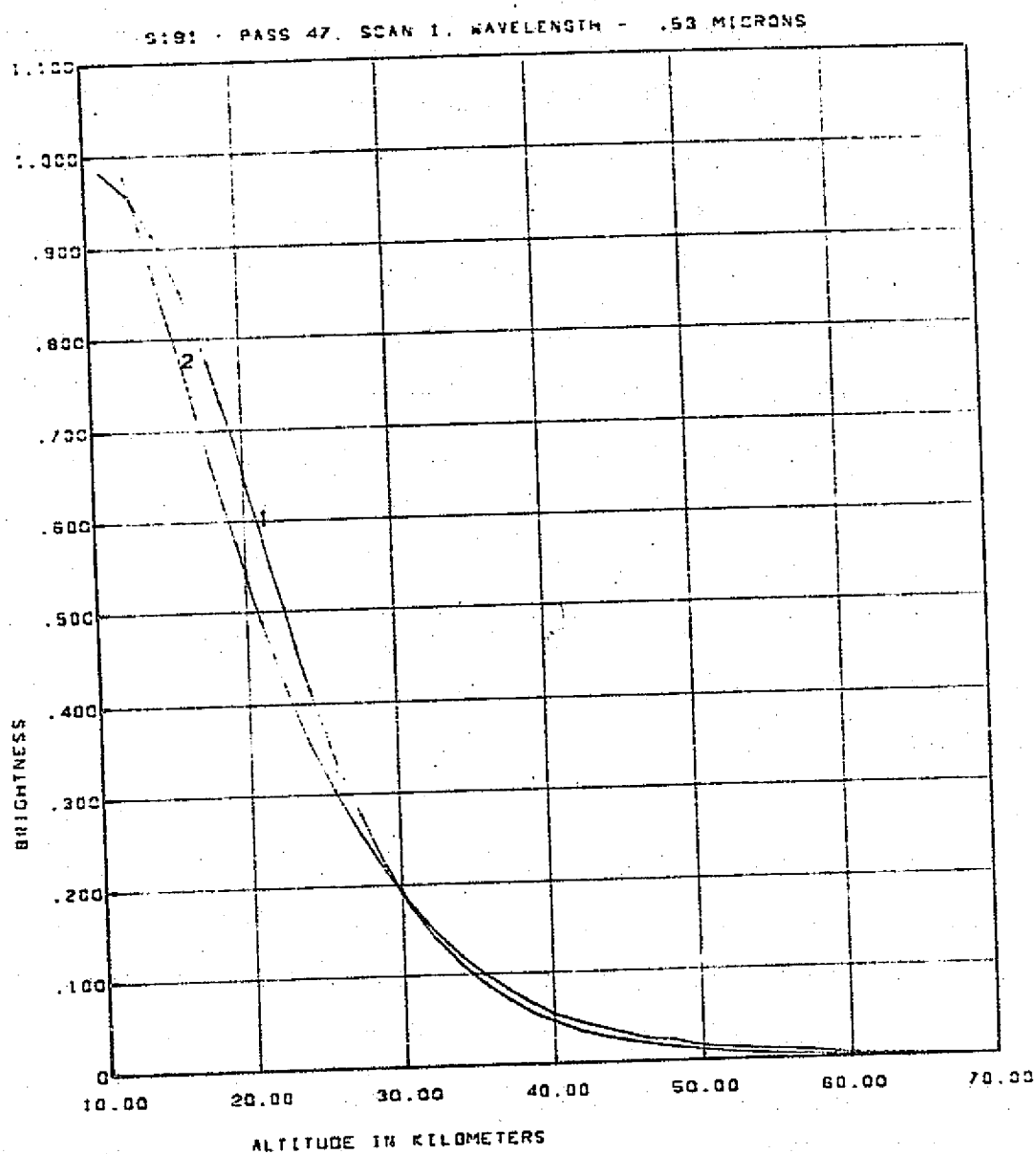


CURVE 1 - RAYLEIGH BETAS. CURVE 2 - RAYLEIGH + 1964 AEROSOL BETAS
 CURVE 3 IS BETAS DERIVED BY INVERSION OF SCALED MEASURED BRIGHTNESS

S19: - PASS 47, SCAN 1, WAVELENGTH - .48 MICRONS



CURVE 1 IS RATIO OF 1984 AEROSOL BETAS OVER RAYLEIGH BETAS.
 CURVE 2 IS RATIO OF DERIVED AEROSOL BETAS OVER RAYLEIGH BETAS.

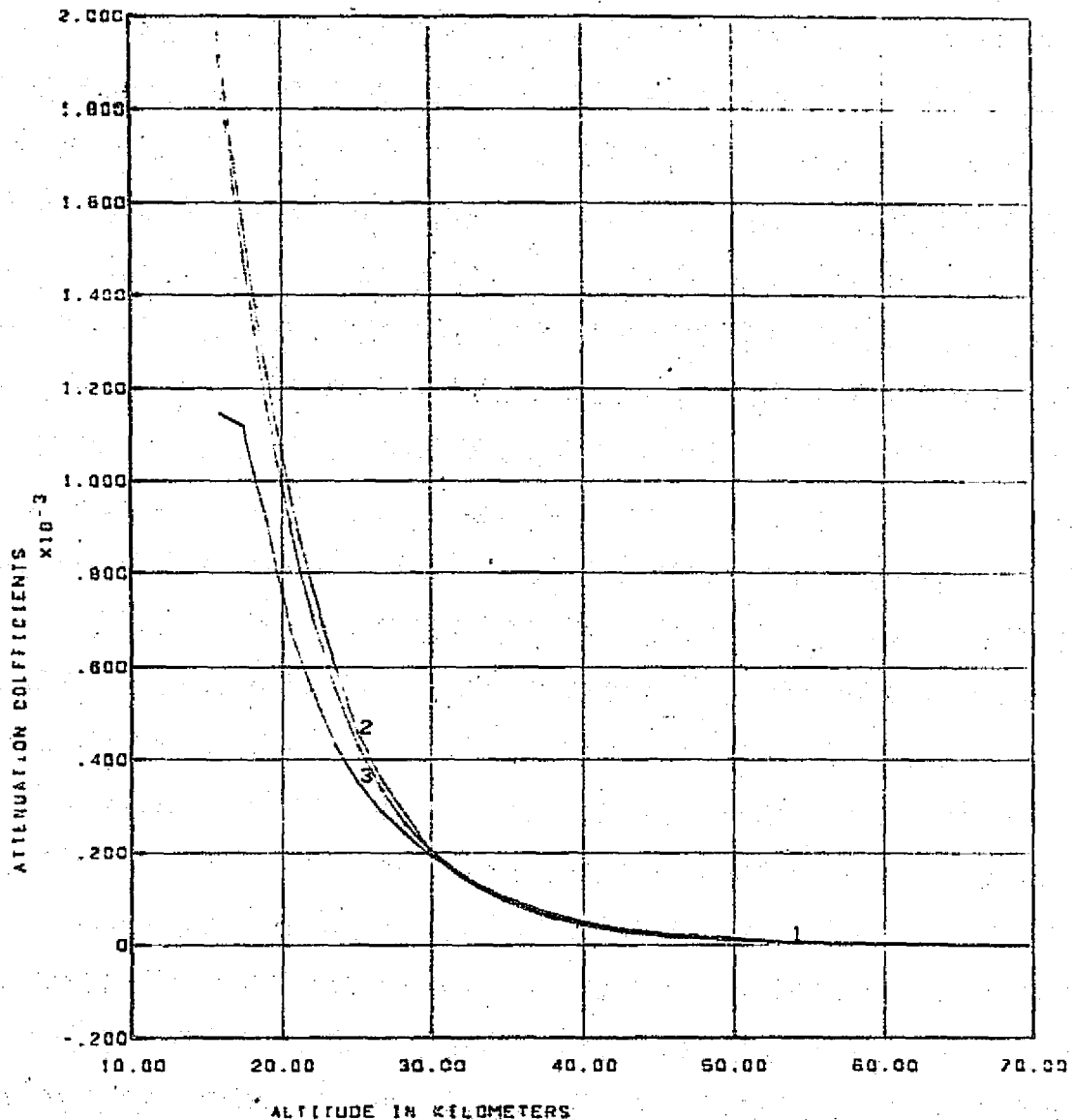


CURVE 1 - BRIGHTNESS MODEL GENERATED FROM RAYLEIGH + 1964 AEROSOL BETAS.
 CURVE 2 - MEASURED BRIGHTNESS SCALED BY 1964 MODEL.

REPRODUCIBILITY OF THE
 ORIGINAL PAGE IS POOR

111

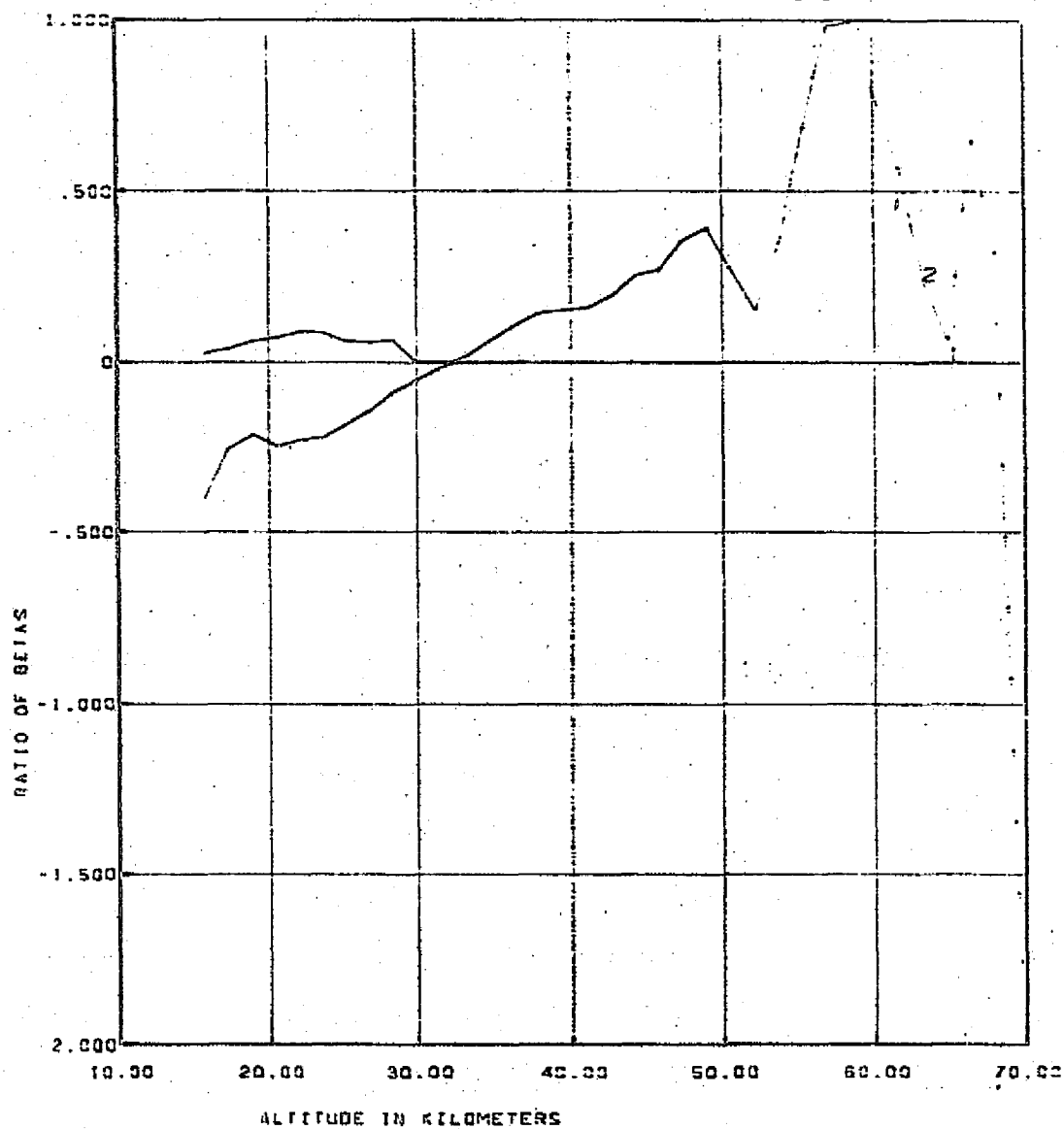
S191 - PASS 47, SCAN 1, WAVELENGTH - .53 MICRONS



CURVE 1 - RAYLEIGH BETAS. CURVE 2 - RAYLEIGH + 1964 AEROSOL BETAS
 CURVE 3 IS BETAS DERIVED BY INVERSION OF SCALED MEASURED BRIGHTNESS

111

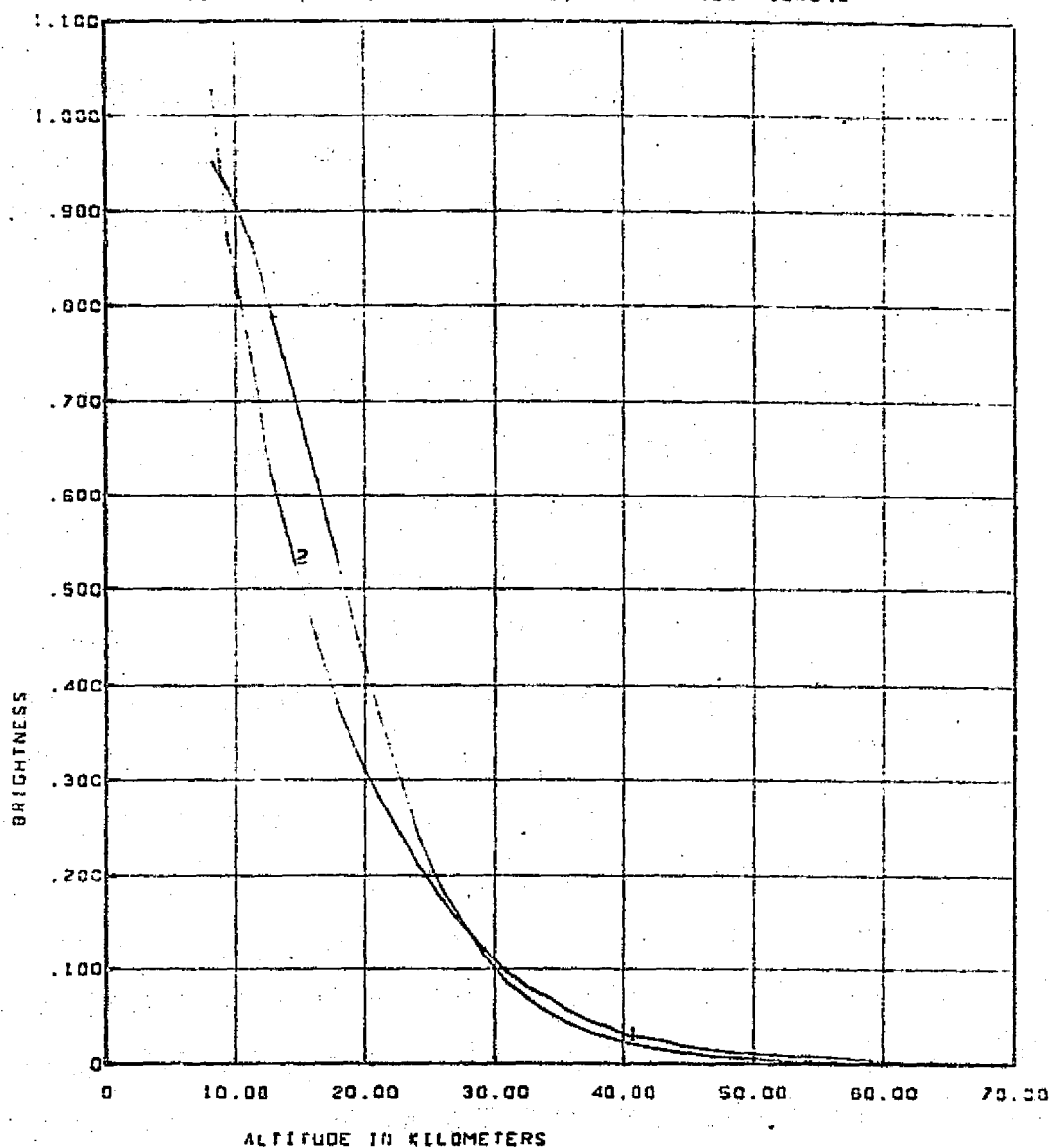
S191 - PASS 47. SCAN 1. WAVELENGTH - .53 MICRONS



CURVE 1 IS RATIO OF 1964 AEROSOL BETAS OVER RAYLEIGH BETAS.
 CURVE 2 IS RATIO OF DERIVED AEROSOL BETAS OVER RAYLEIGH BETAS.

811

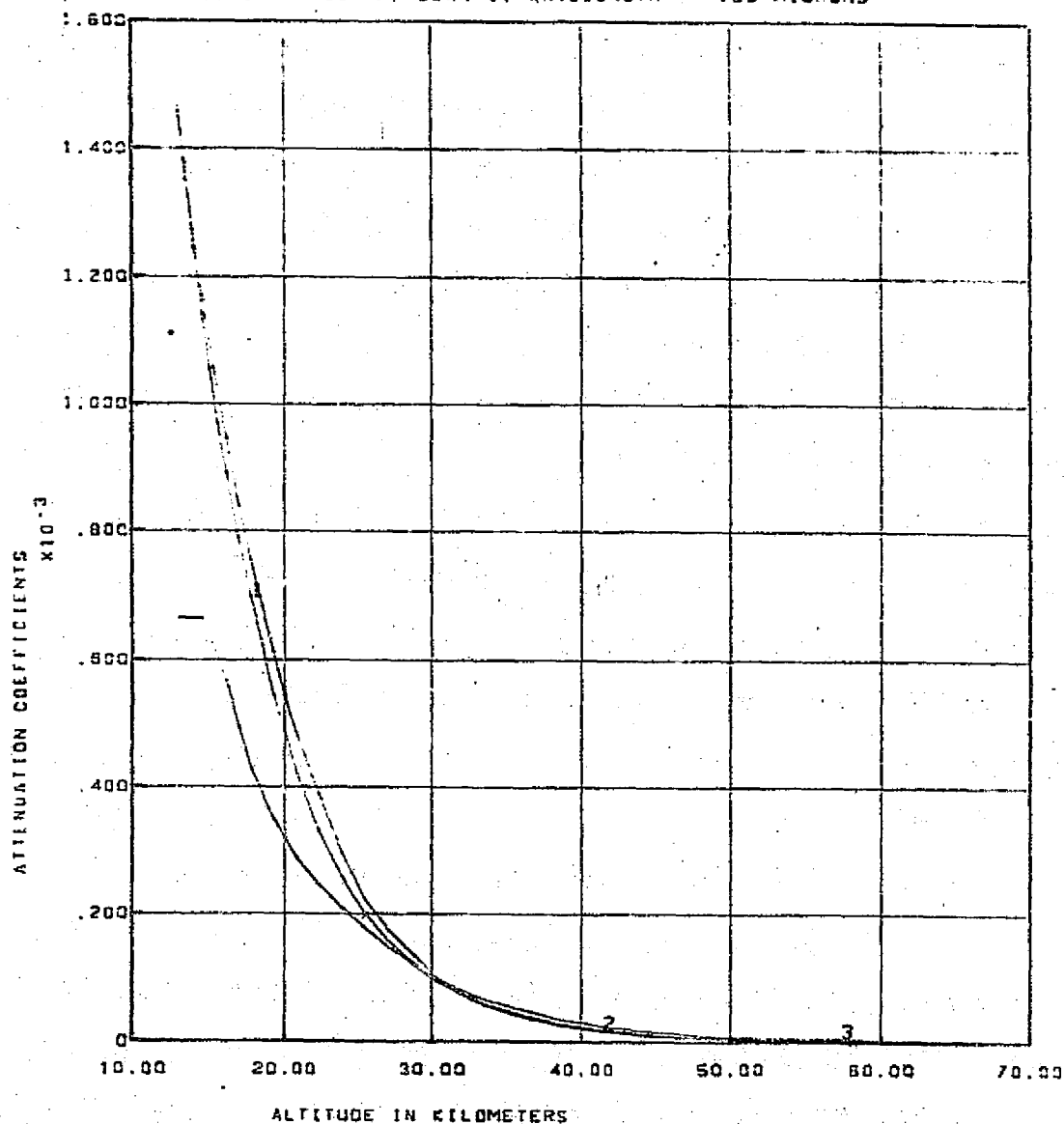
S191 - PASS 47, SCAN 1, WAVELENGTH - .63 MICRONS



CURVE 1 - BRIGHTNESS MODEL GENERATED FROM RAYLEIGH + 1984 AEROSOL BETAS.
 CURVE 2 - MEASURED BRIGHTNESS SCALED BY 1984 MODEL.

211

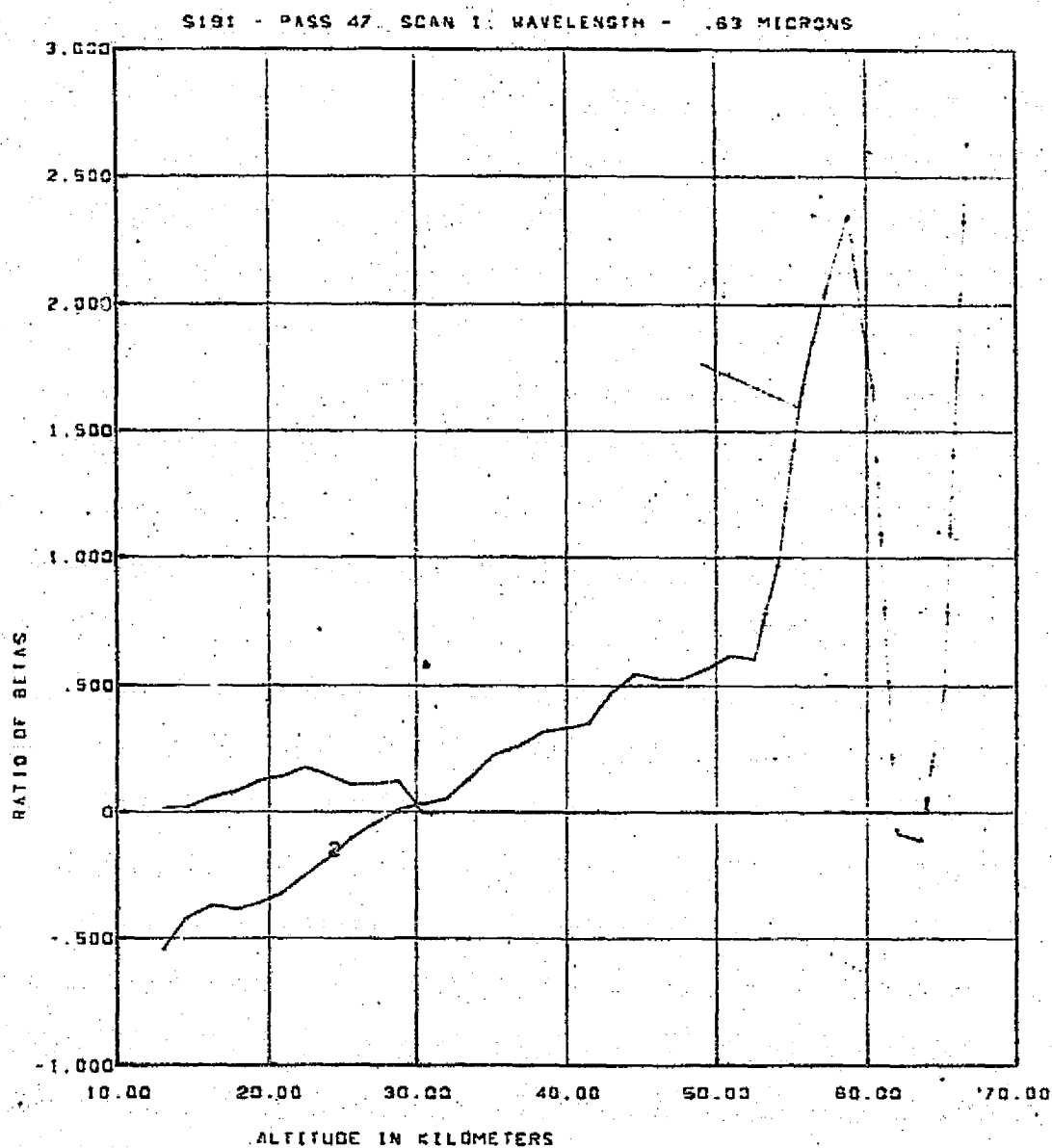
S191 - PASS 47, SCAN 1, WAVELENGTH - .63 MICRONS



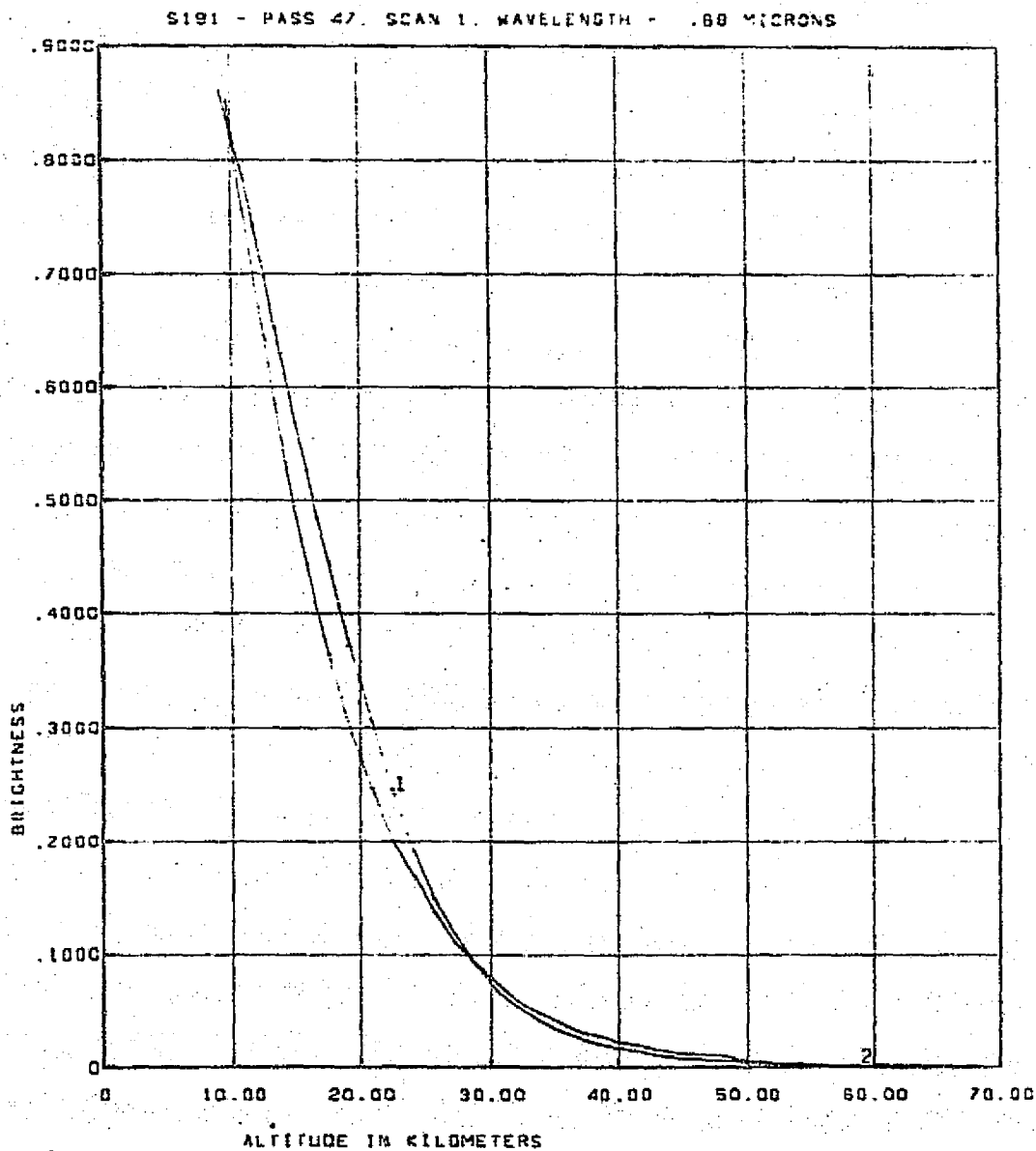
CURVE 1 - RAYLEIGH BETAS. CURVE 2 - RAYLEIGH + 1964 AEROSOL BETAS
CURVE 3 IS BETAS DERIVED BY INVERSION OF SCALED MEASURED BRIGHTNESS

REPRODUCIBILITY OF THE
ORIGINAL PAGE IS POOR

811

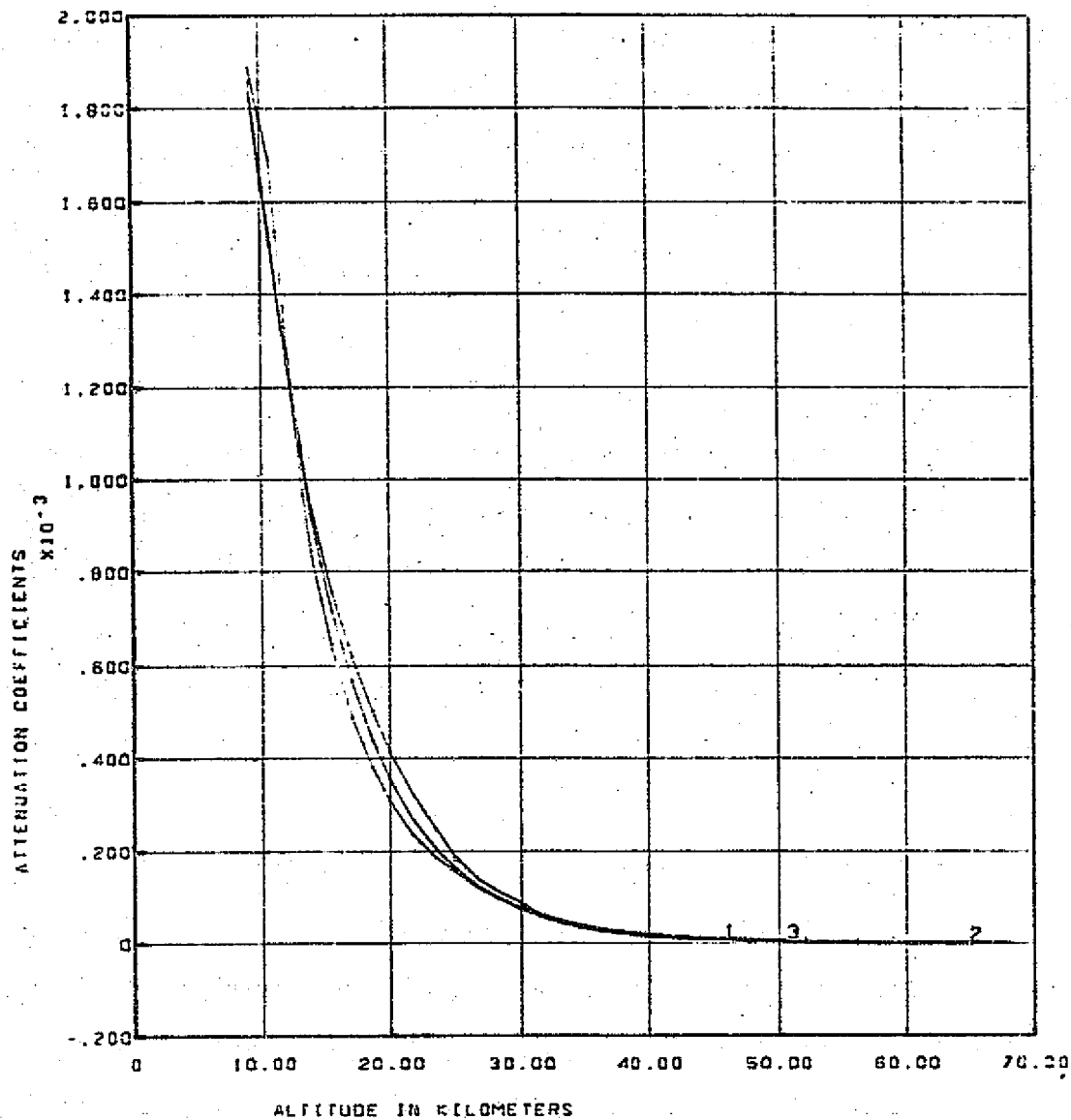


CURVE 1 IS RATIO OF 1984 AEROSOL BETAS OVER RAYLEIGH BETAS.
 CURVE 2 IS RATIO OF DERIVED AEROSOL BETAS OVER RAYLEIGH BETAS.



CURVE 1 - BRIGHTNESS MODEL GENERATED FROM RAYLEIGH + 1964 AEROSOL BETAS.
CURVE 2 - MEASURED BRIGHTNESS SCALED BY 1964 MODEL.

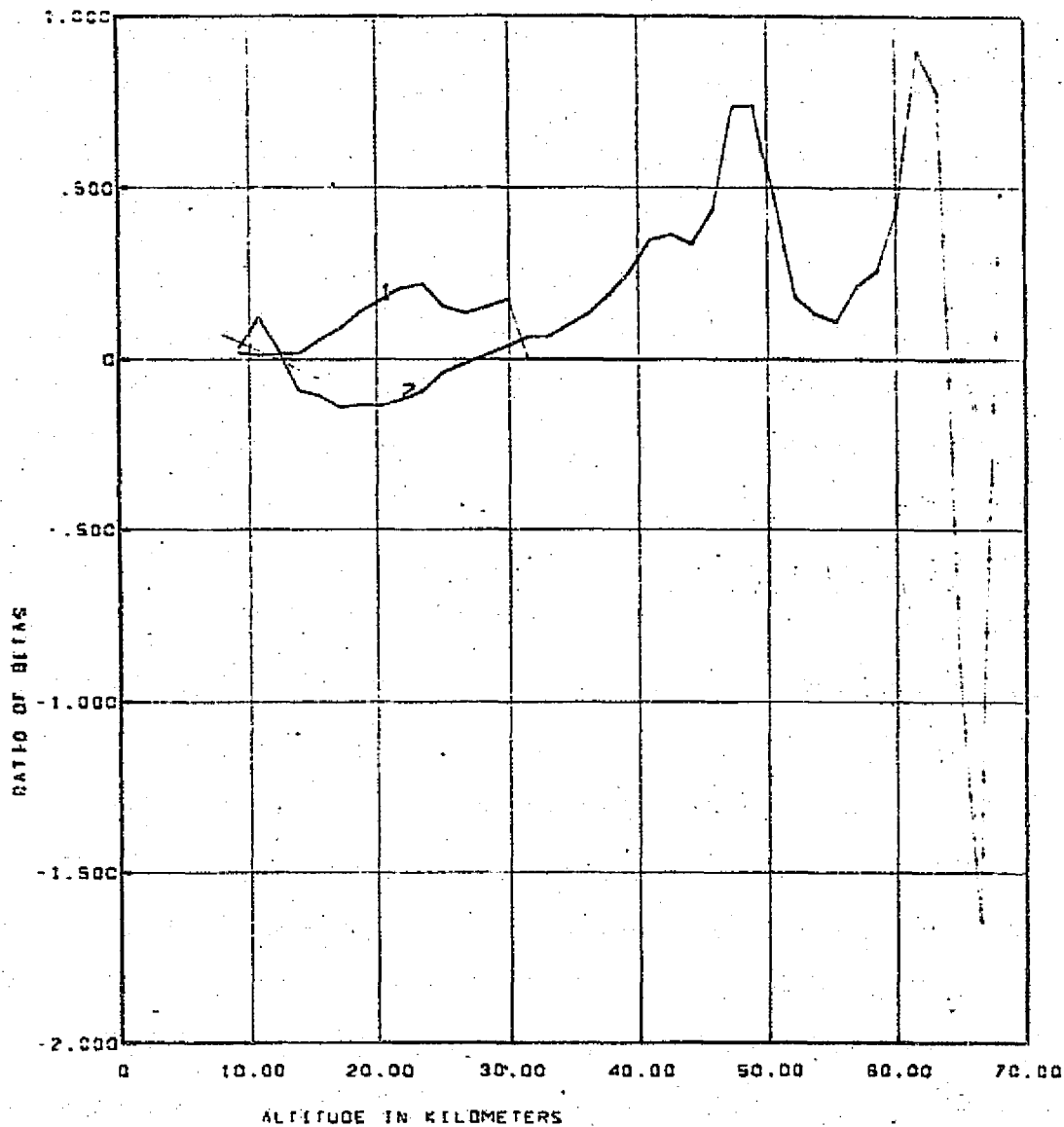
S19: - PASS 47, SCAN 1, WAVELENGTH - .68 MICRONS



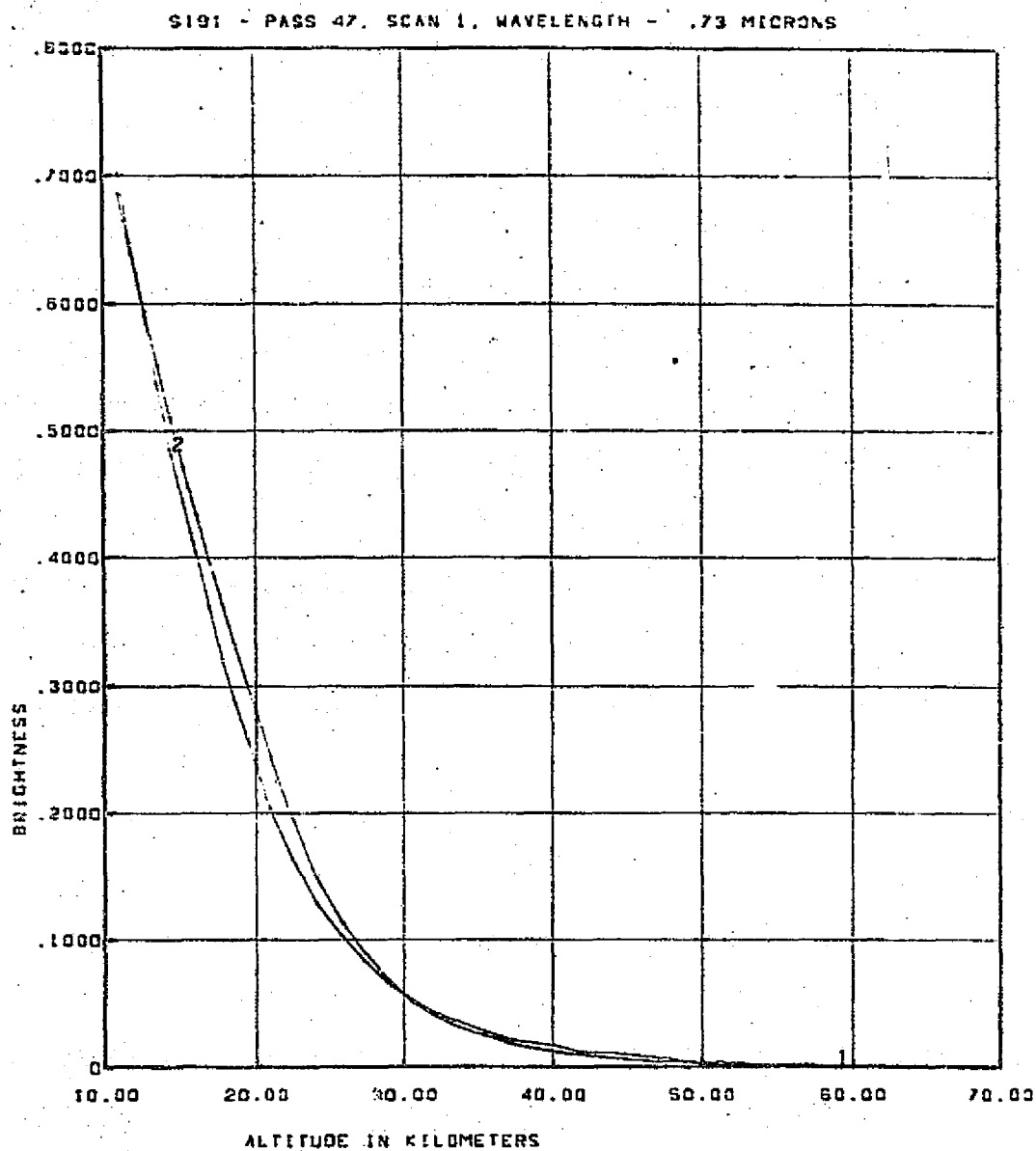
CURVE 1 - RAYLEIGH BETAS. CURVE 2 - RAYLEIGH + 1964 AEROSOL BETAS
CURVE 3 IS BETAS DERIVED BY INVERSION OF SCALED MEASURED BRIGHTNESS

REPRODUCIBILITY OF THE
ORIGINAL PAGE IS POOR

S191 - PASS 47 SCAN 1. WAVELENGTH - .60 MICRONS



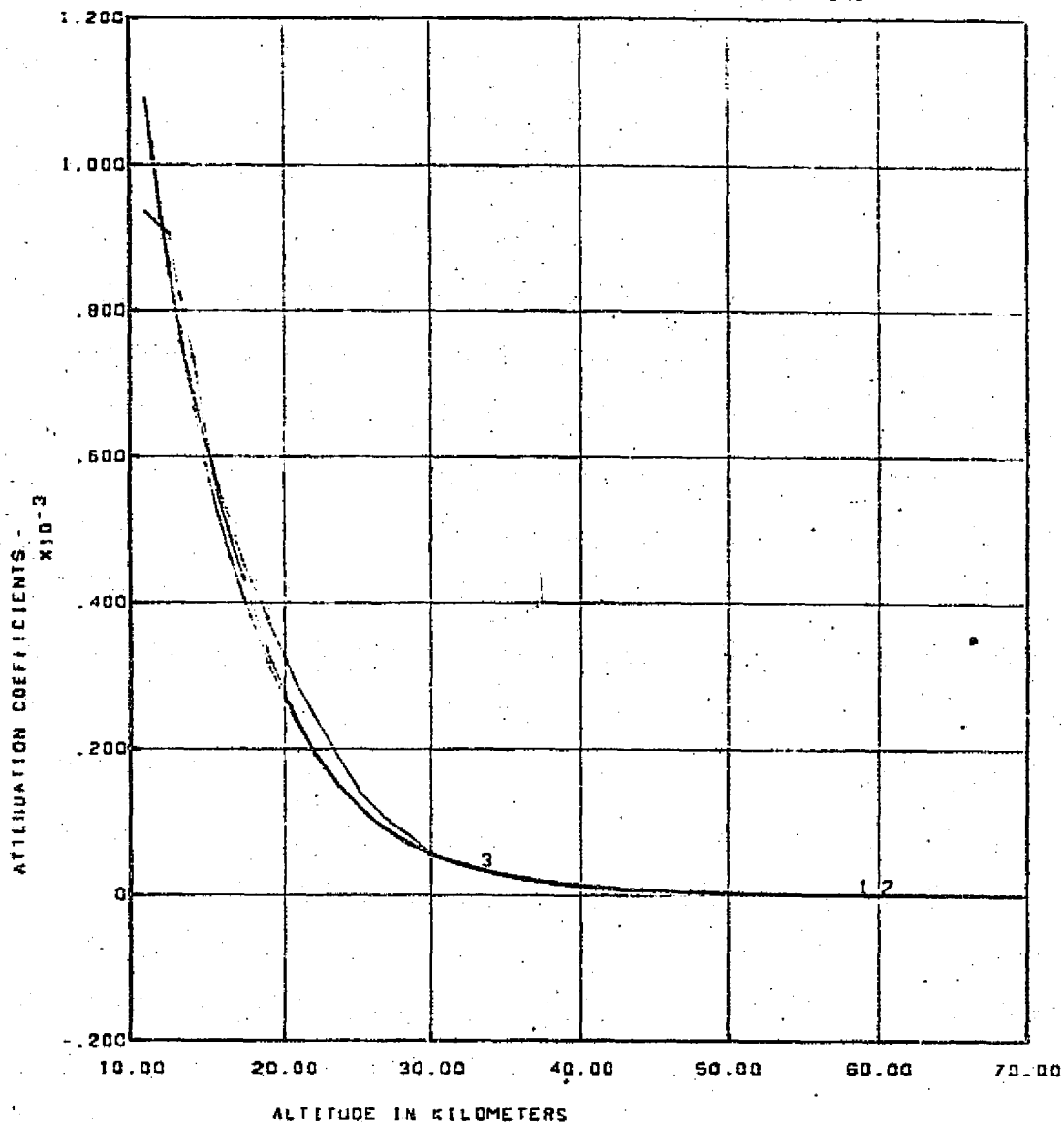
CURVE 1 IS RATIO OF 1964 AEROSOL BETAS OVER RAYLEIGH BETAS.
CURVE 2 IS RATIO OF DERIVED AEROSOL BETAS OVER RAYLEIGH BETAS.



CURVE 1 - BRIGHTNESS MODEL GENERATED FROM RAYLEIGH + 1964 AEROSOL BETAS.
CURVE 2 - MEASURED BRIGHTNESS SCALED BY 1964 MODEL.

11

S191 - PASS 47, SCAN 1, WAVELENGTH - .73 MICRONS

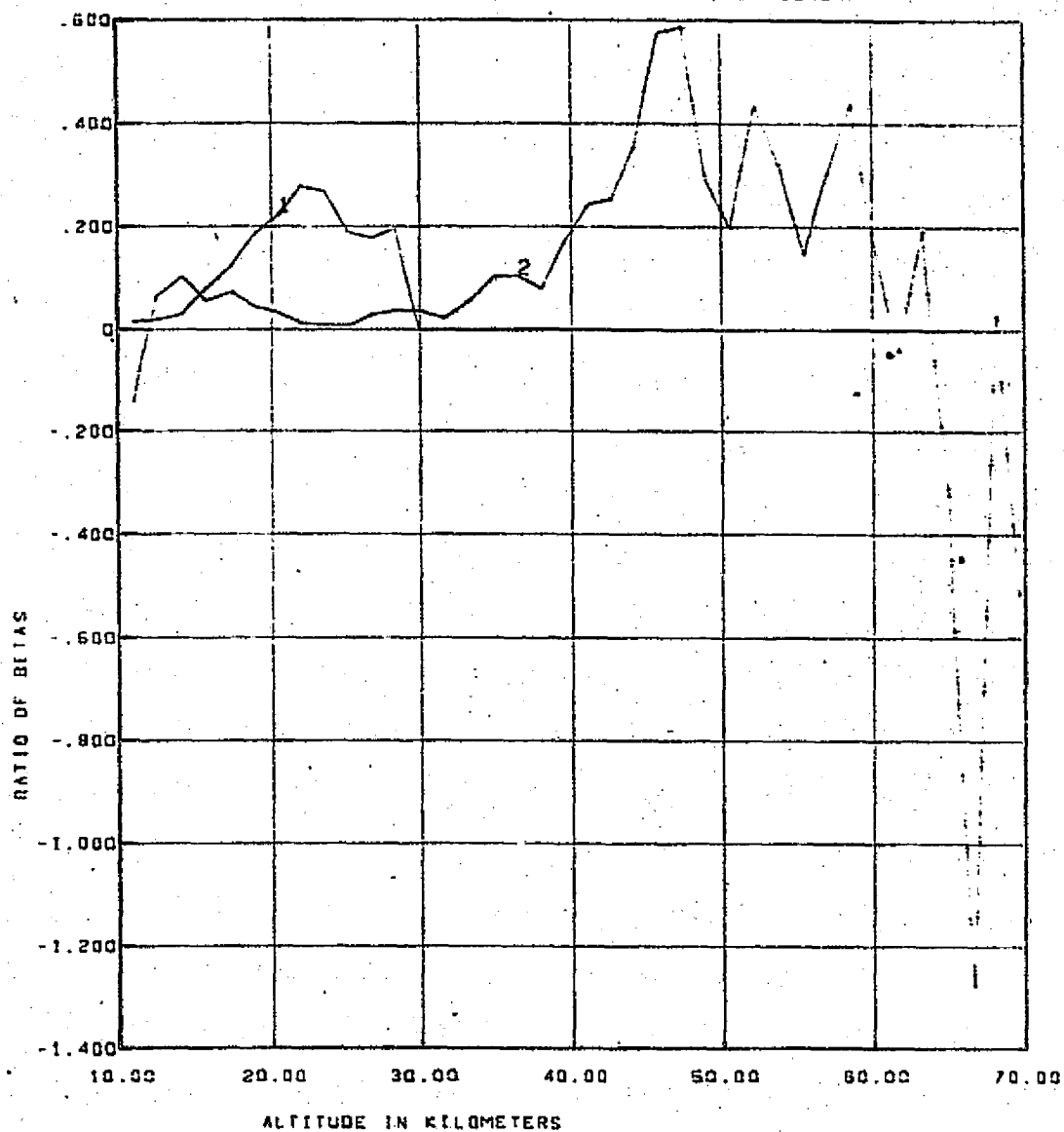


CURVE 1 - RAYLEIGH BETAS. CURVE 2 - RAYLEIGH + 1964 AEROSOL BETAS
 CURVE 3 IS BETAS DERIVED BY INVERSION OF SCALED MEASURED BRIGHTNESS

REPRODUCIBILITY OF THE
 ORIGINAL PAGE IS POOR

811

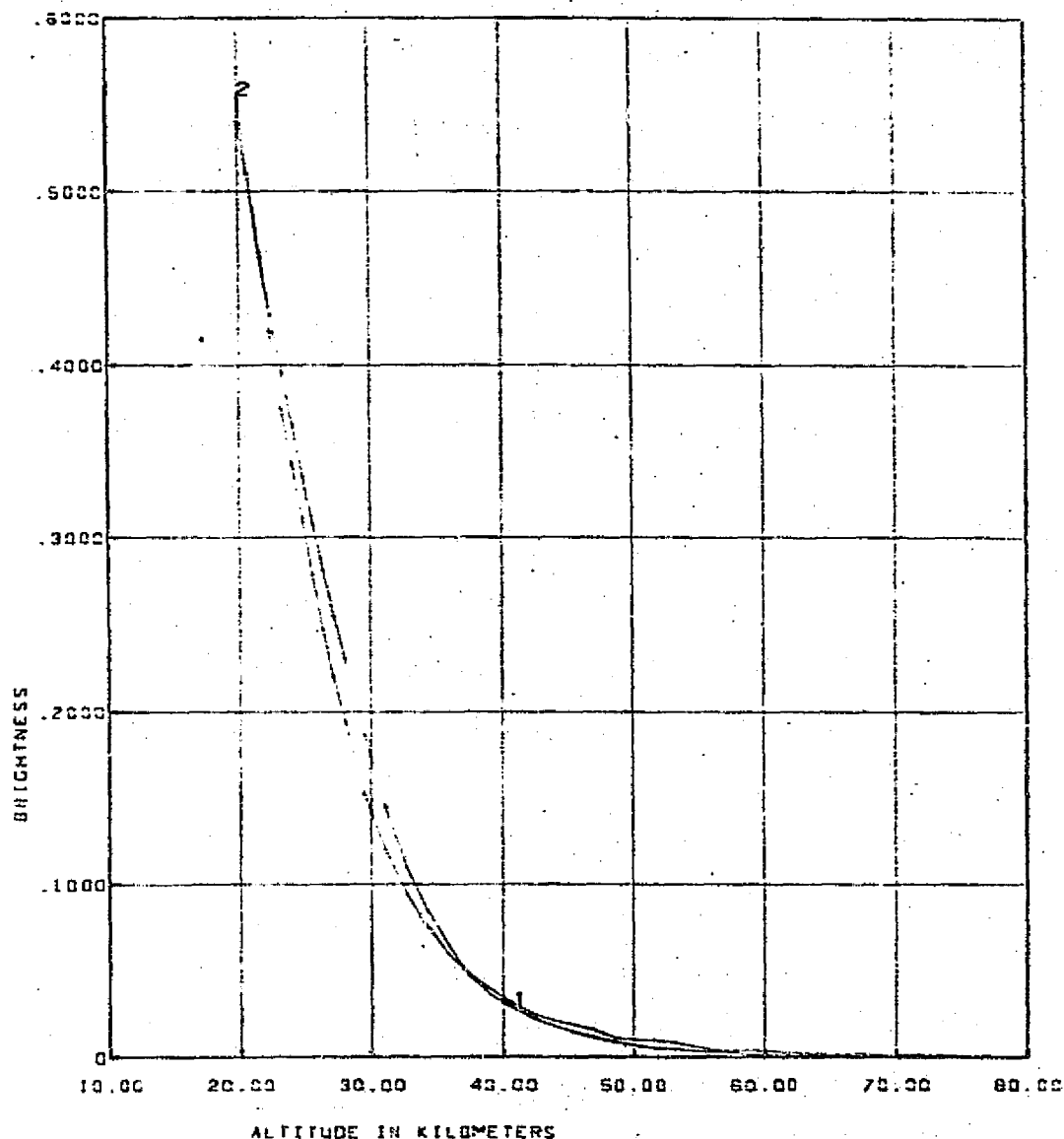
S191 - PASS 47, SCAN 1, WAVELENGTH - .73 MICRONS



CURVE 1 IS RATIO OF 1964 AEROSOL BETAS OVER RAYLEIGH BETAS.
CURVE 2 IS RATIO OF DERIVED AEROSOL BETAS OVER RAYLEIGH BETAS.

810

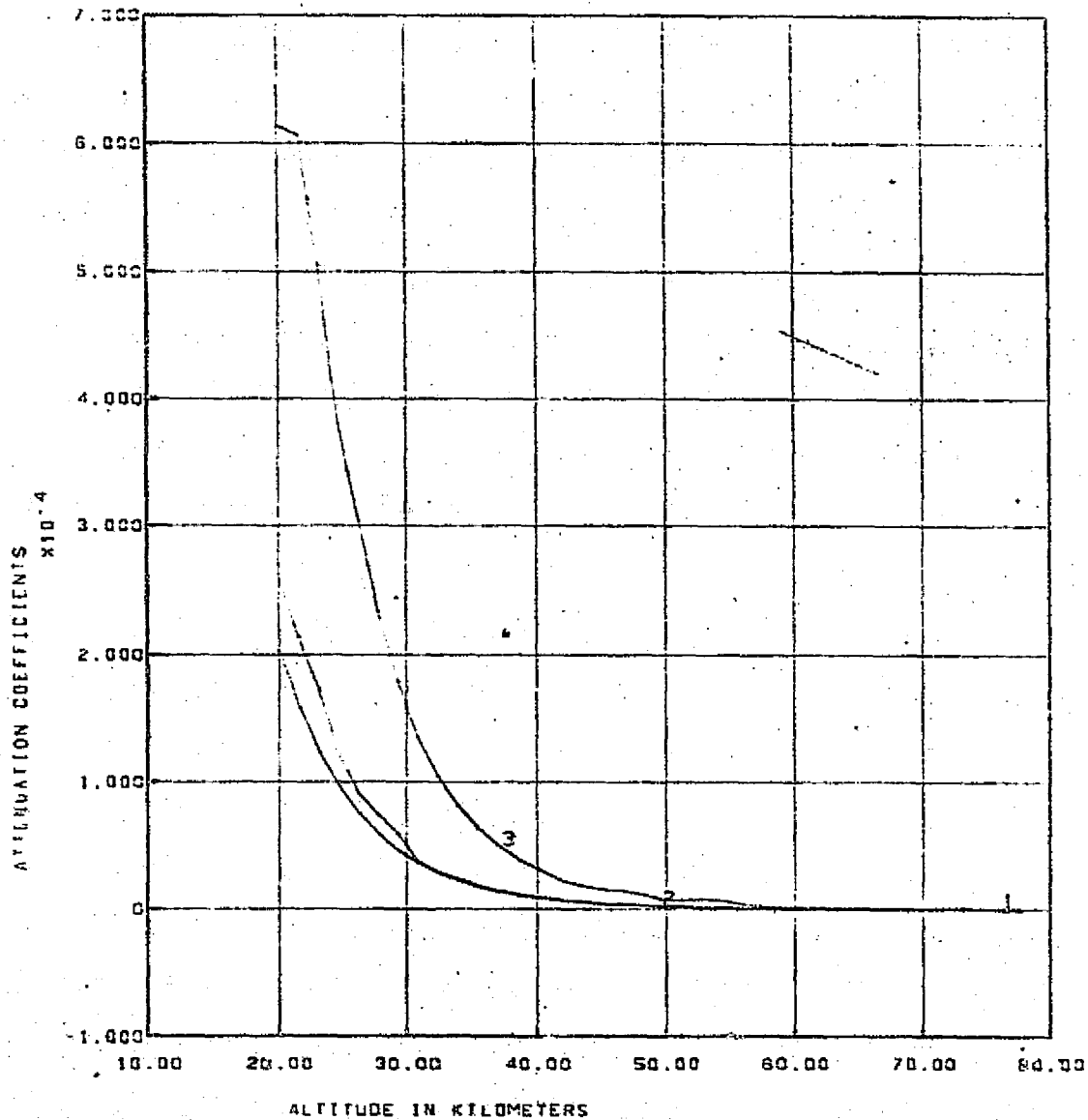
S191 - PASS 47, SCAN 1, WAVELENGTH - .78 MICRONS



CURVE 1 - BRIGHTNESS MODEL GENERATED FROM RAYLEIGH - 1964 AEROSOL BEFAS.
 CURVE 2 - MEASURED BRIGHTNESS SCALED BY 1964 MODEL.

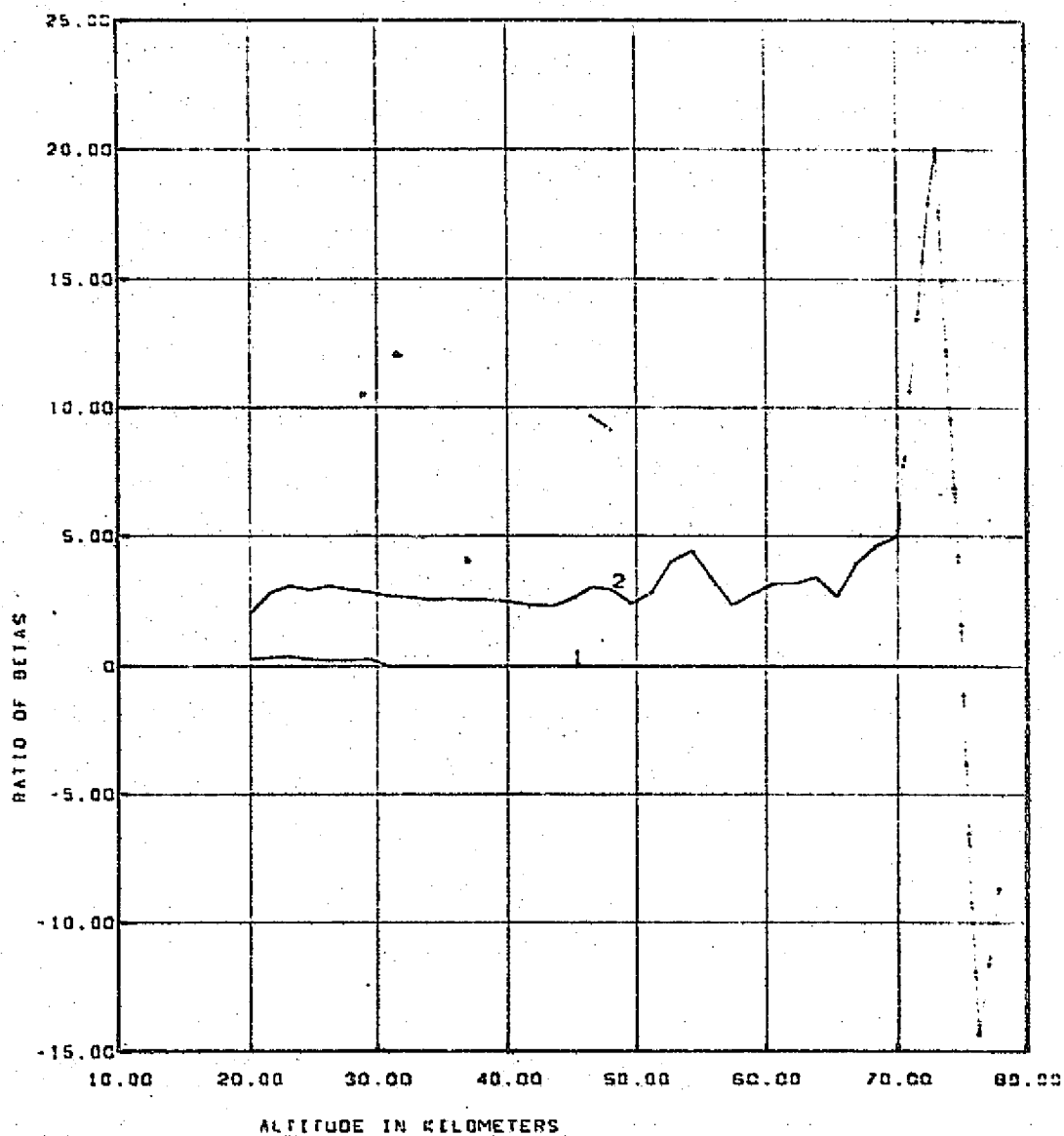
811

S191 - PASS 47 SCAN 1 WAVELENGTH - .70 MICRONS

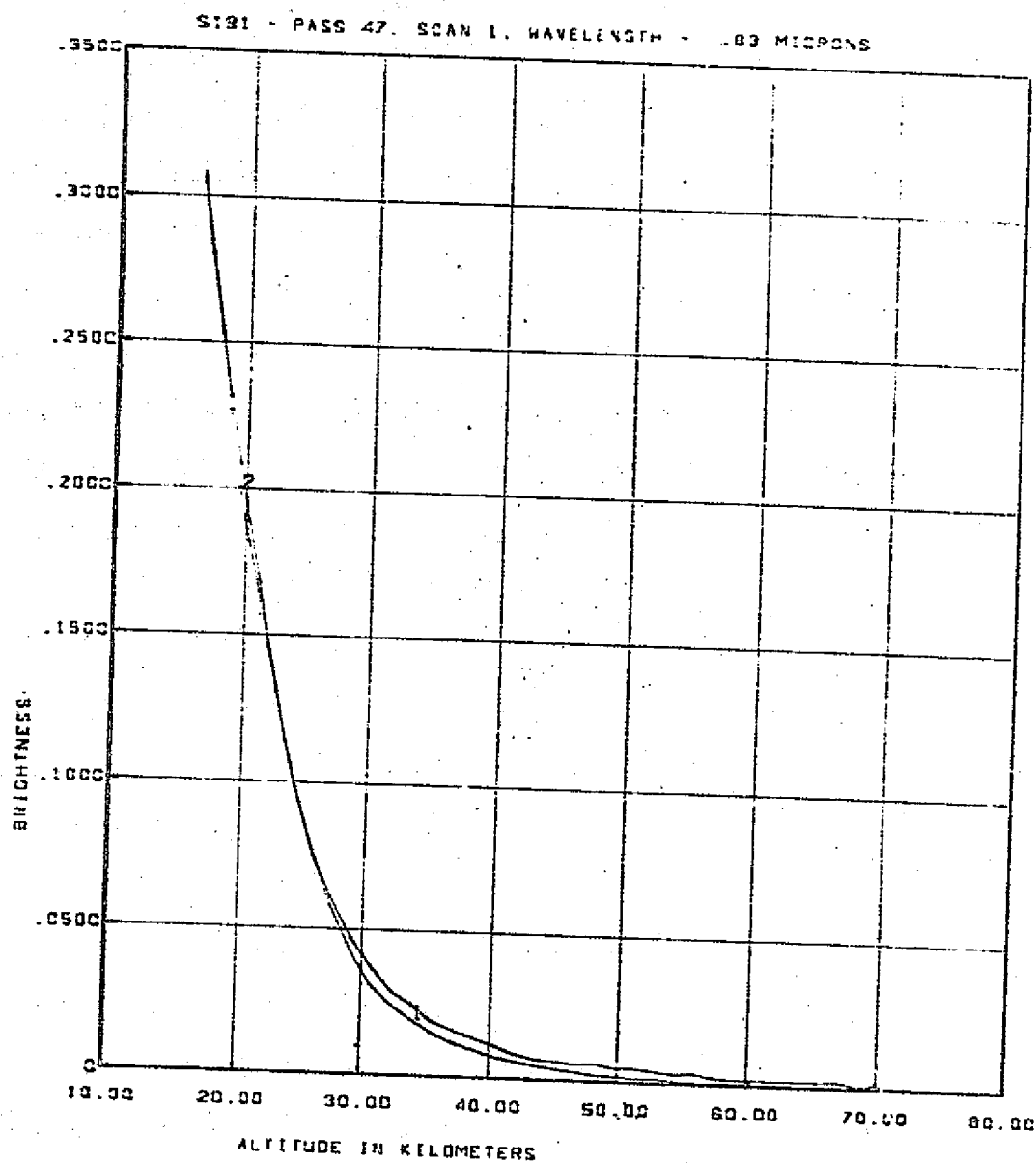


CURVE 1 - RAYLEIGH BETAS. CURVE 2 - RAYLEIGH + 1964 AEROSOL BETAS
CURVE 3 IS BETAS DERIVED BY INVERSION OF SCALED MEASURED BRIGHTNESS

S191 - PASS 47, SCAN 1, WAVELENGTH = .78 MICRONS



CURVE 1 IS RATIO OF 1964 AEROSOL BETAS OVER RAYLEIGH BETAS.
CURVE 2 IS RATIO OF DERIVED AEROSOL BETAS OVER RAYLEIGH BETAS.

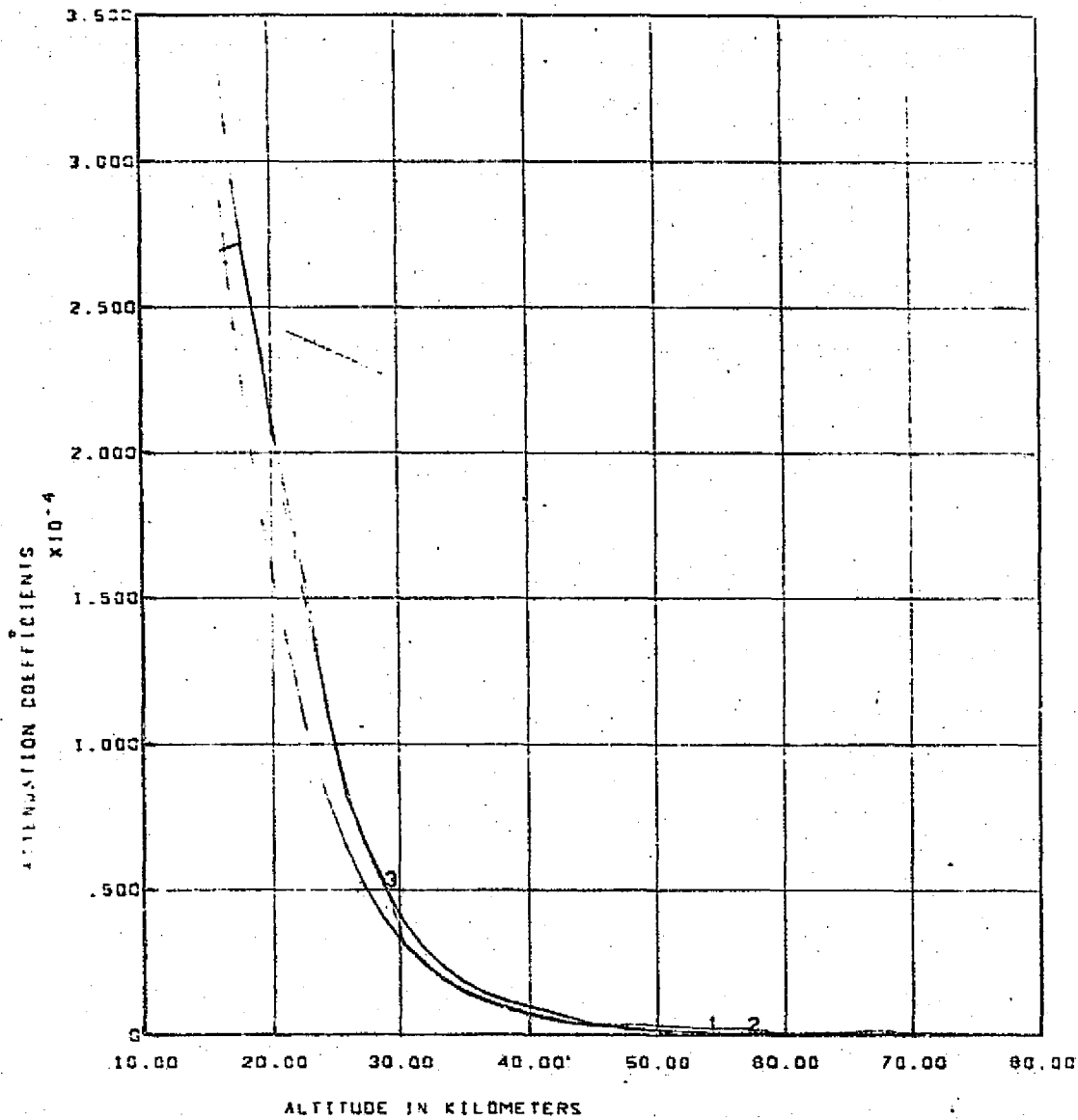


CURVE 1 - BRIGHTNESS MODEL GENERATED FROM RAYLEIGH + 1964 AEROSOL BETAS.
 CURVE 2 - MEASURED BRIGHTNESS SCALED BY 1964 MODEL.

REPRODUCIBILITY OF THE
 ORIGINAL PAGE IS POOR

811

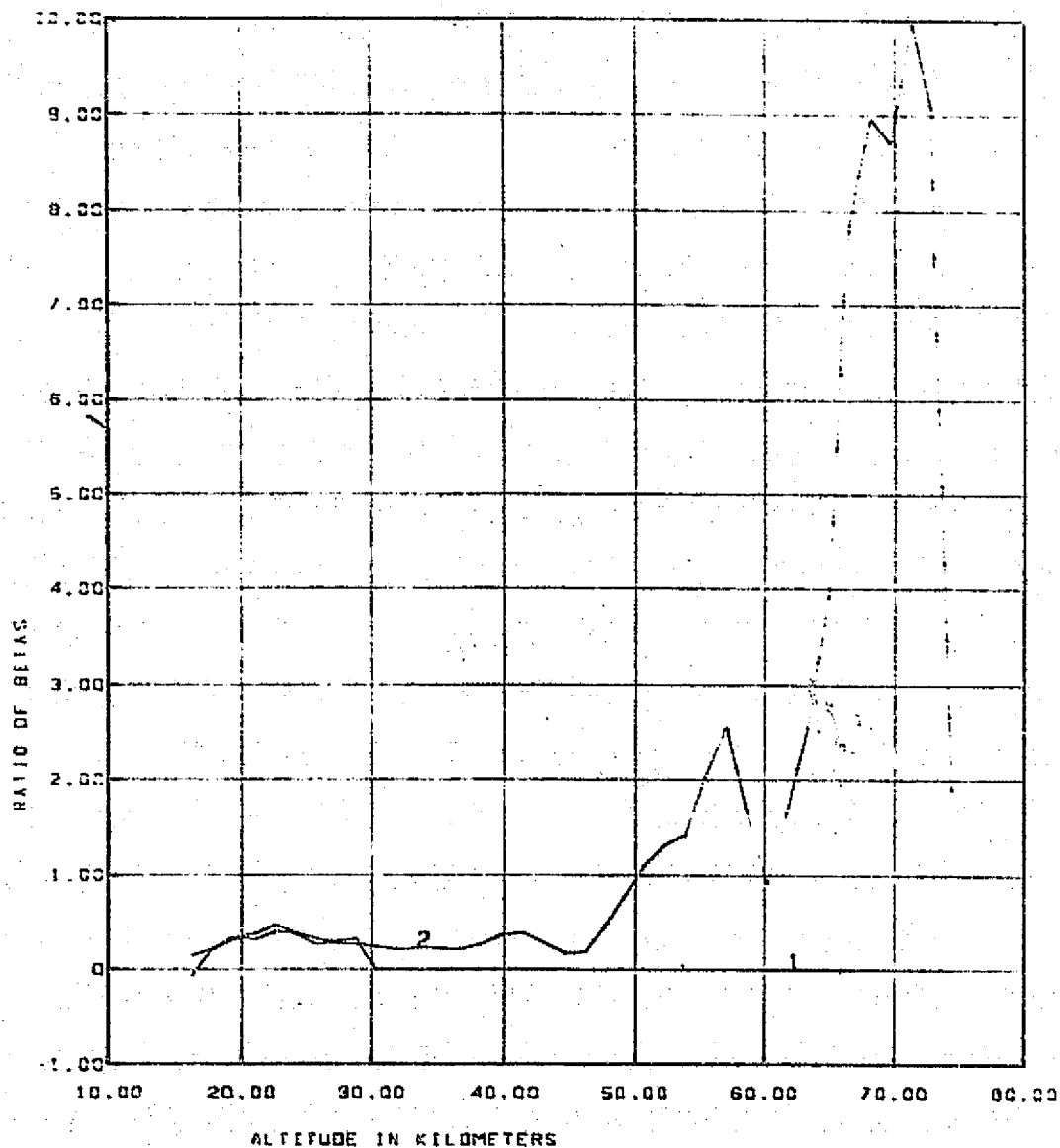
S191 - PASS 47, SCAN 1, WAVELENGTH - .83 MICRONS



CURVE 1 - RAYLEIGH BETAS. CURVE 2 - RAYLEIGH + 1984 AEROSOL BETAS
CURVE 3 IS BETAS DERIVED BY INVERSION OF SCALED MEASURED BRIGHTNESS

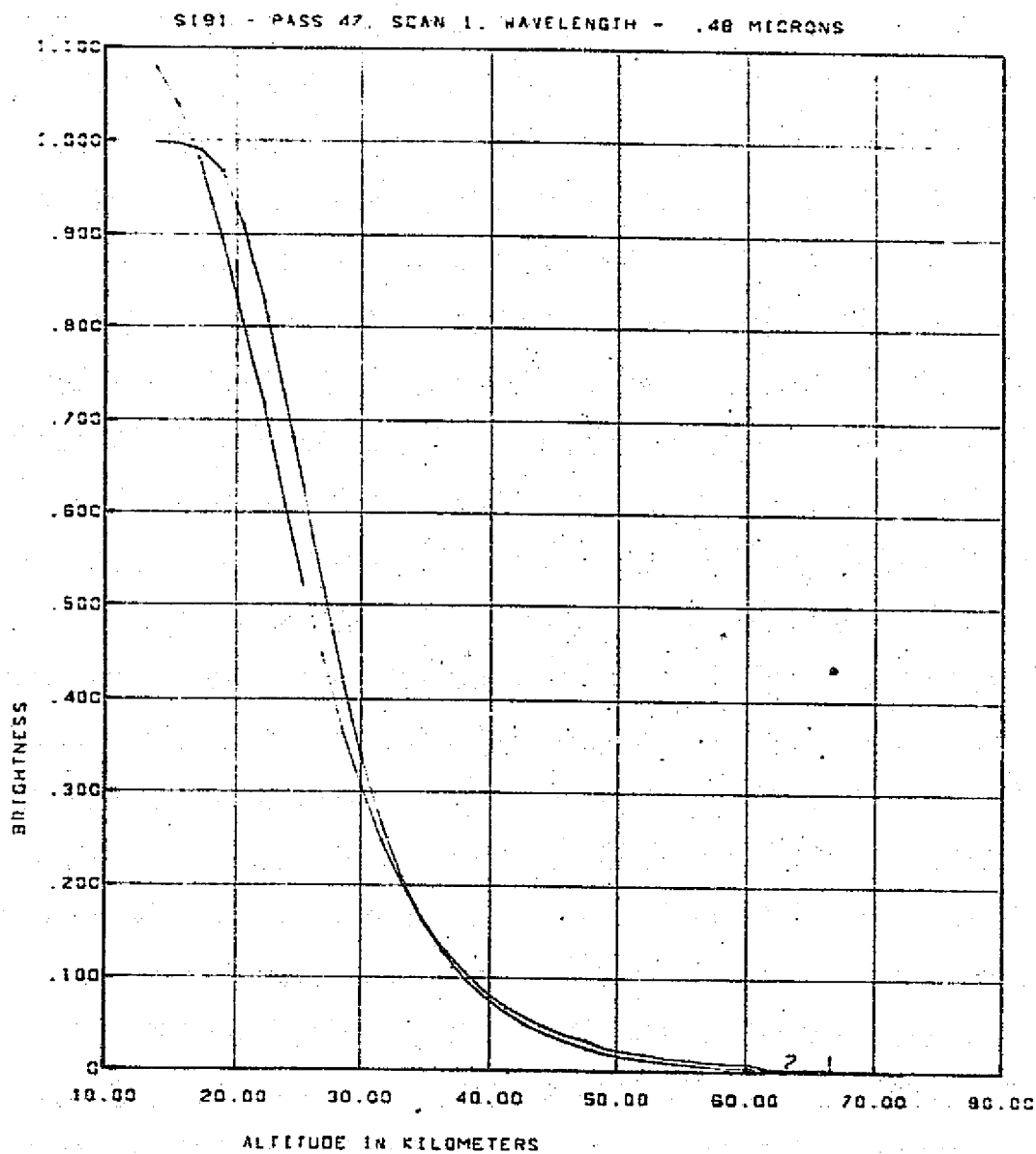
011

S191 PRSS 47. SCAN 1. WAVELENGTH .83 MICRONS



CURVE 1 IS RATIO OF 1964 AEROSOL BETAS OVER RAYLEIGH BETAS.
 CURVE 2 IS RATIO OF DERIVED AEROSOL BETAS OVER RAYLEIGH BETAS.

811

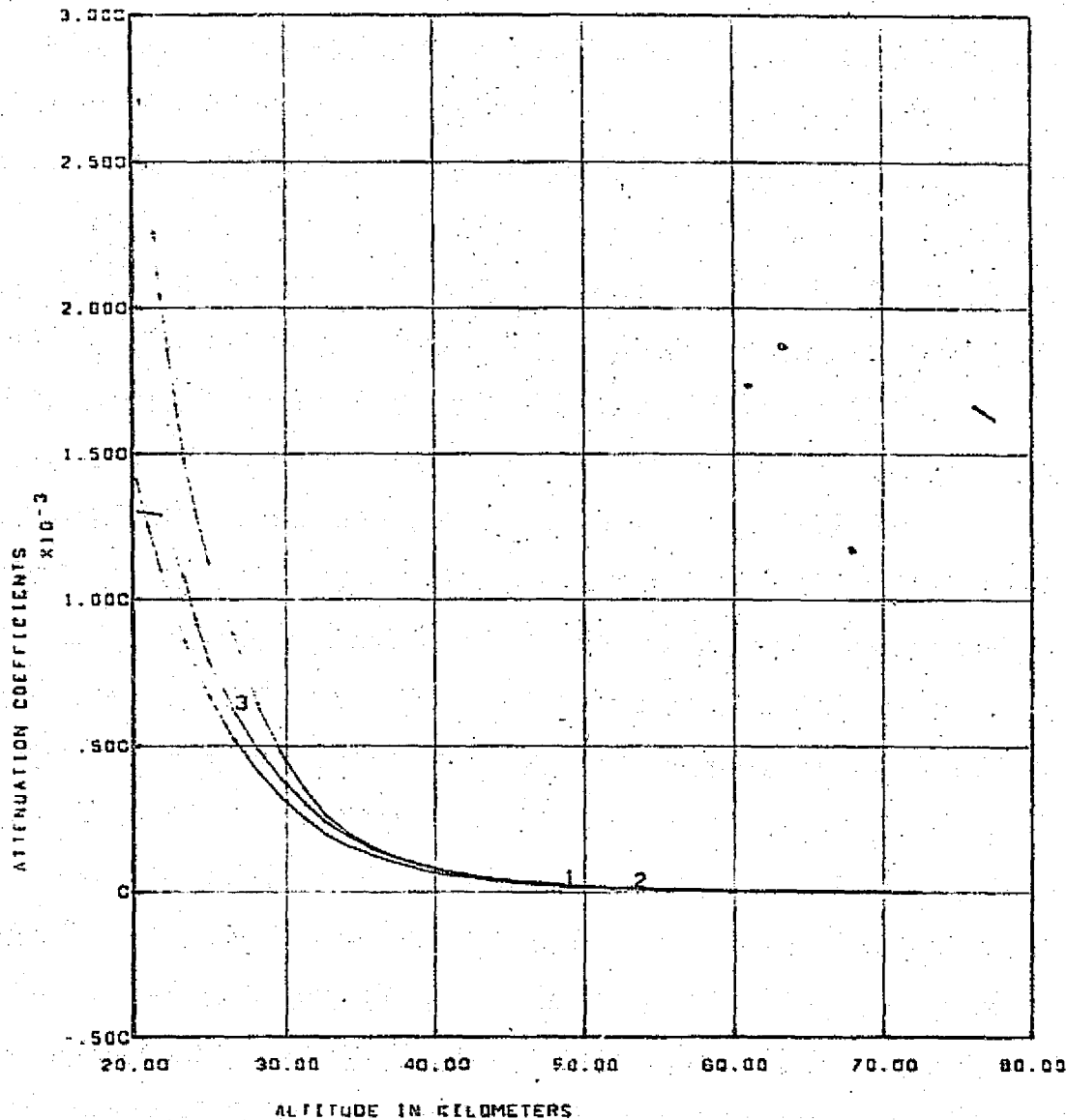


CURVE 1 - BRIGHTNESS MODEL GENERATED FROM RAYLEIGH + 1968 AEROSOL BETAS.
 CURVE 2 - MEASURED BRIGHTNESS SCALED BY 1968 MODEL.

REPRODUCIBILITY OF THE
 ORIGINAL PAGE IS POOR

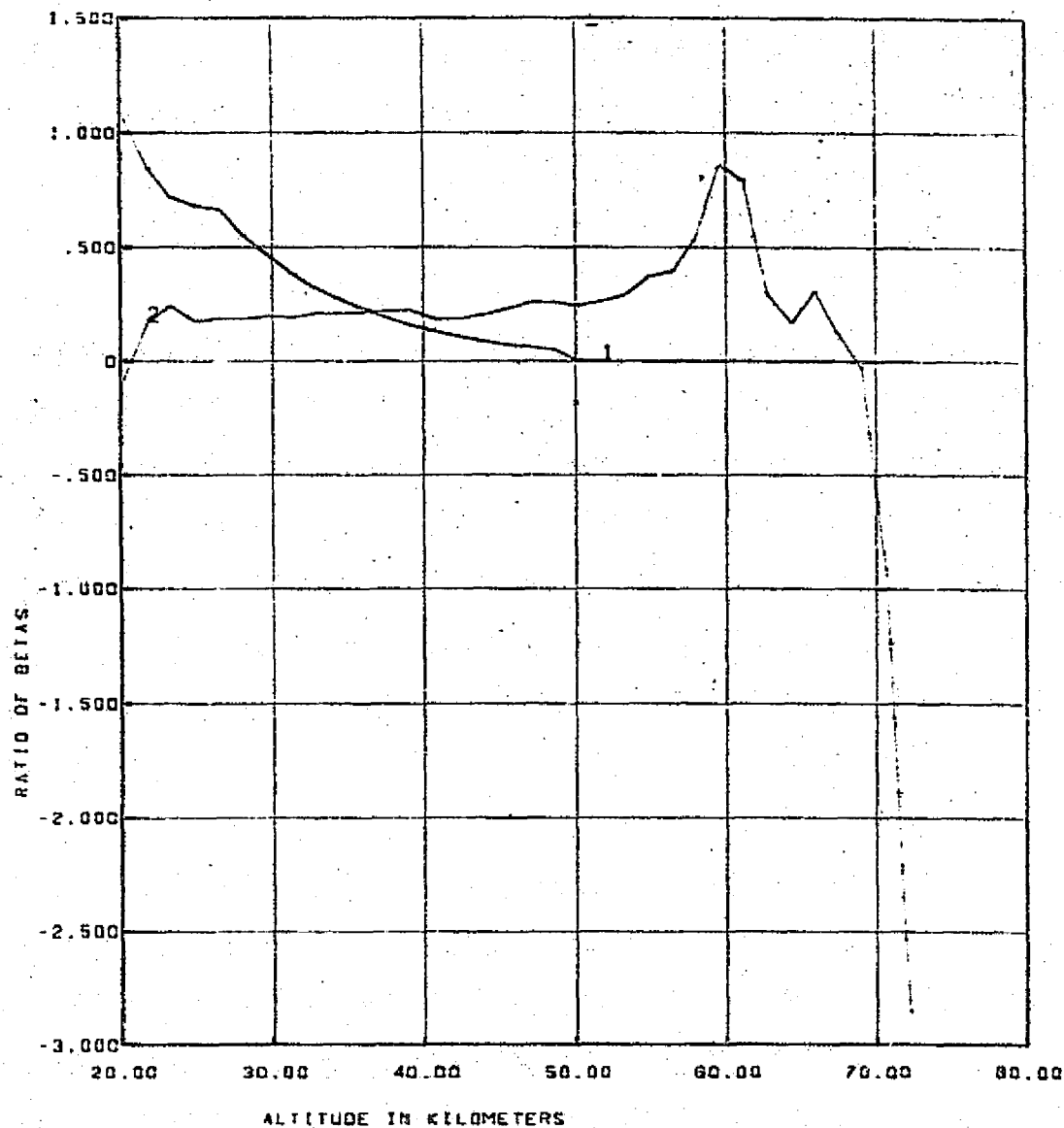
11

S191 - PASS 47, SCAN 1, WAVELENGTH - .40 MICRONS



CURVE 1 - RAYLEIGH BETAS. CURVE 2 - RAYLEIGH + 1968 AEROSOL BETAS
CURVE 3 IS BETAS DERIVED BY INVERSION OF SCALED MEASURED BRIGHTNESS

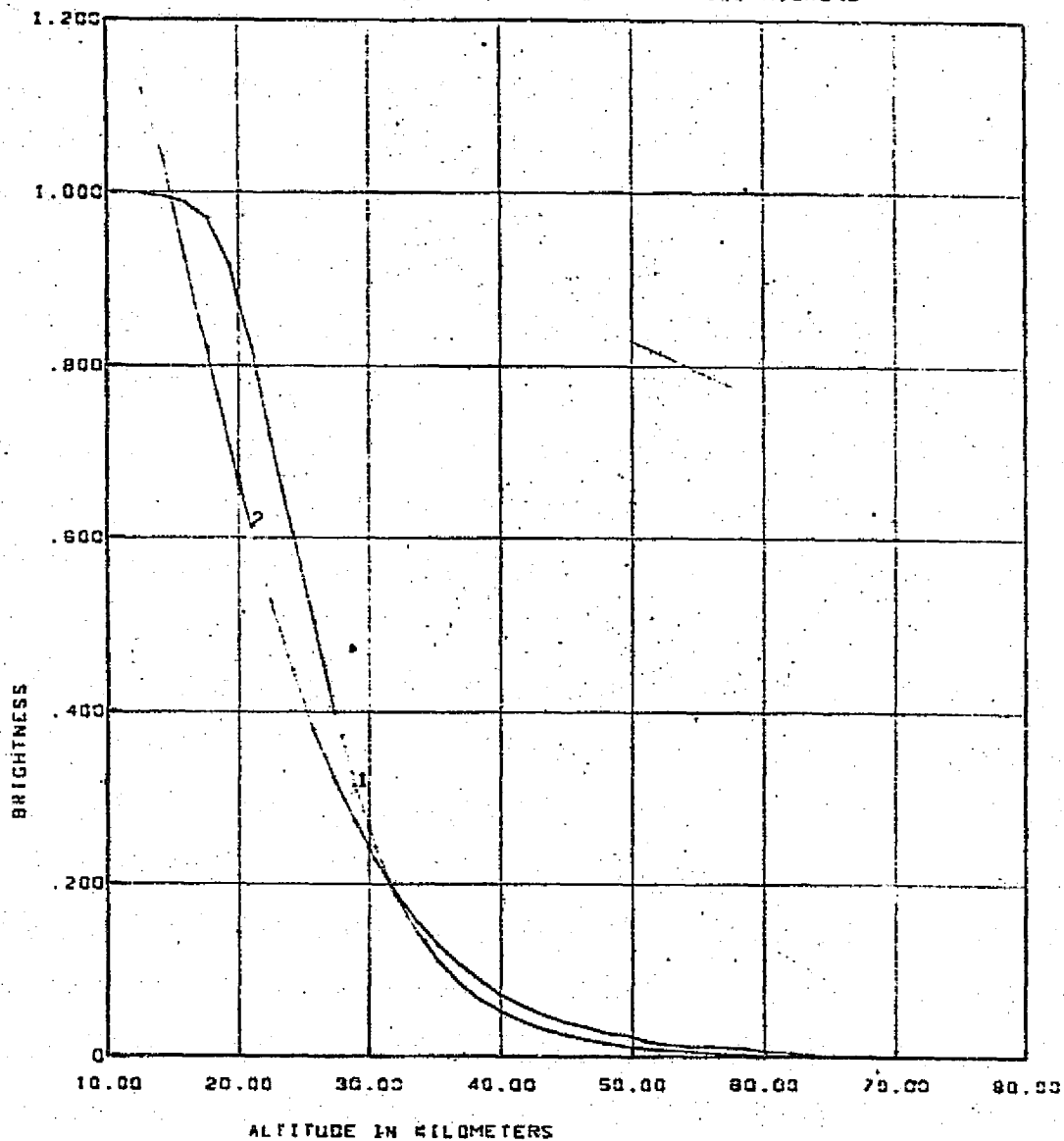
S191 - PASS 47. SCAN 1. WAVELENGTH - .48 MICRONS



CURVE 1 IS RATIO OF 1960 AEROSOL BETAS OVER RAYLEIGH BETAS.
 CURVE 2 IS RATIO OF DERIVED AEROSOL BETAS OVER RAYLEIGH BETAS.

111

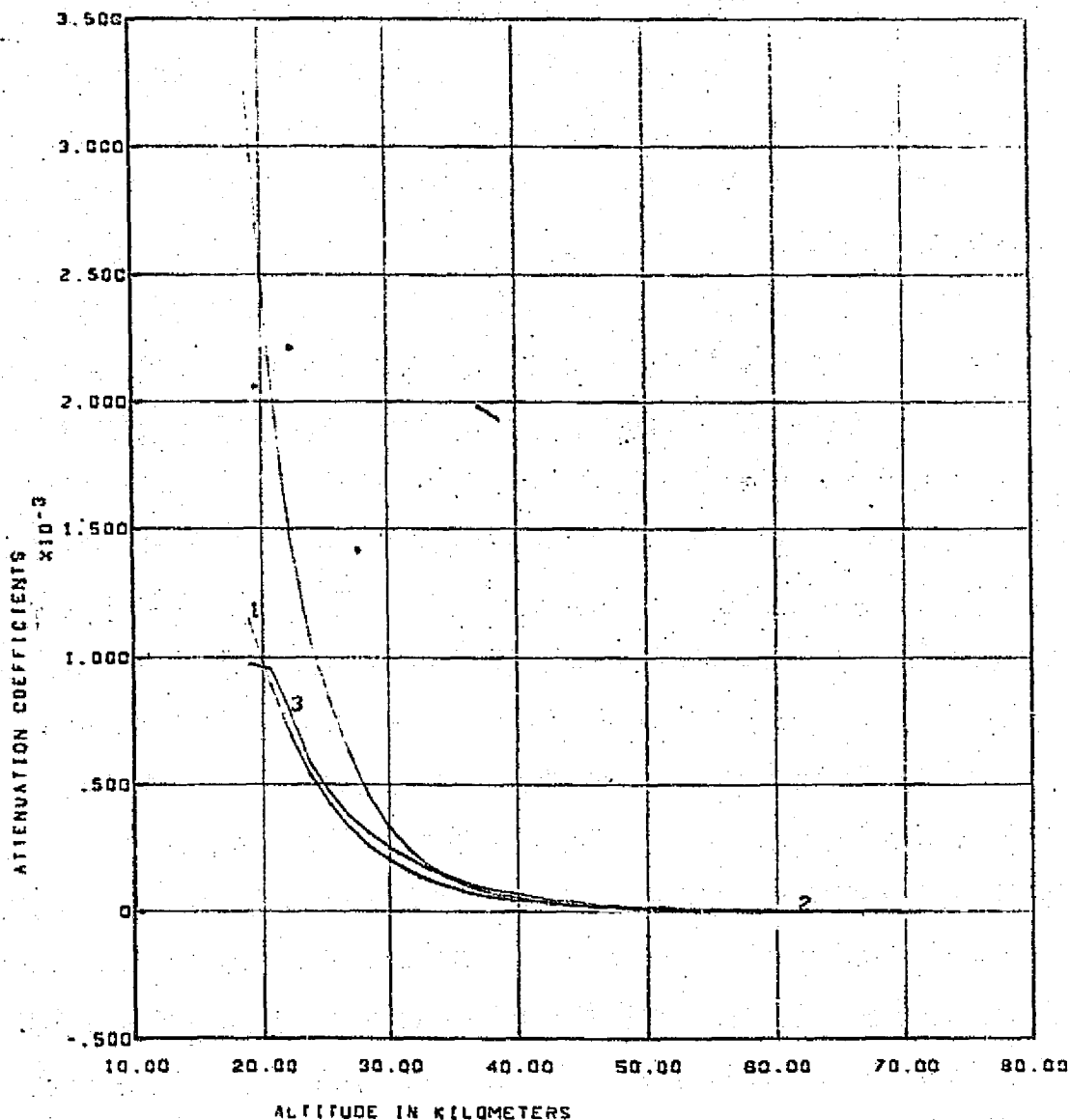
S191 - PASS 47. SCAN 1. WAVELENGTH - .53 MICRONS



CURVE 1 - BRIGHTNESS MODEL GENERATED FROM RAYLEIGH + 1968 AEROSOL BETAS.
 CURVE 2 - MEASURED BRIGHTNESS SCALED BY 1968 MODEL.

REPRODUCIBILITY OF THE
 ORIGINAL PAGE IS POOR

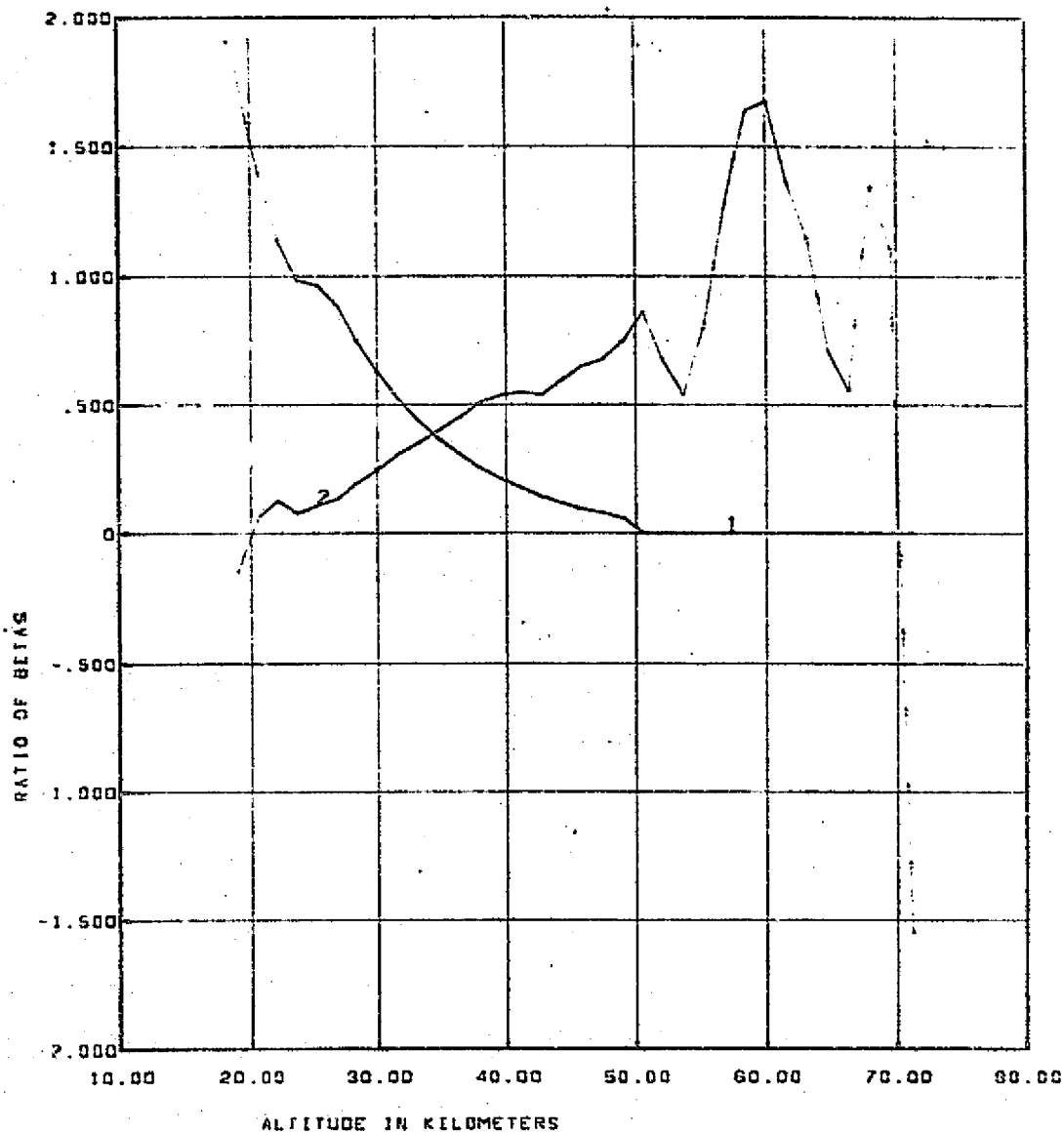
S191 - PASS 47. SCAN 1. WAVELENGTH - .53 MICRONS



CURVE 1 - RAYLEIGH BETAS. CURVE 2 - RAYLEIGH + 1968 AEROSOL BETAS
CURVE 3 IS BETAS DERIVED BY INVERSION OF SCALED MEASURED BRIGHTNESS

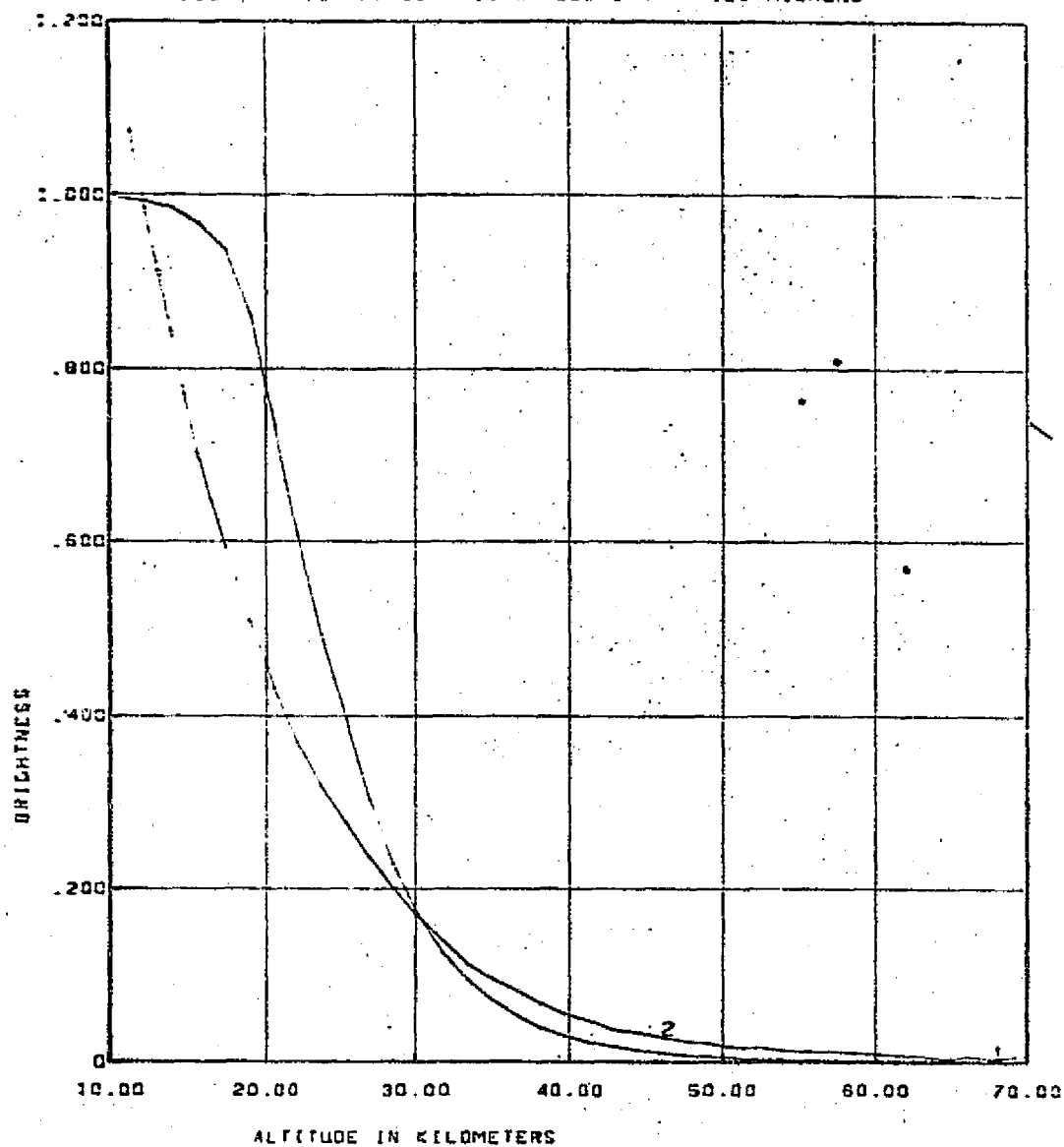
11

S191 - PASS 47. SCAN 1. WAVELENGTH - .53 MICRONS



CURVE 1 IS RATIO OF 1960 AEROSOL BETAS OVER RAYLEIGH BETAS.
 CURVE 2 IS RATIO OF DERIVED AEROSOL BETAS OVER RAYLEIGH BETAS.

S191 - PASS 47 SCAN 1. WAVELENGTH - .83 MICRONS

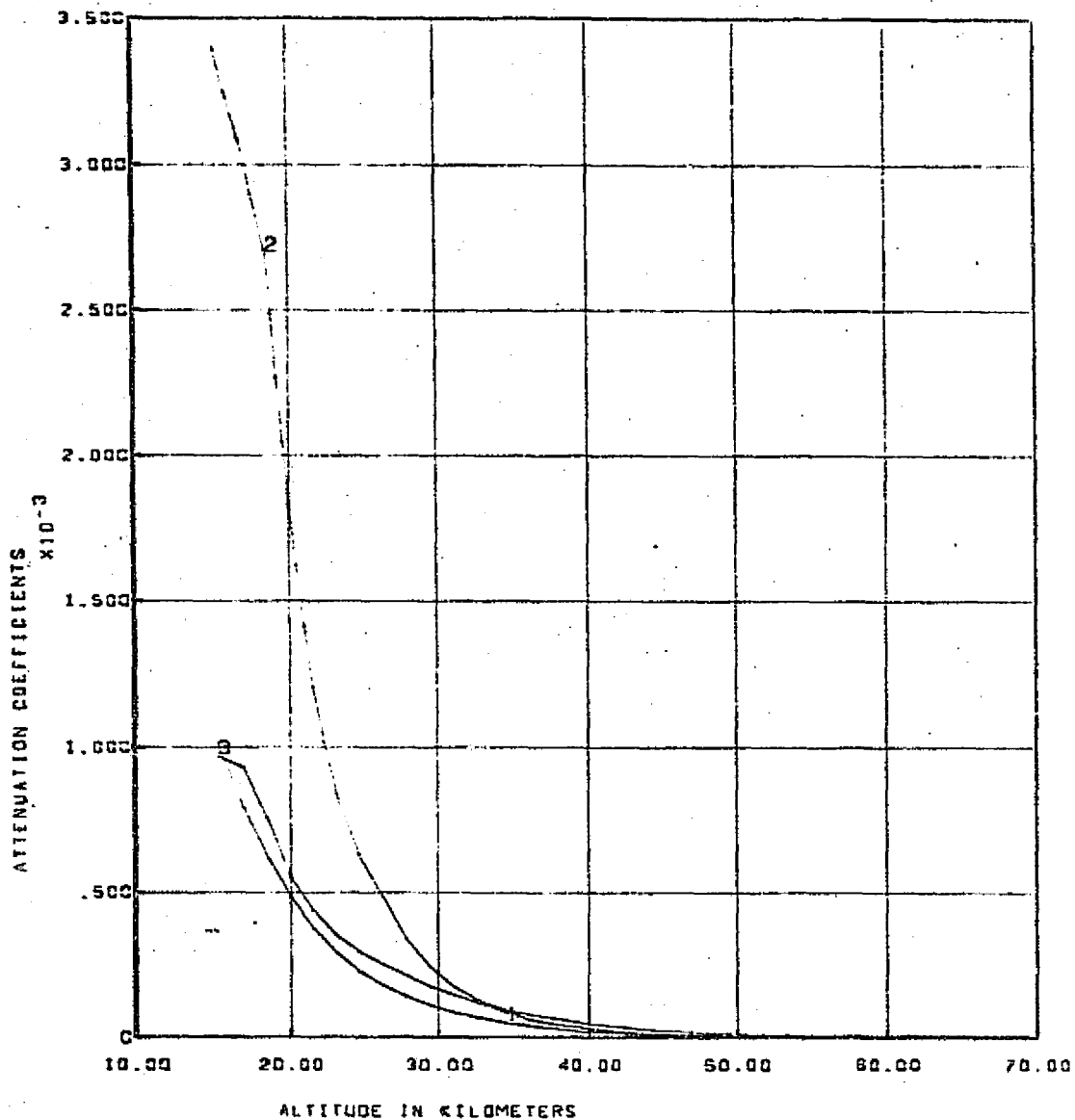


CURVE 1 - BRIGHTNESS MODEL GENERATED FROM RAYLEIGH + 1988 AEROSOL BETAS.
CURVE 2 - MEASURED BRIGHTNESS SCALED BY 1988 MODEL.

REPRODUCIBILITY OF THE
ORIGINAL PAGE IS POOR

011

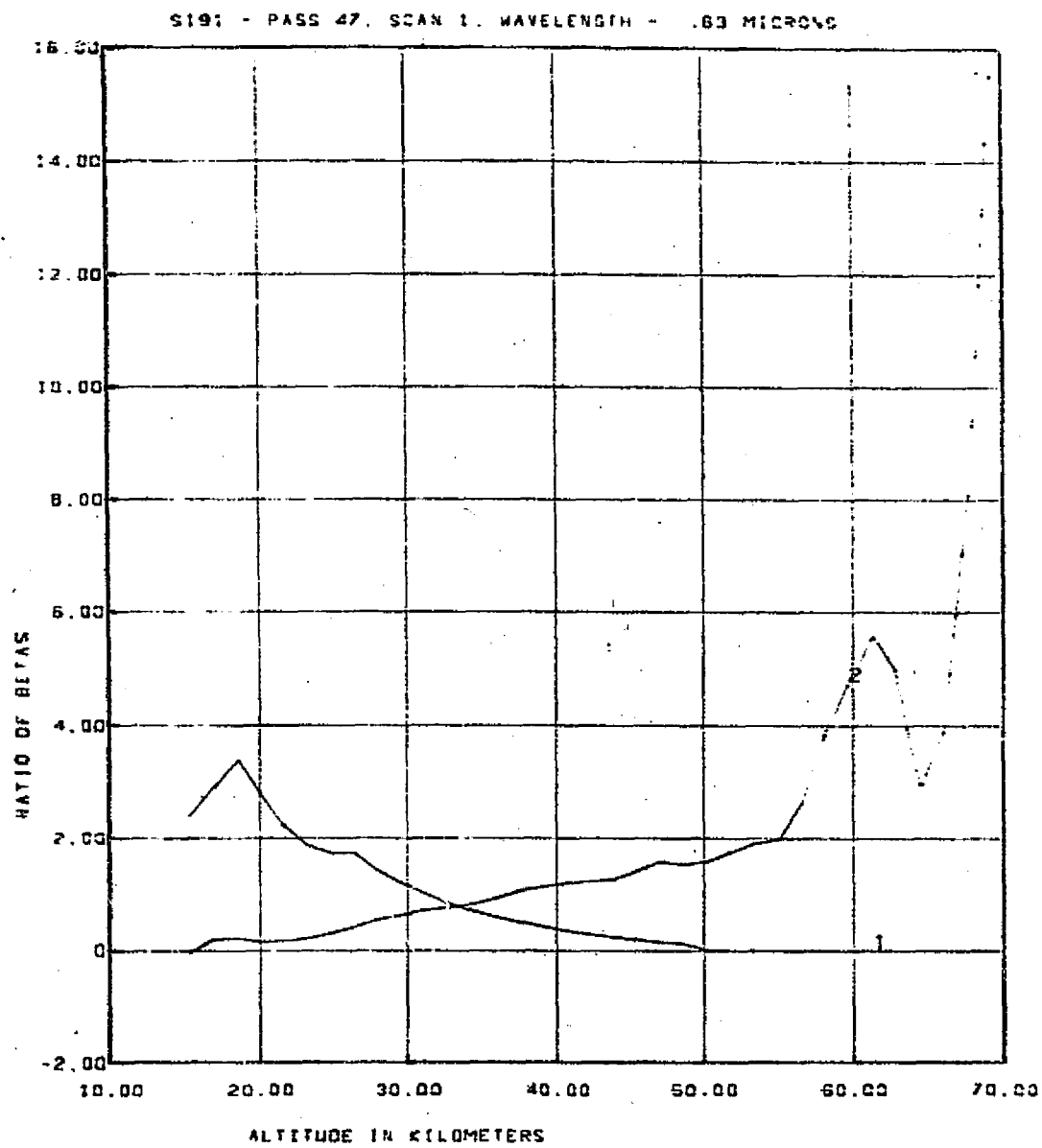
S19: PASS 47, SCAN 1, WAVELENGTH - .63 MICRONS



CURVE 1 - RAYLEIGH BETAS, CURVE 2 - RAYLEIGH + 1968 AEROSOL BETAS
 CURVE 3 IS BETAS DERIVED BY INVERSION OF SCALED MEASURED BRIGHTNESS

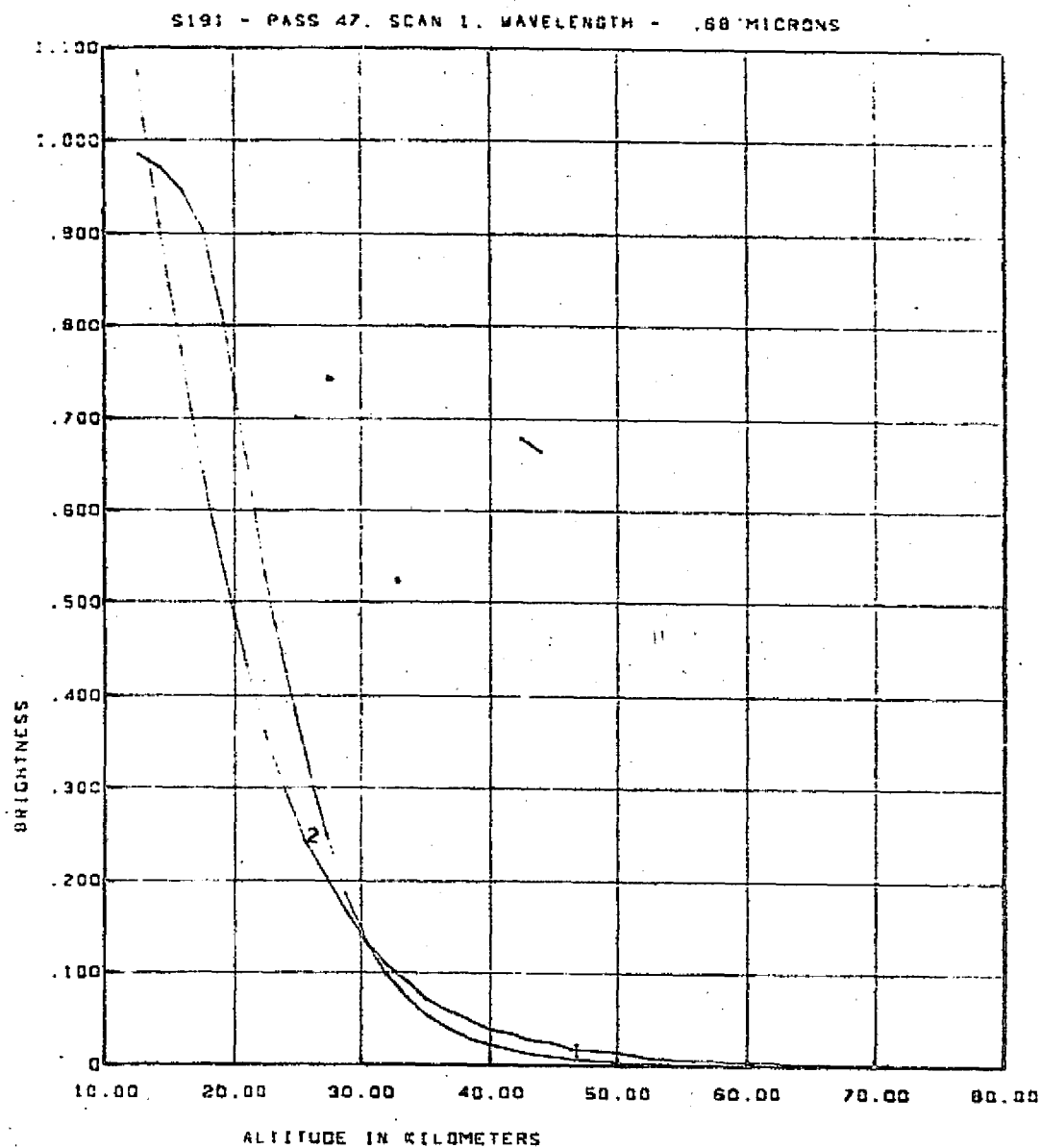
3

111



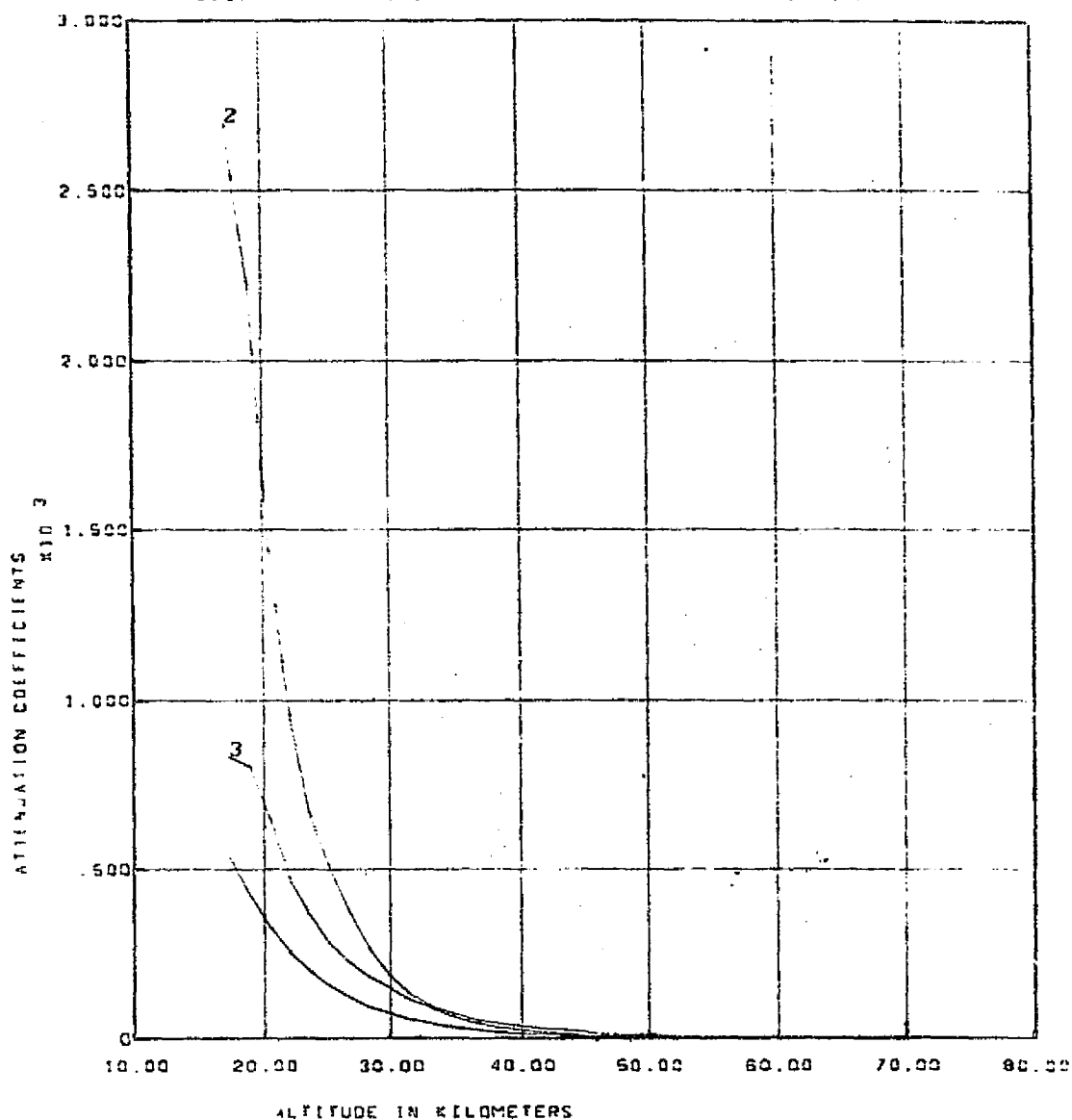
CURVE 1 IS RATIO OF 1968 AEROSOL BETAS OVER RAYLEIGH BETAS.
CURVE 2 IS RATIO OF DERIVED AEROSOL BETAS OVER RAYLEIGH BETAS.

REPRODUCIBILITY OF THE
ORIGINAL PAGE IS POOR



CURVE 1 - BRIGHTNESS MODEL GENERATED FROM RAYLEIGH + 1968 AEROSOL BEFAS.
CURVE 2 - MEASURED BRIGHTNESS SCALED BY 1968 MODEL.

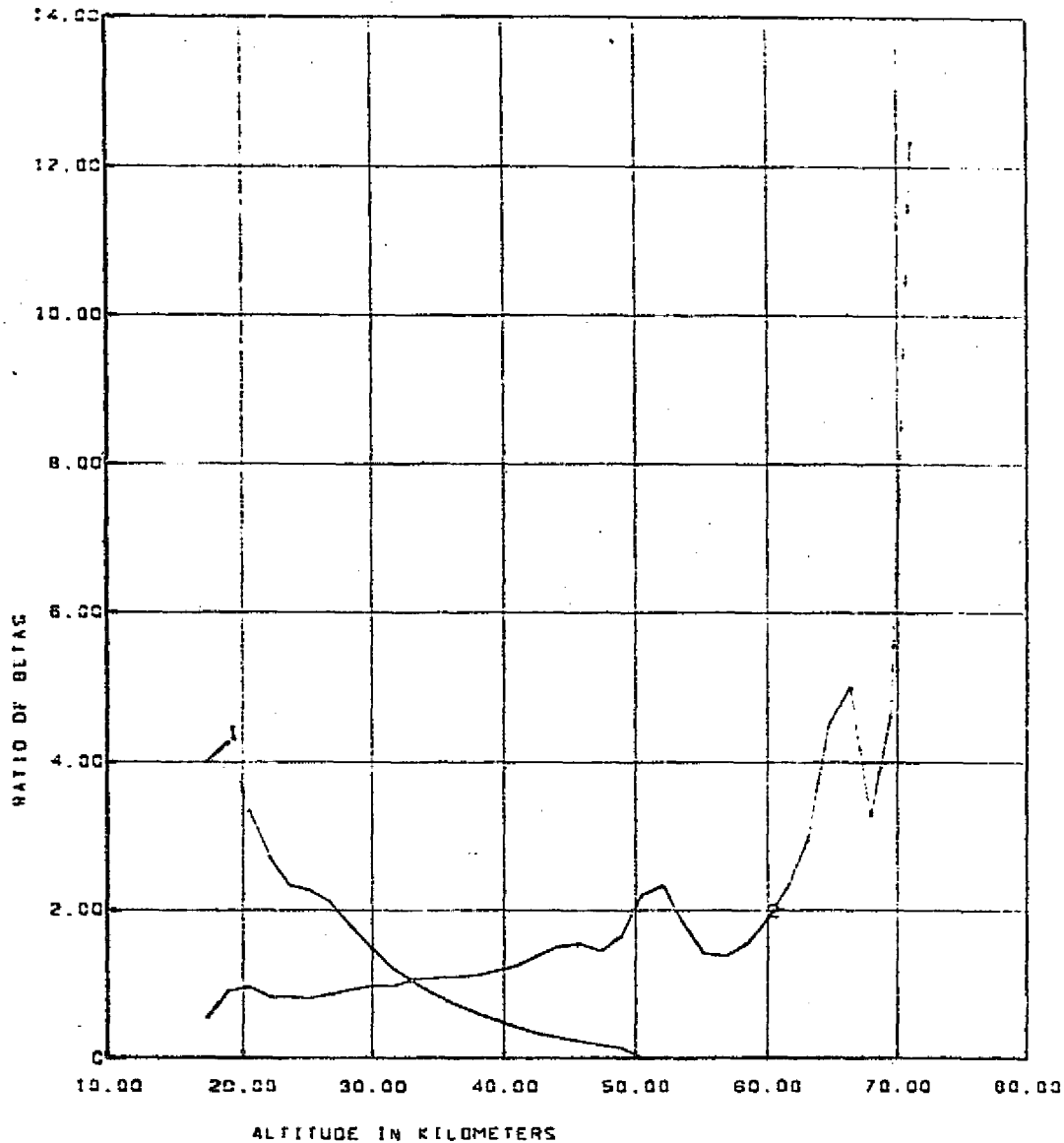
S191 - PASS 47. SCAN 1. WAVELENGTH - .68 MICRONS



CURVE 1 - RAYLEIGH BETAS. CURVE 2 - RAYLEIGH + 1968 AEROSOL BETAS
 CURVE 3 IS BETAS DERIVED BY INVERSION OF SCALED MEASURED BRIGHTNESS

11

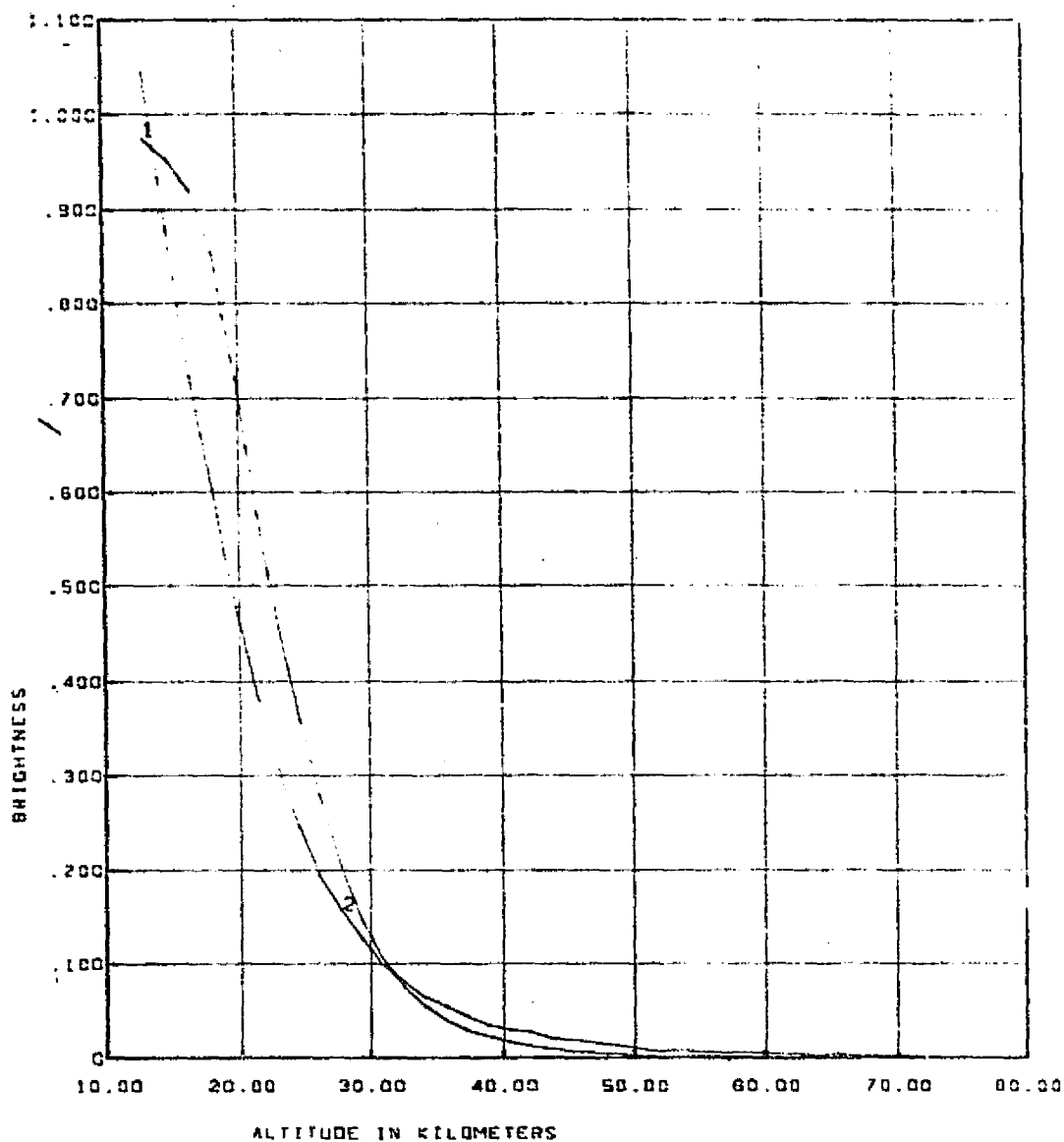
S19: - PASS 47, SCAN 1, WAVELENGTH - .68 MICRONS



CURVE 1 IS RATIO OF 1968 AEROSOL BETAS OVER RAYLEIGH BETAS.
CURVE 2 IS RATIO OF DERIVED AEROSOL BETAS OVER RAYLEIGH BETAS.

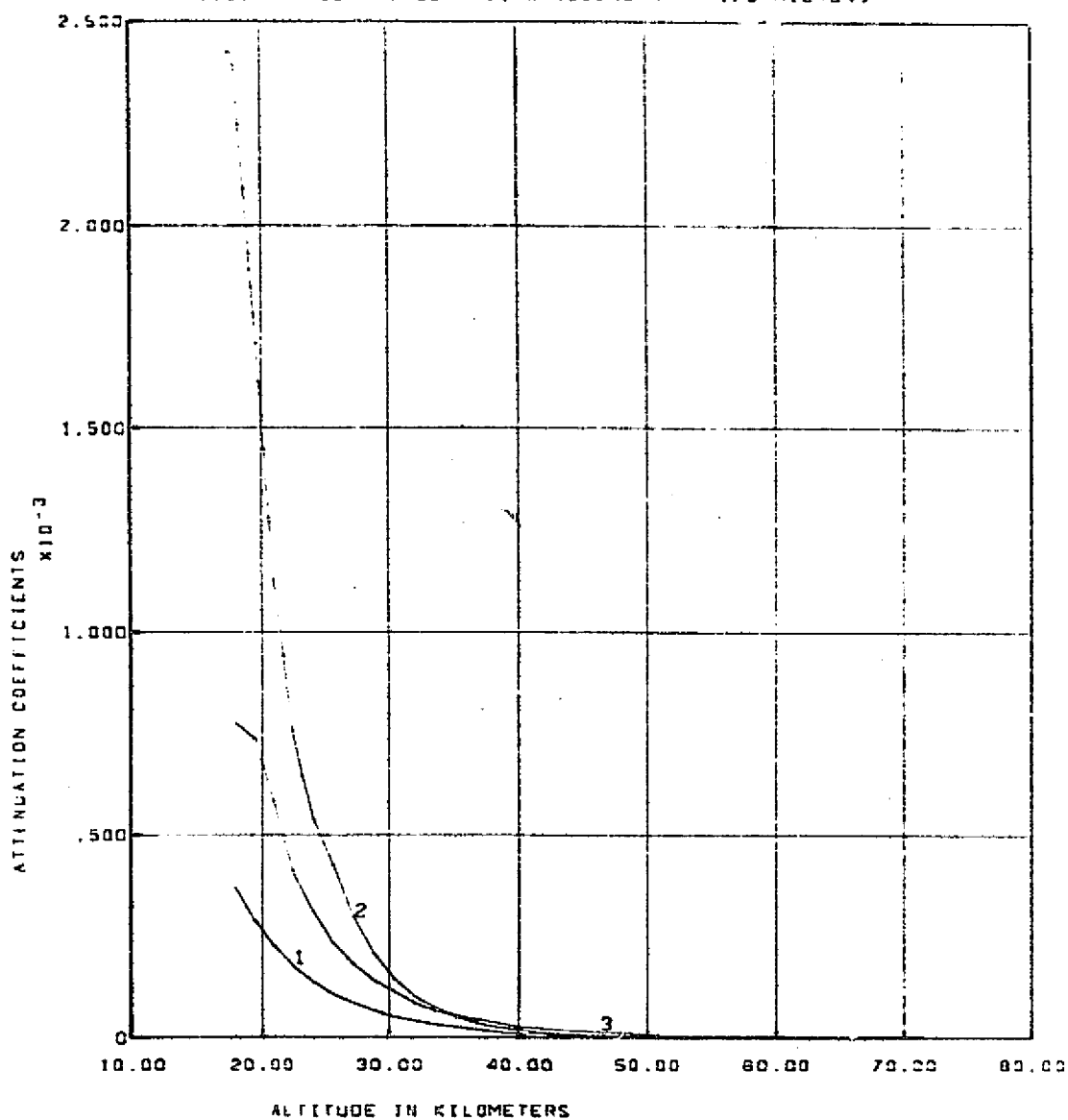
811

S191 - PASS 47 SCAN 1 WAVELENGTH .73 MICRONS



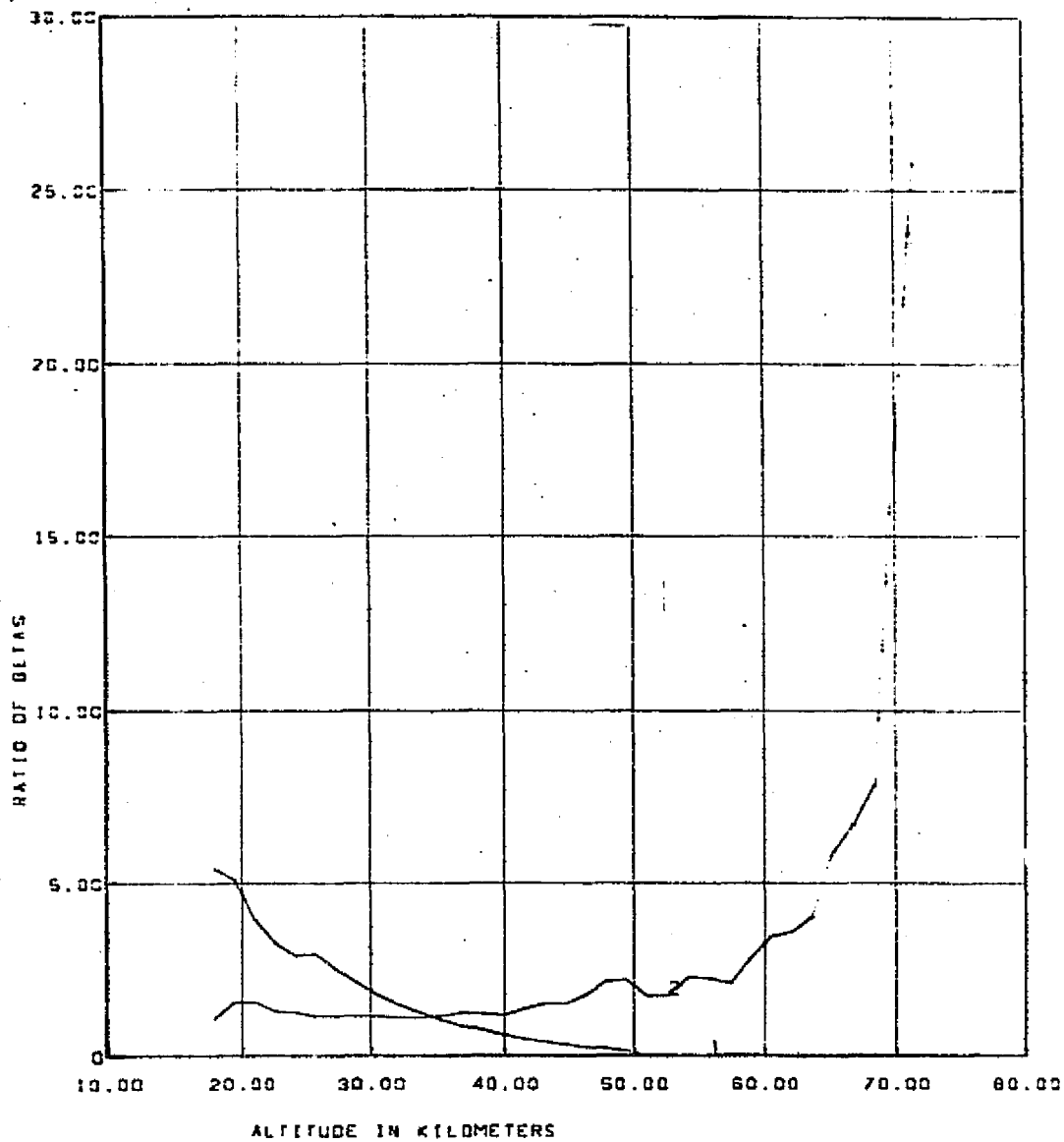
CURVE 1 - BRIGHTNESS MODEL GENERATED FROM RAYLEIGH + 1968 AEROSOL BIAS.
 CURVE 2 - MEASURED BRIGHTNESS SCALED BY 1968 MODEL.

S191 - PASS 47, SCAN 1, WAVELENGTH - .73 MICRONS



CURVE 1 - RAYLEIGH BETAS. CURVE 2 - RAYLEIGH + 1968 AEROSOL BETAS
CURVE 3 IS BETAS DERIVED BY INVERSION OF SCALED MEASURED BRIGHTNESS

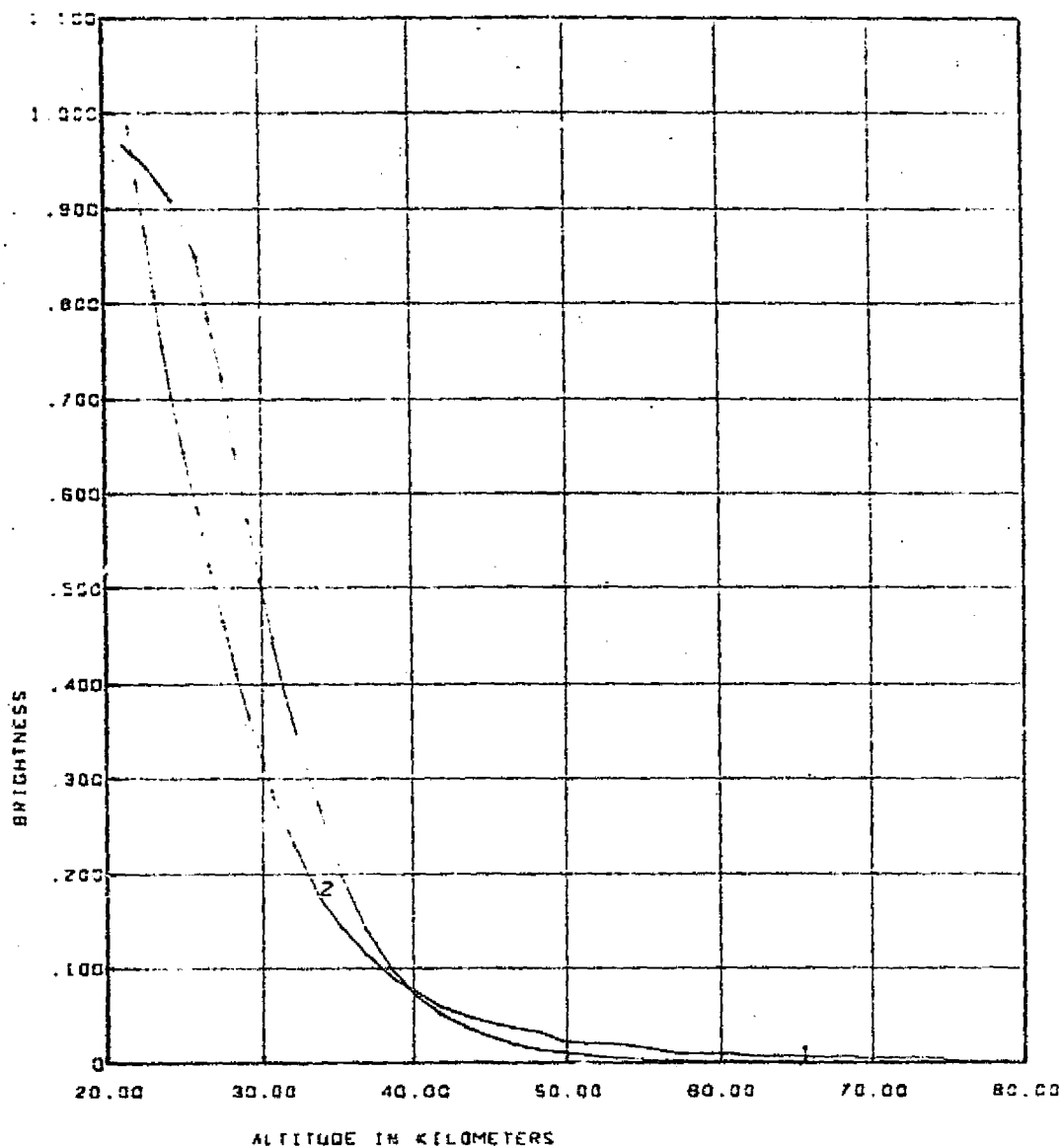
S191 - PASS 47, SCAN 1, WAVELENGTH = 0.73 MICRONS



CURVE 1 IS RATIO OF 1988 AEROSOL BETAS OVER RAYLEIGH BETAS.
CURVE 2 IS RATIO OF DERIVED AEROSOL BETAS OVER RAYLEIGH BETAS.

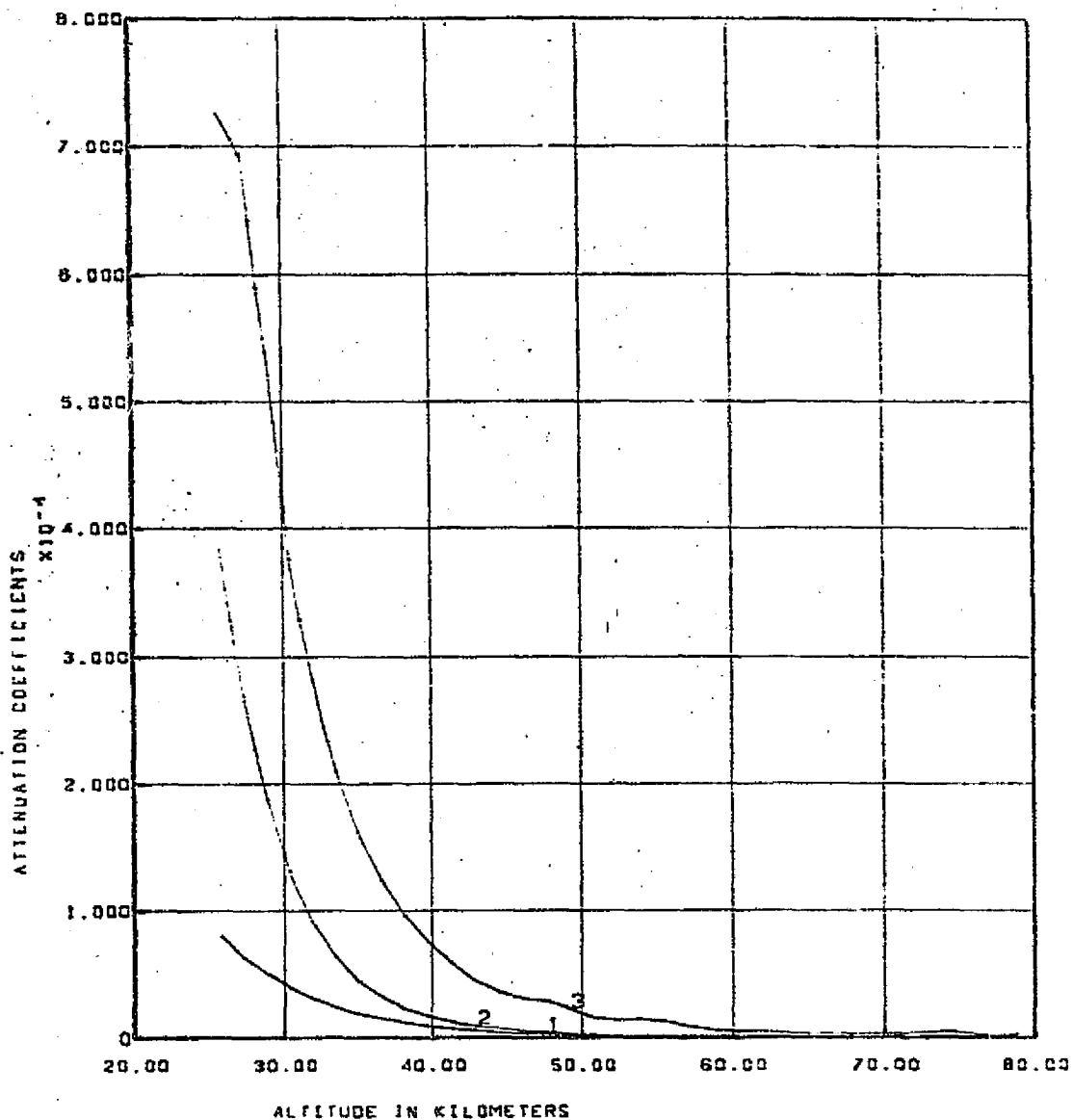
811

S19: PASS 47. SCAN 1. WAVELENGTH - .78 MICRONS



CURVE 1: BRIGHTNESS MODEL GENERATED FROM RAYLEIGH + 1968 AEROSOL BETAS.
 CURVE 2 - MEASURED BRIGHTNESS SCALED BY 1968 MODEL.

S191 - PASS 47, SCAN 1, WAVELENGTH - .78 MICRONS

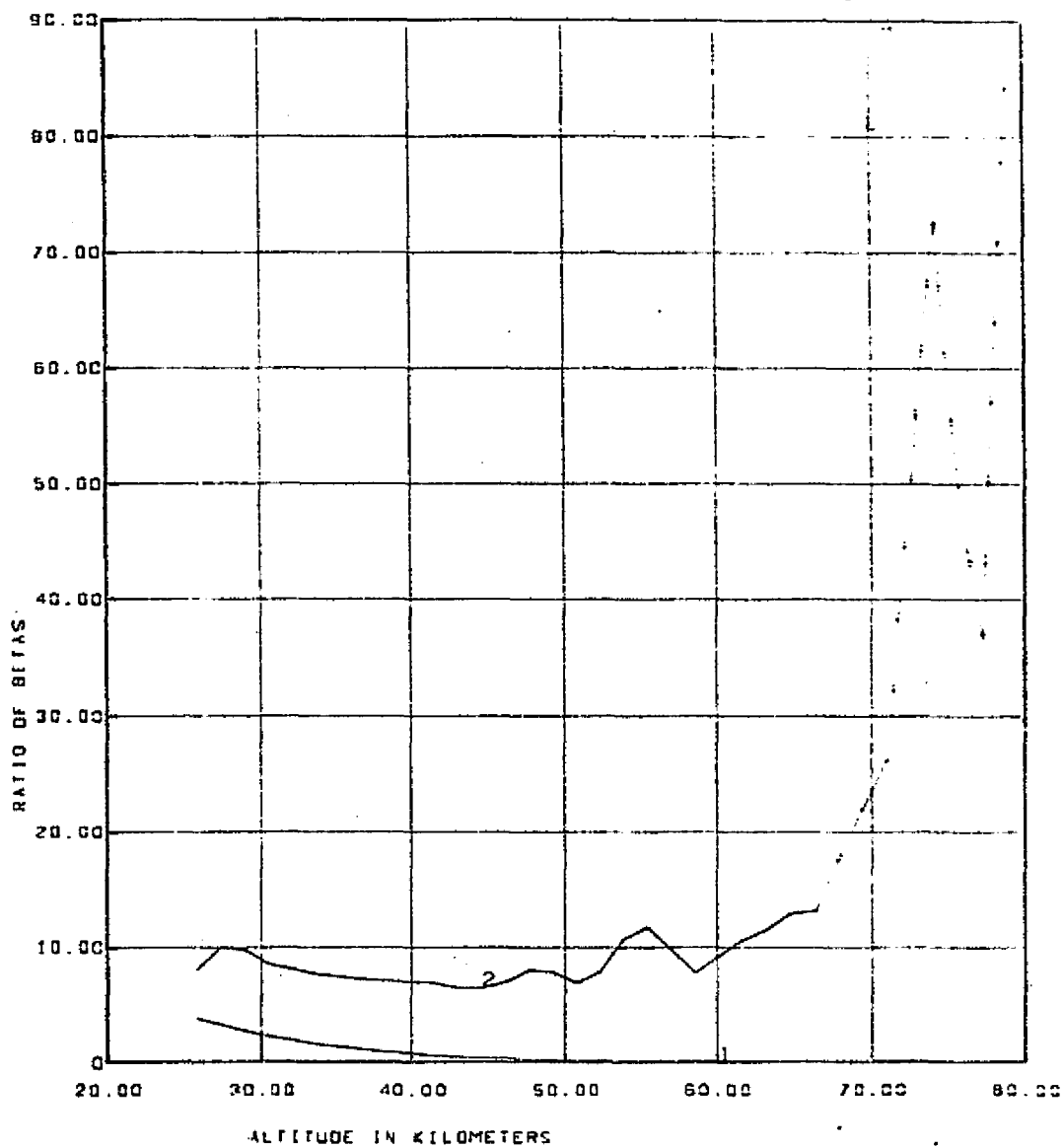


CURVE 1 - RAYLEIGH BETAS, CURVE 2 - RAYLEIGH + 1968 AEROSOL BETAS
 CURVE 3 IS BETAS DERIVED BY INVERSION OF SCALED MEASURED BRIGHTNESS

REPRODUCIBILITY OF THE
 ORIGINAL PAGE IS POOR

111

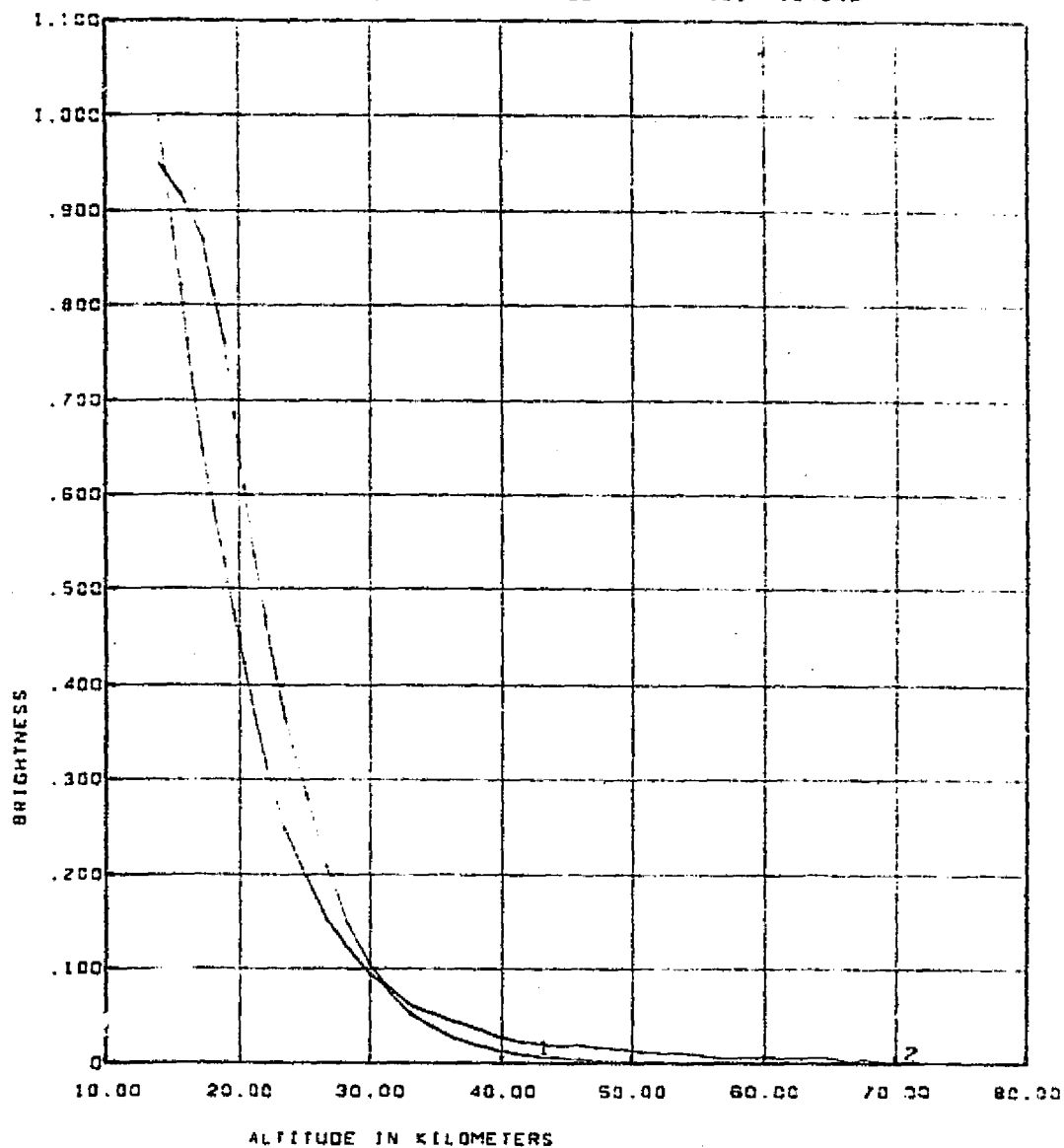
S191 - PASS 47. SCAN 1. WAVELENGTH .78 MICRONS



CURVE 1 IS RATIO OF 1988 AEROSOL BETAS OVER RAYLEIGH BETAS.
 CURVE 2 IS RATIO OF DERIVED AEROSOL BETAS OVER RAYLEIGH BETAS.

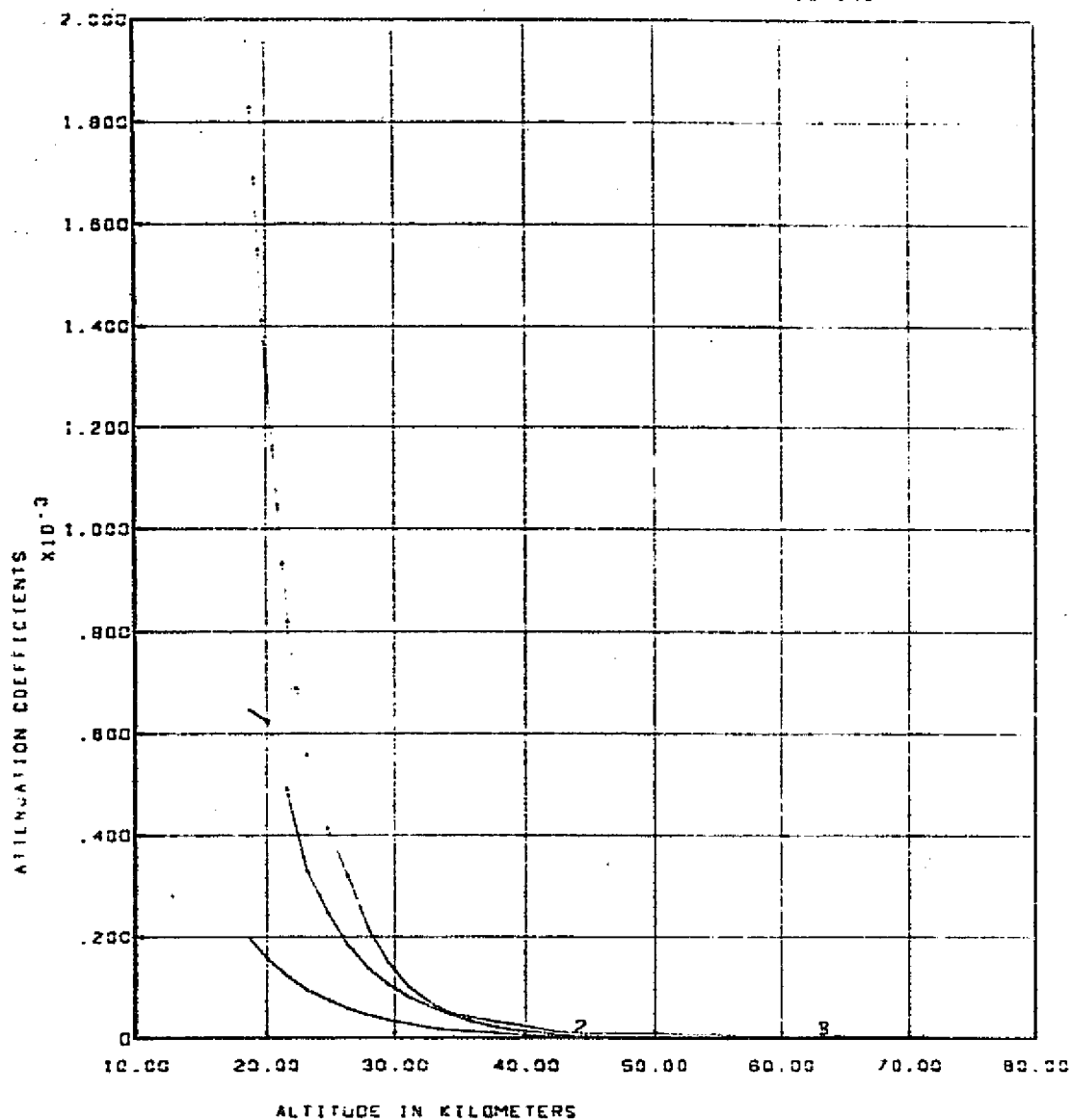
811

S191 - PASS 47, SCAN 1, WAVELENGTH - .83 MICRONS



CURVE 1 - BRIGHTNESS MODEL GENERATED FROM RAYLEIGH + 1968 AEROSOL BETAS.
 CURVE 2 - MEASURED BRIGHTNESS SCALED BY 1968 MODEL.

S19: PASS 47, SCAN 1, WAVELENGTH - .83 MICRONS

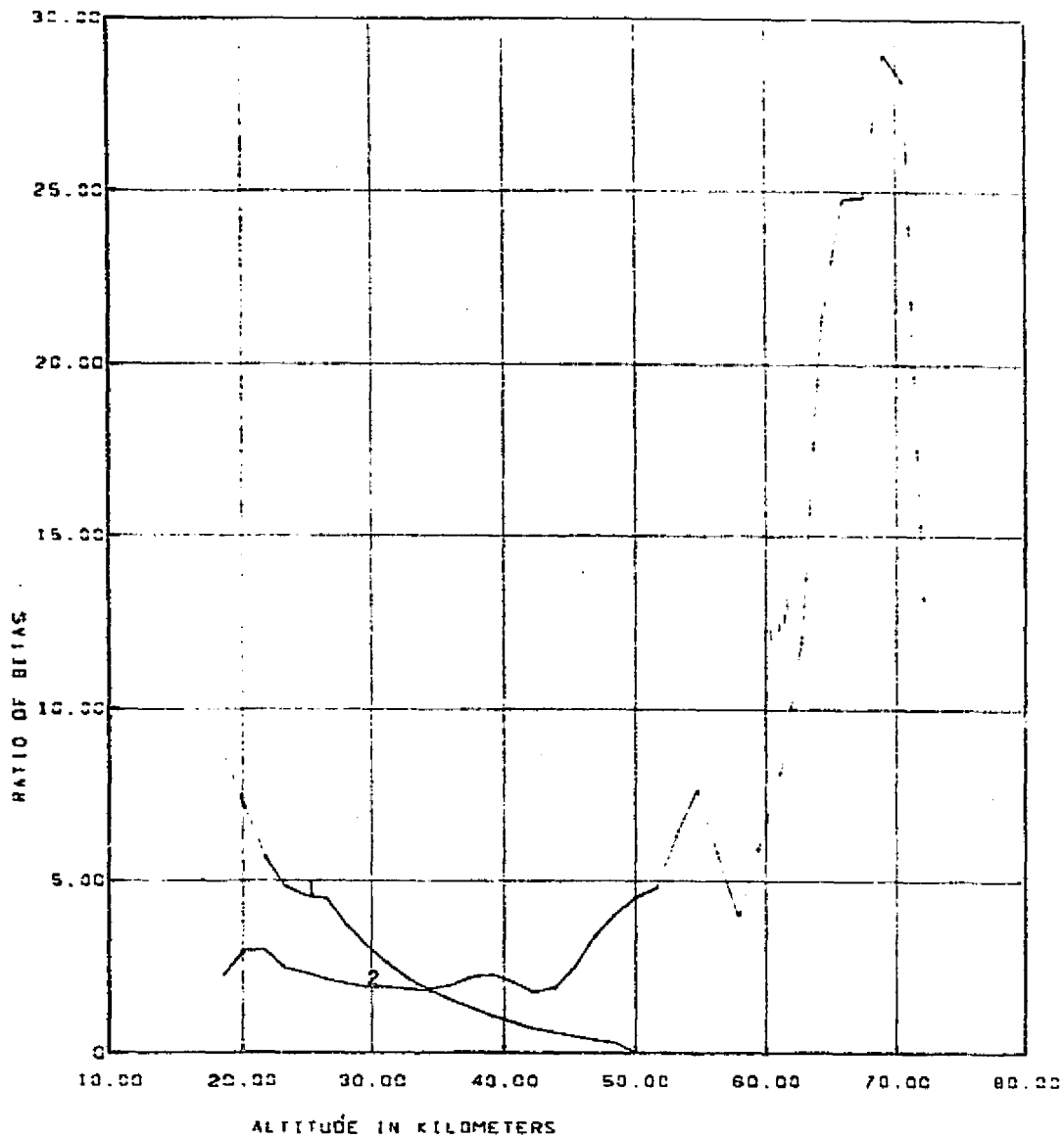


CURVE 1 - RAYLEIGH BETAS. CURVE 2 - RAYLEIGH + 1968 AEROSOL BETAS
CURVE 3 IS BETAS DERIVED BY INVERSION OF SCALED MEASURED BRIGHTNESS

REPRODUCIBILITY OF THE
ORIGINAL PAGE IS POOR

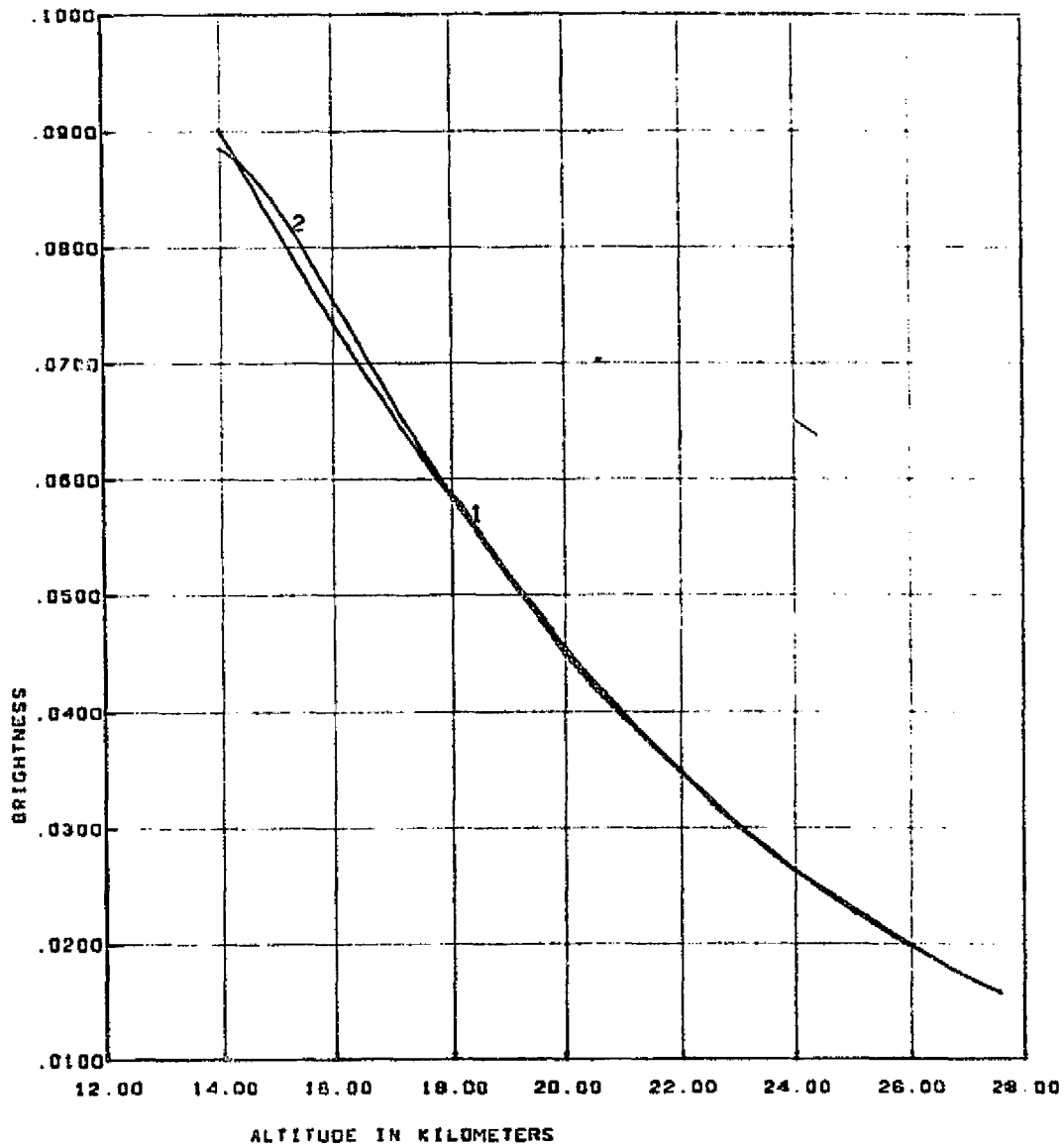
11

S19: PASS 47, SCAN 1, WAVELENGTH - .83 MICRONS



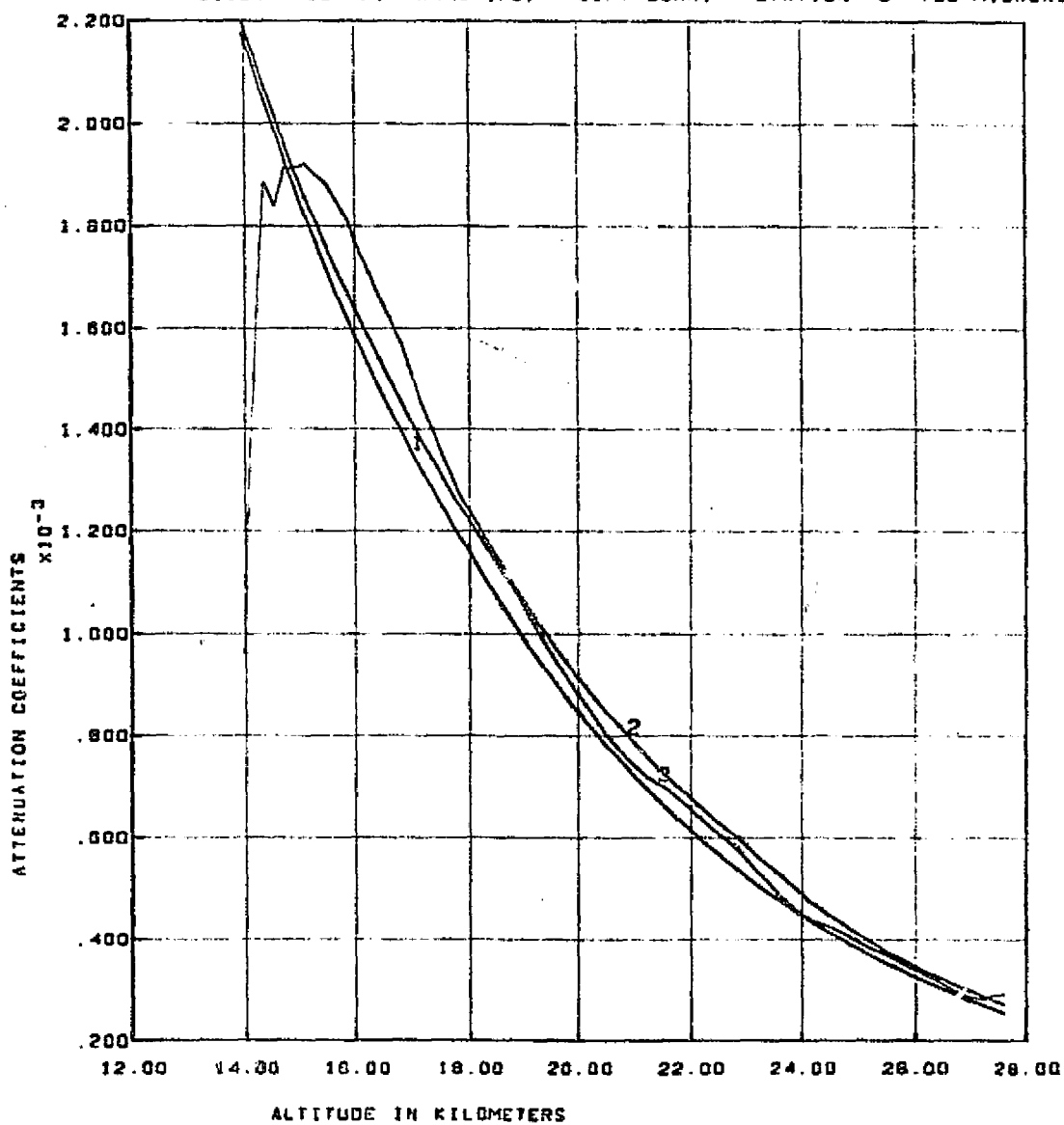
CURVE 1 IS RATIO OF 1968 AEROSOL BETAS OVER RAYLEIGH BETAS.
 CURVE 2 IS RATIO OF DERIVED AEROSOL BETAS OVER RAYLEIGH BETAS.

S190A PASS 47, FRAME 175, LEFT SCAN, STATION 6 - 55 MICRONS.



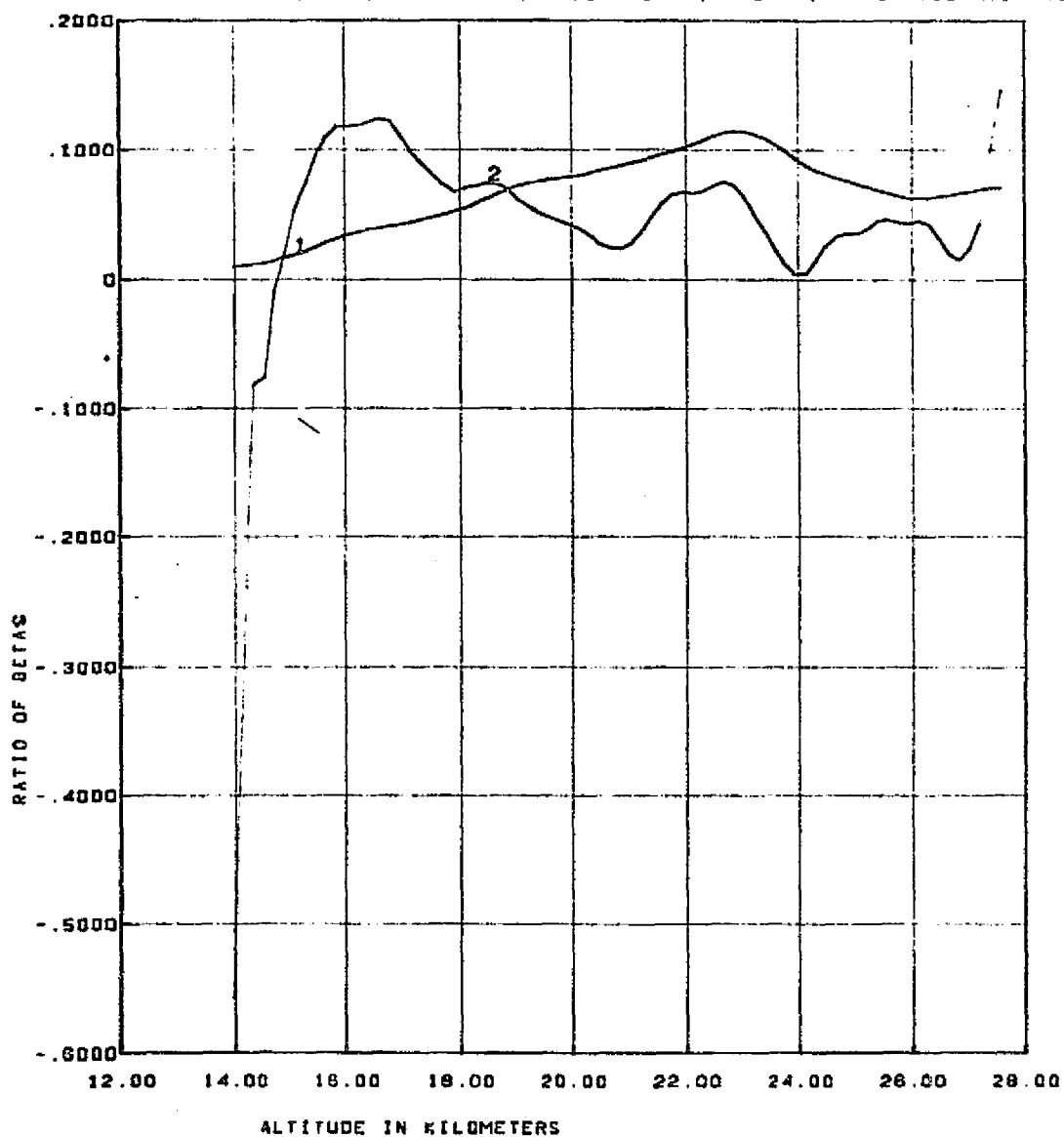
CURVE 1 - BRIGHTNESS MODEL GENERATED FROM RAYLEIGH + 1964 AEROSOL BETAS.
CURVE 2 - MEASURED BRIGHTNESS SCALED BY 1964 MODEL.

S190A PASS 47. FRAME 175. LEFT SCAN. STATION 6 - .55 MICRONS.



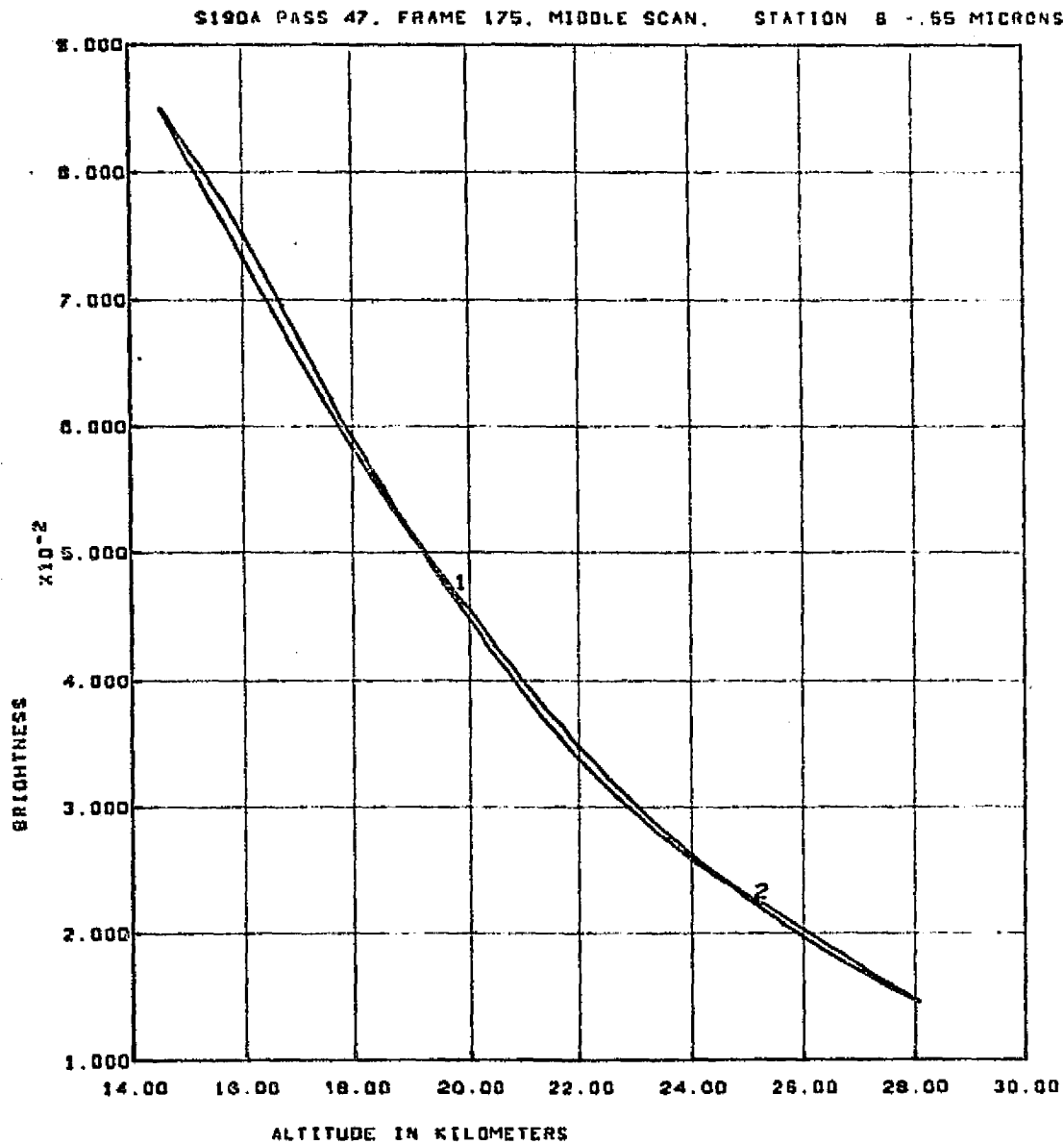
CURVE 1 - RAYLEIGH BETAS. CURVE 2 - RAYLEIGH + 1964 AEROSOL BETAS
CURVE 3 IS BETAS DERIVED BY INVERSION OF SCALED MEASURED BRIGHTNESS

S190A PASS 47, FRAME 175. LEFT SCAN. STATION 8 - .55 MICRONS



CURVE 1 IS RATIO OF 1964 AEROSOL BETAS OVER RAYLEIGH BETAS.
 CURVE 2 IS RATIO OF DERIVED AEROSOL BETAS OVER RAYLEIGH BETAS.

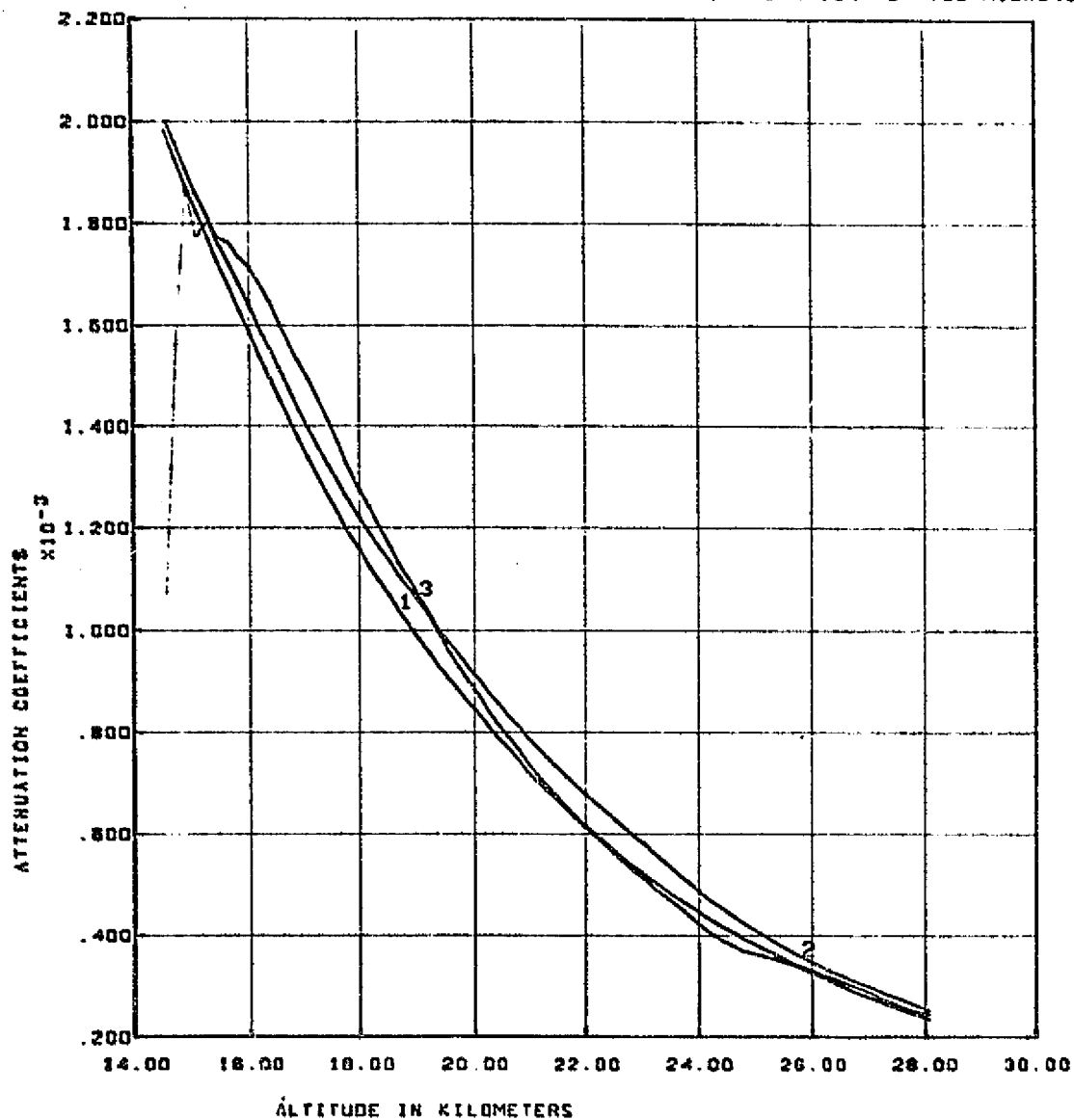
REPRODUCIBILITY OF THE
 ORIGINAL PAGE IS POOR



CURVE 1- BRIGHTNESS MODEL GENERATED FROM RAYLEIGH + 1984 AEROSOL BETAS.
CURVE 2 - MEASURED BRIGHTNESS SCALED BY 1984 MODEL.

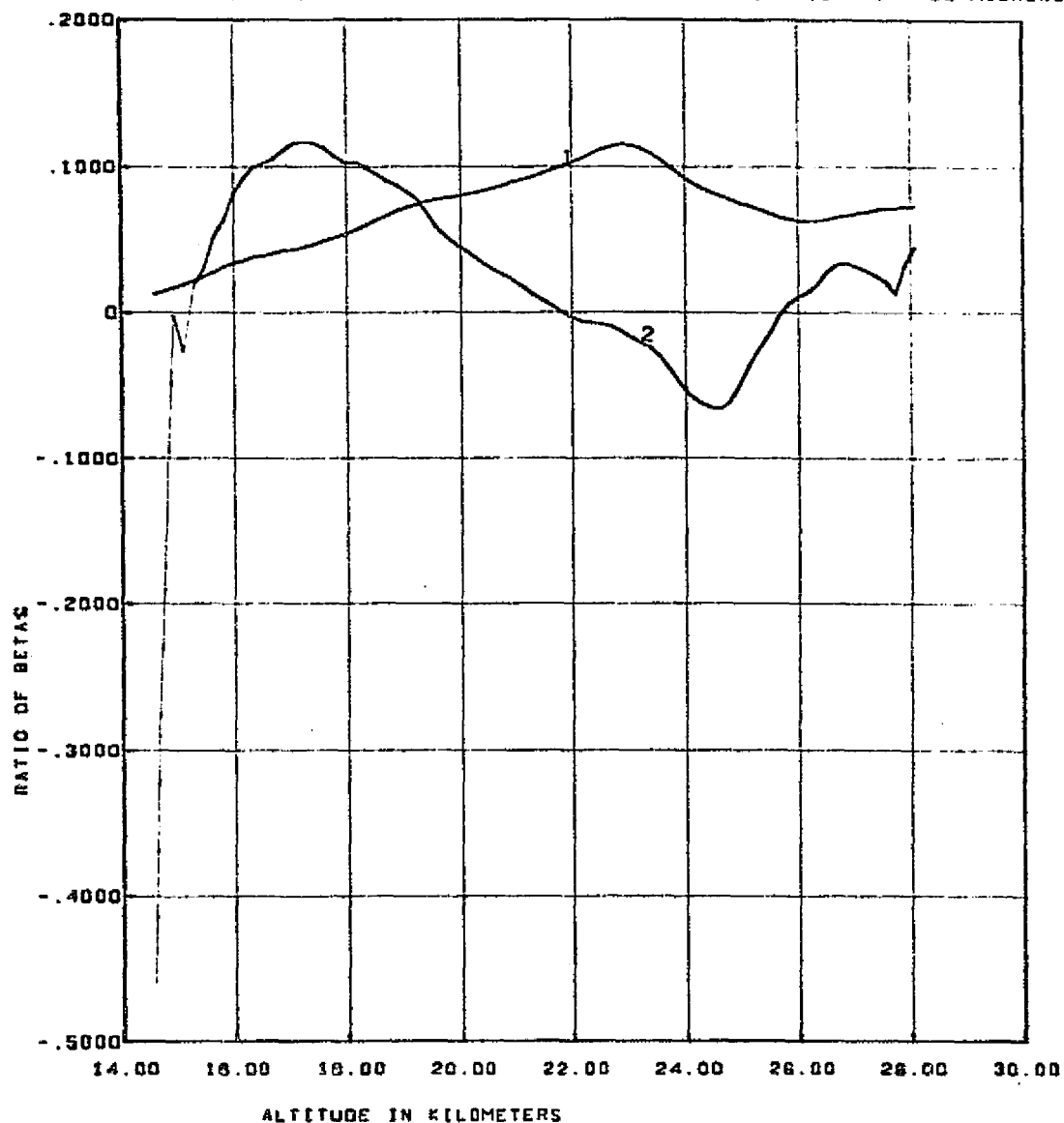
811

S190A PASS 47. FRAME 175. MIDDLE SCAN. STATION B - .55 MICRONS.



CURVE 1 - RAYLEIGH BETAS. CURVE 2 - RAYLEIGH + 1964 AEROSOL BETAS
CURVE 3 IS BETAS DERIVED BY INVERSION OF SCALED MEASURED BRIGHTNESS

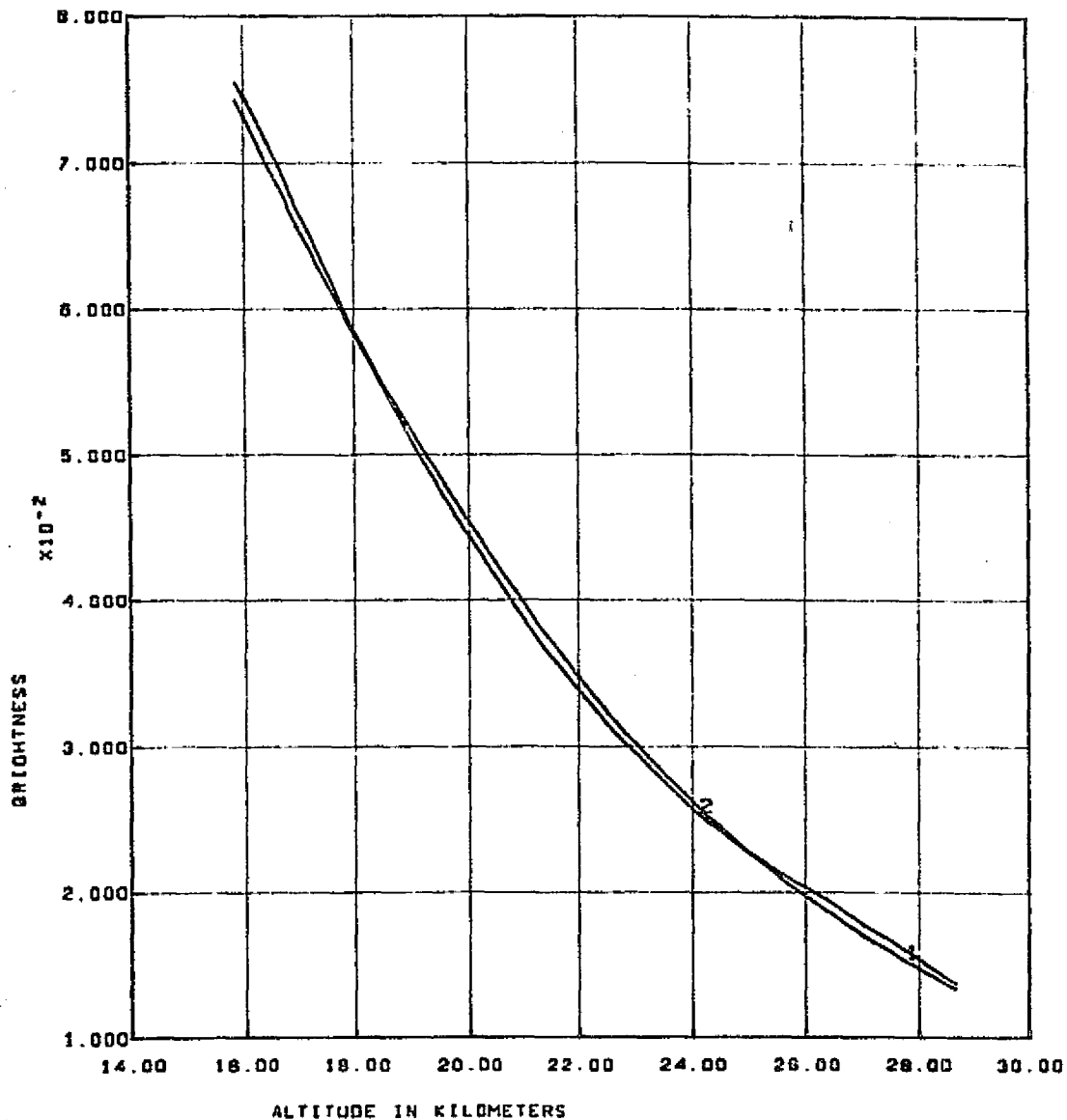
S190A PASS 47. FRAME 175. MIDDLE SCAN. STATION 6 - .55 MICRONS.



CURVE 1 IS RATIO OF 1984 AEROSOL BETAS OVER RAYLEIGH BETAS.
CURVE 2 IS RATIO OF DERIVED AEROSOL BETAS OVER RAYLEIGH BETAS.

REPRODUCIBILITY OF THE
ORIGINAL PAGE IS POOR

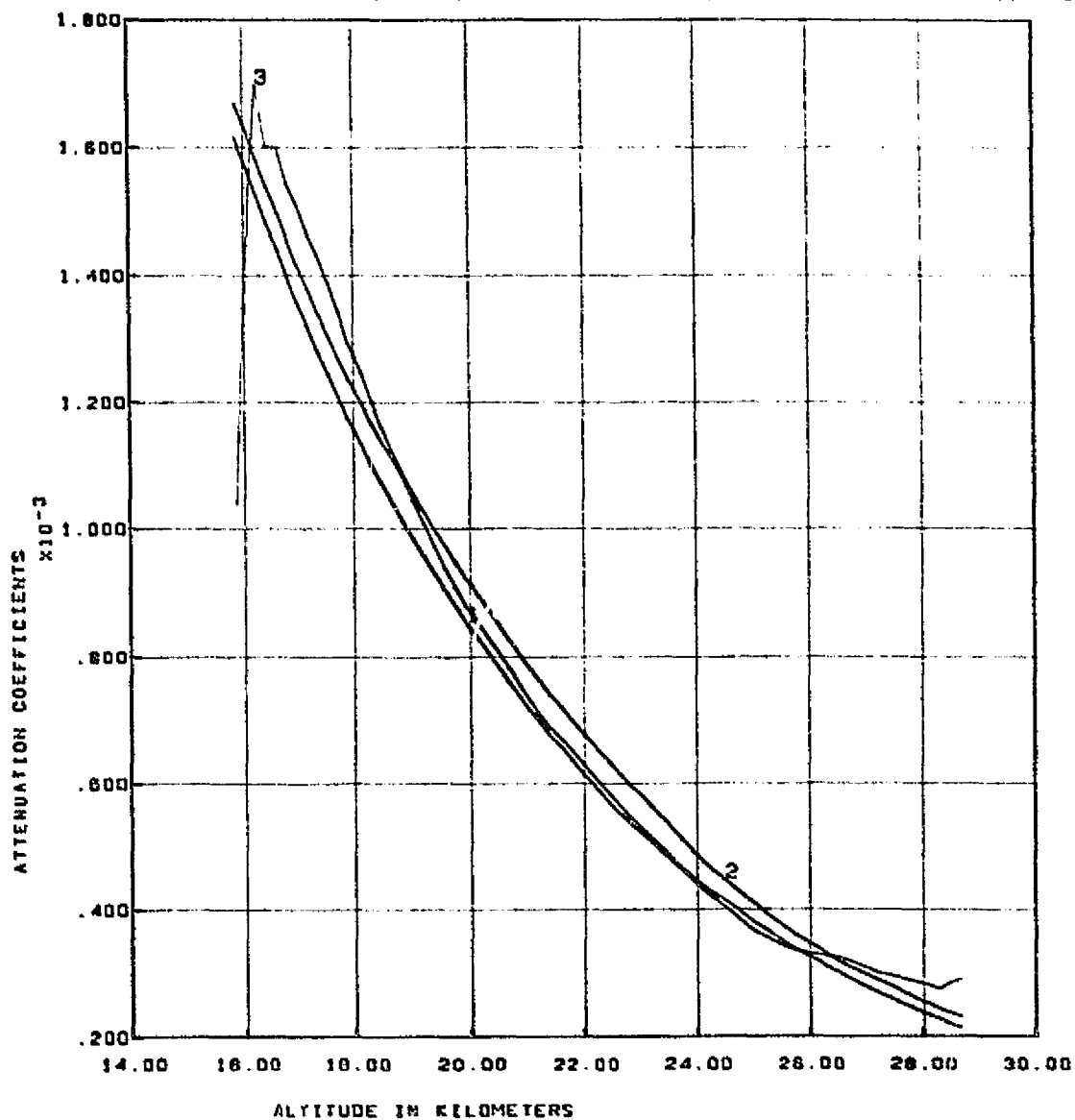
S190A PASS 47, FRAME 175, RIGHT SCAN, STATION 8 - .55 MICRONS.



CURVE 1- BRIGHTNESS MODEL GENERATED FROM RAYLEIGH + 1964 AEROSOL BETAS.
 CURVE 2 - MEASURED BRIGHTNESS SCALED BY 1964 MODEL.

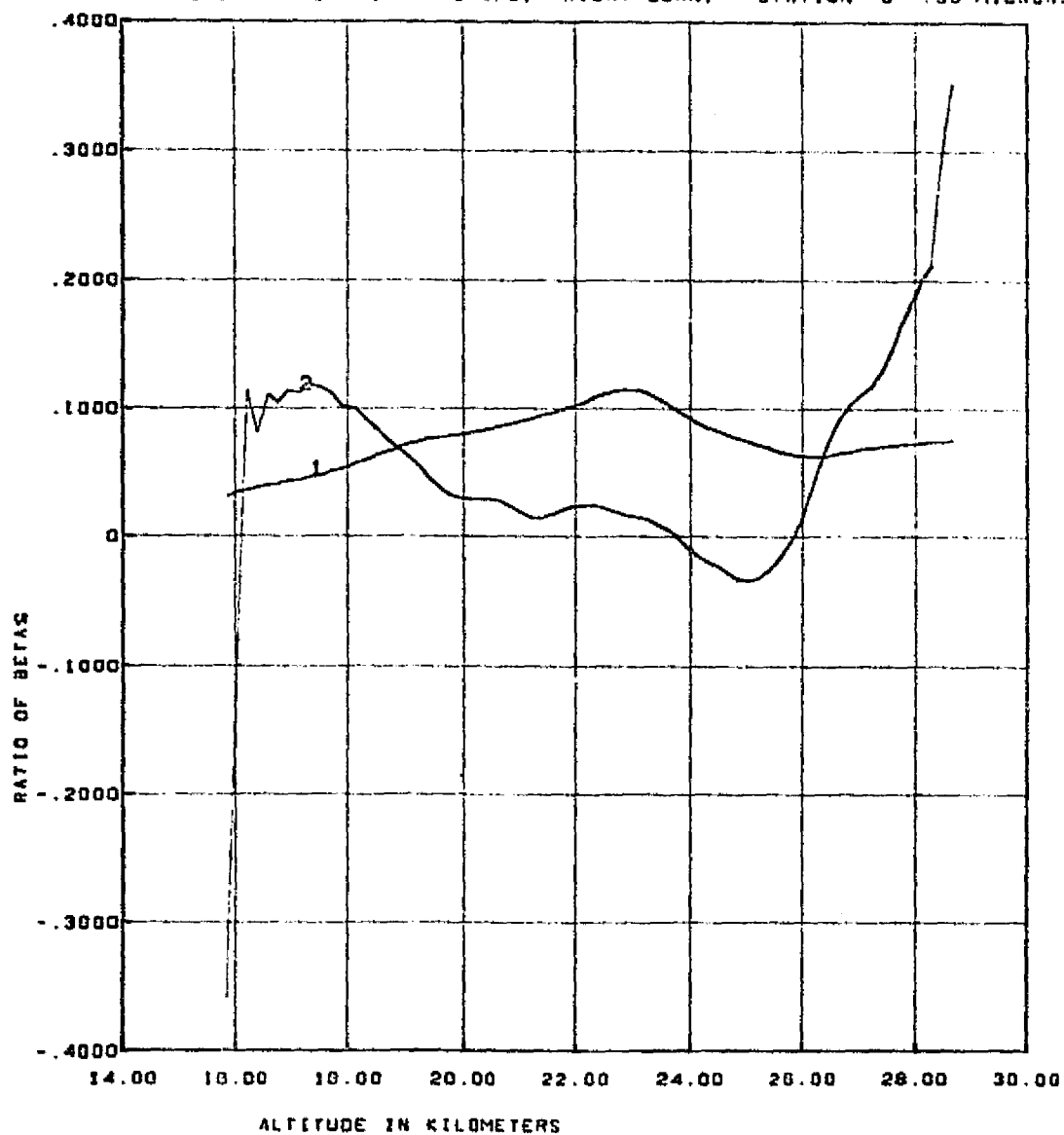
111

S190A PASS 47, FRAME 175, RIGHT SCAN, STATION 8 - .55 MICRONS



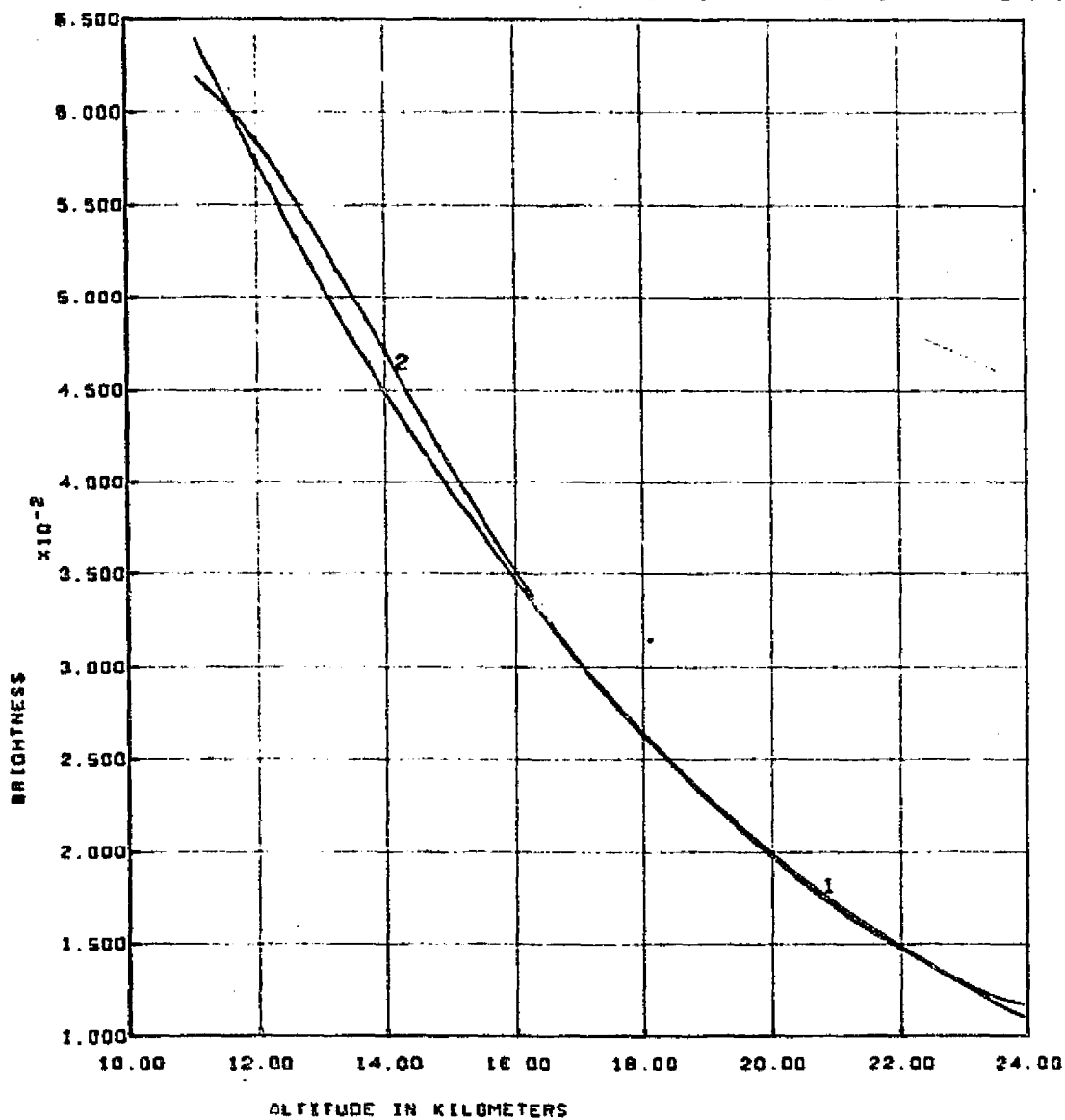
CURVE 1 - RAYLEIGH DETAS. CURVE 2 - RAYLEIGH + 1964 AEROSOL DETAS
 CURVE 3 IS DETAS DERIVED BY INVERSION OF SCALED MEASURED BRIGHTNESS

S190A PASS 47. FRAME 175. RIGHT SCAN. STATION 8 - .55 MICRONS



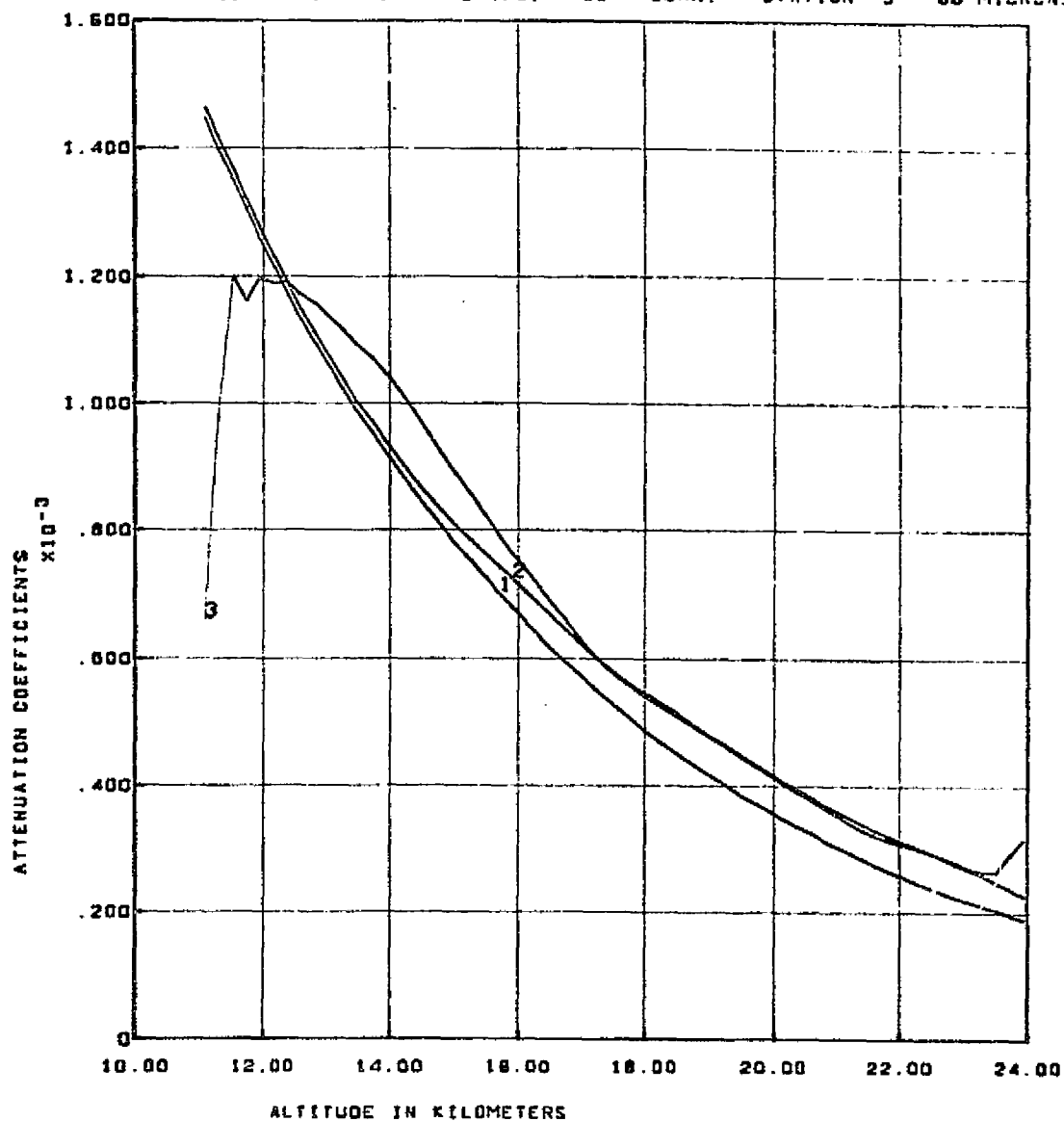
CURVE 1 IS RATIO OF 1964 AEROSOL BETAS OVER RAYLEIGH BETAS.
 CURVE 2 IS RATIO OF DERIVED AEROSOL BETAS OVER RAYLEIGH BETAS.

S19DA PASS 47. FRAME 175. LEFT SCAN. STATION 5 - 68 MICRONS.



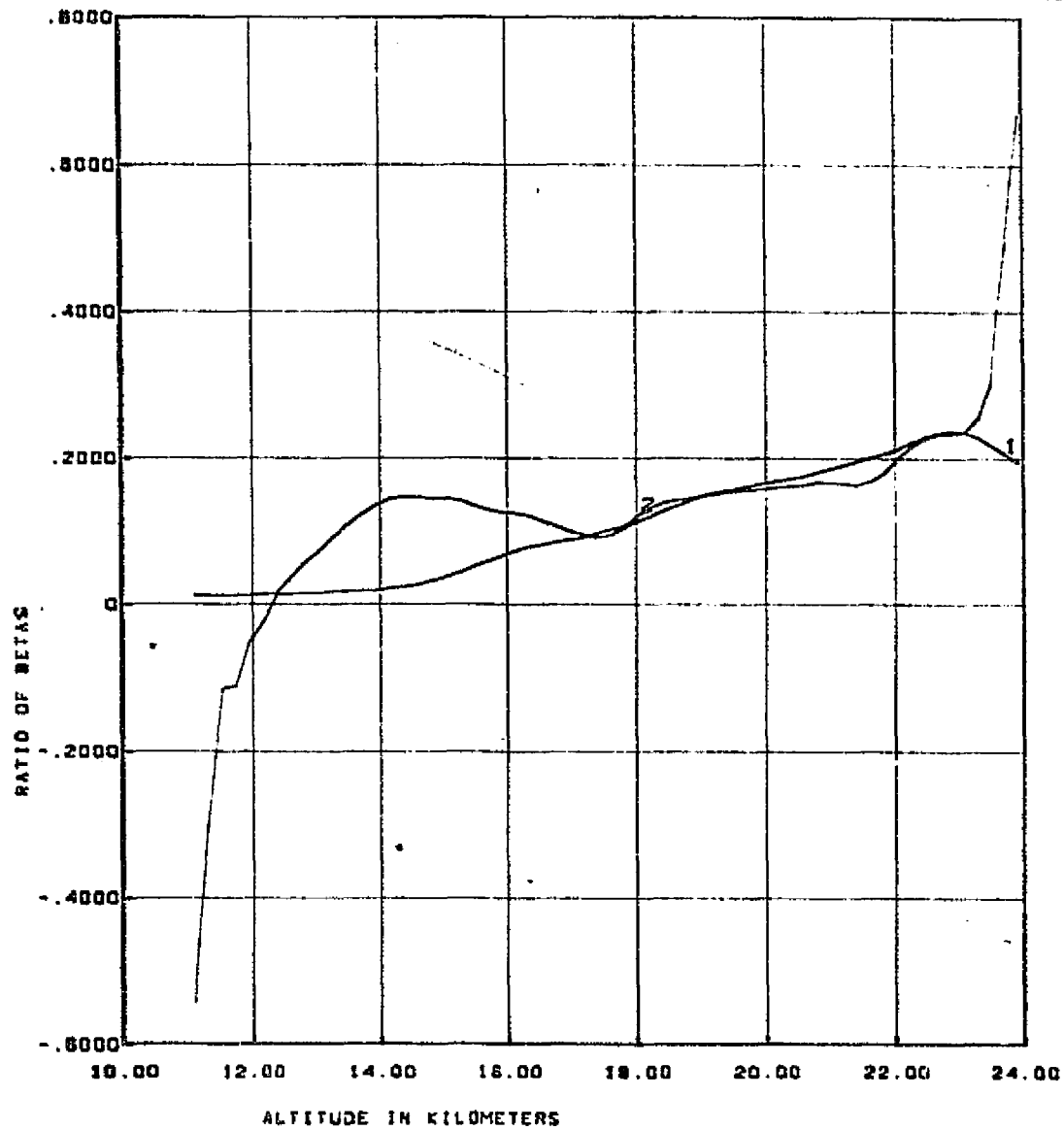
CURVE 1- BRIGHTNESS MODEL GENERATED FROM RAYLEIGH + 1964 AEROSOL BETAS.
CURVE 2 - MEASURED BRIGHTNESS SCALED BY 1964 MODEL.

S190A PASS 47. FRAME 175. LEFT SCAN. STATION 5 - 68 MICRONS



CURVE 1 - RAYLEIGH BETAS. CURVE 2 - RAYLEIGH + 1964 AEROSOL BETAS
CURVE 3 IS BETAS DERIVED BY INVERSION OF SCALED MEASURED BRIGHTNESS

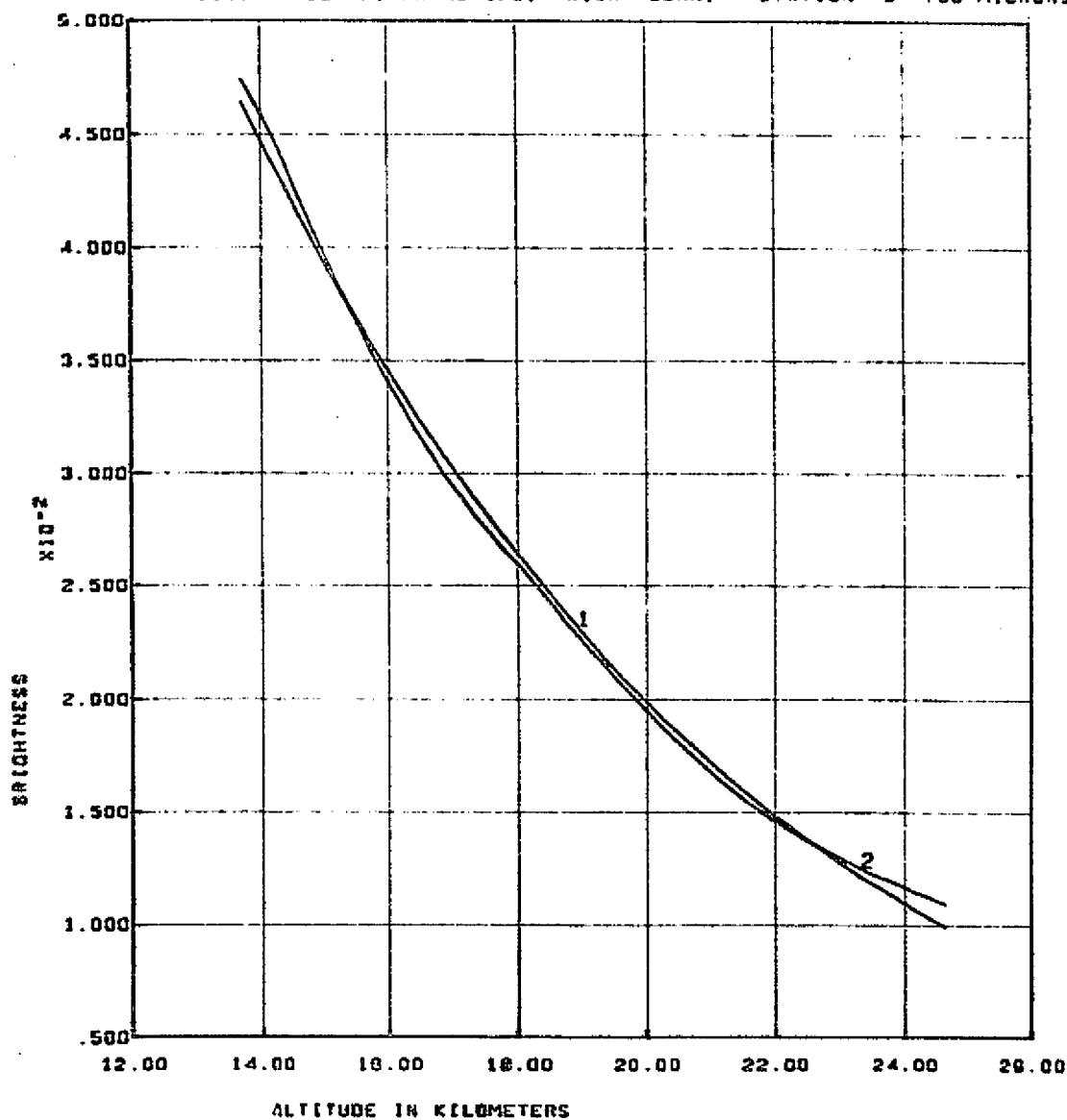
S190A PASS 47. FRAME 175. LEFT SCAN. STATION 5 - .88 MICRONS.



CURVE 1 IS RATIO OF 1984 AEROSOL BETAS OVER RAYLEIGH BETAS.
 CURVE 2 IS RATIO OF DERIVED AEROSOL BETAS OVER RAYLEIGH BETAS.

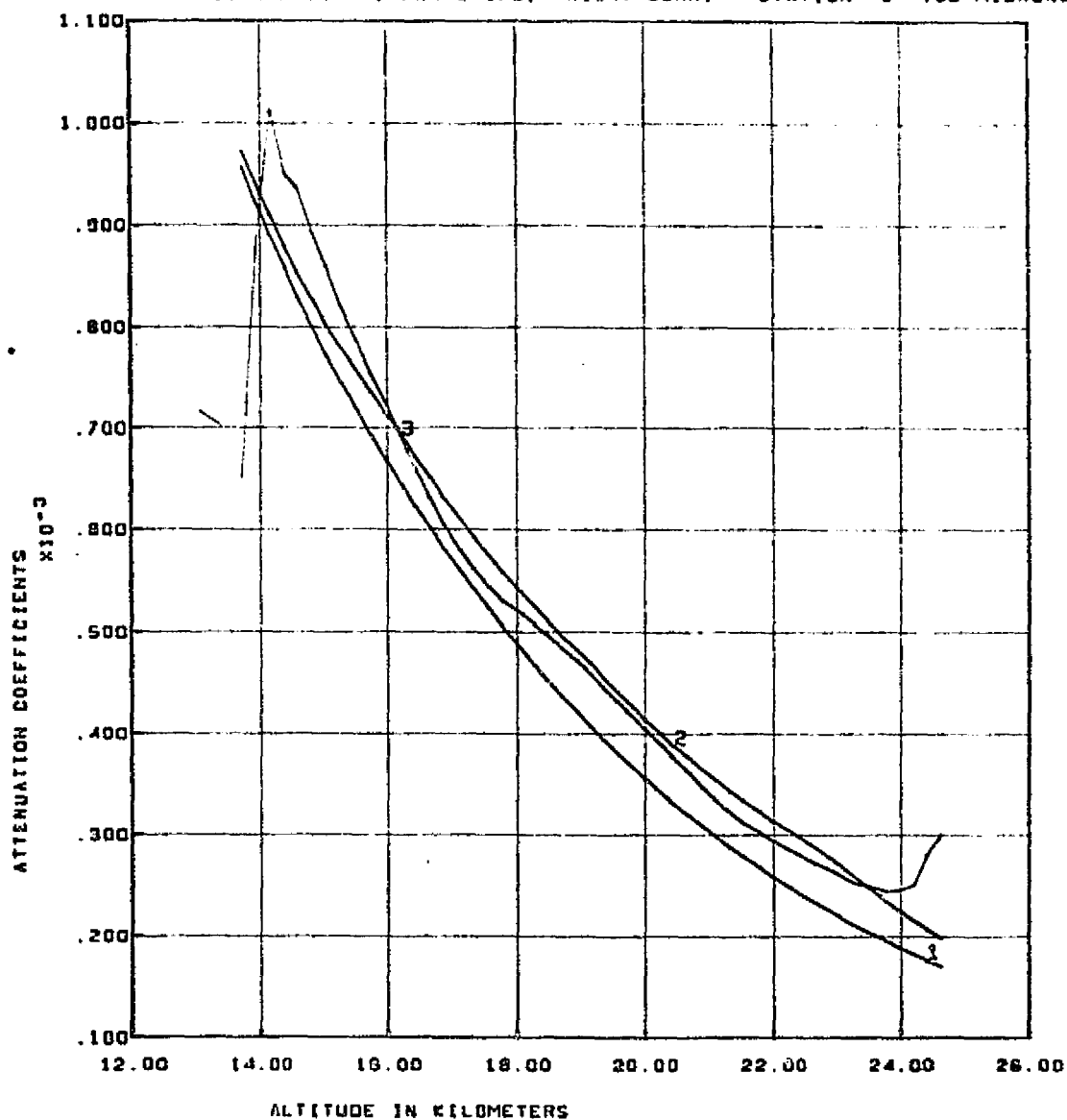
111

S190A PASS 47. FRAME 175. RIGHT SCAN. STATION 5 - .68 MICRONS



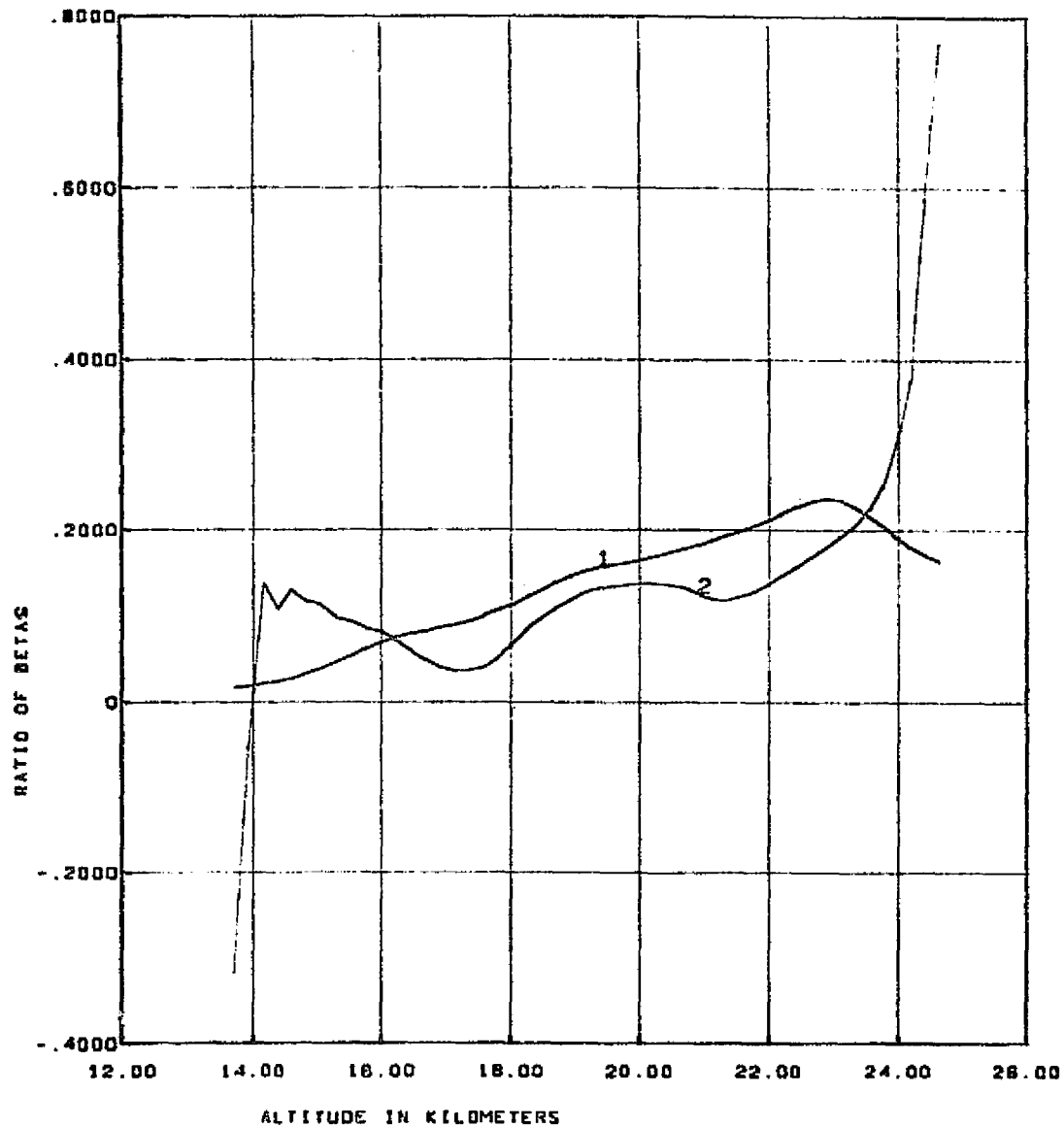
CURVE 1 - BRIGHTNESS MODEL GENERATED FROM RAYLEIGH + 1964 AEROSOL BETAS.
 CURVE 2 - MEASURED BRIGHTNESS SCALED BY 1964 MODEL.

S190A PASS 47, FRAME 175, RIGHT SCAN, STATION 5 -.68 MICRONS



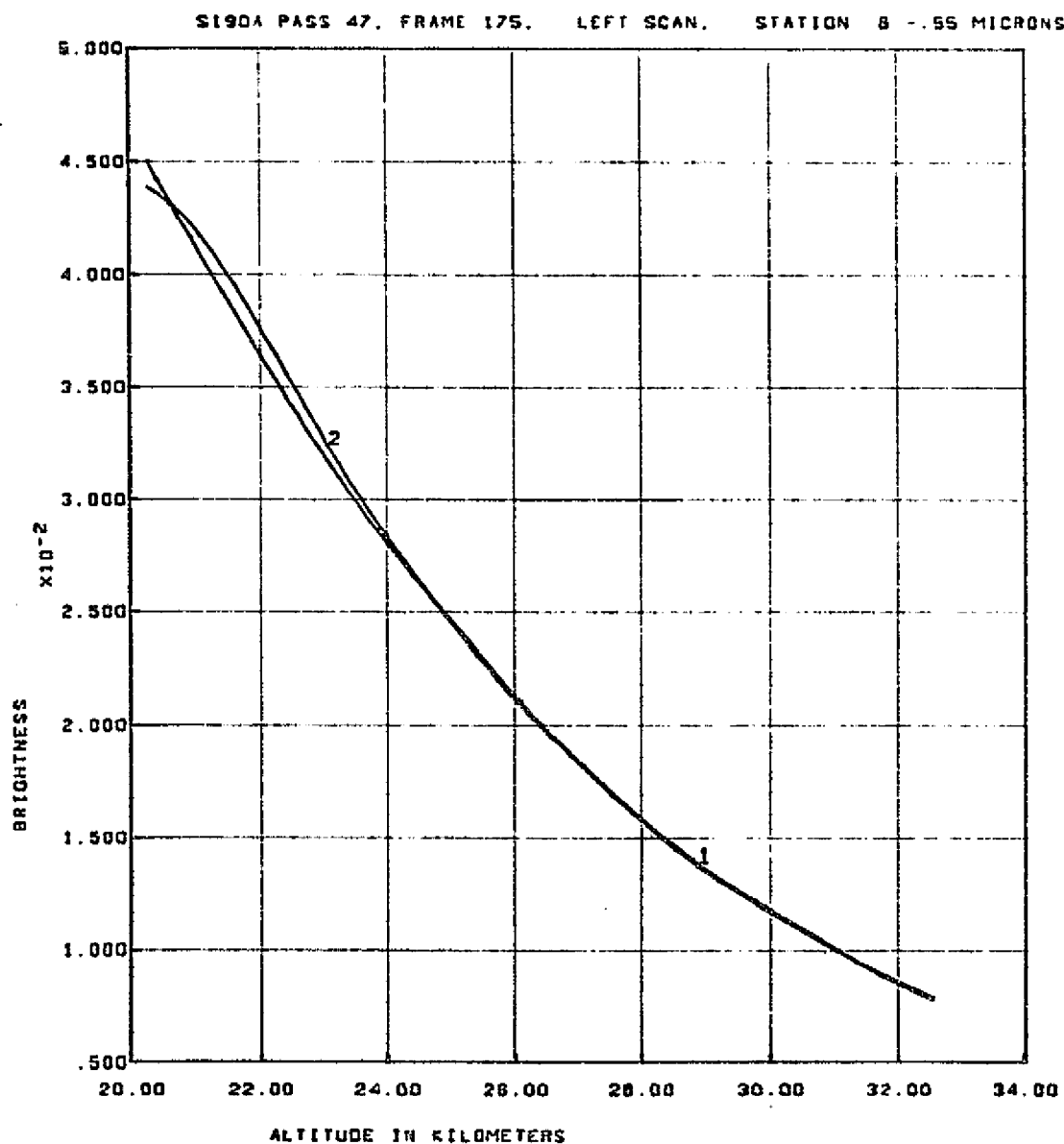
CURVE 1 - RAYLEIGH BETAS. CURVE 2 - RAYLEIGH + 1964 AEROSOL BETAS
CURVE 3 IS BETAS DERIVED BY INVERSION OF SCALED MEASURED BRIGHTNESS

S19DA PASS 47, FRAME 175, RIGHT SCAN, STATION 5 - .68 MICRONS.



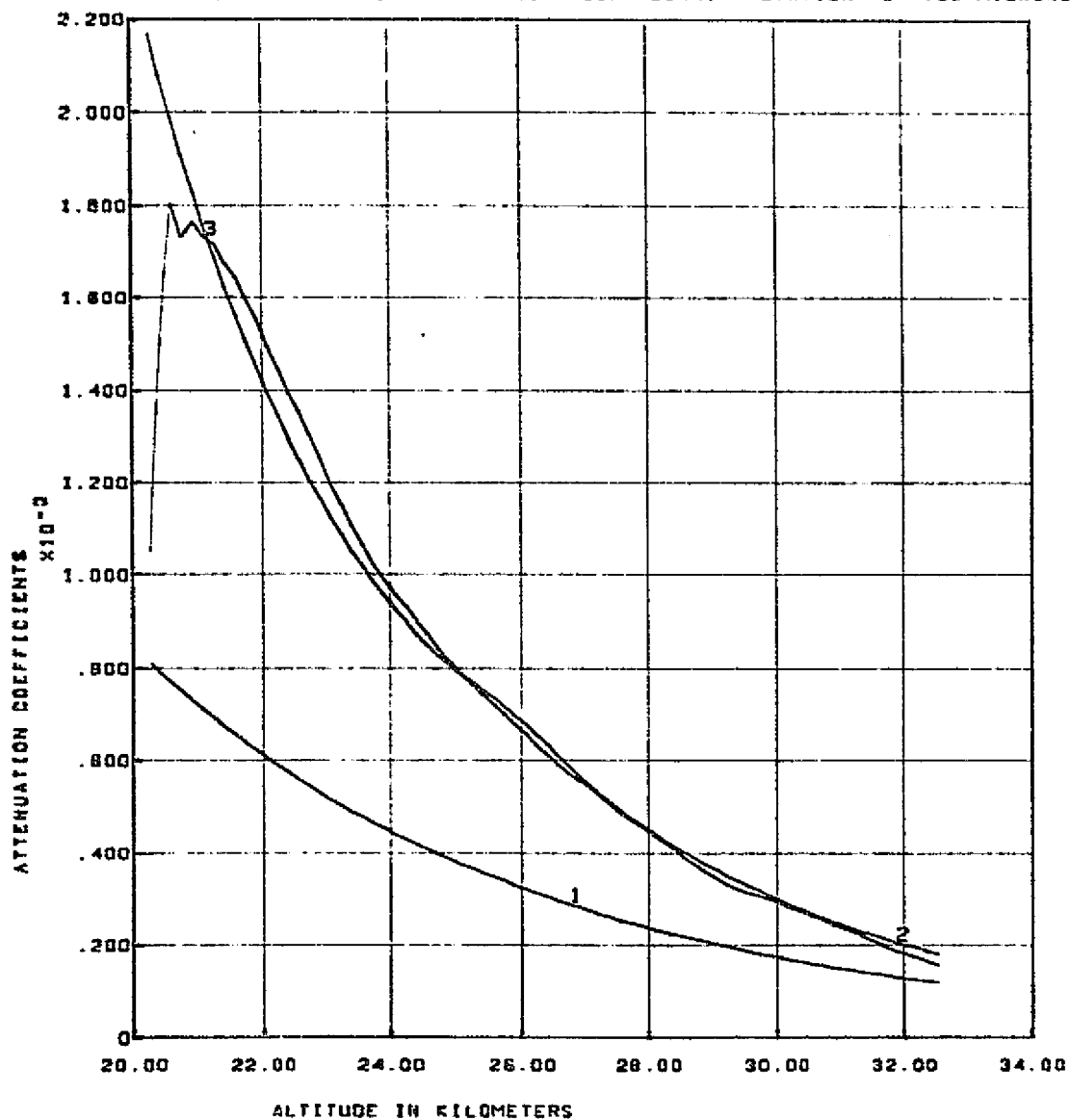
CURVE 1 IS RATIO OF 1964 AEROSOL BETAS OVER RAYLEIGH BETAS.
 CURVE 2 IS RATIO OF DERIVED AEROSOL BETAS OVER RAYLEIGH BETAS.

REPRODUCIBILITY OF THE
 ORIGINAL PAGE IS POOR



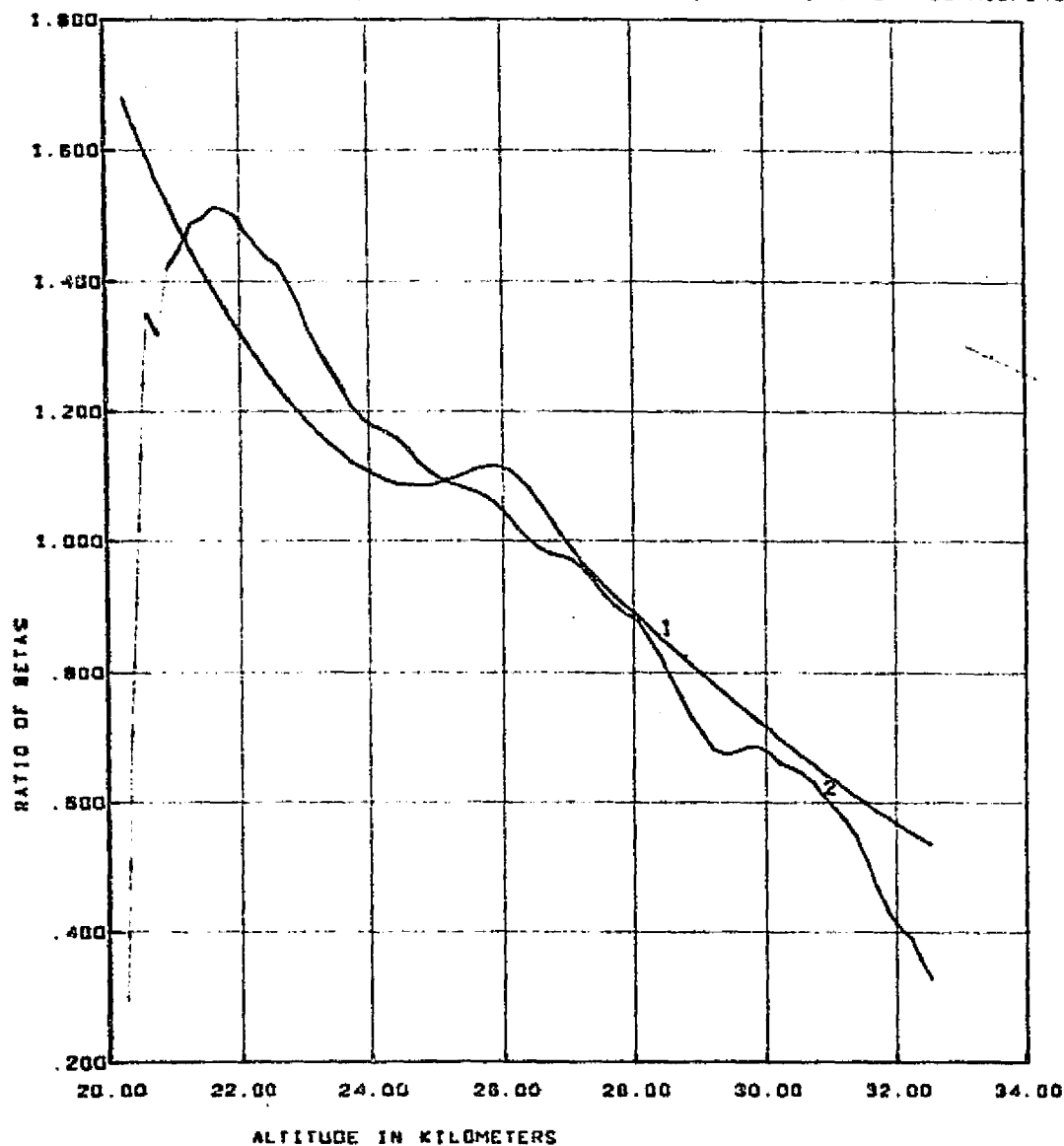
CURVE 1 - BRIGHTNESS MODEL GENERATED FROM RAYLEIGH + 1968 AEROSOL BETAS.
CURVE 2 - MEASURED BRIGHTNESS SCALED BY 1968 MODEL.

S190A PASS 47, FRAME 175, LEFT SCAN, STATION B - .55 MICRONS.

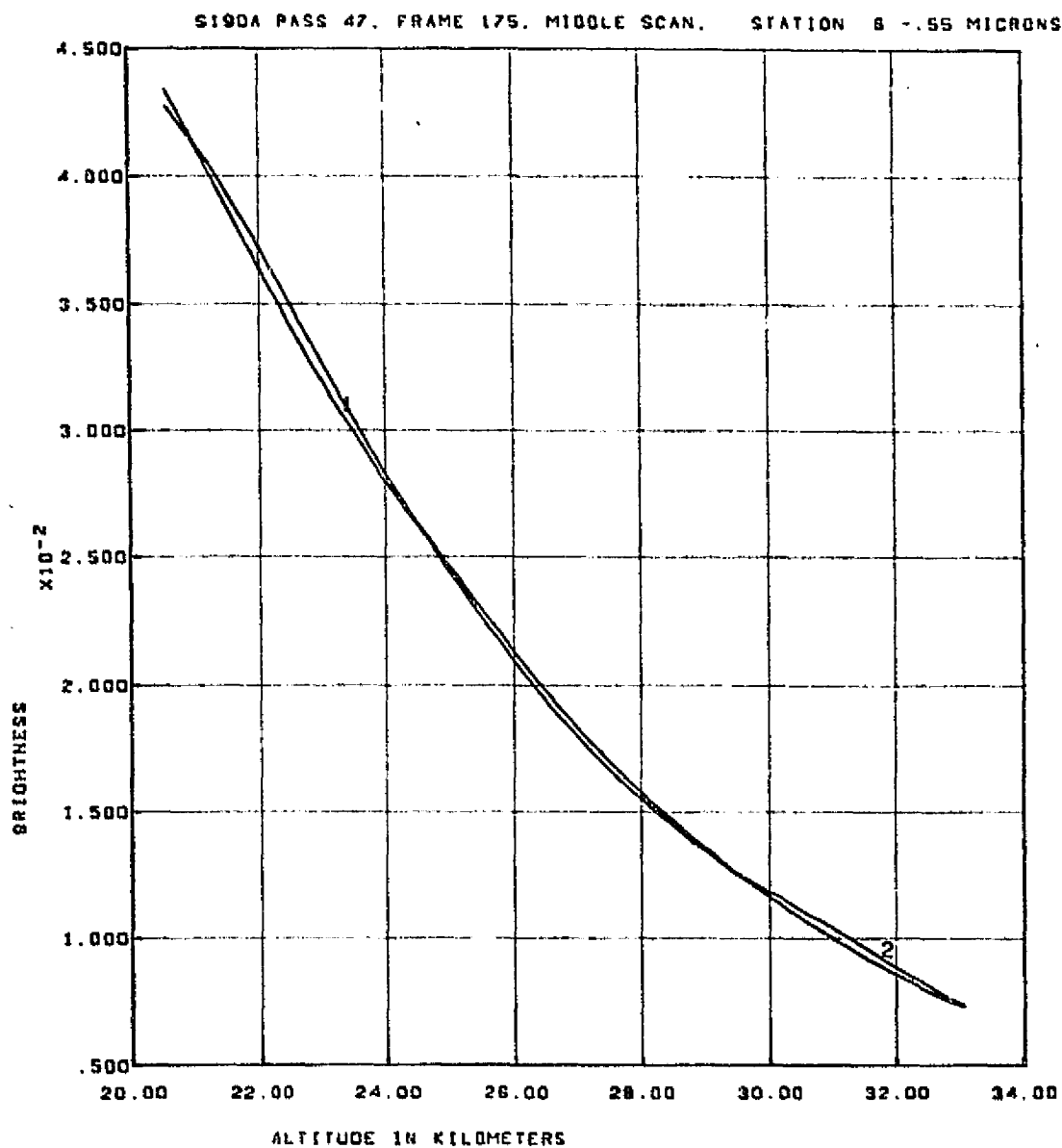


CURVE 1 - RAYLEIGH BETAS. CURVE 2 - RAYLEIGH + 1968 AEROSOL BETAS
CURVE 3 IS BETAS DERIVED BY INVERSION OF SCALED MEASURED BRIGHTNESS

S190A PASS 47. FRAME 175. LEFT SCAN. STATION 8 - .55 MICRONS.



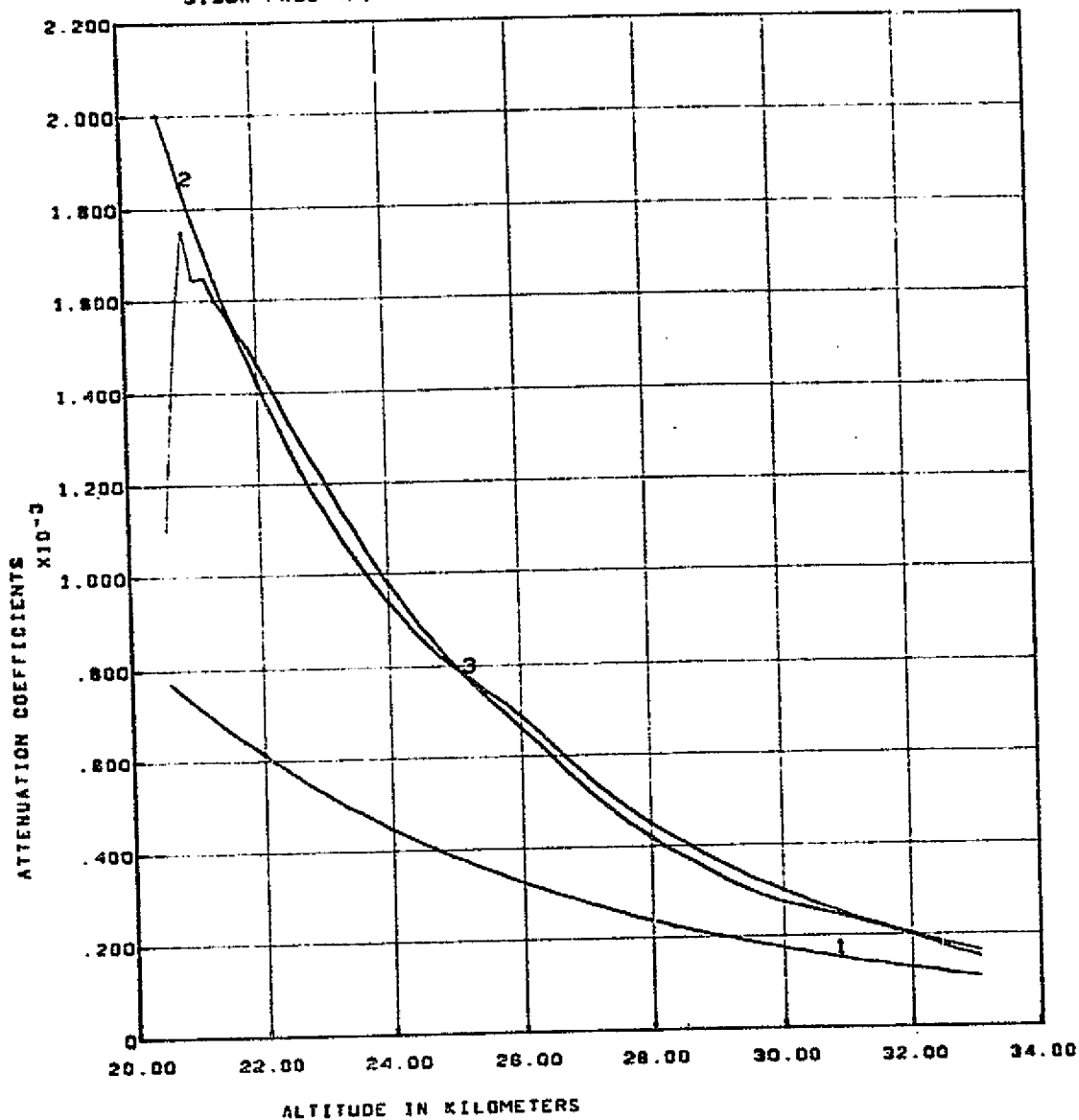
CURVE 1 IS RATIO OF 1988 AEROSOL BETAS OVER RAYLEIGH BETAS.
CURVE 2 IS RATIO OF DERIVED AEROSOL BETAS OVER RAYLEIGH BETAS.



CURVE 1 - BRIGHTNESS MODEL GENERATED FROM RAYLEIGH + 1968 AEROSOL BETAS.
CURVE 2 - MEASURED BRIGHTNESS SCALED BY 1968 MODEL.

011

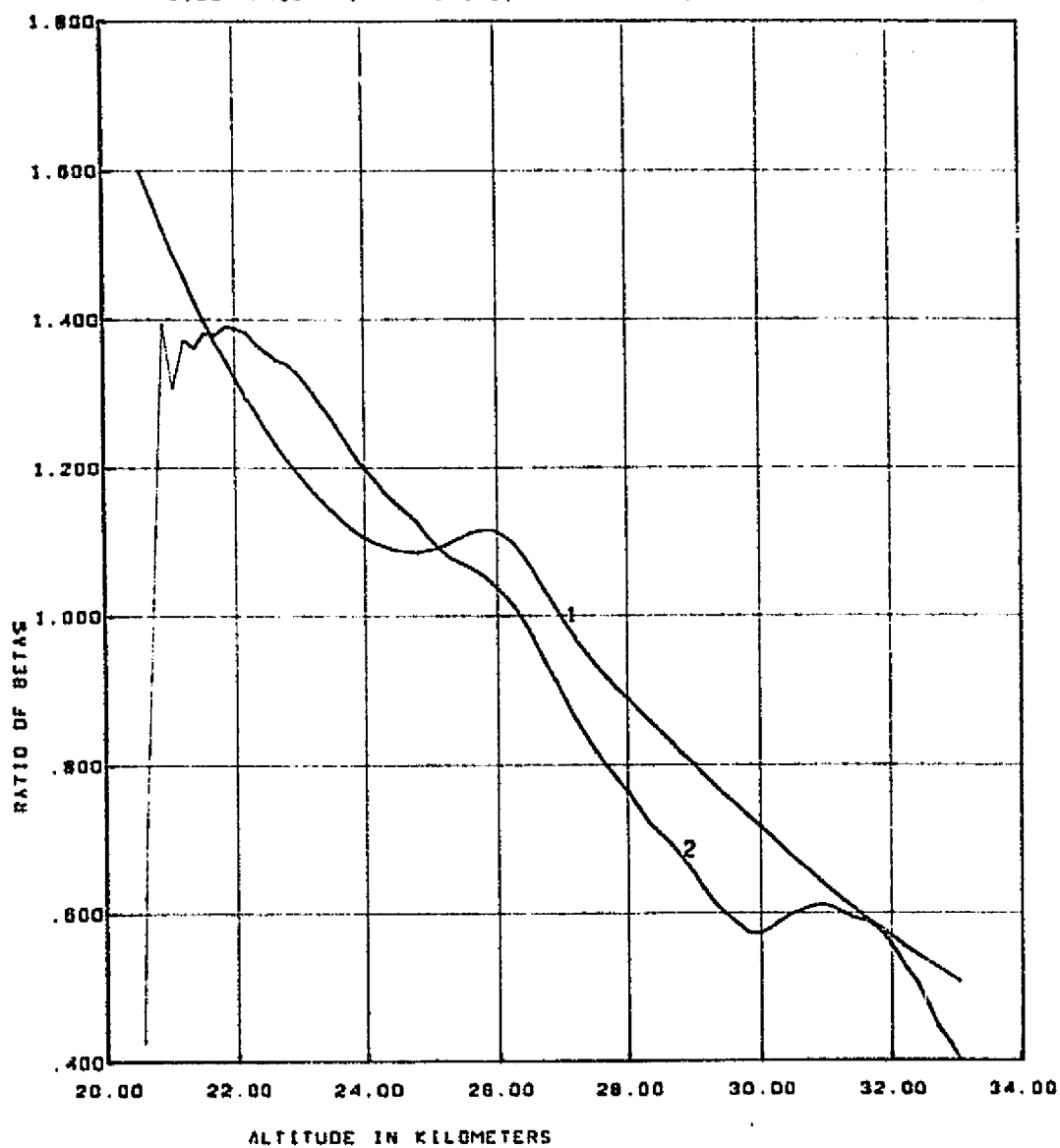
S190A PASS 47. FRAME 175. MIDDLE SCAN. STATION 6 - 55 MICRONS.



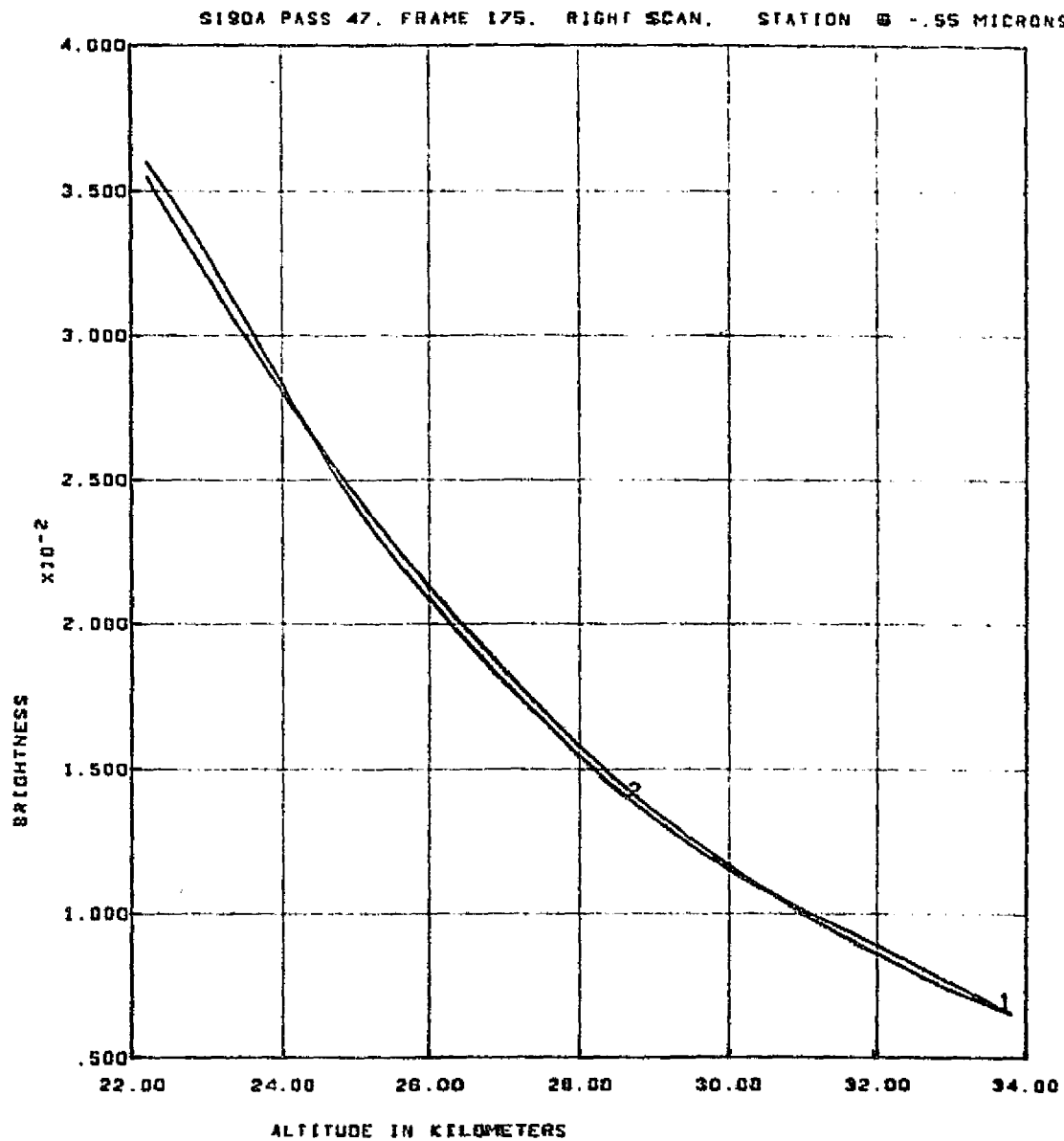
CURVE 1 - RAYLEIGH BETAS. CURVE 2 - RAYLEIGH + 1968 AEROSOL BETAS
CURVE 3 IS BETAS DERIVED BY INVERSION OF SCALED MEASURED BRIGHTNESS

REPRODUCIBILITY OF THE
ORIGINAL PAGE IS POOR

S190A PASS 47, FRAME 175, MIDDLE SCAN. STATION 6 - .55 MICRONS.

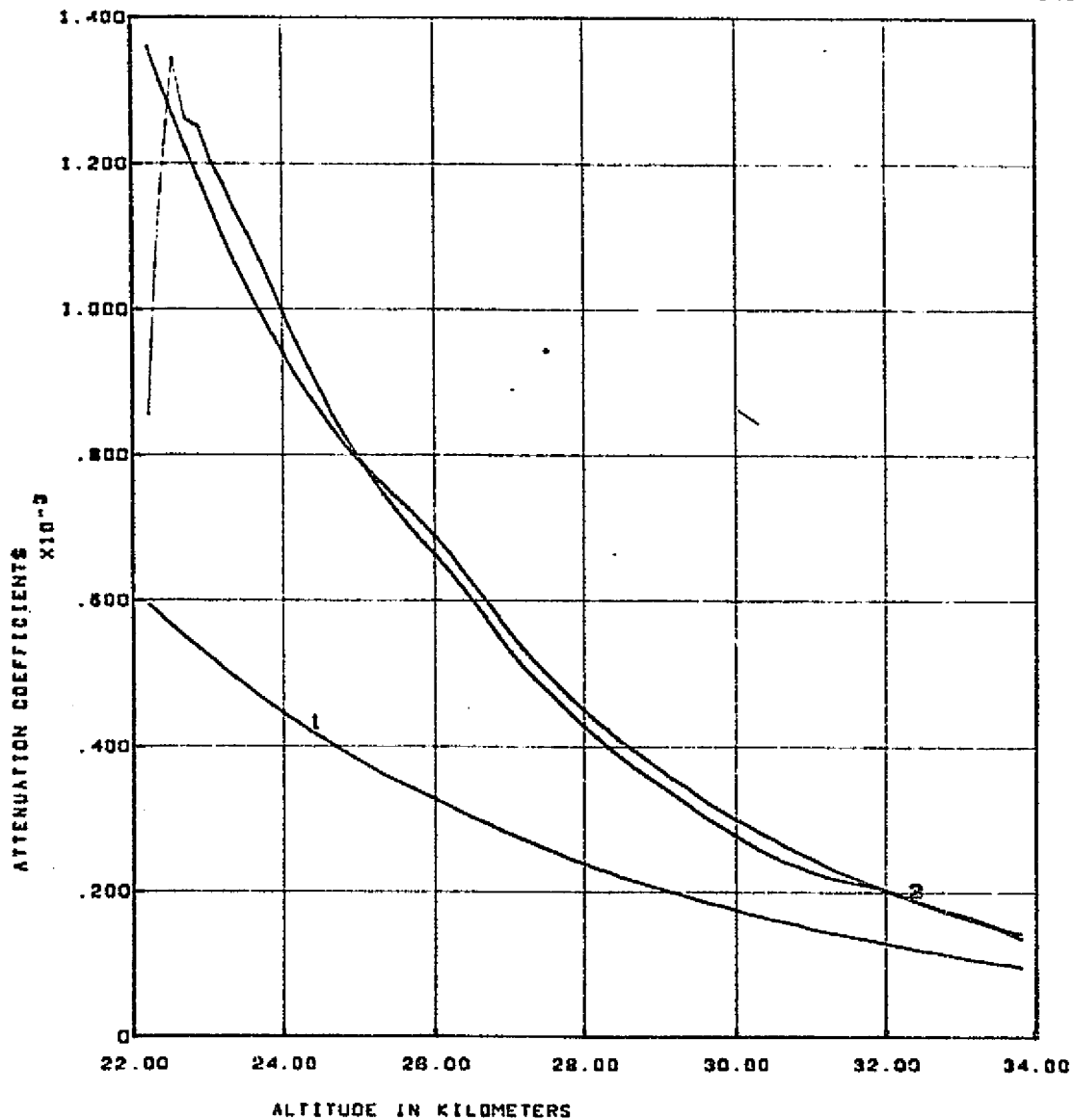


CURVE 1 IS RATIO OF 1988 AEROSOL BETAS OVER RAYLEIGH BETAS.
CURVE 2 IS RATIO OF DERIVED AEROSOL BETAS OVER RAYLEIGH BETAS.



CURVE 1- BRIGHTNESS MODEL GENERATED FROM RAYLEIGH + 1968 AEROSOL BETAS.
CURVE 2 - MEASURED BRIGHTNESS SCALED BY 1968 MODEL.

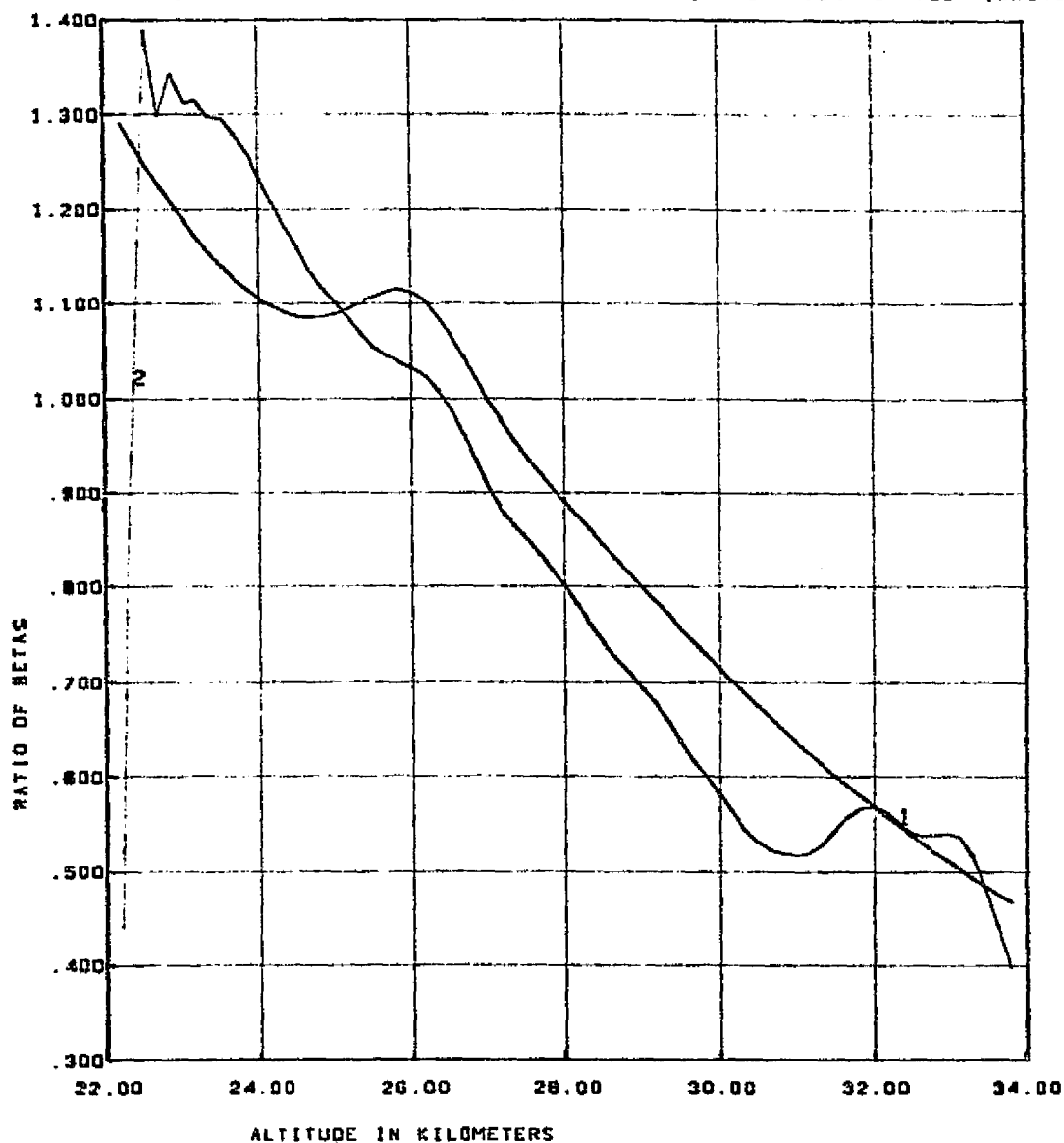
S190A PASS 47, FRAME 175, RIGHT SCAN, STATION 6 - .55 MICRONS.



CURVE 1 - RAYLEIGH BETAS. CURVE 2 - RAYLEIGH + 1968 AEROSOL BETAS
CURVE 3 IS BETAS DERIVED BY INVERSION OF SCALED MEASURED BRIGHTNESS

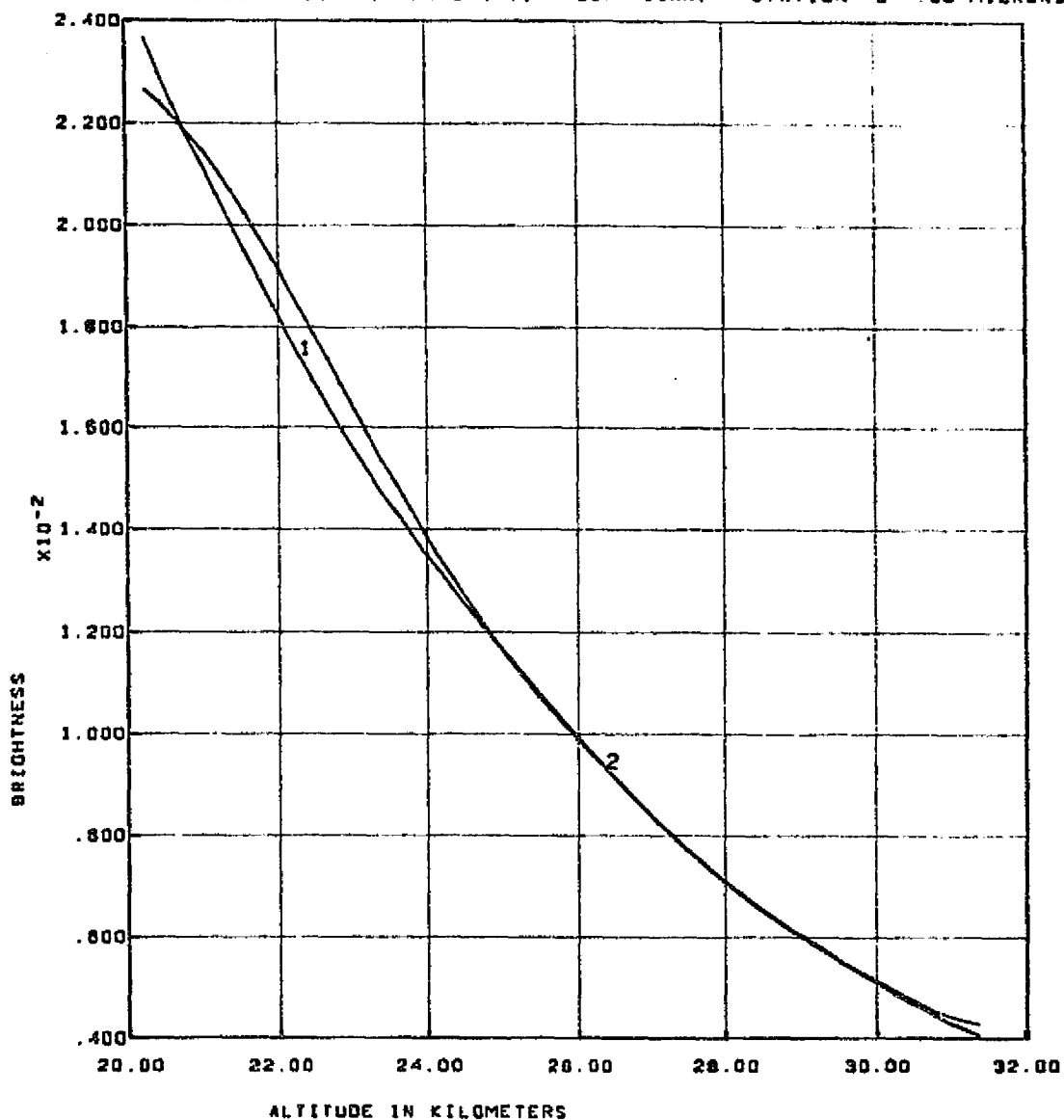
REPRODUCIBILITY OF THE
ORIGINAL PAGE IS POOR

S190A PASS 47. FRAME 175. RIGHT SCAN. STATION 6 - .55 MICRONS.



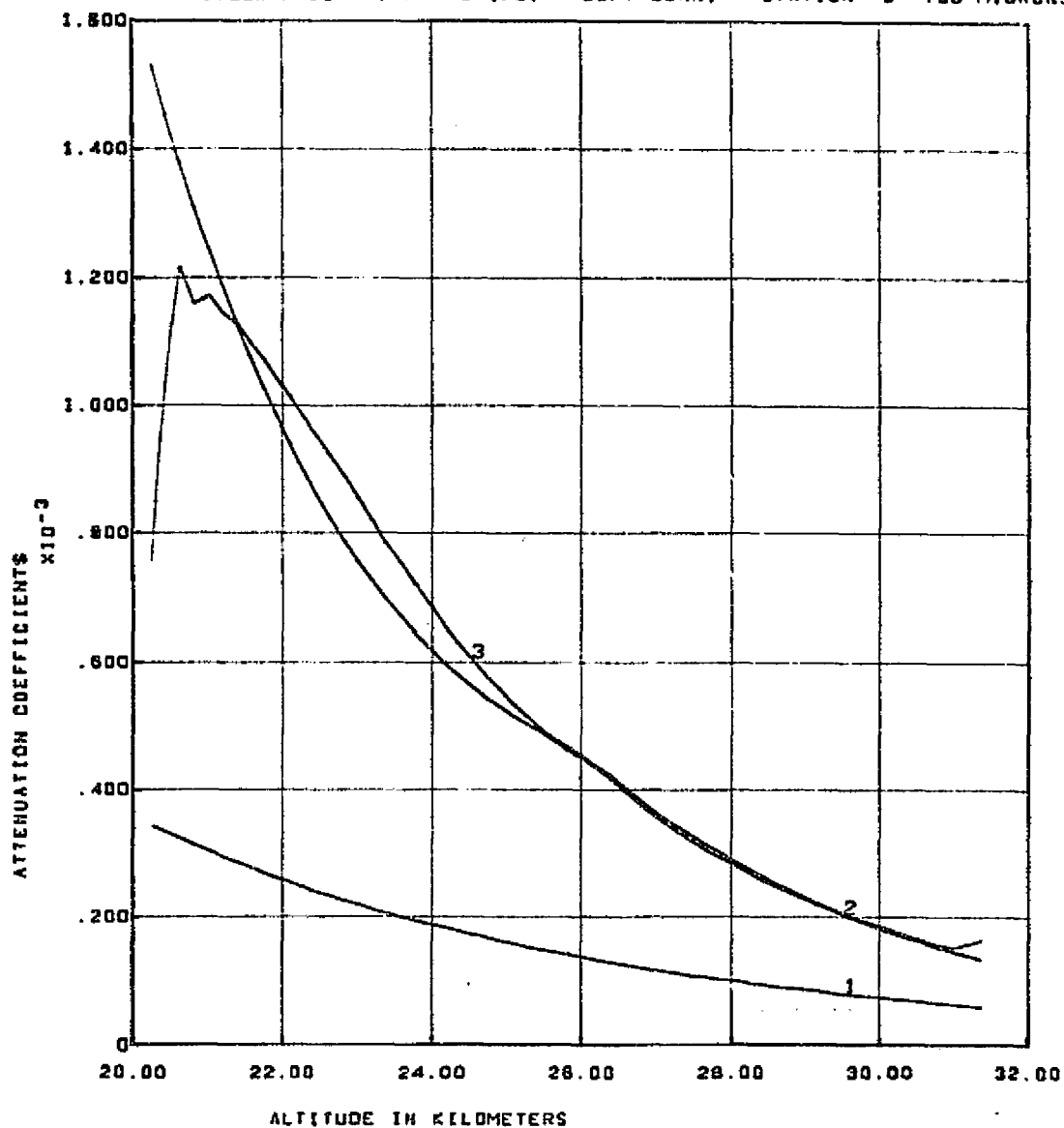
CURVE 1 IS RATIO OF 1968 AEROSOL BETAS OVER RAYLEIGH BETAS.
 CURVE 2 IS RATIO OF DERIVED AEROSOL BETAS OVER RAYLEIGH BETAS.

S190A PASS 47. FRAME 175. LEFT SCAN. STATION 5 - .68 MICRONS



CURVE 1 - BRIGHTNESS MODEL GENERATED FROM RAYLEIGH + 1968 AEROSOL BETAS.
CURVE 2 - MEASURED BRIGHTNESS SCALED BY 1968 MODEL.

S19DA PASS 47. FRAME 175. LEFT SCAN. STATION 5 -.88 MICRONS.

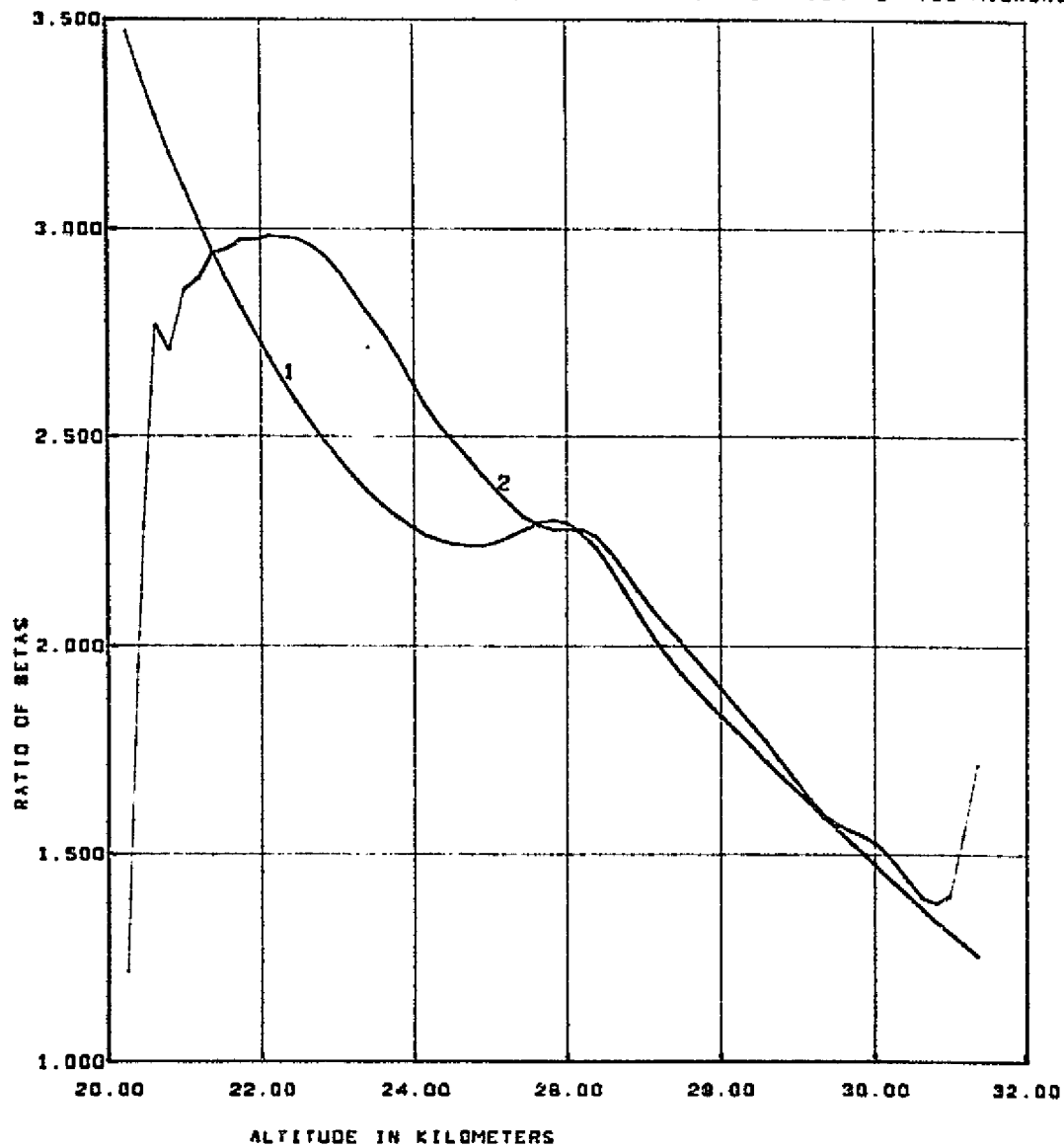


CURVE 1 - RAYLEIGH BETAS. CURVE 2 - RAYLEIGH + 1968 AEROSOL BETAS
CURVE 3 IS BETAS DERIVED BY INVERSION OF SCALED MEASURED BRIGHTNESS

REPRODUCIBILITY OF THE
ORIGINAL PAGE IS POOR

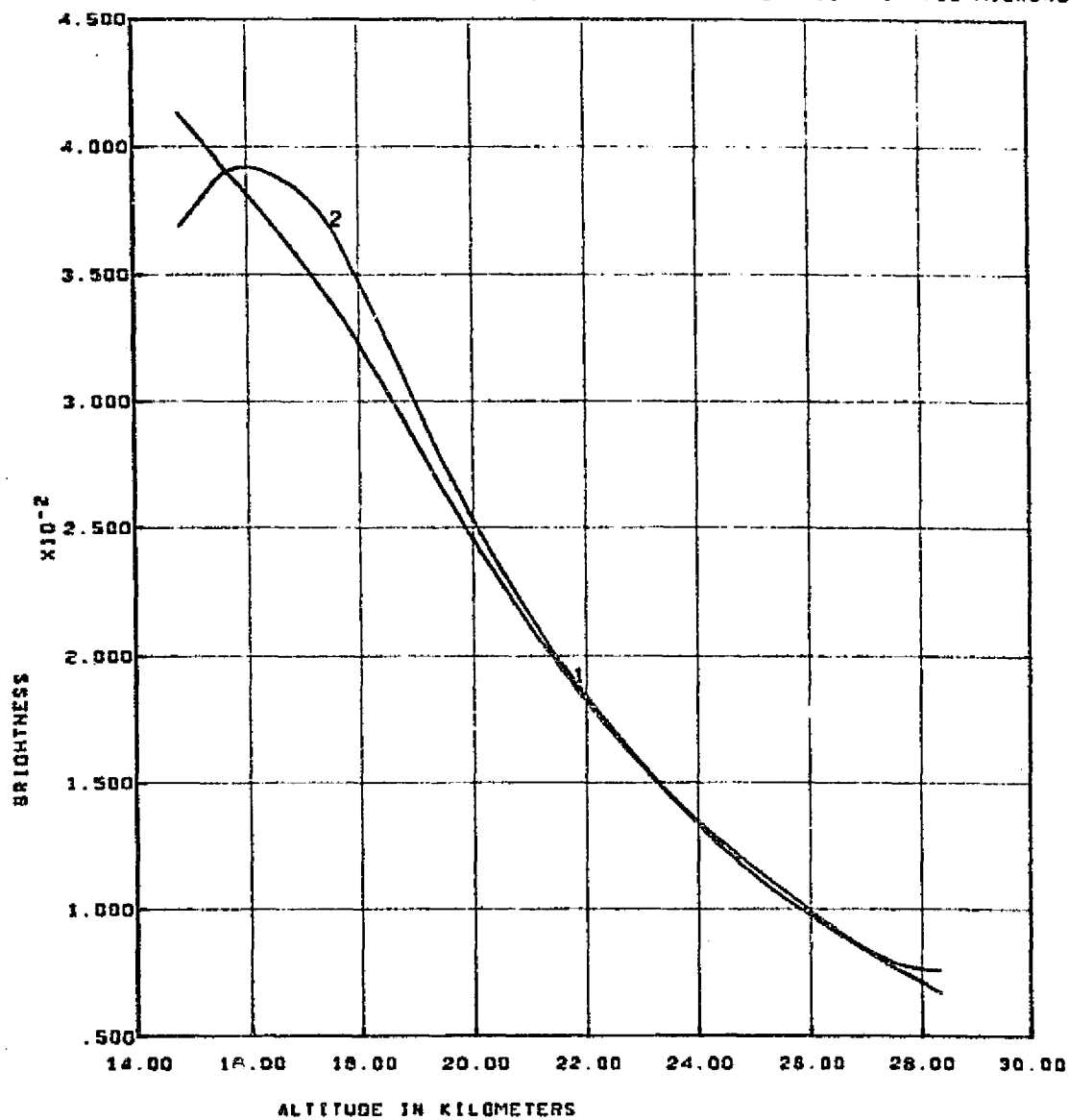
811

S190A PASS 47. FRAME 175. LEFT SCAN. STATION 5 -.68 MICRONS.

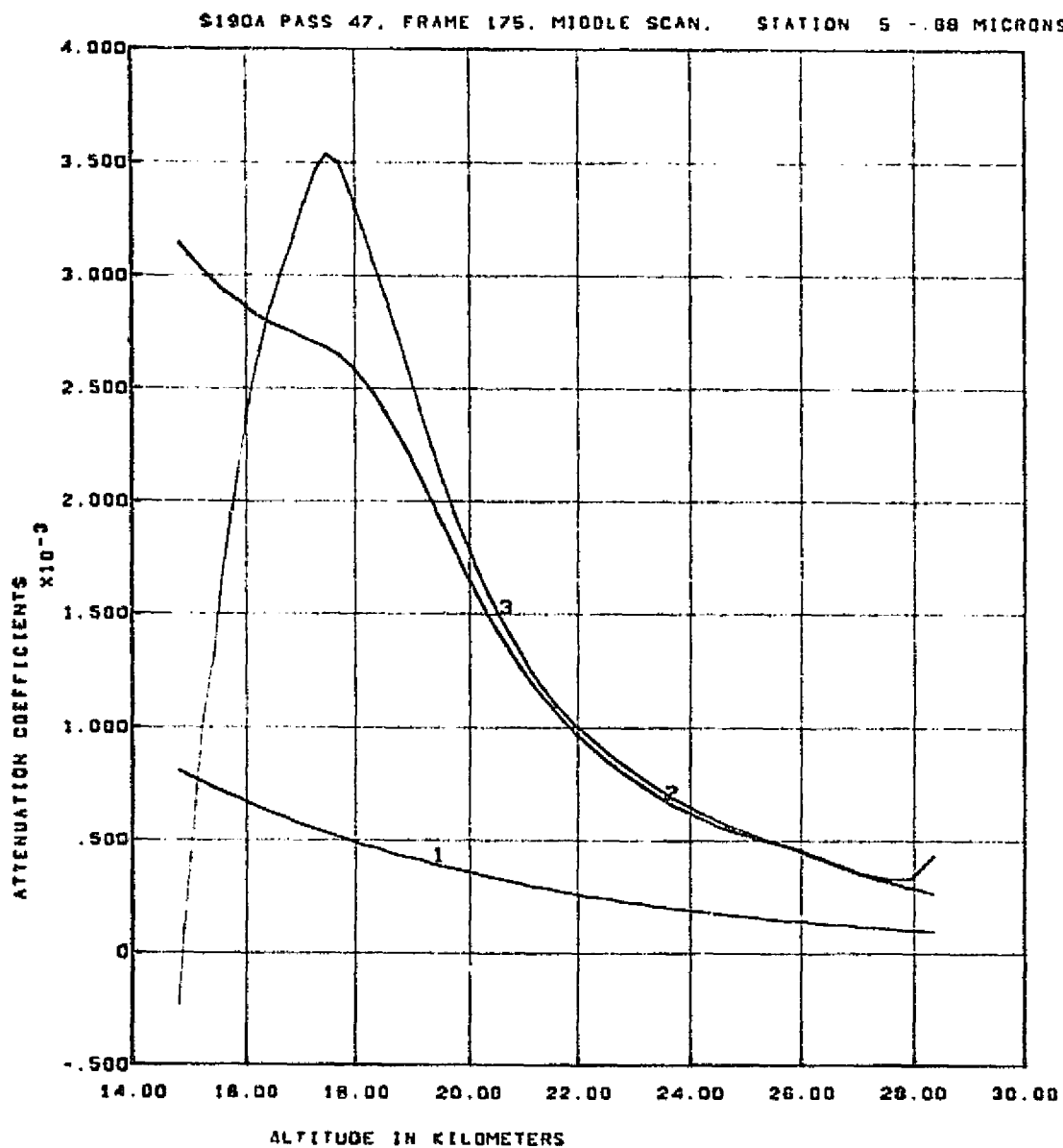


CURVE 1 IS RATIO OF 1968 AEROSOL BETAS OVER RAYLEIGH BETAS.
 CURVE 2 IS RATIO OF DERIVED AEROSOL BETAS OVER RAYLEIGH BETAS.

S190A PASS 47, FRAME 175, MIDDLE SCAN, STATION 5 - .68 MICRONS.



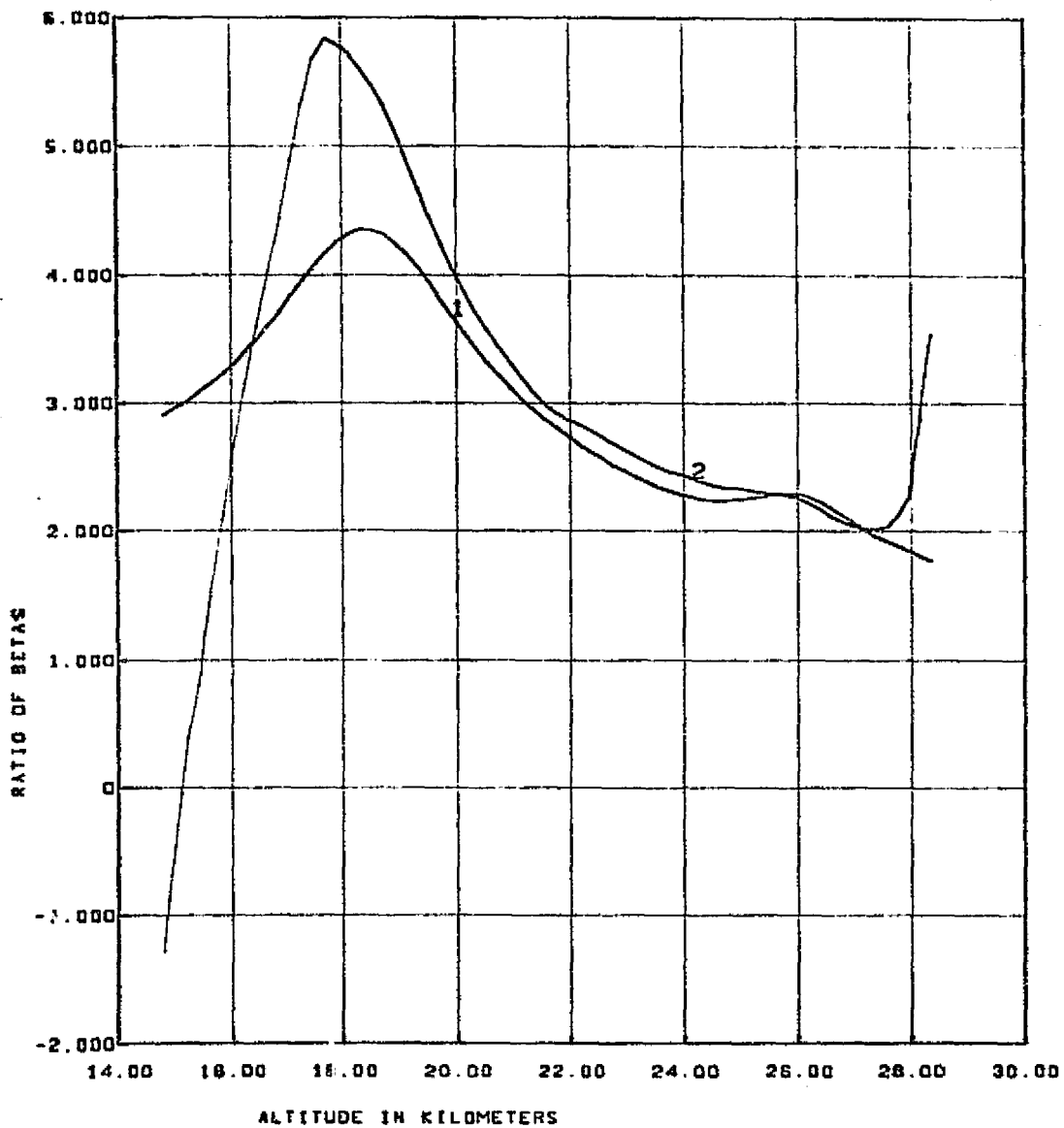
CURVE 1- BRIGHTNESS MODEL GENERATED FROM RAYLEIGH + 1968 AEROSOL BETAS.
CURVE 2 - MEASURED BRIGHTNESS SCALED BY 1968 MODEL.



CURVE 1 - RAYLEIGH BETAS. CURVE 2 - RAYLEIGH + 1960 AEROSOL BETAS
 CURVE 3 IS BETAS DERIVED BY INVERSION OF SCALED MEASURED BRIGHTNESS

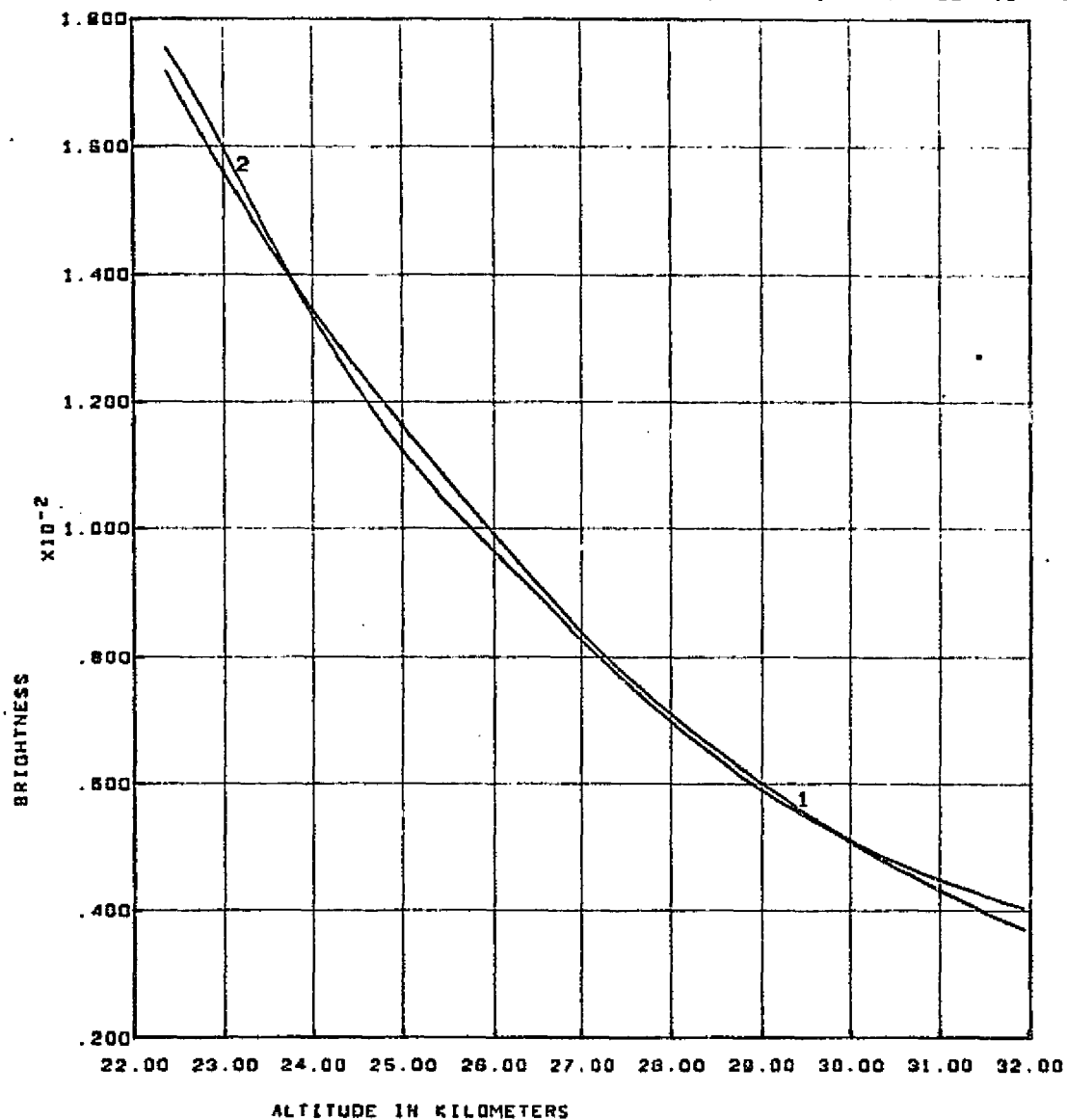
REPRODUCIBILITY OF THE
 ORIGINAL PAGE IS POOR

S19DA PASS 47. FRAME 175. MIDDLE SCAN. STATION 5 - .88 MICRONS.

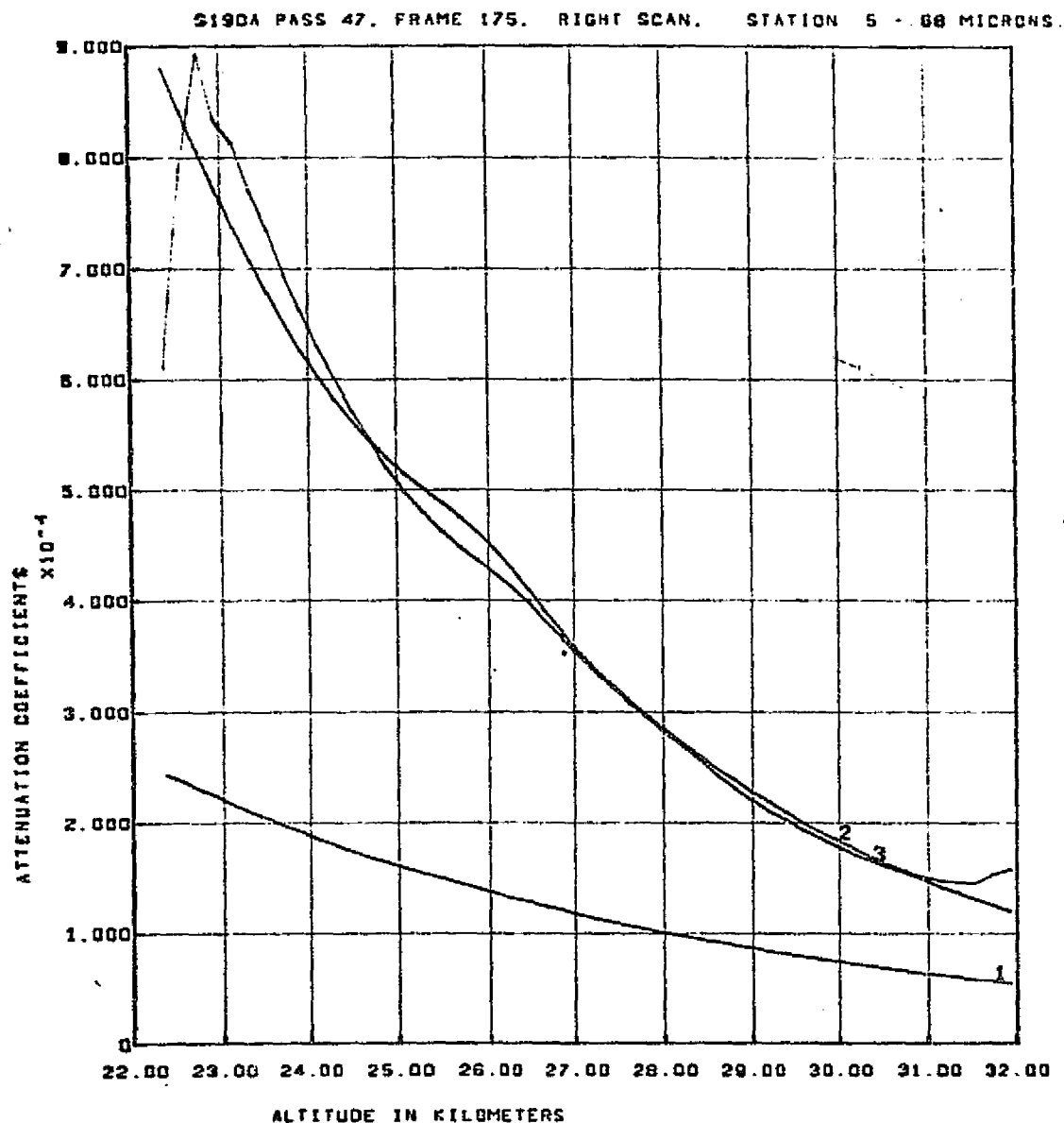


CURVE 1 IS RATIO OF 1968 AEROSOL BETAS OVER RAYLEIGH BETAS.
CURVE 2 IS RATIO OF DERIVED AEROSOL BETAS OVER RAYLEIGH BETAS.

S190A PASS 47. FRAME 175. RIGHT SCAN. STATION 5 - .68 MICRONS.



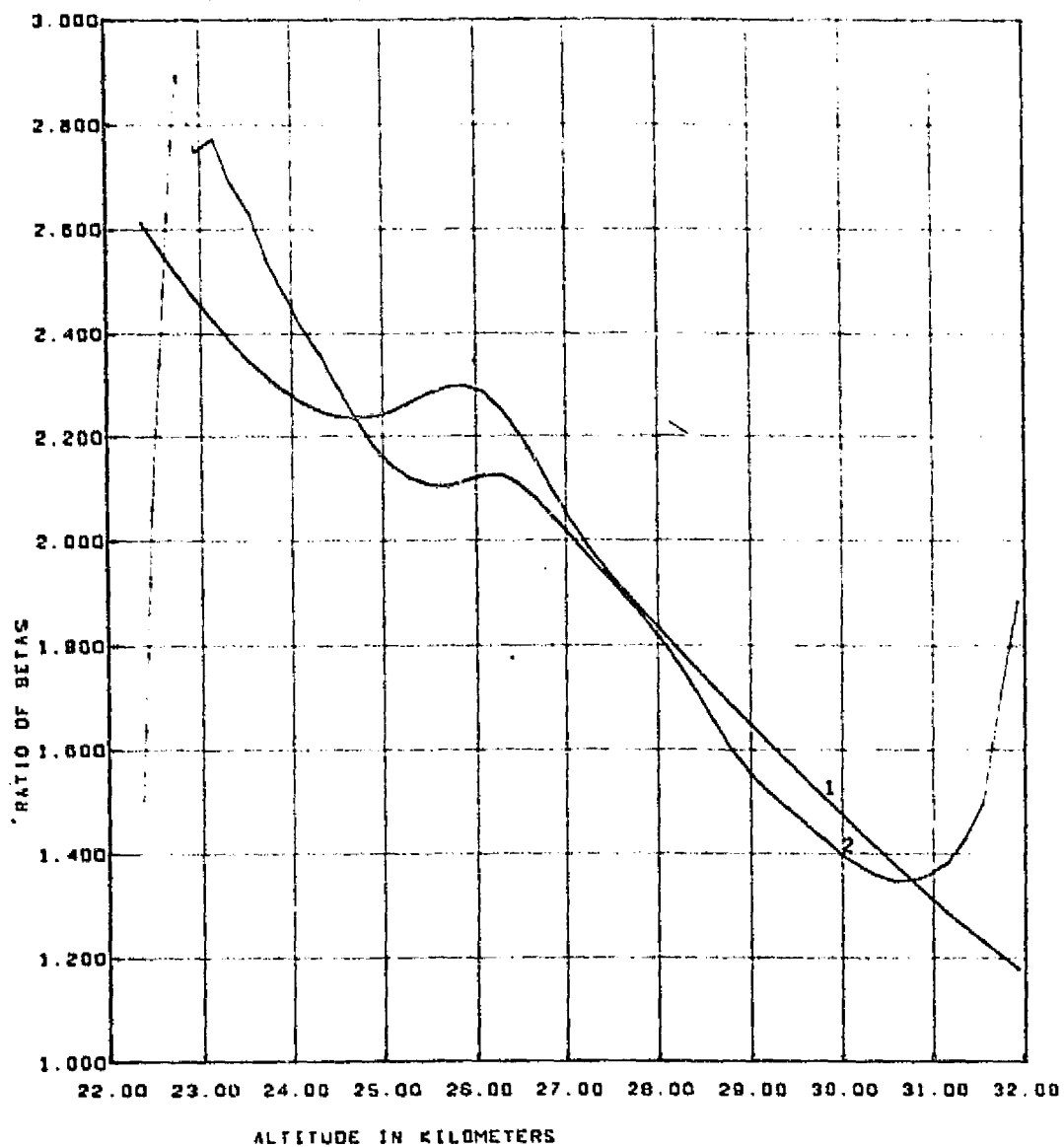
CURVE 1 - BRIGHTNESS MODEL GENERATED FROM RAYLEIGH + 1968 AEROSOL BETAS.
CURVE 2 - MEASURED BRIGHTNESS SCALED BY 1968 MODEL.



CURVE 1 - RAYLEIGH BETAS. CURVE 2 - RAYLEIGH + 1968 AEROSOL BETAS
 CURVE 3 IS BETAS DERIVED BY INVERSION OF SCALED MEASURED BRIGHTNESS

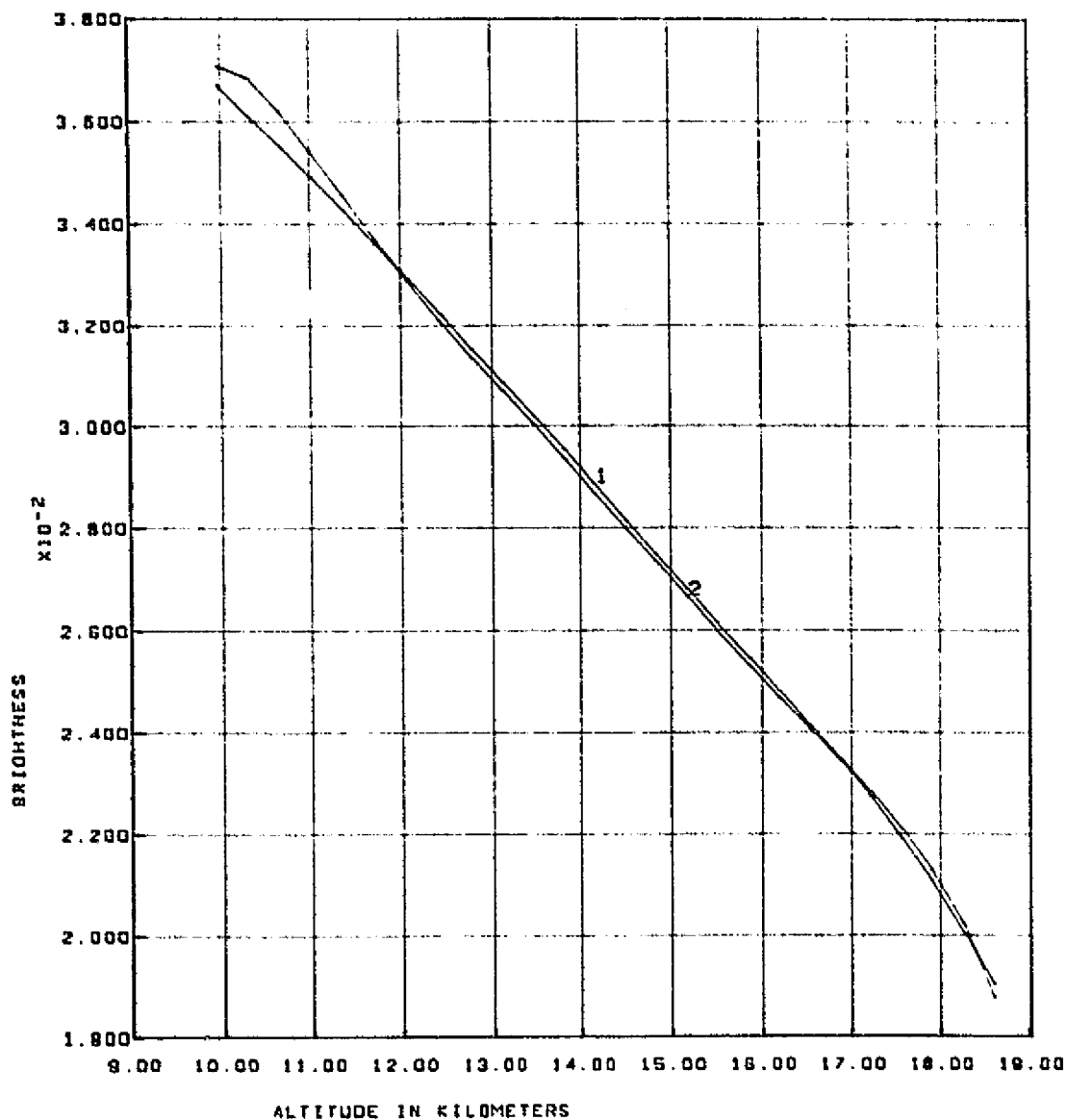
REPRODUCIBILITY OF THE
 ORIGINAL PAGE IS POOR

S190A PASS 47, FRAME 175, RIGHT SCAN, STATION 5 - 68 MICRONS

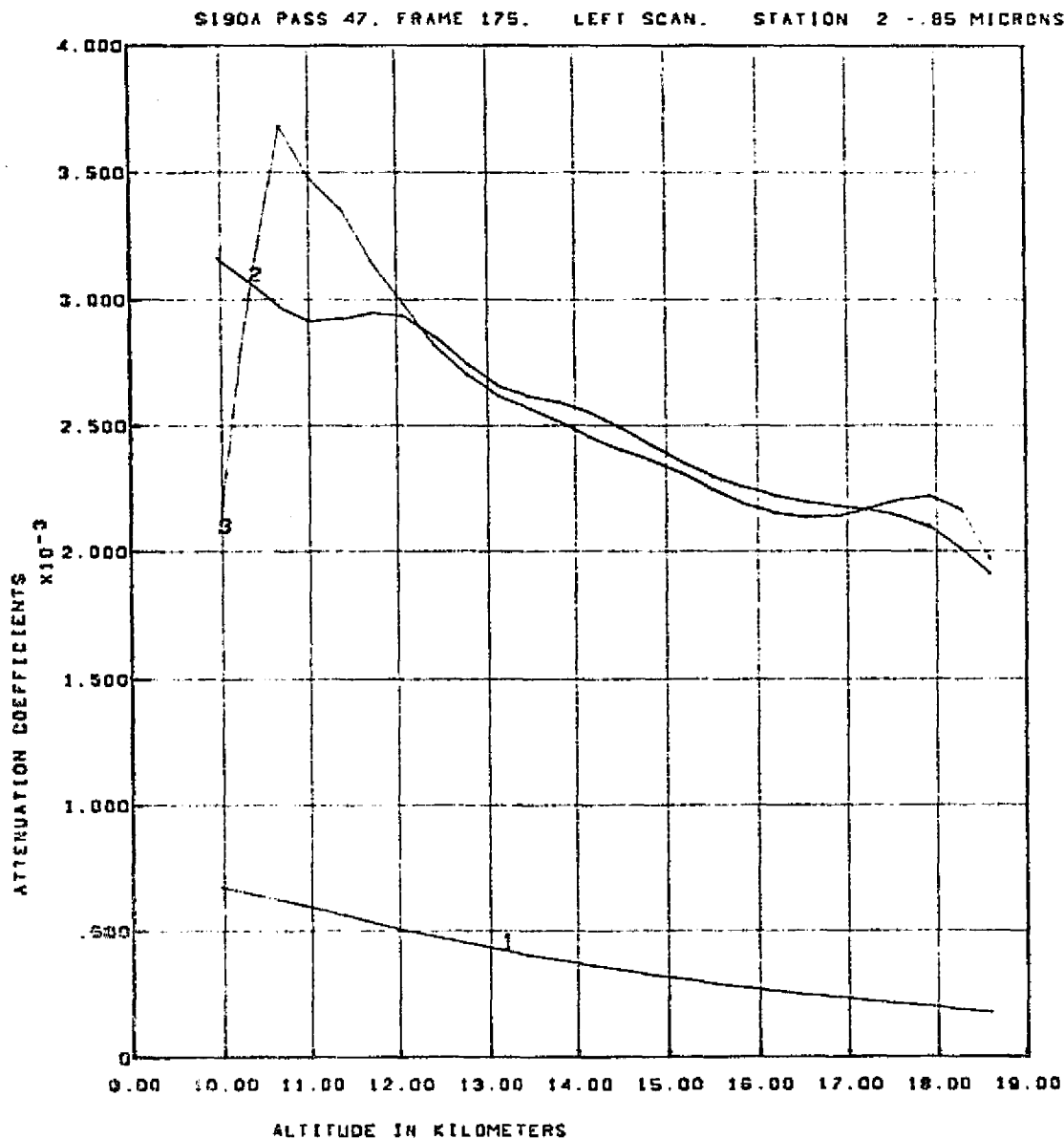


CURVE 1 IS RATIO OF 1968 AEROSOL BETAS OVER RAYLEIGH BETAS.
CURVE 2 IS RATIO OF DERIVED AEROSOL BETAS OVER RAYLEIGH BETAS.

S190A PASS 47, FRAME 175, LEFT SCAN, STATION 2 - 05 MICRONS



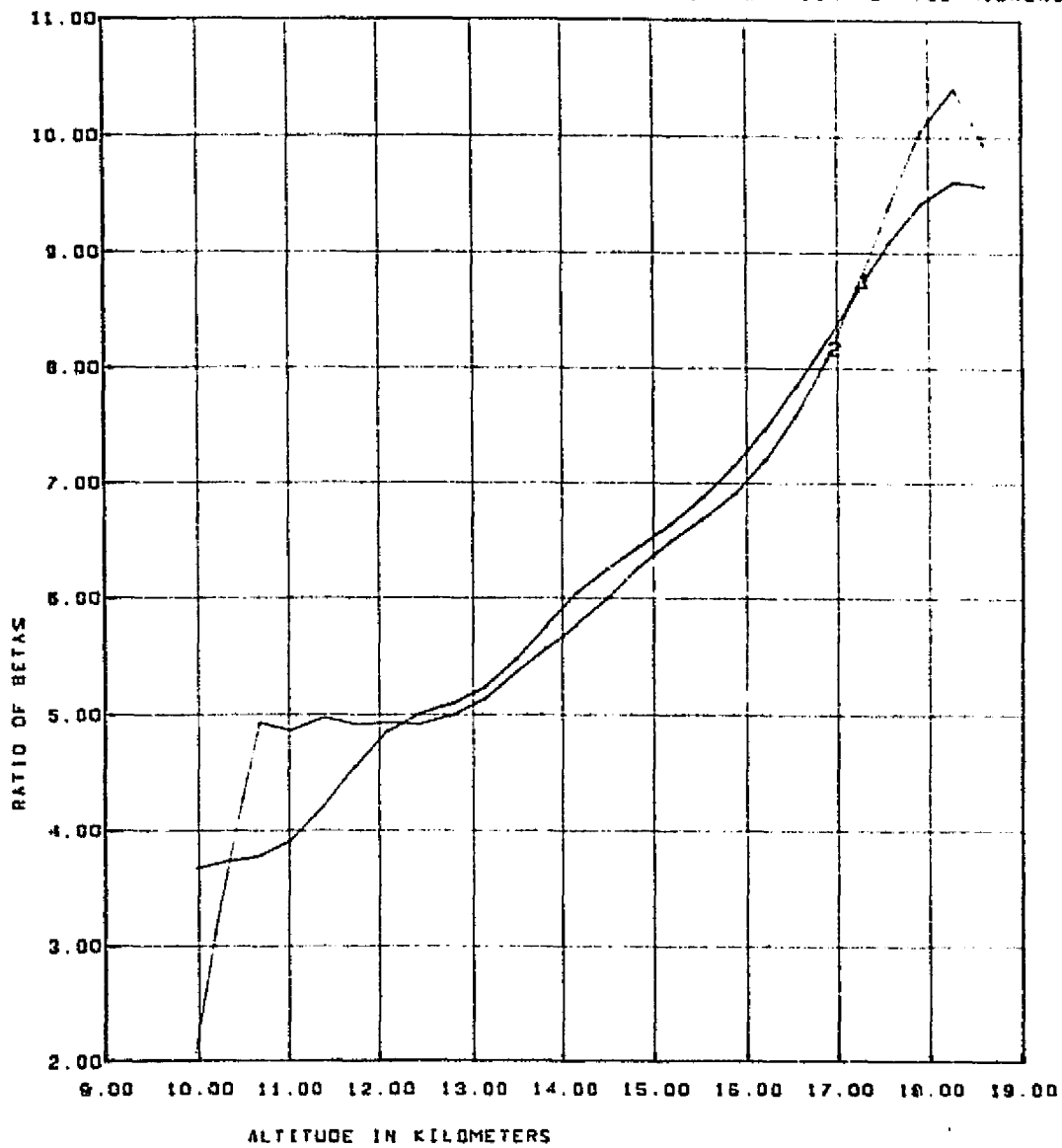
CURVE 1 - BRIGHTNESS MODEL GENERATED FROM RAYLEIGH + 1968 AEROSOL BETAS
 CURVE 2 - MEASURED BRIGHTNESS SCALED BY 1968 MODEL.



CURVE 1 - RAYLEIGH BETAS. CURVE 2 - RAYLEIGH + 1968 AEROSOL BETAS
 CURVE 3 IS BETAS DERIVED BY INVERSION OF SCALED MEASURED BRIGHTNESS

REPRODUCIBILITY OF THE
 ORIGINAL PAGE IS POOR

5190A PASS 47, FRAME 175, LEFT SCAN, STATION 2 - .85 MICRONS.



CURVE 1 IS RATIO OF 196B AEROSOL BETAS OVER RAYLEIGH BETAS.
 CURVE 2 IS RATIO OF DERIVED AEROSOL BETAS OVER RAYLEIGH BETAS.



5.0 SUMMARY AND RECOMMENDATIONS

The investigation results verify the analysis system developed to reduce limb aerosol data. The system is capable of analyzing large volumes of data quickly to yield altitude profiles of attenuation coefficients for each wavelength band. The sensors appear able to penetrate the atmosphere to about 10 Km for the longer wavelengths and to about 20 Km for the shorter wavelengths. The S192 multispectral scanner appears sensitive to an altitude of about 45 Km for the shorter wavelengths. The S191 sensitivity appears to extend to about 70 Km. The S190A duplicate film appears to be sensitive to about 29 Km. The data contained noise which had to be analyzed and removed which subtracted from the time available for aerosol analysis. In general, the sensors appeared adequate to detect stratospheric aerosols although future instruments would benefit from the experience gained through EREP. For example, more effort could be devoted to the pointing accuracy of the instruments thereby avoiding the necessity to compare with models in order to locate the field of view. Accurate radiometric calibration is also critical. Therefore efforts to attain the optimum calibration should be continued.

The problems with the data and the effort it required to solve the problems prevented the analysis of the data for aerosol size distribution and number density in the manner described in the text. This would be a candidate for future work.

In Section 4.0 much analysis results were presented. It was noted that several aerosol layers could be identified with a quantitative measurement of their attenuation coefficients. However, it was also noted that the results were dependent on the model invoked to scale and locate the data. The implication is clear that additional refinement of the models is necessary, also a candidate for future work. The point should be emphasized that the results were only as accurate as the model approximates the stratosphere. This could easily be the cause of inconsistencies. For example, the consistent increase of the values of attenuation coefficients in the lower altitudes above those predicted by the models is most likely due to the single scattering approximation when in fact multiple scattering is actually occurring in this region. Another improvement in the model would be to



include the effects of a scattering function ($P(x)$) (Section 2.1.1) that is dependent on altitude and particle size distribution. If the calibration of the data were inaccurate, a similar error would result in scaling and inverting the data.

Much of the acquired data was not analyzed due to the lack of time caused by data complications, some of which were mentioned above. With the effort devoted to the development of a fairly involved system and with the understanding already gained about the data, continued analysis would be cost effective if stratospheric aerosols remain of interest. Additional effort to improve the models would also be advisable since any improvements are directly extended to the results.

The investigation has unquestionably verified that the described approach can contribute to the analysis of the particulate content of the stratosphere. The approach appears especially suitable to a future satellite which would monitor the changes and variations in the stratosphere between 10 Km and 70 Km. The models used in much of this investigation would in that case become previous measurements. Differences would be interpreted as variations in time or space.



REFERENCES

1. Elterman, L., "Atmospheric Attenuation Model, 1964, in the Ultra-violet, Visible, and Infrared Regions Altitude to 50 Km", Air Force Cambridge Research Laboratories, Environmental Research Paper, No. 46, 1964.
2. Elterman, L., "UV, Visible, and IR Attenuation for Altitudes to 50 Km", Air Force Cambridge Research Laboratories, Environmental Research Paper, No. 285, April 1968.
3. Chandrasekhar, S., Radiative Transfer, Dover Publications, Inc., 1960.
4. Bateman, Harry, Tables of Integral Transforms, Vol. II, McGraw-Hill, 1954, pp 201-212.
5. Phillips, David L., "A Technique for the Numerical Solution of Certain Integral Equations of the First Kind", Journal of the Association of Computer Machinery, Vol. 9, 1962.
6. Twomey, S., "On the Numerical Solution of Fredholm Integral Equations of the First Kind by the Inversion of the Linear System Produced by Quadrature", Journal of the Association of Computer Machinery, Vol. 10, 1963.
7. Pitts, David E. and Kyle, Kirby D., "A Model Atmosphere for Earth Resources Applications", Johnson Space Center, NASA TMX-58033, November 1969.
8. U. S. Standard Atmosphere, 1962, U. S. Government Printing Office, December 1962.
9. Baum, W. A., Code, A. D., "A Photometric Observation of the Occultation of σ Arietis by Jupiter", The Astronomical Journal, Vol. 58, No. 1208, May 1953.
10. Tingey, David L., "An Inversion Technique Developed to Determine Characteristics of Mie Scatterers Differing in Index of Refraction Interspersed in the Stratosphere", Presented at the Conference on Atmospheric Radiation, August 7-9, 1972, American Meteorological Society.